NATO Science for Peace and Security Series - B:
Physics and Biophysics

Uniting Electron Crystallography and Powder Diffraction

Edited by
Ute Kolb
Kenneth Shankland
Louisa Meshi
Anatoly Avilov
William David

Springer

This publication is supported by:

The NATO Science for Peace and Security Programme

Uniting Electron Crystallography and Powder Diffraction

NATO Science for Peace and Security Series

This Series presents the results of scientific meetings supported under the NATO Programme: Science for Peace and Security (SPS).

The NATO SPS Programme supports meetings in the following Key Priority areas: (1) Defence Against Terrorism; (2) Countering other Threats to Security and (3) NATO, Partner and Mediterranean Dialogue Country Priorities. The types of meeting supported are generally “Advanced Study Institutes” and “Advanced Research Workshops”. The NATO SPS Series collects together the results of these meetings. The meetings are co-organized by scientists from NATO countries and scientists from NATO’s “Partner” or “Mediterranean Dialogue” countries. The observations and recommendations made at the meetings, as well as the contents of the volumes in the Series, reflect those of participants and contributors only; they should not necessarily be regarded as reflecting NATO views or policy.

Advanced Study Institutes (ASI) are high-level tutorial courses to convey the latest developments in a subject to an advanced-level audience

Advanced Research Workshops (ARW) are expert meetings where an intense but informal exchange of views at the frontiers of a subject aims at identifying directions for future action

Following a transformation of the programme in 2006 the Series has been re-named and re-organised. Recent volumes on topics not related to security, which result from meetings supported under the programme earlier, may be found in the NATO Science Series.

The Series is published by IOS Press, Amsterdam, and Springer, Dordrecht, in conjunction with the NATO Emerging Security Challenges Division.

Sub-Series

A.	Chemistry and Biology	Springer
B.	Physics and Biophysics	Springer
C.	Environmental Security	Springer
D.	Information and Communication Security	IOS Press
E.	Human and Societal Dynamics	IOS Press

http://www.nato.int/science
http://www.springer.com
http://www.iospress.nl

Series B: Physics and Biophysics

Uniting Electron Crystallography and Powder Diffraction

edited by

Ute Kolb
Johannes Gutenberg University, Mainz, Germany

Kenneth Shankland
University of Reading, UK

Louisa Meshi
Ben-Gurion University of the Negev, Beer-Sheva, Israel

Anatoly Avilov
Institute of Crystallography of the Russian Academy of Sciences, Moscow, Russia

and

William David
STFC Rutherford Appleton Laboratory, Chilton, UK
and
University of Oxford, UK

Published in cooperation with NATO Emerging Security Challenges Division

Proceedings of the NATO Advanced Study Institute on
Uniting Electron Crystallography and Powder Diffraction: an Essential Contribution to the Fight against Terrorism
Erice, Italy
2–12 June 2011

Library of Congress Control Number: 2012954788

ISBN 978-94-007-5585-7 (PB)
ISBN 978-94-007-5579-6 (HB)
ISBN 978-94-007-5580-2 (e-book)
DOI 10.1007/978-94-007-5580-2

Published by Springer,
P.O. Box 17, 3300 AA Dordrecht, The Netherlands.

www.springer.com

Printed on acid-free paper

Preface

The science of crystallography has seen many remarkable developments in the last century. As a basis for experimental techniques, crystallography has evolved from a niche interest to a point where its use in the study of materials is ubiquitous. From the high-pressure phases found in planetary cores to the biomolecules that that define us as individuals, it is crystallography that allows us to determine the three-dimensional structures that are critical to understanding function. As a discipline, crystallography continually evolves to incorporate the latest thinking on material structure and embraces instrumental and computational advances. In particular, powder diffraction and electron crystallography have both undergone rapid development in the last decade, enabling the structure solution and characterization of significantly more complex crystal structures, even when crystallinity exists only over very short length scales.

Powder diffraction and electron crystallography are highly complementary; powder diffraction offers a structural description of bulk samples, while electron crystallography provides information about individual crystals. Given this complementary nature and the rapid advances made in both fields in recent years, it was entirely appropriate that they were covered jointly in the Erice Crystallographic Course of June 2011. The lectures, delivered by experts in their fields, provided a common platform for introducing the basics of their subjects whilst exposing students to the most advanced and cutting-edge topics. This volume contains selected articles derived from these lectures.

The theory and practice of powder diffraction was covered in a sequence of themed days. Fundamentals of the method, laboratory and facility-based instrumentation, methods for structure determination, nanocrystalline materials and quantitative phase analysis were just some of the topics covered. Lecture material was, wherever possible, backed-up by associated demonstrations and workshops, to reinforce learning and comprehension. The electron crystallography element offered an introduction to the fundamentals of electron crystallography, namely; imaging and diffraction, kinematic and dynamical scattering theory. This was followed by the recent advances in 3D electron data collection and processing. As such, it considered structural characterization applied to materials such as small

molecule crystal structures, incommensurate structures and biological crystals. Since the IUCr redefined electron crystallography as 'electrons scattering from crystals', the scope of the term has broadened significantly to incorporate many methods that not only describe crystal structures but also crystal properties, such as magnetism and circular dichroism. Consideration of these topics was incorporated into the latter part of the course. Joint sessions were held for lectures that covered concepts with clear commonality; for example, the application of direct methods of structure determination and the use of combined powder diffraction and electron crystallography in the structure determination of complex materials.

We hope that this volume will provide the reader with a sense of both the breadth and the depth of the courses and serve as a very useful guide to topics and future directions in the study of crystalline and nanocrystalline materials.

Organizing and executing these courses, with approximately 200 participants in total, requires input from a great many people, not least those speakers who willingly gave their time and energy in the hope of exciting and enlightening others. We are grateful to them all. We are extremely grateful to NATO who, as part of their 'Science for Peace and Security' programme, provided substantial funding (ASI 984207) to underpin these courses. Materials development is an extremely important aspect of fostering peace and security, by helping to ease pressure in critical areas such as health care, defence, energy supply and access to information. A cursory glance through this volume will be sufficient to convince the reader that powder diffraction and electron crystallography are mainstays in shaping our understanding of what materials 'are' and how they 'work'. The International Union of Crystallography (IUCr), the European Crystallographic Association (ECA) and the Organisation for the Prohibition of Chemical Weapons (OPCW) also provided substantial funding. We are also grateful to all many companies (ZEISS, FEI, JEOL, App5, Nanomegas, Calidris, AnaliteX, Bruker AXS, Panalytical and ICDD) whose contributions enabled many students to attend the course.

We would also like to express our sincere gratitude to the local organizing committee of 'orange scarves' who, led by Paola Spadon, contributed greatly to the success of the course. We also thank John Irwin and his team for ensuring that the computational facilities ran smoothly. Finally, we would like to acknowledge the pivotal contribution of Lodovico Riva di Sanseverino (1939–2010) to the planning of these Erice-based courses.

Mainz — Ute Kolb
Reading — Kenneth Shankland
Beer-Sheva — Louisa Meshi
Moscow — Anatoly Avilov
Oxford — William I.F. David

Contents

Part I Powder Diffraction

1 Powder Diffraction: By Decades 3
William I.F. David

2 Rietveld Refinement 15
Peter W. Stephens

3 Structure Solution – An Overview 27
Lynne B. McCusker and Christian Baerlocher

4 Inorganic Materials 35
Radovan Černý

5 Organic Compounds 45
Kenneth Shankland

6 Laboratory X-ray Powder Diffraction 53
Pamela Whitfield

7 Synchrotron X-Ray Powder Diffraction 65
Fabia Gozzo

8 Ultrafast Powder Diffraction 83
Andy Fitch and Caroline Curfs

9 Taking It to Extremes – Powder Diffraction Under Non-Ambient Conditions 95
David I.A. Millar and Colin R. Pulham

10 Structure Solution by Charge Flipping 105
Lukáš Palatinus

11 Structure Solution: Global Optimisation Methods 117
Kenneth Shankland

12 Proteins and Powders: Technical Developments 125
Jonathan P. Wright

13 Proteins and Powders: An Overview 137
Irene Margiolaki

14 Parametric Powder Diffraction 149
William I.F. David and John S.O. Evans

15 Powder Diffraction + Computational Methods 165
L'ubomír Smrčok

16 Information on Imperfections 173
Matteo Leoni

17 Pair Distribution Function Technique: Principles and Methods 183
Simon J.L. Billinge

18 Debye Analysis 195
Yuri G. Andreev

19 Quantitative Phase Analysis 207
Ian C. Madsen, Nicola V.Y. Scarlett, and Nathan A.S. Webster

20 Quantifying Amorphous Phases 219
Arnt Kern, Ian C. Madsen, and Nicola V.Y. Scarlett

21 Quantitative Phase Analysis: Method Developments 233
Luca Lutterotti

22 Texture – An Overview 243
Robert B. Von Dreele

23 The Future of Powder Diffraction Is 2-D 251
R.E. Dinnebier and B. Hinrichsen

Part II Electron Crystallography

24 Electron Crystallography – New Methods to Explore Structure and Properties of the Nano World 261
Ute Kolb

25 Image Formation in the Electron Microscope 271
Louisa Meshi

26 Models for Precession Electron Diffraction 281
Laurence D. Marks

27 Structure Solution Using HRTEM 293
Sven Hovmöller

28 Combination of X-ray Powder Diffraction, Electron Diffraction and HRTEM Data 303
Christian Baerlocher and Lynne B. McCusker

29 Automated Electron Diffraction Tomography 315
Ute Kolb

30 Automated Quantitative 3D Electron Diffraction Rotation Tomography 327
Peter Oleynikov

31 Introduction to ADT/ADT3D 337
Tatiana E. Gorelik, Sebastian Schlitt, and Ute Kolb

32 Electrostatic Potential Determined from Electron Diffraction Data 349
Anatoly Avilov

33 Domino Phase Retrieval Algorithm for Structure Solution 359
F.N. Chukhovskii

34 LARBED: Exploring the Fourth Dimension in Electron Diffraction . 369
Christoph T. Koch

35 Shadow Imaging for Charge Distribution Analysis 381
Yimei Zhu and Lijun Wu

36 Electron Diffraction of Protein 3D Nanocrystals 389
Jan Pieter Abrahams, Dilyana Georgieva, Linhua Jiang, and Igor Nederlof

37 Parallel-Beam Diffraction and Direct Imaging in an Aberration-Corrected STEM 399
Ondrej L. Krivanek

38 Electron Diffraction of Commensurately and Incommensurately Modulated Materials 409
Joke Hadermann and Artem M. Abakumov

39 Detection of Magnetic Circular Dichroism Using TEM and EELS ... 419
Stefano Rubino, Jan Rusz, and Peter Schattschneider

Index 429

Contributors

Artem M. Abakumov EMAT, University of Antwerp, Antwerp, Belgium

Jan Pieter Abrahams LIC, Gorlaeus Laboratories, Leiden University, Leiden, The Netherlands

Yuri G. Andreev School of Chemistry, University of St Andrews, Scotland, UK

Anatoly Avilov Institute of Crystallography of Russian Academy of Sciences, ICRAS, Moscow, Russia

Christian Baerlocher Laboratory of Crystallography, ETH Zurich, Zurich, Switzerland

Simon J.L. Billinge Department of Applied Physics and Applied Mathematics, Columbia University, New York, USA

Condensed Matter Physics and Materials Science Department, Brookhaven National Laboratory, Upton NY 11973

F.N. Chukhovskii Institute of Crystallography, The Russian Academy of Sciences, Moscow, Russia

Radovan Černý Laboratory of Crystallography, University of Geneva, Geneva, Switzerland

Caroline Curfs ESRF, Grenoble Cedex, France

William I.F. David ISIS Facility, Science and Technology Facilities Council, Rutherford Appleton Laboratory, Didcot, UK

Inorganic Chemistry Laboratory, University of Oxford, Oxford, UK

R.E. Dinnebier Max-Planck-Institute for Solid State Research, Stuttgart, Germany

John S.O. Evans Department of Chemistry, University of Durham, Durham, UK

Andy Fitch ESRF, Grenoble Cedex, France

Dilyana Georgieva LIC, Gorlaeus Laboratories, Leiden University, Leiden, The Netherlands

Tatiana E. Gorelik Institute of Physical Chemistry, Johannes-Gutenberg University Mainz, Mainz, Germany

Fabia Gozzo Paul Scherrer Institute – Swiss Light Source, 5232 Villigen PSI, Switzerland

Excelsus Structural Solutions S.P.R.L., Brussels, Belgium

Joke Hadermann EMAT, University of Antwerp, Antwerp, Belgium

B. Hinrichsen Max-Planck-Institute for Solid State Research, Stuttgart, Germany

Sven Hovmöller Structural Chemistry, MMK, Stockholm University, Stockholm, Sweden

Linhua Jiang LIC, Gorlaeus Laboratories, Leiden University, Leiden, The Netherlands

Arnt Kern Bruker AXS GmbH, Karlsruhe, Germany

Christoph T. Koch Institute for Experimental Physics, Ulm University, Ulm, Germany

Ute Kolb Institute of Physical Chemistry, Johannes-Gutenberg University Mainz, Mainz, Germany

Ondrej L. Krivanek Nion Co, Kirkland, WA, USA

Matteo Leoni Department of Materials Engineering and Industrial Technologies, University of Trento, Trento, TN, Italy

Luca Lutterotti Dipartimento di Ingegneria dei Materiali e Tecnologie Industriali, Università degli Studi di Trento, Trento, Italy

Ian C. Madsen CSIRO Process Science and Engineering, Clayton South, Melbourne, VIC, Australia

Irene Margiolaki Department of Biology, Section of Genetics, Cell Biology and Development, University of Patras, Patras, Greece

Laurence D. Marks Department of Materials Science and Engineering, Northwestern University, Evanston, IL, USA

Lynne B. McCusker Laboratory of Crystallography, ETH Zurich, Zurich, Switzerland

Louisa Meshi Department of Materials Engineering, Ben-Gurion University of the Negev, Beer-Sheva, Israel

David I.A. Millar School of Chemistry and Centre for Science at Extreme Conditions, The University of Edinburgh, Edinburgh, UK

Igor Nederlof LIC, Gorlaeus Laboratories, Leiden University, Leiden, The Netherlands

Peter Oleynikov Berzelii Centre EXSELENT on Porous Materials, Stockholm University, Stockholm, Sweden

Department of Materials and Environmental Chemistry, Stockholm University, Stockholm, Sweden

Lukáš Palatinus Institute of Physics of the AS CR, Prague 8, Czech Republic

Colin R. Pulham School of Chemistry and Centre for Science at Extreme Conditions, The University of Edinburgh, Edinburgh, UK

Stefano Rubino Department of Engineering Sciences, Uppsala University, Uppsala, Sweden

Jan Rusz Department of Physics and Astronomy, Uppsala University, Uppsala, Sweden

Nicola V.Y. Scarlett CSIRO Process Science and Engineering, Clayton South, Melbourne, VIC, Australia

Peter Schattschneider Institute for Solid State Physics, Vienna University of Technology, Vienna, Austria

Sebastian Schlitt Institute of Mathematics, Johannes Gutenberg University Mainz, Mainz, Germany

Kenneth Shankland School of Pharmacy, University of Reading, Reading, UK

L'ubomír Smrčok Institute of Inorganic Chemistry, Slovak Academy of Sciences, Bratislava, Slovak Republic

Peter W. Stephens Department of Physics and Astronomy, State University of New York (SUNY), Stony Brook, NY, USA

Robert B. Von Dreele Advanced Photon Source, Argonne National Laboratory, Argonne, IL, USA

Nathan A.S. Webster CSIRO Process Science and Engineering, Clayton South, Melbourne, VIC, Australia

Pamela Whitfield National Research Council Canada, Ottawa, ON, Canada

Jonathan P. Wright European Synchrotron Radiation Facility, Grenoble, France

Yimei Zhu Brookhaven National Laboratory, Long Island, NY, USA

Part I
Powder Diffraction

Chapter 1
Powder Diffraction: By Decades

William I.F. David

Abstract This introductory chapter reviews the first 100 years of powder diffraction, decade by decade, from the earliest X-ray powder diffraction measurements of the crystal structure of graphite through to the diversity and complexity of twenty-first century powder diffraction. Carbon features as an illustrative example throughout the discussion of these ten decades from graphite and the disorder of carbon black through to lonsdaleite, the elusive hexagonal polymorph of diamond, and C_{60}, the most symmetrical of molecules. Electronics and computing have played a leading role in the development of powder diffraction, particularly over the past 60 years, and the Moore's Law decade-by-decade rise in computing power is clear in the increasing complexity of powder diffraction experiments and material systems that can be studied. The chapter concludes with a final discussion of decades – the four decades of length-scale from the ångstrom to the micron that not only represent the domain of powder diffraction but are also the distances that will dominate twenty-first century science and technology.

1.1 Powder Diffraction – The First 100 Years

1.1.1 A Brief Preamble

The origins of X-ray diffraction can be traced back to the discovery of X-rays by Wilhelm Conrad Roentgen in the University of Wurzburg in the summer of 1895 [1]. The dramatic early images of the bones of living hands (initially, those of his wife!)

W.I.F. David (✉)
ISIS Facility, Science and Technology Facilities Council, Rutherford Appleton Laboratory, Harwell Science and Innovation Campus, Didcot OX11 0QX, UK

Inorganic Chemistry Laboratory, University of Oxford, South Parks Road, Oxford OX1 3QR, UK
e-mail: bill.david@stfc.ac.uk

U. Kolb et al. (eds.), *Uniting Electron Crystallography and Powder Diffraction*,
NATO Science for Peace and Security Series B: Physics and Biophysics,
DOI 10.1007/978-94-007-5580-2_1,

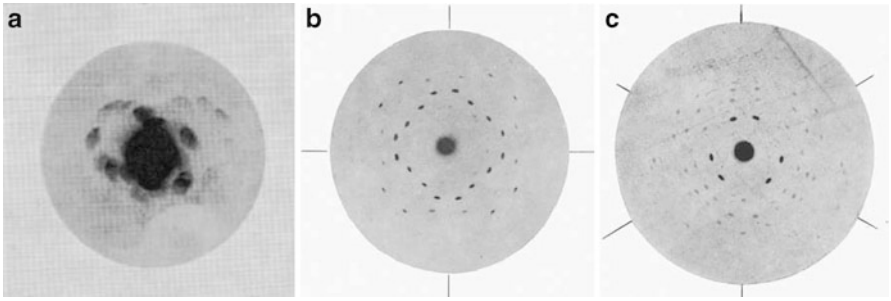

Fig. 1.1 (**a**) Friedrich and Knipping's first successful X-ray diffraction photograph – the crystal was copper sulphate; (**b**) and (**c**) zinc-blende Laue photographs along the four-fold (**b**) and three-fold (**c**) axes from Laue, Friedrich and Knipping, *Sitz. Ger. Bayer. Akademie d. Wiss*, 8 June 1912

created an immediate sensation and, even before the turn of the century, medical applications were quickly developed. Perhaps less well-known was Roentgen's repeated attempts to observe the phenomenon of X-ray diffraction – and he was most likely successful, as his Third Communication on X-rays in March 1897 suggests, in observing diffraction on a few fleeting occasions. Roentgen moved from Wurzburg to Munich in 1900 and in 1901 was accordingly awarded the first Nobel Prize in Physics. The University of Munich was one of the leading universities in the world in the "new physics" and rapidly became the centre of the development of X-rays physics with a roll call of names such as Sommerfeld, Groth, Debye, Ewald and Laue that would define much of the early years of the subject. Laue arrived in Munich in 1909 with interests that ranged across the whole of physics from special relativity and optics to thermodynamics and the theory of radiation. Prompted by Ewald, Laue's intuition led him to an analysis of the first diffraction data collected by his assistants, Friedrich and Knipping. The first diffraction pattern (Fig. 1.1a) was essentially uninterpretable but within weeks the improvement in data quality was not only remarkable but, crucially, also led to an interpretable solution [2] (Fig. 1.1b, c) and the 1914 Nobel Prize in Physics – but only to Laue! The first crystal structure is, however, attributed to the father and son team, W.H. and W.L. Bragg.

On October 18, 1912, only a few months after the first diffraction patterns had been successfully collected, the elder Bragg published his first paper [3] offering an interpretation of the zinc-blended diffraction data published by Laue, Friedrich and Knipping. It was, however, the younger Bragg who, while still a student at Cambridge, came up with a correct analysis of the origins of the diffraction data [4]. Shortly afterwards, the Braggs collected single crystal data and solved the crystal structures of NaCl, KCl, KBr and KI [5] – four crystal structures in the first paper and the Nobel Prize in Physics within 2 years in 1915! Powder diffraction, with its lower intensities, had to wait only a little longer. Some of the first clues are to be found in the 1914 Nobel Prize lecture [6] delivered by Max von Laue who said "Since 1912 much has been done in both fields, and in both sectors W.L. Bragg and W.H. Bragg have taken the first important step beyond the investigations carried out

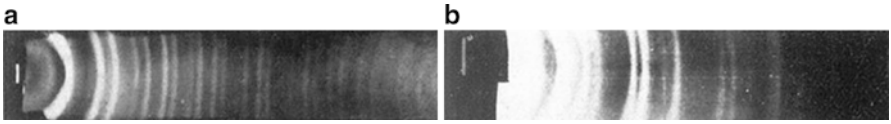

Fig. 1.2 Powder diffraction photographs of (**a**) diamond and (**b**) graphite (Hull 10)

at Munich. It would range far too wide if I were, at this juncture, to compile a fairly comprehensive list of all the researchers who have gained distinction in that research work. I can mention here only the transformation of the process, which proved to be of great importance for the further conduct of the experiments and in which Debye transferred the examination of beautiful, well-formed crystal fragments – which sometimes are obtainable only with considerable difficulty – to research into the finest possible crystal powder."

1.1.2 The First Powder Diffraction Measurements

X-ray powder diffraction has two separate beginnings in Germany, again in Munich, and almost simultaneously in the United States. In Munich, Peter Debye determined that not only powders but also liquids should exhibit distinctive diffraction patterns [7]. Along with Paul Scherrer, Debye performed the first powder diffraction measurements [8] discovering, inter alia, the crystal structure of graphite. The first measurements in the United States happened in very different circumstances – not in a university but in the General Electric Research Laboratory (GERL) in Schenectady, New York by Albert Hull [9]. A chance comment about the unsolved structure of iron by W.H. Bragg, who visited GERL in 1914, drew Hull into the field of X-ray structural analysis and rapidly, although World War 1 interrupted his efforts, he developed many of the essentials of the powder diffraction technique using photographic techniques (see Fig. 1.2) and discussed multi-phase analysis, preferred orientation, the need for sample rotation, wavelength filters, absorption, the importance of sample preparation and the concept of a "lattice constant". The three principal papers [10–12] that Hull published are significant tours-de-force – his first paper alone described the correct crystal structures of iron, silicon, aluminium, magnesium, sodium, lithium, nickel, diamond and graphite. While Debye and Scherrer reported the 3R structure of graphite (space group *R-3m* with hexagonal lattice constants, a = 2.516 Å and c = 10.206 Å), Hull reported the more familiar 2H structure which adopts space group $P6_3/mmc$ with a = 2.47 Å and c = 6.80 Å.

Hull, like Debye, did not stay long in powder diffraction research (indeed, his short time in powder diffraction was essentially a diversion from his research on thermionic valves) but moved on in GERL to invent, among other things, the magnetron which was later used not only to create the microwave oven but also by the British military in the development of radar.

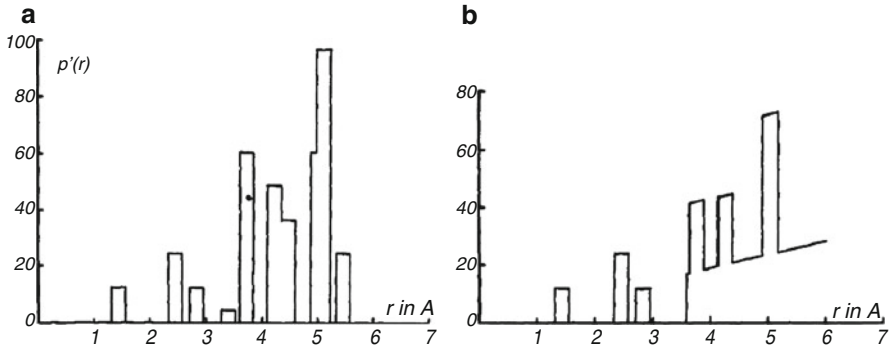

Fig. 1.3 (**a**) Atom distribution in a graphite crystal and (**b**) Atom distribution in carbon black, "a mesomorphic form of carbon, consisting of single graphite layers stacked roughly parallel to one another" [15]. It is noteworthy that while the data are not of the quality obtained with modern instrumentation, the experimental and analytical rigour are all of a standard to aspire!

1.1.3 Towards Disorder

Crystallography developed rapidly in the 1920s and 1930s with an increasing awareness of the power of the technique, particularly when single crystals were available. Powder diffraction, although a powerful tool for fingerprinting and phase identification, suffered (and still does) from a paucity of information compared with what is available from single crystal data. One person deserves a special mention in the development of the powder diffraction technique over the next 30 years and he took the technique in the direction of disorder. Carbon, again, is the principal element of the story; Bertram Warren [13, 14] was the scientist. The Fourier Inversion Method, which provides the pair distribution function, had applied to the diffraction patterns of glass, and Warren was keen to apply the method to other forms of amorphous matter. Carbon black was presumed to be amorphous and Warren collected data from a sample that happened to be in the laboratory. Knowing that carbon black diffracted poorly, he discovered, to his surprise, that the diffraction pattern, when Fourier inverted to provide the atom-atom separations, resulted in a distribution that was remarkably similar to graphite (Fig. 1.3). He concluded, in his first paper on the subject published in 1934 [15], that carbon black was not a truly amorphous form of carbon stating that "the existence of single graphite layers is very definite and therefore the material is at least mesomorphic. The diffraction data indicate a heterogeneous mixture containing particles which range from single graphite layers up to graphite crystals several layers thick." It was a topic that he returned to throughout his career [16–18] – his last carbon-black paper was published in 1965.

Very significantly, Warren discovered that materials did not fit into neatly defined categories of crystalline and amorphous. Powder diffraction is not simply the domain of crystalline systems – or should not be – and a major objective of this

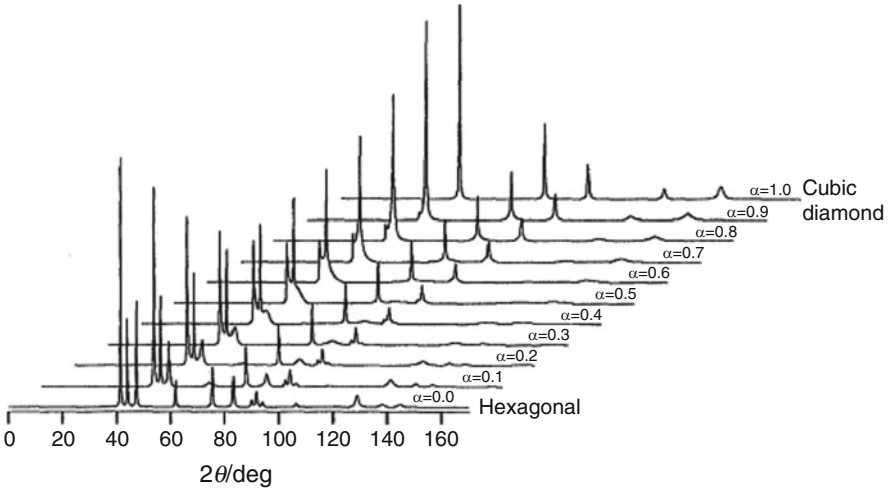

Fig. 1.4 Montage of powder X-ray diffraction patterns calculated as a function of the probability that layers in a diamond crystal will stack in the cubic diamond sequence. Thus $\alpha = 0$ corresponds to pure lonsdaleite and $\alpha = 1$ corresponds to pure diamond [19]

school is to remove the artificial boundaries in the solid-state between crystalline, poorly crystalline and amorphous. Powder diffraction is not synonymous with the Rietveld method – but we are ahead of ourselves – that is the next topic!

As a postscript to this section, it is worth noting that there has been significant subsequent development in the analysis of disordered and partially ordered systems. Deem et al. (1991) [19] produced an elegant program for calculating the diffraction patterns of faulted and strained crystals. Figure 1.4 continues the theme of carbon and illustrates the continuous variation of diffraction pattern from diamond to lonsdaleite, the hexagonal variant of diamond. The peak broadening and appearance and disappearance of peaks are particularly noteworthy. Other major developments have been reviewed by Egami and Billinge [20] and Scardi et al. [21].

1.1.4 Neutron Powder Diffraction and the Rietveld Method

The first neutron diffraction experiments were performed in 1945 by Ernest O. Wollan using the Graphite Reactor at Oak Ridge National Laboratory, USA. He was joined shortly afterwards (June 1946) by Clifford Shull, and together they established the basic principles of the technique and applied it successfully to many different materials, addressing problems such as the structure of ice and the microscopic arrangements of magnetic moments in materials [22]. For this achievement, Shull was awarded one half of the 1994 Nobel Prize in Physics with Bertram Brockhouse (who received the reward for his research on neutron triple-axis

spectrometers and inelastic neutron scattering). Wollan died in 1984 and did not receive the prize that was rightfully his. It is said that the unusually long delay in awarding the prize was due to the politically incorrect association of neutron diffraction analysis with nuclear power!

While Shull and Wollan performed the first neutron powder diffraction measurements, the most significant contribution from neutron diffraction is almost certainly the development of the structure refinement using the full diffraction profile by Hugo Rietveld in the late 1960s [23, 24]. Fame is assured when one's name becomes an adjective and the technique that is ubiquitous today and has enabled the development of the full power of the powder diffraction method is, of course, now called the Rietveld method [25]. Rietveld's two principal papers [23, 24] are elegantly written and the abstract of his 1969 paper succinctly describes the challenge and his solution.

"A structure refinement method is described which does not use integrated neutron powder intensities, single or overlapping, but employs directly the profile intensities obtained from step-scanning measurements of the powder diagram. Nuclear as well as magnetic structures can be refined, the latter only when their magnetic unit cell is equal to, or a multiple of, the nuclear cell. The least-squares refinement procedure allows, with a simple code, the introduction of linear or quadratic constraints between the parameters."

Rietveld's original program not only enabled the refinement of chemical and magnetic structures but also contained constraints, preferred orientation, peak asymmetry, essentially all the current definitions of R-factors, and the generally used formulation of F_{obs}. He even stated that the method can, in principle, also be extended to X-ray powder diagrams, if a satisfactory function can be found to describe the peak profiles. This had to wait a further decade and then, as with the beginnings of powder diffraction, two groups [26, 27] independently adapted the technique to X-ray data. Malmros and Thomas in the University of Uppsala, Sweden applied the Rietveld method to Guinier-Hagg film data while Khattak and Cox at Brookhaven National Laboratory, USA, demonstrated its feasibility with a conventional focussing X-ray powder diffractometer.

1.1.5 Back to Carbon

The principal purpose of this introductory talk has been to present a short – and very selective – history of the development of powder diffraction. Modern powder diffraction – the topic of this 44th International School of Crystallography – spans an enormous breadth of topics [28–31] from archaeology and applied engineering through to pharmaceutical science and protein crystallography. Given this range of modern powder diffraction, it is probably best to finish the story a few years ago. Carbon, in the form of graphite, carbon black, diamond and lonsdaleite have all featured in the decades of powder diffraction and so it is appropriate to finish with the crystal structure of C_{60}, buckminsterfullerene, the most symmetrical of all molecules.

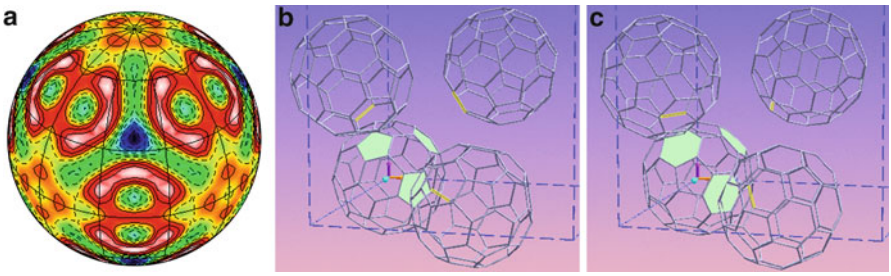

Fig. 1.5 (After [37]) (**a**) the orientation distribution function in the orientationally disordered high temperature phase. *White* represents excess density and *blue* low density – the overall deviation from spherical symmetry is only *ca.*10%; (**b**) and (**c**) the two distinct C_{60} orientations in the low-temperature phase. The orientation with pentagons (**b**) aligned along ∼110 directions pointing towards the C=C bonds are lower in energy than the "hexagon" orientation (**c**). This energy difference is calculated from powder diffraction data alone (color figure online)

C_{60} was first identified in a molecular beam in 1985 by Kroto and colleagues [32] who confirmed its truncated dodecahedral shape and icosahedral symmetry. However, it was the discovery of a synthesis route for bulk C_{60} [33] that led to the dramatic development of fullerenes and subsequently carbon nanotubes. The crystal structure was soon identified to adopt a face-centred cubic lattice [34–36] that contained orientationally disordered molecules at room temperature which ordered below 249 K to a primitive cubic *Pa3* symmetry. Neutron powder diffraction measurements [37] not only determined the subtle deviations from spherical behaviour in the high temperature phase (Fig. 1.5a) but also revealed an orientational glass transition which was explained by the presence of two crystallographically distinct orientations (Fig. 1.5b, c).

The most symmetrical of molecules is itself two-fold disordered in the ordered low-temperature phase and this disorder is paradoxically a consequence of the very high molecular symmetry. More recent neutron powder diffraction analysis [38] has not only obtained very precise measurements of these orientations at 4 K but has also determined the single and double bond lengths to an extreme precision (see Table 1.1) and modelled the orientational single-particle diffuse scattering (Fig. 1.6). These latest results would not have been possible without substantial developments in instrumentation, driven in significant part by advances in electronics (see Sect. 1.2), but also by progress in powder diffraction software – in this case, specifically the implementation of computer algebra in TOPAS [39] (see Table 1.2).

1.2 Powder Diffraction – The Power of Moore's Law

The previous section noted the importance of advances in computing power in the development of the powder diffraction method. It would have been impossible to utilise the Rietveld method without computers and early measurements were

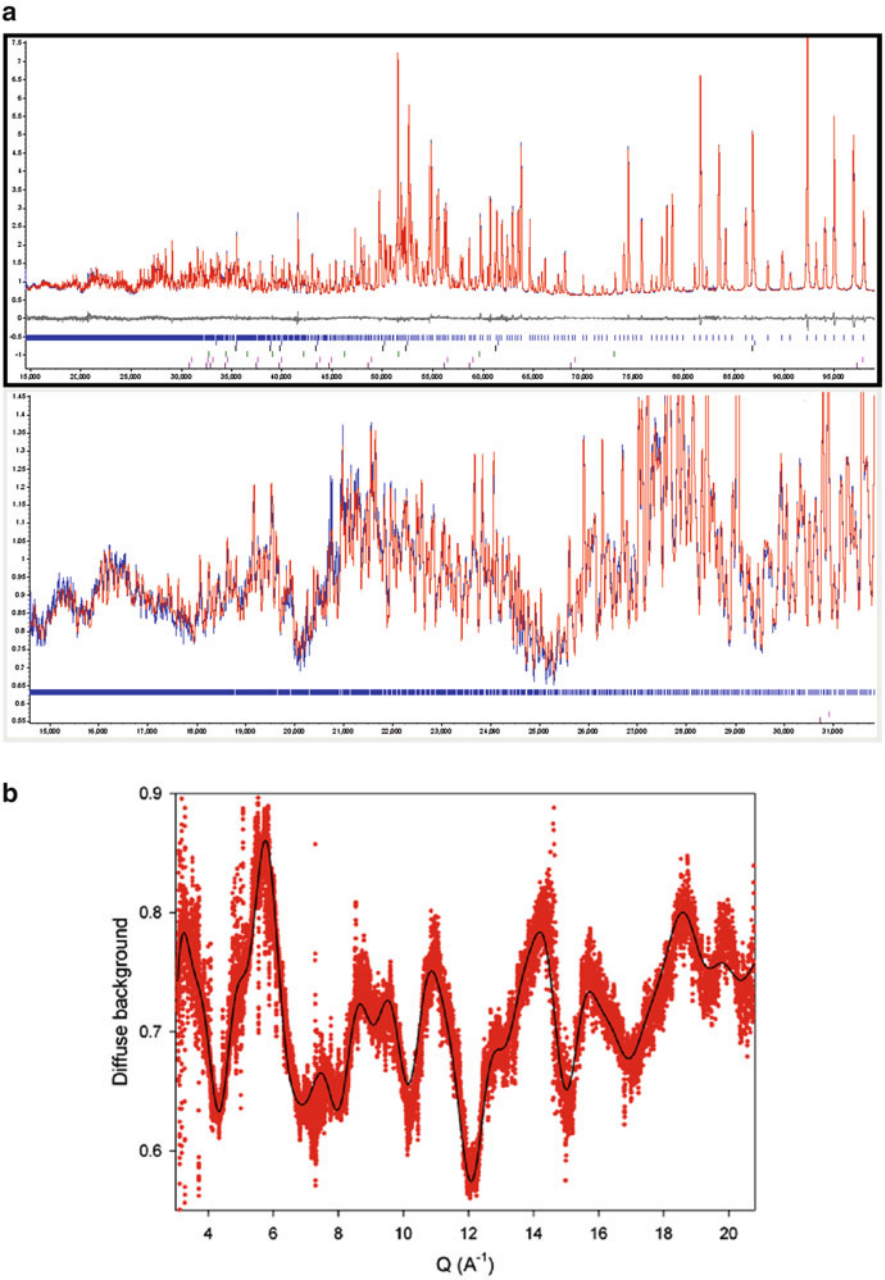

Fig. 1.6 (**a**) Observed and calculated 2007 HRPD neutron powder diffraction of C_{60} at 4 K (*top*) the full range of data from 0.3 to 2.0 Å and (*bottom*) the new range available in 2007 from 0.3 to 0.6 Å containing ∼1,500 new reflections, (**b**) the background fitted in TOPAS as part of a Rietveld refinement using a single molecule diffuse scattering model to a Q_{max} of 21 $Å^{-1}$ [38]

Table 1.1 Structural data for C_{60} obtained from HRPD, ISIS in 1991 and 2007

Year	a (Å)	b_d(Å)	b_s(Å)	ϕ_p (°)	ϕ_h (°)	n_p
1991	14.04212(4)	1.391(18)	1.455(12)	98 (fixed)	38 (fixed)	0.838(2)
2007	14.04225(2)	1.39745(30)	1.44953(15)	99.751(3)	41.915(15)	0.8276(9)

a, b_d and b_d are the 4 K lattice constant and double and single bond lengths while ϕ_p, ϕ_h and n_p are the rotation angles along 111 for "pentagon" and "hexagon" orientation and the fraction of "pentagon" orientation at 5 K. The increase in 2007 precision is a consequence of the larger Q range and also the refinement parameterisation

Table 1.2 Part of the TOPAS input file for the 4 K refinement of C_{60} that defines all atomic positions in the standard orientation based solely on C–C and C=C bond lengths. A single rotation angle C_{60} is required to define the atomic coordinates of each of the "pentagon" and "hexagon" orientations. The script highlights the power of computer algebra in TOPAS to define the refinement in terms of the appropriate parameters [38]

```
prm bsing  1.45022`_0.00014 .
prm bdoub  1.39646`_0.00025.
prm !b0  =  (2.*bsing + bdoub)/(3.*acel) ; :  0.10200`_0.00001
prm !eps = (bsing - bdoub)/(2.*bsing + bdoub);        .
prm !tau 1.6180339887498948482045868343656.
.
prm !xx01 = 0.;.
prm !yy01 = b0*(0.5-eps); :  0.04972`_0.00000.
prm !zz01 = 1.5*b0*tau; :  0.24756`_0.00002.
prm !xx02 = -0.5*b0*tau*(1.+eps); : -0.08355`_0.00001.
prm !yy02 =  0.5*b0*(2.-eps); :  0.10136`_0.00001.
prm !zz02 =  0.5*b0*((1.+eps)*(1.-tau)+3.*tau); :  0.21564`_0.00002.
prm !xx03 = -xx02; :  0.08355`_0.00001.
prm !yy03 =  yy02; :  0.10136`_0.00000.
prm !zz03 =  zz02; :  0.21564`_0.00000.
prm !xx04 = -0.5*b0*(1.+eps);  : -0.05164`_0.00000.
prm !yy04 =  0.5*b0*((1.+eps)*(tau-1.)+3.); :  0.18491`_0.00002.
prm !zz04 =  0.5*b0*tau*(2.-eps);  :  0.16401`_0.00001.
prm !xx05 = -xx04; :  0.05164`_0.00000.
prm !yy05 =  yy04; :  0.18491`_0.00000.
prm !zz05 =  zz04; :  0.16401`_0.00000.
```

restricted by both the computer speed and also the extremely small computer memories compared with modern-day machines. Initially, a single cycle of Rietveld analysis could be measured in hours and diffraction data collection was limited to a few thousand datapoints per day. Figure 1.7 shows the increase in data collection rates for neutron powder diffraction instruments since 1947. The graph follows an exponential Moore's Law growth suggesting that computer memory is the limiting factor, rather than neutron sources, at the frontiers of neutron scattering. Time-of-flight instruments such as GEM and WISH require massive raw files for collecting data as a function of both scattering angle and time of flight. These instruments

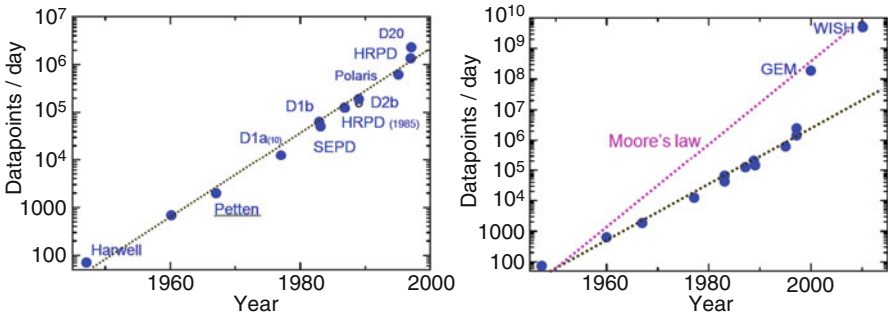

Fig. 1.7 The exponential rise in raw data collection rates for neutron powder diffraction. The early measurements at Harwell by George Bacon were written down by hand – around 100 data points were collected each day. The Petten measurements are attributed to Hugo Rietveld and mark the beginning of the Rietveld method

would be impossible to build and operate without massive data storage and rapid data reduction facilities. The ability to store and collate data rapidly is also crucial in the development of ultra-fast X-ray powder diffraction measurements.

1.3 The Four Most Important Decades – From the Ångstrom to the Micron – The Domain of Powder Diffraction

In the previous sections, we have discussed the development of powder diffraction over the decades of the twentieth century and emphasised the central importance of the decades of growth in computer speed and memory. However, the decades of the twentieth century have not only transformed powder diffraction but all of science and this has been fuelled by the growth in electronics that has taken us, within the span of a single scientific career, from kilobytes to megabytes, gigabytes, terabytes and, just over the horizon, petabytes. But there is another set of decades, the decades of length scales that are also worthy of mention. The shortest length-scale that has meaning in our universe is the Planck length, $\ell_P = \sqrt{(\hbar G/c^3)}$, which represents the granularity of space itself. Coming in at around 1.6×10^{-35} m., it is unbelievably small and, of course, at present is a conjecture and not proven. The smallest distance that has been measured and probed comes in at $\sim 10^{-20}$ m., around 10^{-5} of the diameter of a proton. This is, of course, the domain of particle physics which represents our quest to understand the fundamental particles and interactions and the underlying laws that govern our universe. At the other length of the length spectrum is the dimension of the visible universe itself. Multiplying the estimated age of the universe, 13.75 ± 0.11 billion years, by the speed of light leads to a massive 1.3×10^{26} m. This is domain of astronomy and cosmology where we can observe and understand but cannot touch nor change. Within the 61 orders of magnitude

from the Planck length to the size of the visible universe, there are four decades from the ångstrom to the micron that already dominate the science of the twenty-first century and will continue to define our future technological developments. The ability to synthesise, visualise, understand and modify objects on these length-scales place powder diffraction, along with other techniques such as electron microscopy, at the centre of the discovery and development of twenty-first century science and technology.

References

1. http://www.iucr.org/publ/50yearsofxraydiffraction
2. Friedrich W, Knipping P, von Laue M (1912) Interferenz-Erscheinungen bei Röntgenstrahlen. Sitzungsberichte der Mathematisch-Physikalischen, Classe der Königlich-Bayerischen Akademie der Wissenschaften zu München, pp 303–322
3. Bragg WH (1912) The specular reflexion of X-rays. Nature 90:410
4. Bragg WL (1913) The diffraction of short electromagnetic waves by a crystal. Proc Camb Phil Soc 17:43
5. Bragg WH (1913) The reflection of X-rays by crystals (II). Proc R Soc Lond A 89:246–248; Bragg WL (1913) The structure of some crystals as indicated by their diffraction of X-rays. Proc R Soc Lond A 89:248–277; Bragg WH, Bragg WL (1913) The structure of the diamond. Proc R Soc Lond A 89:277–291
6. von Laue M (1915) Concerning the detection of X-ray interferences, Nobel lecture, http://nobelprize.org/nobel_prizes/physics/laureates/1914/laue-lecture.pdf
7. Debye P (1915) Scattering of X-rays. Ann Physik 46:809–823
8. Debye P, Scherrer P (1916) Interferenzen an regellos orientierten Teilchen im Rontgenlicht. Physik Z 17:277–282
9. http://www.iucr.org/__data/assets/pdf_file/0015/771/hull.pdf
10. Hull AW (1917) A new method of X-ray crystal analysis. Phys Rev 10:661–696
11. Hull AW (1919) A new method of chemical analysis. J Am Chem Soc 41:1168–1175
12. Hull AW (1921) The X-ray crystal analysis of thirteen common metals. Phys Rev 17:571–588
13. http://ww1.iucr.org/people/warren.htm; http://www.iucr.org/__data/assets/pdf_file/0020/785/warren.pdf
14. Warren BE (1969/1990) X-ray diffraction. Addison-Wesley/Dover, Reading/Mineola
15. Warren BE (1934) X-ray powder diffraction study of carbon black. J Chem Phys 2:551–555
16. Biscoe J, Warren BE (1942) An X-ray study of carbon black. J Appl Phys 13:364–371
17. Houska CR, Warren BE (1954) X-ray study of the graphitization of carbon black. J Appl Phys 25:1503–1509
18. Warren BE, Bodenstein P (1966) The shape of two-dimensional carbon black reflections. Acta Crystallogr 20:602–604
19. Treacy MMJ, Newsam JM, Deem MW (1991) A general recursion method for calculating diffracted intensities from crystals containing planar faults. Proc R Soc Lond A 433:499–520. http://www.public.asu.edu/~mtreacy/DIFFaX_manual.pdf
20. Egami T, Billinge SJL (2003) Underneath the Bragg peaks: structural analysis of complex materials. Pergamon Press Elsevier/Oxford University Press, Oxford
21. Scardi P, Ortolani M, Leoni M (2010) WPPM: microstructural analysis beyond the Rietveld method. Mater Sci Forum 651:155–171; Leoni M, Martinez-Garcia J, Scardi P (2010) Mater Sci Forum 651:173–186
22. Shull CG (1995) Early development of neutron scattering. Rev Mod Phys 67:753–757

23. Rietveld HM (1967) Line profiles of neutron powder-diffraction peaks for structure refinement. Acta Crystallogr 22:151–152
24. Rietveld HM (1969) A profile refinement method for nuclear and magnetic structures. J Appl Crystallogr 2:65–71
25. Young RA (ed) (1993) The Rietveld method. Oxford University Press/International Union of Crystallography, Oxford
26. Malmros G, Thomas JO (1977) Least-squares structure refinement based on profile analysis of powder film intensity data measured on an automatic microdensitometer. J Appl Crystallogr 10:7–11
27. Khattak CP, Cox DE (1977) Profile analysis of X-ray powder diffractometer data: structural refinement of La0.75Sr0.25CrO3. J Appl Crystallogr 10:405–411
28. David WIF, Shankland K, McCusker LB, Baerlocher C (eds) (2002) Structure determination from powder diffraction data. Oxford University Press, Oxford
29. Pecharsky V, Zavalij P (2008) Fundamentals of powder diffraction and structural characterization of materials. Springer, New York
30. Kisi EH, Howard CJ (2008) Applications of neutron powder diffraction. Oxford University Press, Oxford
31. Dinnebier RE, Billinge SJL (eds) (2008) Powder diffraction: theory and practice. RSC Publishing, Cambridge
32. Kroto HW, Heath JR, O'Brien SC, Curl RF, Smalley RE (1985) C60: buckminster-fullerene. Nature 318:162–163
33. Krätschmer W, Lowell D, Lamb D, Fostiropoulos K, Huffman DR (1990) Solid C60: a new form of carbon. Nature 347:354–358
34. Heiney PA, Fischer JE, McGhie AR, Romanow WJ, Denenstein AM, McCauley JP Jr, Smith AB III, Cox DE (1991) Orientational ordering transition in solid C60. Phys Rev Lett 66:2911–2914
35. Sachidanandam R, Harris AB (1991) Comment on 'Orientational ordering transition in solid C60'. Phys Rev Lett 67:1467
36. David WIF, Ibberson RM, Matthewman JC, Prassides K, Dennis TJS, Hare JP, Kroto HW, Taylor R, Walton DRM (1991) Crystal structure and bonding of ordered C60. Nature 353:147–149
37. David WIF, Ibberson RM, Matsuo T (1993) High resolution neutron powder diffraction – a case study of the structure of C60. Proc R Soc Lond A Math Phys Eng Sci 442:129–146
38. David WIF, Ibberson RM (2012) in preparation
39. Coelho AA (2011) TOPAS academic; http://wwwtopas-academicnet/

Chapter 2
Rietveld Refinement

Peter W. Stephens

Abstract Rietveld refinement is generally the last stage of structure determination. The determination of unknown structures generally proceeds through a series of hypotheses of lattice, space group, atomic structure, each of which is subject to subsequent verification, so Rietveld refinement is the final test of the correctness of a structure. Unfortunately, there are not such clear tests of the veracity of a Rietveld refinement as there are of single crystal structures, and so a clear understanding of the process is required to judge a correct solution. This chapter will not directly address another frequent use of the technique, quantitative phase analysis, although many of the principles discussed here are relevant. There are any number of widely used programs and this chapter emphasizes the general features of the process over specific implementations.

2.1 Introduction

In powder diffraction, unlike a single crystal experiment, the 3D diffraction pattern is compressed into one dimension. While each (*hkl*) diffraction peak occupies a specific position, the density of peaks rapidly rises with increasing diffraction angle 2θ (or decreasing time of flight in a pulsed neutron experiment) that most peaks are overlapped, and it is a non-trivial task to separate their intensities.[1] A nice example of a pre-Rietveld structure determination from powder x-ray data

[1]For notational convenience I will restrict this discussion to angle-dispersive experiments, with absolutely no prejudice against pulsed neutron techniques.

P.W. Stephens (✉)
Department of Physics and Astronomy, State University of New York (SUNY), Stony Brook, NY 11776, USA
e-mail: pstephens@notes.cc.sunysb.edu

U. Kolb et al. (eds.), *Uniting Electron Crystallography and Powder Diffraction*,
NATO Science for Peace and Security Series B: Physics and Biophysics,
DOI 10.1007/978-94-007-5580-2_2,

is Zachariasen's (1951) solution of cubic Pu_2C_3 [1]. The structure was solved by determining the intensity of a set of diffraction peaks, and then choosing space group and coordinate(s) to fit. This works well for reasonably high symmetry, for relatively simple structures (only the Pu atom was considered in matching intensities, and the number and location of C atoms was inferred), and for people as ingenious as Zachariasen.

The Rietveld method, in use since 1969, goes the other direction [2]. From a hypothesized structure, one calculates the diffraction pattern to compare with the measured diffraction profile, i.e., intensity as a function of 2θ in a step scan. That allows a treatment of overlapping peaks which, we will see, allows the maximum amount of information to be extracted from an experimental pattern. This was originally done for relatively low resolution CW neutron data from a reactor, for which it was possible to give a fairly accurate model lineshape. In general, one imagines that the lineshape, which depends on a convolution of instrumental parameters and sample microstructure, can be specified more or less independently of the crystal structure (peak positions and intensities), so that a simultaneous refinement of lineshape and structure can be factored into reliable information about each, separately. We will return to this point subsequently.

For the purpose of this discussion, we assume that an approximate structural model (lattice parameters, space group, atom positions) is at hand. Our task is to optimize those various parameters, while keeping a close watch for any symptoms that the starting point was incorrect and needs to be revisited. The information in a powder diffraction pattern consists of:

- Peak positions, which depend on lattice dimensions and space group,
- Peak intensities, which depend on the distribution of atoms within the unit cell,
- Peak shapes, which are a convolution of instrumental parameters and the microstructure of the sample.

Crystallographic structure starts with the unit cell, defined by translation vectors $\boldsymbol{a}$, $\boldsymbol{b}$, $\boldsymbol{c}$. Diffraction peaks form a reciprocal lattice spanned by vectors $\boldsymbol{a}^*$, $\boldsymbol{b}^*$, $\boldsymbol{c}^*$ such that any diffraction peak can be specified as $\boldsymbol{Q} = h\boldsymbol{a}^* + k\boldsymbol{b}^* + l\boldsymbol{c}^*$, defined as $\boldsymbol{a}^* = 2\pi(\boldsymbol{b} \times \boldsymbol{c})/\boldsymbol{a}\cdot(\boldsymbol{b} \times \boldsymbol{c})$, *etc*. The diffracting planes for each reflection are separated by $d = 2\pi/|\boldsymbol{Q}|$, and the diffraction condition that the vector difference between incident and diffracted radiation wave vectors $\boldsymbol{k_i}$ and $\boldsymbol{k_f}$ (of equal magnitude $2\pi/\lambda$) is $\boldsymbol{Q} = \boldsymbol{k_f} - \boldsymbol{k_i}$ is equivalent to Bragg's law, $\lambda = 2d\sin\theta$. The above definitions are those commonly used in the physics community; others frequently drop all of the factors of 2π in the equations and definitions in the foregoing paragraph. The position of a peak in a powder pattern can be obtained from the magnitude of $\boldsymbol{Q}$, while the equations above can be put in the convenient form

$$\sin^2\theta = \left(\lambda^2/4d^2\right) = \left(\lambda^2/4\right)\left(Ah^2 + Bk^2 + Cl^2 + Dkl + Ehl + Fhk\right),$$

where the metric parameters $A, \ldots, F$ depend only on the real (or reciprocal) lattice parameters.

In a powder pattern, the integrated intensity of a given peak is

$$I(hkl) = cM_{hkl}\left|\sum_{\text{atoms}\,j} f_j \exp 2\pi i\,[hx + ky + lz]\ \exp -2W\right|^2 \mathrm{g}LP(\theta)$$

Here c is an overall scale factor, M_{hkl} is the multiplicity of the given peak, LP is the Lorentz-Polarization factor, *e.g.*, $LP(\theta) = 1/(\sin\theta \sin 2\theta)$ for x-rays polarized perpendicular to the scattering plane and a detector scanning 2θ with constant solid angle. f_j is the atomic scattering factor of the jth atom, including consideration of partial or mixed occupancy, and $\exp -2\,W$ is the Debye-Waller factor. The sum runs over all atoms in the unit cell, including symmetry equivalent positions generated by the space group. Details of the derivation and implementation of this equation are given in any comprehensive crystallography text, e.g., Giacovazzo [3].

2.2 Lineshape

In order to obtain a computed powder pattern, $Y^{calc}(2\theta)$, one must model the peak shape, taking into account contributions both of the sample microstructure and the diffractometer. Treatment of all of these effects is well beyond the scope of this paper, but we can briefly summarize the usual approach to Rietveld refinement. The comprehensive text edited by Dinnebier and Billinge contains much more detail [4].

Consider the case of an ideal lattice, truncated to spherical shape. Figure 2.1 shows the powder-averaged lineshape, computed from the Debye equation, for a sphere with a diameter of 100 lattice spacings. The full width at half maximum of this peak is $\Gamma = 0.011 \times 2\pi/a$ in Q.

The Scherrer equation, $\mathrm{L} = \mathrm{K}\lambda/\Gamma_{2\theta}\cos\theta$, is frequently used to estimate crystallite size L, where K is a numerical constant having something to do with the (assumed) shape of the grains and $\Gamma_{2\theta}$ is the diffraction peak FWHM in radians. The numerical computation that led to Fig. 2.1 gives $\mathrm{K} \approx 1.10$ for a particle of spherical shape. Powder samples with a single grain size are rare in practice; a distribution of grain sizes will wash out the observed peak shape function and further obscure the relationship between peak width and grain size. For almost all Rietveld refinements of crystal structures, the microstructural details that could be extracted from the lineshape are secondary to the desire to have a simple analytical model, and so one can imagine that the ideal lineshape function might be modeled as a Gaussian or Lorentzian. Figure 2.1 shows Gaussian and Lorentzian lineshapes of the same full width at half maximum, from which it is obvious that the one has tails that are too weak, and the other, too strong. It is generally satisfactory to use an interpolation of the two, for example, a pseudo-Voigt centered at $2\theta_0$,

$$f(2\theta) = \eta\frac{\Gamma/4\pi}{(2\theta - 2\theta_0)^2 + \Gamma^2/4} + (1-\eta)\frac{\sqrt{4\ln 2}}{\Gamma\sqrt{\pi}}\exp -\left(\frac{(2\theta - 2\theta_0)^2}{\Gamma^2}4\ln 2\right)$$

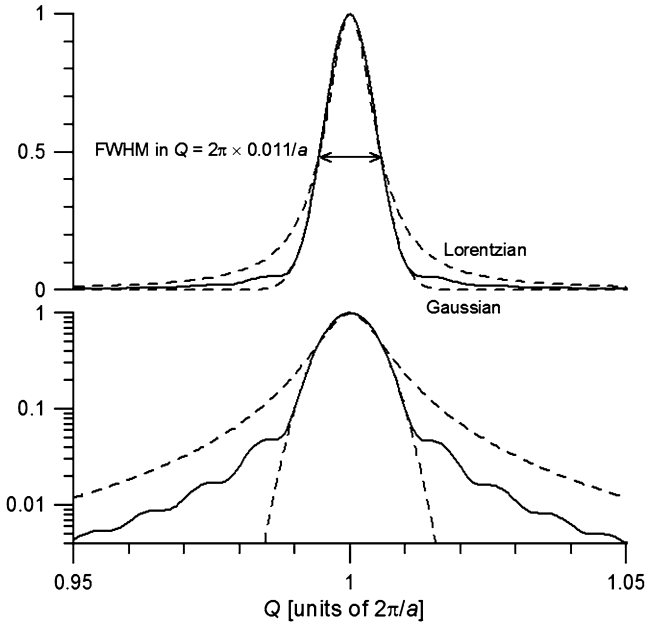

Fig. 2.1 Computed powder lineshape of the (100) peak of a spherical grain, 100 atoms in diameter

normalized to unit integrated intensity, with full width at half maximum Γ, and interpolation parameter η.

Another sample dependent effect frequently encountered is microstrain, whereby the peak width in Q is proportional to the diffraction order, *i.e.*, the width in 2θ grows in proportion to $\tan\theta$. One could rationalize that effect by imagining that some form of disorder causes each crystallite to have a slightly different lattice parameter. A more microscopically satisfying description would come from considering the internal strains within each individual crystallite caused by lattice defects, and then computing the diffraction pattern so produced. However, this requires a lot more effort than is usually justified for a crystal structure analysis.

Especially in high resolution measurements, it is frequently found that fitting experimental lineshapes require more elaborate models of size or strain, *e.g.*, to take account of anisotropic broadening; these are available in most Rietveld software, and are beyond the scope of the current treatment. Combining the effects of size and strain, and imagining that contributions to the width of a diffraction peak can be modeled as a convolution, it is plausible that the observed width in diffraction angle 2θ could be written as $\Gamma_{2\theta} = X/\cos\theta + Y\tan\theta$, where X and Y are parameters that represent the size and strain contributions. (This expression is justified if both contributions are regarded as Lorentzians, whose widths add directly in convolution. For Gaussians, the widths would add in quadrature).

The first application of the Rietveld method was to powder neutron diffraction at a CW source, where the instrumental lineshape is essentially a Gaussian whose

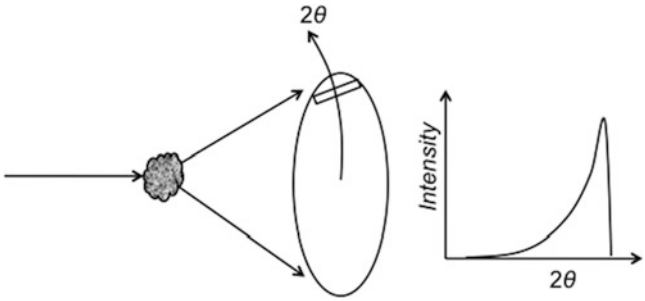

Fig. 2.2 Sketch illustrating the origin of low-angle tails on diffraction peaks due to axial divergence

variance depends on the diffraction angle as $\sigma^2 = U\tan^2\theta + V\tan\theta + W$, where the parameters U, V, and W depend on the width of the collimators, and d-spacings and mosaics of the monochromator [5]. X-ray spectral lines are combinations of several Lorentzians in wavelength, and in high resolution diffractometers with perfect crystals as monochromators and/or analyzers, the intrinsic reflection curves have long ($\Delta\theta^{-2}$) tails. The approach of convoluting the contribution of each optical element, known as fundamental parameters, was described in detail by Klug and Alexander [6]. The utility of fundamental parameters approach has greatly expanded with modern computational techniques, exemplified by Cheary and Coelho [7]. While such methods are extremely powerful, they are generally beyond the scope of this chapter, and so we will restrict our attention to the more widely used empirical lineshape models.

One important aberration in most powder diffractometers is axial divergence. This produces asymmetric peaks, especially at low diffraction angles. The effect may be visualized as shown in Fig. 2.2, where the diffracted radiation from a given order radiates from the sample as a cone. The edges of the detector slit intercept part of that cone below the nominal diffraction angle, and so there is a tail extending to the low angle side of the peak, which is especially pronounced for low diffraction angles. Several analytical treatments of this effect have been published, and it is incorporated in modern Rietveld programs. In the opinion of this author, unsubstantiated numerical approaches to this effect, such as the split-Pearson VII lineshape, should be avoided.

A good point of reference is the lineshape function used in GSAS [8], which is an approximate (pseudo-Voigt) convolution of a Gaussian with variance $\sigma^2 = U\tan^2\theta + V\tan\theta + W + P/\cos^2\theta$ with a Lorentzian of full width at half maximum (FWHM) $\Gamma = X/\cos\theta + Y\tan\theta$ and an asymmetric function to describe axial divergence of the diffracted beam. The origin of these parameters can be traced to elements of the discussion above, although it is not at all clear how to unravel information about sample microstructure from their converged values. Rietveld codes usually incorporate other parameters for instrumental corrections such as detector offset angle, sample displacement, etc.

Since the purpose of Rietveld refinement is to adjust various structural and lineshape parameters to obtain the best agreement between model and data, it is important to be clear on the figure of merit used. Suppose that the data consists of x-ray intensities collected in a step scan of 2θ, so that the observed intensity and standard error at each point are $Y^{obs}(2\theta)$ and $\sigma_{2\theta}$ respectively. (Here we are regarding 2θ as an index spanning the discrete set of measured data points). If $Y^{obs}(2\theta)$ is the number of counts detected, $\sigma_{2\theta}$ is simply $(Y^{obs}(2\theta))^{1/2}$, but it is frequently the case that the intensity is not constant through the scan, *e.g.*, for a synchrotron or pulsed neutron source, or if a variable counting time data collection strategy is in use. In that case, $Y^{obs}(2\theta)$ must be normalized to the dose of radiation reaching the sample while the data point at 2θ was being integrated, and $\sigma_{2\theta}$ scaled by the same factor. If the computed profile is given by $Y^{calc}(2\theta)$, the familiar reduced χ^2 parameter is given by

$$\chi^2 = (N-P)^{-1}\sum_{2\theta}^{N}\left(\frac{Y^{obs}(2\theta)-Y^{calc}(2\theta)}{\sigma_{2\theta}}\right)^2,$$

where N is the number of points in the data set and P is the number of parameters adjusted in the fit. If the deviation between model and observed data is due to the counting statistics alone, one expects χ^2 to be very close to unity. Another parameter frequently used is the weighted profile R-factor, defined as

$$R_{wp} = \sum_{2\theta}\left(\frac{Y^{obs}(2\theta)-Y^{calc}(2\theta)}{\sigma_{2\theta}}\right)^2 \Bigg/ \sum_{2\theta}\left(\frac{Y^{obs}(2\theta)}{\sigma_{2\theta}}\right)^2$$

Again, if differences between model and data are purely due to counting statistics, R_{wp} should approach the expected R-factor, R_{exp}, which is given by

$$R_{exp} = (N-P)\Bigg/\sum_{2\theta}\left(\frac{Y^{obs}(2\theta)}{\sigma_{2\theta}}\right)^2$$

It is evident that $R_{wp}/R_{exp} = \sqrt{\chi^2}$, a number which is also referred to as the "goodness of fit" (GOF).

An obvious question is whether there is some threshold χ^2 or R_{wp} which indicates a correct solution. The answer is no, and this is a source of consternation to people who try to publish refinements, as well as journal editors and referees, who are usually used to the clearer diagnostic signatures of a valid structure from single crystal data. Indeed, in comparing two different Rietveld refinements, even of the same sample, it is not necessarily the case that a better figure of merit indicates superior structural results. This arises partly because the quality of a Rietveld fit depends on details of the data that have little to do with the structure, and partly

because most of the information content in a diffraction pattern is at the higher angles where peaks are generally weaker and more strongly overlapped, but likely have less effect on the refinement statistics than a few strong low angle peaks. For this reason, it is recommended to spend more data collection time on the high angle peaks for the refinement of any complicated material. These issues are discussed in greater detail in several useful papers, *e.g.*, references [9] and [10].

In refining a structure, one must be prepared to examine both the fit and the reasonableness of the result in detail. A paper entitled "Rietveld refinement of a wrong crystal structure" provides a cautionary example, although there are significant danger signals in the example discussed there [11].

2.3 Intensity Estimation and Extraction from Powder Diffraction Pattern

The Rietveld method offers an approximate technique to estimate intensities of partially overlapping peaks from the recorded profile, based in part on the structural model. Imagine that the computed, normalized profile function of the nth diffraction peak is given by $f_n(2\theta)$, so that the computed profile at a given point of the profile is given by

$$Y^{calc}(2\theta) = \sum_{2\theta} I_n \, f_n(2\theta) + B(2\theta)$$

where B is the background function, and I_n is the integrated intensity of the n^{th} diffraction peak. Measured intensity at a given profile point is attributed to all diffraction peaks in proportion to their calculated contribution at that point, i.e.,

$$I_n^{obs} = \sum_{2\theta} \left(Y_i^{obs}(2\theta) - B(2\theta)\right) \frac{I_n^{calc} f_n(2\theta)}{\sum_m I_m^{calc} f_m(2\theta)}$$

One can then compute the standard crystallographic Bragg R factor comparing "observed" and computed intensities,

$$R_B = \sum_n |I_n^{obs} - I_n^{calc}| \Big/ \sum_n I_n^{obs} .$$

Of course, the estimated intensities are obviously biased by the optimistic model-based division of intensity of unresolved peaks.

It is frequently desired to "deconstruct" a powder diffraction profile into a set of integrated intensities of the diffraction peaks present. Armel Le Bail noted

that the Rietveld intensity estimation can be used in an iterative fashion to obtain estimates of the integrated intensities of all peaks in a powder pattern [12]. Cycles of refinement of profile, lattice, and background parameters alternate with reassignments of the set of integrated intensities, and the process is repeated until it converges. Computationally, this is very convenient because most of the work is already performed in the Rietveld program. The method is widely used and has had a tremendous impact on the techniques of structure determination from powder data.

Another method of intensity extraction was pioneered by Pawley, who treated the set of diffraction peak intensities $\{I^{obs}\}$ as parameters in a least squares fit, along side of the profile, lattice, and background parameters [13]. This idea faces the technical obstacle of instability of the refinement when poorly peaks are present. Indeed, the usual Hessian matrix is singular if two peaks have the same position, as occurs, for example, with cubic (333) and (511) reflections. Until relatively recently (~10y), the Pawley method was less used than the Le Bail method, but it is now incorporated into several widely-used Rietveld codes. One direct advantage of the Pawley method is that it provides estimates of the correlation between extracted intensities. This can be used to compare the quality of a structural model much more rapidly than by computing an entire profile R_{wp} [14]. Indeed, it has been shown that no information is lost in reducing a powder diffraction pattern to Pawley intensities and covariance matrix $\boldsymbol{A}$, so that a quality of fit parameter

$$\chi^2 = \sum_{n,m} \left(I_n^{obs} - I_n^{calc}\right)\left(A^{-1}\right)_{nm}\left(I_m^{obs} - I_m^{calc}\right)$$

is just as good as a full pattern Rietveld fit to refine a model (with some subtleties associated with the background) [15]. A similar method has been applied to intensities obtained from a Le Bail fit [16].

Whether the Le Bail or the Pawley method is used, a lineshape fit to an experimental data set is an important intermediate step in determining a crystal structure from powder data. It generally allows accurate refinement of lattice parameters, and a visual inspection can reveal whether a proposed lattice and space group is correct, as well as the presence of impurities. R_{wp} of a Pawley or Le Bail fit can be regarded as the target of a correct structural refinement, insofar as the difference between such a fit and the structural Rietveld refinement lie in the integrated intensities of the diffraction lines.

We now briefly illustrate some of the preceding points by analysis of a sample of Rb_3C_{60} [17]. Figure 2.3a shows the data, collected at a wavelength of 0.69970 Å at beamline X3B1 at the NSLS, in 2002. The experimental conditions were a double crystal Si(111) monochromator and a Ge(111) analyzer, with no focusing optics. The sample was in a 1 mm diameter capillary, spun about its axis to improve the powder statistics. The illuminated area extended about 8 mm along the capillary, and the horizontal (out of scattering plane) slits before the detector were also 8 mm

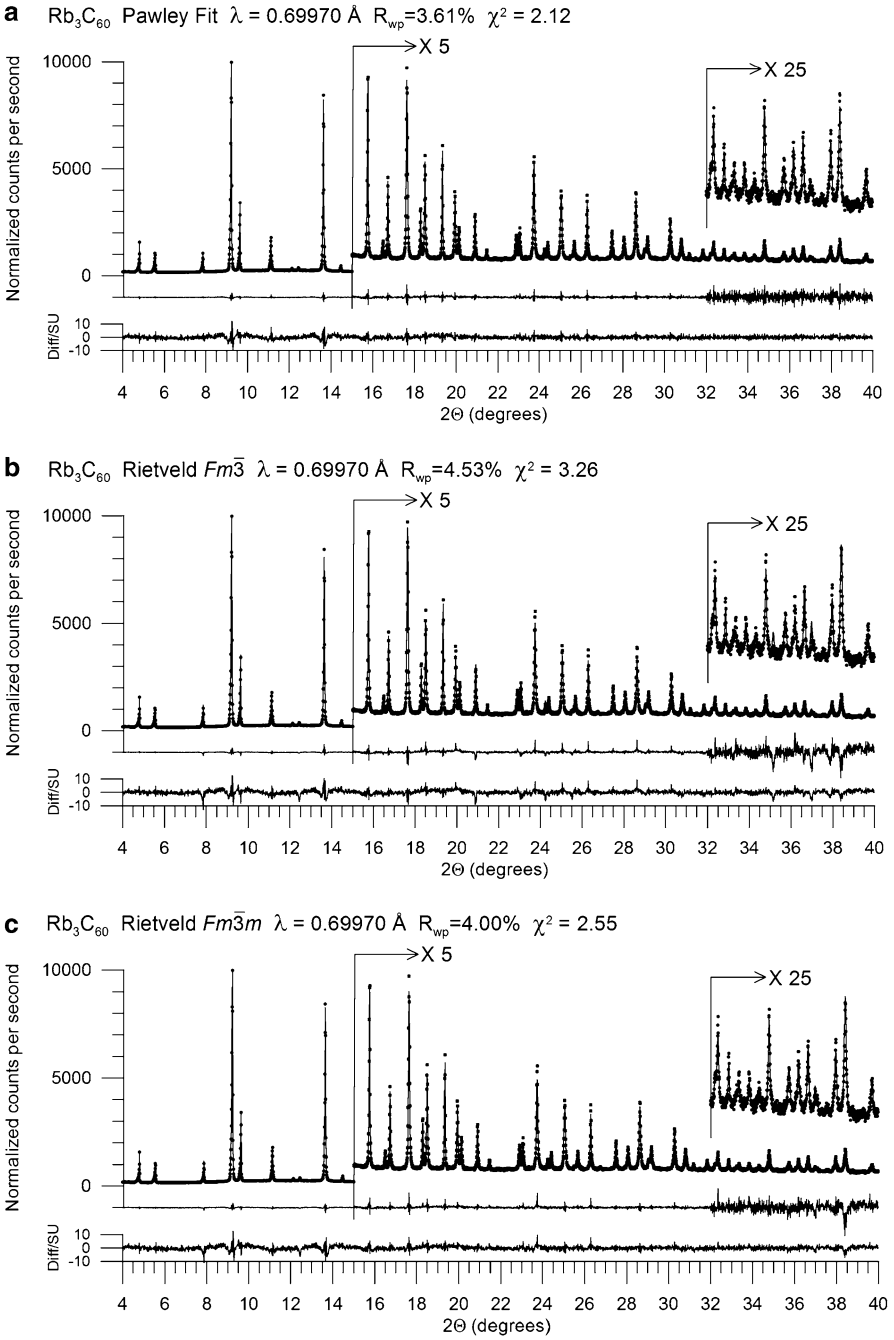

Fig. 2.3 (**a**) Pawley fit to Rb_3C_{60} PXRD data, based on model described in text. Difference curves are shown both in measured intensity (with the same vertical scale changes as the data and model) and as difference divided by the standard uncertainty of each data point (from counting statistics). (**b**) Rietveld refinement in space group $Fm\bar{3}$. (**c**) Rietveld refinement in space group $Fm\bar{3}m$

wide, about 300 mm from the sample. Visual inspection of the data reveals that it has face-centered cubic structure, and shows clearly the aforementioned low angle asymmetry.

Figure 2.3a actually shows a Pawley fit to the data, with axial divergence refined to a value consistent with the known diffractometer geometry, no observable size broadening, and diffraction FWHM proportional to tanθ with roughly equal Gaussian and Lorentzian components. Actually, the strain broadening is slightly anisotropic, with peaks about 30% broader along the {100} directions than along {111}. This can be modeled phenomenologically, and, at least in the case of cubic materials, qualitatively understood as arising from the elastic response to random internal stresses [18]. The background is a quadratic polynomial plus a term in 1/θ, plus a broad (pseudo-Voigt) peak centered at 11.5°. This Pawley fit has Rwp = 3.61%, $\chi^2 = 2.12$, which, frankly, is about as good as it gets.

With the benefit of hindsight, we can immediately solve the structure. The lattice parameter (14.424 Å) is slightly larger than that of an fcc crystal of C_{60}, and a moment's consideration of the cubic close packing of spheres shows that there are two tetrahedral and one octahedral spaces per sphere, which are clearly the sites of the Rb cations, with fractional coordinates (¼, ¼, ¼) and (½, 0, 0) respectively. Examination of a soccer ball leads to the conclusion that it fits naturally into a site of cubic point symmetry, with three-fold axes at the centers of hexagons pointing in the [111] directions, and two-fold axes, at the center of the stitching between two hexagons, pointing in [100] directions. That leads to three crystallographically distinct sites for C atoms: two in general positions (*x, y, z*), and one on the coordinate plane (0*, y, z*). Space group $Fm\bar{3}$ seems the obvious choice, with a multiplicity of 96 in the general position and 48 in the *y*-*z* plane, for a total of 4×60 carbon atoms. Throwing three carbon atoms at random positions, along with the two fixed cations, into a Rietveld program (here, TOPAS, ref. [19]), quickly converges to the decent-looking solution shown in Fig. 2.3b. It was previously noted that even subtle problems in a Rietveld refinement can reveal fundamentally incorrect assumptions. As it happens, Fig. 2.3b is based on an incorrect space group. The fullerene molecule can be rotated by 90° without changing any of the Rb-C distances, which suggests that it could be disordered. Indeed, going to space group $Fm\bar{3}m$ with 50% occupancy of each C position embodies this disorder, and produces the significantly better fit shown in Fig. 2.3c. Despite the small change in refinement statistics, the better fit is clearly evident, especially at high angles. (Note to skeptics – this disorder appears much more clearly in neutron refinements of Rb3C60, as well as in the isostructural K_3C_{60}). The refined bond distances, shown along with refinement statistics in Table 2.1, are also somewhat more plausible in the disordered model. We will stop short of considering further improvements in the model, such as cation vacancies and anisotropic thermal parameters, illustrating the maxim that no Rietveld refinement is ever entirely finished, merely abandoned.

Table 2.1 Refinement statistics and derived bond lengths of Rb_3C_{60} fits shown in Fig. 2.3

	Pawley	$Fm\bar{3}$	$Fm\bar{3}m$
R_{wp} (%)	3.61	4.53	4.00
χ^2	2.12	3.26	2.55
R_B (%)	0.43	2.31	1.26
Double bond (Å)		1.346(5)	1.389(8)
Double bond (Å)		1.347(7)	1.405(6)
Single bond (Å)		1.418(5)	1.442(5)
Single bond (Å)		1.494(5)	1.443(5)
Single bond (Å)		1.504(5)	1.467(7)
Pentagon (deg)		105.0(3)	103.0(4)
Pentagon (deg)		109.9(4)	107.1(2)
Pentagon (deg)		110.0(2)	111.4(4)
Hexagon (deg)		118.2(2)	117.7(3)
Hexagon (deg)		118.4(3)	119.2(4)
Hexagon (deg)		119.9(2)	120.4(2)
Hexagon (deg)		121.6(3)	120.8(4)
Hexagon (deg)		121.9(4)	121.9(2)

References

1. Zachariasen WH (1951) The crystal structure of plutonium sesquicarbide. Argonne National Laboratory report #ANL-4631, Chicago
2. Rietveld HM (1969) A profile refinement method for nuclear and magnetic structures. J Appl Crystallogr 2:65
3. Giacovazzo C (2002) Fundamentals of crystallography, 2nd edn. Oxford University Press, Oxford
4. Dinnebier RE, Billinge SJL (2008) Powder diffraction theory and practice. Royal Society of Chemistry, Cambridge
5. Caglioti G, Paoletti A, Ricci RP (1958) Choice of collimators for a crystal spectrometer for neutron diffraction. Nucl Instrum 3:223–228
6. Klug HP, Alexander LE (1974) X-ray diffraction procedures for polycrystalline and amorphous materials. Wiley, New York
7. Cheary RW, Coelho AA (1992) A fundamental parameters approach to x-ray line-profile fitting. J Appl Crystallogr 25:109
8. Larsen AC, Von Dreele RB (1985) GSAS: General Structure Analysis System, Los Alamos National Laboratory report MS-H805. Los Alamos, New Mexico
9. McCusker LB, Von Dreele RB, Cox DE, Louër D, Scardi P (1999) Rietveld refinement guidelines. J Appl Crystallogr 32:36
10. Toby BH (2006) R factors in Rietveld analysis: how good is good enough? Powder Diffr 21:67
11. Buchsbaum C, Schmidt MU (2007) Rietveld refinement of a wrong crystal structure. Acta Crystallogr B 63:926
12. Le Bail A (2005) Whole powder pattern decomposition methods and applications: a retrospection. Powder Diffr 20:316–326
13. Pawley GS (1981) Unit-cell refinement from powder diffraction scans. J Appl Crystallogr 14:357–361
14. David WIF, Shankland K, Shankland N (1998) Routine determination of molecular crystal structures from powder diffraction data. Chem Commun 8:931–932

15. David WIF (2004) On the equivalence of the Rietveld method and the correlated integrated intensities method in powder diffraction. J Appl Crystallogr B 37:621
16. Pagola S et al (2010) The structure of malaria pigment β-hematin. Nature 404:307; Pagola S, Stephens PW (2010) PSSP, a computer program for the crystal structure solution of molecular materials from X-ray powder diffraction data. J Appl Crystallogr 43:370–376
17. Huq A, Stephens P (2005) Transition temperatures and vacancies in superconducting Rb3C60. Phys Rev B 72:092511
18. Stephens PW (1999) Phenomenological model of anisotropic peak broadening in powder diffraction. J Appl Crystallogr 32:281; Stokes AR, Wilson AJC (1944) The diffraction of x-rays by distorted crystal aggregates. Proc Phys Soc Lond 56:174
19. Bruker AXS (2005) Topas V3: general profile and structure analysis software for powder diffraction data – user's manual; Bruker AXS, Karlsruhe; Coehlo AA (2007) TOPAS academic. Coelho Software, Brisbane. http://www.topas-academic.net

Chapter 3
Structure Solution – An Overview

Lynne B. McCusker and Christian Baerlocher

Abstract The structure solution process consists of a series of steps, each requiring decisions and each depending upon the previous ones having been performed correctly. The preliminary steps involve selecting the best sample, choosing the most appropriate radiation, collecting the data, indexing the pattern, determining the most probable space group(s), and estimating the profile parameters. If extracted intensities are to be used for structure solution, something must be done about the overlapping reflections. They can be equipartitioned, or, if necessary, more sophisticated approaches can be applied to improve the partitioning. At this point, the structure solution algorithm most appropriate for the material and the data must be chosen and applied. Finally, the (partial) structural model has to be completed and refined. The art of structure determination from powder diffraction data lies in finding a viable path through the maze of possibilities.

3.1 Introduction

There has been a veritable explosion in the development of structure determination methodology for powder diffraction data in the last 25 years. What used to be considered a fairly reliable technique for phase identification and perhaps unit cell determination, has become an almost standard one for complete structure analysis: from the determination of a unit cell and space group, to the generation of an approximate structure, to the refinement of that structure. What has caused this modest technique to emerge from the shadow of its immensely superior single-crystal cousin? Certainly, the advances in instrumentation (from radiation sources to detectors and everything in between) and the phenomenal increase in

L.B. McCusker (✉) • C. Baerlocher
Laboratory of Crystallography, ETH Zurich, CH-8093 Zurich, Switzerland
e-mail: lynne.mccusker@mat.ethz.ch; Ch.Baerlocher@mat.ethz.ch

U. Kolb et al. (eds.), *Uniting Electron Crystallography and Powder Diffraction*,
NATO Science for Peace and Security Series B: Physics and Biophysics,
DOI 10.1007/978-94-007-5580-2_3,

readily available computing power have made many of the developments possible. However, the driving force has come from scientists from disciplines as diverse as physics, chemistry, biology, materials science and geology, who need to know the structures of their polycrystalline materials.

Perhaps the beginning can be traced back to the introduction of the Rietveld method of structure refinement in 1969 [1]. It was soon realized that the structural information hidden in a powder diffraction pattern was not only substantial, but retrievable. Then it was only a small step to ask if there was enough, not only to refine an approximate structure, but also to determine one. The fact that the Rietveld method could be adapted from neutrons to X-rays also played a key role here, because X-ray powder diffraction patterns are much easier to come by [2]. Once the first few structure solutions were reported, an increasing number of crystallographers took up the challenge. Even today, they continue to push the limits of powder structure analysis to address increasingly complex problems. Three rich sources of information on this topic, besides this conference, can be found in the book entitled *Structure Determination from Powder Diffraction Data*, first published in 2002 [3], a special issue of *Z. Kristallogr*. devoted to the same topic, published in 2004 [4], and a recent review by David and Shankland [5].

The problems to be overcome in structure determination from powder diffraction data are twofold: (1) the basic phase problem, which is central to all crystallographic structure analyses, whether the data be from a single-crystal or a powder diffraction experiment, and (2) the reflection overlap problem, which is specific to powder diffraction data. No single approach to these two problems has emerged as the optimal one. The best approach always depends upon the nature and complexity of the material under investigation, and the quality of the diffraction data. The whole process can be viewed as finding a viable path through a maze of possibilities (Fig. 3.1). Selecting the best path to take is part of the art of structure solution from powder diffraction data. In the following sections, we will wend our way through this maze.

3.2 The Initial Steps

The structure determination process is a sequential one. That is, each step depends upon the previous one being correct. A mistake made early on in the procedure can make all subsequent steps useless, so a careful approach is usually better than a quick one. It may sound trivial, but structure solution begins with the sample. If the sample is poorly crystallized or contains impurities, structure solution is severely hindered and may become impossible. It is essential that the best sample available be used for the data collection, because all of the following steps are based on these data. It is well worth spending some time on optimizing synthesis conditions to obtain the best possible material.

The first decision to be made is which radiation is best suited to the problem and what parameters should be used for data collection. Are laboratory X-rays

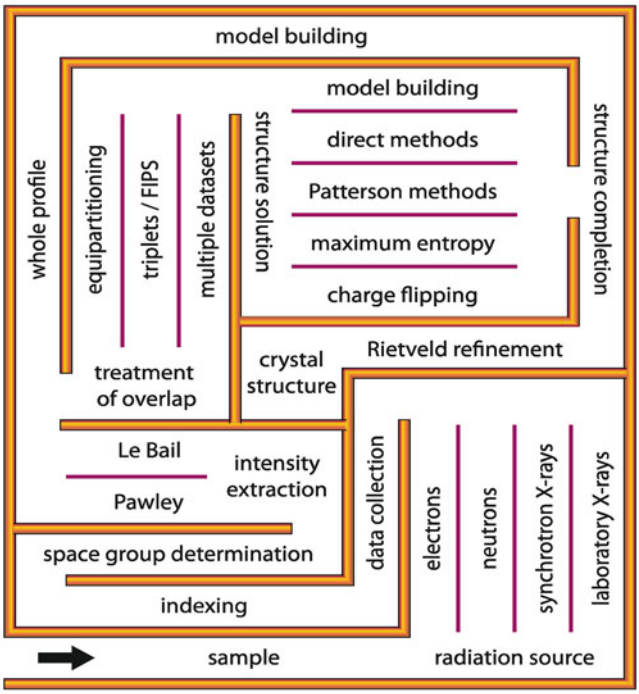

Fig. 3.1 The structure determination maze

sufficient [6] or is the high resolution and/or tunability of a synchrotron source necessary [7]? Would the nature of the sample make a neutron source more appropriate? Is the sample perhaps suited for (nanometer scale) single-crystal electron crystallography?

Once the data have been collected, the pattern has to be indexed and the most probable space group(s) determined. At this point, the positions of the reflections are known and their intensities can be estimated. This is best done with a whole-profile fit, where a peak shape, which can vary as a function of diffraction angle, is assigned to each reflection and its intensity is either refined (Pawley method [8]) or adjusted in an iterative procedure (Le Bail method [9]) to fit the measured data. Fine adjustments to the reflection positions can be made by refining the lattice parameters. This approach to the determination of the reflection intensities can be described as a model-free Rietveld refinement, where the intensities of the reflections rather than the atomic coordinates are optimized [10]. Even if the whole profile rather than the individual reflection intensities are to be used for structure solution, this step is needed to determine the profile parameters (peak width, peak asymmetry, peak shape, peak range, sample displacement, 2θ zero correction, background) and the optimal unit cell. This information is used each time the diffraction pattern of a structural model is calculated, so that it can be compared directly with the measured pattern.

3.3 Treating Overlapping Reflections

If the extracted intensities are to be used as input to the structure solution program, something has to be done about the overlapping reflections. The better these are estimated, the closer one comes to single-crystal data and the better the chances of solving the structure. Usually, however, the intensity of a peak resulting from several (overlapping) reflections is simply divided equally over the contributing reflections. This is known as equipartitioning. Although this approach necessarily yields a number of incorrect intensities, it has proven to be sufficient for structure solution in many cases.

For the more difficult cases, more sophisticated approaches can be used. Two ways of using the information from non-overlapping reflections in conjunction with simple assumptions such as atomicity and positivity to get a rough estimate of the relative intensities of overlapping reflections have been developed [10].

Should these computational approaches fail, an alternative is to attack the problem experimentally. By collecting multiple datasets on a single sample under different, but controlled conditions, additional information about the relative intensities of overlapping reflections can be obtained. For example, if a sample exhibits anisotropic thermal expansion without undergoing a phase transition (i.e. the reflection intensities remain the same), the overlap pattern in a series of diffraction patterns measured at different temperatures will change as the cell parameters change. Reflections that overlap at one temperature may not at another. By combining the information from the different patterns, better estimates of the individual reflection intensities can be derived [11]. A related approach was used by Von Dreele on a protein sample, whose lattice parameters had changed as a result of solvent-induced and radiation-damage induced strains [12]. Another possibility is to exploit (an induced) preferred orientation of the crystallites. If the crystallites are oriented, the differences in the diffraction patterns measured for different sample orientations can be used in a similar way [13].

Whichever approach is used to treat the overlapping reflections, the final result is a list of reflections with their *hkl* indices and their intensities, from which their structure factor amplitudes $|\mathbf{F}|$ can be calculated. That is, the list looks like a single-crystal dataset. The $|\mathbf{F}|$'s are just not as reliable.

3.4 Structure Solution

There are several algorithms to choose from for structure solution, and the best choice will depend upon the problem at hand. In the early days of structure solution from powder diffraction data, the extracted structure factor amplitudes were simply used as input to one of the single-crystal programs (e.g. direct methods, Patterson or maximum entropy algorithms). These all attempt to solve the phase problem from the diffraction data (i.e. in reciprocal space). Today, several algorithms that

take the ambiguity in the intensities of overlapping reflections into account are available. Perhaps the most commonly used structure-solution programs that work in reciprocal space are *EXPO* [14] or *XLENS* [15] for direct methods and *MICE* for maximum entropy [16]. Recently, Rius reported the development of a Patterson-function direct methods program that is particularly well-suited to dealing with powder diffraction data [17].

If reciprocal space methods do not work, structure solution in direct or real space can be tried. This is how single-crystal structures were solved in the days before Patterson and direct methods. That is, a structural model that was consistent with all known information about the material (both diffraction and non-diffraction experimental results) was built, and then its diffraction pattern calculated and compared with the measured one. This is an extremely powerful method, limited only by the imagination of the model builder, and can be used very well with powder diffraction data. The only drawback is that it takes time and patience to build such models and to check them. It also requires considerable experience and chemical intuition to build the correct model. Fortunately, computers have come along, and algorithms for generating chemically sensible models and checking them have been written. These are generally global optimization methods, most commonly based on either simulated annealing or evolutionary algorithms [5]. The two most commonly used programs for this approach are *Fox* [18] and *DASH* [19].

A few algorithms that exploit the advantages of both reciprocal and real space have also been developed for powder diffraction data. The first of these was the zeolite-specific *Focus* algorithm [20], where the reflection intensities are used in conjunction with starting (usually random) phases to generate an electron density map. This map is interpreted in real space using a framework search routine. The largest fragment from this search is then used to generate a new set of phases and these are combined with the extracted intensities to generate a new electron density map. By going back and forth between real and reciprocal space, information in both realms (e.g. the diffraction intensities and the chemical information about zeolite framework structures) are used actively in the structure determination procedure. Similarly, simulated annealing has been combined with direct methods in the newer versions of *EXPO* [21]. The newest algorithm on the scene, charge flipping, is also a hybrid method. It was introduced for single crystals by Oszlányi and Sütő in 2004 [22] and then adapted to powder diffraction data by two separate groups just a few years later [23]. The algorithm combines electron density map generation (generally starting with random phases) in reciprocal space with a density modification in real space (flipping the sign of all densities below a very small positive threshold value). The modified map is then used to calculate new phases, and, as in *Focus*, these are combined with the observed amplitudes to produce a new electron density map for the next cycle. For powder data, an additional loop for the repartitioning of overlapping reflections is added. In the program *Superflip* [24], this repartitioning is coupled to a second density modification in real space involving histogram matching [25]. Coelho has also combined the charge-flipping algorithm with the tangent formula in his program *Topas* [26].

3.5 Structure Completion and Refinement

Whichever method is used to solve the structure, the resulting structural model is usually only approximate and may be incomplete. The final, and often most difficult step of the structure solution procedure, is to complete the model and to refine the structure. Before the atomic coordinates can be refined reliably, all atoms have to be found. To do this, the approximate model is used, not only to calculate the phases of the reflections, but also to partition the intensities of the overlapping ones. Then a difference electron density map (measured structure factor amplitudes partitioned according to the model minus those calculated from the model, combined with phases from the model) can be calculated. This is usually good enough to find the missing atoms and/or to identify problem areas in the model. Finally, the structural parameters are refined using the whole-profile Rietveld method [27].

References

1. Rietveld HM (1969) A profile refinement method for nuclear and magnetic structures. Acta Crystallogr 2:65–71
2. Snyder RL (1993) Analytical profile fitting of X-ray powder diffraction profiles in Rietveld analysis. In: Young RA (ed) The Rietveld method. Oxford University Press, Oxford, pp 111–131
3. David WIF, Shankland K, McCusker LB, Baerlocher C (eds) (2002) Structure determination from powder diffraction data. Oxford University Press, Oxford
4. Baerlocher Ch, McCusker LB (eds) (2004) Structure determination from powder diffraction data. Z Kristallogr 219:782–901
5. David WIF, Shankland K (2008) Structure determination from powder diffraction data. Acta Crystallogr A64:52–64
6. Whitfield P (2013) Laboratory X-ray powder diffraction. In: Kolb U, Shankland K, Meshi L, Avilov A, David WIF (eds) Uniting electron crystallography and powder diffraction, NATO science for peace and security series B: physics and biophysics. Springer, Dordrecht, pp 53–64
7. Gozzo F (2013) Synchrotron X-ray powder diffraction. In: Kolb U, Shankland K, Meshi L, Avilov A, David WIF (eds) Uniting electron crystallography and powder diffraction, NATO science for peace and security series B: physics and biophysics. Springer, Dordrecht, pp 65–82
8. Pawley GS (1981) Unit cell refinement from powder diffraction scans. J Appl Crystallogr 14:357–361
9. Le Bail A, Duroy H, Fourquet JL (1988) Ab-initio structure determination of LiSbWO4 by X-ray powder diffraction. Mater Res Bull 23:447–452
10. David WIF, Sivia DS (2002) Extracting integrated intensities from powder diffraction patterns. In: David WIF, Shankland K, McCusker LB, Baerlocher C (eds) Structure determination from powder diffraction data. Oxford University Press, Oxford, pp 136–161
11. (a) Fernandes P, Shankland K, David WIF, Markvardsen AJ, Florence AJ, Shankland N, Leech CK (2008) A differential thermal expansion approach to crystal structure determination from powder diffraction data. J Appl Crystallogr 41:1089–1094. (b) Wright JP (2004) Extraction and use of correlated integrated intensities with powder diffraction data. Z Kristallogr 219:791–802
12. Von Dreele RB (2007) Multipattern Rietveld refinement of protein powder data: an approach to higher resolution. J Appl Crystallogr 40:133–143
13. Baerlocher Ch, McCusker LB, Prokic S, Wessels T (2004) Exploiting texture to estimate the relative intensities of overlapping reflections. Z Kristallogr 219:803–812

14. Altomare A, Caliandro R, Camalli M, Cuocci C, Giacovazzo C, Moliterni AGG, Rizzi R (2004) Automatic structure determination from powder data with EXPO2004. J Appl Crystallogr 37:1025–1028
15. Rius J, Frontera C (2007) Application of the constrained S-FFT direct-phasing method to powder diffraction data XIII. J Appl Crystallogr 40:1035–1038
16. Gilmore C, Dong W, Bricogne G (1999) A multisolution method of phase determination by combined maximization of entropy and likelihood. VI. The use of error-correcting codes as a source of phase permutation and their application to the phase problem in powder, electron and macromolecular crystallography. Acta Crystallogr A55:70–83
17. Rius J (2011) Patterson-function direct methods for structure determination of organic compounds from powder diffraction data XVI. Acta Crystallogr A67:63–67
18. Favre-Nicolin V, Cerny R (2004) A better FOX: using flexible modelling and maximum likelihood to improve direct-space ab initio structure determination from powder diffraction. Z Kristallogr 219:847–856
19. David WIF, Shankland K, van de Streek J, Pidcock E, Motherwell WDS, Cole JC (2006) DASH: a program for crystal structure determination from powder diffraction data. J Appl Crystallogr 39:910–915
20. Grosse-Kunstleve RW, McCusker LB, Baerlocher C (1997) Powder diffraction data and crystal chemical information combined in an automated structure determination procedure for zeolites. J Appl Crystallogr 30:985–995
21. Altomare A, Caliandro R, Cuocci C, Giacovazzo C, Moliterni AGG, Rizzi R, Platteau C (2008) Direct methods and simulated annealing: a hybrid approach for powder diffraction data. J Appl Crystallogr 41:56–61
22. Oszlányi G, Sütő A (2004) Ab initio structure solution by charge flipping. Acta Crystallogr A60:134–141
23. (a) Wu J, Leinenweber K, Spence JCH, O'Keeffe M (2006) Ab initio phasing of X-ray powder diffraction patterns by charge flipping. Nat Mater 5:647–652. (b) Baerlocher Ch, McCusker LB, Palatinus L (2007) Charge flipping combined with histogram matching to solve complex crystal structures from powder diffraction data. Z Kristallogr 222:47–53
24. Palatinus L, Chapuis G (2007) SUPERFLIP – a computer program for the solution of crystal structures by charge flipping in arbitrary dimensions. J Appl Crystallogr 40:786–790
25. Zhang KYJ, Main P (1990) Histogram matching as a new density modification technique for phase refinement and extension of protein molecules. Acta Crystallogr A46:41–46
26. Coelho AA (2007) A charge-flipping algorithm incorporating the tangent formula for solving difficult structures. Acta Crystallogr A63:400–406
27. (a) Stephens P (2013) Rietveld refinement. In: Kolb U, Shankland K, Meshi L, Avilov A, David WIF (eds) Uniting electron crystallography and powder diffraction, NATO science for peace and security series B: physics and biophysics. Springer, Dordrecht, pp 15–26

Chapter 4
Inorganic Materials

Radovan Černý

Abstract The separation of compounds by inorganic/organic boundary is of less importance for the structure determination by diffraction methods. More important for the diffraction is how the atoms build up larger building units and the crystal itself. A molecular/non-molecular boundary is therefore relevant for the choice of a structure determination method. Non-molecular compounds – also called extended solids – are constructed by bonds that extend "infinitely" in three dimensions through a crystal. These non-molecular crystals usually crystallize with higher symmetries, and atoms often occupy special Wyckoff positions. A review of actual methodology is given first, and then highlights and pitfalls of structure determination from powder diffraction, its problems and their solutions are shown and discussed using selected examples.

4.1 *Ab Initio* Structure Determination – Polyhedral Description

Inorganic compounds usually do not contain isolated molecules. This does not mean a particular difficulty for the *ab initio* structure solution methods working entirely in the reciprocal space (RSM). However, it becomes a difficulty for the methods working entirely (global optimization methods) in the direct space (DSM) and using the chemical knowledge in this space (for a comprehensive review on the methods see [1]). The structure solution algorithm working in the direct space has to know how to define basic structural blocks of the crystal which are then manipulated (optimized) by the algorithm.

R. Černý (✉)
Laboratory of Crystallography, University of Geneva, Geneva, Switzerland
e-mail: Radovan.Cerny@unige.ch

U. Kolb et al. (eds.), *Uniting Electron Crystallography and Powder Diffraction*,
NATO Science for Peace and Security Series B: Physics and Biophysics,
DOI 10.1007/978-94-007-5580-2_4,

The choice of the structural blocks is easy when isolated molecules are present in the crystal like in organic or coordination compounds where the molecules are easily described by a finite number of the internal molecular coordinates (bonding distances, angles and dihedral angles). A molecule is naturally an isolated structural block that can be moved in the unit cell, and deformed from its planar form. No sharing of atoms between the molecules occurs. The situation becomes rather unclear when one tries to model the crystal structure of a non-molecular compound. The definition of a finite structural block for a crystal like iron or sodium chloride is not unambiguous; should it be one atom, first coordination sphere of each atom, structural sheet of finite thickness, the asymmetric unit?

Coordination polyhedra, typically the first coordination spheres, of selected atoms, which will generate the whole inorganic crystal structure, can always be identified. These polyhedra will share corners, edges or faces. A wide range of polyhedra can be defined, and these are naturally described using again bond distances, angles and dihedral angles. Sharing of atoms between the polyhedra is either evident (for example exclusive corner sharing of SiO_4 tetrahedra in aluminosilicates [2]), or can be better described generally with an automatic, adaptive routine, the Dynamical Occupancy Correction (DOC) which handles also the special Wyckoff positions as it is used in the program Fox [3]. The optimization algorithm of DSM must be able to move smoothly the building blocks to the positions when they share atoms or to move an atom on the special position, while also allowing separation of the building blocks or moving the atom *away* from the special position, without *any* intervention from the user.

The polyhedra are typically described using Z-matrices as for the molecules [3]. The restraint-based description [4] of the polyhedra then solved some pitfalls of Z-matrices, however, with less benefit for the non-molecular compounds. A careful choice of the structural blocks may significantly improve the convergence of the DSM as illustrated on the example of AlMePO-γ phosponate [5] where the modelling by two free Al atoms converges faster than the modelling by AlO_4 tetrahedron and AlO_5 trigonal bipyramid.

4.2 Direct or Reciprocal Space Method?

The principal difference between DSM and RSM and an advantage of the former is that DSM does not require the extraction of integrated intensities of individual reflections which are needed for RSM. In the case of powder patterns of inorganic compounds showing often broad peaks, because of particular sample synthesis like mechanochemistry (ball-milling) or in situ studies of phase transformations and non ambient studies the DSM are the only option as no reliable integrated intensities can be extracted. An excellent example that has been solved *ab initio* by both DSM and RSM, and shows effectiveness of both approaches when well crystallized samples

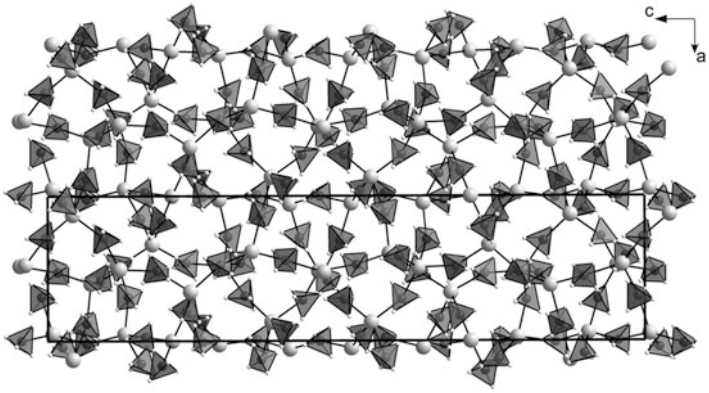

Fig. 4.1 Structure of $Mg(BH_4)_2$ viewed along the hexagonal *b* axis, showing two unit cells. *Dark grey* (partially transparent) tetrahedra are BH_4 units; Mg atoms in *light grey*

are available, is $Mg(BH_4)_2$ (Fig. 4.1). With 55 atoms in the asymmetric unit it represents one of the most complex atomic arrangements ever solved from powder diffraction data. The correct structure was found independently by DSM [6] and by RSM [7]. In both cases high resolution synchrotron data were required for indexing. In the DSM approach, the structure was modelled by five free Mg atoms and ten rigid tetrahedral BD_4 groups, and optimized jointly with synchrotron and neutron data by using the program Fox [3]. The correct structure was recognized after several hours of optimization (guidelines for efficient use of Fox can be found in [8]). In the RSM approach, the structure was solved with the aid of the program EXPO [9] using only synchrotron data. The positions of Mg and B atoms were recognized in electron density maps. In both cases the structure was refined by Rietveld refinement keeping the borohydride groups rigid.

4.3 Need for Accurate Unit Cell Content

Knowledge of the chemical composition and estimation of the unit cell content are the necessary information for most structure solution algorithms. The DSM may successfully work with overestimated cell content as the DOC can simply merge excess atoms (but does not create missing atoms!).

The recently discovered borohydrides $AZn_2(BH_4)_5$ ($A = $ Li, Na) [10] are an example how important is the correct estimation of the unit cell content for an unknown phase. In a parallel study [11] the chemical composition of the ball milled product was wrongly estimated as $AZn(BH_4)_3$, and led to structural models that

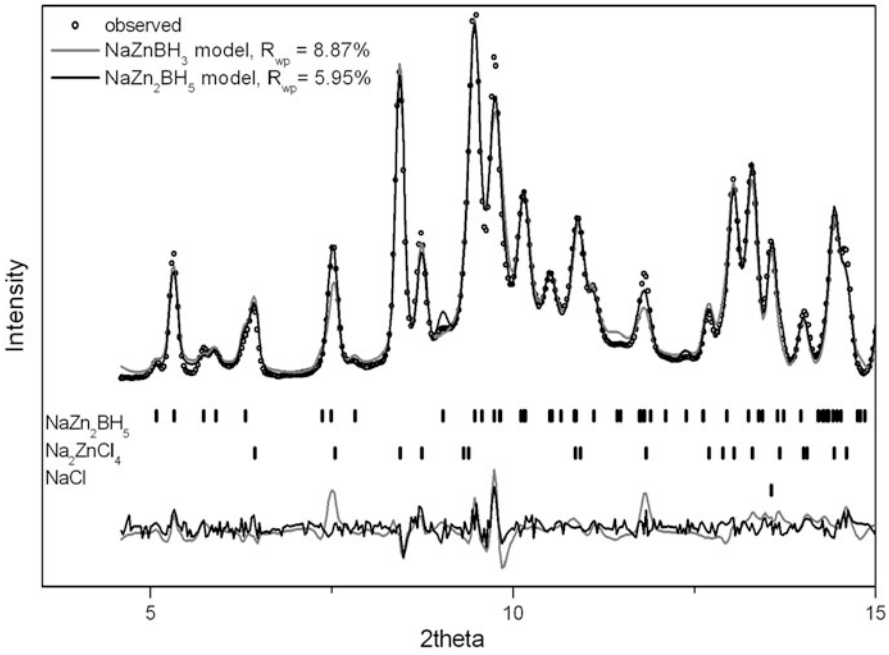

Fig. 4.2 Comparison of Rietveld plots for wrong, $NaZn(BH_4)_3$, and correct, $NaZn_2(BH_4)_5$, structural models, both in the same monoclinic cell (s.g. $P2_1/c$, $a = 9.440(4)$, $b = 16.573(4)$, $c = 9.110(2)$ Å, $\beta = 112.99(3)°$)

have shortcomings in Rietveld plots (Fig. 4.2.) which are not easily detectable from the powder diffraction data. Such a structural model can have balanced interatomic forces as shown by the DFT optimization, but does not correspond to a stable polymorph at given conditions.

The only warning about the wrong structural model came from the significant increase of the cell volume (+5.2%) in the DFT optimized structure, because of higher cell content (16 cations and 24 anions) compared to the correct model (12 cations and 20 anions). It means also that the wrong model is more packed (34.52 $Å^3$/ion) than the correct one (40.81 $Å^3$/ion) as calculated on DFT optimized cells. Another warning about the wrong model could have been certainly obtained from the measured density, a difficult experiment for a relatively reactive powder. In the case of multiphase samples containing new phase with unknown exact chemical composition it is therefore crucial to perform the synthesis of starting mixtures in several different ratios of the starting compounds. This procedure allows deducing the chemical composition of the new phase from molar fractions of known phases in different mixtures.

4.4 Structure Validation and Verification

A post-experimental DFT-optimization helps to validate new structures, locate light atoms (hydrogen), especially when using high-pressure diffraction data [12], and even correct the symmetry and some structural details as shown on following examples:

The difficulty in finding the correct orientation of BH_4 tetrahedra led to the overlooked two-fold axes in the $Mg(BH_4)_2$ space group symmetry originally identified as $P6_1$ [6, 7]. The DFT optimization of the structural model [13] has suggested the true symmetry as $P6_122$, which was then unambiguously confirmed by the single crystal X-ray diffraction [14]. The fact that the structural solution has been found independently by DSM and RSM in the lower Laue symmetry 6/*m* of the space groups $P6_1$ rather than in the true Laue symmetry 6/*mmm* of the true space groups $P6_122$ can be also understood by more degree of freedom (*hkl* and *khl* are independent) in 6/*m* allowing to correct the systematic errors of the powder diffraction data (grain statistics) having the symmetry 6/*mmm*.

In the case of $Li_4Al_3(BH_4)_{13}$ (*P*-43*n*) the DFT optimization [15] of the experimental structure has corrected the orientation of the complex anion $[Al(BH_4)_4]^-$ and modified so the bonding scheme in the structure from isolated complex ions $[(BH_4)Li_4]^{3+}$ and $[Al(BH_4)_4]^-$ rather to a 3D-framework structure (Fig. 4.3). The corrected model was indeed confirmed by the Rietveld refinement. A similar situation occurred for a nanocrystalline inorganic–organic hybrid compound $VO(C_6H_5COO)_2$ [16] where the correct orientation of the VO_6 octahedron was revealed by the DFT calculation.

The post-experimental DFT-optimization of the crystal structures allows achieving the global minimum in the Rietveld refinement which is not easily visible from the diffraction data only, and can be thus highly recommended.

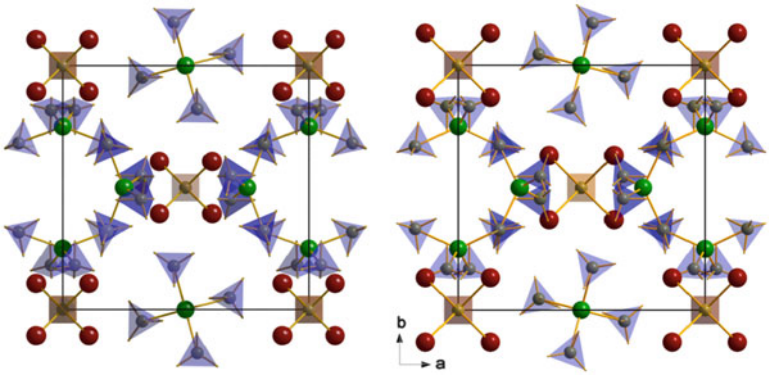

Fig. 4.3 Unit cell of $Al_3Li_4(BH_4)_{13}$ as solved from SR-XPD (*left*) and as corrected by DFT optimization (*right*). Complex cation $[(BH_4)Li_4]^{3+}$ centred by BH_4 tetrahedron in brown (*light grey*), complex anion $[Al(BH_4)_4]^-$ centred by Al atom in green (*dark grey*) (color figure online)

4.5 Symmetry Guided Refinement, Phase Transitions

The analysis of crystal symmetry plays an important role in the structure solution/refinement of inorganic compounds. The most complex inorganic structures were solved from powder diffraction data by the symmetry analysis of superstructures based on a well described average structure. Good example is α-$Bi_2Sn_2O_7$, a 176 atom crystal structure based on a pyrochlore structure [17]. Other example of symmetry guided refinement is the parametric Rietveld refinement [18], *i.e.* constraining the crystallographic parameters by set of equations which may have a physical basis, and follow the crystal symmetry. Structural phase transitions are one of the examples [19].

4.6 Multiphase Samples, Impurities

Solid state route synthesis is a method often used for the preparation of inorganic compounds. The resulting products may contain more than one phase like unreacted starting components and side reactions products. As the bottle-neck of the *ab initio* structural studies is still indexing of the powder data, multiphase samples introduce an additional complication.

A successful strategy consists of the so-called 'decomposition-aided indexing', which utilizes *in situ* diffraction as a function of the temperature (*T*-ramping) up to the decomposition/melting temperature of different phases. This procedure allows to separate diffraction peaks of individual phases as illustrated in Fig. 4.4 by synchrotron powder diffraction data for a ball milled KBH_4-$ScCl_3$ mixture [20].

The T-ramps (as well as any set of powder patterns collected as a function of external stimuli like pressure, excitation by a light) play an important role in the analysis of multiphase samples, as already mentioned. The studies of physical properties (thermal dilatation, compressibility), and of phase transitions are of course the original reason of the non-ambient diffraction studies.

4.7 Weak Superstructures and Lattice Pseudo-Symmetry

The arrangement of atoms in the lattice of an inorganic compound may show a small deviation from an arrangement with higher symmetry or shorter periodicity. A typical example are metal hydrides where this deviation is created by positioning H atoms in the matrix of metal atoms which becomes then only slightly deformed or by positioning a lower symmetry structural block like BH_4 tetrahedron on a high symmetry Wyckoff site. Because of a small deformation of the metal matrix and the low scattering power of hydrogen for X-rays, the splitting of peaks caused by lowering the symmetry is not very strong and the superstructures peaks are very weak in X-ray patterns as was the case of $Mg_6Co_2H_{11}$ [21] or $Y(BH_4)_3$ [22, 23].

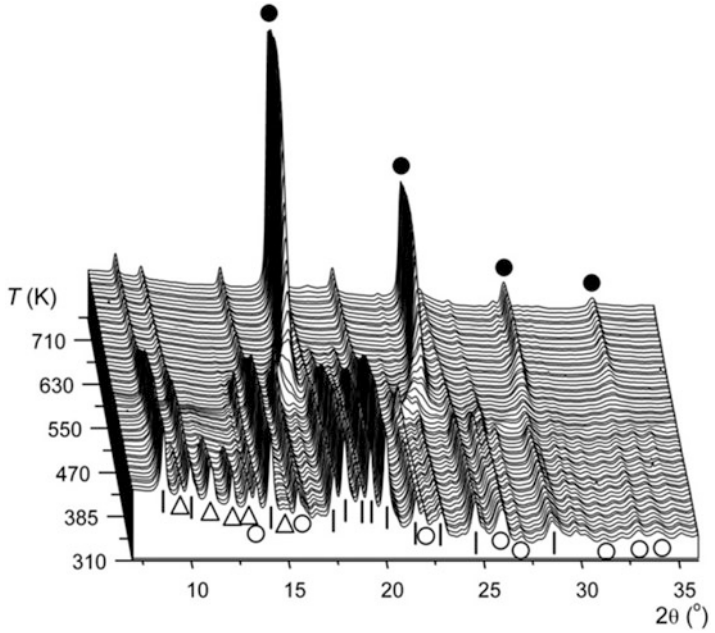

Fig. 4.4 *In situ* synchrotron radiation X-ray powder diffraction data for a ball milled sample of KBH_4-$ScCl_3$ (2:1) (*RT* to 580 K, $\Delta T/\Delta t = 5$ K/min, $\lambda = 0.9707$ Å). Only utilization of T-ramping allowed for determination of attribution of observed peaks to individual phases, $KSc(BH_4)_4$ and K_3ScCl_6, and led to a successful indexing of the RT-powder pattern. Symbols: Δ $KSc(BH_4)_4$, | K_3ScCl_6,○ KBH_4 and • KCl

4.8 Chemical and Positional Disorder – Local Structures

Chemical disorder is often observed in metal alloys where metal sites may have mixed occupation. When the occupation of individual sites by different metals is not statistically random, it can be analyzed provided the scattering contrast between the metals is strong enough. It can be achieved either using the X-ray and neutron data jointly or by resonant X-ray scattering. Note that for the case of n atomic species (including vacancies) on one Wyckoff site, one needs $n - 1$ diffraction patterns with different contrast between the scatterers under the question. An example of the analysis of the multi-substituted $LaNi_5$ alloy is given in [24].

Positional atomic disorder may show a local order (short range order) which can be studied from the diffuse intensity of the scattered radiation. The diffuse scattering from polycrystalline samples may be studied by using the Pair Distribution Function (see [25] for more details) like local hydrogen ordering in Laves phases [26].

4.9 Powder vs. Single Crystal

Independent studies of the orthorhombic (*Cmca*) $Mg_{1+x}Ir_{1-x}$ by single-crystal and powder diffraction methods [27] have allowed a comparison of the structural results obtained by two different methods on a compound having rather a complex crystal structure with 304 atoms in the unit cell. The investigated volume in the reciprocal space was approximately the same in both experiments, but with more than 4,000 unique reflections and redundancy factor of 7 for single crystal experiment and 754 unique non-overlapped reflections for the powder data. The atomic positional parameters from both methods are identical within 3–4 times standard uncertainties (s.u.) of the powder diffraction with the s.u. of the powder diffraction by one order of magnitude higher than corresponding s.u. of single crystal results. On the contrary the s.u. of the lattice parameters were by more than one order lower in favour of the powder diffraction.

It is sometimes possible to find a single grain of sufficient size for X-ray single crystal diffraction in an apparently powder sample, as was the case for $Li_4BN_3H_{10}$ [28] or $LiBH_4$ [29]. Even a multi-domain single crystal obtained by a low temperature annealing of an air- and moisture-sensitive $Mg(BH_4)_2$ has produced more accurate structural results than powder diffraction [14].

4.10 Conclusions

The powder diffraction on inorganic compounds is not a routine work. A crystallographer has to face numerous crystallographic challenges: complex structures, superstructures, pseudo-symmetries, twinning, chemical and positional disorder, local order, and structural solution from low quality data. On the other hand many powerful tools are available: resonant scattering, total scattering analysis, fast in-situ data collection. The good knowledge of basic crystallographic concepts like symmetry analysis, theory of scattering including diffuse effects, aperiodic crystals, and knowledge of limits and accuracy of powder data helps to avoid erroneous conclusions. The final cut should be always left to the crystal chemistry analysis.

Acknowledgments The author wants to thank to all users of Fox, and especially to them who have kindly provided the details of their work when solving the crystal structures.

References

1. David WIF, Shankland K, McCusker LB, Baerlocher C (eds) (2002) Structure determination from powder diffraction data. Oxford University Press, Oxford
2. Deem MW, Newsam JM (1989) Determination of 4-connected framework crystal structures by simulated annealing. Nature 342:260–262

3. Favre-Nicolin V, Černý R (2002) FOX, "Free objects for crystallography": a modular approach to ab initio structure determination from powder diffraction. J Appl Crystallogr 35:734–743
4. Favre-Nicolin V, Černý R (2004) A better FOX: using flexible modeling and maximum likelihood to improve direct-space ab initio structure determination from powder diffraction. Z Kristallogr 219:847–856
5. Edgar M, Carter VJ, Tunstall DP, Grewal P, Favre-Nicolin V, Cox PA, Lightfoot P, Wright PA (2002) $Al_2(CH_3PO_3)_3$: Structure solution of a novel aluminium methylphosphonate using a new simulated annealing program and powder X-ray diffraction data. Chem Commun 8:808–809
6. Černý R, Filinchuk Y, Hagemann H, Yvon K (2007) Magnesium borohydride: synthesis and crystal structure. Angew Chem Int Ed 46:5765–5767
7. Her J-H, Stephens PW, Gao Y, Soloveichik GL, Rijssenbeek J, Andrus M, Zhao J-C (2007) Structure of unsolvated magnesium borohydride $Mg(BH_4)_2$. Acta Crystallogr B63:561–568
8. Černý R, Favre-Nicolin V (2007) Direct space methods of structure determination from powder diffraction: principles, guidelines and perspectives. Z Kristallogr 222:105–113
9. Altomare A, Caliandro R, Camalli M, Cuocci C, Giacovazzo C, Moliternia AGG, Rizzi R (2004) Automatic structure determination from powder data with EXPO2004. J Appl Crystallogr 37:1025–1028
10. Ravnsbæk D, Filinchuk Y, Cerenius Y, Jakobsen HJ, Besenbacher F, Skibsted J, Jensen TRM (2009) A series of mixed-metal borohydrides. Angew Chem Int Ed 48:6659–6663
11. Černý R, Kim KC, Penin N, D'Anna V, Hagemann H, Sholl DS (2010) $AZn_2(BH_4)_5$ (A = Li, Na) and $NaZn(BH_4)_3$: structural studies. J Phys Chem C 114:19127–19133
12. Filinchuk Y, Chernyshov D, Nevidomskyy A, Dmitriev V (2008) High-pressure polymorphism as a step towards destabilization of $LiBH_4$. Angew Chem Int Ed 47:529–532
13. Dai B, Sholl DS, Johnson JKJ (2008) First-principles study of experimental and hypothetical $Mg(BH_4)_2$ crystal structures. Phys Chem C 112:4391–4395
14. Filinchuk Y, Černý R, Hagemann H (2009) Insight into $Mg(BH_4)_2$ with synchrotron X-ray diffraction: structure revision, crystal chemistry, and anomalous thermal expansion. Chem Mater 21:925–933
15. Lindemann I, Ferrer RD, Dunsch L, Filinchuk Y, Cerný R, Hagemann H, D'Anna V, Lawson Daku LM, Latevi M, Schultz L, Gutfleisch O (2010) $Al_3Li_4(BH_4)_{13}$: a complex double-cation borohydride with a new structure. Chem Eur J 16:8707–8712
16. Djerdj I, Cao M, Rocquefelte X, Černý R, Jagličič Z, Arcon D, Potocnik A, Gozzo F, Niederberger M (2009) Structural characterization of a nanocrystalline inorganic–organic hybrid with fiberlike morphology and one-dimensional antiferromagnetic properties. Chem Mater 21:3356–3369
17. Evans IR, Howard JAK, Evans JSO (2003) α-$Bi_2Sn_2O_7$ – a 176 atom crystal structure from powder diffraction data. J Mater Chem 13:2098–2103
18. Stinton GW, Evans JSO (2007) Parametric Rietveld refinement. J Appl Crystallogr 40:87–95
19. Müller M, Dinnebier RE, Ali Naveed Z, Campbell BJ, Jansen M (2010) Direct access to the order parameter: parameterized symmetry modes and rigid body movements as a function of temperature. Mater Sci Forum 651:79–95
20. Černý R, Ravnsbæk DB, Severa G, Filinchuk Y, D'Anna V, Hagemann H, Haase D, Jensen CM, Jensen TR (2010) Structure and characterization of $KSc(BH_4)_4$. J Phys Chem C 114:19540–19549
21. Černý R, Bonhomme F, Yvon K, Fischer P, Zolliker P, Cox DE, Hewat A (1992) Hexamagnesium dicobalt undecadeuteride $Mg_6Co_2D_{11}$: containing CoD_4 and CoD_5 complex anions conforming to the 18-electron rule. J Alloy Compd 187:233–241
22. Ravnsbæk DB, Filinchuk Y, Černý R, Ley MB, Haase D, Jakobsen HJ, Skibsted J, Jensen TR (2010) Thermal polymorphism and decomposition of $Y(BH_4)_3$. Inorg Chem 49:3801–3809
23. Frommen C, Aliouane N, Daledda S, Fonneløp JE, Grove H, Lieutenant K, Llamas-Jansa I, Sartori S, Sørby MH, Hauback BCJ (2010) Crystal structure, polymorphism, and thermal properties of yttrium borohydride $Y(BH_4)_3$. Alloy Compd 496:710–716

24. Joubert J-M, Černý R, Latroche M, Percheron-Guégan A, Yvon K (1998) Site occupancies in the battery electrode material $LaNi_{3.55}Mn_{0.4}Al_{0.3}Co_{0.75}$ as determined by multiwavelength synchrotron powder diffraction. J Appl Crystallogr 31:327–332
25. Egami T, Billinge SJL (2003) Underneath the Bragg-peaks: structural analysis of complex materials. Pergamon Press, Oxford
26. Ropka J, Cerný R, Paul-Boncour VJ (2011) Local deuterium order in apparently disordered Laves phase deuteride $YFe_2D_{4.2}$. J Solid State Chem 184(9):2516–2524
27. Černý R, Renaudin G, Favre-Nicolin V, Hlukhyy V, Pöttgen R (2004) $Mg_{1+x}Ir_{1-x}$ ($x = 0$, 0.037 and 0.054), a binary intermetallic compound with a new orthorhombic structure type determined from powder and single-crystal X-ray diffraction. Acta Crystallogr B 60:272–281
28. Filinchuk YE, Yvon K, Meisner GP, Pinkerton FE, Balogh MP (2006) On the composition and crystal structure of the new quaternary hydride phase $Li_4BN_3H_{10}$. Inorg Chem 45: 1433–1435
29. Filinchuk YE, Chernyshov D, Černý R (2008) The lightest borohydride probed by synchrotron diffraction: experiment calls for a new theoretical revision. J Phys Chem C 112:10579–10584

Chapter 5
Organic Compounds

Kenneth Shankland

Abstract For many years, powder X-ray diffraction was used primarily as a fingerprinting method for phase identification in the context of molecular organic materials. In the early 1990s, with only a few notable exceptions, structures of even moderate complexity were not solvable from PXRD data alone. Global optimisation methods and highly-modified direct methods have transformed this situation by specifically exploiting some well-known properties of molecular compounds. This chapter will consider some of these properties.

5.1 Introduction

Molecular organic materials tend to crystallise in low-symmetry space groups (some 80% crystallise in one of five space group, $P2_1/c$, P-1, $P2_12_12_1$, $P2_1$ and $C2/c$ [1], with % updated for Nov 2010 release of the CSD) and as such exhibit substantial accidental reflection overlap, particularly at high values of 2θ. This, coupled with the fact that molecular materials do not, in general, have strongly scattering elements present to boost measurable intensities at high angle means that it is particularly difficult to extract accurate reflection intensities. As such, the application of unmodified direct methods of crystal structure determination is generally unsuccessful. Spurred on by this failing, numerous groups have developed global optimisation based methods of structure determination, where the position, orientation and conformation of a molecule are adjusted in such a way as to maximise the agreement between observed and calculated diffraction data [2]. Clearly, to be able to perform such an optimisation, one must have a fairly accurate model of the molecule

K. Shankland (✉)
School of Pharmacy, University of Reading, Whiteknights, PO Box 224, Reading, UK
e-mail: k.shankland@reading.ac.uk

U. Kolb et al. (eds.), *Uniting Electron Crystallography and Powder Diffraction*,
NATO Science for Peace and Security Series B: Physics and Biophysics,
DOI 10.1007/978-94-007-5580-2_5,

being studied. The vast number of previously determined organic crystal structures provides a rich source of prior information that can be used in the construction of such models ready for optimisation. This is discussed in more detail below.

5.2 Molecular Connectivity

In single-crystal diffraction, it is not generally necessary to know the molecular connectivity in advance of the diffraction experiment, as the wealth of diffraction data, coupled with the power of direct (and other) methods of structure determination/completion means that the molecular structure usually emerges directly from the Fourier maps. In the case of powder diffraction, this is not normally the case and when applying global optimisation methods, it is necessary to know the molecular connectivity (or at least, a large part of it) in advance of structure determination. This is a significant constraint, but is not as restrictive as it seems at first sight; analytical techniques such as mass spectrometry and NMR can be used to determine 2D connectivity quickly and accurately and many diffraction problems consist of solving the structures of new crystalline forms of previously well-characterised molecules. That said, if the 2D connectivity supplied is wrong in any significant regard, it is unlikely that the structure determination will succeed and the crystallographer should always be alert to this possibility. If a new structure is being studied, one can frequently find significant molecular 'chunks' of the structure in existing crystal structures. In this regard, the Cambridge Structural Database (CSD) and its associated search interface ConQuest (Fig. 5.1) are essential tools [3], as is a good molecular modelling program with which one can edit retrieved structures to delete unwanted atoms or add new ones.

In the construction of a molecular model, one generally does not have to worry about the *exact* positions of hydrogen atoms, as their individual contribution to the scattering from any given point of the unit cell is relatively small. However, collectively, their contribution to the overall scattering can be significant and they should be included in the molecular model whenever possible.

Once a model of the molecule being studied has been constructed, it should be carefully checked for chemical sense – this is discussed in more detail in a separate section below.

5.3 Molecular Volume

Many molecular modelling programs (e.g. Marvin [4]) will quickly calculate a volume for any given isolated molecule. These values can be extremely useful as the powder pattern indexing stages, as the experimentally determined unit cell volume should be able to accommodate a crystallographically sensible number of molecular units. If the value of V_{cell}/V_{mol} makes crystallographic sense, this is a very good indicator of the correctness of the solution, above and beyond whatever the indexing

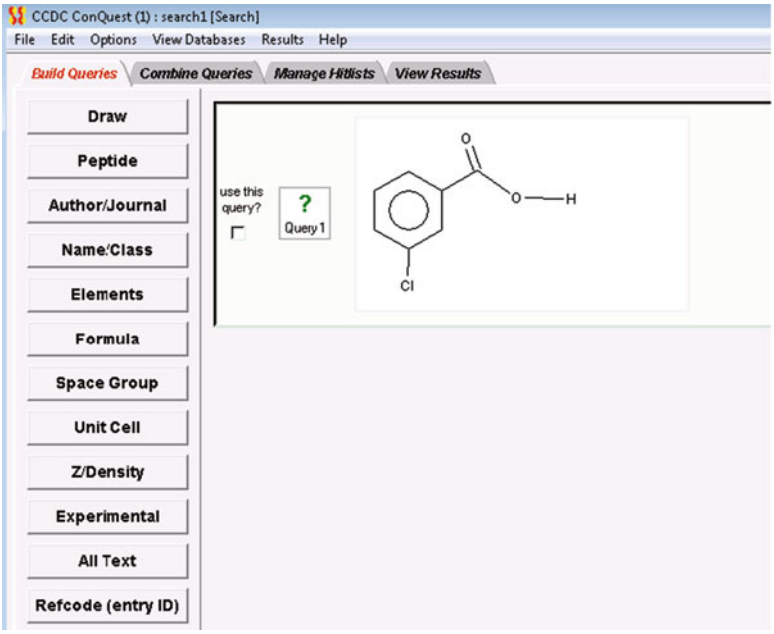

Fig. 5.1 Search options in the ConQuest program, with the 'Draw' option being used to search for all crystal structures containing the sketched substructure. This particular fragment matches 92 structures in the November 2010 version of the CSD

figures of merit suggest. In considering the calculation of $V_{\text{cell}}/V_{\text{mol}}$, it should be remembered that the V_{mol} obtained for an isolated molecule cannot be used "as is", as it does not take into account the crystal packing index. Fortunately, this is easily corrected by the use of an average crystal packing index of 0.7 i.e. $V_{\text{cell}}/(V_{\text{mol}} \div 0.7)$.

The 18 Å rule [5], where the estimated molecular volume of an organic material is obtained by counting all the non-hydrogen atoms in the structure and multiplying this number by 18 $Å^3$, is commonly used on account of its speed and simplicity. The figure of 18 $Å^3$ per atom is an average value derived from a survey of crystal structures in the Cambridge Structural Database. In 2002, Hofmann introduced a more specific formula [6], again based on observed crystal structures, but with individual volume terms for each atom type present in the structure. The formula is given in simplified form below:

$$V_{mol} = \sum_{i=1}^{x} n_i v_i$$

where the summation is over the x different atom types in the molecule, n_i is the number of atoms of the ith type in the structure and v_i is a volume contribution (in $Å^3$, derived from the CSD) for the ith atom type. This method is very accurate and should be used in preference to the 18 $Å^3$ rule.

5.4 Molecular Description

The 2D connectivity of a molecule has to be translated into a 3D description for use in global optimization. This is generally a two-stage process: (1) perform the 2D to 3D conversion (if required), and (2) convert the 3D description into a format suitable for the optimisation program. The 2D to 3D conversion can be performed in a variety of ways but is generally done with a molecular modeling program. The specifics of such programs lie outside the scope of this summary, but regardless of the method used, the output structure should be checked carefully against the expectation values before use (see Sect. 5.6). The output structure will have atomic coordinates in a Cartesian frame and may or may not retain the explicit connectivity information. For global optimisation, were this collection of N atoms to be optimised as freely moving objects, there would be $3N$ parameters. However, to do so would neglect the fact that we actually know a great deal about the molecular geometry [7]. Any two directly bonded atoms in a molecular structure sit at well-defined distances from one another, and these distances are not greatly influenced by the environment of the crystal structure. As such, a bond length may generally be considered to be a fixed entity and not one that requires to be optimised. Bond angles created by three connected atoms are similarly well-defined, mainly by the molecular environment as opposed to the crystallographic one. They are 'softer' than bond lengths (in that it takes considerably less energy to induce a deviation from the value found in an isolated molecule) but may generally be considered to be fixed entities that do not require to be optimised. Bond torsion angles (defined as the angle between two bonds A–B and C–D, viewed along a common bond B–C), are extremely 'soft' in comparison to bond lengths and angles, as changing the bond torsion changes only non-bonded contact distances. As such, they are considered to be flexible entities whose values cannot (in general) be assigned in advance and that must be parameters in the global optimisation.

Using an internal coordinate description of the molecule [7, 8] is a convenient way of encoding this prior molecular knowledge and serves to reduce considerably the number of parameters that needs to be determined. A very simple example is shown in Fig. 5.2.

It is worth mentioning, however, that in some cases, it may be advantageous to allow some variation in bond lengths and angles during the optimisation process [9].

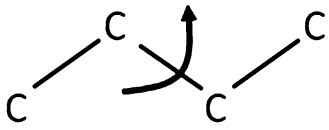

Fig. 5.2 A simplified molecular model for butane, with H atoms omitted. The bond lengths are known to be 1.54 Å and the bond angles are known to be 109.5°. The arrow shows a torsion angle whose exact value cannot be specified in advance of the optimisation. The 12 degrees of freedom associated with the use of independent atoms are reduced to 7 (six positional, one torsional) when an internal coordinate description is used

5.5 Other Sources of Prior Information

Although the values of flexible torsion angles in a structure cannot, in general, be specified in advance, that is not to say that one cannot infer probable values in advance of an optimisation. It should come as no surprise that molecular conformations within crystal structures populate low-lying areas of an energy surface and as such, it is possible to either (a) attempt to calculate in advance likely molecular conformations based on isolated molecule calculations[1], or (b) examine ensembles of existing crystal structures in order to determine energetically favorable confirmations; see, for example [10]. The latter is conveniently achieved through the Conquest or Mogul [11] front ends to the Cambridge Structural Database and Fig. 5.3 shows the result obtained for the facile example of the amide bond. Few distributions are as well defined as the one shown in Fig. 5.3, but it still possible to use the distributions to influence the way in which torsional parameters in the

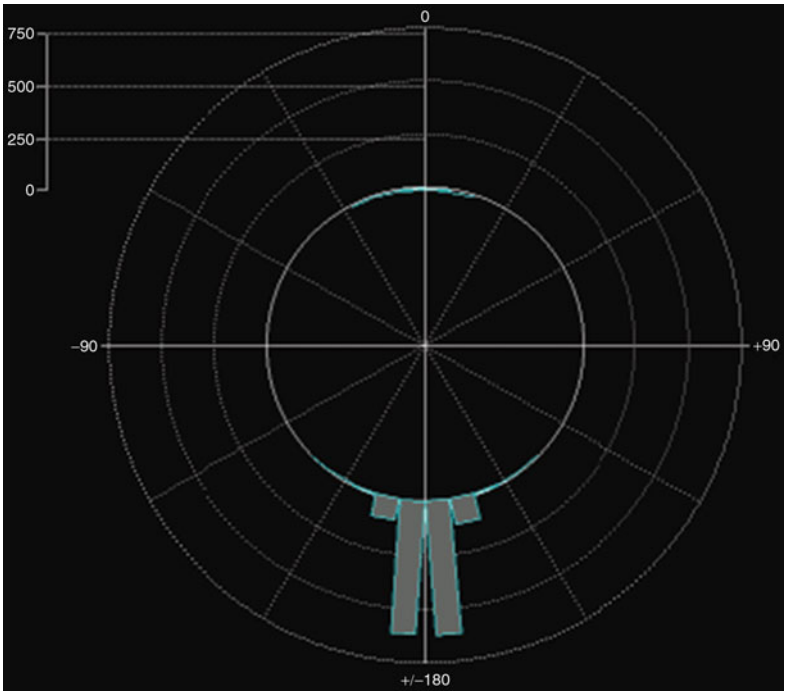

Fig. 5.3 A polar plot of the torsion angle associated with the amide bond (–C(=O)–NH–) in crystal structures in the Nov 2010 CSD release. The plot summarises some 1,573 observations and shows clearly that the amide bond is *trans* planar

[1]Carrying such calculations to their logical periodic conclusion brings us to the domain of crystal structure prediction.

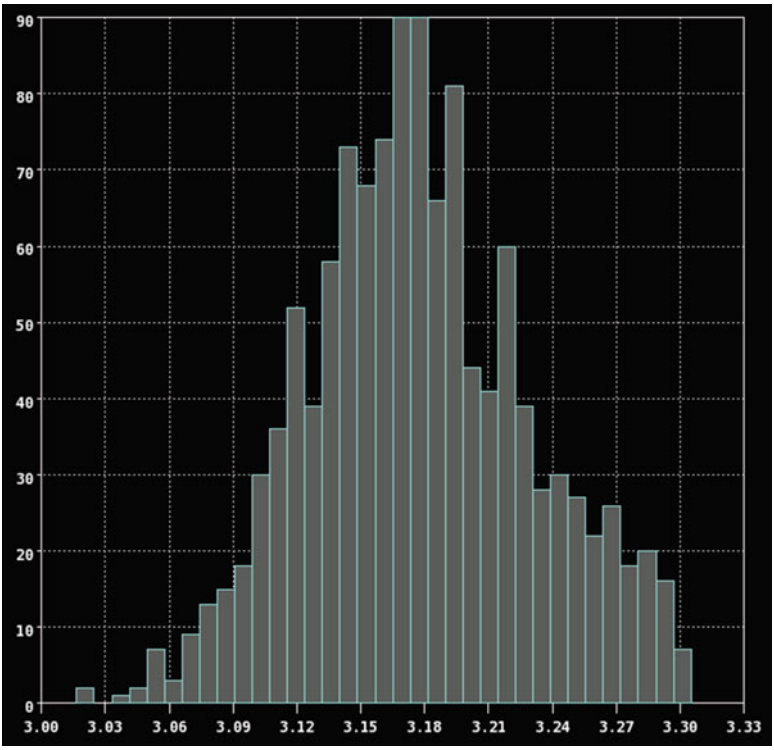

Fig. 5.4 A histogram of the distance (Å) associated with the intermolecular contact $N^{+}\cdots Cl^{-}$ in crystal structures containing the motif $R\text{-}NH_3{}^{+}\cdots Cl^{-}$. Only structures with an *R* factor less than 5% were included in the search of the Nov 2010 CSD release. The plot summarises some 1,200 observations and shows clearly that the chloride ion is consistently located at a distance of 3.18 ± 0.05 Å from the positively-charged nitrogen atom

optimization are varied. For problems involving multiple torsion angles, significant reductions in the search space can be achieve, with consequent benefits for both speed of solution and frequency of success [12].

For problems involving more than one fragment in the asymmetric unit, information about non-bonded contacts can also be also derived from the CSD using either the Conquest or Isostar front ends. Both distance and direction information can be obtained quickly and easily. Such information can be incorporated into the internal coordinate description of the fragments in order to reduce the degrees of freedom in the search. For the case shown in Fig. 5.4, the distance information can be included in the form of a virtual bond and the angle information (not shown) in the form of a virtual angle. Only one degree of freedom is saved (i.e. three positional for the Cl^{-} ion are reduced to two internal) but the resultant internal degrees of freedom are very highly restrained, leading to a significant reduction in the search space [13].

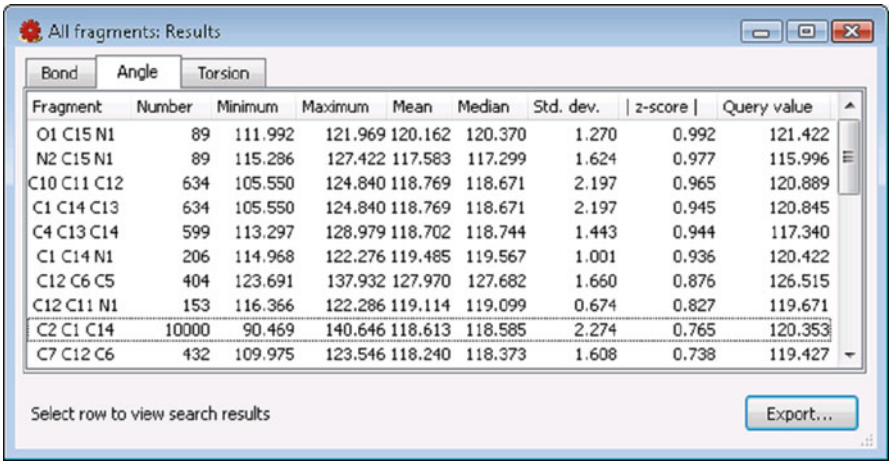

Fig. 5.5 The Mogul summary output of bond angles in CBMZPN01. Bong angle values in the input structure ("Query value" column) can be quickly compared with the observed distribution of similar angles present in structures in the CSD

5.6 Structure Checking

As mentioned earlier, when a model is constructed and ready for global optimisation against the measured diffraction data, it is wise to check to make sure that the model does not contain any bond lengths or angles that deviate too far from expected (previously observed) values. In this regard, the Mogul [14] front end to the CSD is an extremely valuable tool that makes this process straightforward. Figure 5.5 shows the results of a check performed on the molecular structure of carbamazepine as recorded in CSD refcode CBMZPN01. These results make it easy to identify any length, angle or torsion that deviates significantly from expectation values and that might need modification in the input model.

5.7 Summary

There are many different ways of constructing molecular models ready for global optimisation and this document has concentrated on arriving at the most accurate internal coordinate description. As highly accurate computational methods (such as DFT) become more widely used on the desktop, they will form an extremely valuable addition to the range of tools than can be brought to bear on this problem.

Acknowledgements I am especially grateful to the staff of the CCDC in Cambridge, with whom we have explored the applicability to powder diffraction of many of the tools mentioned here.

References

1. Mighell AD, Himes VL, Rodgers JR (1983) Space-group frequencies for organic-compounds. Acta Crystallogr A 39:737
2. Shankland K, David WIF (2002) Global optimisation. In: David WIF, Shankland K, McCusker LB, Baerlocher C (eds) Structure determination from powder diffraction data. Oxford University Press, Oxford
3. Allen FH (2002) The Cambridge structural database: a quarter of a million crystal structures and rising. Acta Crystallogr B58:380–388
4. http://www.chemaxon.com/products/marvin/
5. Kempster CJ, Lipson H (1972) Rapid method of assessing number of molecules in unit-cell of an organic crystal. Acta Crystallogr B 28:3674
6. Hofmann DWM (2002) Fast estimation of crystal densities. Acta Crystallogr B 58:489
7. Shankland K (2004) Whole-molecular constraints – the Z-matrix unravelled. IUCR commission on crystallographic computing newsletter no. 4. http://www.iucr.org/__data/assets/pdf_file/0003/6384/iucrcompcomm_aug2004.pdf
8. Leach AR (2001) Molecular modelling: principles and applications, 2nd edn. Prentice-Hall, Harlow
9. Favre-Nicolin V, Cerny R (2004) A better FOX: using flexible modelling and maximum likelihood to improve direct-space ab initio structure determination from powder diffraction. Z Kristall 219:847
10. Shankland N, Florence AJ, Cox PJ, Wilson CC, Shankland K (1998) Conformational analysis of Ibuprofen by crystallographic database searching and potential energy calculation. Int J Pharm 165:107
11. Bruno IJ, Cole JC, Lommerse JPM, Rowland RS, Taylor R, Verdonk ML (1997) Isostar: a library of information about non-bonded interactions. J Comput Aided Mol Des 11:525–537
12. Florence AJ, Shankland N, Shankland K, David WIF, Pidcock E, Xu XL, Johnston A, Kennedy AR, Cox PJ, Evans JSO, Steele G, Cosgrove SD, Frampton CS (2005) Solving molecular crystal structures from laboratory X-ray powder diffraction data with DASH: the state of the art and challenges. J Appl Crystallogr 38:249
13. Nowell H, Attfield JP, Cole JC, Cox PJ, Shankland K, Maginn SJ, Motherwell WDS (2002) Structure solution and refinement of tetracaine hydrochloride from X-ray powder diffraction data. New J Chem 26:469
14. Bruno IJ, Cole JC, Kessler M, Luo J, Motherwell WDS, Purkis LH, Smith BR, Taylor R, Cooper RI, Harris SE, Orpen AG (2004) Retrieval of crystallographically-derived molecular geometry information. J Chem Inf Comput Sci 44:2133–2144

Chapter 6
Laboratory X-ray Powder Diffraction

Pamela Whitfield

Abstract Laboratory diffractometers form the introduction to powder diffraction for most researchers. On a basic level for phase ID, etc., one diffractometer is very much like another. However when configuring a system for more challenging and advanced experiments, a variety of options and choices confront the experimentalist. Rather than cover the basics of diffractometer operation and geometry we will discover how a good understanding of the concepts behind laboratory diffractometers and their components is vital to getting the best from a system and pushing the limits of what can be achieved with lab instrumentation. Laboratory instrumentation will never compete with the sheer power and resolution of a synchrotron beamline. However, by departing from the conventional setups, it can be surprising what may be achieved in-house without resorting to the delay and inconvenience of synchrotron beamtime proposals.

6.1 Introduction

Although there have been many recent developments in software and instrumentation, the most basic Bragg-Brentano geometry used by many laboratory instruments is unchanged. It is a parafocusing geometry with a X-ray tube source and scintillation detector, with or without a monochromator. The biggest change has been the increasing use of position sensitive detectors, although in many instances the underlying parafocusing geometry is unchanged. This is not the forum to describe the basic geometry of diffractometers, and the reader is referred to the classical book by Jenkins and Snyder [1] or more recent texts [2–4] for further details.

P. Whitfield (✉)
National Research Council Canada, 1200 Montreal Road, Ottawa, ON K1A 0R6, Canada
e-mail: Pamela.Whitfield@nrc-cnrc.gc.ca

U. Kolb et al. (eds.), *Uniting Electron Crystallography and Powder Diffraction*,
NATO Science for Peace and Security Series B: Physics and Biophysics,
DOI 10.1007/978-94-007-5580-2_6,

6.2 Challenges in Everyday Powder Diffraction

Some researchers during their career are fortunate enough to be in the position to purchase one or more new powder diffractometers and write the specifications themselves. In many instances the standard system with a copper tube is not the best configuration. In order to obtain the best instrument for the job a few basic questions need to be answered.

The instrument should be matched to the type of sample to be analyzed – there is no laboratory configuration that will be good for every conceivable sample. This can be a challenge in a multi-user environment with a wide variety of sample types, where certain compromises may be necessary. The first question should always be "what are my samples?" Organic samples with low X-ray absorption and inorganic samples with high X-ray absorption tend to require different configurations to obtain high quality data. Organic samples are usually best served with a transmission geometry, while inorganics tend to require reflection geometry. The second question should be "how much sample do I have?" Very small samples may require capillary geometry or a specialist microdiffractometer to obtain the best results. The third question should be what elements do I have? The experienced analyst will come to regard sample fluorescence as one of their biggest enemies. Avoidance is much preferable to dealing with fluorescence after the fact.

6.2.1 Fluorescence

Fluorescence occurs when elements in a sample absorb a portion of the incident radiation and re-emit it at different energies (inelastic scattering). Effectively intensity is taken from the Bragg peaks and distributed into the background, producing a poor quality diffraction pattern. The most problematic elements (most often transition metal elements) for each type of X-ray tube are known, so it can often be avoided by selecting a suitable X-ray energy (Table 6.1). The different X-ray tubes, both common and uncommon are shown in Table 6.2. Unfortunately, in a multiuser/multisample environment it may not be possible to avoid generating fluorescence. This can be problematic where high-speed position sensitive detectors are used, as secondary X-ray optics to remove fluorescence often can't be used.

Scintillation detectors can easily be fitted with a graphite secondary monochromator which is very effective at removing the background due to fluorescence. There is an additional penalty in terms of peak intensity but the improvement in data quality is usually more than worth it. If a secondary monochromator isn't available,

Table 6.1 Problematic transition metal elements for Cu and Co X-ray tubes

X-ray tube	Problematic transition metal elements
Cu	Co, Fe, Mn
Co	Mn, Cr, Ti

Table 6.2 Different X-ray tubes available for laboratory X-ray diffractometers listed by increasing Kα1 energy

Anode	Energy (KeV)	Wavelength (Å)	Uses
Cr	5.4	2.290	Lowest energy. Used for stress analysis, SAXS and samples with large d-spacings (clays)
Fe	6.4	1.936	Rare tube, low power, used by some groups for Mn-containing samples
Co	6.9	1.789	Fe-containing samples to reduce fluorescence. Common in analysis of steel and minerals
Cu	8.0	1.541	Most common energy. Well matched to distances in lattice planes. X-ray detectors often optimized for CuKα
Mo	17.5	0.709	Small unit cell samples, highly absorbing samples, in-situ work. Common in single crystal
Ag	22.2	0.559	Very rare tube. Highest practical energy available. Very penetrating, best for PDF work

the peak-to-background ratio (P/B) can be improved somewhat by optimizing the electronic discriminators of the detector. P/B is important in structure analysis – the Rietveld round robin showed that a P/B of 50 or better is needed for accurate atomic positions in a structure refinement to remove uncertainty in the background fitting [5]. The discriminators determine the X-ray energies that the detector will 'throw away' and ignore. The degree of discrimination for scintillation detectors and PSDs is limited compared to energy-discriminating Si(Li) detectors but can go some way to improving the P/B of the data collected.

6.3 Beyond the Sales Brochure

The sales brochures tell you what vendor can guarantee the instrument will do. To find out what a lab diffractometer is *really* capable of requires an understanding of the different concepts behind diffractometer geometry and the different components (radiation properties, optics, detectors, software, etc.). Customized sample environments benefit greatly from a good design/fabrication shop due to the precision required. Integration with diffractometer systems and control software can require some fore-thought in terms of controllers and computer I/O systems.

6.3.1 High-Energy Radiation with Lab Diffractometers

MoKα is commonly used in single crystal diffractometers, but has recently become quite rare in powder diffraction. Older systems with scintillation detectors are

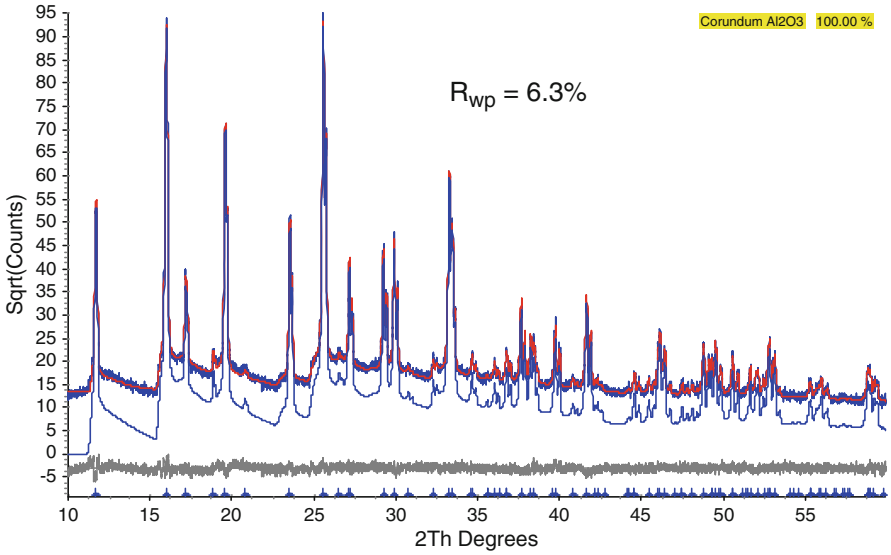

Fig. 6.1 (**a**) Rietveld fit to data from SRM1976 corundum collected using MoKα and a Zr Kβ filter using a modified emission profile. The calculated profile includes the low-angle step and high angle tail caused by the Kβ filter

perfectly capable of operating with higher energies, but many of the modern generation PSD detectors are much more limited in their wavelength capabilities, and in some instances will only operate with CuKα.

Even if your detector will operate with higher energies there are some potential issues when using MoKα or AgKα. In the absence of a monochromator it is customary to use a Kβ filter. With CuKα this does induce some subtle and hardly noticeable artefacts in the background. However, with MoKα and AgKα they are very noticeable and may cause serious problems in data analysis. Attempting to fit these artefacts with a conventional background in a Rietveld analysis fails miserably. However, modifying the emission profile either empirically or using a function written for the purpose can do a reasonable job as shown in Fig. 6.1. The calculated profile in Fig. 6.1 shows the low-angle step and high-angle tail present on all the intense reflections.

6.3.1.1 Laboratory Pressure Cells

One of the obvious applications for high energy X-rays is for laboratory-based pressure cells. Here the attraction of higher energies is the improved penetration through the cell windows and sample. The key to obtaining a reasonable time resolution is sufficient transmission of X-rays reaching a detector that ideally has good detection efficiency at higher X-ray energies.

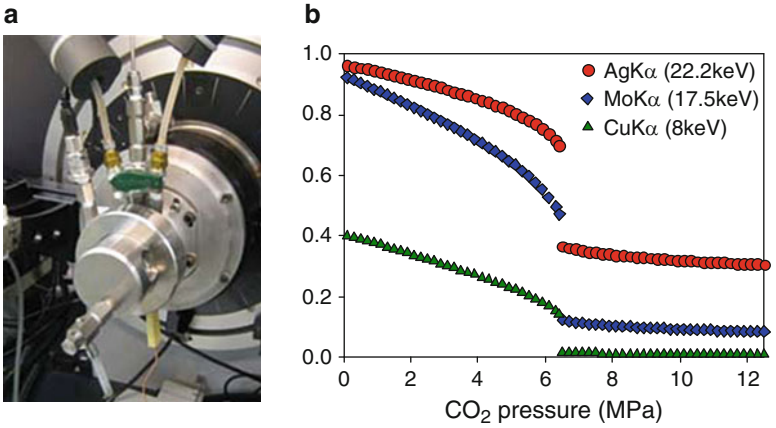

Fig. 6.2 (**a**) 125 bar CO_2 laboratory pressure cell and (**b**) the theoretical X-ray transmission through the cell with different X-ray energies

Gas Pressure Cell at the National Research Council

A 1st generation 125 bar, 200°C pressure cell was constructed [6] for studying crystallization of polymers under CO_2 pressure (Fig. 6.2a). The design was a modification of a literature design [7] to meet the ASME Boiler and Pressure Vessel Code [8]. The use of high energy X-rays was dictated by the transmission through the 1/8 in. beryllium windows and the dense, pressurized CO_2. The theoretical transmission with different X-ray energies is shown in Fig. 6.2b.

This cell was used with MoKα and a Vantec-1 PSD detector with a 8° window. This configuration was capable of producing good data with reasonable time resolution either in scanning or snapshot mode. The reaction kinetics of the carbonation of wollastonite ($CaSiO_3$) was studied using quantitative Rietveld analysis with this cell [9]. Data from different pressures and temperatures such as that showed in Fig. 6.3 allowed an activation energy for the carbonation of wollastonite to be calculated.

High Pressure Acid Leaching Studies at CSIRO

The group of Ian Madsen and Nicola Scarlett at CSIRO have been studying reaction processes occurring during high pressure acid leaching of nickel laterite ores [10, 11]. Industrially this process takes place in an autoclave to stop the acid boiling. Studying the reaction *in-situ* requires penetrating a mixture of a solid and an acidic solution, leading to use of MoKα radiation to reduce attenuation. To reduce absorption a thick-walled 1 mm quartz capillary is used as shown in Fig. 6.4, together with an Inel diffractometer and a 120° PSD detector. A hot air heater was used to heat the sample and the capillary was oscillated as opposed to fully rotated due to the connection of the pressure line. Maximizing the counting efficiency of this detector with MoKα required the use of a custom counting gas mixture.

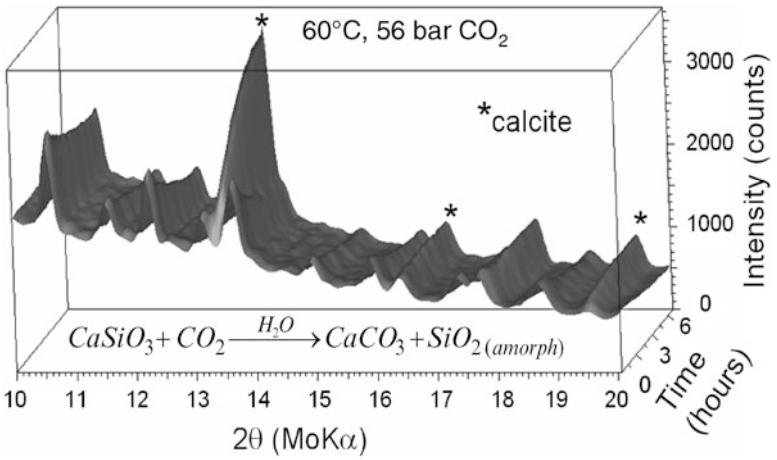

Fig. 6.3 In-situ data showing the carbonation of $CaSiO_3$ over a period of 6 h at 60°C and under 56 bar CO_2 pressure

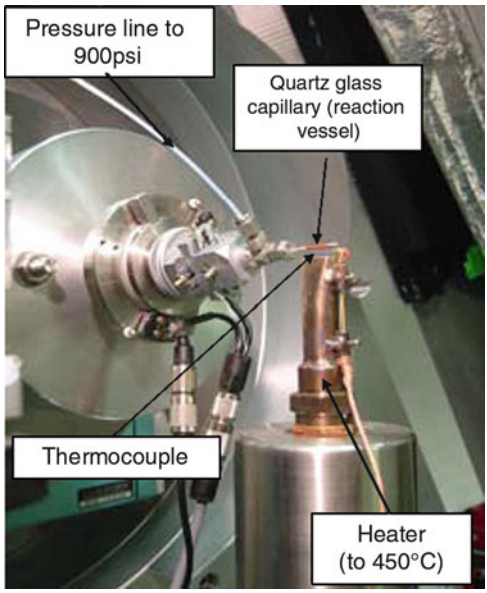

Fig. 6.4 Capillary cell used for the high pressure acid leaching experiments. This setup was used both in laboratory and synchrotron experiments

The sample was either a slurry or powder. For powdered samples the acid solution is forced into the powder by pressure. The lack of delay between fluid injection and data collection allows a long series of 2 min datasets to be collected from the exact moment of acid injection. An example dataset from the leaching experiments is shown in Fig. 6.5.

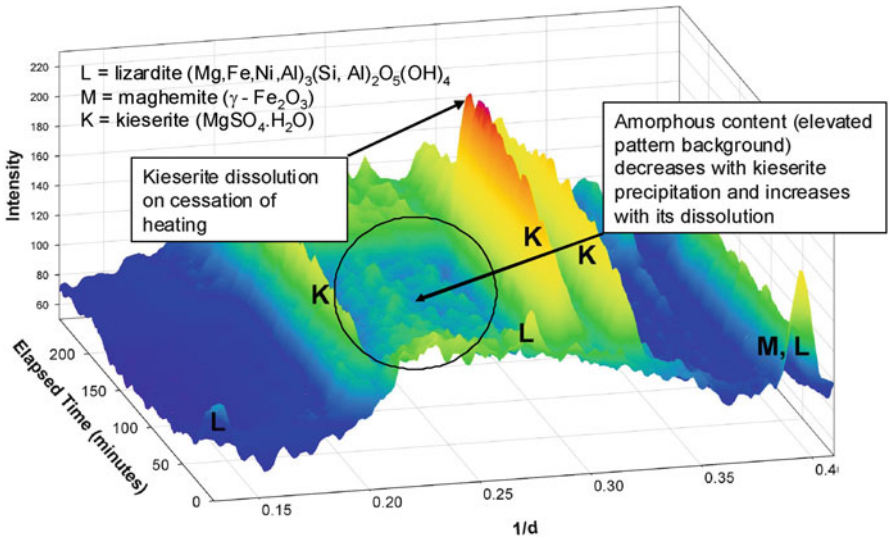

Fig. 6.5 Example dataset from high pressure acid leaching experiments

6.3.1.2 Highly Absorbing Capillary Samples

Capillary samples in a laboratory setting are usually restricted to samples with low linear absorption with CuKα – often organics. When a small quantity of a new mineral with the composition PbF_2 appeared, the use of a laboratory instrument is not the first thing that comes to mind. The use of MoKα with a 0.3 mm capillary produced decent looking data but had an excessive absorption for a publication-quality Rietveld refinement. Rather than use synchrotron radiation, AgKα radiation with a focusing primary mirror optic was used to obtain data with an acceptable absorption of $\mu R < 3$. The data was of sufficient quality for a multi-phase refinement (Fig. 6.6) of the new mineral that has the same cubic structure as synthetic β-PbF_2. This structure refinement was used in a submission to the International Mineralogical Association and corresponding journal paper [12].

6.3.2 Low Temperature Capillary Experiments

Liquid nitrogen cryostream systems are standard equipment in single crystal instruments. However, the upright goniometer of most powder diffractometers conspires to reduce the space in front the doors, and no easy access is available for the semi-flexible vacuum insulated transfer line. A customized setup was assembled using different supplied components that integrated with the diffractometer control software. The laminar flow of nitrogen gas co-axial along the capillary cools samples to 80 K without icing either the capillary or the goniometer head.

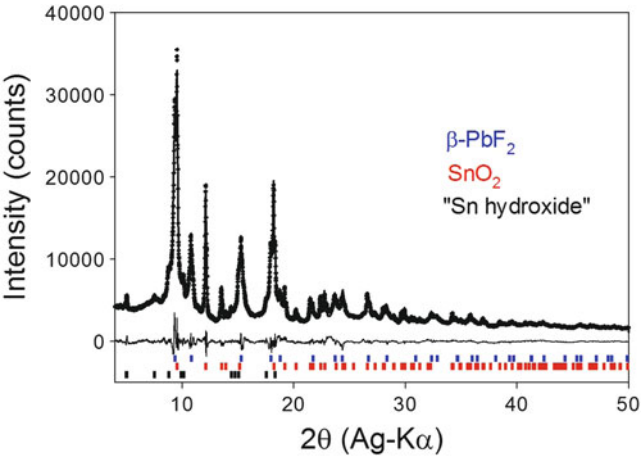

Fig. 6.6 Rietveld refinement of the β-PbF_2 mineral with the intimately associated phases SnO_2 and a new, uncharacterized "Sn hydroxide" mineral

This setup allowed for very rapid quenching of samples including liquid solvents. Combined with an optimized diffractometer configuration of a CuKα tube, focusing primary mirror and a Vantec-1 detector with a 10° window, very rapid data collection was possible. Very satisfactory data could be collected between 10° and 60° 2θ in 4 min (Fig. 6.7) to the extent that crystal structures could be determined *ab-initio* from some datasets using simulated annealing. Refinements of the structures were carried out using Variable Count Time (VCT) data [13] to rebalance the loss of intensity in the peak-rich high angle region.

6.3.3 Modified Relative Humidity (RH) Stage

Not every problem needs the design and construction of equipment from scratch. In many instances modification of an existing stage can extend its capabilities. Ron Peterson at Queens University has taken a commercial Anton Paar THC stage and modified it to better control the RH and collect data from thin layers of sample [14]. Accurate control of RH is problematic as any cold-points in the gas-circuit will lead to condensation and a drop in the RH of the gas stream. This has been tackled by using the water from a recirculating bath to make the system isothermal from the initial gas-mixing, along jacketed gas-lines and a water jacket around the chamber. Accurate RH readings from the chamber are taken using a chilled mirror hygrometer mounted as shown in Fig. 6.8. Kapton film windows and a PANalytical X'Celerator PSD detector allow for rapid data collection with CoKα to reduce fluorescence in the iron-containing samples. An example dataset from this system can be seen in Fig. 6.9, showing the phase behavior between $FeSO_4{\cdot}4H_2O$ and $FeSO_4{\cdot}7H_2O$ at a fixed temperature of 40°C but varying the RH.

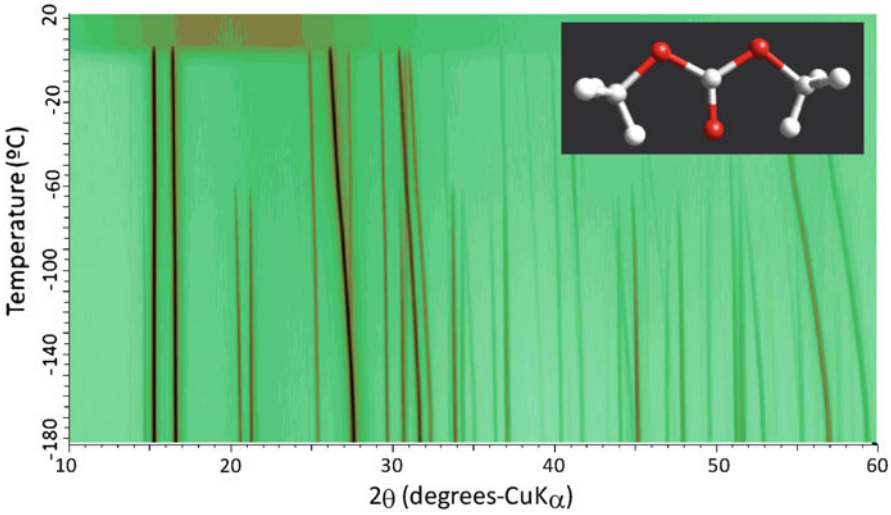

Fig. 6.7 Diffraction data from the solvent dimethyl carbonate between −180 and +20°C. Repeated rapid quenching to 82 K was used to determine reproducibility and improve particle statistics. The data were collected every 5°C and each dataset was collected in approximately 4 min

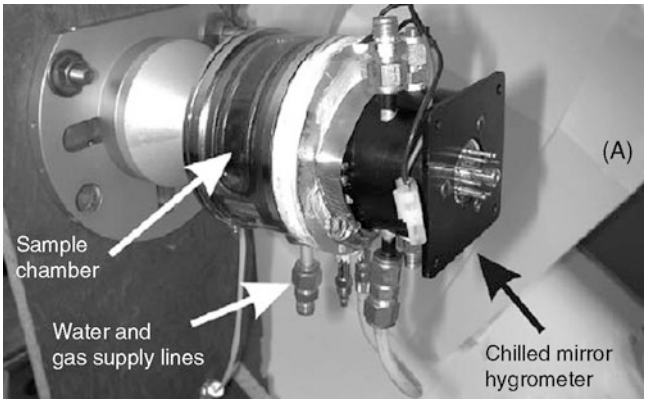

Fig. 6.8 Photo of the modified relative humidity cell showing the chilled mirror hygrometer and some of the water-jacketed gas lines

6.4 Conclusions

A good understanding of the concepts and components of a laboratory diffractometer allows for effective design for advanced experimental setups. Being open to the possibilities of non-standard configurations allows the researcher to push the limits of what is possible in the laboratory. This may involve the use of more

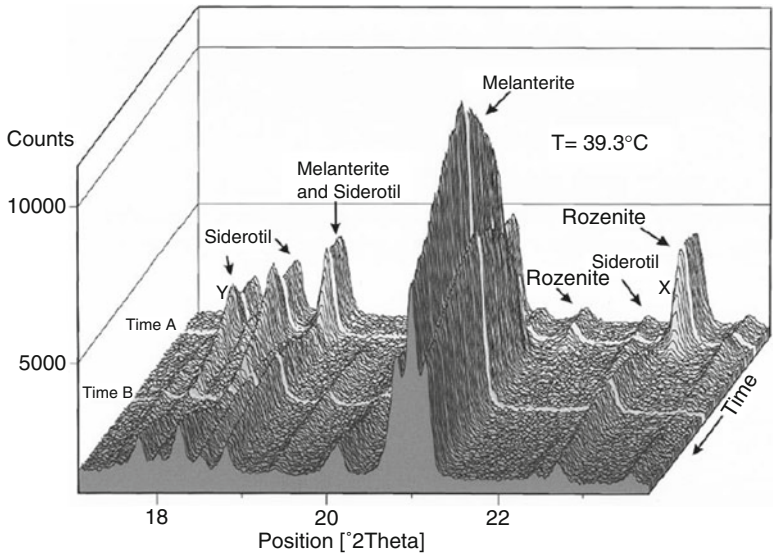

Fig. 6.9 Data showing phase behaviour between $FeSO_4 \cdot 4H_2O$ (rozenite) and $FeSO_4 \cdot 7H_2O$ (melanterite) at 40°C while varying the RH. The experiment started with RH = 57%, increased to 76% at *Time A* and reduced to 68% at *Time B*

exotic X-ray tubes, different instrument optics, customized sample environments or a combination of these. Although the time and effort required to yield results may be considerable, the potentially unique capabilities can open up new areas of research that could be very productive over an extended period.

Acknowledgments The author would like to thank Ian Madsen and Nicola Scarlett of CSIRO, Melbourne, Australia and Ron Peterson of Queens University, Kingston, Canada for kindly allowing their work to be used as examples.

References

1. Jenkins R, Snyder R (1996) Introduction to X-ray diffractometry. Wiley-Interscience, New York
2. Clearfield A, Riebenspies J, Bhuvanesh N (eds) (2008) Principles and applications of powder diffraction. Wiley-Blackwell, Oxford
3. Pecharsky V, Zavalij P (2008) Fundamentals of powder diffraction and structural characterization of materials, 2nd edn. Springer, New York
4. Dinnebier RE, Billinge SJL (eds) (2008) Powder diffraction: theory and practice. Royal Society of Chemistry, London
5. McCusker LB, Von Dreele RB, Cox DE, Louër D, Scardi P (1999) Rietveld refinement guidelines. J Appl Crystallogr 32:36

6. Whitfield PS, Nawaby AV, Blak B, Ross J (2008) Modified design and use of a high pressure environmental stage for laboratory X-ray powder diffractometers. J Appl Crystallogr 41:350
7. van Groos AF K, Guggenheim S, Cornell C (2003) Environmental chamber for powder X-ray diffractometers for use at elevated pressures and low temperatures. Rev Sci Instrum 74:273
8. Boiler and Pressure Vessel Code (2004) American Society of Mechanical Engineers. ASME, New York, USA
9. Whitfield PS, Mitchell LD (2010) In situ laboratory X-ray powder diffraction study of wollastonite carbonation using a high pressure stage. Appl Geochem 24:1635
10. Madsen IC, Scarlett NVY, Whittingham BI (2005) Pressure acid leaching of nickel laterite ores: an in situ diffraction study of the mechanism and rate of reaction. J Appl Crystallogr 38:927
11. Scarlett NVY, Madsen IC, Whittingham BI (2008) Time-resolved diffraction studies into the pressure acid leaching of nickel laterite ores: a comparison of laboratory and synchrotron X-ray experiments. J Appl Crystallogr 41:572
12. Mills SJ, Kartashov PM, Gamyanin GN, Whitfield PS, Kern A, Guerault H, Raudsepp M (2011) Fluorocronite, the natural analogue of β-PbF_2, from the Sakha Republic, Russian federation. Eur J Mineral 23:695-700
13. Madsen IC, Hill RJ (1994) Collection and analysis of powder diffraction data with near-constant counting statistics. J Appl Crystallogr 27:385
14. Peterson RC, Grant AH (2005) Dehydration and crystallization reactions of secondary sulfate minerals found in mine waste: in situ powder diffraction experiments. Can Miner 43:1171

Chapter 7
Synchrotron X-Ray Powder Diffraction

Fabia Gozzo

Abstract The large breadth of the Synchrotron Radiation X-ray Powder Diffraction (SR-XRPD) technique inevitably requires that we make a certain number of choices in its discussion. Assuming you already have some knowledge of SR and XRPD, we explore the peculiar features that arise from combining them. From the perspective of a beamline scientist, we discuss aspects influencing the beamline optics, diffractometer, detectors and sample environments with attention to details important to perform outstanding SR-XRPD experiments. We begin with a brief overview of SR characteristics and properties and finish with a few SR-XRPD highlights. An extensive literature citation is provided for those who want to delve deeper into those topics that are inevitably not completely covered here.

7.1 Properties of Synchrotron Radiation

When a charged particle is accelerated or decelerated it emits electromagnetic (e.m.) radiation. This is what happens, for example when an electron moves along a curved trajectory. If the speed v of the electron is much smaller than the speed of light c ($v \ll c$) the emitted e.m. radiation (called ***cyclotron radiation***) is uniformly distributed around the moving electron. When the electron's speed reaches values close to the speed of light ($v \sim c$), relativistic effects dramatically change the properties of the emitted radiation making it a very attractive source of radiation for a large variety of experiments. The emitted radiation is called ***synchrotron radiation*** from the specific type of particle accelerator (the electron synchrotron) in which it

F. Gozzo (✉)
Paul Scherrer Institute – Swiss Light Source, 5232 Villigen PSI, Switzerland

Excelsus Structural Solutions S.P.R.L, Brussels, Belgium
e-mail: fabia.gozzo@excels.us

U. Kolb et al. (eds.), *Uniting Electron Crystallography and Powder Diffraction*,
NATO Science for Peace and Security Series B: Physics and Biophysics,
DOI 10.1007/978-94-007-5580-2_7,

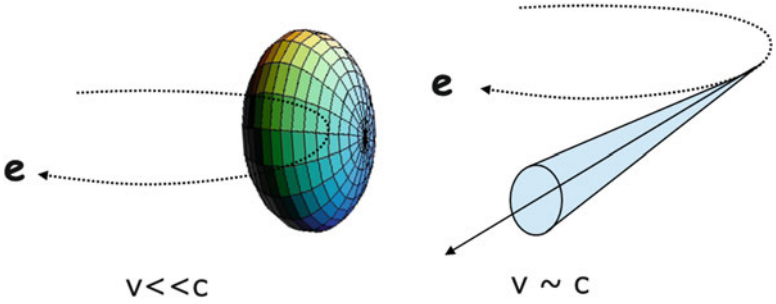

Fig. 7.1 Pictorial representation of the radiation emitted by an electron moving along a curved trajectory: when its speed **v** is much smaller than the speed of light (*left*) and **v** $\sim$ **c** (*right*)

was first observed in 1947 [1]. Figure 7.1 is a pictorial representation of cyclotron and synchrotron radiation. Today it is hard to believe that SR has not been always perceived as a precious good. Initially considered only a side negative effect in high-energy physics accelerators that needed to be investigated and minimized, it took almost 20 years for SR to become a fundamental tool in physics, chemistry, biology and medical science.

The history of synchrotron radiation is truly fascinating and the interested reader can find a few dedicated reviews in [2–4].

The main characteristics of synchrotron radiation are here summarized [5–7]:

1. **Tunable photon energy** (or wavelength) over a wide spectral range.
2. **Spectral Brightness** (or brilliance) defined as the flux per unit area of the radiation source per unit solid angle of the radiation cone per unit spectral bandwidth: **[Brightness] = [photons/s/0.1% BW/mm^2/mrad^2]** that tells us how collimated and intense the emitted photon beam is per unit spectral bandwidth. Relativistic effects ($v \sim c$) alter the angular distribution of the emitted SR, which is then concentrated around a direction tangential to the storage ring orbit (see Fig. 7.1). The divergence of the SR emitted by the single particle is approximately given by $1/\gamma$, where γ is the particle (typically electrons) energy E_e in units of its rest energy: $\gamma = E_e / m_0 c^2 = 1 \Big/ \sqrt{1 - (v/c)^2}$.
3. **Polarization**: the emitted radiation is linearly polarized with the electric vector parallel to the plane of the orbit. Above and below the plane of the orbit, it is elliptically polarized.
4. **Pulsed time structure** of the source, defined by the duration (order of psec) and the separation between pulses (order of nsec or longer if requested). It depends on the size of the ring (a fixed parameter) and the number of circulating bunches that can be changed by changing the electron current I, usually measured in mA.
5. **Coherence**: *transverse* (or *spatial* or *lateral*) and *longitudinal* (or *temporal*) coherence, the former depending on the size and angular spread of the source, the latter on its wavelength bandwidth $\Delta\lambda$.

Although these properties qualitatively characterize all SR facilities, the detailed characteristics of a given facility determine its specific numbers [5–7]. For example, the Swiss light Source is a 2.4 GeV facility, where 2.4 GeV refers to the electron energy E_e defined before. The value of E_e and the average magnetic field B produced by the storage ring dipoles (also called *bending magnets*) influence the effective radius of curvature ρ of the storage ring (i.e. the radius of curvature that the ring would have without the straight sections that host wigglers and undulators): $\rho = cte\ E_e[GeV]/B[T]$. The value of E_e and B also affects the critical photon energy: $h\nu_c = 3hc\gamma^3/4\pi\rho \Rightarrow h\nu_c\,[keV] \approx 0.67\,E_e^2[GeV]\,B[T]$, i.e. the value that divides the spectral distribution of the emitted radiation into two parts of equal total power. The critical energy obviously sets a limit to the maximum photon energy that the given facility would be able to provide out of its bending magnets.

The SR characteristics can be further tuned and enhanced if the radiation is extracted from the so-called *insertion devices* (wigglers and undulators, accommodated in the straight sections of the storage ring). Wigglers and undulators characterize 3rd generation synchrotron sources. They are **multiple magnets** that force the electrons to perform a *slalom course* instead of going along a straight line when they traverse them and, therefore, emit e.m. radiation at each oscillation. What makes multiple magnets wigglers or undulators is essentially the amount of deviation from a straight path (i.e. the size of the excursions inside the device) that they force the electrons to undergo, large for wigglers and small for undulators. This in turn depends on the spatial period λ_u of the magnet array (smaller for undulators) and the amplitude of the oscillating magnetic field B (larger for wigglers), the latter essentially defined by the magnetic properties of the materials. Figure 7.2 shows how the electron oscillations differ for wigglers and undulators.

Since λ_u and B define the wiggler- or undulator-like character of a multiple magnet (wiggler: longer λ_u, stronger B; undulator: shorter λ_u, weaker B), the best parameter to define if a periodic insertion device behaves like a wiggler or an undulator is the dimensionless K parameter, $K \approx 0.934\,B[T]\,\lambda_u[cm]$ whose value is ~1 for undulators and ≫1 for wigglers.

It should be clear that without relativistic effects, the SR wavelength would not be in the desired short-wavelength range. For example, an undulator with period $\lambda_u = 1.4$ cm would produce radiation of the order of its period, that is in the radio frequency range. Relativistic effects (Lorentz contraction and Doppler effect) shorten the λ of the emitted radiation in the laboratory reference system by the relativistic factor $2\gamma^2$:

$$\lambda_1 \approx \frac{\lambda_u}{2\gamma^2}\left(1 + \frac{K^2}{2} + \gamma^2\theta^2\right) \overset{\text{for collection angles } \theta \text{ close to zero}}{\approx} \frac{\lambda_u}{2\gamma^2}\left(1 + \frac{K^2}{2}\right).$$

For K small (<0.4) the emitted intensity is mostly concentrated at the fundamental wavelength λ_1. As K increases by applying higher B values, however, the motion of the electrons inside the multiple magnets is no longer a pure sinusoidal

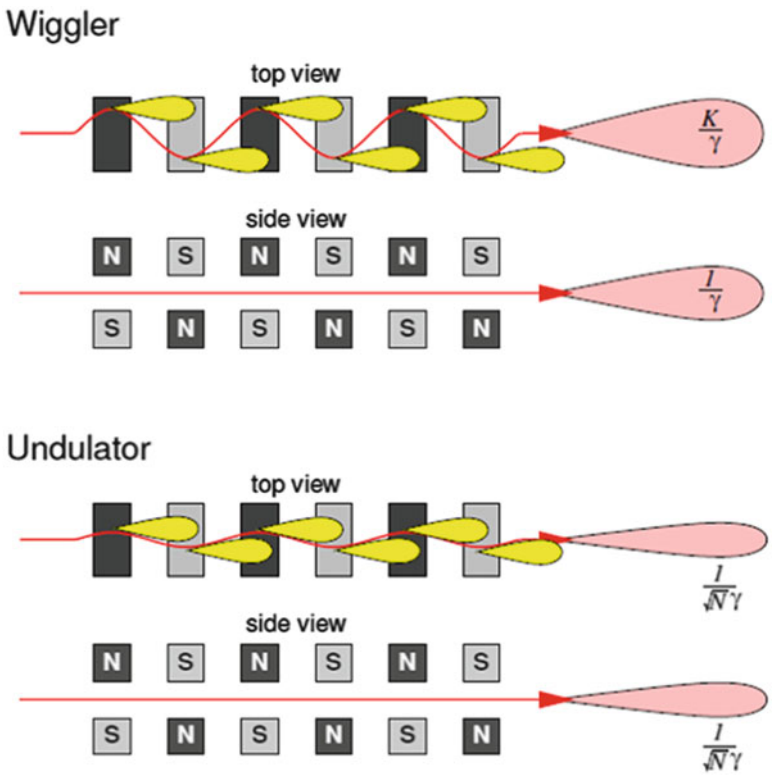

Fig. 7.2 Schematic representation of the electron beam behavior in a wiggler or an undulator (Courtesy P.Willmott [7])

transverse motion and not negligible intensity is also emitted corresponding to higher harmonics λ_n [5–7]:

$$n\lambda_n \approx \frac{\lambda_u}{2\gamma^2}\left(1+\frac{K^2}{2}\right) \approx \frac{13.056\,\lambda_u[cm]}{E_e^2[GeV]}\left(1+\frac{K^2}{2}\right).$$

The energy of the emitted radiation depends, therefore, on K but how close in energy are the harmonics and how the intensity is distributed among the fundamental wavelength and its harmonics also depends on K.[1] Tuning K, therefore,

[1]The higher is the value of K, the closer are to each other the generated harmonics. Therefore, a wiggler can be thought as an undulator with an extremely high number of harmonics so close to each other to generate a continuous bending magnet-like spectrum. The wiggler continuous spectrum is also characterized by the critical photon energy $h\nu_c \propto E_c^2$, B, where B is now the amplitude of the "local" magnetic field. Because wigglers are characterized by higher B value, they shift the maximum emitted photon energy towards values higher than those of bending magnets.

allows us to change the intrinsically discrete character of the undulator emission spectrum (spectrum with well separated emission lines) into a sort of continuous-like spectrum by smoothly swap from the fundamental λ_1 to the higher harmonics while tuning the K parameter. It remains intrinsically different from the continuous emission spectrum of the bending magnet and wiggler radiation, but it allows covering uninterruptedly a wide energy range.

Another important figure of merit characterizing SR is its angular spread in both the direction perpendicular θ_v and parallel θ_h to the storage ring plane. Referring to [6] for a derivation, we find that:

Wigglers: $\theta_v \approx \frac{1}{\gamma}; \quad \theta_h \approx \frac{K}{\gamma}$

Undulators: $\theta_v = \theta_h \approx \frac{1}{\gamma\sqrt{nN}}$ (n: harmonic number, N: number of periods)

Bending magnets: $\theta_v \approx \frac{1}{\gamma}; \quad \theta_h \approx$ no intrinsic limitation

The *unlimited* horizontal angular spread characterizing bending magnets is due to the fact that here the emission direction of the radiation changes as the electrons move inside the storage ring and, therefore, the SR is emitted in the horizontal plane as a search light. In practice, the value of θ_h is limited by the obviously limited acceptance of the beamline optics and explains why one single bending magnet occasionally serves more than one bending magnet beamline.

7.2 SR-XRPD Beamline Optics

Once SR is extracted, depending on the planned experiments, the SR beam will be ad-hoc *conditioned* by appropriate beamline optics. Beamline optics together with the choice of a given magnetic device allow the same synchrotron facility to host beamlines operating over very different energy ranges (e.g. from the infra-red up to the hard X-rays in a medium energy facility like the SLS[2]).

In the case of powder diffraction, the ultimate achievable overall angular (FWHM) resolution depends on (but not only) the energy resolution $\Delta\lambda/\lambda$ and the degree of collimation of the photon beam. Therefore, the beamline optics for a high-resolution PD station should provide a highly monochromatic and collimated beam. On the other hand, for experiments requiring fast acquisition times (e.g. time-resolved XRPD) and/or "photon-hungry" experiments (e.g. Pair Distribution Function data collection), the ability to focus the X-ray beam is very important. The beamline optics should, therefore, ideally provide dynamic focusing capabilities.

Beamline optics for SR-XRPD usually consists of a monochromator (typically a double crystal monochromator DCM) and one or two mirrors [8–12]. A channel cut can replace or follow the DCM to further improve the energy resolution [13].

[2]Since the optics needs to be optimized for the specific working energy range and the specific experiment, each beamline covers only a portion of the entire range covered by the given facility.

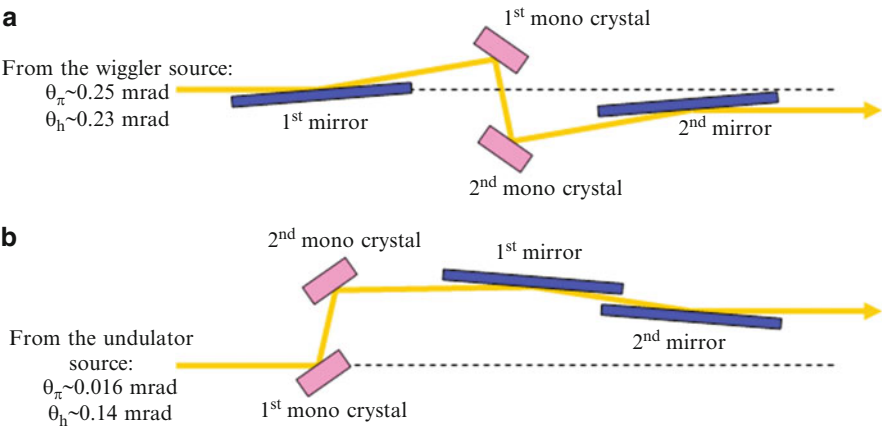

Fig. 7.3 Schematic representation of the SLS-MS beamline optics based on a wiggler (**a**) and on an undulator (**b**) source

As a representative example of SR-XRPD beamline optics, we discuss the optics characterizing the Swiss Light Source Materials Science (SLS-MS) beamline before and after its upgrade to an undulator beamline, started in October 2010.

The SLS-MS beamline started being operative in 2001 and for ∼10 years it has been the only wiggler beamline at the SLS and the one delivering the hardest X-rays (5–40 keV) [8]. Back in 2001, in medium energy facilities, a wiggler was in fact the only option to reach photon energies as high as 40 keV with usable intensities. The maximum achievable photon energy that the 2001 undulator technology was able to achieve was ∼25 keV with a U19, a prototype at that time (Schmidt Th, Ingold G, 2006, private communication).

The discovery of stronger magnetic materials (i.e. with higher B) and the improvement of the *in-vacuum* undulator technology have made it possible to design and construct a new *in-vacuum* undulator with a shorter $\lambda_u = 14$ mm period (therefore called U14 (Schmidt Th, Ingold G, 2006, private communication)). A shorter λ_u allows the energy of the fundamental and higher harmonics to be shifted towards higher values, whereas higher B values allow one to keep the K value essentially constant ($K \propto B \cdot \lambda_u$). With the prototype U14 therefore, the SLS-MS beamline still covers the 5–40 keV energy range, but with all the advantages of an undulator beamline, namely enhanced brilliance and intrinsic collimation of the beam.

Figure 7.3 shows a schematic view of the SLS-MS beamline optics based on a wiggler (2001–2010) and an undulator source (2010-on). With the wiggler source, the first optical element is a vertically collimating Rh-coated Si mirror followed by a Si(111) DCM and a second Rh-coated Si refocusing mirror. The DCM main axis of rotation defines the selected wavelength via Bragg's law: $2d_{Si(111)} \sin\theta = n\lambda$. In a DCM, however, the energy resolution totally relies on the degree of collimation of the incoming photon beam (see Fig. 7.4).

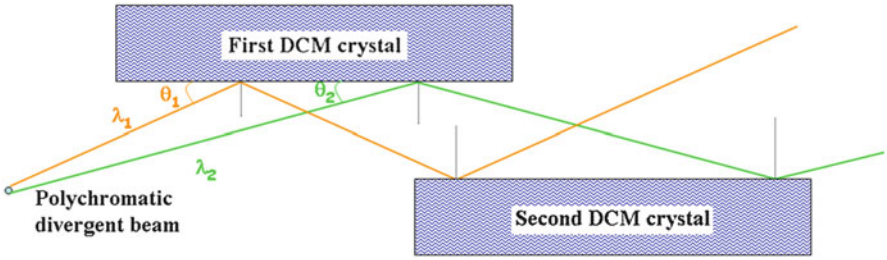

Fig. 7.4 Schematic view of a DCM: λ_1 and λ_2 are two discrete wavelengths belonging to the polychromatic divergent incident beam satisfying Bragg law for the same interplanar distance d of the DCM crystal and a combination (λ_i, θ_i) of photon wavelength and Bragg angles

We have seen that the intrinsic divergence of a photon beam generated by a wiggler source is relatively large ($\sim 0.25 \times 2.3$ mrad^2 at the SLS-MS) and, therefore, it imperatively requires the use of a collimating mirror placed before the DCM. The second crystal of the DCM is a bendable crystal which provides a collimated or a focused beam in the sagittal (horizontal) plane and guarantees a fixed beam exit height. Finally, the beam is reflected onto the second mirror, which can either be bent, and deliver a focused beam or kept flat and deliver a collimated beam (high-angular resolution set up).

The SLS-MS beamline optics based on an undulator source is also schematically described in Fig. 7.3. The photon beam can now directly be sent on the DCM being the fairly small undulator beam residual divergence in the vertical (diffraction) plane comparable with that of the wiggler beam after collimation from the first mirror. Why still having two mirrors? For essentially two reasons:

- The ability to focus the beam down to approximately 200×9 μm^2 (unfocused beam size 2.9×0.34 mm^2) for all photon energies, but to this purpose one single mirror would have been enough.
- To get an horizontal and fixed beam exit.
- Higher harmonics suppression to better than 10^{-7} that can only be achieved with two mirrors working close to the critical angle α_c for total external reflection [14].

For the purpose of the efficient suppression of the higher harmonics, whether the mirrors are placed before or after the DCM does not play any role. Placing them after the DCM, however, allows us to preserve the beam coherence when working with only one or no mirrors.

7.3 Powder Diffractometer

The mechanical properties of SR powder diffractometers need to be consistent with ultra-high-resolution requirements. Mechanical accuracy and precision (reproducibility) of ± 1–2 and resolution of 1 arcsec usually characterize SR powder diffractometers [8–13, 15].

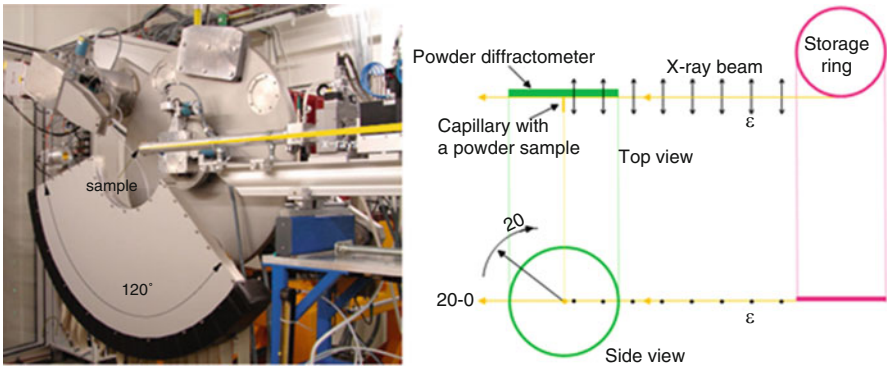

Fig. 7.5 The SLS-MS powder diffractometer (*left*). A pictorial description explaining why the diffraction plane is vertical (*right*)

Figure 7.5 (left) shows the SLS-MS powder diffractometer as an example. If you are used to laboratory diffractometers, what probably immediately strikes you is the size and weight and the vertical plane of diffraction.

The considerable size and weight guarantee high mechanical stability, whereas the choice of the vertical plane as diffraction plane is related to the linear polarization property of the SR beam in the plane of the electron orbit. As pictorially described by Fig. 7.5, if the diffraction plane is perpendicular to the electron orbit (storage ring plane), the electric field $\boldsymbol{\varepsilon}$ associated with the incoming e.m. radiation will always be at 90° with respect to the scattered beam for all 2θ values. In other words, there will not be a 2θ dependence of the scattered intensity from the 2θ and the polarization factor $P = 1$.

The SLS-MS powder diffractometer consists of three coaxial independent rotary tables and it is the result of a joint SLS and Rotary Precision Instrument® development project. The central table (ω-axis) hosts the sample or sample environment. The other two tables host two independent detection systems: a multi-crystal analyzer detector [16] and a wide-angle (120°) silicon solid state microstrip 1-D position sensitive detector (MYTHEN II) [17] that we discuss later.

7.4 Detectors

A comprehensive overview of detectors is beyond the scope of this chapter. Through examples of detectors widely used at synchrotron facilities, however, we define and discuss a few relevant detector-related concepts, namely ***angular selectivity***, ***position sensitivity***, ***point-,1D-*** or ***2D-***detectors, ***direct*** or ***indirect conversion***, ***single-photon-counting*** or ***integrated*** detectors.

Angular selectivity refers to the selection of the diffracted beam by means of a crystal (called, therefore***, crystal analyzer***) oriented at the appropriate Bragg angle, before reaching the detector. Without a crystal in the secondary beam, the diffracted rays are assigned an angular value based on the position at which they hit the detector, therefore called ***position-sensitive*** detector. Intensity that arrives at the analyzer crystal from inelastic scattering (i.e. fluorescence emission, Compton scattering), air scattering is suppressed providing an ultra-high angular (FWHM) resolution, a high signal-to-noise (S/N) and a high signal-to-background (S/B). In addition to that, the angular selectivity makes the angular (FWHM) resolution independent of the sample dimension (capillary diameter in transmission measurements) and its accurate positioning at the center of the diffractometer.

Analyzer detectors – These are detectors (typically point-detectors) that include a crystal analyzer in the secondary beam. Angular selectivity is very costly in terms of diffracted intensity and a smart solution to recover some of the lost intensity was found by Hodeau et al. in 1998 [16] with their ***multicrystal analyzer detector*** design. Their idea consisted in placing n independent analyzer crystals as a fan at a fixed offset and simultaneously collecting the diffracted signal with the detector following each crystal. The counting statistics are, then, increased by n but the counting time still remains of the order of min or hours.

Position sensitive detectors – These are 1- or 2-D detectors that identify the value of the 2θ scattering angle from the position at which the diffracted ray reaches the detector. 2-D detectors record the full Debye-Scherrer rings whereas the 1-D detectors only one section of them, whose width is defined by the detector aperture and make, therefore, the implicit assumption that the selected sections are representative of the whole rings. The MYTHEN detector is a 1-D position silicon solid state detector. It is an *in-house* development at the Paul Scherrer Institut conceived for time-resolved powder diffraction experiments [17]. It is a modular 1-D detector with over 30,000 elements covering an angular range of 120° in 2θ (24 modules, each covering 5°). Depending on the dynamic range (4–24 bits), the read out time ranges between 90 and 250 μs whereas its frame rate (1 frame = 1 diffraction pattern) ranges from 10 Hz (24 modules, 24 bits) to 600 Hz (1 module, 4 bits). Figure 7.6 explains the principle of operation of solid state detectors. MYTHEN performances in terms of high angular (FWHM) and d-spacing resolution, S/N and S/B are comparable with those of analyzer detectors with a counting efficiency at least two orders of magnitude higher and acquisition times several orders of magnitude shorter. These outstanding characteristics make MYTHEN also ideal for the structural analysis of radiation-sensitive materials, such as organic compounds, and for applications to total scattering techniques for which high real space resolution data (i.e. high values of the momentum transfer $Q = 2\pi\sin\theta/\lambda$), high S/B, high S/N ratios and a remarkable counting statistics over the entire angular range are of paramount importance.

As all position-sensitive detectors, MYTHEN does not perform an angular selection of the diffracted beam and is, therefore, sensitive to inelastic scattering

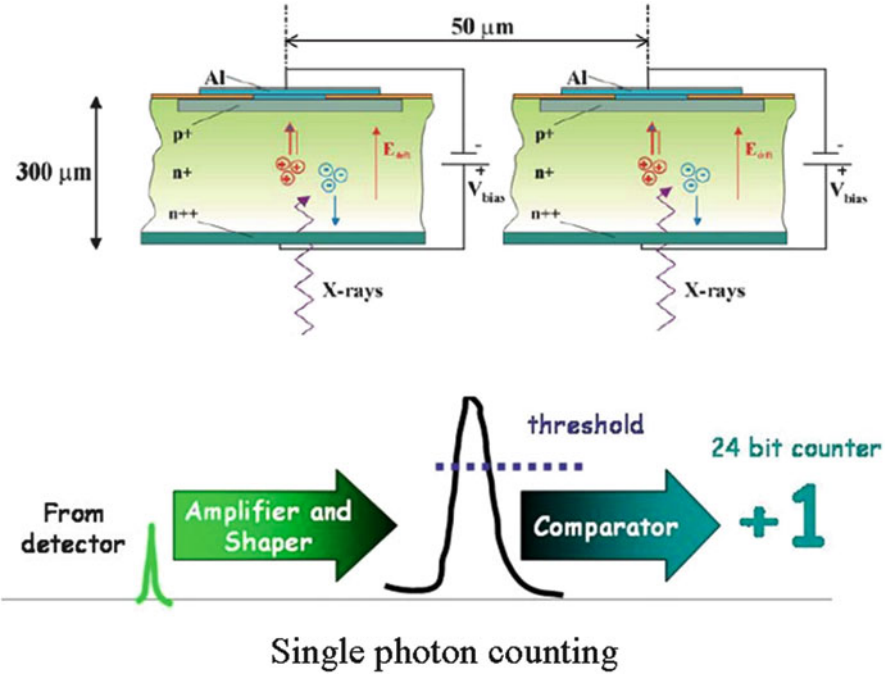

Fig. 7.6 Principle of operation of a solid state detector like MYTHEN

signals and its intrinsic angular resolution (∼0.004° in 2θ) is relaxed by the sample dimension. What makes MYTHEN very special among conventional position sensitive detectors, however, is connected to the fact of being a ***direct conversion single photon counting*** detector. When X-ray photons arrive on the silicon sensor (see Fig. 7.6), they are absorbed and produce free charge (electron–hole pairs) whose number is proportional to the energy of the X-ray photon. The created charge is, then, separated by a voltage V_{bias} applied to the junction and travels to the electrodes where it results in a pulse. The pulse is then amplified, shaped and compared to a user-defined threshold. Only the signal whose amplitude is above this threshold is counted. Properly chosen for the given experiment, the threshold rejects, therefore, all unwanted signal (e.g. electronic noise, fluorescence signal).

Solid state detectors are, therefore, based on the production of charge directly from the X-ray photons without the intermediate conversion into visible light in a phosphor screen (which normally poses limitations on the spatial resolution because of light diffusion). Their efficiency depend on the photon energy and for Si and 300 μm sensor thickness (as for MYTHEN) is 100% at 7 keV but already 15% at 25 keV, making them not ideal for photon energies above 40 keV. The PSI detector group is presently working on thicker Si sensors and detectors made with different absorbing materials.

For powder diffraction, 2-D detectors (e.g. **I**mage **P**late, **C**harged **C**oupled **D**evices, amorphous-Si **F**lat **P**late, **P**ixel **D**etectors) are also often employed. They simultaneously collect full Debye-Scherrer rings and their direct-space resolution is directly proportional to their size and inversely proportional to the angular (FWHM) resolution. With MYTHEN, the FWHM and d-spacing resolutions are instead decoupled.

In Image Plate (IP) detectors [18], the core of the detector is a storage phosphor screen and the creation of an image requires illuminating the plate twice: the first exposure, to the radiation of interest, "writes" the image, and the second, to a visible-laser, "reads" the image. After the initial exposure, excited electrons in the phosphor material remain "trapped" in color centers (so-called F-centers) in the crystal lattice that constitutes the image plate until stimulated by a second illumination. The emitted visible light is, then, recorded by a photomultiplier. In terms of efficiency, dynamic range and read-out times the IP detectors are not very competitive and CCD or amorphous-Si Flat Plate detectors are often preferred.

At the APS 1-ID beamline [19], a high-sensitivity (quantum efficiency $>65\%$), fast-readout (up to 30 Hz) a-Si Flat Plate (FP) detector has been installed for in-situ fast PDF acquisitions at high Q values (Qmax >35 Å-1). FP detectors are based on amorphous-silicon thin-film-transistor (TNT)/photodiode arrays coupled to X-ray scintillators. The coupling with scintillators that convert the X-rays into visible light makes them very efficient even with the hard X-ray photon beams.

Charged Coupled Devices (CCD) detectors performances are, to some extend, in between the IP and the a-Si FP detectors. Reference [19, Table 1] provides a suitable comparison among these three different detector technologies. CCDs consist of a photoactive region (usually epitaxial p^+-Si) and a transmission region (the CCD, properly speaking). As for the IP and the a-Si FP, it is based on the conversion of the X-rays into visible light by means of scintillators.

All the 2-D detectors discussed above are ***integrating detectors***. They collect the totality (elastically and inelastically scattered plus noise) of the signal reaching the detector without setting a discriminating threshold, as MYTHEN does.

The 2-D version of MYTHEN is the PILATUS pixel detector [20]. Apart from all the advantages of the single photon counting mode discussed for MYTHEN, PILATUS has a readout time of 5 ms, a dynamic range of 20 bits and a pixel size of $172\ \mu m \times 172\ \mu m$. Pixel 2D detectors have, however, quite small area/pixel ratio, which often make IPs and CCDs a preferred choice for XRPD [17] MYTHEN and PILATUS are now commercialized by the spin-off company DECTRIS [21].

7.5 SR-XRPD Highlights

The remarkable developments of instrumentation, computer technology, experimental techniques (e.g. anisotropic thermal expansion and texture methods by Brunelli et al. [22] and Wessels et al. [23] and methodologies (e.g. global optimization techniques by David and Shankland [24]; resolution bias algorithm by

Altomare et al. [25]; charge flipping by Oszlanyi et al. [26]) that have characterized the powder diffraction technique of the last 10–15 years, have made it an undoubtedly powerful tool for both structural solution and refinement and microstructural analysis of a large variety of materials. Not only is powder diffraction a valuable alternative to single crystal diffraction when appropriate single crystals cannot be obtained, but it is often the preferable choice for *in-situ*, non-ambient and time-resolved analyses and for the analysis of materials at the nanoscale [27, 28].

We discuss here a few experiments performed at synchrotron facilities as examples of recent SR-XRPD applications. They do not constitute an overview of outstanding SR-XRPD applications, but a restricted choice due to the limited available time and space. Not discussed but of special note are SR-XRPD applications to the structural analysis of proteins that will be the subject of two chapters by Irene Margiolaki and Jonathan Wright, pioneers in this field with their co-workers at the ESRF [29]; the *in-situ* studies of polymorphism of chocolate where polymorphic transformation in coca butter have been studied *in-situ* and in real time as a function of temperature and in parallel to the rheological properties of fats [30]; the study of the dependence of the photocatalytic activity of TiO_2 nanocrystals (a *smart textile* material of industrial interest) on the nanocrystals size and shape by means of a combination of SR-XRPD and total scattering methods based on the Debye function [31].

7.6 Structural Solution of Small Organic Molecules

Ab-initio structural solution and refinement of small organic molecular compounds (e.g. pharmaceuticals) is one of the fields where advanced SR-XRPD instrumentation and new methodologies are perfectly married to each other. Although successful structural solutions from powders have been achieved using laboratory data [32], for increased complexity of the system under investigation the outstanding quality of SR-XRPD data is often the key for the success of their structural solution. Small organic molecular compounds, however, are often strongly affected by radiation damage, a normally unavoidable side effect of SR [33]. Therefore, the combination of SR properties with the very high counting efficiency of the SR detectors discussed before, allows collecting data of outstanding quality before irreversible changes in the compound occur. At the SLS-MS powder beamline we have devoted considerable efforts to optimizing the beamline optics, the calibration of the 1-D single-photon counting detector MYTHEN II, the experimental set up and the data collection strategy. Furthermore, the remarkable counting statistics of MYTHEN II even at subsec acquisition times allows us to study *in-situ* the details of structural transformations. Figure 7.7 shows as an example the diffraction patterns of S-bupivacaine hydrochloride, a long-acting anesthetic drug of the amide type used for local anesthesia [34], recorded at the SLS-MS powder station using the Si(111) multicrystal analyzer detector and MYTHEN II at 50% reduced beam intensity.

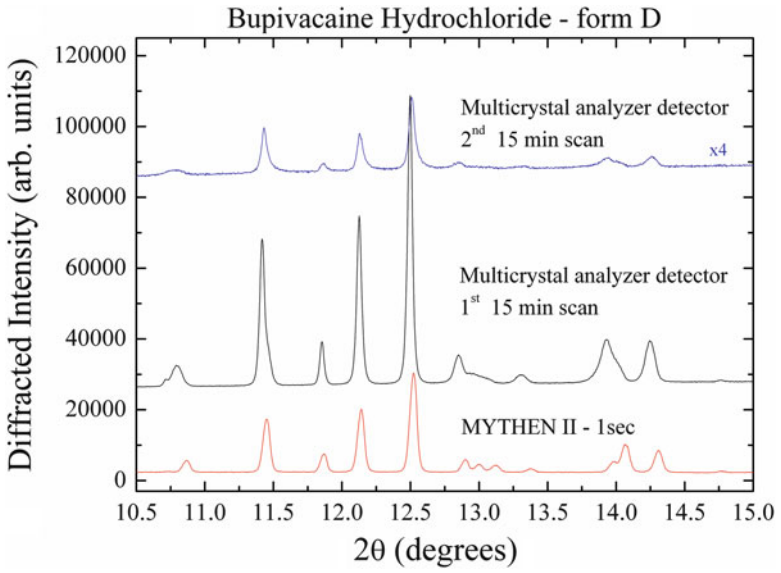

Fig. 7.7 Detail of the SR-XRPD pattern of form D of S-bupivacaine recorded at 12 keV with the multicrystal detector for 15 min and with MYTHEN II in 1 s

The first and second powder diffraction patterns recorded by the multicrystal analyzer detector were acquired for 15 min by continuously moving the detector arm between 0° and 50° in 2θ, whereas several 1 s diffraction patterns were collected with MYTHEN covering simultaneously 120° in 2θ. A comparison of the first and second multicrystal analyzer diffraction patterns clearly shows that the first 15 min of measurements already damaged the sample and that the damage was already not negligible after the acquisition of the first 10°. The structures at 13° and 14° are strongly compromised by the radiation damage. Successive multiple 1 s data acquisition with MYTHEN, always at reduced intensity, showed that the powder was stable for at least 2–3 min (Fig. 7.7 shows one of these 1 s runs). While the analyzer detector data were not usable for indexation and structural solution, MYTHEN data delivered a successful structural solution of form D of bupivacaine in $P2_12_12_1$ space group type (Gozzo et al., 2010, personal communication).

Another example of structural solution and refinement achieved with MYTHEN II data is the study of the polymorphism of carprofen, which undergoes a subtle isostructural transformation as a function of temperature and whose structure was not accessible with analysis of laboratory data [35]. Figure 7.8 shows the molecular packing of the metastable form of carprofen (left) and its molecular scheme (right) indicating the internal degrees of freedom of the molecule. It was found that the main difference between polymorph I and II structures was the rotation of the propane skeleton about the C–C bond (torsion 1 in Fig. 7.8) and that form II was characterized by configurational disorder.

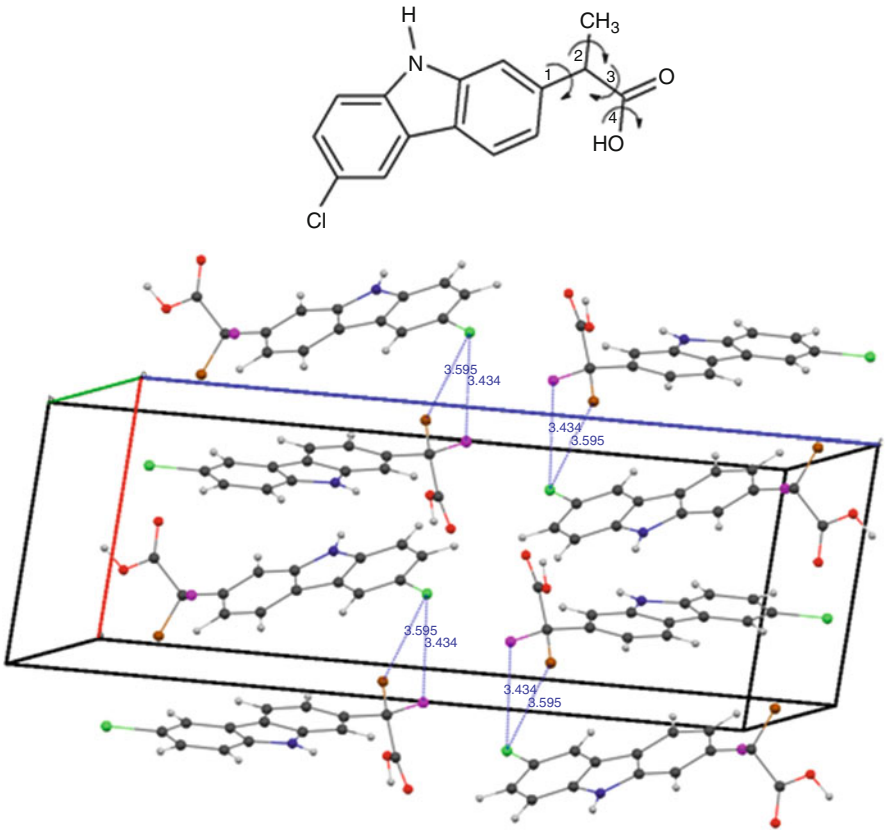

Fig. 7.8 Molecular packing diagram of polymorph II of carprofen showing both the carbon atom of the predominant and the disordered configurations. The H atoms of the methyl group directly involved in the configurational disorder have been omitted for clarity. A complete discussion of the structure of carprofen can be found in [35]

7.7 Microwave-Assisted Heating

Microwaves can be efficiently used as source of heating during the chemical synthesis of materials. Due to its low energy consumption and ultrafast heating and cooling rates, the latter essential for the preservation of nanoscale features in bulk nanostructured solids, microwave-assisted heating has recently received a lot of attention as a valid alternative to conventional methods [36, 37]. Its development and scaling up to industrial applications depends, however, on the understanding of the mechanisms behind it, which in turn is related to the ability to follow in-situ and in real time the evolution of materials during heating and cooling. In 2007, Vaucher, Nicula and co-workers [37] have performed at the SLS-MS powder station the first in-situ microwave heating experiments using synchrotron radiation and MYTHEN I detector (Fig. 7.9).

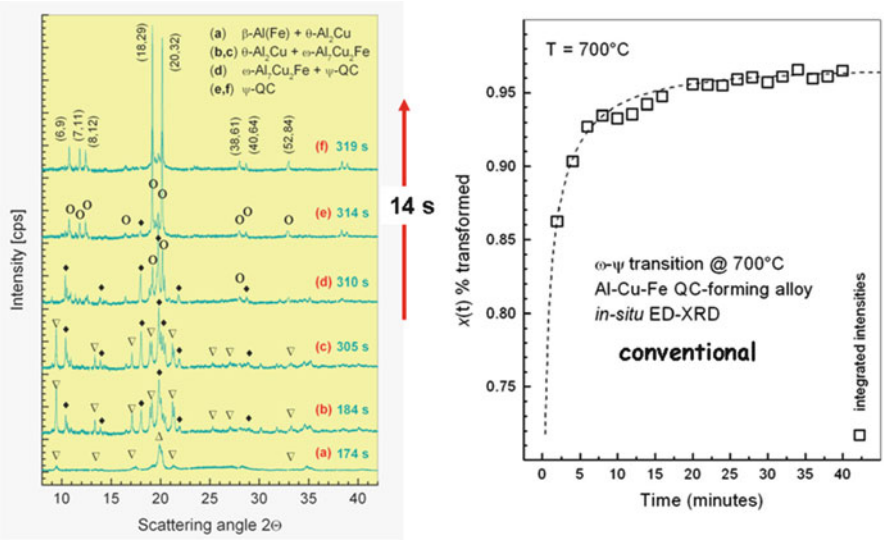

Fig. 7.9 *Left*: sequence of solid-state transitions leading to the formation of single-phase quasicrystals [35]. *Up-triangles* β-Fe(Al); *down-triangles* θ-Al2Cu; *diamonds* ω-Al7Cu2Fe; *open circles* ψ-phase. *Right*: rate of transformation of θ → ψ phases at 700 C with conventional heating. Courtesy Sebastian Vaucher

Figure 7.9 (left) shows the evolution in time of the solid state phase transformations during microwave heating of metallic nanopowders of Al, Cu and Fe to form single phase quasicrystals. The comparison of the transformation rate between microwave assisted and conventional heating (Fig. 7.9, right) shows for the former an exceptional rate enhancement. After 40 min at 700°C only 96% of the sample is transformed into the QC phase with conventional heating, whereas the same transition is fully completed in less than 10 s if microwaves are employed.

7.8 Self-Propagating Exothermic Reactions

Ultra-fast SR-XRPD experiments were performed by Fadenberger and co-workers to study *in-situ* the dynamics of structural transformations occurring in Self-Propagating Exothermic Reactions (SPER). For the first time this was performed with the angular (FWHM) resolution necessary to identify and follow the formation and evolution of phases [38]. Self-Propagating Exothermic Reaction (SPER) are self-sustained thermal processes that interest industry for their reduced energy consumption via targeted delivery of the heat in the desired area. The understanding of the mechanisms driving self-propagating reactions requires monitoring the reactions and the induced phase transformations as they occur. The high flame front

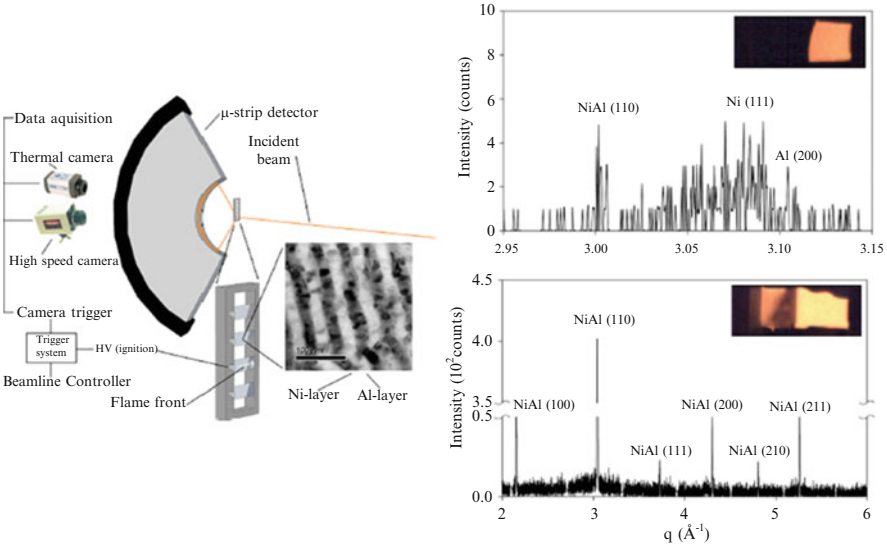

Fig. 7.10 *Left*: SPER experimental set-up for *in-situ* SR-XRPD with MYTHEN II. *Right above*: 1–1.125 ms after ignition (acquisition time of 0.125 ms) showing superimposed peaks of reactants and the formed NiAl. *Right, below*: identification of NiAl phase 8–9 ms after ignition (acquisition time of 1 ms). Courtesy Konrad Fadenberger

velocities (1–20 m/s) characterizing SPER require, therefore, diffraction analysis at the submilliseconds scale with angular resolutions and statistics appropriate for phase identification.

Figure 7.10 shows the experimental set up of an *in-situ* SPER experiment performed on nanoscale foils of $Ni_{0.9}V_{0.1}$-Al multilayers at the SLS-MS beamline using MYTHEN II detector, in combination with high-speed (HS) optical and infrared (IR) imaging [36].The experiment starts with the foil ignition via a high-voltage electric spark generated by a central trigger system, which simultaneously triggers the HS and thermal cameras and the MYTHEN II detector.

The HS and thermal cameras start recording optical and thermal images while MYTHEN starts recording successive XRPD patterns. XRPD frames were recorded using 0.125, 0.25, 1 and 5 ms acquisition times with dead times between successive frames of 0.125 or 20 ms, depending on the acquisition time. Figure 7.10 shows the complex SPER experimental set up and two of the multiple XRPD frames recorded by MYTHEN II at 0.125 ms (above) and 1 ms (below) acquisition time at 1 and 8 ms from ignition, respectively. The patterns remarkably show the change in composition of the films occurring over extremely short times.

Acknowledgements Behind successful SR beamlines there is always a team of people (always smaller than necessary) working enthusiastically together and sharing the many heavy tasks. At the SLS-MS we are, in alphabetic order: Antonio Cervellino, Fabia Gozzo, Michael Lange,

Dominik Meister, and Philip Willmott. At the MS, we also have the chance to closely work with a fantastic detector group at PSI, which has delivered at PSI and worldwide outstanding new detector technology. MS is particularly grateful to Bernd Schmitt and Anna Bergamaschi.

References

1. Elder FR, Gurewitsch AM, Langmuir RV, Pollock HC (1947) Radiation from electrons in a synchrotron. Phys Rev 71:829–830
2. Blewett J (1998) Synchrotron radiation – early history. Synchrotron Radiat 5:135–139
3. Baldwin GC (1975) Origin of synchrotron radiation. Phys Today 9
4. Helliwell JR (1998) Synchrotron Radiation and Crystallography: the First 50 Years. Acta Crystallogr A 54:738–749
5. Margaritondo G (1988) Introduction to synchrotron radiation. Oxford University Press, New York
6. Margaritordo G (2002) Elements of synchrotron light. Oxford University Press, New York
7. Willmott P (2011) An introduction to synchrotron radiation: techniques and applications. Wiley, Chichester
8. Patterson BD, Abela R, Auderset H, Chen Q, Fauth F, Gozzo F, Ingold G, Kuehne H, Lange M, Maden D, Meister D, Pattison P, Schmidt T, Schmitt B, Schulze-Briese C, Shi X, Stampanoni M, Willmott PR (2005) The materials science beamline at the Swiss Light Source: design and realization. Nucl Instrum Methods A 540:42–46
9. Toby BH, Huang Y, Dohan D, Carroll D, Jiao X, Ribaud L, Doebbler JA, Suchomel MR, Wang J, Preissner C, Klinea D, Mooneya TM (2009) Management of metadata and automation for mail-in measurements with the APS 11-BM high-throughput, high-resolution synchrotron powder diffractometer. J Appl Crystallogr 42:990–993
10. Wallwork KS, Kennedy BJ, Wang D (2007) The High Resolution Powder Diffraction Beamline for the Australian Synchrotron. AIP Conf Proc 879(1):879–882
11. Tang CC, Roberts MA, Azough F, Leach C, Freer R (2002) Synchrotron X-ray Diffraction Study of Ba4.5Nd9Ti18O54 Microwave Dielectric Ceramics at 10-295 K. J Mater Res 17:675–682
12. Masson O, Dooryhee E, Cheary RW, Fitch AN (2001) Instrumental Resolution Function of the ESRF Powder Diffraction Beamline BM16. Mater Sci Forum 300:378–381. See also: http://www.esrf.eu/UsersAndScience/Experiments/StructMaterials/ID31
13. Van Beek W, Safonova OV, Wiker G, Emerich H (2011) SNBL, a dedicated beamline for combined in situ X-ray diffraction, X-ray absorption and Raman scattering experiments. Ph Transit 84(8):726–732
14. Birkholz M (2006) Thin film analysis by X-ray scattering. Wiley, Weinheim
15. Gozzo F, Schmitt B, Bortolamedi T, Giannini C, Guagliardi A, Lange M, Meister D, Maden D, Willmott PR, Patterson BD (2004) First experiments at the Swiss Light Source Materials Science beamline powder diffractometer. J Alloy Compd 362:206–217
16. Hodeau J-L, Bordet P, Anne M, Prat A, Fitch AN, Dooryhee E, Vaughan G, Freund A (1998) Nine crystal multianalyzer stage for high-resolution powder diffraction between 6 and 40 keV. SPIE Proc 3448:353–361
17. Bergamaschi A, Cervellino A, Dinapoli R, Gozzo F, Henrich B, Johnson I, Kraft P, Mozzanica A, Schmitt B, Shi X (2010) The MYTHEN detector for X-ray powder diffraction experiments at the Swiss Light Source. J Synchrotron Radiat 17(5):653–668
18. Chupas PJ, Qiu X, Hanson JC, Lee PL, Grey CP, Billinge S (2003) Rapid-acquisition pair distribution function (RA-PDF) analysis. J Appl Crystallogr 36:1342–1347
19. Chupas PJ, Chapman KW, Lee PL (2007) Applications of an amorphous silicon-based area detector for high-resolution, high-sensitivity and fast time-resolved pair distribution function measurements. J Appl Crystallogr 40:463–470

20. Schlepuetz CM, Herger R, Willmott PR, Patterson BD, Bunk O, Broennimann C, Henrich B, Huelsen G, Eikenberry EF (2005) Improved data acquisition in grazing-incidence X-ray scattering experiments using a pixel detector. Acta Crystallogr A 61:418
21. See extensive technical information on the company web site at: http://www.dectris.com
22. Brunelli M, Wright JP, Vaughan GBM, Mora AJ, Fitch AN (2003) Solving Larger Molecular Crystal Structures from Powder Diffraction Data by Exploiting Anisotropic Thermal Expansion. Angew Chem 115:2075–2078
23. Wessels T, Baerlocher C, McCusker LB (1999) Single-crystal-like diffraction data from polycrystalline materials. Science 284:477–479
24. David WIF, Shankland K (2008) Structure determination from powder diffraction data. Acta Crystallogr A 64:52–64
25. Altomare A, Cuocci C, Giacovazzo C, Maggi S, Moliterni A, Rizzi R (2009) Correcting electron-density resolution bias in reciprocal space. Acta Crystallogr A 65:183–189
26. Oszlanyi G, Suto A, Czugler M, Parkanyi L (2006) Charge flipping at work: a case of pseudosymmetry. J Am Chem Soc 128:8392–8839
27. David WIF, Shankland K, McCusker LB, Baerlocher C (eds) (2002) Structure determination from powder diffraction data. Oxford University Press, Oxford
28. Guagliardi A, Masciocchi N (eds) (2010) Diffraction at the nanoscale: nanocrystals, defective & amorphous materials. Insubria University Press, Como
29. Margiolaki I, Wright JP, Fitch AN, Fox GC, Von Dreele, RB (2005) Synchrotron X-ray powder diffraction study of hexagonal turkey egg-white lysozyme. See also: Powder crystallography on macromolecules. Acta Crystallogr D61:423–432. See also: Margiolaki I, Wright, JP (2008) Acta Crystallogr A64:169–180
30. Padar S, Merhle YE, Windhab EJ (2009) Shear-induced crystal formation and transformation in cocoa butter. Cryst Growth Des 9:4023–4031; See also: ESRF highlights at www.esrf.eu/UsersAndScience/Publications/Highlights
31. Cernuto G, Masciocchi N, Cervellino A, Colonna GM, Guagliardi A (2011) Size and Shape Dependence of the Photocatalytic Activity of TiO2 Nanocrystals: A Total Scattering Debye Function Study. J Am Chem Soc 133:3114–3119
32. Harris KDM (2002) Structure determination of molecular materials from powder diffraction data. Curr Opin Solid State Mater Sci 6:125–130
33. Niederwanger V, Gozzo F, Griesser U (2009) Characterization of Four Crystal Polymorphs and a Monohydrate of S-Bupivacaine Hydrochloride (Levobupivacaine Hydrochloride). J Pharm Sci 98:1064–1074
34. Holton JM (2009) A beginner's guide to radiation damage. J Synchrotron Radiat 16:133–142
35. Bruni G, Gozzo F, Capsoni D, Bini M, Macchi P, Simoncic P, Berbenni V, Milanese C, Girella A, Ferrari S, Marini A (2011) Thermal, Spectroscopic, and Ab Initio Structural Characterization of Carprofen Polymorphs. J Pharm Sci 100(6):2321–2332
36. Vaucher S, Nicula R (2008) Frontiers in microwave process monitoring. Chem Today 26(3):38–39
37. Vaucher S, Nicula R, Catala-Civera JM, Patterson B, Schmitt B (2008) In situ synchrotron radiation monitoring of phase transitions during microwave heating of Al–Cu–Fe alloys. J Mater Res 23(1):170–175
38. Fadenberger K, Gunduz IE, Tsotsos C, Kokonou M, Gravani D, Brandstetter D, Bergamaschi S, Schmitt B, Mayrhofer PH, Doumanidis CC, Rebholz C (2010) In situ observation of rapid reactions in nanoscale Ni-Al multilayer foils using synchrotron radiation. Appl Phys Lett 97:144101

Chapter 8
Ultrafast Powder Diffraction

Andy Fitch and Caroline Curfs

Abstract An overview is given of the use of powder synchrotron-X-ray and neutron diffraction to study very fast physical or chemical processes that require time resolution of 500 ms or less. The experimental requirements to obtain data of good quality are considered, including the incident flux, detector characteristics, and the different strategies possible for irreversible and reversible processes. The latter are accessible via a stroboscopic approach whereas the former require the maximum rates of data acquisition. Some recent studies are described, drawn from the areas of combustion synthesis, metallurgy and catalysis. The exploitation of the bunch structure of a synchrotron ring to obtain time resolution in the sub-ns range with the pump-probe stroboscopic approach is also illustrated.

8.1 Introduction

An important use of powder diffraction is in the study of samples that are undergoing some sort of structural modification of a physical or chemical nature. Such experiments are often designed to investigate the kinetics and the mechanism of the process, which can be a phase transition caused by a change of the temperature, pressure or other external condition, or a chemical reaction taking place in the sample. Modern powder instruments, particularly at sources of penetrating radiation such as neutrons or high-energy synchrotron X-rays, allow sophisticated sample environments to be exploited, with great flexibility in the design of *in-situ* experiments to study evolving systems. The question naturally arises as to just how fast a process can be usefully measured.

A. Fitch (✉) • C. Curfs
ESRF, BP 220, F-38043 Grenoble Cedex, France
e-mail: fitch@esrf.fr; curfs@esrf.fr

U. Kolb et al. (eds.), *Uniting Electron Crystallography and Powder Diffraction*,
NATO Science for Peace and Security Series B: Physics and Biophysics,
DOI 10.1007/978-94-007-5580-2_8,

For measuring rapidly there are several technical issues to consider. For example, rapid processes require powder diffraction patterns to be recorded with appropriate time resolution – on the timescale of s, ms, μs, or faster still? – needing a detector system that can acquire data and be read out fast enough. However, simply registering patterns at enormous speed is of little use if the quality of the data is not sufficient to reveal the relevant details of the sample on that time scale. For the fastest, irreversible processes therefore, both high flux at the sample and efficient detectors are required. A high flux at the sample can be obtained by appropriate design of the source and instrumental optics, possibly focusing, and maximizing the energy spread of the radiation used to probe the sample.

For reversible processes, the stroboscopic approach can be used, in which the process under investigation is cycled and diffraction patterns registered during a small time window are accumulated over a number of cycles, progressively building up the statistical quality of the pattern. During the course of the experiment, the time window probes different parts of the cycle so as to cover it as required.

As a general rule, speed has to be traded against *d*-spacing or angular resolution. High resolution involves selecting only those neutrons or X-rays with an energy lying in a narrow range and whose trajectory from the source to the detector via the sample follows a stringently defined path (i.e. with a low divergence for the radiation incident on the sample and a tightly defined angular acceptance range for the detector, so as to have an exact measure of the Bragg angle θ). This necessarily excludes a large fraction of the photons or neutrons from the source or scattered by the sample which do not fulfill the criteria and so is a relatively inefficient process. Rapidly acquiring data of adequate statistical quality for meaningful analysis requires the maximum number of photons or neutrons to contribute to the diffraction pattern. Thus the selection criteria on the recorded radiation need to be relaxed by increasing the energy spread of the radiation and by allowing more pathways through the instrument (greater divergence), thus reducing the overall resolution.

8.2 Instrumentation

Fast data collection requires a fixed multi-channel detector system that can record the whole of the diffraction pattern essentially in one cycle. Scanning a detector system through the *d*-spacing range of interest necessarily takes a few seconds so is too slow to measure the fastest processes.

If working with monochromatic radiation and an angular-dispersive instrument then a fast-readout two-dimensional area detector or a one-dimensional position sensitive detector is the system of choice. 2-D detectors that have been found suitable for use with hard X-rays include the Frelon camera, based on CCD technology, and developed at the ESRF [1], and commercially available large flat-panel detectors, developed primarily for medical imaging at hard energies, which

have been exploited at speeds of up to 30 Hz [2–4]. A 1-D detector can be emulated by applying a mask to an area detector and only reading out the region of interest. Using the Frelon camera at beamline ID11 at ESRF, a time resolution of 10 ms has been achieved in this way with a 64×1 rebin of the data on the CCD chip [1]. Other read-out modes exist, such as rapidly transferring the electronic image to the masked part of the plate, which is read while the plate is re-exposed.

The best one-dimensional curved PSD for X-rays is the modular Mythen detector developed at the Paul-Scherrer Institute in Switzerland [5]. These detectors can be found on the powder diffraction beamlines at the Swiss Light Source, the Australian synchrotron, and Diamond in the UK. Based on Si technology, (at the time of writing), the detector is limited to detecting X-rays of up to $\approx$25 keV (0.5 Å wavelength). At SLS the detector covers 120° in 2θ, 30,720 channels, that can be read in parallel in 250 μs, with plans to be able to read even faster.

At ILL Grenoble, the angular-dispersive powder neutron diffractometer D20 [6] is equipped with a large curved microstrip PSD covering 153.6° in 2θ in 0.1° steps. The detector can be read in around 160 ms so giving a maximum time resolution of about 6 Hz. At ANSTO in Sydney, the high intensity powder diffractometer Wombat [7] is equipped with a similar curved PSD, covering 120° in steps of 0.125°. The detectors of both instruments can be used in stroboscopic mode.

With polychromatic radiation – which automatically exploits a greater fraction of the radiation from the source – the neutron time-of-flight approach is ideal, or for synchrotron radiation an energy-dispersive solid-state detector is required. Both methods work with detectors positioned at known 2θ angles that record the diffraction pattern by discriminating the wavelength or energy of each detected neutron or photon. For the fastest measuring rates multiple detectors are required. Examples of neutron powder diffractometers with extensive detector coverage are GEM [8] at ISIS, and the recently opened POWGEN [9] at the SNS (Oak Ridge). The former has a detector area of 7.27 m^2 covering scattering angles from 1.2° to 171.4°, and the latter, when completed, will have more than 40 m^2 of detectors from 10° to 170° 2θ (about 4 sr of detector coverage, some 240,000 individual elements).

With energy-dispersive measurements the detector consists of a liquid-nitrogen-cooled semiconducting Ge crystal. The energy of an absorbed X-ray photon, typically within the range 10–150 keV depending on the source, promotes electrons to the conduction band in proportion to its energy. By analyzing the amplitude of the charge pulses arriving from the crystal, the energy of the absorbed photon is determined with a multi-channel analyzer. The conversion from photon energy (in keV) to wavelength (in Å) is $E = 12.398/\lambda$ (where $12.398 \approx hc/e \times 10^7$). The energy resolution of such a detector is modest, around 2%. Owing to the need to take into account several energy-dependent effects, e.g. absorption and scattering factors, the shape of the incident X-ray spectrum, and the detector response, modeling the intensities of the powder diffraction pattern in a Rietveld refinement is generally difficult.

8.3 Examples

For the fastest processes, synchrotron radiation is generally expected to have the best performance, because of the very high flux from the source. However, neutrons, because of their penetrating power, can be used with larger samples, which can compensate to some extent.

8.4 Combustion Synthesis

This is a technique for synthesizing materials that exploits the high exothermic heat of reaction to promote a self-sustaining reaction, either by propagation from a point of ignition, or by heating the whole sample volume to a point where reaction occurs essentially simultaneously throughout. A number of advantages are cited for such an approach including reduced energy requirements, rapid reaction rates, and combined synthesis and sintering of the final product.

D20 at ILL was used at its peak-flux wavelength of 1.3 Å to investigate a number of systems by heating pre-pressed pellets of the starting products, 10–20 g, in a standard furnace for powder neutron diffraction until reaction was initiated [10–14]. Patterns were collected for 200–500 ms with readout of the detector requiring 80–400 ms. For the formation of Ti_3SiC_2 from a stoichiometric mixture of Ti, SiC and C five stages of the process were identified, including the transformation of α-Ti to β-Ti, the pre-ignition exothermic formation of intermediate TiC_x phases, the very rapid (sub-second) formation of a single intermediate phase, corresponding to a solid solution of Si in TiC. After an incubation period of a few seconds the product Ti_3SiC_2 nucleates and precipitates out as the temperature falls. Lattice parameter variations were used to estimate the bulk temperature and indicated that ≈2,600 K was attained. Rietveld analysis allowed the amount of each phase present to be determined, from which kinetic parameters were derived via a non-isothermal form of the Avrami equation. An activation energy of ≈45 kJ mol^{-1} was estimated for the nucleation and growth of the product phase. During cooling, the temperature deviated positively from an exponential decrease over a part of the range because of the release of latent heat correlated with the precipitation of the product phase. Analogous to differential thermal analysis, it was possible from this to estimate the enthalpy of formation of Ti_3SiC_2 as −76 kJ mol^{-1} [15].

On beamline ID11 at ESRF several systems have been studied in the self-propagating mode [1, 16–21]. Discs of the reactants were pressed, 20 mm in diameter × ≈2 mm thick, which were mounted in transmission with a 200 × 200 μm^2 monochromatic beam in the range 40–50 keV. The beam characteristics were chosen to obtain a balance between incident flux, penetration through the sample, the size of the combustion front, the grain size, and the angular resolution. Ignition via an electrically heated wire led to the propagation of the reaction through the sample at speeds of up to 100 mm s^{-1}, monitored with the 2-D Frelon camera with the temperature estimated via a pyrometer. The time resolution was typically in the

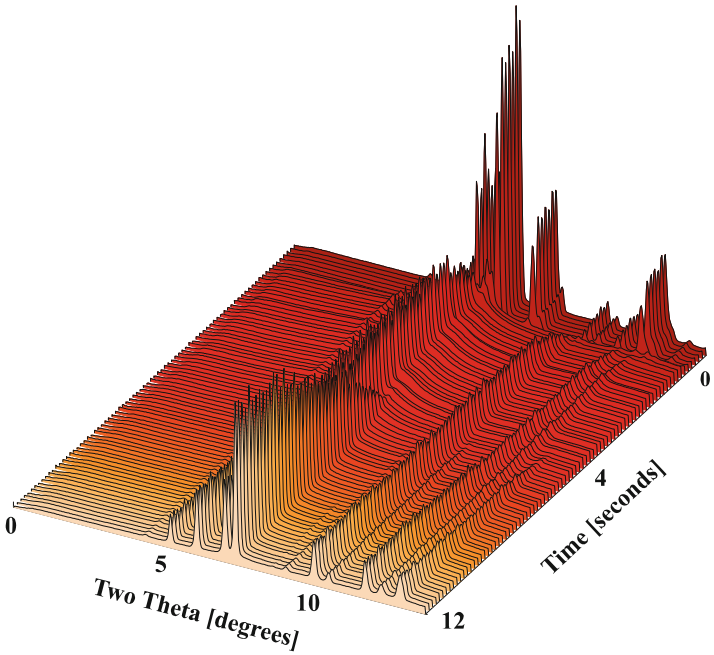

Fig. 8.1 Powder diffraction patterns of the Al-Ni-Ti-C system during self-propagating combustion synthesis measured on ID11 [17]

range 65–135 ms when exploiting the whole area of the detector and 20 ms when masking and rebinning on the chip as in the synthesis of Jacobsite, Fe_2MnO_4 [1]. Systems studied included the synthesis if TiC-NiAl (Fig. 8.1), TiC-WC and TiC-TiB_2 composites, Al-Ni intermetallics, TiC-FeTi cermets. For the TiC-NiAl system, for example, the formation of TiC accompanies the melting of Al then Ni and the formation of a (probably) ternary phase before the final formation of NiAl during cooling. The final product has small TiC particles embedded in a matrix of NiAl.

On beamline X11A at the NSLS Brookhaven the formation of several refractory carbides and diborides (of Ti, Zr, Nb, Hf or Ta) was studied in a specially built reaction chamber allowing operation under vacuum or in the presence of different reactive or inert gasses [22]. The chamber is equipped with a 2,048-channel 50-mm photodiode array covering 30° in 2θ, and a pyrometer. Data were collected in 50–200 ms at an energy of 8 keV in reflection mode.

Energy-dispersive measurements of the formation of barium, lithium and magnesium zinc ferrites were made on station 16.4 at the SRS Daresbury [23]. The reaction is driven by the oxidation of iron which is highly exothermic. Reaction was carried out in oxygen, and with the addition of sodium perchlorate as an internal oxidizing agent. Three energy-dispersive detectors were set at low 2θ angles of 1.8°, 4.7° and 7.5° and measurements were made in reflection with a 100 μm diameter white beam from the wiggler source. The time resolution was 100 ms. Measurements were

also made under an applied magnetic field using a 1.1 T permanent magnet with a cylindrical bore of 20 mm diameter. The X-ray beam direction was parallel to the axis of the bore and the fixed scattering geometry made the measurements possible. The magnetic field was seen to induce a transient phase identified as magnetite in the synthesis of barium ferrite.

8.5 Metallurgy

Processing of metals is an area where rapid changes of state are involved, such as during welding [24–28], heat treatment [29–32], and quenching [33, 34], etc. To understand the effects induced by these actions, detailed microscopic structural information is required.

At BL-10-2 at SSRL (Stamford), (beamline based on a multipole wiggler), rapid, *in-situ* powder diffraction patterns were recorded as gas tungsten arc spot welds were made on carbon-manganese steel bars [24, 25]. To prevent oxidation the experiments were performed under a helium atmosphere, and used a 50-mm photodiode array covering 24–54° 2θ with a time resolution of 100 ms (260 μm X-ray spot) or 50 ms (730 μm spot size) at an X-ray energy of 12.0 keV. The fcc-to-bcc ($\gamma \rightarrow \alpha$) transition on cooling happened twice as fast as the bcc-to-fcc ($\alpha \rightarrow \gamma$) transition on heating reflecting, most probably, differences in the heating and cooling rates. Subtle changes in *d*-spacings indicated the precipitation of carbide or the relief of residual stress during heating. Detailed analysis indicated that there were differences in microstructure between the weld fusion zone and the nearby heat-affected zone (HAZ). The same experimental arrangement was also used to study welding of stainless steel at two positions in the HAZ, 0.2 and 0.7 mm from the fusion zone boundary, to investigate the transformation of austenite (γ phase) to ferrite (δ phase) on heating, and back on cooling [26]. Volume fractions, peak positions and widths were tracked and correlated with the temperature calculated via a numerical heat transfer and fluid flow model.

Time resolution of down to 10 ms was exploited at Spring-8 (Japan) using undulator beamline 46XU to study solidification during welding of martensitic steel using X-rays of energies 18 or 30 keV and a large area pixel detector [28]. In a further development, fast diffraction measurements during heat treatment of mild steel and low-temperature transformation steel were combined with concurrent fast laser scanning confocal microscopy, allowing insight into the origin and morphology of the observed microstructural changes accompanying phase transitions on cooling [29].

NiTi shape memory alloy wires must be annealed, modifying the cold-worked deformed microstructure, and mechanically constrained to set the wire, to give the shape-memory properties. Practically, heating can be done via an electrical pulse. ID11 was used to study the transformation of a wire under rapid electrical heating with applied tensile force and simultaneous electrical resistivity measurements [32]. By masking the detector and rebinning on the chip, a time resolution of 10 ms

was obtained. Marked changes in microstructure and strain were apparent from monitoring the evolution of the 011 reflection of the austenitic phase present, depending on the power dissipated during the thermal treatment.

8.6 Catalysis

Many chemical processes are catalyzed by metallic nanoparticles such as platinum or gold. Studying such systems by conventional diffraction is hampered because of the effect of particle-size broadening on the diffraction pattern. Nevertheless the structure of such systems can be studied by measuring to high Q values (where $Q = 4\pi \sin\theta/\lambda$), then Fourier transforming to give the pair distribution function (PDF). Measuring to high Q requires hard X-ray energies and, if not scanning to high 2θ, a large 2-D detector such as the GE medical imaging detector [3, 4] installed at the APS (Illinois), which moreover has a time resolution of 30 Hz. Thus the reduction of PtO_2 to Pt metal by hydrogen at 200°C was studied at an energy of 77 keV (just below the Pt K edge to minimize fluorescence) while recording data up to $\approx$25 $Å^{-1}$. The individual patterns collected in 130 ms could be suitably converted to yield a PDF showing the overall course of the reaction. In a similar experiment, catalytic Pt nanoparticles were prepared in situ by reducing with hydrogen a deposit of H_2PtCl_6 on a TiO_2 support [35]. The support forms the bulk of the system, but nevertheless sensitivity to the Pt particles is achieved by adopting the differential PDF approach whereby the PDF of the bare support (measured under equivalent conditions) is subtracted from the total PDFs obtained from the individual patterns. It is evident that the reduction follows pseudo-zero-order kinetics, and by performing the measurements at different temperatures (100, 150 and 200°C) an Arrhenius plot allows an activation energy for the reduction of a nanoparticle to be estimated at about 50 kJ mol^{-1}, a quantity very difficult to obtain by any other means.

At ESRF beamline ID15B diffraction patterns from 2% of Pd nanoparticles ($\approx$3 nm diameter) supported on alumina were recorded using high energy (86.8 keV) X-rays with a time resolution of 2 Hz [36]. During the measurements the atmosphere was cycled between CO and NO, in simulation of a working car exhaust catalyst. The reactions were also monitored by diffuse reflectance infrared spectroscopy (DRIFTS) and mass spectroscopy (MS) of the effluent gas. A complementary experiment applied time resolved dispersive EXAFS at the Pd K edge in combination with DRIFTS and MS. During the CO cycle the Pd cell parameter was seen to increase linearly with time accompanied by the production of CO_2 then reverse when switched to NO flow. The studies show that CO dissociates on the surface of the nanoparticles to produce CO_2 and PdC_x (lattice expansion consistent with $x \leq 0.06$). Under NO, the PdC_x is converted back to Pd, with the emission of CO_2 and nitrogen gas. The IR spectroscopic measurements indicate moreover that the formation of the PdC_x also promotes the adsorption of CO in a linear configuration (PdCO) compared to a bridging (Pd_2CO) arrangement.

8.7 Stroboscopic Measurements

Commercial, doped, polycrystalline lead zirconate titanate (PZT) piezoelectric ceramics were measured in a cyclic electric field of ± 400 V mm^{-1} at frequencies up to 500 Hz via the stroboscopic approach using WOMBAT [37]. Each detected neutron is time stamped and subsequently binned together with others that have been scattered from the sample at the equivalent time in the electrical cycle. The data resulting from the sum of many cycles can be represented relative to just a single cycle. An effective time resolution of 30 μs is available using this approach. Shifts in peak positions indicate the level of piezoelectric strain generated by the field and showed no dependence on frequency. Time-of-flight neutron diffraction studies performed at ISIS on a related system using ENGIN-X [38] showed time and orientation dependence of the lattice strains [39]. Possible mechanisms for the observed behavior were discussed.

Rather than using the detector to time the arrival of the scattered radiation, the source can be pulsed to give the time frame for stroboscopic measurements. This is particularly appropriate at a synchrotron where tight bunches of electrons are in fact circulating in the storage ring. Specific ring-filling modes can be exploited to enhance the possibilities for time-resolved studies. Thus at ESRF, when operating in 16-bunch mode, an intense pulse (70 ps duration) of X-rays is emitted from the ring every 180 ns as each bunch of electrons flashes past the entrance to a beamline. A high-speed chopper in the X-ray beam can be used to select the source frequency desired for any particular experiment. Of particular note are pump-probe experiments, whereby a very short laser pulse (of the order 100 fs) excites the sample, which is then probed with an X-ray pulse a chosen delay time later. The diffraction pattern can be simply accumulated over a number of cycles on a passive 2-D detector like an image plate, because of the intrinsic low dark current for these devices. Accurate electronics are required to synchronize the laser and chopper with the bunch clock tracking the electron bunches in the storage ring.

Two examples studied at the ESRF on beamline ID09B are 4-(dimethylamino) benzonitrile and 4-(diisopropylamino)benzonitrile [40, 41], whose fluorescence properties indicate that photo-excitation leads to the formation of an intramolecular charge-transfer state. Powder diffraction patterns were collected over 10 min at a frequency of 897 Hz at delay times ranging from -150 ps (i.e. as a reference before the laser excitation) to 2,500 ps after excitation. Only about 5% of the molecules are excited by the laser, so the diffraction pattern is from a structure containing both excited and ground-state molecules. Rietveld refinement of the structure from the diffraction patterns gave the number of excited (distorted) molecules as a function of delay time, and the nature of the molecular change induced by the photo-excitation. For the isopropyl analogue, an exponential decay time of 6.3 (± 2.8) ns was observed for the excited molecules (compared to 3.28 ns seen spectroscopically). The main distortion to the molecules was a change in the torsion angle between the diisopropylamino group and the benzene ring from 13° to 14° determined from the pre-excitation patterns (14.3° in the single-crystal structure) to 10 (± 1–2)°.

Such experiments give the highest time resolution currently possible for powder diffraction experiments, though future experiments using free-electron lasers are being considered [42].

8.8 Data Analysis

Measuring data at high speed produces a large number of powder patterns that need to be analyzed, to extract lattice parameters, phase fractions, structural parameters, etc. as required to understand the behavior of the system. Modern Rietveld refinement programs (e.g. GSAS, Fullprof, Topas) allow a series of patterns to be processed. One approach takes the output from pattern n as the input to pattern $n + 1$, sequentially progressing through the series, (but watch out for abrupt changes as the system evolves). Another way is to analyze several datasets simultaneously in a single refinement, tying together chosen parameters between patterns so as to vary according to an underlying theoretical model or to follow an empirical evolution, i.e. essentially fitting to a data surface rather than to the individual patterns [43]. For example, instead of refining the lattice parameters for each pattern, the thermal expansion coefficients can be refined, defining how the lattice parameters vary over the series. Care is required in analyzing patterns from time-resolved measurements as they are necessarily compromised by the need to measure rapidly. However you choose to analyze your data, good luck.

References

1. Labiche JC et al (2007) The fast readout low noise camera as a versatile X-ray detector for time resolved dispersive EXAFS and diffraction studies of dynamic problems in materials science, chemistry and catalysis. Rev Sci Instrum 78:091301
2. Daniels JE, Drakopoulos M (2009) High-energy X-ray diffraction using the Pixium 4700 flat-panel detector. J Synchrotron Radiat 16:463–468
3. Chupas PJ, Chapman KW, Lee PL (2007) Applications of an amorphous silicon-based area detector for high-resolution, high-sensitivity and fast time-resolved pair distribution function measurements. J Appl Crystallogr 40:463–470
4. Lee JH et al (2008) Synchrotron applications of an amorphous silicon flat-panel detector. J Synchrotron Radiat 15:477–488
5. Bergamaschi A et al (2010) The MYTHEN detector for X-ray powder diffraction experiments at the Swiss Light Source. J Synchrotron Radiat 17:653–668
6. Hansen TC, Henry PF, Fischer HE, Torregrossa J, Convert P (2008) The D20 instrument at the ILL: a versatile high-intensity two-axis neutron diffractometer. Meas Sci Technol 19:034001
7. Studer AJ, Hagen ME, Noakes TJ (2006) Wombat: the high-intensity powder diffractometer at the OPAL reactor. Physica B 385–386:1013–1015
8. Hannon AC (2005) Results on disordered materials from the GEneral Materials diffractometer, GEM, at ISIS. Nucl Instrum Method A 551:88–107
9. http://www.jcns.info/POWGEN

10. Riley DP, Kisi EH, Wu E, Hansen T, Henry P (2010) Applications of in situ neutron diffraction to optimisation of novel materials synthesis. Studying kinetics with neutrons, Springer Series in solid state sciences, vol 161. Springer, Berlin/Heidelberg, pp 123–148
11. Kisi EH, Riley DP (2003) Neutron diffraction studies of self-propagating high-temperature synthesis. IUCr Comm Powder Diffr Newsl 29:18–20
12. Riley DP, Kisi EH, Hansen TC, Hewat AW (2002) Self-propagating high-temperature synthesis of Ti3SiC2: I, ultra-high-speed neutron diffraction study of the reaction mechanism. J Am Ceram Soc 85:2417–2424
13. Kisi EH, Riley DP, Curfs C (2006) Ultra-high speed neutron diffraction studies of combustion synthesis. Physica B 385–386:487–492
14. Riley DP, Kisi EH, Hansen TC (2008) Self-propagating high-temperature synthesis of Ti3SiC2: II. Kinetics of ultra-high-speed reactions from in situ neutron diffraction. J Am Ceram Soc 91:3207–3210
15. Kisi EH, Riley DP (2002) Diffraction thermometry and differential thermal analysis. J Appl Crystallogr 35:664–668
16. Curfs C, CanoI G, Vaughan GBM, Rodríguez MA, Turillas X, Kvick A (2000) Intermetallic-ceramic composites synthesis by SHS. Time-resolved studies using synchrotron radiation X-rays. Int J SHS 9:331–339
17. Curfs C, Cano IG, Vaughan GBM, Turillas X, Kvick A, Rodríguez MA (2002) TiC-NiAl composites obtained by SHS: a time-resolved XRD study. J Eur Ceram Soc 22:1039–1044
18. Contreras L, Turillas X, Vaughan GBM, Kvick A, Rodríguez MA (2004) Time-resolved XRD study of TiC-TiB2 composites by SHS. Acta Mater 52:4783–4790
19. Contreras L, Turillas X, Mas-Guindal MJ, Vaughan GBM, Kvick A, Rodríguez MA (2005) Synchrotron diffraction studies of TiC/FeTi cermets obtained by SHS. J Solid State Chem 178:1595–1600
20. Mas-Guindal MJ, Contreras L, Turillas X, Vaughan GBM, Kvick A, Rodríguez MA (2006) Self-propagating high-temperature synthesis of TiC-WC composite materials. J Alloys Compd 419:227–233
21. Curfs C, Turillas X, Vaughan GBM, Terry AE, Kvick A, Rodríguez MA (2007) Al-Ni intermetallics obtained by SHS; A time-resolved X-ray diffraction study. Intermetallics 15:1163–1171
22. Wong J, Larson EM, Waide PA, Frahm R (2006) Combustion front dynamics in the combustion synthesis of refractory metal carbides and di-borides using time-resolved X-ray diffraction. J Synchrotron Radiat 13:326–335
23. Parkin IP, Pankhurst QA, Affleck L, Aguas MD, Kuznetsov MV (2001) Self-propagating high temperature synthesis of BaFe12O19, Mg0.5Zn0.5Fe2O4 and Li0.5Fe2.5O4; time resolved X-ray diffraction studies (TRXRD). J Mater Chem 11:193–199
24. Wong J (2003) Phase mapping and transformation dynamics in fusion welds. IUCr Comm Powder Diffr Newsl 29:26–30
25. Wong J, Ressler T, Elmer JW (2003) Dynamics of phase transformations and microstructure evolution in carbon-manganese steel arc welds using time-resolved synchrotron X-ray diffraction. J Synchrotron Radiat 10:154–167
26. Palmer TA, Elmer JW, Babu SS (2004) Observation of ferrite/austenite transformations in the heat affected zone of 2205 duplex stainless steel spot welds using time resolved X-ray diffraction. Mater Sci Eng A 374:307–321
27. Stone HJ, Bhadeshia HKDH, Withers PJ (2008) In situ monitoring of weld transformations to control weld residual stresses. Mater Sci Forum 571–572:393–398
28. Komizo Y, Terasaki H (2010) In-situ observation of solidification behavior during welding. Mater Sci Forum 638–642:3722–3726
29. Terasaki H, Komizo Y (2011) Diffusional and displacive transformation behavior in low carbon-low alloy steels studied by a hybrid in situ observation system. Scr Mater 64:29–32
30. Elmer JW, Palmer TA, Specht ED (2007) In situ observation of sigma phase dissolution in 2205 duplex stainless steel using synchrotron X-ray diffraction. Mater Sci Eng A 459:151–155

31. Zhang D, Terasaki H, Komizo Y (2009) In situ observation of phase transformation in Fe-0.15C binary alloy. J Alloys Compd 484:929–933
32. Malard B, Pilch J, Sittner P, Delville R, Curfs C (2011) In situ investigation of the fast microstructure evolution during electropulse treatment of cold drawn NiTi wires. Acta Mater 59:1542–1556
33. Epp J, Hirsch T, Curfs C (2012) In situ X-Ray diffraction analysis of unexpected carbon partitioning during quenching of low carbon steel. Metall Mater Trans A 43:2210–2217
34. Epp J, Hirsch T, Kuznetsov A, Curfs C Martensite self-tempering in a ball bearing steel: in situ X-ray diffraction analysis during quenching (in preparation)
35. Chupas PJ, Chapman KW, Jennings G, Lee PL, Grey CP (2007) Watching nanoparticles grow: the mechanism and kinetics for the formation of TiO2-supported platinum nanoparticles. J Am Chem Soc 129:13822–13824
36. Newton MA, Michiel MD, Kubacka A, Fernández-García M (2010) Combining time-resolved hard X-ray diffraction and diffuse reflectance infrared spectroscopy to illuminate CO dissociation and transient carbon storage by supported Pd nanoparticles during CO/NO cycling. J Am Chem Soc 132:4540–4541
37. Pramanick A et al (2010) In situ neutron diffraction studies of a commercial, soft lead zirconatetitanate ceramic: response to electric fields and mechanical stress. Appl Phys A 99:557–564
38. Santisteban JR, Daymond MR, James JA, Edwards L (2006) ENGIN-X: a third-generation neutron strain scanner. J Appl Crystallogr 39:812–825
39. Jones JL et al (2007) Time-resolved and orientation-dependent electric-field-induced strains in lead zirconatetitanate ceramics. Appl Phys Lett 90:172909
40. Davaasambuu J, Durand P, Techert S (2004) Experimental requirements for light-induced reactions. J Synchrotron Radiat 11:483–489
41. Techert S, Zachariasse KA (2004) Structure determination of the intramolecular charge transfer state in crystalline 4-(diisopropylamino)benzonitrile from picoseconds X-ray diffraction. J Am Chem Soc 126:5593–5600
42. Blome C, Tschentscher T, Davaasambuu J, Durand P, Techert S (2005) Femtosecond time-resolved powder diffraction experiments using hard X-ray free-electron lasers. J Syncrotron Radiat 12:812–819
43. Stinton GW, Evans JSO (2007) Parametric Rietveld refinement. J Appl Crystallogr 40:87–95

Chapter 9
Taking It to Extremes – Powder Diffraction Under Non-Ambient Conditions

David I.A. Millar and Colin R. Pulham

Abstract Structural studies of materials under elevated pressures provide a fascinating insight into the physical and chemical behaviour of matter under the wide range of conditions experienced throughout the Universe. Both x-ray and neutron powder diffraction techniques play a crucial role in structural studies and are therefore at the forefront of high-pressure research. These notes provide a short introduction to the principles and experimental practice of high-pressure powder diffraction techniques.

9.1 Introduction

Although on the surface of the Earth we rarely experience pressures that deviate significantly from 1 atm, much of the Universe experiences a much wider range of pressures that span the near vacuum of outer space to the pressure at the centre of a neutron star (estimated to be 10^{30} atm). Even on Earth there is a significant variation – at the bottom of the Mariana Trench in the Pacific Ocean at a depth of 11,000 m, the pressure is over 1,000 atm, and the pressure at the centre of the Earth is 3.5 million atmospheres. Under this range of extreme conditions, structural and chemical changes in materials can be dramatic – proteins are denatured; pathogenic bacteria are destroyed; ice melts above 100°C; graphite turns to diamond; and non-metals become metallic. Such conditions also provide a rich regime for geochemical synthesis – diamonds, garnets, and perovskites are just a few of the many minerals produced under extreme conditions within the Earth. The domain of pressure therefore provides an exciting additional dimension to explore structure, chemical

D.I.A. Millar • C.R. Pulham (✉)
School of Chemistry and Centre for Science at Extreme Conditions, The University of Edinburgh, King's Buildings, West Mains Road, Edinburgh EH9 3JJ, UK

U. Kolb et al. (eds.), *Uniting Electron Crystallography and Powder Diffraction*,
NATO Science for Peace and Security Series B: Physics and Biophysics,
DOI 10.1007/978-94-007-5580-2_9,

reactivity, and physical properties. At the same time it provides a powerful way to test computational models, with a particular focus on the validation of the efficacy of intermolecular potentials.

It is for these reasons that high-pressure research attracts such interest across a wide range of disciplines that includes: geosciences; physics; chemistry; materials science; biology; engineering; and astronomy. Since physical properties are intrinsically linked to structure, structural studies are key to understanding how matter behaves under extreme conditions. Both x-ray and neutron powder diffraction techniques therefore play a crucial role in such structural studies. These notes will therefore provide a short introduction to high-pressure powder diffraction techniques.

9.2 Techniques

High-pressure structural science is a particularly good example of an area that relies upon the complementarity of various techniques to achieve the final aim of the structural characterisation of novel materials. The advances in this field are intertwined with the evolution of complex sample environments for experiments at elevated temperatures and/or pressures, as well as the development of techniques for the collection and analysis of spectroscopic and diffraction data under extreme conditions. In particular, developments of high brightness X-ray and neutron sources, coupled with the enhancement of associated detectors, have played a major part in advancing powder diffraction studies at extreme conditions [1].

9.2.1 The Diamond-Anvil Cell

High-pressure X-ray diffraction measurements are generally performed using a gasketed diamond-anvil cell (DAC). The premise for this device is relatively simple; the sample is placed between two diamond faces (culets) and is subjected to high pressures when a force pushes the opposed anvils together (see Fig. 9.1). The DAC utilised in this work was based on developments by Merrill and Bassett in 1974 [2]. The small size ($\sim$5 cm diameter) and relative ease of use make these cells extremely versatile and perfectly suited for high-pressure X-ray diffraction studies. Depending on the size of the culets and the gasket hole, pressures beyond 100 GPa can be obtained. Note that in high-pressure research it is common to find various units used, sometimes interchangeably, as a measure of pressure. Gigapascals (GPa) may be related to other units as follows:

$$1\,\text{GPa} = 10\,\text{kbar} = 9869.2\,\text{atm}.$$

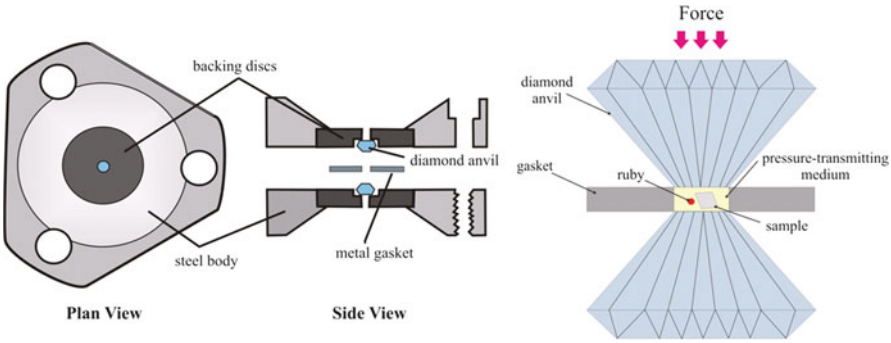

Fig. 9.1 Schematic representation of Merrill-Bassett diamond-anvil cell

The experimental set-up for a typical high-pressure X-ray powder diffraction experiment is represented in Fig. 9.2a. Data are collected on an image plate detector and are generally processed according to the procedure outlined for ambient-pressure powder diffraction, although in some cases it may also be necessary to mask out intense single-crystal reflections arising from the diamond anvils to ensure no anomalies occur in the I_{obs} *vs* 2θ profile. The image can then be integrated to provide the one-dimensional powder diffraction pattern using programs such as Fit2D [3].

It is also possible to mask intense powder diffraction rings due to the tungsten gasket, although should this interfere with sample peaks it is also possible to perform Rietveld refinements in which the tungsten diffraction pattern is incorporated. Finally the data can be integrated to give a plot of diffraction intensity against scattering angle. The large background common to such data collections is due to Compton (inelastic) scattering from the diamonds and can be subtracted prior to data refinement.

9.2.2 Radiation Sources

Whilst in principle it is possible to record powder diffraction patterns on laboratory instruments using conventional sealed sources (e.g. Mo-K_α), far superior results can be obtained using synchrotron sources that combine high flux with tuneable wavelength and low divergence. Beam diameters of less than 30 μm are easily obtained and hence allow one to record diffraction patterns for heterogeneous samples and without contamination from the DAC components. In such studies, however, great care must be taken to ensure effective powder averaging of such a small sample volume. This is typically achieved by ensuring that the DAC is loaded with a very finely ground powder and rocking the DAC through an angle of 5–20°.

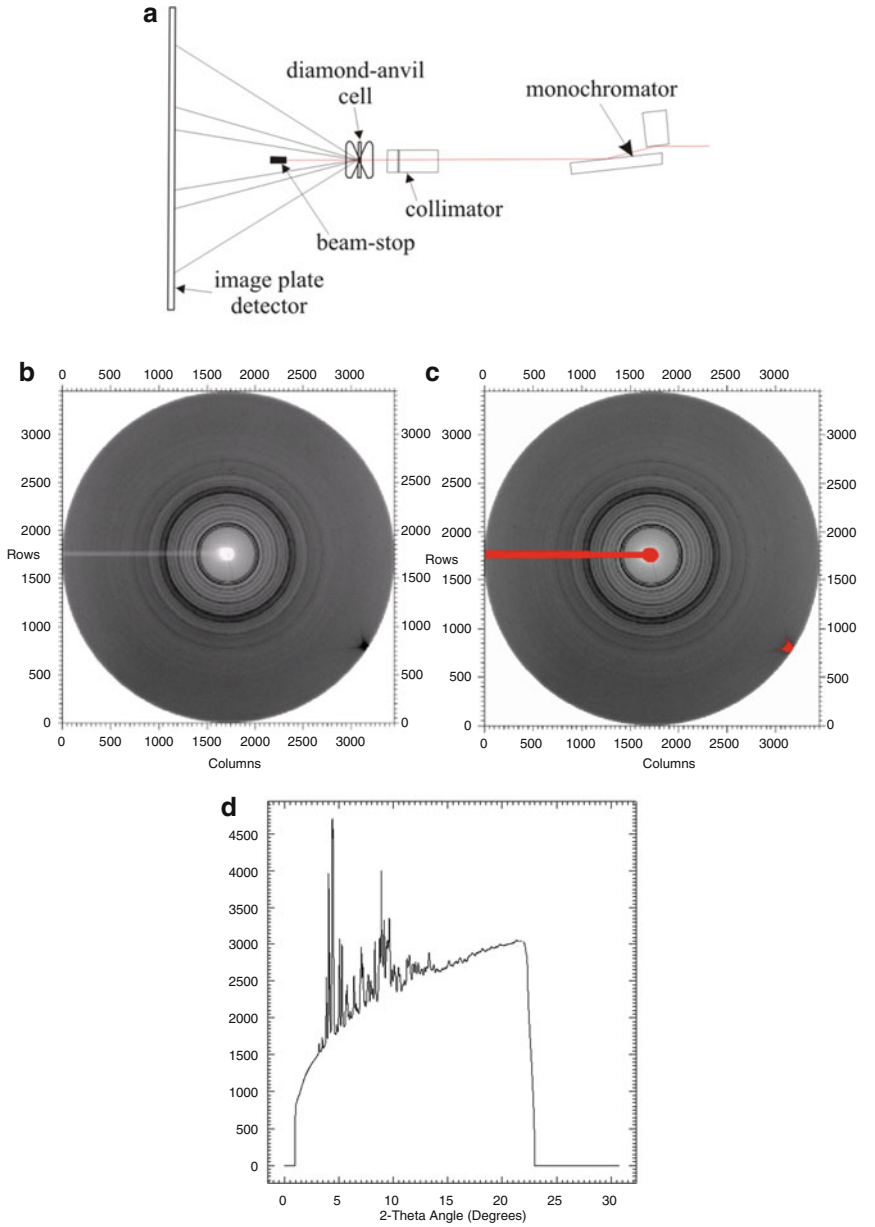

Fig. 9.2 (**a**) Schematic illustrating the key components of a high-pressure X-ray powder diffraction experiment. (**b**)–(**d**) Schematic illustrating the stages of data reduction. The raw image is shown in (**b**). The *concentric rings* correspond to the diffracted intensities from the sample; the *dark spot* at the edge of the image is an intense diamond reflection

9.2.3 Pressure Measurement in the DAC

Direct pressure measurement from the applied force is both inaccurate and impractical. Instead, Piermarini *et al.* demonstrated that a small chip or sphere of ruby (Al_2O_3:Cr^{3+}) could serve as a continuous pressure sensor within the DAC by utilising its laser-induced fluorescence [4]. Indeed the simplicity of the ruby fluorescence method for *in situ* pressure calibration is without question a contributing factor to the widespread application of diamond-anvil cell techniques and, as such, was the subject of an extensive review by Syassen in 2008 [5]. The spectral lines of ruby undergo a pronounced redshift with applied pressure; the R_1 electronic transition shows a linear dependence with pressure up to at least 20 GPa at ambient temperature [4].

9.2.4 The Paris-Edinburgh Cell

Neutron diffraction experiments require sample volumes *ca* 10^6 times larger than those required for X-ray powder diffraction, thus precluding the use of diamond-anvil cells. High-pressure neutron diffraction experiments were therefore severely limited until the advent of the Paris-Edinburgh cell (P-E Cell), developed in 1992, which extended the pressure range to 10–20 GPa [6]. The popularity of the P-E Cell arose from its (relatively) light-weight design and its portability – the Paris-Edinburgh cell weighs ∼50 kg, in contrast to other commercial devices of the time with comparable sample volume that weighed close to 1 tonne. This portability, coupled with the fact that loads can be applied to the cell by a hydraulic ram while it remains *in situ* on the beamline, greatly simplified high-pressure experiments. The P-E Cell is also an opposed-anvil device, like the diamond-anvil cell and the Bridgman cell. In this construction, however, the sample is compressed between anvils made of either tungsten carbide (WC) or sintered diamond, see Fig. 9.3a. Early designs utilised null-scattering TiZr toroidal gaskets located into corresponding grooves machined into the anvil faces to confine the sample and, generally, a solid pressure-transmitting medium. Compression studies using the preferred fluid pressure-transmitting media (methanol:ethanol and iso:n-pentane) were limited to *ca* 2.0 GPa before anvil failure. It was realised that complete encapsulation of the sample and pressure-transmitting medium in two flanged hemispherical caps (TiZr) would prevent the fluid media coming into direct contact with the anvil surface [7]. In this way the anvils were shown to be protected and the available pressure range for hydrostatic studies were extended up to the freezing pressure of methanol:ethanol (*i.e.* ∼10 GPa). The encapsulated gasket is compared to the 'standard' TiZr toroidal gasket in Fig. 9.3b.

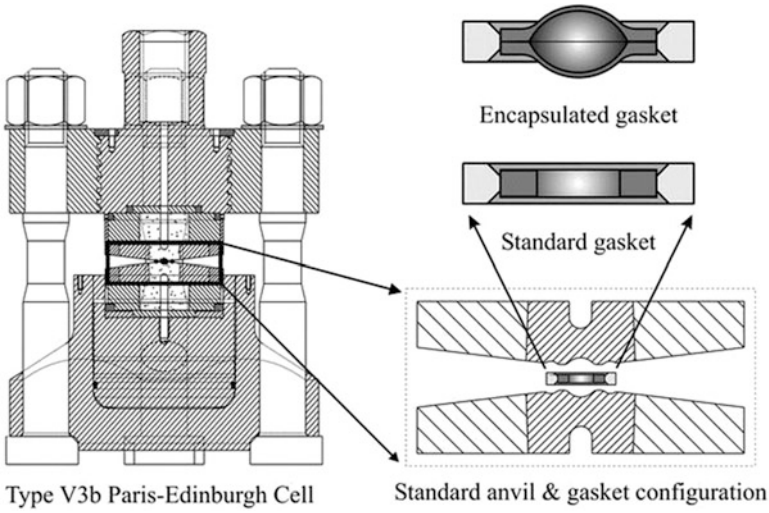

Fig. 9.3 (**a**) Cross-section of the Paris-Edinburgh cell (V3b) and (**b**) a comparison of the standard and encapsulated gaskets [7]

9.2.5 Pressure Measurement in the Paris-Edinburgh Cell

Unlike the diamond-anvil cell, the Paris-Edinburgh cell does not allow optical access to the sample chamber and therefore a method for pressure calibration other than the ruby fluorescence method had to be developed. Instead, small quantities of internal pressure calibrants are used, typically either NaCl(s) or Pb(s). Both materials have clearly defined equations of state which means that the unit cell volume of the chosen calibrant (as determined by Rietveld refinement of the powder diffraction patterns) is directly related to the pressure within the gasket.

9.3 Pressure-Transmitting Media

In most powder diffraction experiments it is desirable to ensure that the stress applied to the sample is homogeneous and that the sample is free of any differential stress or induced shear strain over the entire pressure range of the experiment. In order to achieve these conditions, the powder must be immersed in a medium that displays hydrostatic behaviour. The consequences of a non-hydrostaticity include: inhomogeneous strain in the crystallites leading to broadening of Bragg peaks with associated loss of resolution and signal-to-noise; modification of the relative evolution of unit cell parameters; and difficulties in measuring the pressure using the ruby-fluorescence technique. Non-hydrostatic stresses may therefore adversely affect results from equation of state and elasticity studies, especially those aimed at

Table 9.1 Nominal hydrostatic limits of pressure-transmitting media (From refs. [12] and [13])

Medium	Hydrostatic limit/GPa
4:1 methanol:ethanol	9.8–10.5
16:3:1 methanol:ethanol:water	10.5
Anhydrous 2-propanol (isopropanol)	4.2
Glycerol	1.4
1:1 Pentane:iso-pentane	7.4
Silicone oil (various viscosities)	0.9
Fluorinert	2.0
Argon	1.9
Nitrogen	3.0
Neon	15
Helium	23

obtaining accurate pressure derivatives of elastic moduli. Non-hydrostatic stresses can also promote or suppress phase transitions [8, 9] and they can promote the amorphisation of crystalline samples [10, 11]. Table 9.1 shows the nominal hydrostatic limits of some common pressure-transmitting media. There is considerable variation within the literature about the precise values of hydrostatic limits – this arises because of the different ways that loss of hydrostaticity can be assessed. The onset of line-broadening of the fluorescence spectra of ruby chips immersed in the medium has often been used, but ruby is a relatively stiff material with a bulk modulus of about 254 GPa and is thus intrinsically less sensitive to non-hydrostatic stresses than most minerals or molecular compounds. Furthermore, the fluorescence spectra are intrinsically broad as a result of defects and strains within the ruby crystals, unless the crystallites have been very carefully annealed. More recently a systematic, more sensitive, ruby-fluorescence study has been performed, which monitored values of the pressure gradients across the sample chamber for the pressure-solidified medium [12]. An alternative method for monitoring non-hydrostatic stresses is to measure the widths of the diffraction peaks of quartz single crystals [13]. Quartz is available as gem-quality samples that have intrinsically sharp diffraction peaks and it has a low bulk modulus, which make the peak positions and widths sensitive to small non-hydrostatic stresses. Gigahertz ultrasonic interferometry has also been used to detect the onset of the pressure-induced glass transition in methanol:ethanol mixtures [13].

It should also be noted that neutron experiments require the use of fully deuterated pressure-transmitting media since hydrogen-containing material produces a strong background due to the large incoherent cross section of hydrogen.

9.4 Further Reading

References [14, 15], which represent proceedings of previous Erice Schools, give a flavour of research in the field of high-pressure crystallography. Reference [16] is an informative review of high-pressure chemistry that highlights some of the

fascinating structural changes induced by elevated pressures. References [17–21] provide a combination of tutorial and critical reviews that cover a range of high-pressure research from simple metals through molecular compounds to ceramic materials.

Acknowledgments We thank Dstl and EPSRC for contributions toward a studentship, and the Diamond Light Source and the ISIS Neutron and Muon Facility for the provision of beamtime. We are extremely grateful to Dr Bill Marshall (ISIS) for a longstanding and fruitful collaboration.

References

1. Merrill L, Bassett WA (1974) Miniature diamond anvil pressure cell for single crystal x-ray diffraction studies. Rev Sci Instrum 45:290
2. Norby P, Schwarz U (2008) Powder diffraction under non-ambient conditions. In: Dinnebier RE, Billinge SJL (eds) Powder diffraction theory and practice. Royal Society of Chemistry, Cambridge
3. Hammersley AP, Svensson SO, Hanfland M, Fitch AN, Hausermann D (1996) Two-dimensional detector software: from real detector to idealised image or two-theta scan. High Press Res 14:235
4. Piermarini GJ, Block S, Barnett JD, Forman RA (1975) Calibration of the pressure dependence of the R1 ruby fluorescence line to 195 kbar. J Appl Phys 46:2774
5. Syassen K (2008) Ruby under pressure. High Press Res 28:75
6. Besson JM, Nelmes RJ, Hamel G, Loveday JS, Weill G, Hull S (1992) Neutron powder diffraction above 10 GPa. Physica B180–181:907
7. Marshall WG, Francis DJ (2002) Attainment of near-hydrostatic compression conditions using the Paris-Edinburgh cell. J Appl Crystallogr 35:122
8. Decker DL, Petersen S, Debray D, Lambert M (2004) Pressure-induced ferroelastic phase transition in $Pb_3(PO_4)_2$: a neutron-diffraction study. Phys Rev B 19:3552
9. Resel R, Oehzelt M, Shimizu K, Nakayama A, Takemura K (2004) On the phase-transition in anthracene induced by high pressure. Solid State Commun 129:103
10. Haines J, Léger JM, Gorelli F, Hanfland M (2001) Crystalline post-quartz phase in silica at high pressure. Phys Rev Lett 87:15503
11. Machon D, Dmitriev VP, Bouvier P, Timonin PN, Shirokov VB, Weber HP (2003) Pseudoamorphization of Cs_2HgBr_4. Phys Rev B 68:144104
12. Klotz S, Chervin J-C, Munsch P, Le Marchand G (2009) Hydrostatic limits of 11 pressure transmitting media. J Phys D: Appl Phys 42:075413
13. Angel RJ, Bujak M, Zhao J, Gatta GD, Jacobsen SD (2007) Effective hydrostatic limits of pressure media for high-pressure crystallographic studies. J Appl Crystallogr 40:26
14. Boldyreva E, Dera P (eds) (2010) High-pressure crystallography. Springer, Netherlands
15. Katrusiak A, McMillan P (eds) (2004) High-pressure crystallography, NATO science series II: mathematics, physics and chemistry, vol 140. Kluwer Academic Publishers, London
16. Grochala W, Hoffmann R, Feng J, Ashcroft NW (2007) The chemical imagination at work in very tight places. Angew Chem Int Ed 46:3620
17. Goncharov AF, Hemley RF (2006) Probing hydrogen-rich molecular systems at high pressures and temperatures. Chem Soc Rev 35:899
18. Santoro M, Gorelli FA (2006) High pressure solid state chemistry of carbon dioxide. Chem Soc Rev 35:918

19. Fabbiani FPA, Pulham CR (2006) High-pressure studies of pharmaceutical compounds and energetic materials. Chem Soc Rev 35:932
20. McMahon MI, Nelmes RJ (2006) High-pressure structures and phase transformations in elemental metals. Chem Soc Rev 35:943
21. Horvath-Bordon E, Riedel R, Zerr A, McMillan PF, Auffermann G, Prots Y, Bronger W, Kniep R, Kroll P (2006) High-pressure chemistry of nitride-based materials. Chem Soc Rev 35:987

Chapter 10
Structure Solution by Charge Flipping

Lukáš Palatinus

Abstract Charge flipping is an iterative structure solution method based on the alternating modification of an electron density in direct space and structure factors in reciprocal space. It has been successfully applied to a range of crystallographic problems, including structure solution from powder diffraction data and from electron diffraction data obtained by the precession electron diffraction method. For electron diffraction no modification of the basic algorithm is necessary. For the structure solution from powder diffraction the histogram matching technique proved to be a powerful method to improve the quality of the solutions and use the algorithm to solve quite complex structures.

10.1 Introduction

Introductory note: Reading of this chapter assumes a basic knowledge of crystallographic terms and concepts. Reader unfamiliar with these concepts will find them in several text books on the subject, for example in an excellent treatise Fundamentals of Crystallography [1].

The phase problem in crystallography is almost as old as structural crystallography itself. For a long time, the approaches to this problem have been driven by the attempts to reduce the computational complexity of the solution methods because of the limited (or non-existent) access to powerful computers. Lots of effort has been invested in the development of Patterson and direct methods in order to make them as computationally efficient as possible.

L. Palatinus (✉)
Institute of Physics of the AS CR, v.v.i., Na Slovance 2, 182 21 Prague 8, Czech Republic
e-mail: palat@fzu.cz

U. Kolb et al. (eds.), *Uniting Electron Crystallography and Powder Diffraction*,
NATO Science for Peace and Security Series B: Physics and Biophysics,
DOI 10.1007/978-94-007-5580-2_10,

The advent of cheap computer power available on almost everyone's desk has allowed the development of methods that are conceptually simpler than the classical methods at the expense of higher requirements for computing power. Among these techniques are direct-space methods (simulated annealing, genetic algorithms . . .) and extensions of the classical direct methods, like Shake-and-Bake [2, 3]. Recently, a new class of methods based neither on the direct methods nor on direct-space approaches have emerged. These methods are based on an iterative modification of an image in both direct and reciprocal (Fourier) space, and can therefore be referred to as dual-space iterative methods.

10.2 Dual-Space Iterative Methods

The diffraction experiment provides information about the amplitudes of the Fourier coefficients of the scattering density, but the phases of the structure factors are lost. In the case of X-ray diffraction by a crystal, the scattering density is the electron density in the unit cell of the crystal. For diffraction by electrons the scattering density is the electrostatic potential. The knowledge of the Fourier amplitudes imposes constraints on possible electron densities (the *amplitude constraints*), but these constraints alone are not sufficient for the solution of the phase problem. To solve the phase problem without serious ambiguities, we have to define additional constraints that allow us to discriminate between physically meaningful and meaningless electron densities. The weakest and most general constraint is the requirement for the electron density to remain positive (*positivity constraint*). Another obvious constraint follows from the fact that crystals consist of individual atoms. We could thus require that the electron density contains only a limited number of significant peaks, and the rest of the unit cell is filled by almost zero density. A weaker variant of this constraint is the mere requirement that only a small part of the unit cell has significant density, with the rest being zero. In this weaker formulation there is no explicit assumption that the significant density is grouped into separated point-like peaks. We can call this condition a *sparseness constraint*. All these constraints are defined with respect to the electron density rather than its Fourier coefficients, and they are therefore direct-space constraints in contrast to the amplitude constraint, which is defined in reciprocal space.

Whatever constraint we choose, we can now reformulate the solution of the phase problem from a different perspective. In the space that contains all possible electron densities, we seek the subset of densities that fulfill both the amplitude constraint and some of the direct space constraints. This subset is an intersection of the subsets fitting the amplitude constraint and the direct-space constraint. We are therefore looking for an intersection of two subsets in the space of electron densities. The sets of densities that fulfill the constraints are termed constraint sets.

The problem of finding an element from the intersection of two (or more) constraint sets has been treated by mathematicians since long time ago. In the special case of *convex feasibility* or *convex optimization* problems, where all

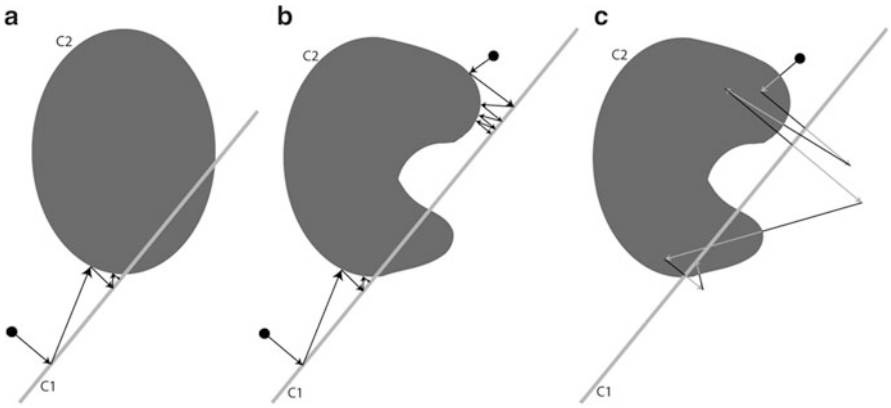

Fig. 10.1 Finding the inter-section of two constraint sets. (**a**) Convex constraint sets and repeated projections. (**b**) Non-convex constraint sets and repeated projections. (**c**) Non-convex constraint sets and repeated overprojections

sets are convex, well-defined iterative procedures exist with proven convergence properties [4]. For instance, the intersection between two convex constraint sets is always reached simply by alternating projections onto the first and the second set (Fig. 10.1a). In crystallography, the set associated with the amplitude constraint is unfortunately non-convex. In such case the algorithms developed for convex sets are not guaranteed to work, because they can get trapped in local minima (Fig. 10.1b). It is nevertheless useful to use the terminology and approaches developed for the convex feasibility problem. The two main elements constituting the basis of the algorithms are the constraint sets and the projections onto them. We have already discussed the constraints. Now let us consider the projections. For the purposes of this chapter a projection P is a mapping from an arbitrary point ρ in the image space onto the nearest point of the constraint set C:

$$P : P_\rho \in C \text{ and } \left\| P_\rho - \rho \right\| = \min$$

Applying a projection to an arbitrary density results in a new density that belongs to the constraint set. A projection P_F that projects an arbitrary density ρ on the amplitude constraint C_A can be written as:

$$P_F = \Phi^{-1} A \Phi$$

where Φ represents a Fourier transform, and A an operation on the Fourier coefficients such that the phases remain intact, and the amplitudes are replaced with the experimental amplitudes. It is obvious from Fig. 10.1b that "naively" alternating the projections onto the first and second constraint set can only be successful sometimes, but it is prone to stagnation at local minima. This drawback can be

overcome by replacing simple projections by relaxed projections (*overprojections*), or combining these relaxed projections in more elaborate schemes. A relaxed projection R is defined as:

$$R = P + \gamma(P - I)$$

Thus, a relaxed projection is obtained by a "prolongation" of the vector from ρ to P_ρ by a factor γ. The special case $\gamma = 1$ is called a reflection. Figure 10.1c illustrates that using relaxed projections may allow the iteration to escape from a local minimum.

Multiple different combinations of projections have been suggested in the literature (see [5] for overview), but it must be emphasized that not all possible combinations are useful. A good algorithm must be designed in such a way that it searches the image space efficiently, *i.e.* it does not get trapped in local minima, and explores large parts of the image space. On the other hand, if the iteration approaches the true solution, it must converge close to the solution, and not diverge again. Clearly, the algorithm must be a balance between the perturbing aspect necessary to explore the search space, and the stabilizing aspect needed for the stability at the solution.

10.3 The Charge-Flipping Algorithm

Several dual space algorithms can be described in the frame-work of repeated (over) projections onto the constraint sets. Among them the charge flipping algorithm [6–8] has gained the widest attention, and is currently the main dual-space iterative method used to solve structures in practical crystallography. The basic algorithm can be briefly described as an alternation of a simple projection onto the amplitude constraint set followed by an overprojection onto the positivity constraint set. However, the exact implementation deviates somewhat from this general scheme, and we will discuss these deviations later.

Figure 10.2 shows the flow chart of the basic algorithm. The electron density ρ is sampled on a grid with $N_{pix} = N_1 \times N_2 \times N_3$ pixels. The density values ρ_i are evaluated in each pixel $i = 1, \ldots, N_{pix}$ of the grid. $|F^{obs}(\mathbf{h})|$ are the experimental amplitudes of the structure factors. The algorithm is initiated in the zeroth cycle by assigning random starting phases $\varphi_{rand}(\mathbf{h})$ to all experimental amplitudes and making all unobserved amplitudes equal to zero:

$$F^{(0)}(\mathbf{h}) = \begin{cases} |F^{obs}(\mathbf{h})| \exp(i\varphi_{rand}(\mathbf{h})) & \text{if } |F^{obs}(\mathbf{h})| \text{ is known} \\ 0 & \text{otherwise} \end{cases}$$

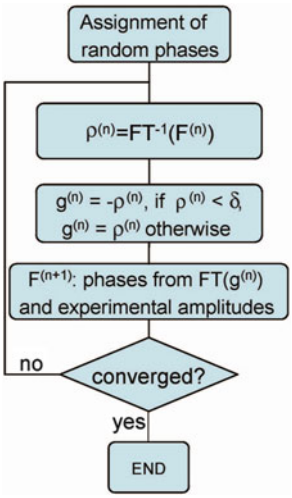

Fig. 10.2 The flow chart of the basic charge flipping algorithm

The iteration cycle then proceeds as follows:

1. The density $\rho^{(n)}$ is calculated by inverse Fourier transform of $F^{(n)}$.
2. The modified density $g^{(n)}$ is obtained by flipping the density of all pixels with density values below a small positive threshold δ and keeping the rest of the pixels unchanged:

$$g_i^{(n)} = \begin{cases} \rho_i^{(n)} & \text{if } \rho_i^{(n)} > \delta \\ -\rho_i^{(n)} & \text{if } \rho_i^{(n)} \leq \delta \end{cases}$$

3. Temporary structure factors $G^{(n)}(\mathbf{h}) = \left|G^{(n)}(\mathbf{h})\right| \exp(i\varphi_G^{(n)}(\mathbf{h}))$ are calculated by Fourier transform of $g^{(n)}$.
4. New structure factors $F^{(n+1)}$ are obtained by combining the experimental amplitudes with the phases of $G^{(n)}$ and setting all non-measured structure factors to zero:

$$F^{(n+1)}(\mathbf{h}) = \begin{cases} \left|F^{obs}(\mathbf{h})\right| \exp(i\varphi_G^{(n)}(\mathbf{h})) & \text{if } \left|F^{obs}(\mathbf{h})\right| \text{ is known} \\ 0 & \text{otherwise} \end{cases}$$

These structure factors then enter the next iteration cycle.

Let us analyze the steps in detail. Steps 1 and 3 are just Fourier transforms that transform the quantities between direct and reciprocal space. Steps 2 and 4 are the actual modifications. Step 4 is a standard projection onto the amplitude constraint set, as described in the previous section. To understand the meaning of step 2 let us first define a *significance pseudoprojection* as an operation that

sets all density values below the (small, but positive) threshold δ to zero. This operation can be understood as a combination of the positivity projection (all negative densities are set to zero), and the sparseness projection (small density values are considered insignificant and set to zero). If we combine the definition of the significance pseudoprojection and the definition of an overprojection, we see that the charge flipping operation is an overprojection with $\gamma = 1$ associated with the significance pseudoprojection. But why do we call the significance pseudoprojection a pseudoprojection, and not simply a projection? Because this operation does not minimize the distance between the original and modified density, and therefore it does not match the definition of projection introduced above. For example, for the value of δ equal to 0.5, the constraint set consists of all densities with density values either exactly zero or larger than 0.5. Consider now a density value 0.4. The minimum change of this value to bring it onto the constraint set is to increase it by 0.1–0.5. However, the significance pseudoprojection is defined so that this value becomes zero, i.e. a change by −0.4. As a result, the charge flipping operation cannot be understood as an overprojection in the strict sense. The difference might seem unimportant, but tests show that replacing the charge flipping operation by a true overprojection visibly decreases the efficiency of the algorithm.

The basic algorithm has been extended several times to improve the efficiency and to widen its applicability [8]. One improvement involves the replacement of the amplitude projection by the corresponding overprojection. This simple extension significantly improves the ability of the algorithm to solve complex structures. Another improvement has been obtained by introducing a so-called π-half variant of the amplitude projection. In this variant, the amplitudes of the weak reflections are not modified in step 4 of the algorithm, but their phase is shifted by $\pi/2$:

$$F^{(n+1)}(\mathbf{h}) = \begin{cases} \left|F^{obs}(\mathbf{h})\right| \exp(i\varphi_G^{(n)}(\mathbf{h})) & \text{if } \left|F^{obs}(\mathbf{h})\right| \text{ is known and strong} \\ \left|G^{(n)}(\mathbf{h})\right| \exp(i\varphi_G^{(n)}(\mathbf{h}) + \frac{\pi}{2}) & \text{if } \left|F^{obs}(\mathbf{h})\right| \text{ is known and weak} \\ 0 & \text{otherwise} \end{cases}$$

Typically around 20% of the weakest reflections are treated as weak.

An extension of the algorithm towards scattering densities that are not strictly positive (like neutron scattering densities in presence of isotopes of some elements) is possible by a modification of the flipping operation. In this so-called *band flipping* variant [9] only densities between $+\delta$ and $-\delta$ are multiplied by -1. This operation leaves large negative densities intact, and allows the development of negative peaks.

10.4 Practical Considerations

The charge flipping algorithm has many practical aspects that are not fundamental, but are important for application of the algorithm to real problems. Let us comment on the two most important aspects.

10.4.1 Data Completeness

Charge flipping requires atomic resolution to work. That means that the resolution should be better than 1.2 Å for organic structures. The limit can be relaxed to 1.6 Å or even more for structures containing heavier atoms. Being a method based on Fourier transform, charge flipping is more sensitive to data completeness than direct methods. It is especially harmful to remove strong reflections from the data set. This, unfortunately, happens in practice, if strong reflections are saturated during the exposure, and then removed from the data set as unreliable. It is recommended to include the strong reflections in the data set for solution, even if their intensity is less reliable. These reflections should, however, be removed before the structure refinement procedure.

10.4.2 Symmetry Determination

An important aspect of the algorithm is the handling of symmetry. During the iteration no symmetry is imposed on the density. The algorithm is said to "solve the structures in $P1$". Any attempt to use the symmetry information during the iteration has so far resulted in a decreased or at least unchanged efficiency of the algorithm. The symmetry is, of course, indirectly encoded in the diffraction intensities, and therefore the reconstructed electron density contains the proper symmetry. As a result the symmetry can be estimated from the electron density. This is an important advantage, because the symmetry analysis can be based both on the experimental amplitudes and reconstructed phases rather than only on the amplitudes [10]. Consequently, the symmetry analysis does not suffer from ambiguities between centrosymmetric and noncentrosymmetric space groups. It is also less sensitive to the noise in the data. In the analysis of systematic absences a handful of false strong reflections (arising for example due to diffuse scattering) can obscure the detection of the corresponding symmetry element. The analysis of the density, on the other hand, relies on the full density in the unit cell, and is therefore much more robust.

Sometimes, however, the solution is not sufficiently accurate to detect small deviations from a higher symmetry. This can happen for example, if large parts of the structure (say all heavy atoms) match a higher symmetry, and only a few light atoms break the symmetry. The best practice in symmetry determination is therefore combining both standard symmetry analysis based on the distribution of diffraction intensities, and the symmetry analysis of the electron density reconstructed by charge flipping in $P1$.

10.5 Applications of Charge Flipping to Powder Diffraction Data

A powder diffraction diagram can be considered as a projection of the 3D diffraction pattern onto one dimension. Such projection inevitably results in the overlap of reflections in the pattern and consequently in the loss of information about the intensity of individual reflections.

Using some of the decomposition procedures (Le Bail or Pawley decomposition [11, 12]) it is possible to extract approximate reflection intensities from the powder diagram. Some of these intensities can be very accurate, but those exhibiting heavy overlap will be estimated with a significant inaccuracy. Nevertheless, such a set of intensities can be considered as a noisy single crystal data set.

If the reflection overlap is not too severe, the charge flipping algorithm can solve structures directly from the extracted intensities. In such case the structure solution process is not different from the structure solution from single crystal data. Such solutions are especially successful if synchrotron radiation data are available [13, 14].

However, as the reflection overlap increases, the quality of the data set decreases to the point when the density map reconstructed by charge flipping becomes uninterpretable, although not completely wrong. We then stand in front of the following problem: we have a partial solution, and we would like to modify the solution in such a way that with the help of the modified solution we can obtain a better guess for the individual intensities that are overlapped in the diffraction pattern.

The first attempt to make such modification was to use the ratio of $|G^{(n)}(\mathbf{h})|$ of the overlapped reflections, and modify their $|F(\mathbf{h})|$ to have the same ratio while keeping the total intensity of the overlapped group of reflections equal to the experimentally determined value [15]. However, this approach does not bring any really new information in the iteration process, and it has so far not gained wider application.

An alternative approach has been developed by Baerlocher et al. [13]. It was noted that the partial solution from the original, noisy data exhibited typical distributions of the density values (density histograms), which were different from the density histograms of the correct solutions (Fig. 10.3). The technique called histogram matching [16] is used successfully in protein crystallography to improve the estimated reflection phases by modifying a partial solution so that its histogram matches the expected histogram. For powder diffraction this idea was modified, and the histogram matching is used to improve the estimates of *intensities* rather than phases.

The flowchart of the complete algorithm is shown in Fig. 10.4. The heart of the algorithm is the original charge flipping algorithm. However, after every n cycles (n being typically between 20 and 100), the current density $\rho^{(n)}$ is submitted to a histogram matching procedure, which modifies the density values so that histogram of the modified density matches the expected histogram. Structure factors

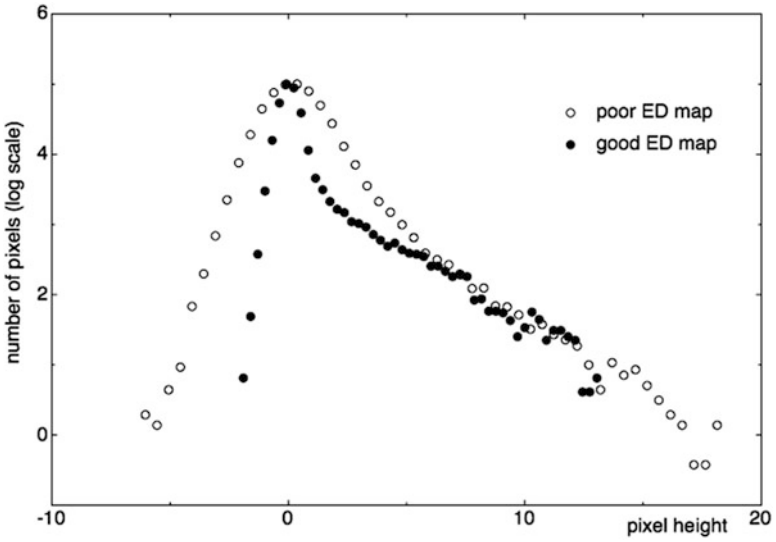

Fig. 10.3 Density histogram of a partial solution obtained by charge flipping from powder diffraction data, and a histogram of a good solution from [13]

calculated from such modified density are different from the original structure factors. Because it can be assumed that the density was improved by the histogram matching procedure, the calculated structure factors should also be improved, and in particular the ratios of the structure factor amplitudes are probably closer to the correct values than in the original dataset extracted from the powder pattern. These ratios can thus be used to repartition the intensities in overlapped reflection groups. The charge flipping algorithm then continues with the improved data set, and the whole metacycle of n cycles of charge flipping followed by histogram matching is repeated until convergence.

This algorithm proved to be successful in solution of several complex structures [13]. For extremely difficult problems the algorithm can be combined with additional information obtained from high-resolution electron microscopy, and such combination then resulted in solution of some of the most complex zeolite structures known to date [17, 18].

10.6 Structure Solution from Electron Diffraction Data

Electron diffraction data have long been deemed generally unsuitable for *ab initio* solution of crystal structures. This is because the dynamical effects present in the electron diffraction scramble the intensities to such an extent that the structure-solution techniques, which are based on the kinematical theory of diffraction, do

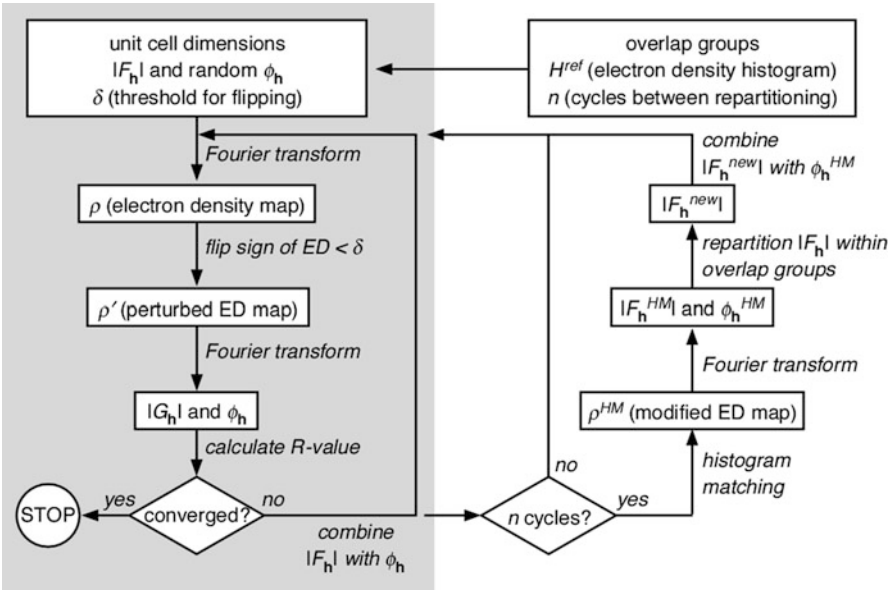

Fig. 10.4 The flowchart of the charge flipping algorithm with histogram matching (From [13])

not work anymore. The situation has changed a few years ago, when the precession electron diffraction method gained more attention. With this method the electron beam precesses with high frequency along the surface of a cone with the vertex on the sample. The motion of the beam is compensated under the sample so that the resulting diffraction pattern is still point-like. The intensities in such pattern are then integrals over all orientations of the incident beam along the cone. As a result, some of the dynamical effects are averaged out, and the intensities are closer to intensities predicted by kinematical theory.

Despite of this important advance the PED intensities are not perfectly kinematical, and they exhibit non-negligible dynamical effects. Therefore, from the point of view of the structure solution, the intensity data from PED can be considered a very noisy kinematical data set.

Charge flipping does not make any use of atomic scattering factors, because it operates only with the scattering density. Therefore, charge flipping can be, in principle, applied without any modifications to precession electron diffraction data.

Practical applications of charge flipping can be hindered by the incompleteness of the data set. Traditionally the intensity data are recorded as a set of oriented zone-axis patterns. Such a data set can have severe gaps and relatively low completeness even at low diffraction angles. As mentioned earlier, such incomplete data set is not suitable for charge flipping. Recently, however, 3D diffraction tomography technique is becoming more and more popular [19, 20]. In this technique the sample is rotated in small steps, and a diffraction pattern is recorded in each step.

The intensities are then extracted from the collected images analogically to the standard procedure used in X-ray crystallography, and the data set is complete within the limits of the tilt of the sample holder.

The application of charge flipping to solution of crystal structures from precession electron diffraction data is still in its very beginning. The first demonstration on a structure of barium sulphate has been made by Mugnaioli et al. [21]. Eggeman et al. [22] showed a solution of the structure of erbium pyrogermanate by charge flipping, and proposed a special treatment of symmetry to enhance the quality of the structure solution from sparse intensity data. Recently charge flipping was successfully applied to a structure solution of a complex aperiodic structure of copper silicogermanate Cu_{3+x}(Si,Ge) [23]. The latter example illustrates the potential of charge flipping for the solution of complex structures. The full potential and limitation of the application still remains to be explored.

References

1. Giacovazzo C, Monaco HL, Artioli G, Viterbo D, Ferraris G, Gilli G, Zanotti G, Catti M (2002) Fundamentals of crystallography, 2nd edn. Oxford University Press, Oxford
2. DeTitta GT, Weeks CM, Thuman P, Miller R, Hauptman HA (1994) Structure solution by minimal function phase refinement and Fourier filtering: theoretical basis. Acta Crystallogr A 50:203–210
3. Weeks CM, DeTitta GT, Hauptman HA, Thuman P, Miller R (1994) Structure solution by minimal function phase refinement and Fourier filtering: II. Implementation and applications. Acta Crystallogr A 50:210–220
4. Combettes P (1997) Hilbertian convex feasibility problem: convergence of projection methods. Appl Math Optim 35:311–330
5. Thibault P (2007) Algorithmic methods in diffraction microscopy. Dissertation, Cornell University
6. Oszlányi G, Sütő A (2004) Ab initio structure solution by charge flipping. Acta Crystallogr A60:134–141
7. Oszlányi G, Sütő A (2005) Ab initio structure solution by charge flipping. II. Use of weak reflections. Acta Crystallogr A61:147–152
8. Oszlányi G, Sütő A (2008) The charge flipping algorithm. Acta Crystallogr A63:156–163
9. Oszlányi G, Sütő A (2007) Ab initio neutron crystallography by the charge flipping method. Acta Crystallogr A 63:156–163
10. Palatinus L, van der Lee A (2008) Symmetry determination following structure solution in P1. J Appl Crystallogr 41:975–984
11. Le Bail A, Duroy H, Fourquet JL (1988) Ab initio structure determination of LiSbWO6 by X-ray powder diffraction. Mater Res Bull 23:447–452
12. Pawley GS (1981) Unit-cell refinement from powder diffraction scans. J Appl Crystallogr 14:357–361
13. Baerlocher C, McCusker L, Palatinus L (2007) Charge flipping combined with histogram matching to solve complex crystal structures from powder diffraction data. Z Kristalogr 222:47–53
14. Le Bail A, Cranswick L (2009) Third structure determination by powder diffractometry round robin (SDPDRR-3). Powder Diffr 24:254–262
15. Wu JS, Leinweber K, Spence JCH, O'Keefe M (2006) Ab initio phasing of X-ray powder diffraction patterns by charge flipping. Nat Mater 5:647–652

16. Zhang KYJ, Main P (1990) Histogram matching as a new density modification technique for phase refinement and extension of protein molecules. Acta Crystallogr A 46:41–46
17. Baerlocher C, Gramm F, Massuger L, McCusker LB, He ZB, Hovmoller S, Zou XD (2007) Structure of the polycrystalline zeolite catalyst IM-5 solved by enhanced charge flipping. Science 315:1113–1116
18. Baerlocher C, Xie D, McCusker LB, Hwang SJ, Chan IY, Ong K, Burton AW, Zones SI (2008) Ordered silicon vacancies in the framework structure of the zeolite catalyst SSZ-74. Nat Mater 7:631–635
19. Kolb U, Gorelik T, Kuebel C, Otten MT, Hubert D (2007) Towards automated diffraction tomography: part I – data acquisition. Ultramicroscopy 107:507–513
20. Zhang D, Oleynikov P, Hovmoller S, Zou X (2010) Collecting 3D electron diffraction data by the rotation method. Z Krist 225:94–102
21. Mugnaioli E, Gorelik T, Kolb U (2009) Ab initio structure solution from electron diffraction data obtained by a combination of automated diffraction tomography and precession technique. Ultramicroscopy 109:758–765
22. Eggeman A, White T, Midgley P (2009) Symmetry-modified charge flipping. Acta Crystallogr A65:120–127
23. Palatinus L, Klementová M, Dřínek V, Jarošová M, Petříček V (2011) An incommensurately modulated structure of η'-phase of Cu3+xSi determined by quantitative electron diffraction tomography. Inorg Chem 50(8):3743–3751

Chapter 11
Structure Solution: Global Optimisation Methods

Kenneth Shankland

Abstract The direct location of atomic positions from electron density maps generated using conventional direct methods solutions is a far more difficult exercise when using powder data as opposed to single crystal data. Global optimisation methods that involve the assessment of trial crystal structures in real space offer a powerful alternative method of structure solution that circumvents the map interpretation stage by directly maximising the agreement between calculated and observed diffraction intensities.

11.1 Introduction

Given a known unit cell, space group, and a set of atomic coordinates with corresponding atom types, the structure factors for a trial crystal structure may be easily calculated. The agreement between these structure factors and a set of experimentally determined structure factor intensities (obtained from, for example, a Pawley or LeBail refinement against a powder pattern) can be easily quantified using a measure such as the |F| R-factor:

$$R = \sum_{\mathbf{h}} ||F_{\mathbf{h}}^{o}| - K\,|F_{\mathbf{h}}^{c}|| \Big/ \sum_{\mathbf{h}} |F_{\mathbf{h}}^{o}|$$

where the summation is over the list of observed intensities [1].

K. Shankland (✉)
School of Pharmacy, University of Reading, Whiteknights, PO Box 224, Reading, UK
e-mail: k.shankland@reading.ac.uk

U. Kolb et al. (eds.), *Uniting Electron Crystallography and Powder Diffraction*,
NATO Science for Peace and Security Series B: Physics and Biophysics,
DOI 10.1007/978-94-007-5580-2_11,

Fig. 11.1 The number of stationary point χ^2 values located on the χ^2 hypersurface of FFB. The χ^2 agreement factor is as defined in [3]. A total of one million minimisations was run in order to locate the ca. quarter of a million stationary points

χ^2 range	No. of χ^2 values
$0 < \chi^2 \leq 200$	10
$200 < \chi^2 \leq 400$	453
$400 < \chi^2 \leq 600$	138,491
$600 < \chi^2 \leq 800$	74,208
$800 < \chi^2 \leq 1{,}100$	1085
Total	214,527

The chances of guessing all of the atomic positions in a crystal structure correctly in a single step are negligible, even if significant amounts of prior chemical information are incorporated into the formulation of those positions (see, for example the Chapter 5). As such, the coordinates of the trial structure must be adjusted in order to explore the function that describes the agreement between the calculated and measured diffraction data, with a view to maximising the level of agreement, which equates to minimizing the R-factor (or some equivalent fit criterion, such as χ^2). This function has *N*-dimensions, where *N* is the number of structural parameters associated with the formulation of the model being optimised. The process of structure solution is therefore equivalent to searching for, and locating the position of, the minimum value of an *N*-dimensional agreement hypersurface. Though the exact topology of the surfaces varies from problem to problem, it is the topology (as opposed to the number of dimensions) that determines how difficult it is to locate the global minimum – were it everywhere convex, for example, containing just one minimum, local minimisation from any point would always locate the global minimum. In fact, a typical hypersurface in the context of structure solution exhibits multiple stationary points – this is easily verified by employing multiple local minimisations, starting from random trial structures each time. Figure 11.1 shows the results of such a verification exercise, for the relatively simple 13 dimensional problem of solving the crystal structure of famotidine form B from powder data fitted to 1.75 Å resolution [2].

These stationary points may be divided into two sets: (a) the *global* minimum that corresponds to the fully determined crystal structure and (b) *local* minima and saddle points that correspond to incorrectly determined crystal structures. In a structure *refinement*, it is assumed that the starting model is sufficiently close to the true crystal structure that the agreement function value lies within the radius of convergence of the *N*-dimensional well that surrounds the global minimum. In these circumstances, least-squares can quickly locate the precise global minimum. In structure solution, this is unlikely to be the case and so global optimisation algorithms, that possess the ability to escape from local minima, are employed. Figure 11.2 shows a block outline of a generic global optimisation strategy for powder diffraction.

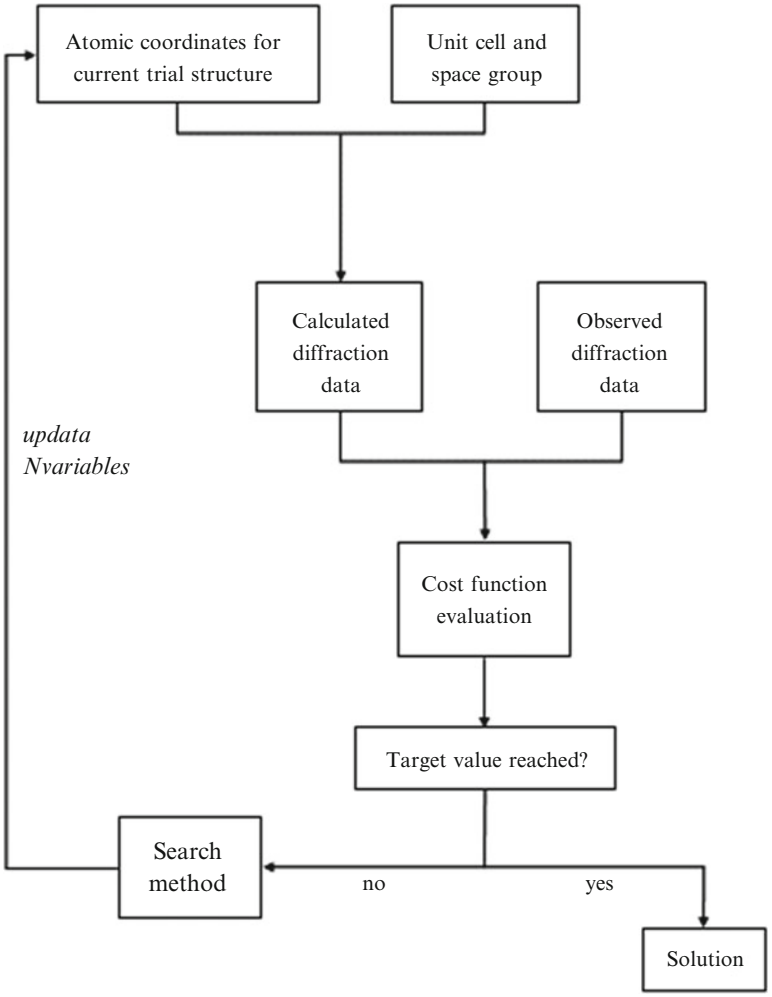

Fig. 11.2 A generic flowchart for implementing a global optimisation approach to crystal structure solution. The target value is usually some small multiple of the best R_{wp} or χ^2 obtained from a Pawley or LeBail fit to the data

11.2 Search Methods

A wide range of search methods, designed to locate the global minimum in a structure solution context, have been employed. Any 'Monte-Carlo' method involves some element of random sampling; the term 'Reverse Monte-Carlo' is sometime used in the context of the solution of disordered crystal structures [4]. Here, we use the term 'global optimisation' to represent both *search* and *optimisation* algorithms, bearing in mind that 'global search' and 'global optimisation' are normally used interchangeably in the literature [5].

The global optimisation problem in powder diffraction is analogous to the conformational search problem in molecular modelling [6], with the additional complication that the position and orientation of the molecule in the unit cell must also be identified. It is therefore unsurprising that many of the optimisation methods employed in molecular modelling are transferable to the crystal structure solution problem.

The simplest approach is to perform an exhaustive grid search over the parameter space of interest, and this has been applied successfully to some problems in powder diffraction [7, 8]. However, the 'combinatorial explosion' that arises when dealing with large numbers of parameters renders the approach somewhat limited in applicability.

Simulated annealing (SA) is the most widely used optimisation method for SDPD. References [9–14] all describe SA-based approaches and associated computer programs. It is effective and requires only a limited number of control parameters. A single SA run is only *guaranteed* to find the global minimum after an infinite number of steps, but in practice, the global minimum is normally located in a finite number of steps. There are many variants on the basic SA algorithm. For example, rather than simply reduce the temperature of the system at a preset rate [11], the rate of cooling can be linked to function value fluctuations [3]. Parallel tempering, has also been used to good effect [14]. SA is intrinsically a sequential process but is easily adapted to parallel computing environments in the context of *parametric execution*. For example, multiple SA runs can be started in parallel, in order to ensure that the same function minimum can be located several times from different random starting points [15, 16]. SA has been responsible for the vast majority of crystal structures from powder data solved using the global optimisation approach and has even been combined with direct methods of structure solution to provide an additional powerful tool [17].

Genetic algorithms (GAs) are an approach to global optimisation that borrow heavily from the Darwinian theory of evolution and been widely applied to optimisation problems such as molecular docking [18]. In structure solution, each trial crystal structure is treated as an individual defined by a collection ('chromosome') of variables ('genes'). The fitness of an individual is (generally) nothing more than the figure of merit that describes how well calculated and observed diffraction data agree. The genetic operators of crossover and mutation are applied to generate new structures from a population of individuals, with the fittest members having the highest probability of surviving into subsequent generations. Applied to the powder diffraction problem [19–21] they have proven effective, but are not as widely used as SA. Closely-related evolutionary algorithms have also been applied to the powder problem [22] though they have not found wide adoption. As with SA, there are a great many variants on the basic theme. For example, Lamarkian evolution assumes that an individual is not a fixed-fitness entity, but rather one that improves during its lifetime and that such improvements are coded back into the chromosome. This notion can be incorporated into computer code by use of a *local* optimiser,

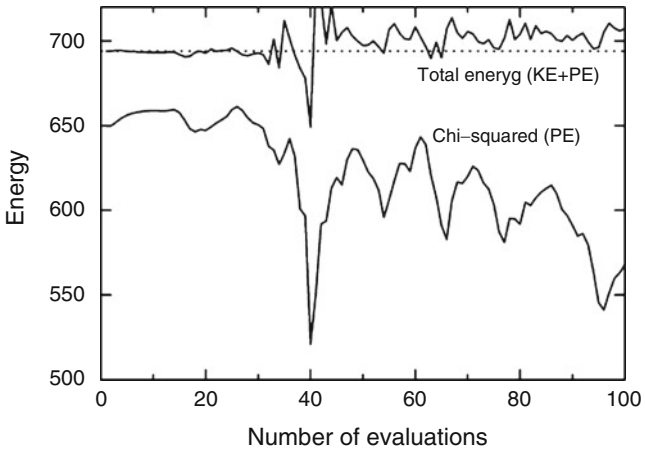

Fig. 11.3 The potential energy (FOM for fit to the data) and total energy (kinetic energy plus potential energy) evaluated over a single MD trajectory during the crystal structure solution of capsaicin. The initial total energy is shown as a dotted line in order to highlight the total energy fluctuations arising from the finite MD step size

which quickly pulls each candidate GA solution to location of the closest function minimum before the genetic operators are applied. Unsurprisingly, this can improve the convergence rate of a GA significantly [23].

Both SA and GAs are examples of *stochastic* algorithms, but *deterministic* algorithms can also be employed in the context of global optimization. An excellent example is the hybrid Monte Carlo (HMC) approach [24] – the algorithm combines the key components of molecular dynamics (MD) and Monte Carlo (MC) simulations to achieve efficient sampling of phase space, allowing a crystal structure to be solved more effectively than using a SA-based approach. Put simply, the trial crystal structure can be considered to be a hypothetical particle moving over a hypersurface, following a trajectory determined by its initial momentum and the local gradient of the hypersurface. As the total "energy" of the system must be conserved throughout a particular particle trajectory, a promising structure (i.e. one lying on a low point of the hypersurface) is said to have low potential energy and high kinetic energy. It is this high kinetic energy component that allows the particle to subsequently move uphill and thus escape local minima. Figure 11.3 shows how the algorithm explores the potential energy surface and how the finite step size in the MD component results in an accumulation of errors in the total energy. It is here, at the end of a single MD trajectory, that the MC component is invoked to decide whether or not the trajectory should be accepted or rejected, in a way similar to the move accept/reject step in SA.

Other approaches have been investigated and sometimes incorporated into SDPD schemes. For example, the downhill simplex can be employed towards the end of a global optimisation as a robust method for quickly and efficiently descending to

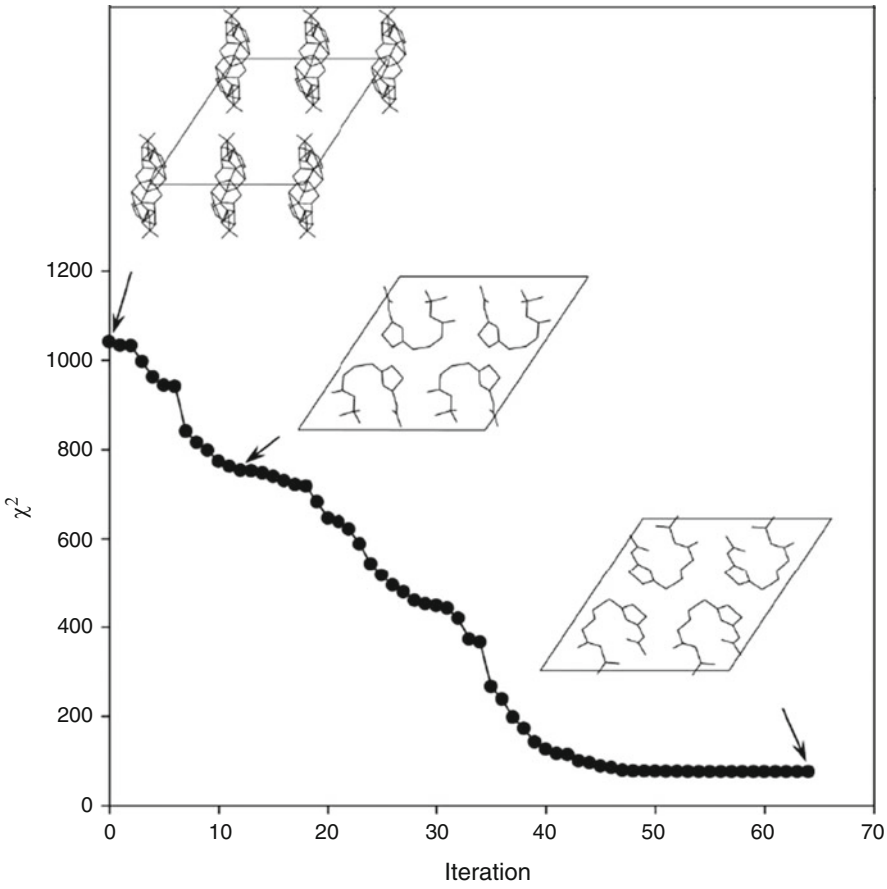

Fig. 11.4 χ^2 (hypersurface FOM) values at each of the 64 iterations of a single successful quasi-Newton Raphson minimisation of the structure of famotidine form B i.e. one that reaches the global minimum of $\chi^2 = 75.3333$. The unit cell contents (viewed down the *b*-axis) of the structure are shown at 3 points along the path

the lowest point on the hypersurface from the lowest point located by the global optimisation method [25]. Recently, it has been shown (somewhat unexpectedly) that simple local minimizers can in fact locate the global minimum from a completely random start point [2]. Furthermore, they do so with a frequency higher than that expected if one assumes that all stationary points have an equal probability of location. Figure 11.4 shows the trajectory of one successful quasi-Newton Raphson minimisation for the structure of famotidine form B (13 degrees of freedom). Whilst this plot appears similar to the 'ridge-and-cliff'-type plots sometimes used to illustrate the progress of global optimisation algorithms, there is an important distinction; the latter show *only* the lowest hypersurface values encountered as a function of time, whereas Fig. 11.4 shows *all* hypersurface values encountered,

confirming the monotonically decreasing nature of the path. The starting structure is clearly randomised and a recognisable structure appears after only 30 iterations, with the structure clearly solved by iteration 50. Significantly, minimisation takes less than 50 μs to execute on a single core of a 2.5 GHz Xeon E5420 CPU.

The contribution of global optimisation methods to structure solution has been, and continues to be, highly important but there is clearly still significant room for development in the coming years.

Acknowledgements I am extremely grateful to my collaborators Bill David, Tony Csoka, Anders Markvardsen, John Johnston, Gareth Didlick and Chris Rowlatt, all of whom have played crucial roles in helping me explore the global optimisation landscape.

References

1. Shankland K, David WIF (2002) Global optimisation. In: David WIF, Shankland K, McCusker LB, Baerlocher C (eds) Structure determination from powder diffraction data. Oxford University Press, Oxford
2. Shankland K, Markvardsen AJ, Rowlatt C, Shankland N, David WIF (2010) A benchmark method for global optimization problems in structure determination from powder diffraction data. J Appl Crystallogr 43:401
3. David WIF, Shankland K, Shankland N (1998) Routine determination of molecular crystal structures from powder diffraction data. Chem Commun 931
4. Keen DA (1998) In: Billinge SJL, Thorpe MF (eds) Local structure from diffraction. Plenum Press, New York
5. Hazelrigg GA (1996) Systems engineering: an approach to information based design. Prentice-Hall International, Upper Saddle River
6. Leach AR (2001) Molecular modelling: principles and applications, 2nd edn. Prentice-Hall, Harlow
7. Hammond RB, Roberts KJ, Docherty R, Edmondson M (1997) Computationally assisted structure determination for molecular materials from X-ray powder diffraction data. J Phys Chem B 101:6532
8. Dova E, Goubitz K, Driessen R, Sonneveld E, Chernyshev V, Schenk H (2001) Structure determination of two organometallic complexes from powder data using grid-search techniques. Materials Science Forum 378–371:798
9. Andreev YG, MacGlashan GS, Bruce PG (1997) Ab initio solution of a complex crystal structure from powder-diffraction data using simulated-annealing method and a high degree of molecular flexibility. Phys Rev B 55:12011
10. Engel GE, Wilke S, Konig O, Harris KDM, Leusen FJJ (1999) PowderSolve – a complete package for crystal structure solution from powder diffraction patterns. J Appl Crystallogr 32:1169
11. Putz H, Schon JC, Jansen M (1999) Combined method for ab initio structure solution from powder diffraction data. J Appl Crystallogr 32:864
12. Pagola S, Stephens PW, Bohle DS, Kosar AD, Madsen SK (2000) The structure of malaria pigment beta-haematin. Nature 404:307
13. Coelho AA (2001) Whole-profile structure solution from powder diffraction data using simulated annealing. J Appl Crystallogr 33:899
14. Favre-Nicolin V, Cerny R (2004) FOX: modular approach to crystal structure determination from powder diffraction. Epdic 8:433–4, Trans Tech Publications Ltd.

15. Griffin TAN, Shankland K, van de Streek J, Cole J (2009) GDASH: a grid-enabled program for structure solution from powder diffraction data. J Appl Crystallogr 42:356
16. Rohlíček J, Husák M, Favre-Nicolin V (2011) FOX.Grid – a grid computing extension of the Fox program for ab initio structure determination from powder diffraction. http://vincefn.net/Fox/Manual/Fox.Grid
17. Altomare A, Caliandro R, Giacovazzo C, Moliterni AGG, Rizzi R (2003) Solution of organic crystal structures from powder diffraction by combining simulated annealing and direct methods. J Appl Crystallogr 36:230
18. Jones G, Willett P, Glen RC, Leach AR, Taylor R (1997) Development and validation of a genetic algorithm for flexible docking. J Mol Biol 267:727
19. Kariuki BM, Serrano-Gonzalez H, Johnston RL, Harris KDM (1997) The application of a genetic algorithm for solving crystal structures from powder diffraction data. Chem Phys Lett 280:189
20. Shankland K, David WIF, Csoka T (1997) Crystal structure determination from powder diffraction data by the application of a genetic algorithm. Z Kristall 212:550
21. Deng XD, Dong C (2011) EPCryst: a computer program for solving crystal structures from powder diffraction data. J Appl Crystalogr 44:230
22. Chong SY, Tremayne M (2006) Combined optimization using cultural and differential evolution: application to crystal structure solution from powder diffraction data. Chem Commun 4078
23. Turner GW, Tedesco E, Harris KDM, Johnston RL, Kariuki BM (2000) Implementation of Lamarckian concepts in a Genetic Algorithm for structure solution from powder diffraction data. Chem Phys Lett 321:183
24. Johnston JC, David WIF, Markvardsen AJ, Shankland K (2002) A hybrid Monte Carlo method for crystal structure determination from powder diffraction data. Acta Crystallogr A 58:441
25. David WIF, Shankland K, Van de Streek J, Pidcock E, Motherwell WDS, Cole JC (2006) DASH: a program for crystal structure determination from powder diffraction data. J Appl Crystallogr 39:910

Chapter 12
Proteins and Powders: Technical Developments

Jonathan P. Wright

Abstract Protein powder samples offer many technical challenges for powder diffraction experiments and data analysis. Samples are sensitive to radiation damage and the large unit cells lead to severe peak overlaps, creating interesting challenges. Powder diffraction remains as the unique tool to characterize certain polymorphic forms of crystalline proteins.

Some 12 years ago Von Dreele published a Rietveld refinement of the structure of the protein myoglobin from powder diffraction data [1]. For many crystallographers this came as a surprise; could it be possible to refine a 1,261 atom structure using only a powder diagram? This landmark achievement was the result of a system of stereochemical restraints which keeps the local atomic geometry correct while the secondary and tertiary structures of the molecule were determined by the powder data. This work generalizes to many different protein structures, almost all proteins mainly consist of a folded polymeric chain of amino acids, so that the same restraint macros can be re-used. By making his work available to the community in the GSAS software package [2] Von Dreele has helped many of us to join him in working at an exciting new frontier in powder diffraction.

Since that breakthrough there has been good deal of progress and other reviews are already available [3, 4]. This chapter focuses mainly on technical aspects and should be complementary to previous reviews, and also to the next chapter from Irene Margiolaki which gives more scientific results.

Technical developments come about when we address difficult challenges. A few proteins, such as lysozyme, offer highly crystalline samples with huge unit cells so

J.P. Wright (✉)
European Synchrotron Radiation Facility, 6 rue Jules Horowitz, BP-220,
Grenoble F-38043, France
e-mail: wright@esrf.fr

U. Kolb et al. (eds.), *Uniting Electron Crystallography and Powder Diffraction*,
NATO Science for Peace and Security Series B: Physics and Biophysics,
DOI 10.1007/978-94-007-5580-2_12,

that we can obtain stunning diffraction patterns and really push our instrumentation to the limits [5]. Making a complete analysis of such a rich dataset then encourages progress on software and algorithms too. With these new methods in hand, proteins provide a rich source of poorly crystalline samples and difficult problems which motivate us to optimize our strategies as far as possible.

Protein structures are unlike small molecule or inorganic crystal structures in a couple of important ways; we rarely have "atomic resolution" in the data and so we cannot resolve individual atomic positions, also, large regions of the unit cell may be filled with liquid water. The "structural resolution" is usually quoted in Ångstroms and corresponds to the real space resolution for which the data can provide an electron density map. A "high resolution" crystal structure is one where we can actually see the atoms, and would be somewhat better than 2 Å. If we can obtain a structural resolution of around 3 Å we may expect to see how the protein chain is folded and packed into the crystal. At resolutions lower than about 10 Å the peak intensities are strongly affected by the disordered solvent in the structure, but still give information about how the molecules pack into the unit cell. Many of the technical developments have been motivated to increase the structural resolution we can obtain as far as possible.

The structural resolution we can obtain for a powder depends on the sample and instrumentation, as for a single crystal. However, quite unlike single crystal data, the numerical resolution is strongly affected by the size of the unit cell of the sample. In a powder pattern the density of overlapping peaks gets worse as we go further out into the reciprocal lattice. Even with high resolution instrumentation it is rare to get more than about 1,000 peaks out of a powder diagram. This leads to a conclusion that the structural resolution we may obtain for a sample is on the order of the size of the asymmetric unit divided by 10, or in other words, $10 \times 10 \times 10$ independent voxels. This limit may be too cautious if there is high solvent content or other favorable effects, but nevertheless, it gives a useful guide as to what can be expected for structural resolution from powder data. For a small protein with a unit cell of 20–30 Å we may resolve amino acid side chains (2–3 Å), but for a large macromolecular complex, we will probably remain limited to seeing only the tertiary structures from powder data.

The strong contribution of the liquid water in a protein crystal structure causes large changes in the low angle peak intensities. These differences may be modeled by a Babinet model where all atoms are assumed to be embedded in a continuous electron density from which they displace a local volume. This model modifies the atomic scattering factors according to:

$$F = F_0 - A \exp\{-8\pi^2 U \sin^2\theta/\lambda^2\}$$

This Babinet model was originally implemented for powder data in the GSAS software package [2]. "A" represents the average electron density of the solvent and takes values of 3–6 and "U" is a thermal parameter falling in the range 1–10. The equivalent model is also now available in Topas; see reference [6] for details on how to use Topas with protein data. An alternative approach which is more

common in protein crystallography is to fill the empty parts of the unit cell with a uniform density. Then a Fourier transform is carried out to get the structure factor of these solvent regions. An advantage of this method is that empty regions of the unit cell which are too small to contain water can be excluded. This method has been implemented in the protpow software [7]. Until recently the main drawback of the map based methods were that they were not differentiable for least squares fitting, but this too has been addressed in a recent publication [8]. We may hope that this new differentiable model will improve the fitting of low resolution powder data, as soon as it can be implemented into the various software packages.

In order to solve or refine any complex structure from a powder sample we should try to get the best possible data. More time spent on the sample preparation and experiment will make any analysis easier. We want to get data with good counting statistics and very sharp diffraction peaks, but these two goals lead to a conflict, when we improve the peak resolution, we tend to cut down the count rate. Proteins present a problem as the counts we can collect are limited by radiation damage in the sample.

Cooling the sample to cryogenic temperatures reduces the rate of radiation damage by a factor of about 80 in most protein samples. Protocols for cryoprotection of single crystal samples are almost universally used nowadays and many single crystal synchrotron beamlines allow samples to be delivered and loaded onto the diffractometer while remaining always at low temperatures. For powder diffraction, cryocooling turns out to be more difficult than expected. The problem is avoiding the formation of crystalline ice, which causes large strains and damage to the protein crystals. By cooling a sample very quickly we can avoid ice formation and instead obtain amorphous ice. Typically this process can be favoured by adding a cryoprotectant chemical to the mother liquor which disrupts the formation of crystalline ice.

We compared the effects of a series of different cryoprotectant molecules in a systematic study [9] where we found that higher concentrations of cryoprotectants worked better. We also found that the peak broadening due to strain is proportional to the unit cell change which occurred when the sample was frozen. Since then, Yves Watier [10] has further developed cryoprotection strategies for powders at ESRF by using annular samples and kapton capillaries. A thin annular sample can be prepared by inserting an empty capillary up the centre of a previous filled capillary sample. The thin sample can then be cooled much more rapidly and uniformly when plunging into liquid nitrogen, in comparison to the regular capillary sample, where the core of the sample is insulated from the outside. This procedure is also helped by the relatively high thermal conductivity of kapton at low temperatures. Unfortunately, some small amounts of peak broadening are still induced by cryocooling a sample, so that the data are not as sharp as can be obtained at room temperature.

While a cryocooled sample will last for many hours in the X-ray beam, even at an undulator beamline at the ESRF, at room temperature the lifetime is around 10 min. When a large sample is available, radiation damage problems may be avoided at ID31 at the ESRF due to the invention of a translating capillary spinner. A series

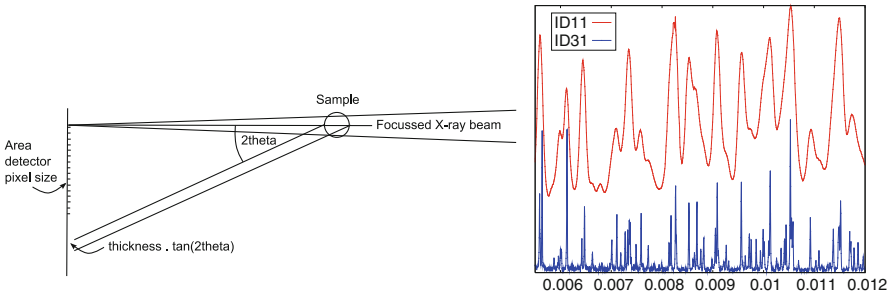

Fig. 12.1 *Left*, geometrical contributions to the peak width in area detector powder diffraction. *Right*, comparison of data for Typsin plotted versus 1/resolution^2 for an analyser crystal instrument (ID31) and an area detector (ID11)

of short scans are collected and then the capillary is translated to give a fresh area of sample for the next scan. By coupling this spinner with a sample changing robot one can continuously replenish the sample as it is destroyed by the X-ray radiation. In this way, the data which can be obtained at ID31 are usually limited by the quantity of sample that is available. Small samples are unfortunately very common, especially when the protein has to be expressed from bacteria. This forces us to turn to area detectors or cryocooling to improve the counting statistics.

By using a 1D strip [11] or 2D area detector [12], we may record many more of the photons scattered by the sample in comparison to the use of a scanning bank of point detectors. The instrumental resolution we can obtain in this case is given mainly by the sample dimensions and the point spread function (typically similar to the pixel size) of the detector system. Many single crystal diffraction beamlines are available at synchrotrons for protein crystallography, and these too may be used for powder diffraction. Getting a good powder diagram requires that the rings recorded on the detector are as narrow as possible, which is helped by focusing the X-ray beam at the detector surface. To overcome the point spread of the detector, it is better to have a very large area detector with many pixels. A cost effective way to make a modest sized are detector appear larger is to place it on a translation stage and scan it. Then the powder diagram can be reconstructed in software by calibrating the detector position and integrating each image separately. The peak width that can be obtained with an area detector is limited by several contributions other than the intrinsic sample broadening:

– Detector pixel size (point spread)
– X-ray beam size at the detector surface
– X-ray band pass and divergence
– Projected sample thickness

The beam size and point spread contributions give an angular broadening which is reduced when the detector distance is increased. The sample thickness broading (Fig. 12.1) depends on tan2θ as well as the sample to detector distance, so that this contribution is reduced for peaks at lower 2θ angles, e.g., it is less problematic

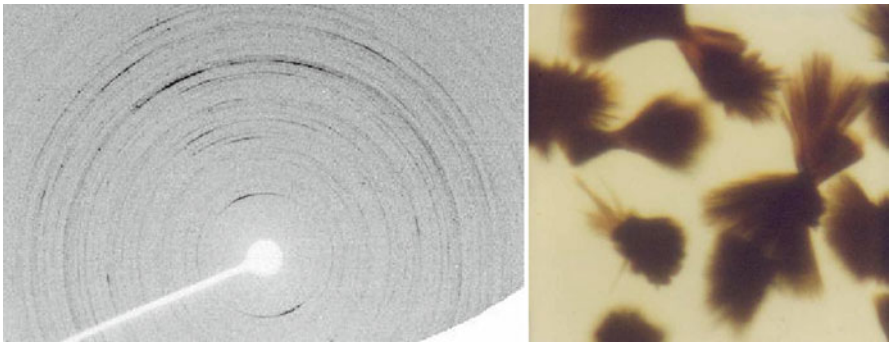

Fig. 12.2 Powder data for myoglobin and the bundles of needles which give rise to these strong preferred orientation effects

for very large unit cells as in proteins. While most of the broadening effects are reduced by moving the detector further back, this does reduce the overall 2θ range. The range can be recovered by scanning the detector, or purchasing one with more pixels. Finally, the bandpass contribution is determined by the X-ray source and optics and contributes as $\cot\theta\, d\theta$, so is typically unimportant for proteins at small θ.

By using a lens focusing system at beamline ID11 at the ESRF [13] we are able to focus the X-ray beamsize to less than 10 μm at the detector surface, making this contribution negligible. The band pass of our Laue-Laue monochromator is about 3×10^{-3} and the pixel size is about 50 μm. If the sample to detector distance is around 1.5 m and the wavelength is 0.3–0.4 Å then we have sufficient resolution to index even very large unit cells [14]. The resolution can be improved by using a thinner sample, or by moving the detector even further back. A similar system at Spring8 uses an image plate and gives a peak width resolution of 0.028° [15].

A great advantage of area detector data, especially for screening samples, is that you get an extra dimension of information about the sample, in comparison to a traditional 1D powder diagram. If the sample shows strong preferred orientation, this is immediately obvious in the area detector images as the rings do not show a uniform intensity around the azimuth (Fig. 12.2). This is explored in greater detail in Chapter 22. We have observed strong preferred orientation effects in a number of proteins. While such images offer strong encouragement for obtaining more "single crystal" like data from powder samples, we still struggle to get strong data at high scattering angles with such samples. This is mainly the technical difficulty of obtaining a large sample while preserving the preferred orientation effect, and also keeping the crystallites wet and immobilised. Ideally a series of images should be collected as the sample rotates, which means overcoming radiation damage problems.

Occasionally, single crystals can be found in a sample which appears to be a powder when viewed in an optical microscope. When data are collected using an area detector and a small beam size we often observe spots superimposed on the powder rings. Then we can perform the same experiment as for single crystal

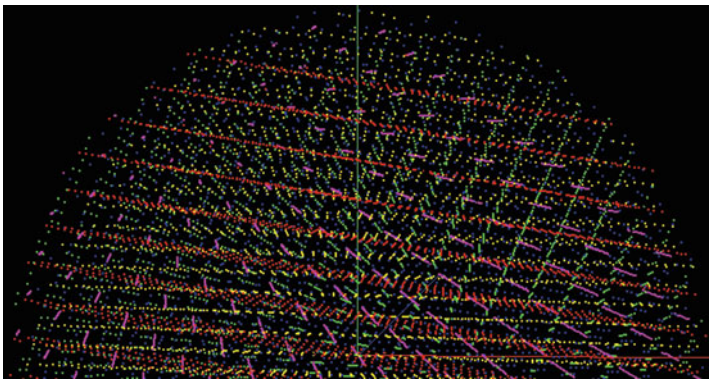

Fig. 12.3 Simulation of five overlapping 3D lattices from a multi-crystal sample of triclinic lysozyme to 3 Å resolution. The peaks were indexed to individual grains in the sample automatically using the index_unknown.py script

diffraction, record a series of pictures as the sample is rotated. Indeed, any powder sample is just a collection of individual single crystals, and if we can make the beam size small enough we may always hope to resolve the individual diffraction spots on the rings. The challenge is then to assign each individual diffraction spot to an individual crystallite in the sample. A good deal of progress has been made in this area thanks to the "TotalCrystallograpy" project [16].

An outline of an algorithm that was developed specifically for indexing protein multi-crystal data is given here. Peak positions the detector are converted into scattering vectors in reciprocal space using the ImageD11 software package [17]. Then the observed peaks are treated as indexed peaks in an arbitrary, but very large sized unit cell. If we make a Patterson map using the data indexed in such a large cell, we will find origin Patterson peaks at the lattice positions of the individual crystallites in the sample. Choosing one of the origin peaks out of this Patterson map will give one of the lattice vectors of one of the crystallites in the sample. We may attempt to group the lattice vectors together by observing which peaks are indexed by multiple Patterson vectors, or simply by a brute force method which picks triplets of vectors from the map. Once the peaks have been assigned to crystals they may be integrated as usual. Figure 12.3 shows a set of 5 superposed lattices which have been indexed using this procedure as implemented in the index_unknown.py script in the ImageD11 software package [17]. The script has also been successful in indexing a number of small molecule crystal samples, as well as the protein multicrystal samples for which it was designed [18].

When we cannot induce crystallographic texture or resolve diffraction spots from individual crystallites, we are faced with the powder overlap problem. One of the ways we can try to alleviate this problem is to persuade the peaks to move a little with respect to each other, so that the pattern of peak overlaps changes. Then by fitting the various patterns to a single set of integrated intensities we can unravel the intensities of the individual contributions. This method has been used

for structure solution of several small molecules [19, 20] and is now often exploited for protein data collections. Many external variables can be used to perturb the unit cell, including; temperature, pressure, pH, humidity, salt concentration and radiation damage.

A multipattern fit using such data can be used to enhance the estimation of overlapped peaks in an intensity extraction. These peaks can then be used for molecular replacement structure solution [12, 21] and typically enhance the signal to noise ratio compared to a single pattern fit. Alternatively the multiple datasets can be combined for a Rietveld refinement of the crystal structure [22, 23]. The multiple histogram approach for Rietveld refinement leads to more stable fits than with a single pattern.

In order to attack the crystallographic phase problem we have also exploited anisotropic variations in the unit cell [24] to improve the data. Currently the majority of software for solving the phase problem is only available for single crystal data, and so we need to extract integrated intensities from the powder profiles. By using likelihood based criteria we are able to improve the estimation of overlapped peaks in intensity extractions, especially in space groups where symmetry systematically enhances certain peaks [25]. Using very heavy atoms, Gadolinium with lysozyme, uranium with elastase, we were able to measure significant changes in peak intensities in the heavy atom derivatives [26]. These intensity changes were sufficient to unambiguously locate the heavy atoms in the unit cell and the find the shapes of the solvent channels in the structure. By adding data from another heavy atom derivative, based on Holmium, to the lysozyme data, it was possible to find shown the shape of a protein molecule [27]. Electron density maps showing the backbone of the protein molecule were of sufficient quality to be interpreted by automatic software.

Suppression of radiation damage has been critical to being able to collect powder data for proteins at elemental absorption edges. In order to detect small differences due to anomalous scattering good counting statistics are required. In the study of $PtBr_6$ binding to lysozyme [28] data were recorded at the f′ dip wavelength which corresponds to the inflection point on the absorption edge. This is in contrast to single crystal MAD experiments where a wavelength at the top of the absorption edge will be selected. The reasoning for this is as follows; atomic scattering factors near and absorption edge are given by:

$$f = f_0 + f' + \mathrm{if}''$$

For any reflection (hkl) there will always be another reflection (-h-k-l) which overlaps it exactly. The contribution of f′ to the structure factor summation is the same for both of these reflections, however, the contribution of the f″ part has a phase shift which is opposite for the two reflections in the Friedel pair. Therefore we should experimentally maximize the f′ variation. This has been explored in detail by Prandl [29, 30]. Figure 12.4 shows how the contributions add up:

By using a cryocooled sample and collecting data at both the Br and Pt edges Helliwell et al. [28] were able to recover the positions of the heavy elements in the

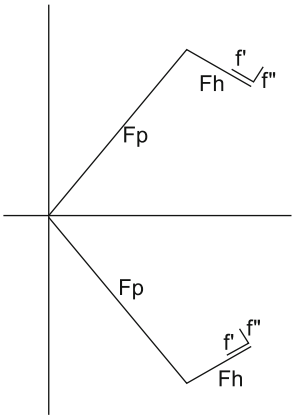

Fig. 12.4 Protein (Fp) and heavy atom (Fh) contributions to the structure factor for a Friedel pair. At the absorption edge f′ and f″ modify the Fh contribution

unit cell. These show up clearly in difference Fourier maps. Once the heavy atom substructure has been obtained, the next step is to compute an electron density map for the protein. While a range of single crystal software packages are available, more optimized methods have recently been developed for MAD phasing of powder data [31, 32].

When we refine complex structures we are often not sure that the changes we make to a model offer a genuine improvement, or whether we are merely fitting the noise which is present in the data. One useful figure of merit that has been developed for protein crystallography is the free R-factor. The idea is exclude a fraction of the dataset from the refinement and then watch how the model predicts these excluded peaks as the fitting progresses. One can think of this procedure as hiding some data from our refinement software which we can use to monitor progress. In a powder diagram it does not work to remove some individual data points for this computation, as they can easily be interpolated based on their neighbors. A method was proposed by the author in terms of a refinement based on extracted correlated integrated intensities [33]. To apply the same idea in a Rietveld refinement one would need to allow the free-R reflections to vary so that they fit the pattern as well as possible, and then compare them to the computed values from the model. In practice this could be achieved either by including their intensities as free variables (as in a Pawley refinement) or, perhaps with less programming effort, by using Lebail extraction for these peaks. One just needs to replace Icalc by Iobs from the previous cycle only for free-R flagged reflections, and then compute the R-factors as usual.

The future outlook for protein powder diffraction is bright and there are still many opportunities for cross fertilization of ideas. By combining powder diffraction data with NMR and molecular dynamics simulations we may expect to go further in the size and complexity of powder structures that can be tackled. Moreover, as our knowledge of protein structure becomes more and more detailed, based on the results of the many single crystal structures that are produced in the PDB databank, we may get better at producing restraints for low resolution crystallography. A

recent development of DEN refinement [34] added a new restraint which was highly effective for low resolution single crystal structures; we may hope it will be equally useful for powder data.

Powder diffraction as a technique has many applications outside of structure solution, and continues to play an important industrial role in phase identification. Recent developments at the free electron laser would seem to suggest that the size limitation for single crystal diffraction no longer exists [35], and so that 1 day there might be fewer structural problems which are only amenable to powder diffraction, but probably not for a few more years. Nevertheless, for polymorph characterization and in-situ experiments, powder diffraction will continue to offer unique insights to the structural behavior of macromolecular crystals.

Acknowledgements I am especially grateful to my collaborators in this adventure into protein powder diffraction; Irene Margiolaki, Yves Watier and Andy Fitch and all of the students and colleagues who have carried the work that was summarized here. We thank the ESRF for provision of synchrotron beamtime.

References

1. Von Dreele RB (1999) Combined Rietveld and stereochemical restraint refinement of a protein crystal structure. J Appl Crystallogr 32:1084–1089
2. Larson AC, Von Dreele RB (1994) General Structure Analysis System (GSAS), Los Alamos National Laboratory Report LAUR, pp 86–748. see: http://www.ccp14.ac.uk/solution/gsas/
3. Margiolaki I, Wright JP (2008) Powder crystallography on macromolecules. Acta Crystallogr A64:169–180
4. Von Dreele RB (2003) Protein crystal structure analysis from high-resolution X-ray powder-diffraction data. Methods Enzymol 368:254–267
5. Margiolaki I, Wright JP, Fitch AN, Fox GC, Labrador A, Von Dreele RB, Miura K, Gozzo F, Schiltz M, Besnard C, Camus F, Pattison P, Beckers D, Degen T (2007) Powder diffraction studies on proteins: an overview of data collection approaches. Zeitschrift für Kristallographie Suppl 26:1–13
6. Watier Y, Fitch AN (2010) Protein powder diffraction with Topas. Mater Sci Forum 651: 117–129
7. Hartmann CG, Nielsen OF, Ståhl K, Harris P (2010) In-house characterization of protein powder. J Appl Crystallogr 43:876–882
8. Fenn TD, Schnieders MJ, Brunger AT (2010) A smooth and differentiable bulk-solvent model for macromolecular diffraction. Acta Crystallogr D66:1024–1031
9. Jenner MJ, Wright JP, Margiolaki I, Fitch AN (2007) Successful protein cryocooling for powder diffraction. J Appl Crystallogr 40:121–124
10. Watier Y (2011) Powder diffraction studies of proteins. Ph.D thesis, University Joseph Fourier, Grenoble
11. Bergamaschi A, Cervellino A, Dinapoli R, Gozzo F, Henrich B, Johnson I, Kraft P, Mozzanica A, Schmitt B, Shi X (2010) The MYTHEN detector for X-ray powder diffraction experiments at the Swiss Light Source. J Synchrotron Radiat 17:653–668
12. Doebbler JA, Von Dreele RB (2009) Application of molecular replacement to protein powder data from image plates. Acta Crystallogr D65:348–355

13. Vaughan GBM, Wright JP, Bytchkov A, Rossat M, Gleyzolle H, Snigireva I, Snigirev A (2011) X-ray transfocators: focusing devices based on compound refractive lenses. J Synchrotron Radiat 18:125–133
14. Papageorgiou N, Watier Y, Saunders L, Coutard B, Lantez V, Gould EA, Fitch AN, Wright JP, Canard B, Margiolaki I (2010) Preliminary insights into the non structural protein 3 macro domain of the Mayaro virus by powder diffraction. Zeitschrift für Kristallographie 225:576–580
15. Oka T, Miura K, Inoue K, Ueki T, Yagi N (2006) High-resolution powder diffraction study of purple membrane with a large Guinier-type camera. J Synchrotron Radiat 13:281–284
16. See http://www.totalcryst.dk/
17. Wright JP http://sourceforge.net/apps/trac/fable/wiki/imaged11
18. Paithankar KS, Sorensen HO, Wright JP, Schmidt S, Poulsen HF, Garman EF (2011) Simultaneous X-ray diffraction from multiple single crystals of macromolecules. Acta Crystallogr D 67:608–618
19. David WIF, Shankland K, Shankland N (1998) Routine determination of molecular crystal structures from powder diffraction data. Chem Commun 931
20. Brunelli M, Wright JP, Vaughan GBM, Mora AJ, Fitch AN (2003) Solving larger molecular crystal structures from powder diffraction data by exploiting anisotropic thermal expansion. Angew Chem Int Ed 42:2029–2032
21. Margiolaki I, Wright JP, Wilmanns M, Fitch AN, Pinotsis N (2007) Second SH3 Do-main of ponsin solved from powder diffraction. J Am Chem Soc 129:11865–11871
22. Basso S, Fitch AN, Fox GC, Margiolaki I, Wright JP (2005) High-throughput phase-diagram mapping via powder diffraction: a case study of HEWL versus pH. Acta Crystallogr D61: 1612–1625
23. Von Dreele RB (2007) Multipattern Rietveld refinement of protein powder data: an approach to higher resolution. J Appl Crystallogr 40:133–143
24. Besnard C, Camus F, Fleurant M, Dahlström A, Wright JP, Margiolaki I, Pattison P, Schiltz M (2007) Exploiting X-ray induced anisotropic lattice changes to improve intensity extraction in protein powder diffraction: application to heavy atom detection. Zeitschrift für Kristallographie Suppl 26:39–44
25. Wright JP, Markvardsen AJ, Margiolaki I (2007) Likelihood methods with protein powder diffraction data. Z Kristallogr Suppl 26:27–32
26. Wright JP, Besnard C, Margiolaki I, Basso S, Camus F, Fitch AN, Fox GC, Pattison P, Schiltz M (2008) Molecular envelopes derived from protein powder diffraction data. J Appl Crystallogr 41:329–339
27. Basso S, Besnard C, Wright JP, Margiolaki I, Fitch AN, Pattison P, Schiltz M (2010) Features of the secondary structure of a protein molecule from powder diffraction data. Acta Crystallogr D66:756–776
28. Helliwell JR, Bell AMT, Bryant P, Fisher S, Habash J, Madeleine H, Irene M, Kaenket S, Yves W, Wright JP, Yalamanchilli S (2010) Time-dependent analysis of K2PtBr6 binding to lysozyme studied by protein powder and single crystal X-ray analysis. Zeitschrift für Kristallographie 225:570–575
29. Prandl W (1990) Phase determination and Patterson maps from multiwave powder data. Acta Crystallogr A46:988–992
30. Prandl W (1994) Phase determination from X-ray powder diffraction data. II. Partial Patterson maps and the localization of anomalously scattering atoms. Acta Crystallogr A50:52–55
31. Altomare A, Burla MC, Cuocci C, Giacovazzo C, Gozzo F, Moliterni A, Polidori G, Rizzi R (2009) MAD techniques applied to powder data: finding the structure given the sub-structure. Acta Crystallogr A65:291–299
32. Altomare A, Belviso BD, Burla MC, Campi G, Cuocci C, Giacovazzo C, Gozzo F, Moliterni A, Polidori G, Rizzi R (2009) Multiple-wavelength anomalous dispersion techniques applied to powder data: a probabilistic method for finding the substructure via joint probability distribution functions. J Appl Crystallogr 42:30–35

33. Wright JP (2004) Extraction and use of correlated integrated intensities with powder diffraction data. Zeitschrift für Kristallographie 219:791–802
34. Schroeder GF, Levitt M, Brunger AT (2010) Super-resolution biomolecular crystallography with low-resolution data. Nature 464:1218–1222
35. Chapman HN, Fromme P, Barty A, White TA, Kirian RA, Aquila A, Hunter MS, Schulz J, DePonte DP, Weierstall U (2011) Femtosecond X-ray protein nanocrystallography. Nature 470:73–77

Chapter 13
Proteins and Powders: An Overview

Irene Margiolaki

Abstract Following the seminal work of Von Dreele, powder X-ray diffraction studies on proteins are being established as a valuable complementary technique to single crystal measurements. A wide range of small proteins have been found to give synchrotron powder diffraction profiles where the peak widths are essentially limited only by the instrumental resolution. The rich information contained in these profiles, combined with developments in data analysis, has stimulated research and development to apply the powder technique to microcrystalline protein samples. In this chapter, progress in using powder diffraction for macromolecular crystallography is reported.

13.1 Introduction

In recent years, modern powder diffraction techniques have been applied to several microcrystalline proteins. The use of high-resolution synchrotron data, together with new analysis procedures, has stimulated exciting progress which is showing that powders can offer unique opportunities for the structural characterization of proteins and are complementary to existing methods. The developments in experimental methods and instrumentation have been absolutely essential, and they have been discussed recently in another article [1]. Perhaps the most enticing goal for any crystallographer is to solve new structures; we discuss the progress and prospects for powder diffraction data in this area. We then describe in some of the structural

I. Margiolaki (✉)
Department of Biology, Section of Genetics, Cell Biology and Development, University of Patras, GR-26500, Patras, Greece
e-mail: imargiola@upatras.gr

U. Kolb et al. (eds.), *Uniting Electron Crystallography and Powder Diffraction*, NATO Science for Peace and Security Series B: Physics and Biophysics,
DOI 10.1007/978-94-007-5580-2_13,

refinements which have been carried out for powders using single or multiple pattern fitting and the Rietveld method. The application of the powder diffraction method to phase identification in mixtures and crystal screening is also discussed.

13.2 Structure Solution

If powder data contain enough information to refine the structure of a small protein, then it follows that the structure might also be solved from the same data. We are choosing an inclusive definition of 'solving' a protein structure in this context. The use of stereochemical restraints and introduction of prior knowledge, such as the amino acid sequence, will be used to fill in missing information at high resolution. Powder data can certainly be used to uncover new structural information at low or even modest resolution, and we expect to see this becoming a more common approach in the future. As water molecules have been seen in at least two refinements already [1, 2], we can be confident that powder data will be sufficient to unravel new structural information.

13.2.1 The Molecular Replacement Method

In the molecular replacement method [3], a model for a protein molecule is proposed based on other known structures of proteins which have similar amino acid sequences. This model is then oriented and positioned in the unit cell to match the experimental data for the unknown structure. In this era of structural genomics [4], the quality of the search models is expected to improve dramatically so that molecular replacement using a powder diagram may be sufficient to confirm that a new protein is indeed similar to one that is previously known. Proteins are often found in a variety of different organisms with very similar amino acid sequences, or are expressed with a few modified residues to investigate the effects these changes have on the protein. There are only six degrees of freedom to be determined per molecule in solving a structure by molecular replacement. The first three give the orientation and the second three give the position of the molecule with respect to the symmetry elements of the space group. Relatively low resolution data can often be used for molecular replacement problems. A resolution of 6 Å can be sufficient and a cut-off of 3 Å is often applied. Typically, even with single-crystal data, the highest resolution data are not so useful as the details of the model structure will not be correct at high resolution anyway. The solution of the structure of T3R3 insulin by Von Dreele et al. [5] is the first example of the molecular replacement method at work. In our own laboratory, we have been able to successfully use the MOLREP software [6] together with powder data for a variety of small proteins. Integrated intensities are extracted [7] from the powder profile and then treated as if they came from a single crystal, ignoring the overlap problem. Fortunately, the molecular replacement method tolerates errors in the input data as if they were

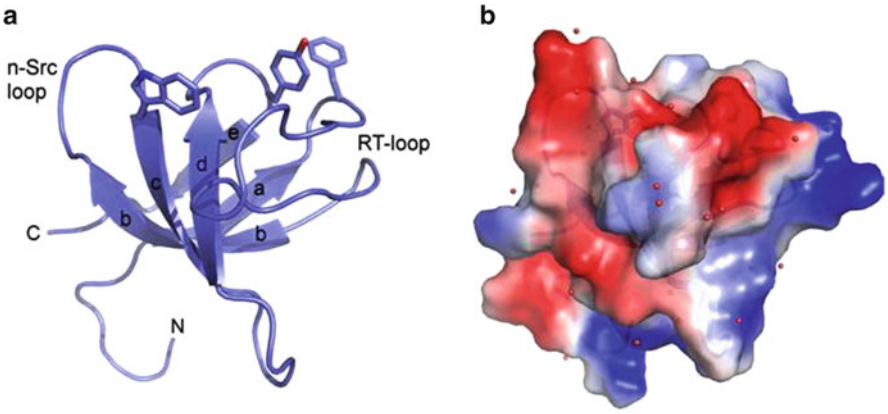

Fig. 13.1 Powder-diffraction structure of the ponsin SH3.2 domain. (**a**) *Ribbon* representation of the SH3.2 indicating the secondary structure elements of the domain. The main hydrophobic residues of the binding interface as well as the positions of the n-Src and RT loops are indicated. (**b**) Electrostatic potential representation of domain identifying additionally the water molecules as *spheres* [1]. This figure was generated using PYMOL (http://pymol.sourceforge.net/)

due to errors in the model for the structure. In the cases of turkey [8] and hen [9] egg white lysozymes, there was a clear distinction of the correct structure which was proposed by MOLREP from the second best, and in both cases these were the correct positions and orientations for the molecule in the unit cell. After determining the position and orientation of a model for the protein molecule in the unit cell, it is of critical importance to be able to go through the structure and identify the regions that are different in the new protein compared to the initial model. A more recent example is the structure solution of the second SH3 domain (SH3.2) of ponsin via molecular replacement. The high-quality extracted intensities from the measured profiles led to the unique determination of an unknown 544-atom protein structure from powder data. The search model had a moderate similarity (38% sequence identity) and was sufficient for molecular replacement and model building based on electron-density maps. Figure 13.1 illustrates the structure of the SH3.2 domain derived from powders [1]. Another example of a molecular replacement style approach is the use of phase angle or structural information from another technique, combined with data collected using powder methods. Oka et al. [10] have investigated the structure of purple membranes, which comprise two-dimensional crystals of bacteriorhodopsin trimers. They collected high-resolution synchrotron powder diffraction data using a 1 m path length Guinier-type camera at beamline BL40B2 at SPring-8. By combining extracted intensities up to a resolution of 4.2 Å with phases from cryoelectron microscopy, they were able to produce an electron-density map. The data from the synchrotron improved the resolution for purple membrane compared to that attained previously with laboratory X-rays (intensities extracted up to ∼7 Å) and opens up the possibility of studying these systems under a wider range of conditions.

Recently, we have extended our studies on the 160 amino-acid nsP3 protein macro domain of the Mayaro virus (MAYV), an emerging virus of South American tropic regions, by means of powder diffraction on microcrystalline precipitants. These results correspond to the first structural data existing in the literature since 1954 when the virus was isolated in Trinidad [11, 12]. Comparison with known structures of sequence-homologous Chikungunya virus (CHIKV) macro domains [13] indicate that MAYV adopts a trigonal/hexagonal structure associated with a looser molecular packing. The cell dimensions of MAYV are significantly altered in comparison to CHIKV and the unit cell is composed of six molecules and 58% solvent. Structure solution via the molecular replacement technique and refinement of MAYV are currently in progress [14].

13.2.2 The Isomorphous Replacement Method

When there is no starting model available for a protein molecule, then we face the crystallographic phase problem. The isomorphous replacement method [15] determines the phases of X-ray reflections by comparing data from a series of crystals which contain different additive heavy atoms. This method was already in common use prior to the application to proteins for the determination of organic structures by comparing crystalline salts with differing cations or anions. The first application to proteins [16] was used to determine the signs of centric reflections in haemoglobin. In order to use the isomorphous replacement method, one needs to collect data for a protein with and without the added heavy atom and to be able to measure and interpret the differences in the data due to the added atoms. Difficulties arise when the addition of the heavy atom perturbs the structure leading to non-isomorphism and differences that can no longer be simply interpreted by a few atoms. With powder data, we can determine whether or not a particular heavy atom has formed a derivative by comparing the unit-cell parameters, which are normally perturbed by the addition of a heavy atom. In the case of a gadolinium derivative of hen egg white lysozyme (HEWL) [17], we prepared derivatives using different concentrations of Gd and also different pH values in order to alleviate the peak-overlap problem. Extracted intensities were then used to solve for the atomic positions of the Gd atoms using SHELXD [18] and then refinement of the heavy-atom substructure and phasing were carried out using Sharp [19]. Similarly, in the case of a uranium derivative of elastase [20], the peak-overlap problem was reduced by comparing data sets that had been exposed to the X-ray beam for different amounts of time. The gradual changes in unit-cell parameters due to radiation damage changed the pattern of peak overlaps sufficiently to deconvolute the overlapping peaks. The U atom is clearly visible in a difference Patterson map from native and derivative data sets and phasing using Sharp proceeds to give a solvent mask which clearly and correctly delineates the protein and solvent regions [17]. Recently, two heavy-atom derivatives of tetragonal HEWL (a gadolinium derivative and a holmium derivative) were crystallized at

room temperature. Using synchrotron radiation, high-quality powder patterns were collected in which pH-induced anisotropic lattice-parameter changes were exploited in order to reduce the problem of overlapping reflections. The phasing power of two heavy atom derivatives in a multiple isomorphous replacement (MIR) analysis enabled molecular structural information to be obtained up to approximately 5.3 Å resolution. At such a resolution, features of the secondary structure of the lysozyme molecule could be accurately located using programs dedicated to that effect. In addition, the quoted resolution was sufficient to determine the correct hand of the heavy-atom substructure which leads to an electron-density map representing the protein molecule of proper chirality [21].

13.3 Rietveld Fits to High-Resolution Synchrotron Powder Data

In 1999, the first protein structure refinement using powder data was reported [22] for metmyoglobin. High-angular resolution synchrotron data from beamline X3B1 ($\lambda = 1.14991$ Å) at the National Synchrotron Light Source (NSLS), Brookhaven National Laboratory, USA, were used for the refinement. A key characteristic of the powder profile was the observation of very sharp reflections associated with the highly crystalline protein sample. By combining a suite of stereochemical restraints with the measured diffraction profile, a successful refinement of the atomic positions of the 1,260-atom protein was achieved (pdb code 1f6h). In order to carry out this refinement, Von Dreele upgraded the GSAS [23] software package in several ways. A suite of stereochemical restraints, as are normally used in low-resolution refinements with single crystal data, were implemented with automatic recognition of atom and bond types for the standard amino acid residues. A novel restraint was introduced to describe the two-dimensional pseudo-potential surface of a Ramachandran plot [24]. Also, a Babinet's principle solvent correction was used to account for the disordered solvent within the crystal structure. The excellent Rietveld fit obtained was a breakthrough, showing for the first time that a crystal structure refinement could be carried out for a protein molecule from powder data. The following year, the structure of a new variant of the T3R3 human insulin–Zn complex, produced by mechanical grinding of a polycrystalline sample, was solved and refined from a powder [5]. It was determined that the reversible grinding-induced phase change is accompanied by 9.5° and 17.2° rotations of the two T3R3 complexes that comprise the crystal structure. These results were later born out by a single-crystal study [25] at cryogenic temperatures (100 K). The possibility of using powder diffraction data on microcrystalline protein samples for detection of ligands in protein–ligand complexes was illustrated by the studies of HEWL complexes with N-acetylglucosamine (NAGn, n = 1–6) oligosaccharides [26, 27]. The location of each NAGn could be found from difference Fourier maps generated from structure factors extracted during preliminary Rietveld refinements. Full

NAGn–protein structures were subjected to combined Rietveld and stereochemical restraint refinements and revealed binding modes for NAGn that depended on the length of the NAG oligosaccharide. The series of refined powder structures are available in the pdb database via access codes 1ja2, 1ja4, 1ja6, 1ja7, 1sf4, 1sf6, 1sf7, 1sfb and 1sfg. These studies showed that powder diagrams can give useful electron density maps for protein samples and show unambiguously that a powder sample can be sufficient for structural analysis. Following the tradition in the powder diffraction community, Von Dreele has made the GSAS software package freely available, including the most recent features for refinements of protein structures. We were able to benefit from this generous philanthropy to use the package in our laboratory to carry out a Rietveld refinement of the structure of turkey egg white lysozyme [8]. By carefully balancing the restraint weights with a highly resolved powder diagram collected at beamline ID31 at the ESRF, we were able to produce an excellent fit and refined model (pdb code: 1xft). In the course of refining this structure using GSAS, we also became convinced that powder methods can indeed be applied to such large structures.

Structure refinements can be improved by the use of multiple datasets, provided there are not significant changes in structure factors between the different data sets. Two independent investigations of HEWL showed that the use of multiple patterns associated with slightly different lattice parameters leads to enhanced extracted intensities and more robust structure refinements [2, 9] using a modified version of GSAS which could account for small lattice strains in different patterns. In our laboratory, we prepared a total of 44 different polycrystalline HEWL precipitates at 277 K and room temperature and in the pH range between 6.56 and 3.33 [9]. High resolution powder diffraction data were collected at room temperature ($\lambda = 1.249826$ Å, ID31, ESRF). The anisotropic effect of pH of crystallization on the lattice dimensions of tetragonal HEWL shifts the peaks significantly and alleviates the peak-overlap problem. We selected four patterns across the range of pH for use in a multi-pattern Rietveld refinement [28] in order to extract an average structural model for tetragonal HEWL using the GSAS software. Some differences between diffraction patterns could be accounted for by allowing the solvent-scattering coefficients to differ for each one of the four histograms following the observation that the largest observed differences in peak intensities were mainly at low angles. A more detailed description of this refinement can be found elsewhere [9] and the model is deposited in the pdb database with access code 2a6u. We found that this approach resulted in a much smoother and more robust refinement than previously experienced with single-pattern fits and produced a structural model with excellent stereochemistry. Von Dreele has also applied a multi-pattern approach to HEWL but using data sets obtained from an image plate and approaching single-crystal resolution limits (dmin $\approx$ 2 Å). The patterns differ due to changes in salt concentration and radiation-induced lattice strains. Anisotropic changes in the unit cell are taken into account in all of these refinements using a special profile function implemented in GSAS (No. 5). Using this function, only one set of unit-cell parameters is refined and those corresponding to the other patterns are related via a strain ($\Delta d/d$) of the reciprocal metric tensor elements. By selecting different combinations of data sets, Von Dreele refined three structural models and

was able to add water molecules in each case (pdb codes 2hs7, 2hs9 and 2hso). Many of these water molecules are conserved between the three models and have also been found in single-crystal structures. The stereochemistries of the resulting multi-dataset models show significant improvements in comparison to previous single-pattern powder refinements. In one of our most recent studies of the second SH3 domain of ponsin [9], we exploited radiation-induced anisotropic lattice strains in a specially modified multi-pattern Pawley refinement taking into consideration likelihood criteria for partitioning overlapped peaks [29]. The outcome of this analysis was a set of improved extracted intensities, in excellent agreement with single-crystal intensities later obtained by an independent experiment. The powder extracted data were sufficient for the structure solution of the domain via the molecular replacement method.

Maximum-likelihood refinement improved the phases to a level where we could trace the main-chain alterations, build additional residues where needed and eventually place the correct side chains along the sequence; a substantial result from powder diffraction data. The protein conformation was refined in a multiple-data-set stereochemically restrained Rietveld analysis taking advantage of sample-induced anisotropic lattice strains. We further benefited from an approach combining multiple-data-set Rietveld analysis and periodical OMIT map [30] computation, to reduce the bias of the final model, extending the resolution limits to levels comparable to single-crystal measurements, and even detecting several water molecules bound to the protein [1]. The refined model is deposited in the pdb database with access code 2O31 and is illustrated in Fig. 13.1.

13.4 Crystal Screening

Powder diffraction has been exploited as a technique for fingerprinting different crystalline substances and allows rapid phase identification and quantification of mixtures. High-resolution powder instrumentation is designed to obtain the sharpest possible peaks in reciprocal space and also to determine accurate peak positions. These features are complementary to area-detector single-crystal experiments, where the aim is normally to measure diffraction peaks at the highest possible scattering angles, to improve the direct-space resolution in an electron-density map. By exploiting the excellent reciprocal-space resolution of powder instruments, a variety of complementary studies can be carried out which are typically more difficult to do with single crystals. Powder samples contain many millions of individual crystallites and give information about the bulk properties of a material; there is no question of whether a particular crystallite is representative of the whole sample.

Wherever microcrystalline proteins come into use as biomaterials or medicines, there will be an increasingly important role for powder diffraction to play. There are many added benefits from using a crystalline form of an already existing drug: it permits better control over the release rate into the system by an optimisation of the crystals size and polymorphism, and it should also offer an extended shelf-life and

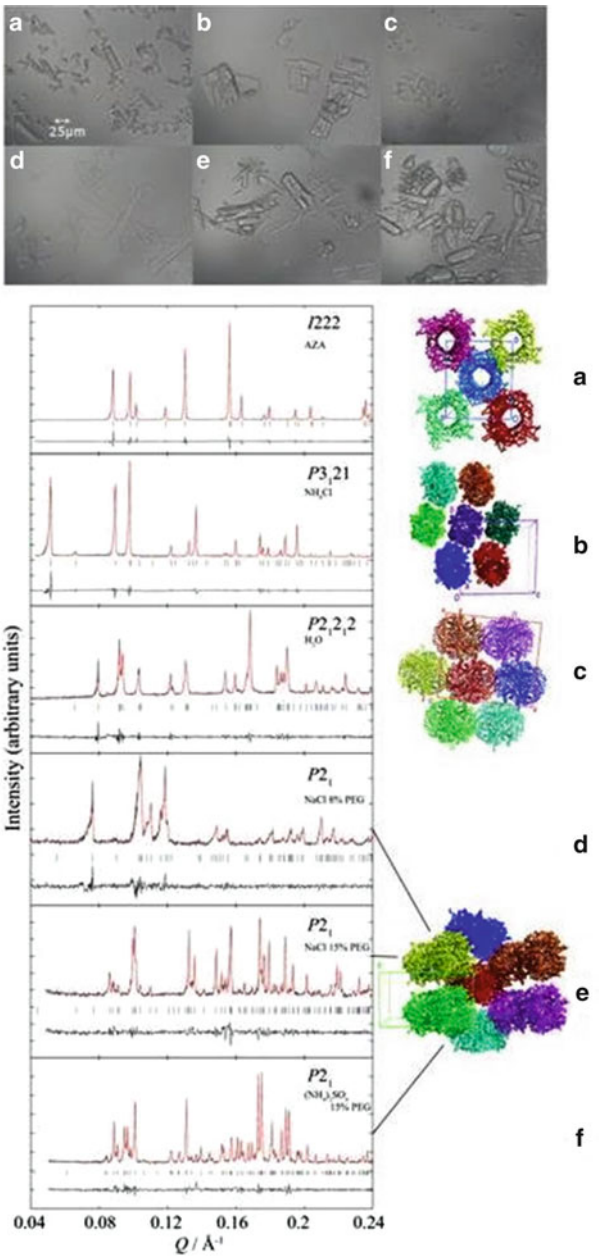

Fig. 13.2 ***Upper panel***: Optical microscopy images of Uox micro-crystals prepared at different conditions. (**a**) Uox ligand-free with NH^4Cl and 15% PEG 8000, (**b**) Uox ligand-free with NaCl and 15% PEG 8000, (**c**) Uox ligand-free with $(NH^4)^2SO^4$ and 15% PEG 8000, (**d**) Uox ligand-free with 10% PEG, (**e**) Uox ligand-free with KCl and 10% PEG 8000, (**f**) Uox complexed to AZA with NaCl and 10% PEG 8000. ***Lower panel***: Selected Q-region of the LeBail fits for six distinct phases of Uox [40]. Projection in the *ab* plane of candidate structure models available in the pdb (**a**) 1R51 [44], (**b**) 1WS3 [45], (**c**) 1XXJ [45], (**d**), (**e**), and (**f**) 1XY3 [45]

a reduction in production costs [31–37]. Microcrystalline forms of protein-based drugs tend to be slower acting as the crystallites must dissolve before acting. Crystallite size and polymorphism both affect dissolution rates and so they are important factors in understanding formulations.

To date, our studies on microcrystalline Human Insulin (HI) [38, 39] and Urate oxidase/Rasburicase (Uox) [40] suspensions using the powder diffraction method have revealed a high degree of polymorphism upon variation of their physicochemical environment (i.e. pH, ligand binding etc.). Even more important was our discovery of two new biologically active Insulin-phenol complexes which were later on characterized via single crystal methods [41]. In the case of Uox, a key protein component of currently existing drugs (i.e. Fasturtec) helping body to eliminate uric acid [42, 43] , a previously unknown, biologically active polymorph was discovered when crystallization was performed in the absence of any chemical additives. The structure solution of the latter Uox form is currently in progress. Part of the current research within our group is devoted to the structural characterization of an extensive series of Insulin-ligand complexes and Uox polymorphs, prepared at different crystallization conditions (pH, ionic strength, crystallization agent) which are potential drug targets. Figure 13.2 shows crystalline Uox samples, Le Bail fits for six distinct phases of Uox identified from powders and the corresponding candidate structure models available in the PDB.

13.5 Conclusions

In the last 10 years, the use of powder data with macromolecules has gone from being an ambitious suggestion to a respectable practice. A series of demonstration experiments and data analyses has been carried out which establishes the validity of the methodology. Although developments are still in progress for phasing methods and structure solution, there are already molecular-replacement and structure-refinement methods that are now mature enough for consumption by the more adventurous protein crystallographer. The solution of the structure of the SH3 domain of ponsin shows how powder diffraction is already moving ‘beyond lysozyme’ and is a technique ready to tackle genuine biological problems.

Acknowledgments I am grateful to Dr. A.N. Fitch & Dr. J.P. Wright for their continuous input, advice and support during this project. I would like to thank six undergraduate students from the University of Bath who have worked with us 1 year each: S. Basso, L. Knight, S. Dagogo, M. Jenner, I. Collings, L. Saunders as well as our PhD student, Y. Watier. Many thanks to my three M.Sc. students at the department of biology of the University of Patras (UPAT): Miss Evdokia-Anastasia Giannopoulou, Foteini Karavasili & Eleni Kotsiliti. Special thanks go to Drs. R.B. Von Dreele, M. Norrman, G. Schluckebier, M. El Hajji, F. Bonnete, M. Giffard, N. Papageorgiou, B. Canard, B. Coutard, M. Wilmanns and N. Pinotsis, and also Dr. M. Schiltz and his group, for the provision of interesting samples, their help and collaboration. I am grateful to the UNESCO and L’OREAL foundations for the international fellowship for women in science (2010). Finally, we thank the ESRF for provision of synchrotron beam time and UPAT for provision of facilities and financial resources.

References

1. Margiolaki I et al (2007) Second SH3 domain of ponsin solved from powder diffraction. J Am Chem Soc 129:11865–11871
2. Von Dreele RB (2007) Multipattern Rietveld refinement of protein powder data: an approach to higher resolution. J Appl Crystallogr 40:133–143
3. Rossmann MG (1990) The molecular replacement method. Acta Crystallogr A46:73–82
4. Stevens RC et al (2001) Global efforts in structural genomics. Science 294:89–92
5. Von Dreele RB (2000) The first protein crystal structure determined from high-resolution X-ray powder diffraction data: a variant of T_3R_3 human insulin-zinc complex produced by grinding. Acta Crystallogr D56:1549–1553
6. Vagin A, Teplyakov A (1997) MOLREP: an automated program for molecular replacement. J Appl Crystallogr 30:1022–1025
7. Wright JP (2004) Extraction and use of correlated integrated intensities with powder diffraction data. Z Kristallogr 219:791–802
8. Margiolaki I et al (2005) Synchrotron X-ray powder diffraction study of Turkey egg-white Lysozyme. Acta Crystallogr D61:423–432
9. Basso S et al (2005) High throughput phase diagram mapping via powder diffraction: a case-study of HEWL versus pH. Acta Crystallogr D61:1612–1625
10. Oka T et al (2006) High-resolution powder diffraction study of purple membrane with a large Guinier-type camera. J Synchrotron Radiat 13:281–284
11. Anderson CR et al (1957) Mayaro virus: a new human disease agent II. Isolation from blood of patients in Trinidad. Am J Trop Med Hyg 6:1012–1016
12. Causey OR, Maroja OM (1957) Mayaro virus: a new human disease agent. III. Investigation of an epidemic of acute febrile illness on the river Guama in Pará, Brazil, and isolation of Mayaro virus as causative agent. Am J Trop Med Hyg 6:1017
13. Malet H et al (2009) The crystal structures of Chikungunya and Venezuelan equine encephalitis virus nsP3 macro domains define a conserved adenosine binding pocket. J Virol 83:6534
14. Papageorgiou N et al (2010) Preliminary insights into the non structural protein 3 macro domain of the Mayaro virus by powder diffraction. Z Kristallogr 225:576
15. Perutz MF (1956) Isomorphous replacement and phase determination in non-centrosymmetric space groups. Acta Crystallogr 9:867–873
16. Green DW et al (1954) The structure of Hemoglobin. IV. Sign determination by the isomorphus replacement method. Proc R Soc Lond Ser A 225:287
17. Wright JP et al (2007) Likelihood methods with protein powder diffraction data. J Appl Crystallogr 41:329–339
18. Uson I, Sheldrick GM (1999) Advances in direct methods for protein crystallography. Curr Opin Struct Biol 9:643–648
19. La Fortelle E, Bricogne G (1997) Maximum-likelihood heavy-atom parameter refinement for multiple isomorphous replacement and multiwavelength anomalous diffraction methods. Methods Enzymol 276:472–494 316
20. Besnard C et al (2007) Exploiting X-ray induced anisotropic lattice changes to improve intensity extraction in protein powder diffraction: application to heavy atom detection. Z Kristallogr Suppl 26:39–44
21. Basso S et al (2010) Features of the secondary structure of the protein molecule from powder diffraction data. Acta Crystallogr D66:756–761
22. Von Dreele RB (1999) Combined Rietveld and stereochemical restraint refinement of a protein crystal structure. J Appl Crystallogr 32:1084–1089
23. Larson AC, Von Dreele RB (2004) General Structure Analysis System (GSAS), Los Alamos National Laboratory Report LAUR, Los Alamos, USA, pp 86–748
24. Ramachandran GN et al (1963) Stereochemistry of polypeptide chain configurations. J Mol Biol 7:95–99
25. Smith GD et al (2001) The structure of T6 bovine insulin. Acta Crystallogr D57:1091–1100

26. Von Dreele RB (2001) Binding of N-acetylglucosamine to chicken egg lysozyme: a powder diffraction study. Acta Crystallogr D57:1836–1842
27. Von Dreele RB (2005) Binding of N-acetylglucosamine oligosaccharides to hen eggwhite lysozyme: a powder diffraction study. Acta Crystallogr D61:22–32
28. Rietveld HM (1969) A profile refinement method for nuclear and magnetic structures. J Appl Crystallogr 2:65–71
29. Wright JP et al (2007) Likelihood methods with protein powder diffraction data. Z Kristallogr 26:27–32
30. Bhat TN (1988) Calculation of an OMIT map. J Appl Crystallogr 21:279–281
31. Yang MX et al (2003) Crystalline monoclonal antibodies for subcutaneous delivery. Proc Natl Acad Sci USA 100:6934–6939
32. Basu S et al (2004) Protein crystals for the delivery of biopharmaceuticals. Expert Opin Biol Ther 4:301–317
33. Havelund S (2009) US Patent 2009/0010854A9 331
34. Brader ML, Sukumar M (2005) US Patent 2005/0054818A1 332
35. Rabinow BE (2004) Nanosuspensions in drug delivery. Nat Rev Drug Discov 3:785–796
36. Aguiar AJ et al (1967) Effect of polymorphism on the absorption of chloramphenicol from chloramphenicol palmitate. J Pharm Sci 56:847–853
37. Bauer J et al (2001) Ritonavir: an extraordinary example of conformational polymorphism. Pharm Res 18:859–866
38. Knight L et al (2007) Protein powder diffraction – pH variation studies of insulin. Acta Crystallogr A63:s243
39. Karavassili F et al (2012) Structural studies of human insulin cocrystallized with phenol or resorcinol via powder diffraction. Acta Crystallogr 68(12):1632–1641
40. Collings I et al (2010) Polymorphism of micro-crystalline Urate Oxidase from Aspergillus flavus. Acta Crystallogr D66:539–548
41. Norrman M, Schluckebier G (2007) Crystallographic characterization of two novel crystal forms of human insulin induced by chaotropic agents and a shift in pH. BMC Struct Biol 7:83
42. McGrath BM, Walsh G (eds) (2005) Directory of therapeutic enzymes. CRC Press, Boca Raton
43. Wu X et al (1992) Two independent mutational events in the loss of urate oxidase during hominoid evolution. J Mol Evol 34:78–84
44. Retailleau P et al (2004) Complexed and ligand-free high-resolution structures of urate oxidase (Uox) from Aspergillus flavus: a reassignment of the active-site binding mode. Acta Crystallogr D60(3):453–462
45. Retailleau P et al (2005) Urate oxidase from Aspergillus flavus: new crystal-packing contacts in relation to the content of the active site. Acta Crystallogr D61(3):218–229

Chapter 14
Parametric Powder Diffraction

William I.F. David and John S.O. Evans

Abstract The rapidity with which powder diffraction data may be collected, not only at neutron and X-ray synchrotron facilities but also in the laboratory, means that the collection of a single diffraction pattern is now the exception rather than the rule. Many experiments involve the collection of hundreds and perhaps many thousands of datasets where a parameter such as temperature or pressure is varied or where time is the variable and life-cycle, synthesis or decomposition processes are monitored or three-dimensional space is scanned and the three-dimensional internal structure of an object is elucidated. In this paper, the origins of parametric diffraction are discussed and the techniques and challenges of parametric powder diffraction analysis are presented. The first parametric measurements were performed around 50 years ago with the development of a modified Guinier camera but it was the automation afforded by neutron diffraction combined with increases in computer speed and memory that established parametric diffraction on a strong footing initially at the ILL, Grenoble in France. The theoretical parameterisation of quantities such as lattice constants and atomic displacement parameters will be discussed and selected examples of parametric diffraction over the past 20 years will be reviewed that highlight the power of the technique.

W.I.F. David (✉)
ISIS Facility, Science and Technology Facilities Council, Rutherford Appleton Laboratory, Harwell Science and Innovation Campus, Didcot OX11 0QX, UK

Inorganic Chemistry Laboratory, University of Oxford, South Parks Road, Oxford OX1 3QR, UK
e-mail: bill.david@stfc.ac.uk

J.S.O. Evans
Department of Chemistry, University of Durham, South Road, Durham DH1 3LE, UK
e-mail: john.evans@durham.ac.uk

U. Kolb et al. (eds.), *Uniting Electron Crystallography and Powder Diffraction*,
NATO Science for Peace and Security Series B: Physics and Biophysics,
DOI 10.1007/978-94-007-5580-2_14,

14.1 Parametric Powder Diffraction – The Beginnings

While many papers before 1960 reported multiple powder diffraction measurements, it was the development of a modification to the Guinier camera (Fig. 14.1a) by Lenné [1] that marks the beginning of parametric powder diffraction. Lenné's modification was profound but simple and involved translating a film cassette across a narrow aperture that defined the equatorial plane of scattering. Simon [2] developed a modified version for air-sensitive samples and these cameras were used extensively over the next two decades to monitor structural changes, principally as a function of temperature. An example of some early work on the ferroelastic phase transition in $LaNbO_4$ [3] is presented in Fig. 14.1b which clearly shows the continuous transformation from monoclinic to tetragonal symmetry. While these photographs gave an excellent oversight into the behaviour of materials, extracting quantifiable data involved using microdensitometry where the transmission of light, pixel by pixel, through the photograph was digitised. Given the computing power and available memory, analysis of a single photograph of the complexity presented in Fig. 14.1b was a major undertaking.

The next major breakthrough in parametric powder diffraction was to occur with neutrons not X-rays. The Rietveld method [4, 5] was developed initially for neutron powder diffraction and its application to X-ray scattering came a decade later [6, 7].

By the late 1970s, profile refinement was well-established for neutron powder diffraction and the Institut Laue et Langevin (ILL), Grenoble was at the forefront of the development of neutron scattering techniques. Two powder diffractometers were commissioned; the high resolution diffractometer, D1a, which was represented the state of the art in structural precision and accuracy from powder diffraction data and D1b, a medium resolution neutron powder diffractometer, with a large area

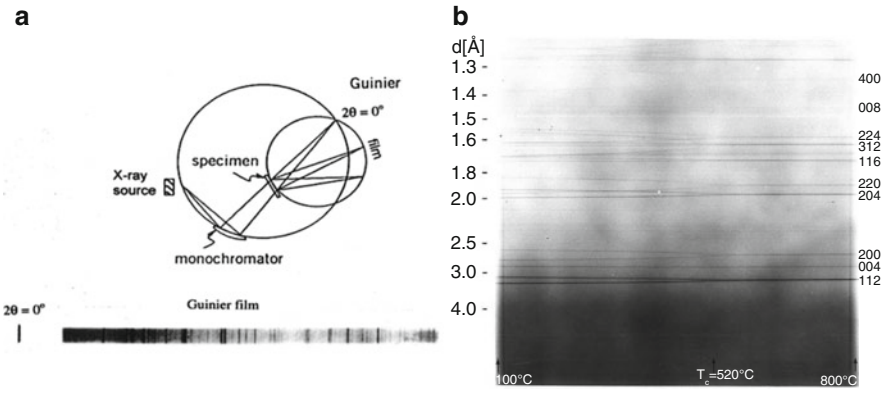

Fig. 14.1 (**a**) the Guinier camera geometry with the ribbon of illuminated film along the equatorial plane; (**b**) a Guinier-Simon photograph of ferroelastic $LaNbO_4$ covering the approximate temperature range from 100 to 800°C [3]. The monoclinic-tetragonal transition is clearly visible at ∼590°C and it is possible to see the anisotropic increase in line-broadening (particularly for the 220 reflection) around the phase transition

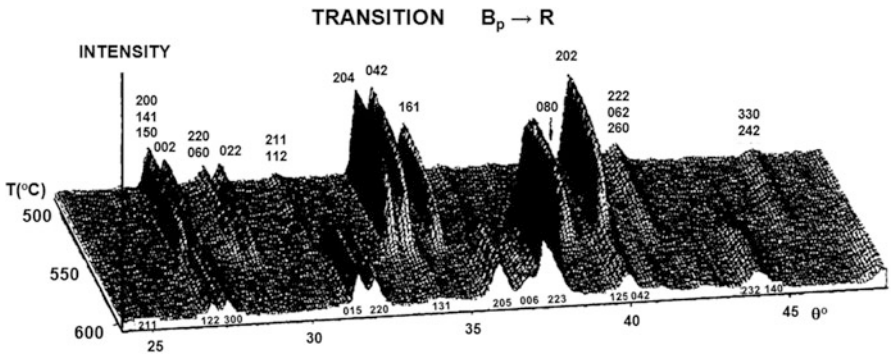

Fig. 14.2 A typical thermodiffractogram from D1b: the temperature dependence of the neutron powder diffraction pattern of $Sr_2Co_2O_5$ showing one of five phase transitions Bp and R refer to the paramagnetic brownmillerite-type and rhombohedral structures of $Sr_2Co_2O_5$ [9]

position sensitive detector. In the late 1970s, a complete D1a dataset was collected in 6–12 h, but D1b data could be collected in minutes. Jean Pannetier, the D1b instrument scientist at the time, developed the technique of thermodiffractometry [8] which defines the beginning of parametric powder diffraction analysis. A typical mid-1980s example from D1b of the complex evolution of a crystal structure, that of $Sr_2Co_2O_5$ [9], is presented in Fig. 14.2.

14.2 Crystal Structure Parameters: Some Equations

Parametric powder diffraction measurements yield a wealth of information about the variation of structural parameters as a function of an external variable such as temperature or pressure. In this section, we discuss the variation of crystallographic parameters such as lattice constants and displacement parameters as a function of temperature. Equations of state as a function of pressure have also been derived and applied to powder diffraction data [10] but these will not be discussed in this chapter. Perhaps the simplest temperature dependence to explore is associated with the thermal motion of an atom – the displacement parameter. Each atom in a crystal structure vibrates around a mean position defined by its crystallographic coordinates. The potential around this equilibrium position is, to a good approximation, quadratic in nature. The temperature dependence of the mean square displacement, $<u^2>$, of such a quantum system, mass m, vibrating with frequency, ω, is given by $<u^2> = (\hbar/2m\omega)\coth(\hbar\omega/2kT)$ (see [11]). Strictly speaking, this argument, originally derived by Einstein, pertains not to individual atoms but to phonons but the assumption generally works well for displacement parameters. This is illustrated in Fig. 14.3 which shows the difference in libration parameters between ND_3 and BD_3 rotation in ammonia borane, ND_3BD_3.

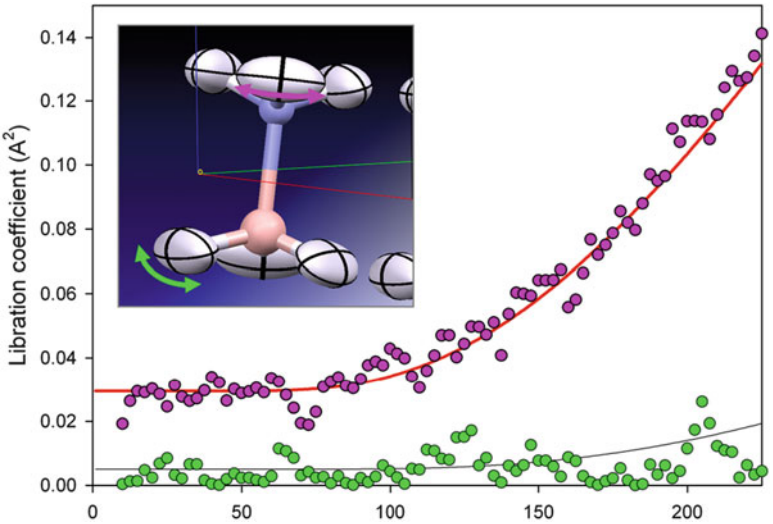

Fig. 14.3 The coefficients for ND_3 and BD_3 libration in ammonia borane. As observed by NMR, the ND_3 libration is larger and has a lower frequency than BD_3

The approximate equations that determine thermal expansion may also be derived from a quantum-mechanical analysis. Thermal expansion is, however, a consequence of anharmonic potentials as it is usually easier for bonds to expand than contract. Following [11], the temperature dependence of the mean position, a, of a weak anharmonic potential of the form $V(x) = \frac{1}{2}mw^2x^2 + kx^3$ is given by the formula $a = 3k\hbar \coth(\hbar\omega/2kT)/2m^2\omega^3$. In simpler terms, this Einstein oscillator behaviour may be expressed as

$$\frac{(a - a(T=0))}{T} = \frac{(\Theta_E/T)}{\exp(\Theta_E/T) - 1}$$

One final caveat – basic modelling of specific heat data (see, for example, Kittel (1976) [12]) suggests that a more correct formulation is a low-frequency, quadratic density of states model originally formulated by Debye

$$\frac{(a - a(T=0))}{T} = \frac{3}{(\Theta_D/T)^3}\int_0^{\Theta_D/T} \frac{\xi^3}{\exp(\xi) - 1} d\xi$$

$$= \left[\frac{\pi^4}{5(\Theta_D/T)^3} - \sum_{n=1}^{\infty}\left(3 + \frac{9}{(n\Theta_D/T)} + \frac{18}{(n\Theta_D/T)^2} + \frac{18}{(n\Theta_D/T)^3}\right)\frac{\exp(n\Theta_D/T)}{n}\right]$$

This formulation is straightforward to implement in a least squares analysis. A good example of the use of this parametric fitting is solid C_{60} which we will use in this chapter to illustrate a number of different aspects of parametric powder

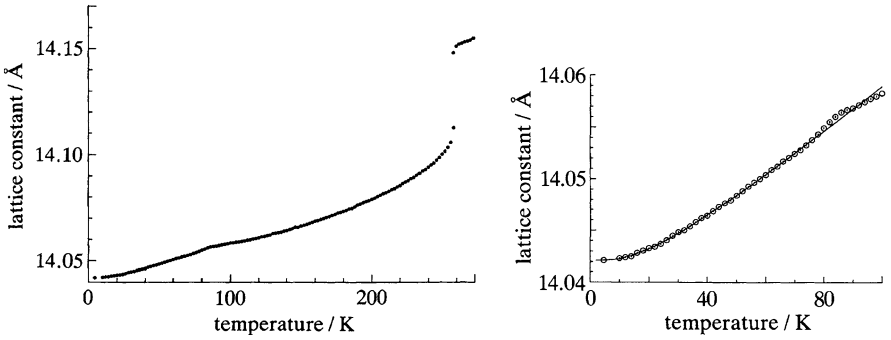

Fig. 14.4 (**a**) the cubic cell constant of C_{60} as a function of temperature from 4 to 272 K and (**b**) observed (*circles*) and calculated (*line*) C_{60} lattice constant below the orientational glass transition. The data were fitted between 4 and 70 K using a combined Debye and Einstein model

diffraction. High resolution neutron powder diffraction data of solid C_{60} were collected on HRPD at ISIS using a 2.5 g sample [13]. After an initial long 3½ h. run at 4 K, the temperature was raised in 2 K intervals from 10 to 272 K. Each dataset was collected for 20 min. with 5 min. allowed for temperature equilibration. The resulting refined lattice parameters are presented in Fig. 14.4a and have been precisely determined with $a(4\text{ K}) = 14.04212(2)$Å, $a(170\text{ K}) = 14.07080(10)$Å and $a(272\text{ K}) = 14.15425(20)$Å. This high precision is important for the extraction of non-crystallographic information which will be discussed further in Sect. 14.4.

The C_{60} lattice constant shows two significant features at ~80 and ~260 K. The upper feature corresponds to an orientational melting of C_{60}. Above this transition temperature, T_c, the orientation distribution is close to isotropic; below T_c, C_{60} hops between two sets of distinct crystallographic orientations – the lower energy, major orientation is characterised by pentagonal face directed along the 110 direction while the higher energy, minor orientation is characterised by hexagonal face along 110. The lower feature at ~80 k, shown clearly in the expanded plot Fig. 14.4b, corresponds to an orientational glass transition. Above this temperature, C_{60} is rotating sufficiently quickly to maintain thermodynamic equilibrium and the relative fractions of major and minor orientations follow a Boltzmann distribution. This will be discussed further in Sect. 14.4.

Below the orientational glass transition, the fractions of major and minor orientations are quenched at the glass transition temperature value. The lattice constant behaviour is typical of substances at low temperature. The roughly linear dependence with temperature above *ca.* 50 K levels off to a constant value at the lowest temperatures. In specific heat data analysis, both the Debye and Einstein models described above can look superficially similar as the evaluation of the specific heat involves an integration, and consequent smoothing, over phonon frequencies. The same also holds for lattice constant analysis. With high precision data, however, the relative merits of a Debye, Einstein or approximate combination can be discriminated in both specific heat and lattice parameter quantities. This has

been found to be the case in the analysis of C_{60}. Working with data between 4 and 70 K, a 'Debye-only' model gave a significantly poorer fit ($\chi^2 = 12.1$) to the data than an 'Einstein-only' model ($\chi^2 = 1.53$). A single Debye + single Einstein model gave an improved fit ($\chi^2 = 1.20$). No further parameters could be justifiably introduced to improve the fit. The fitted lattice constant is given by

$$a(T) = 14.042\,103(36) + 0.000\,157(8) \times a_{\mathrm{D}}(52.0(6)/T) + 0.000\,65(9) \times a_{\mathrm{E}}(93(8))/T$$

The derived Debye and Einstein temperatures are 52(6) K and 93(8) K which are close to anticipated values obtained from specific heat data.

14.3 Refining a Complete Experiment – "Surface" Refinements

In the previous section, we discussed the parametric fitting of structural quantities such as lattice constants and displacement parameters as a function of an experiment variable such as temperature and pressure. In this section, we explore the possibility and advantages of going beyond the serial refinement of a set of diffraction data to the simultaneous refinement of all the diffraction data together [14, 15]. The simple idea behind this approach is that if one has an ensemble of data collected under evolving conditions of a variable such as time, temperature, pressure or chemical environment (a "surface" of diffraction data) many of the key parameters one extracts from a Rietveld refinement can be derived from the whole set of data rather than from a single (noisy) data set. A trivial example might be the zero-point of a diffractometer during a series of time resolved experiments. The physical instrumental misalignment leading to this correction is unlikely to change during the course of the experiment, and the variable is therefore best determined from all data sets simultaneously rather than from each individual set independently. In this way one can sometimes extract "good information" from individually "bad data". An additional key feature of the parametric approach to data analysis is that physically sensible conditions may be imposed on the refined parameters in a flexible manner. This is extremely useful – and, indeed, essential, when the information content in individual data sets is sufficiently low (e.g. due to low data quality or a complex structural model) that a number of different models can provide an equivalent fit.

One area where this approach is potentially very powerful is in the quantitative phase analysis of materials with complex or closely related structures. For example, WO_3 undergoes a series of phase transitions on cooling as shown schematically in Fig. 14.5 in which the material evolves from a hypothetical high-temperature, high-symmetry cubic form to a series of lower symmetry forms of increasing complexity. [16–21].

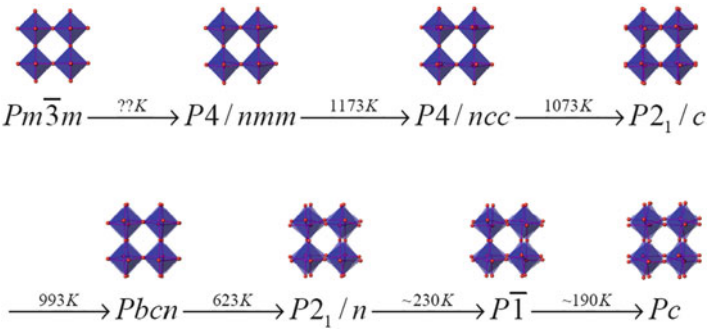

Fig. 14.5 The sequence of phase transitions in WO_3

Figure 14.6a shows a two-dimensional "film plot" of powder diffraction data recorded on cooling a sample of monoclinic $P2_1/n$ WO_3 from 300 to 90 K. Data were collected using a Bruker d8 diffractometer equipped with a pHeniX cryostat using Cu K_α radiation, with each dataset recorded for 20 min. The difficulty in performing a quantitative analysis of such diffraction data arises from the displacive nature of the transitions only resulting in small changes in atomic coordinates, which in turn leads to relatively minor changes in the diffraction pattern.

In fact, as shown by Fig. 14.6b, if we consider a small region of the diffraction pattern around 24° 2θ all three phases of WO_3 have peaks in this 2θ region, with similar intensities. If one fits a single experimental dataset it is therefore possible for the "incorrect" structure to distort to fit the diffraction data. For example, even though the material is predominantly in the monoclinic $P2_1/n$ form at room temperature the $P\bar{1}$ structural model, which has more degrees of freedom, can distort to fit the experimental data as well as a $P2_1/n$ model. This makes quantitative analysis of an evolving mixture of $P2_1/n$ and $P\bar{1}$ phases extremely challenging. Figure 14.6 shows the implications of this on quantitative Rietveld refinement on the data in Fig. 14.5a as a function of temperature. Here all 100 data sets have been fitted independently using three-phase Rietveld refinement. A total of 91 parameters were used to fit each data set, requiring 9,100 refined parameters in total.

It is clear from Fig. 14.7a that the evolution of refined phase fractions as a function of temperature makes little chemical sense. It is extremely unlikely, for example, that abrupt and reverse changes of the type apparently observed at 180 and 200 K occur. This suggests that the refinements have found false minima. This occurs despite each refinement being set up as carefully as possible, with variables constrained to lie within sensible minimum and maximum ranges of ideal values. That these are false minima is further shown by Fig. 14.7b where the apparent temperature dependence of refined cell volumes is clearly non-physical. Clearly independent Rietveld refinement of these data is not the optimal approach.

Figure 14.8 shows results from fitting the same data using a parametric approach in which all patterns were fitted simultaneously. To fit the data, three simple

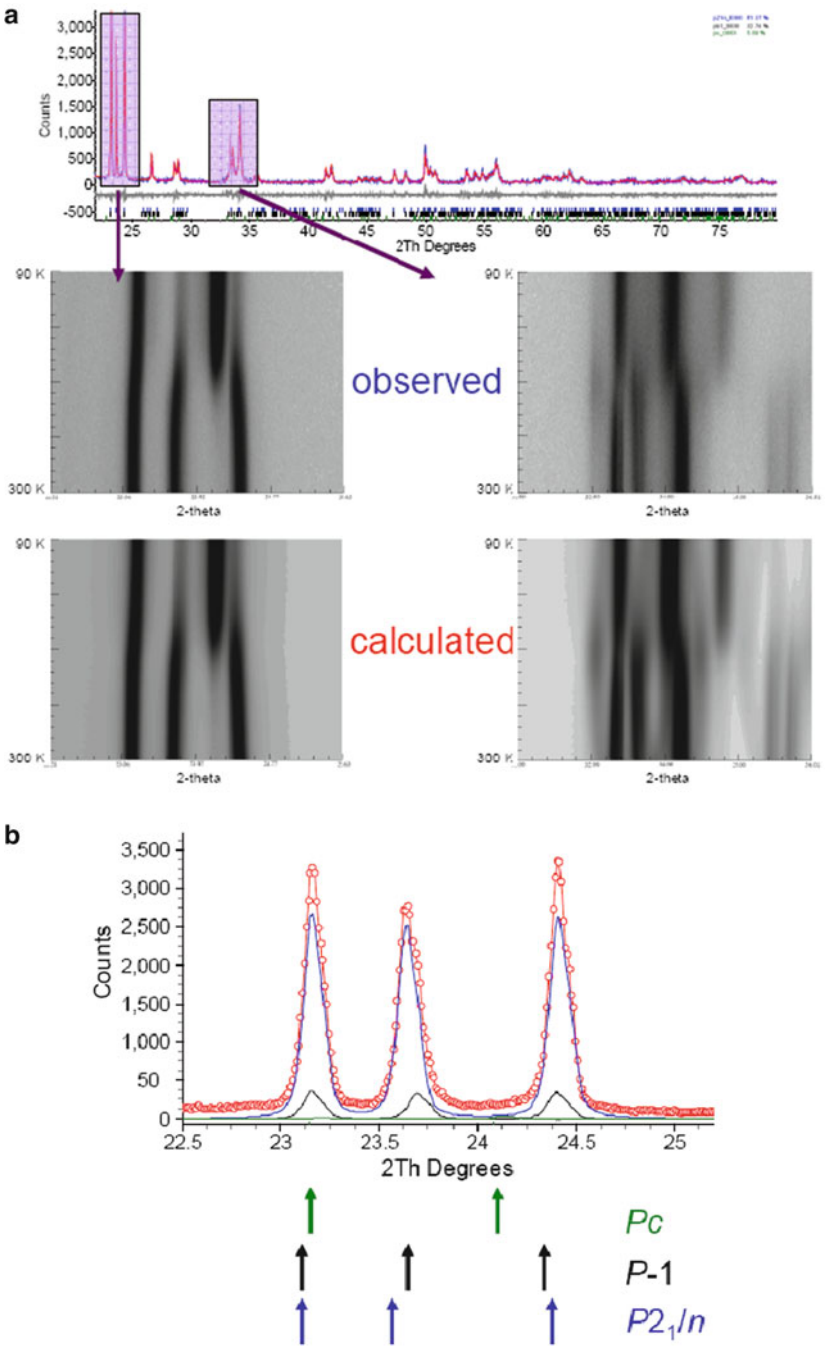

Fig. 14.6 (**a**) Surface "film plot" showing changes in two regions of the diffraction pattern of WO_3 on cooling. Observed and calculated surfaces from a parametric refinement are shown and (**b**) 300 K diffraction data showing predicted reflection positions for the {200} family of reflections. The 2θ range corresponds to that shown in *left hand* zoomed region of Fig. 14.6a

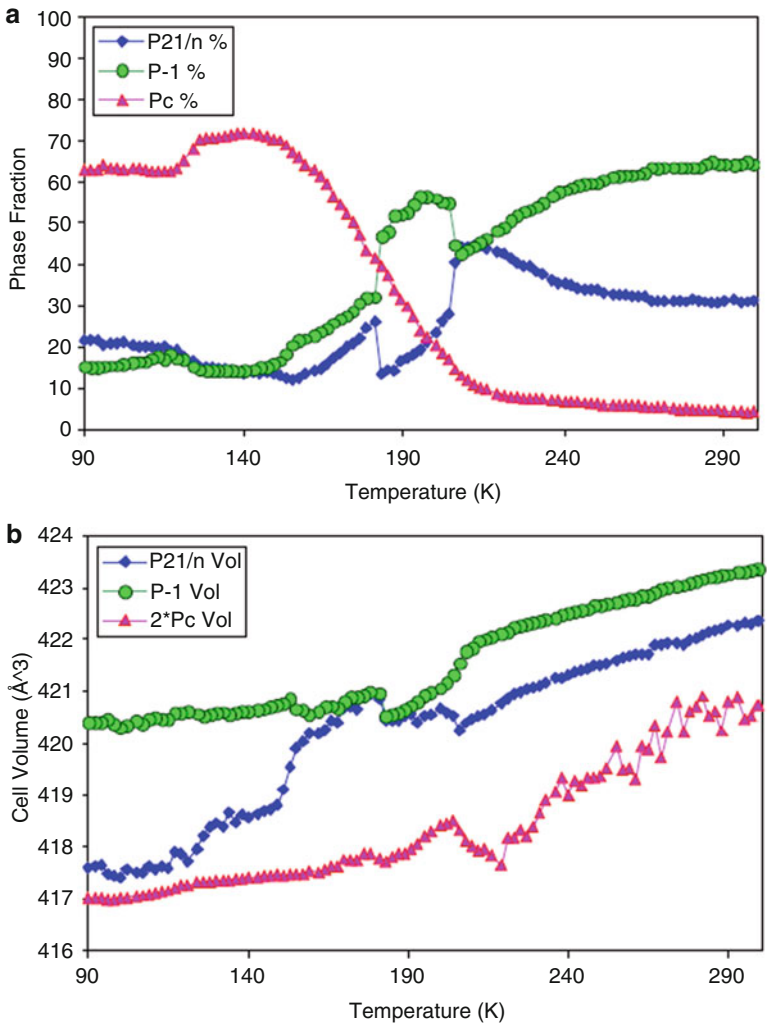

Fig. 14.7 (**a**) Phase fractions and (**b**) cell volumes of $P2_1/n$, $P\bar{1}$ and Pc forms of WO_3 obtained by independent Rietveld refinement

assumptions were made. Firstly, it was assumed that the cell parameters of each individual phase show a smooth variation with temperature. The specific variation was not imposed on the data, but cell parameters of the three phases were parameterised using the following expression, $a(T) = a(0) + c_1/(\exp(\theta/T) - 1)$ (see Sect. 14.2) where coefficients $a(0)$, c_1 and θ were refined from the diffraction data. For variable unit-cell angles, a second-order polynomial was used. Secondly, it was assumed that the temperature factor refined for each atomic site should increase smoothly with temperature. The same Einstein functional form was used as for

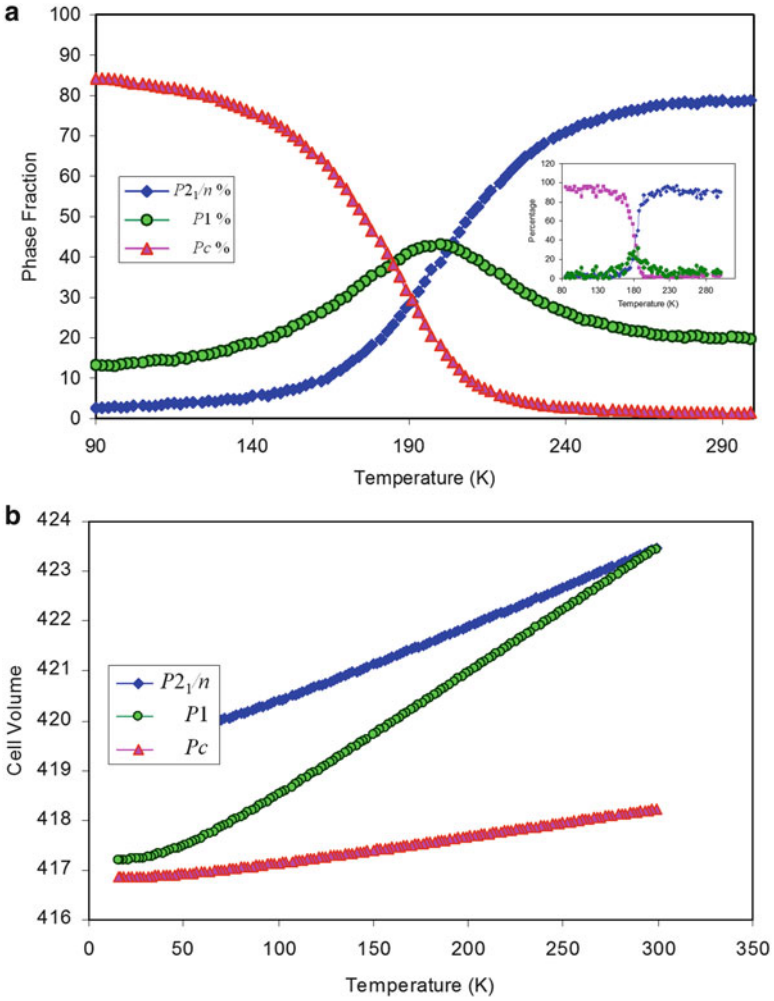

Fig. 14.8 (**a**) Phase fractions and (**b**) cell volumes of $P2_1/n$, $P\bar{1}$ and Pc forms of WO_3 obtained by parametric Rietveld refinement. Note that volumes extrapolate into temperature regions where individual phases no longer exist

the lattice constants (see Sect. 14.2). Finally, the peak shape description was set up such that each individual phase had an identical peak shape description at all temperatures. In this fashion, a single Rietveld refinement was performed with 1,102 parameters fitted simultaneously to all 100 datasets [22]. This led to the phase fractions and cell volumes shown in Fig. 14.8. The extracted phase fractions make much more chemical sense and vary in a smooth fashion with temperature even though they were not constrained in any way. The values also agree well with those extracted from analysis of neutron data on a similar sample (inset to Fig. 14.7a).

The parametrically fitted cell parameters also make physical sense in that they give rise to comparable volume coefficients of expansion for each phase as expected.

The success of this approach has two basic origins. The most important influence is the fact that the three-phase model, with each phase constrained to have cell parameters which evolve with temperature in a physically sensible way, must simultaneously fit each experimental data set. This essentially prevents the $P\bar{1}$ phase, for example, distorting to fit the room temperature data, as the distortions required to do so would prevent accurate fitting of data recorded around 200 K, where more of the $P\bar{1}$ phase is present. Secondly, the parametric approach to modelling peak shapes means that the peak-shape parameters for an individual phase are dominated by the temperature regions of the diffraction surface when it is actually present. This prevents, for example, peak shapes for the *Pc* phase becoming infinitely broad in regions of the data where the phase is not present, "mopping up" minor errors in fitting the experimental background and influencing the quantitative refinement. In essence the parameters modelling an individual phase are determined by regions of the data where the phase is present rather than regions where it is not.

The approach used to fit the data in this example is entirely general and the degree of complexity, in terms of which variables are parameterised and which functions are used, is the choice of the analyst. It is possible, for example, to parameterise atomic coordinates, peak shape parameters or background functions as required. One criticism of the approach is that one imposes a certain physical form on the evolution of variables which may not be correct. In fact, this objection can turn out to be a major strength. If an inappropriate parametric form is chosen for a given variable, or if the overall model is not sufficiently flexible to model all the features of the diffraction surface the inadequacy is often revealed in a plot of R-factor against data set number for the parametric refinement. Normally one would expect a smooth evolution in R-factor (e.g. as data quality improves slightly on cooling). If the parametric model is incorrect one sees unexpected variations (e.g. humps in certain temperature regions) with temperature. When data sets are refined independently these tell-tale variations can be lost as the Rietveld model can distort in non-physically sensible ways to fit an individual data set and the distinguishing power of the R-factor is reduced.

14.4 Parametric Powder Diffraction – Beyond Crystal Structure

In this section, we illustrate the possibility of obtaining significant non-crystallographic properties from parametric diffraction. We use the example of solid C_{60} [13] and continue our discussion from Sect. 14.2 focussing on the low-temperature ordered phase and, in particular, the orientational glass transition around 80 K. Below this transition, the proportions of the two orientations are fixed. There is a slight rise around the glass transition temperature, T_g and this is attributed

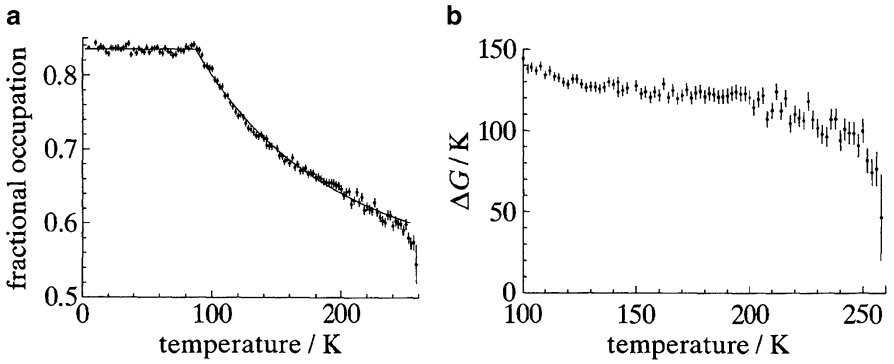

Fig. 14.9 (**a**) The fractional occupation, p_P, of the more energetically favourable, major orientation as a function of temperature. The sum of major, p_P, and minor, p_H, sums to unity. The quenching of the relative populations of major and minor orientation fractions at the glass transition of ∼90 K is clearly evident. The fitted line above 90 K corresponds to a refined energy difference of 122(4) K (11.0(3)meV) between the two orientations. There are clear departures from this behaviour above 200 K; (**b**) the free energy difference between the two orientations obtained the relative major and minor orientation populations

to the fact that the cooling rate (*ca.* 1 K min^{-1}) is substantially faster than the heating rate (i.e. the experiment duration). The re-orientational hopping thus unlocks at a lower temperature than the original 'quenching' temperature. This effect is more prominent in the lattice parameter and can be used to determine the relaxation rate and hence the re-orientational correlation. A model for this effect is developed later in this section. Above T_g, the decrease in major orientation fraction may be expressed in terms of a Boltzmann distribution since thermal equilibrium is achieved. The energy difference between major and minor orientations, ΔG, may be expressed by the equation

$$\text{and thus} \quad (p_H / p_P) = ([1 / p_P] - 1) = \exp(-\Delta G / kT)$$
$$\Delta G = -kT \ln((1 / p_P) - 1).$$

A least squares fit assuming ΔG to be constant between 90 and 200 K gives fair but not excellent agreement (Fig. 14.9a). The derived value for the energy difference is 122(3) K. Above 200 K, there are clear precursor effects of the orientational order – disorder transition at 260 K. Evaluation of the energy difference, ΔG, calculated point by point from the above equation emphasises these precursor effects and clearly indicates that ΔG is not precisely constant between 90 and 200 K and that there is therefore an additional entropic contribution (Fig. 14.9b).

Previously in this section, attention was drawn to the anomalous rise in the major orientation fraction at the glass phase transition temperature. This was explained in terms of the differing rates of initial cooling (*ca.* 1 K min^{-1}) and heating. The latter corresponds to the experimental time of *ca.* 25 min. (i.e. 12.5 K min^{-1}). The slower

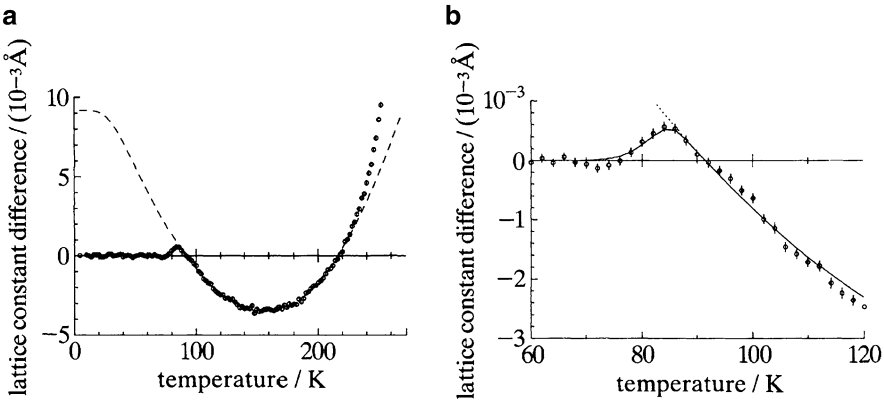

Fig. 14.10 (**a**) The lattice constant difference between the observed and calculated C60 lattice constant. From this, the relative volumes of pentagonal and hexagonal orientations may be obtained; (**b**) the lattice constant difference fitter to a recursive function that model the return to thermal equilibrium around the glass transition temperature. Reorientation times extracted by the method lead to an accurate estimate of the reorientation activation energy

rate of heating implies that the system will unquench at a lower temperature and that the approach to thermal equilibrium will be distinguishable when thermal relaxation rate (the inverse of the reorientational correlation time) is around an order of magnitude longer than the experimental time. This behaviour is particularly evident in the temperature variation of the lattice parameter as an anomalous rise in the vicinity of the glass transition. As an example of obtaining non-crystallographic data, a model is developed that explains the lattice parameter anomaly below T_g and enables relaxation rates to be determined and hence the reorientational activation energy to be derived.

Consider the information in Fig. 14.10a below the orientational glass transition temperature, T_g. The plotted data provide a baseline that corresponds to a fixed major/minor orientation ratio. The dotted line represents the thermodynamically stable, but unattainable, population ratio. As T_g is approached, thermal relaxation begins to occur. The lattice constant rises above the 'quenched' baseline. Relaxation does not approach completion, however, until T_g.

The approach to thermal equilibrium is, however, a cumulative effect which, when accounted for, leads to the conclusion that the relaxation rate, $\tau(T_k)$, at the kth temperature step may be obtained from the equation

$$\left(u_k \Big/ \left[1 - \sum_{r=1}^{k-1} u_r \right] \right) \approx [1 - \exp(-T_{\text{exp}} / \tau(T_k))]$$

where the experiment time, $T_{\text{exp}} \approx 25$ min, $u_k = \Delta a_k / z_k$ is the deviation of the plotted data from the baseline and z_k is the difference between the theoretical equilibrium lattice constant and the baseline. The relaxation rate can thus be obtained in a

recursive manner. A starting point of 70 K was found to be adequate. The relaxation rates obtained are listed in the following table:

Temperature/K	τ (derived)/s	τ (calc)/s
74	8.47×10^4	8.18×10^4
76	3.51×10^4	3.31×10^4
78	1.32×10^4	1.40×10^4
80	5.89×10^3	6.21×10^3
82	3.20×10^3	2.86×10^3

The functional form of this anomalous lattice parameter model is shown in Fig. 14.9b where it can be seen to provide an excellent fit to the data. Note that the full lattice constant range in this figure is only 0.004 Å. The variation in relaxation rate of more than an order of magnitude between 74 and 82 K permits a precise Arhennius formulation to be obtained. Writing $\tau(T) = \tau_0 \exp(E_a/kT)$ yields τ_0 to be $10^{-10\pm1}$ s and a reorientational activation energy of 219(7) meV in excellent agreement with other techniques. This parametric powder diffraction study of C_{60} not only yields an accurate account of the temperature variation of the crystal structure of C_{60} through the orientational glass and order–disorder transitions but also provides detailed information about reorientation times and the relative energies of and the activation energy between the two crystallographically distinct orientations. Similar properties may be obtained from studying in-situ reactions and in operando processes.

14.5 Conclusions

Most modern X-ray and neutron powder diffractometers have the potential to collect datasets in a matter of minutes and indeed with synchrotron radiation the timescales can be significantly shorter. Combining sophisticated sample environment, substantial computer memory and speed and advanced computer programs, it is possible with parametric powder diffraction not only to investigate the temperature and pressure evolution of a material through complex phase transitions but to perform a very wide range of more complex experiments. These include in-situ synthesis reactions, in-operando material systems such as batteries, hydrogen storage materials, hydration/dehydration and gas absorption/desorption and the pixel-by-pixel scanning of materials at the micron level. By performing advanced parametric analysis it can be possible to extract "non-crystallographic" information such as rate constants, activation energies, temperature and others from diffraction data. It also becomes possible to introduce physically meaningful constraints or restraints to an entire body of diffraction data and obtain "high quality" information from individually "low quality" data.

Acknowledgements We would like to thank our colleagues, Richard Ibberson (ISIS, now NIST), Takasuke Matsuo (Osaka) and Graham Stinton (Durham, now Edinburgh) for their collaboration in the C_{60} and WO_3 parametric diffraction studies discussed in this chapter. We particularly would

like to thank and acknowledge the huge contribution that Alan Coelho has made that underpins this work. His computer program, Topas, is simply crucial in enabling the most complex parametric diffraction experiments to be analysed and understood.

References

1. Lenné H-U (1961) Die Böhmit-Entwässerung, verfolgt mit einer neuen Röntgenheizkamera (Engl translation: "The dehydration of Boehmite observed with a new X-ray heating cam-era"). Z Krist 116:190–209
2. Simon A (1970) Eine Methode zur Untersuchung extrem luftempfindlicher Substanzen mit der. Guinier-Methode. J Appl Crystallogr 3:11–18
3. David WIF (1981) Structural studies of ferroic ABO4 crystals, D. Phil thesis, University of Oxford, Oxford, UK
4. Rietveld HM (1967) Line profiles of neutron powder-diffraction peaks for structure refinement. Acta Crystallogr 22:151–152
5. Rietveld HM (1969) A profile refinement method for nuclear and magnetic structures. J Appl Crystallogr 2:65–71
6. Malmros G, Thomas JO (1977) Least-squares structure refinement based on profile analysis of powder film intensity data measured on an automatic microdensitometer. J Appl Crystallogr 10:7–11
7. Khattak CP, Cox DE (1977) Profile analysis of X-ray powder diffractometer data: structural refinement of La0.75Sr0.25CrO3. J Appl Crystallogr 10:405–411
8. Pannetier J (1986) Thermodiffractometry. Chem Scr 26(A):131–139
9. Rodriguez-Carvajal J, Gonzalez-Calbet JM, Grenier JC, Pannetier J, Anne M (1987) Phase transitions in Sr2Co2O5: a neutron thermodiffractometry study. Solid State Comm 62:231–234
10. http://www.iucr.org/resources/commissions/crystallographiccomputing/newsletters/1/fitting-equations-of-state (and references therein)
11. Feynman RP (1972) Statistical mechanics: a set of lectures. W. A. Benjamin, Inc/Advanced Book Program, Reading, pp 52–55
12. Kittel C (1976) Introduction to solid state physics. Wiley, New York
13. David WIF, Ibberson RM, Matsuo T (1993) High resolution neutron powder diffraction: a case study of C60. Proc R Soc Lond A 442:129–146
14. Stinton GW, Evans JSO (2007) Parametric Rietveld refinement. J Appl Crystallogr 40:87–95
15. Evans JSO (2010) Advanced input files and parametric quantitative analysis using Topas. Mater Sci Forum 651:1–9
16. Campbell BJ, Evans JSO, Perselli F, Stokes HT (2007) Rietveld refinement of structural distortion-mode amplitudes. http://iucrcomputing.ccp14.ac.uk/iucrtop/comm/ccom/newsletters/2007nov/
17. Howard CJ, Luca V, Knight KS (2002) High temperature phase transitions in tungsten trioxide – the last word? J Phys Condens Matter 14:377–387
18. Salje EKH, Rehmann S, Pobell F, Morris D, Knight KS, Herrmannsdorfer T, Dove MT (1997) Crystal structure and paramagnetic behaviour of epsilon-WO_{3-x}. J Phys Condens Matter 9:6563–6577
19. Vogt T, Woodward PM, Hunter BA (1999) The high-temperature phases of WO_3. J Solid State Chem 144:209–215
20. Woodward PM, Sleight AW, Vogt T (1995) Structure refinement of triclinic tungsten trioxide. J Phys Chem Solids 56:1305–1315
21. Woodward PM, Sleight AW, Vogt T (1997) Ferroelectric tungsten trioxide. J Solid State Chem 131:9–17
22. David WIF, Evans JSO, Sleight AW (1999) Direct evidence for a low-frequency phonon mode mechanism in the negative thermal expansion compound ZrW2O8. Europhys Lett 46:661–666

Chapter 15
Powder Diffraction + Computational Methods

L'ubomír Smrčok

Abstract It is proposed that the application of computational methods provides an attractive route towards structures, whose accuracy is well-comparable to that typical for single crystal standards. Although theoretical calculations and powder diffraction seemingly represent completely disjunctive sets, it is demonstrated that they could meet at three stages of structure analysis from powders – initial model building, structure refinement and crystal chemical analysis.

15.1 Introduction

A restricted amount of structural information extractable from a powder diffraction pattern strongly limits the accuracy of structural data resulting from Rietveld refinement, which usually follows a structure solution step. If the information content of a powder pattern is insufficient and we are, this reality notwithstanding, interested in accurate structure, it is time to turn out our attention to other methods of refinement. Basically, there are two possible routes. The first one, introducing various improvements to the Rietveld method is the subject of other contributions to this School. In this place we will focus on the second direction and will point to the advantages of symbiosis of powder diffraction with several types of theoretical (quantum chemistry) calculations. Although theoretical calculations and powder diffraction seemingly represent completely disjunctive sets, we will show how they could meet at three stages of structure analysis from powders – initial model building, structure refinement and crystal chemical analysis based on the refined parameters.

L'. Smrčok (✉)
Institute of Inorganic Chemistry, Slovak Academy of Sciences, Dúbravská cesta 9,
SK-845 36 Bratislava, Slovak Republic
e-mail: Lubomir.Smrcok@savba.sk

U. Kolb et al. (eds.), *Uniting Electron Crystallography and Powder Diffraction*,
NATO Science for Peace and Security Series B: Physics and Biophysics,
DOI 10.1007/978-94-007-5580-2_15,

15.2 Molecular Calculations

The first occasion a crystallographer comes across a theoretical calculation during structure solution is, as a rule, preparatory step dedicated to building of a structural model to be used in (*i*) a future structure solution in the direct space, or (*ii*) for geometrical analysis of electron density maxima obtained by a calculation in reciprocal space. Seen from the quantum chemistry side "a model building" corresponds to optimization of the geometry of a molecule, starting either from a very approximate outline based on a combination of the fragments taken from a choice of databases, or even on the oracle nicknamed chemical intuition.

In case of organic molecules one is normally satisfied with relatively simple quantum chemistry molecular calculation, frequently referred to as "calculations in vacuum". Both terms are equivalent and in fact only emphasize the fact, that the geometry of the subject is not influenced by its environment. Such calculations can be easily accomplished by any standard quantum chemistry package (Gaussian, Turbomole, Gamess, NWChem, ADF, etc. . . .) as this path is the most used and hence the best tuned and debugged. For simple organic compounds reasonable results are normally obtained at DFT level of theory by making use of one from the family of hybrid functionals (e.g. B3LYP) combined with the split valence ("Pople") basis sets augmented by diffuse and polarization functions. For example, the 6–31+G* basis (the symbol stands for the basic 6–31G basis augmented with polarization denoted by * and diffuse functions denoted by +) will provide satisfactory results in the vast majority of the cases [1, 2].

It should be however noted, that optimization of a flexible molecular geometry under the absence of any "environment" ("external field") is likely to provide the values of torsional angles disagreeing with the values obtained in the subsequent structure solution and refinement. If the differences are striking, one should, before accusing any of the method of its total or partial malfunction, carefully evaluate the impact of the external field and/or of formation of intra- and intermolecular hydrogen bonds. In any case, the shape of a flexible molecule ought to be optimized also during the direct space structure solution, of course only if the accuracy of the experimental data permits. A word of warning: semiempirical methods belonging to the NDO group (CNDO, INDO, MNDO, AM1, PM3, . . .) though fast, are known not giving very accurate molecular geometries.

While preparing the building blocks of a future organic structure usually does not pose any important problem worth explicitly mentioning, this need not be the case for metal-organic or inorganic compounds. Geometry of a representative cluster (a polyhedron) of the atoms (a central atom of a transition metal surrounded by medium sized organic ligands or water, for instance) playing the role of "molecule" can be to a certain degree influenced by a spin state of a transition metal. Furthermore, presence of very heavy atoms in the structure could call for application of so called Effective Core Pseudopotential (ECP) in place of the basis functions approximating the inner (core) shells of the atoms. This approach not

only saves the computational time due to the reduction of dimensionality of the problem, but modern relativistic pseudopotentials also take care about the important part of relativistic effect, which plays non-negligible role for atoms beyond the first transition metal row. Note that when using an ECP, the valence parts of the basis functions of all atoms in the molecule should be consistent and one is discouraged from mixing of principally different types of bases.

15.3 Solid State Calculations

Inasmuch as structure solution process usually provides only approximate positions of atoms, an improvement of their accuracy is desirable. Standard "powder" refinements nowadays almost exclusively rely on a few variants of Rietveld idea, that the parameters of a function approximating the diffraction profiles can be refined by a non-linear weighted least-squares procedure simultaneously with the atomic parameters. Due to the notorious problems with accurate and cheap description of powder diffraction profiles, with instrumental and sample effects and in particular with a low number of structure factors compared to the number of refined atomic parameters, the accuracy of the resulting structures is, more often than not, markedly inferior to that typical for the current single crystal standards.

Although several improvements of this procedure have been already proposed (restrained and rigid body refinements, just among others; see e.g. [3, 4] and the references cited therein), the problem with a low number of uncorrelated/inaccurate structure factors persists. As the elements of the Jacobian matrix related in Rietveld method to structural parameters are calculated considering the structure factors and not the individual profile intensities, any bias in the former is involuntarily transferred to the accuracy of the refined atomic parameters. In reality, accuracy of any powder refinement is smaller or at maximum identical to the accuracy of a single crystal refinement based on the same numbers of independently collected structure factors and refined parameters. Unfortunately, in a common practice this is the ideal point never reachable as the accuracy of structure factors from a powder pattern is always lower, especially due to overlap of the individual diffractions caused by collapse of 3D diffraction pattern to 1D or due to various sample effects.

A remedy to the chronic difficulty of standard powder refinements, which is the aforementioned lack of information extractable from a powder pattern, could be structure optimization by energy minimization in the solid state. If we (for the lack of space) restrict ourselves only to the solid-state DFT methods, we realize that the size of problems tractable on a laboratory computer nowadays reaches $\sim$1,000 atoms per unit cell – in dependence on the level of approximation used by the concrete computational method. This number greatly exceed the widely accepted limits for powder refinements, which frequently fail in providing accurate results even for the structures with much, much smaller numbers of atoms. Moreover, since theoretical calculations are frequently done in the $P1$ space group, simultaneous

optimization of the geometries of possibly symmetrically equivalent units within a unit cell provides a good measure of internal consistency of structure optimization and/or solution.

The main "crystallographic" advantage of this approach is that all atoms in a structure are on equal footing, i.e. not weighted by their scattering abilities. For organic structures (in fact, not only for them) it implies direct access to accurate geometry of hydrogen bonds, whose knowledge is in good deal of cases essential for understanding of physicochemical properties of a compound. Secondly, a shape of the molecule or of a fragment (polyhedron) in an "inorganic" structure is further optimized under the constraints imposed by a crystal field. Last but not least, by exploiting the resulting wavefunction several interesting quantities like electronic or vibrational densities of states, distribution of the electron density in a crystal, stress tensors, etc. are easily accessible. The approach to handling of lattice parameters is twofold. Either they are refined in advance e.g. by Le Bail technique and kept fixed in the course of optimization of the atomic coordinates, or their values are refined along with the atomic coordinates. Validity of both these approaches has been a subject of long discussions with many pros and cons. In short, the main argument of the "pros" group is that, that without the cell parameters "the optimized structure is not in the minimum" (. . . of total energy), while the second group proclaims that the accuracy of the lattice parameters obtained from a crystallographic experiment is as a rule much more accurate than that of those obtained by energy minimization and there is hence no need to make it worse.

Such a combined approach to powder structure solution and refinement was to our best knowledge pioneered by Dinnebier et al. [5] in their study of a rigid ferrocene-based macrocycle, $C_{48}H_{44}B_4Fe_2N_8O_4$, crystallizing in a relatively large monoclinic ($C2/c$) cell ($V = 4152.8$ Å^3). In order to decrease the number of the optimized atom coordinates the calculation was done in the reduced cell with $V/2$. The initial structure models were generated by Monte Carlo method using the synchrotron data and the atomic coordinates were refined by energy minimization in the solid state. Refined structures were put to Rietveld refinement and the profile parameters were improved, while keeping the atomic coordinates fixed. This study was soon followed by the structure solution followed by the refinement by crystal energy minimization of the red polymorph of tetrahexylsexitiophene [6]. The powder pattern was collected with a laboratory diffractometer and the structure solved by Monte Carlo technique. Nearly identical solution in the space groups $C2/m$, $C2$ and $P-1$ were found, of which the first was at last chosen.

Since then, two different attitudes to co-existence of classic crystallographic Rietveld refinement and the refinement by crystal energy minimization have developed. The first and the more frequently used, gives more weight to standard Rietveld refinement and uses theoretical calculation only to refine positions of hydrogen atoms and/or for "validation" of a refined structure (see [7–14] for examples). The second approach, on the contrary, is based on the presumption that it is unlikely that Rietveld refinement with all atoms relaxed can provide sufficiently accurate structural data for the structures built from more than few atoms. Rietveld refinement is therefore used only for estimation of isotropic displacement parameters and/or

selected "profile" parameters, like preferred orientation correction (e.g. [15–21]). Like the first approach, also the second has been successfully applied to organic, metal-organic and inorganic compounds. Note, however, that the lists of the papers belonging to any of these groups are not claimed to be complete and the author apologizes for omissions.

The requirements for successful application of energy minimization in structure refinement are however stricter than those typical for a standard Rietveld refinement. First of all, the model must be complete, i.e. no dangling bonds resulting from omission of atoms (intentional or accidental) are allowed. Partial occupancies of atomic positions are not possible and must be modeled by a supercell simulating distribution of atoms and vacancies. The optimization path could depend on the initial configuration, as the optimization of atomic coordinates by energy minimization is not, in spite of his robustness, the method of global minima. Fortunately, in case of a configuration being rather far from a reasonable minimum, its accuracy can be improved by molecular dynamics approach. A way towards improvement of resulting accuracy is application of d-DFT method (e.g. [22]). This pragmatic approach may, however, bring unwanted variability into energy calculations, unless the empirical correction terms ("d") are rigorously defined.

Although there is a variety of computer programs for theoretical calculation in the solid state available, two of them are probably at the leading edge: CASTEP [23] and VASP [24].[1] Both these codes employ pseudopotentials to approximate the inner (core) shells of atoms and plane waves as a basis set describing the valence charge density. In spite of the effort invested to construction of pseudopotentials of various flavors, the user should always carefully consider their quality, especially when dealing with the atoms from the opposite corners of the periodic table in one structure. Plane waves in place of the basis set have for the solid state calculations several advantages over the localized basis functions typical for molecular calculations. Using FFT procedure one can calculate the electronic structure using plane-waves basis set in reciprocal rather than in the direct space, making the calculation less computationally demanding. A good beginner's guide to the art of solid state calculations is provided in the review paper by Gillan [25].

15.4 Post-optimization Calculations

The last stage where theory meets experiment is post-optimization applications of theoretical methods not only for the molecules (fragments) cut from a structure, but also for "bulk". These applications are not by any means any by-products and require each a special attention. The first group in principle employs very similar methods as those used at the model building stage, but calculation of some derived

[1] Because it is not the role of this contribution to provide a comprehensive list of all the approaches and of the relevant computer codes, a reader is asked to visit e.g. http://www.psi-k.org/codes.shtml

quantities require a higher accuracy of the calculations and hence larger basis sets or even a higher level of theory. A very typical post-optimization application is detailed analysis of hydrogen bonds geometry including calculation of the relevant binding energies or vibration analysis. The next widely accepted "chemical" application, which can prove useful especially when comparing properties of a series of structurally similar compounds, is estimation of the atomic charges followed by calculation of the dipole moment and, optionally, of its components. Sadly, importance of the atomic charges is in many cases overestimated and obvious arbitrariness in their calculation frequently ignored. Projected densities of electronic states obtained from a calculation in the solid state provide a good picture of bonding conditions in a crystal and are frequently correlated to the selected physical properties. Calculated vibrational densities of states can aid interpretation of vibrational (IR, Raman, INS) spectra by revealing significance of the individual modes.

Quite a prominent chemical application calculated at the molecular level is Natural Bond Orbitals (NBO) method, which transforms a given wave function into a localized form, corresponding to the one-center ("lone pairs") and two-center ("bonds") elements of the chemist's Lewis structure picture. In NBO analysis, the input atomic orbital basis set is transformed via natural atomic orbitals (NAOs) into natural bond orbitals (NBOs). Resulting NBOs correspond to the image, in which two-center bonds and lone pairs are localized [26, 27]. Examples of application of NBO in interpretation of the variations in bond distances in the crystal structures is e.g. in [17] or in [28]. In the second case also the concept of inequivalent hybridization [29] was applied to explain variations in some bond angles in the aminoethylene substituent attached to flourophenyl from their expected ideal values. Another nice example of symbiosis of crystallography, though here single-crystal, and theoretical calculations is a combined structure solution of $[Ag_{26}In_{18}S_{36}C_{l6}(dppm)_{10}(thf)_4][InCl_4(thf)]_2$ [30]. Although the structure was solved from X-ray single crystal data, the assignment of several atom positions solely on the basis of X-ray analysis was impossible due to close scattering factors of the pairs Ag/In and S/Cl and very similar bond lengths for Ag-S and In-S. The correct assignment was found by molecular DFT/TZVPP calculation.

Acknowledgement This contribution was partially supported by Slovak Grant Agency VEGA under the contract 2/0150/09. My thanks are to P. Mach for his critical reading of a draft of the text and also to R. Skorczyk, whom I have never met, but whose paper [31] has many years ago triggered my interest in the field of solid-state calculations.

References

1. Cramer CJ (2002) Essentials of computational chemistry. Wiley, Chichester
2. Szabo A, Ostlund NS (1989) Modern quantum chemistry: introduction to advanced electronic structure theory. McGraw-Hill, New York
3. Immirzi A (2009) Constraints and restraints in crystal structure analysis. J Appl Crystallogr 42:362–364

4. Afonine PV, Grosse-Kunstleve RW, Urzhumtsev A, Adams PD (2009) Automatic multiple-zone rigid-body refinement with a large convergence radius. J Appl Crystallogr 42:607–615
5. Dinnebier RE, Ding L, Kuangbiao M, Neumann MA, Tanpipat N, Leusen FJL, Stephens PW, Wagner M (2001) Crystal structure of a rigid ferrocene-based macrocycle from high-resolution X-ray powder diffraction. Organometallics 20:5642–5647
6. Neumann MA, Tedesco C, Destri S, Ferro DR, Porzio W (2002) Bridging the gap – structure determination of the red polymorph of tetrahexylsexithiophene by Monte Carlo simulated annealing, first-principles DFT calculations and Rietveld refinement. J Appl Crystallogr 35:296–303
7. Bhattacharya A, Kankanala K, Pal S, Mukherjee AK (2010) A nimesulide derivative with potential anti-inflammatory activity: synthesis, X-ray powder structure analysis and DFT study. J Mol Struct 975:40–46
8. Brodski V, Peschar R, Schenk H, Brinkmann A, Van Eck ERH, Kentgens APM, Coussens B, Braam A (2004) Structure of melaminium dihydrogenpyrophosphate and its formation from melaminium dihydrogenphosphate studied with powder diffraction data, solid-state NMR, and theoretical calculations. J Phys Chem B108:15069–15076
9. Das U, Chattopadhyay B, Mukherjee M, Mukherjee AK (2011) Crystal structure and electronic properties of three phenylpropionic acid derivatives: a combined X-ray powder diffraction and quantum mechanical study. Chem Phys Lett 501:351–357
10. Kaduk JA (2002) Terephthalate salts of dipositive cations. Acta Crystallogr B58:815–822
11. Kaduk JA (2002) Aromatic carboxylate salts terephthalates. Trans Am Crystallogr Assoc 37:63–84
12. Kaduk JA, Toft MA, Golab JT (2010) Crystal structure of antimony oxalate hydroxide, Sb(C2O4)OH. Powder Diffr 25:19–24
13. Whitfield PS, Le Page Y, Davidson IJ (2009) Ab initio structure determination of the low temperature phase of succinonitrile from X-ray powder diffraction data – coping with potential poor quality using DFT ab initio methods. Powder Diffr 23:292–299
14. Whitfield PS, Mitchell LD, Lepage Y, Margeson J, Roberts AC (2010) Crystal structure of the mineral strontiodresserite from laboratory powder diffraction data. Powder Diffr 25:322–328
15. Florence AJ, Bardin J, Johnston B, Shankland N, Griffin TAN, Shankland K (2009) Structure determination from powder data: Mogul and CASTEP. Z Krist Suppl 30:215–220
16. Jorík V, Scholtzová E, Segl'a P (2008) Combined powder diffraction and solid-state DFT study of [Cu(2,6-dimethoxynicotinate)(2)(muronicol)(2)](n) complex. Z Krist 223:524–529
17. Smrčok L', Jorík V, Scholtzová E, Milata V (2007) Ab initio structure determination of 5-anilinomethylene-2,2-dimethyl-1,3-dioxane-4,6-dione from laboratory powder data – a combined use of X-ray, molecular and solid-state DFT study. Acta Crystallogr B63:477–484
18. Smrčok L', Brunelli M, Boča M, Kucharík M (2008) Structure of K2TaF7 at 993 K: the combined use of synchrotron powder data and solid-state DFT calculations. J Appl Crystallogr 41:634–636
19. Smrčok L', Bitschnau B, Filinchuk Y (2008) Low temperature powder diffraction and DFT solid state computational study of hydrogen bonding in NH4VO3. Cryst Res Technol 44:978–984
20. Smrčok L', Kucharík M, Tovar M, Žižak I (2009) High temperature powder diffraction and solid state DFT study of beta-cryolite (Na3AlF6). Cryst Res Technol 44:834–840
21. Smrčok L', Černý R, Boča M, Macková I, Kubíková B (2010) K3TaF8 from laboratory X-ray powder data. Acta Crystallogr C66:I16–I18
22. van de Streek J, Neumann MA (2010) Validation of experimental molecular crystal structures with dispersion-corrected density functional theory of calculations. Acta Crystallogr B66:544–558
23. Milman V, Refson K, Clark SJ, Pickard CJ, Yates JR, Gao S-P, Hasnip PJ, Probert MIJ, Perlov A, Segall MD (2010) Electron and vibrational spectroscopies using DFT, plane waves and pseudopotentials CASTEP implementation. J Mol Struct (THEOCHEM) 954:22–35
24. Hafner J (2000) Atomic-scale computational materials science. Acta Mater 48:71–92
25. Gillan MJ (1997) The virtual matter laboratory. Contemp Phys 38:115–130

26. Reed AE, Curtiss LA, Weinhold F (1988) Intermolecular interactions from a natural bond orbital, donor-acceptor viewpoint. Chem Rev 88:899–926
27. Weinhold F, Landis C (2005) Valency and bonding: a natural bond orbital donor-acceptor perspective. Cambridge University Press, Cambridge
28. Langer V, Mach P, Smrčok L', Milata V (2009) (E)-Methyl 2-[(2-flourophenyl) aminomethylene]-3-oxobutanoate: X-ray and density functional (DFT) study. Acta Crystallogr C65:o183–o185
29. Bent HA (1961) An appraisal of valence-bond structures and hybridization in compounds of the first-row elements. Chem Rev 61:276–311
30. Ahlrichs R, Eichhőfer A, Fenske D, Hampe O, Kappes MM, Nava P, Olkowska-Oetzel J (2004) Synthesis and structure of [Ag26In18S36Cl6(dppm)10(thf)4] [InCl4(thf)]2 – a combined approach of theory and experiment. Angew Chem Int Ed 43:3823–3827
31. Skorczyk R (1976) The calculation of crystal energies as an aid in structural chemistry 1: a semi-empirical potential field model with atomic constants as parameters. Acta Crystallogr A32:447–452

Chapter 16
Information on Imperfections

Matteo Leoni

Abstract Line Profile Analysis is the common name given to those methods allowing microstructure information to be extracted from the breadth and shape of the peaks in a diffraction pattern. A fast analysis is always possible via traditional techniques such as the Scherrer formula, Williamson-Hall plot and Warren-Averbach method, but at the expenses of the physical meaning of the result. A more sound alternative is offered by the Whole Powder Pattern Modelling, allowing physical information to be extracted from diffraction data in a self-consistent way.

16.1 Introduction

Nanostructured materials are still a hot topic in current research. An obvious choice for the analysis of the microstructure of such systems would be microscopy, as the sub-nm resolution can be easily achieved on last generation Transmission Electron Microscopes (TEMs) and Scanning Probe Microscopes (SPMs). However, obvious does not always mean better. SPMs mainly provide morphological information, whereas the TEM, albeit accessing morphology and microstructure information, is limited to the analysis of a few grains, a too small range to guarantee a good statistical significance of the measurements.

A possible alternative is certainly offered by indirect methods such as powder diffraction. The microstructure information is contained, highly integrated, in a single powder diffraction pattern: already at the beginning of last century, in fact, it was observed a close relationship between e.g. the breadth of a diffraction peak and

M. Leoni (✉)
Department of Materials Engineering and Industrial Technologies, University of Trento, via Mesiano 77, 38123 Trento, TN, Italy
e-mail: Matteo.Leoni@unitn.it

U. Kolb et al. (eds.), *Uniting Electron Crystallography and Powder Diffraction*, NATO Science for Peace and Security Series B: Physics and Biophysics,
DOI 10.1007/978-94-007-5580-2_16,

the microstructure of the scattering domains. In the years, several techniques have been proposed for the so-called Line Profile Analysis (LPA), mainly grouped into two broad classes characterised by a totally different approach to the problem:

- pattern decomposition (PD) i.e. fitting of the individual peaks in the pattern using some bell-shaped function and *a posteriori* analysis of the parameters of the fit
- pattern modelling (PM) i.e. fitting of a set of microstructure models to the entire diffraction pattern.

Most of the traditional techniques of LPA, still widely employed by the scientific community, fall in the first category. They are e.g. the well known Scherrer formula (SF), Williamson-Hall (WH) plot and Warren-Averbach (WA) method [1–8].

They all pretend to give some microstructure information under the form of *average domain size* and *microstrain*: in most practical cases, however, the true meaning of those terms and the theory behind those methods are highly overlooked. Pattern modelling is the modern answer to most of the limitation of traditional LPA. The information provided e.g. by the Whole Powder Pattern Modelling [9–11] is in fact tightly bound to the physics of the material (e.g. a domain size distribution is refined, and a quantitative account of the sources of microstrain is given) and the model is refined directly on the data for full consistency. A brief account for traditional and advanced models is here given. For further details, an extensive account is provided in the old and recent literature [5, 6, 12–15].

16.2 Integral Breadth Methods

Scherrer formula relates the Full-Width at Half-Maximum (FWMH) of a diffraction peak in Bragg position $2\theta_B$ with a so-called *average crystallite size* $<D>$. To render the approach independent of the actual shape of the $\{hkl\}$ peak, the FWHM is usually replaced with the so-called Integral Breadth (IB) $\beta_{\{hkl\}}$ i.e. the ratio between peak area and peak maximum. With this definition, SF reads:

$$\beta_{\{hkl\}}(2\theta) = \lambda K_\beta \,/\left(\langle D\rangle \cos\,\theta_{\{hkl\}}\right) \tag{16.1}$$

where λ is the wavelength, K_β is the so-called Scherrer constant for the given shape and $\theta_{\{hkl\}}$ is Bragg angle. In reciprocal space, we can analogously write $\beta_{\{hkl\}}(d^*) = K_\beta/<D>$ being d^* the reciprocal space variable. The Scherrer constant in Eq. (16.1) can be calculated for any given domain shape and in general depends on *hkl* (see e.g. [8]).

The meaning of the *average crystallite size* obtained from the SF is not obvious. In fact, applying the idea of Bertaut [16, 17], <D> is an average of the length of the columns in which the shape can be subdivided along the scattering direction. Therefore it does not represent the average size of a physical object, the quantity of usual interest. For non-spherical sizes, the average crystallite size depends on the *hkl* and the same value can be obtained with different shapes.

In order to compare the broadening corresponding to different directions and try to increase the level of information that can be extracted, Williamson and Hall [2] proposed to plot the FWHM or the IB in reciprocal space. For an isotropic domain (direction-independent size), this plot is expected to be constant in reciprocal space. An increase in the integral breadth with the distance from the origin of the reciprocal space is observed, and the following model is employed:

$$\beta\left(d^*\right) = K_\beta / \langle D \rangle + 2 \cdot \left\langle \varepsilon^2 \right\rangle^{1/2} \cdot d^* \tag{16.2}$$

being the combination of Scherrer formula with the differential of Bragg's law. The first term in (16.2) is again named *average crystallite size* (extrapolation of the integral breadth to the origin of the reciprocal space), whereas the second is the so-called *microstrain* or *root mean strain*. The true meaning of this approach and of the corresponding results is seldom considered.

In fact, even if the WH formalism seems straightforward, there is no physical reason for summing the two contributions up. As breadths are additive only for Lorentzians, the Williamson-Hall formalism is strictly valid only for Lorentzian peaks, condition seldom met in practice. Alternatives have been proposed to cover all Gauss/Lorentz-type combinations [18, 19], being complete from a mathematical point of view but poor from a physical one.

The meaning of the size term in Eq. (16.2) is that of the Scherrer formula. In the real case of polydispersed domains, the *average crystallite size* provided by the SF and WH plot is different from the first moment of the size distribution. If we assume a certain shape for the domains, we can see that this size is in fact the ratio between two high order moments of the size distribution [20].

Quoting the result of the SF or WH as "average size" may thus lead to confusion or misinterpretation.

The microstrain contribution is quite an abstract concept as it provides an evidence for the presence of defects, but it does not identify their source. It should also be borne in mind that the microstrain term accounts for the breadth of the local strain distribution: should the microstrain be constant or average to a non-zero value, a residual strain (leading to shift in peak position) would be present.

16.3 Fourier Methods

A first step towards the use of the full information contained in a diffraction peak was the introduction of the Warren-Averbach method [3–6], the father of all Fourier methods of LPA. If $x = s - s_{\{hkl\}}$ is the distance in reciprocal space with respect to Bragg position $s_{\{hkl\}}$, then the peak profile $h(x)$ in the powder diffraction pattern of a polycrystalline material results from the folding of an instrumental profile $g(x)$ with sample-related effects $f(x)$ (microstructure) [5, 6]:

$$h(x) = \int f(x) g\,(y - x)\, dy = f(x) \otimes g(x) \tag{16.3}$$

The Fourier Transform (FT) allows an easier handling of this expression: the convolution theorem, in fact, states that the FT of a convolution can be obtained as the product of the Fourier transforms of the functions to be folded. In synthesis:

$$H(L) = FT\,[h(x)] = FT\,[f(x)] \cdot FT\,[g(x)] \tag{16.4}$$

where L is the variable conjugate to x. The original h(x) function can be obtained by inverse Fourier transform of $H(L)$. In traditional Fourier methods, the $f(x)$ is obtained by inverting Eq. (16.4) and is further split into size ($A^S(L)$) and a strain or distortion ($A^D(L)$) components:

$$C(L) = FT\,[f(x)] = FT\,[h(x)]\,/FT\,[g(x)] = A^S(L)A^D(L) \tag{16.5}$$

The separation becomes trivial if size effects are considered as isotropic and thus independent of the diffraction order (true for spherical domains). Strain effects, in fact, depend on the diffraction order (and thus the reciprocal space variable) and can be expressed, in a first order approximation, as: $A^D(L) = <\cos 2\pi L n \varepsilon_L> = 1 - 2\pi^2 L^2 n^2 <{\varepsilon_L}^2>$ where ε_L is the strain averaged over the length L. A suitable plot of $\ln(FT[f(x)]) = \ln(A^S(L)) + \ln(A^D(L))$ as a function of n^2 is the practical tool for Warren-Averbach analysis. A size term, with meaning similar to that of the SF, can be obtained in this case by taking the intercept of the initial slope of $A^S(L)$ [5]. The chain of operations leading to the result is quite long and several approximations are made: the consistency between data and result cannot be readily verified.

A few extensions of the WA method have been proposed. In the Multiple Whole Profile Fitting (MWP) [21, 22], for instance, simple models for the size and strain terms $A^S(L)$ and $A^D(L)$ are fitted to the Fourier coefficients extracted from the experimental data. Arbitrary data pre-processing is necessary to separate the peaks and to extract their Fourier transform. Even if transforms of multiple peaks are simultaneously used, the method is nowadays scarcely employed, as fitting in Fourier space leads to results that cannot be easily checked on the measured data.

16.4 Whole Powder Pattern Modelling

A leap forward in LPA was the introduction of reciprocal-space full pattern techniques such as the Whole Powder Pattern Fitting (WPPF) [9, 23–25] and the Whole Powder Pattern Modelling (WPPM) [9–11, 20, 23–45] or variants of it [21, 22, 46–48]. In those techniques, model parameters are directly refined on the entire pattern as in the Pawley [49] and Rietveld methods (RM [50–52]). We can somehow consider the WPPM as the dual of the Rietveld method as they have common bases, but complementary targets: structural refinement in RM, microstructural refinement in WPPM. The major differences lay in the generation of the peak profiles (Fourier plus reciprocal space in WPPM, angular in the RM) and in the treatment of the peak shape (peaks from microstructure models in WPPM, and Williamson-Hall or effective models in the RM).

Using some microstructure model in the Rietveld method to improve the fit and to extract extra information is certainly an advance over traditional LPA, as the whole pattern is employed. The structural constraint on peak intensities can however pose serious problems, as it can bias the microstructure extraction. It would be ideal to model structure and microstructure simultaneously, but it is advised to perform the microstructure studies with the least degree of biasing to correctly take into account the subtle features of each profile.

The WPPM starts from the Fourier approach of Eq. (16.3) and (contrary to traditional methods) works in a convolutive way. Each peak in the pattern is built as:

$$I_{hkl}\left(s - s_{hkl}\right) = k(s)\, h\left(s - s_{hkl}\right) = k(s) \int C(L) \mathrm{e}^{2\pi i L \cdot (s - s_{hkl})} dL \tag{16.6}$$

where $k(s)$ groups all geometrical and structural factor that are constant or known functions of s (e.g., structure factor, Lorentz-polarization factor). This equation is not fully general, as it implicitly assumes that the broadening contributions act on the entire $\{hkl\}$ reflection family and thus that a multiplicity term (included in $k(s)$) can be used. Certain defects (e.g. faults), can however act independently on each member of the reflection family, leading to:

$$I_{\{hkl\}}\left(s - s_{\{hkl\}}\right) = \sum_{hkl} w_{hkl} I_{hkl}\left(s - s_{\{hkl\}} - \delta_{hkl}\right) \tag{16.7}$$

where w_{hkl} is a weight function, $(s - s_{\{hkl\}} - \delta_{\mathrm{hkl}}) = (x - \delta_{\mathrm{hkl}})$ is the reciprocal-space distance from the centroid of the (hkl) component and δ_{hkl} is the shift from the reciprocal-space point $s_{\{hkl\}}$ corresponding to the Bragg position in the absence of defects. The sum in Eq. (16.7) is over independent profile sub-components, selected on the basis of the specific defects (e.g. 4 for $\{111\}$ when faults are present in the *fcc* case: selection is based on the value of $\mathrm{h} + \mathrm{k} + \mathrm{l}$ that can be ± 3 or ± 1).

The whole pattern is synthesised as sum of peaks obtained by means of Eqs. (16.6) and (16.7) plus background and aberrations. The desired parameters are then refined by fitting the model to the measured data using a nonlinear least squares routine. Full consistency between data and model is thus preserved.

Any broadening contribution can enter the convolution chain and can therefore be included in Eq. (16.6). The most common broadening sources in a real case are certainly those related to the non-ideal nature of the instrument, the finite size of the coherently diffracting domain (size effect) and to the presence of defects such as e.g. dislocations and faults. Taking this into account, the $C(L)$ reads:

$$C(L) = T^{IP}(L) A^{S}_{hkl}(L) \left\langle \mathrm{e}^{2\pi i \cdot \psi_{hkl}(L)} \right\rangle \left\langle \mathrm{e}^{2\pi i \cdot \phi_{hkl}(L)} \right\rangle \tag{16.8}$$

where $T^{IP}(L)$ and $A^{S}{}_{hkl}$ are the FT of the instrumental profile (IP) and domain size components, respectively, and the terms in brackets (<>) are average phase factors related to lattice distortions (ψ) and faulting (ϕ). A plug and play behaviour is thus envisaged: new broadening sources can be considered by including the

corresponding complex FT in the product of Eq. (16.8). Expressions are available for a wide selection of cases of practical interest [10–15, 20, 23–35, 53, 54] including a size distribution of domains with given shape, the effects of dislocations and stacking faults, grain surface relaxation, antiphase boundaries, distribution of cell parameters, just to cite some. The method is conveniently implemented in a flexible and freely available software [31] allowing the analysis of X-rays, synchrotron, neutron or electron diffraction patterns.

A warning should be given here: the physical bases of the approach should always be considered. The WPPM is certainly valid if the broadening sources are diluted and independent, i.e. if the correlation between defects can be neglected. If this does not apply, then cross terms start playing a role: errors can arise if this is not properly done and therefore the WPPM needs being revised. For example, in the case of extended faulting and heavy interaction between structure and microstructure, a possible alternative to traditional models has been proposed in [55].

16.5 Example of Analysis

The analysis of a nanocrystalline ceria specimen produced by sol–gel (details are given in [36]) is proposed using traditional and advanced techniques of LPA. The diffraction pattern collected on a laboratory instrument over ca. 24 h is shown in Fig. 16.1a. TEM shows spherical domains with a distribution of diameters approximately lognormal (cf. bar plot in Fig. 16.1b, evaluated on 800 isolated grains [36]).

The application of Scherrer formula to the most intense {111} peak is proposed in Fig. 16.1c: no fitting, no background and no peak overlapping were considered. From the FWHM of the peak, it is possible to estimate an average $<D>/K_\beta$ of 5.8 nm. The actual size value depends on the Scherrer constant K_β and therefore on the domain shape.

To improve the result, all peaks were simultaneously fitted using pseudo-Voigt functions, properly considering the instrumental profile contribution. The corresponding IB was employed for the WH analysis (cf. Fig. 16.1d). Linear fitting leads to $\beta(d^*) = 0.019 + 0.008d^*$. Despite the clear presence of a microstrain ($<\varepsilon^2>^{1/2} = 0.004$), the size is 5.3 nm, i.e. smaller than the SF result. This is a caveat that instrumental effects *must* always be considered in the analysis.

Residual anisotropic broadening is clear in the WH plot (errors are small and points do not lie on the line), and can be ascribed to the presence of dislocations. The WPPM analysis was conducted assuming the presence of a lognormal distribution of spherical domains (compatible with TEM) and of dislocations. The modelled pattern is shown in Fig. 16.1a together with the experimental data: the residual is flat and the GoF is close to 1 [36], witnessing the perfect match of data and model.

The resulting WPPM size distribution is proposed in Fig. 16.1b superimposed to the TEM result. The mean size is 4.4 nm, quite far from SF and WH results. A better agreement (3.98 nm) is obtained if the correcting factor ¾ (valid of a

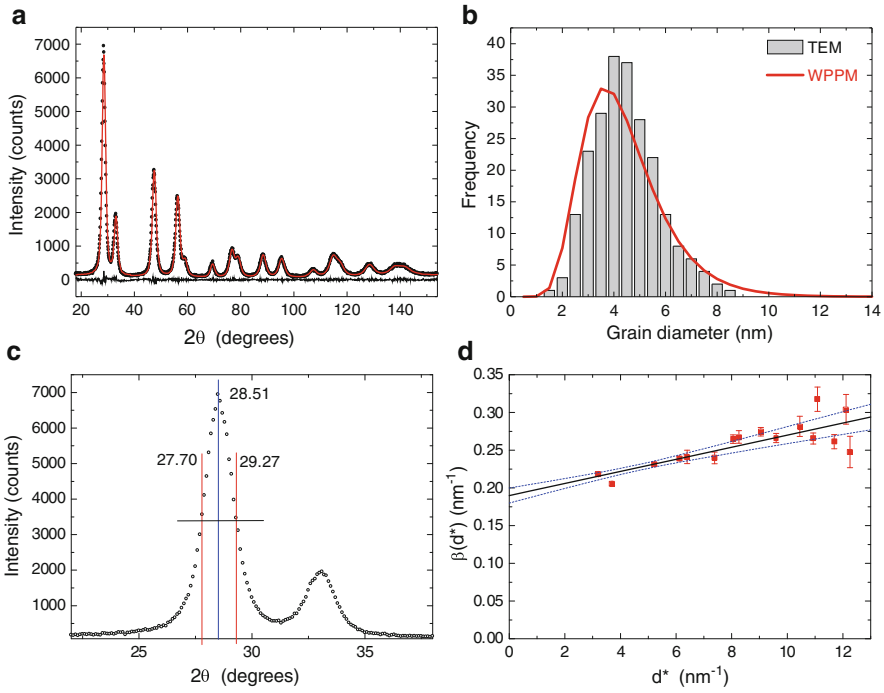

Fig. 16.1 (**a**) Experimental pattern (*dots*), WPPM result (*line*) and difference curve (*line below*). Comparison between TEM and WPPM size distributions is proposed in (**b**). The analysis using Scherrer formula and Williamson-Hall plot are shown in (**c**) and (**d**) respectively

lognormal distribution of spheres [20]) is applied to the WH result to extract the first moment of the distribution. What is clear, however, is that or a well behaving specimen (narrow monomodal distribution), the breadth of the peaks gives at least an order of magnitude estimate of the size. Considering that CeO_2 is a ceramic, a high dislocations density is also obtained (1.4×10^{16} m^{-2}): the value corresponds to ca. 1 dislocation every few grains, in agreement with TEM observations [26].

A final word should be dedicated to the number of parameters employed in the analysis: excluding Scherrer formula, clearly inappropriate here, the WH plot involved the use of 67 parameters (4 parameters for each of the 16 peaks +3 for the background). Conversely just 26 were necessary for the WPPM (16 intensities, 1 cell parameter, 2 size, 3 dislocations, 3 background, 1 specimen displacement). A higher quality result is thus obtained with less model parameters, further suggesting that modern LPA methods are mature enough for a more frequent use.

Acknowledgments The author wishes to thank Prof. P. Scardi for continuous support, critical reading and useful discussions. The PM2K software implementing the WPPM method and the DIFFaX+ code for the analysis of systems with heavy faulting are both available on request from the author. A free license is granted for academic and non-profit use.

References

1. Scherrer P (1918) Bestimmung der Grösse und der inneren Struktur von Kolloidteilchen mittels Röntgenstrahlen. Nachr Ges Wiss Goettingen Math-Phys Kl:98–100
2. Williamson GK, Hall WH (1953) X-ray line broadening from filed aluminium and wolfram. Acta Metall 1:22–31
3. Warren BE, Averbach BL (1950) The effect of cold-work distortion on X-ray patterns. J Appl Phys 21:595–600
4. Warren BE, Averbach BL (1952) The separation cold-work distortion and particle size broadening in X-ray patterns. J Appl Phys 23:497–512
5. Warren BE (1969) X-ray diffraction. Addison-Wesley, Reading
6. Klug HP, Alexander LE (1974) X-ray diffraction procedures for polycrystalline and amorphous material. Wiley, New York
7. Langford JI, Louër D (1996) Powder diffraction. Rep Prog Phys 59:131–234
8. Langford JI, Wilson AJC (1978) Scherrer after sixty years: a survey and some new results in the determination of crystallite size. J Appl Crystallogr 11:102–113
9. Scardi P, Leoni M, Dong YH (2000) Whole diffraction pattern-fitting of polycrystalline fcc materials based on microstructure. Eur Phys J B 18:23–30
10. Scardi P, Leoni M (2004) Whole powder pattern modelling: theory and application. In: Mittemeijer EJ, Scardi P (eds) Diffraction analysis of the microstructure of materials. Springer, Berlin, pp 51–91
11. Scardi P, Leoni M (2002) Whole powder pattern modelling. Acta Crystallogr A 58:190–200
12. Snyder RL, Fiala J, Bunge HJ (eds) (1999) Microstructure analysis from diffraction. Oxford University Press, Oxford
13. Mittemeijer EJ, Scardi P (eds) (2004) Diffraction analysis of the microstructure of materials. Springer, Berlin
14. Guagliardi A, Masciocchi N (2010) Diffraction at the nanoscale. Nanocrystals, defective & amorphous materials. Insubria University Press, Como
15. Scardi P, Dinnebier R (eds) (2010) Extending the reach of powder diffraction modelling. Trans Tech Publications Ltd., Zurich
16. Bertaut EF (1949) X-ray study of the distribution of crystallite dimensions in a crystalline powder [in French]. CR Acad Sci Paris 228:492–494
17. Bertaut EF (1950) Raies de Debye-Scherreretrépartition des dimensions des domaines de Bragg dans les poudrespolycristallines. Acta Crystallogr 3:14–18
18. Scardi P, Leoni M, Delhez R (2004) Line-broadening analysis using integral breadth methods: a critical review. J Appl Crystallogr 37:381–390
19. Balzar D (1999) Voigt-function model in diffraction line-broadening analysis. In: Snyder RL, Fiala J, Bunge HJ (eds) Microstructure analysis from diffraction. Oxford University Press, Oxford
20. Scardi P, Leoni M (2001) Diffraction line profiles from polydisperse crystalline systems. Acta Crystallogr A 57:604–613
21. Ungár T, Gubicza J, Ribárik G, Borbély A (2001) A crystallite size distribution and dislocation structure determined by diffraction profile analysis: principles and practical application to cubic and hexagonal crystals. J Appl Crystallogr 34:298–310
22. Ribárik G (2008) Modeling of diffraction patterns properties. PhD thesis, Eötvös University, Budapest
23. Scardi P, Dong YH, Leoni M (2001) Line profile analysis in the Rietveld method and whole-powder-pattern fitting. Mater Sci Forum 378–381:132–141
24. Scardi P (2002) Profile modelling versus profile fitting in powder diffraction. Z Kristallogr 217:420–421
25. Scardi P, Leoni M (2006) Line profile analysis: pattern modelling versus profile fitting. J Appl Crystallogr 39:24–31

26. Leoni M, Scardi P (2004) Surface relaxation effects in nanocrystalline powders. In: Mittemeijer EJ, Scardi P, Mittemeijer EJ, Scardi P (eds) Diffraction analysis of the microstructure of materials. Springer, Berlin, pp 413–454
27. Leoni M (2004) Grain surface relaxation and grain interaction in powder diffraction. Mater Sci Forum 1–10:443–444
28. Scardi P, Leoni M (2005) Diffraction whole-pattern modelling for the study of anti-phase domains in Cu3Au. Acta Mater 53:5229–5239
29. Leoni M, Scardi P (2004) Nanocrystalline domain size distributions from powder diffraction data. J Appl Crystallogr 37:629–634
30. Armstrong N, Leoni M, Scardi P (2006) Some considerations concerning Wilkens' theory of dislocation line-broadening. Z Kristallogr Suppl 23:81–86
31. Leoni M, Confente T, Scardi P (2006) PM2K: a flexible program implementing whole powder pattern modelling. Z Kristallogr Suppl 23:249–254
32. Scardi P, Leoni M, Faber J (2006) Diffraction line profile from a disperse system: a simple alternative to Voigtian profiles. Powder Diffr 21:270–277
33. Leoni M, Martinez-Garcia J, Scardi P (2007) Dislocation effects in powder diffraction. J Appl Crystallogr 40:719–724
34. Estevez-Rams E, Leoni M, Scardi P, Aragon-Fernandez B, Fuess H (2003) On the powder diffraction pattern of crystals with stacking faults. Phil Mag 83(36):4045–4057
35. Martinez-Garcia J, Leoni M, Scardi P (2009) A general approach for determining the diffraction contrast factor of straight-line dislocations. Acta Crystallogr A 65:109–119
36. Leoni M, Di Maggio R, Polizzi S, Scardi P (2004) An X-ray diffraction methodology for the microstructural analysis of nanocrystalline powders: application to cerium oxide. J Am Ceram Soc 87:1133–1140
37. Scardi P (2005) Microstructure and lattice defects in highly deformed metals by X-ray diffraction whole powder pattern modelling. Z Metall 9:698–702
38. De Giudici G, Biddau R, D'Incau M, Leoni M, Scardi P (2005) Reactivity of nanocrystalline fluorite powders: defect density threshold. Geochimicaet Cosmochimica Acta 69(16): 4073–4083
39. Scardi P, Leoni M, Lamas DG, Cabanillas ED (2005) Grain size distribution of nanocrystalline systems. Powder Diffr 20(4):353–358
40. Leoni M, De Giudici G, Biddau R, D'Incau M, Scardi P (2006) Analysis of polydisperse ball-milled fluorite powders using a full pattern technique. Z Kristallogr Suppl 23:111–116
41. Scardi P, Leoni M, D'Incau M (2007) Whole powder pattern modelling of cubic metal powders deformed by high energy milling. Z Kristallogr 222:129–135
42. Scardi P, Leoni M, Straffelini G, GiudiciG D (2007) Microstructure of Cu-Be alloy triboxidative wear debris. Acta Mater 55:2531–2538
43. Scardi P, D'Incau M, Leoni M (2007) Full pattern methods for the analysis of plastically deformed materials. Solid State Phenom 130:27–32
44. D'Incau M, Leoni M, Scardi P (2007) High energy grinding of FeMo powders. J Mater Res 22:1744–1753
45. Pesenti H, Leoni M, Scardi P (2008) XRD line profile analysis of calcite powders produced by 318 high energy milling. Z Kristallogr Suppl 27:143–150
46. Ungár T (2004) Microstructure parameters from X-ray diffraction peak broadening. Scripta Mater 51:777–781
47. Ribárik G, Gubicza J, Ungár T (2004) Correlation between strength and microstructure of ball-milled Al–Mg alloys determined by X-ray diffraction. Mater Sci Eng A 387–389:343–347
48. Balogh L, Ribárik G, Ungár T (2006) Stacking faults and twin boundaries in fcc crystals determined by X-ray diffraction profile analysis. J Appl Phys 100:023512
49. Pawley GS (1981) Unit-cell refinement from powder diffraction scans. J Appl Crystallogr 14:357–361
50. Rietveld HM (1967) Line profiles of neutron powder-diffraction peaks for structure refinement. Acta Crystallogr 22:151–152

51. Rietveld HM (1969) A profile refinement method for nuclear and magnetic structures. J Appl Crystallogr 2:65–71
52. Young RA (ed) (1993) The Rietveld method. Oxford University Press, Oxford
53. Leineweber A, Mittemeijer EJ (2004) Diffraction line broadening due to lattice-parameter variations caused by a spatially varying scalar variable: its orientation dependence caused by locally varying nitrogen content in ε-$FeN_{0.433}$. J Appl Crystallogr 37:123–135
54. van Berkum JGM (1994) Strain fields in crystalline materials. PhD thesis, Technische Universiteit Delft, Delft, The Netherlands
55. Leoni M, Gualtieri A, Roveri N (2004) Simultaneous refinement of structure and microstructure of layered materials. J Appl Crystallogr 37:166–173

Chapter 17
Pair Distribution Function Technique: Principles and Methods

Simon J.L. Billinge

Abstract One of the frontiers when studying complex and nanostructured materials is the characterization of structure on the nanoscale. We describe how the atomic pair distribution function analysis of powder diffraction data can be used to this end, and what kind of structural information can be obtained in different situations.

17.1 Introduction

This chapter is adapted from a description of the PDF method described in Chapter 16 of "*Powder Diffraction: Theory and Practice*" [1]. Increasingly, materials that are under study for their interesting technological or scientific properties are highly complex. They are made of multiple elements, have large unit cells and often low dimensional or incommensurate structures [2]. Increasingly also, they have aperiodic disorder: some aspect of the structure that is different from the average crystal structure. In the case of nanoparticles the very concept of a crystal is invalid as the approximation of infinite periodicity is no longer a good one. Still we would like to study the structure of these materials. Powder diffraction is an important method for characterizing these materials, but we have to go beyond the Bragg equation and crystallographic analysis.

The "total scattering" approach treats both the Bragg and diffuse scattering on an equal basis [3]. Powder diffraction data are measured in much the same way as in a regular powder measurement. However, explicit corrections are made for

S.J.L. Billinge (✉)
Department of Applied Physics and Applied Mathematics, Columbia University, New York, NY, USA

Condensed Matter Physics and Materials Science Department, Brookhaven National Laboratory, Upton, NY 11973, USA
e-mail: sb2896@columbia.edu

U. Kolb et al. (eds.), *Uniting Electron Crystallography and Powder Diffraction*, NATO Science for Peace and Security Series B: Physics and Biophysics,
DOI 10.1007/978-94-007-5580-2_17,

extrinsic contributions to the background intensity from such things as Compton scattering, fluorescence, scattering from the sample holder, and so on. The resulting coherent scattering function *I(Q)* is a continuous function of Q, the magnitude of the scattering vector,

$$Q = |\boldsymbol{Q}| = 2k \sin\theta = \frac{4\pi \sin\theta}{\lambda} \tag{17.1}$$

with sharp intensities where there are Bragg peaks, and broad features in between, the diffuse scattering. In general we like to work with a normalized version of this scattering intensity, *S(Q)*. This is the intensity normalized by the incident flux per atom in the sample. *S(Q)* is the total-scattering structure function. It is a dimensionless quantity and the normalization is such that the average value, $\langle S(Q)\rangle = 1$. Despite the tricky definition, it is worth remembering that *S(Q)* is nothing other than the powder diffraction pattern that has been corrected for experimental artifacts and suitably normalized.

To get a good resolution in real-space, the *S(Q)* must be measured over a wide range of Q-values. The coherent intensity (the features) in *S(Q)* die out with increasing Q due to the Debye-Waller factor which comes from thermal and quantum zero-point motion of the atoms, as well as any static displacive disorder in the material. By a Q-value of 30–50 Å^{-1} (depending on temperature and stiffness of the bonding) there are no more features in *S(Q)* and there is no need to measure it to higher-Q. Still, this is much higher than conventional powder diffraction experiments using laboratory x-rays or reactor neutrons. The maximum Q attainable in back-scattering from a copper-K_α tube is around 8 Å^{-1} and from a Mo-K_α tube 16 Å^{-1}.Routine total-scattering measurements can be made using laboratory sources with Mo or Ag tubes; however, for the highest real-space resolution, and the smallest statistical uncertainties, synchrotron data are preferred. In the case of neutron scattering, spallation neutron sources are ideal for this type of experiment.

Total scattering *S(Q)* functions appear different to standard powder diffraction measurements because of the Q-range studied, but also because of an important aspect of the normalization: the measured intensity is divided by the total scattering cross-section of the sample. For neutrons, this scattering cross-section is simply $\langle b\rangle^2$, where b is the coherent neutron scattering length of the atoms of the material in units of barns. The angle brackets denote an average. The scattering length, b, is constant as a function of Q and so is just part of the overall normalization coefficient. However, in the case of x-ray scattering, the sample scattering cross-section is the square of the atomic form-factor, $\langle f(Q)\rangle^2$, which becomes very small at high-Q. Thus, during the normalization process the data at high-Q are amplified (by being divided by a small number). This has the effect that even rather weak intensities at high-Q, which are totally neglected in a conventional analysis of the data, become rather important in a total-scattering experiment. Because the signal at high-Q is weak it is important to collect the data in that region with good statistics. This is illustrated in Fig. 17.1.

Thus, the value added of a total scattering experiment over a conventional powder diffraction analysis is the inclusion of diffuse scattering as well as Bragg peak

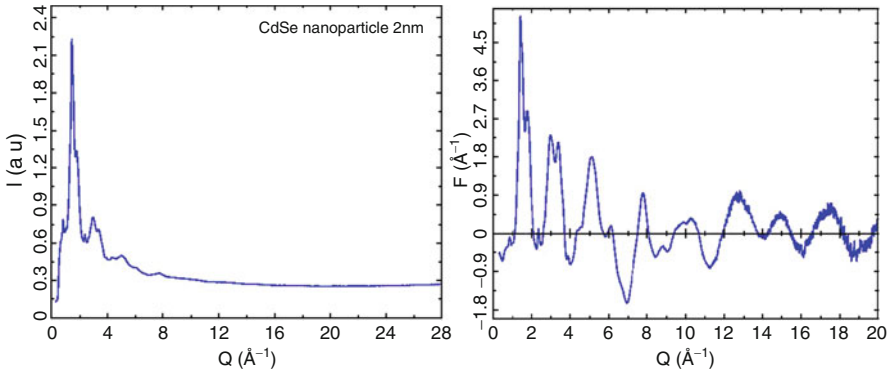

Fig. 17.1 Comparison of raw data and normalized reduced total scattering structure function F(Q) = Q[S(Q)−1]. The sample is a powder of 2 nm diameter CdSe nanoparticles and the data are x-ray data from 6ID-D at the Advanced Photon Source at Argonne National Laboratory. The raw data are shown in the left panel. The high-Q data in the region Q > 9 appear smooth and featureless (*left panel*). However, after normalizing and dividing by the square of the atomic form-factor, important diffuse scattering is evident in this region of the diffraction pattern (*right panel*)

intensities in the analysis, and the wide range of Q over which data are measured. In fact, the total scattering name comes from the fact that *all* the coherent scattering in *all* of Q-space is measured.

Total scattering data can be analyzed by fitting models directly in reciprocal-space (i.e., the *S(Q)* function is fit). However, an interesting and intuitive approach is to Fourier transform the data to real-space to obtain the atomic pair distribution function (PDF), which is then fit in real-space. The reduced pair distribution function, *G(r)*, is related to *S(Q)* through a Sine Fourier transform according to

$$G(r) = \frac{2}{\pi} \int_{Q\,\mathrm{min}}^{Q\,\mathrm{max}} Q[S(Q) - 1] \sin(Qr)\, dQ \tag{17.2}$$

Examples of a *G(r)* functions are shown in Fig. 17.2.

It has peaks at positions, r, where pairs of atoms are separated in the solid with high probability. For example, there are no peaks below the nearest neighbor peak at ∼2.5 Å which is the Cd-Se separation in CdSe [4]. However, in addition to the nearest-neighbor information, valuable structural information is contained in the pair-correlations extending to much higher values of r. In fact, with high Q-space resolution data, PDFs can be measured out to tens of nanometers (hundreds of angstroms) and the structural information remains quantitatively reliable.

There are now many classes of problems that have been studied using total scattering analysis. Traditionally it was used for liquids [5] and amorphous materials, more recently for the study of disorder in crystalline materials, and now with increasing popularity it is used to study nanostructured materials. A number of recent reviews [3, 6, 7] give examples of modern applications of the PDF method.

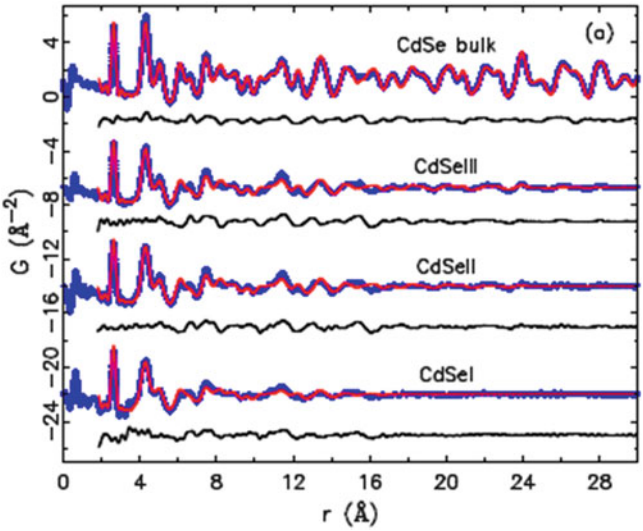

Fig. 17.2 PDFs in the form of G(r) from bulk CdSe, and from a series of CdSe nanoparticles. The *blue curve* at the *bottom* is the PDF obtained from the data shown in Fig. 17.1. The *thick lines* are from the data, with *thin lines* on *top* from models of the local structure in these nanoparticles. Offset below are *difference curves* between the model and the data (Figure adapted from [4]) (color figure online)

17.2 Theory

The basis of the total scattering method is the normalized, measured, scattering intensity from a sample, total scattering structure function, $S(Q)$ [3, 8, 9]. The wavevector, Q, is a vector quantity and in general the intensity variation, $S(Q)$, will depend on which direction one looks in Q-space. However, when the sample is isotropic, for example, a powder, it depends only on the magnitude of Q and not its direction.

Similarly, the Fourier transform of the scattered intensity, in the form of $S(Q)$, yields the reduced atomic pair distribution function, $G(r)$, defined by Eq. 17.2. This is strictly correct when the sample is made of a single element. We will discuss an approximate extension that works excellently in practice, to the more interesting case of multiple elements.

The inverse transformation of Eq. 17.2 can be defined and it yields the structure function $S(Q)$ in terms of $G(r)$,

$$S(Q) = 1 + \frac{1}{Q}\int_0^\infty G(r)\sin(Qr)\,dr. \tag{17.3}$$

There are a number of similar correlation functions related to $G(r)$ by multiplicative and additive constants. They contain the same structural information but are subtly different in some detail. $G(r)$ is the function obtained directly from the

Fourier transform of the scattered data. The function oscillates around zero and asymptotes to zero at high-r. It also tends to zero at $r = 0$ with the slope $-4\pi\rho_0$, where ρ_0 is the average number density of the material. From a practical point of view $G(r)$ is attractive because the random uncertainties on the data (propagated from the measurement) are constant in r [3]. This means that fluctuations in the difference between a calculated and measured $G(r)$ curve have the same significance at all values of r. Thus, for example, if the observed fluctuations in the difference curve decrease with increasing r this implies that the model is providing a better fit at longer distances (perhaps it is a model of the average crystallographic structure). This inference cannot be made directly from a difference curve to $\rho(r)$ or $g(r)$. A further advantage of the $G(r)$ function is that the amplitude of the oscillations gives a direct measure of the structural coherence of the sample. In a crystal with perfect structural coherence, oscillations in $G(r)$ extend to infinity with a constant peak-peak amplitude [10]. In the $G(r)$ from a real crystal the peak-peak amplitude of the signal gradually falls off due to the finite Q-resolution of the measurement, which is then the limitation on the spatial coherence of the measurement rather than the structural coherence itself. A higher Q-resolution results in data extending over a wider range of r. In samples with some degree of structural disorder, the signal amplitude in $G(r)$ falls off faster than dictated by the Q-resolution and this becomes a useful measure of the structural coherence of the sample. For example, it can be used to measure the diameter of nanoparticles.

Another function often denoted $g(r)$ is called the pair distribution function. It is normalized so that, as $r \to \infty$, $g(r) \to 1$ and has the property that for r shorter than the distance of closest approach of pairs of atoms $g(r)$ becomes zero. It is closely related to the pair density function, $\rho(r) = \rho_0 g(r)$. Clearly, $\rho(r)$ oscillates about, and then asymptotes to, the average number density of the material, ρ_0 at high-r and becomes zero as $r \to 0$. The relationship between these correlation functions is given by

$$G(r) = 4\pi r\,(\rho(r) - \rho_0) = 4\pi\rho_0 r(g(r) - 1) \tag{17.4}$$

Finally we describe the radial distribution function, $R(r)$ given by

$$R(r) = 4\pi r^2 \rho(r) \tag{17.5}$$

which is related to $G(r)$ by

$$G(r) = \frac{R(r)}{r} - 4\pi r\rho_0 \tag{17.6}$$

The $R(r)$ function is important because it is the most closely related to the physical structure since $R(r)dr$ gives the number of atoms in an annulus of thickness dr at distance r from another atom. For example, the coordination number, or the number of neighbors, N_C, is given by

$$N_C = \int_{r_1}^{r_2} R(r)dr \tag{17.7}$$

where r_1 and r_2 define the beginning and ending positions of the RDF peak corresponding to the coordination shell in question. This suggests a scheme for calculating PDFs from atomic models. Consider a model consisting of a large number of atoms situated at positions r_ν with respect to some origin. Expressed mathematically, this amounts to a series of delta functions, $\delta(r - r_\nu)$. The RDF is then given as

$$R(r) = \frac{1}{N} \sum_{\nu} \sum_{\mu} \delta(r - r_{\nu\mu}) \tag{17.8}$$

where $r_{\nu\mu} = |r_\nu - r_\mu|$ is the magnitude of the separation of the ν-th and μ-th ions and the double sum runs twice over all atoms in the sample. Later we address explicitly samples with more than one type of atom, but for completeness we give here the expression for *R(r)* in this case:

$$R(r) = \frac{1}{N} \sum_{\nu} \sum_{\mu} \frac{b_\nu b_\mu}{\langle b \rangle^2} \delta(r - r_{\nu\mu}) \tag{17.9}$$

where the b terms are the Q-independent coherent scattering lengths for the νth and μth atoms and $\langle b \rangle$ is the sample average scattering length. In the case of x-rays, the b terms are replaced with atomic number, Z.

17.3 Experimental Methods

Total scattering measurements have basically the same requirements as any powder diffraction measurement. Special requirements for high-quality total scattering data are the following:

1. Data measured over a wide Q-range. This requires wide scattering angles and/or short-wavelength incident radiation.
2. Good statistics, especially at high-Q where the scattering signal is weak.
3. Low background scattering. It is important to measure weak diffuse scattering signals accurately which is difficult on top of high backgrounds.
4. Stable set-up and accurate incident intensity monitoring. The data are normalized by incident intensity. It is important that the incident beam and detector characteristics do not change in an uncontrolled way during the course of the experiment, or that this can be corrected, for example, by monitoring the incident beam intensity as is done at synchrotron x-ray and spallation neutron measurements.

X-ray experiments can be carried out using laboratory diffractometers with Mo or Ag sources which give Q-ranges up to $Q_{max} \sim 14$ and 20 Å^{-1}, respectively. These are less than optimal values for Q_{max}, but acceptable for straightforward characterization of nanostructured materials at room temperature. Optimally, x-ray experiments are

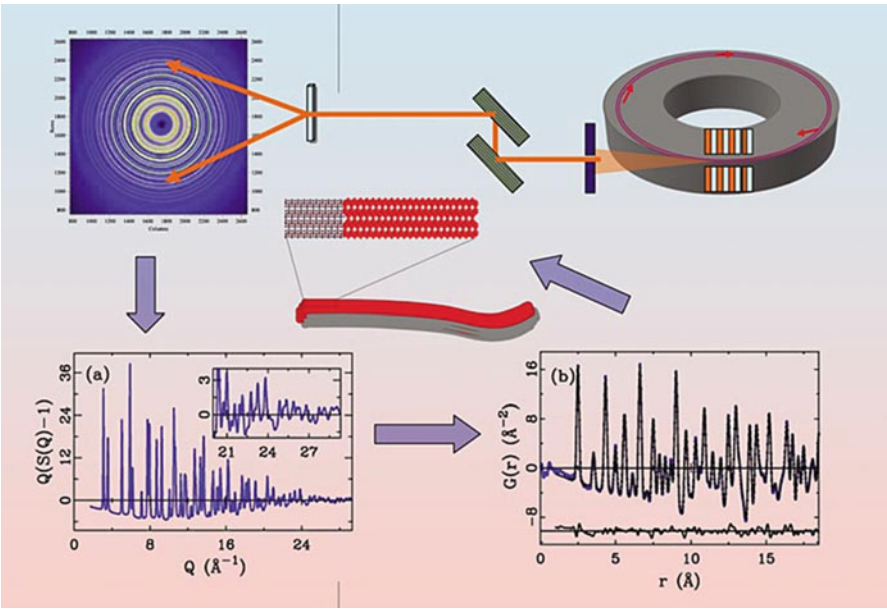

Fig. 17.3 Schematic of the rapid acquisition RAPDF x-ray data collection method

carried out at x-ray synchrotron sources using high incident energy x-rays. These can be done with incidence energies in the vicinity of 30–45 keV in conventional Debye-Scherrer geometry (for instance using be beamlines such as X31 at ESRF or 11BM at APS that are constructed for regular powder diffraction). However, more common, these days, is to use the rapid acquisition PDF mode (RAPDF) in which data for a PDF is collected in a single-shot using a planar 2D detector [11]. This is illustrated in Fig. 17.3.

Dedicated beamlines have been constructed at APS for this purpose (11ID-B and 11ID-C) with similar beamlines under construction at NSLS (X17A), ESRF and NSLS-II. In this geometry, incident x-rays of energy 60–150 keV are fired through a sample and collected on a large area image-plate detector placed behind the sample. The experiment consists of ensuring the incident beam is perpendicular and centered on the detector and the sample, then exposing the image plate. Depending on the strength of scattering and the sensitivity of the detector, exposures for good PDFs in excess of $Q_{max} = 30$ Å^{-1} can be obtained in as little as 100 ms, and typically a few seconds to minutes. This compares to data collection times of 8–12 h with conventional non-parallel counting approaches, even at the synchrotron. The RAPDF measurement is ideal for time-resolved and parametric measurements, of local structure through phase transitions for example. The Q-resolution of these measurements is very poor because of the geometry, and this limits the r-range of the resulting data from crystalline materials. However, most modeling is carried out over rather narrow ranges of r and this represents a very good tradeoff. Where a

wide *r*-range is necessary for the measurement (to study some aspect of intermediate range order on length-scales of 5–10 nm for, example) the Debye-Scherrer geometry diffractometers can be used.

In the case of neutron measurements, the requirement of short-wavelengths really limits experiments to time-of-flight spallation neutron sources. Reactor sources with hot moderators would give good quality data for PDF studies, but are in short supply. The requirements for a spallation neutron powder diffractometer are laid out in the list of experimental requirements above. Normal time-of-flight powder diffractometers can be used provided the length of the flight-path and frequency of operation are such to allow good fluxes of neutrons with short wavelength (0.2–0.4 Å). Currently neutron guides do not propagate these short-wavelength neutrons effectively so shorter flight-path diffractometers with or without guides give the best data. Currently the instruments of choice are NPDF at the Lujan Center at Los Alamos National Laboratory in the USA and GEM at ISIS, Rutherford Laboratory, in the UK. The former was upgraded with PDF experiments in mind and has excellent stability on a water moderator and low backgrounds, though data collection time is not quite at the level of GEM. New powder diffractometers are coming on line at the Spallation Neutron Source at Oak Ridge National Laboratory (NOMAD and POWGEN) that will give unprecedented data-rates and will be suitable for PDF studies.

A number of data correction programs are available for free download and these take care of the corrections and normalizations needed to obtain PDFs from raw data. These can be browsed at the ccp14 software website [12]. Commonly used, and generally easy to use, programs are Gudrun [13] and PDFgetN [14] for spallation neutron data and PDFgetX2 [15, 16] for x-ray data. PDFgetX2 has the corrections implemented for accurate analysis of RAPDF data. Details of the corrections are beyond the scope of this article, but can be found in some detail in "*Underneath the Bragg peaks: structural analysis of complex materials"* by Egami and Billinge [3].

17.4 Extracting Structural Information from Total Scattering

Here we confine ourselves to real-space modeling whereby the PDF of the model is calculated and compared to an experiment. Fitting the PDF is generally done with models described by a small number of atoms in a unit cell (which may or may not be the crystalline unit cell) and yields information about the very local structure.

Information can be extracted directly from the PDF in a model-independent way because of its definition as the atom-pair correlation function. The position of a peak in the PDF indicates the existence of a pair of atoms with that separation. There is no intensity in *R(r)* for distances less than the nearest-neighbor distance, $r < r_{nn}$ and a sharp peak at r_{nn}. This behavior is very general and true even in atomically disordered systems such as glasses, liquids and gasses. In crystals, because of the

long-range order of the structure, all neighbors at all lengths are well defined and give rise to sharp PDF peaks. The positions of these peaks give the separations of pairs of atoms in the structure directly and the width contains information about thermal motion of the atoms, or static disorder. In general, it is not possible to tell directly from the data whether a PDF peak broadening is static or dynamic in nature, though this can sometimes be inferred by fitting temperature dependence to a dynamical model such as the Debye model.

When a well-defined PDF peak can be observed, we can determine information about the number of neighbors in that coordination shell around an origin atom by integrating the intensity under that peak, as shown in Eq. 17.7. In the case of crystalline Ni there are four Ni atoms in the unit cell (fcc structure). Each nickel ion has 12 neighbors at 2.49 Å [17]. When we construct our PDF we will therefore place 48 units of intensity at position $r = 2.49$ Å (the weighting factor, $b_m b_n / \langle b \rangle^2$, is unity since there is only one kind of scatterer) and divide by $N = 4$ since we put 4 atoms respectively at the origin. Thus, integrating the first peak will yield 12 which is the coordination number of Ni. The same information can be obtained from multi-element samples if the chemical origin of the PDF peak, and therefore the weighting factor, is known. If, as is often the case, PDF peaks from different origins overlap this process is complicated. Information can be extracted by measuring the chemical specific differential or partial-PDFs directly [18], by fitting the peaks with a series of Gaussian functions, or better, by full-scale structural modeling.

Atomic disorder in the form of thermal and zero-point motion of atoms, and any static displacements of atoms away from ideal lattice sites, give rise to a distribution of atom-atom distances. The PDF peaks are therefore broadened resulting in Gaussian shaped peaks. The width and shape of the PDF peaks contain information about the real atomic probability distribution. For example, a non-Gaussian PDF peak may suggest an anharmonic crystal potential.

Modeling the data reveals much more information that straight model independent analysis. The most popular approach for real-space modeling is to use PDFfit, and its replacement PDFfit2 and PDFgui [19, 20], a full-profile fitting method analogous to the Rietveld method [21] but where the function being fit is the PDF.

Parameters in the structural model, and other experiment-dependent parameters, are allowed to vary until a best-fit of the PDF calculated from the model and the data derived PDF is obtained, using a least-squares approach. The sample dependent parameters thus derived include the unit cell parameters (unit cell lengths and angles), atomic positions in the unit cell expressed in fractional coordinates, anisotropic thermal ellipsoids for each atom and the average atomic occupancy of each site.

We highlight here the similarities and differences with conventional Rietveld. The main similarity is that the model is defined in a small unit cell with atom positions specified in terms of fractional coordinates. The refined structural parameters are exactly the same as those obtained from Rietveld. The main difference from conventional Rietveld is that the *local* structure is being fit which contains information about short-range atomic correlations. There is additional information in the data, which is not present in the average structure, about disordered and short-range

ordered atomic displacements. To successfully model these displacements it is often necessary to utilize a "unit cell" which is larger than the crystallographic one. It is also a common strategy to introduce disorder in an average sense without increasing the unit cell. For example, in the example where an atom is sitting in one of two displaced minima in the atomic potential, but its probability of being in either well is random, can be modeled as a split atomic position with 50% occupancy in each well. This is not a perfect, but a very good, approximation of the real situation and is very useful as a first order attempt at modeling the data.

This "Real-space Rietveld" approach is proving to be very useful and an important first step in analyzing PDFs from crystalline materials. This is because of two main reasons. First, its similarity with traditional Rietveld means that a traditional Rietveld derived structure can be compared *quantitatively* with the results of the PDF modeling. This is an important first step in determining whether there is significant evidence for local distortions beyond the average structure. If evidence exists to suggest that local structural distortions beyond the average structure are present, these can then be incorporated in the PDF model. The second strength of the real-space Rietveld approach is the simplicity of the structural models making it quick and straightforward to construct the structural models and making physical interpretations from the models similarly quick and straightforward. The most recent version of the PDFfit code comes with a user-friendly graphical user interface facilitating many tasks in the data analysis, called PDFgui and PDFfit2 [19].

PDFfit was originally designed to study disorder and short-range order in crystalline materials with significant disorder such as nanoporous bulk materials. It has also found extensive use in studying more heavily disordered materials such as nanocrystalline materials and nanoporous materials and this looks set to increase in the future.

17.5 Conclusions

This chapter contains a brief account of the theory behind the PDF method and the basic methods for obtaining suitable data, analyzing it and extracting nanostructural information from it. Interest in the technique is growing rapidly as the quality of structural information obtainable from it improves due to methodological advances, and as more and more researchers seek to make and characterize materials on the nanoscale.

Acknowledgements Work in the Billinge group is supported by the US-Department of Energy, Office of Science, through grant DE-AC02-98CH10886 and by the US National Science Foundation through grant DMR-0703940.

References

1. Dinnebier RE, Billinge SJL (2008) Powder diffraction: theory and practice. The Royal Society of Chemistry, Cambridge
2. Billinge SJL, Levin I (2007) The problem with determining atomic structure at the nanoscale. Science 316:561–565
3. Egami T, Billinge SJL (2003) Underneath the Bragg peaks: structural analysis of complex materials. Pergamon Press/Elsevier, Oxford
4. Masadeh AS, Bozin ES, Farrow CL, Paglia G, Juhás P, Karkamkar A, Kanatzidis MG, Billinge SJL (2007) Quantitative size-dependent structure and strain determination of CdSe nanoparticles using atomic pair distribution function analysis. Phys Rev B 76:115413
5. Soper AK (1996) Empirical potential Monte Carlo simulation of fluid structure. Chem Phys 202:295–306
6. Billinge SJL, Kanatzidis MG (2004) Beyond crystallography: the study of disorder nanocrystallinity and crystallographically challenged materials. Chem Commun 2004:749–760
7. Proffen T, Billinge SJL, Egami T, Louca D (2003) Structural analysis of complex materials using the atomic pair distribution function – a practical guide. Z Kristallogr 218:132–143
8. Warren BE (1999) X-ray diffraction. Dover, New York
9. Klug HP, Alexander LE (1974) X-ray diffraction procedures for polycrystalline and amorphous materials, 2nd edn. Wiley, New York
10. Levashov VA, Billinge SJL, Thorpe MF (2005) Density fluctuations and the pair distribution function. Phys Rev B 72:024111
11. Chupas PJ, Xiangyun Qiu, Hanson JC, Lee PL, Grey CP, Billinge SJL (2003) Rapid acquisition pair distribution function analysis (RA-PDF). J Appl Crystallogr 36:1342–1347
12. URL:http://www.ccp14.ac.uk/
13. Information can be found at the ISIS disordered materials group website: http://www.isis.rl.ac.uk/disordered/dmgroup_home.htm
14. URL: http://pdfgetn.sourceforge.net/
15. Xiangyun Qiu, Thompson JW, Billinge SJL (2004) PDFgetX2: a GUI driven program to obtain the pair distribution function from X-ray powder diffraction data. J Appl Crystallogr 37:678
16. URL: http://www.pa.msu.edu/cmp/billinge-group/programs/PDFgetX2/
17. Wyckoff RWG (1967) Crystal structures, vol 1, 2nd edn. Wiley, New York
18. Price DL, Saboungi ML (1998) Anomalous X-ray scattering from disordered materials. In: Billinge SJL, Thorpe MF (eds) Local structure from diffraction. Plenum, New York
19. Farrow CL, Juhás P, Jiwu Liu, Bryndin D, Bozin ES, Bloch J, Proffen T, Billinge SJL (2007) PDFfit2 and PDFgui: computer programs for studying nanostructure in crystals. J Phys Condens Mat 19:335219
20. URL: http://www.diffpy.org/
21. Young RA (1993) The Rietveld method, vol 5 of international union of crystallography monographs on crystallography. Oxford University Press, Oxford

Chapter 18
Debye Analysis

Yuri G. Andreev

Abstract Violation of 3D translational symmetry often precludes extraction of accurate structural information from powder diffraction data using the established methods of structure refinement. Prone to turbostratic distortions, layered structures and nano objects, with anisotropic crystallite size and non-uniform deformation, are the prime examples of compounds that provide a considerable challenge for diffraction studies. Application of the fundamental diffraction equation of Debye provides a means of establishing the arrangement of atoms with any degree of structural disorder.

18.1 Introduction

The arrival of the Rietveld method initiated the renaissance of powder diffraction methodology as a tool for structure refinement [1]. It took another 25–30 years after that for the powder diffraction method to end the total dominance of single-crystal diffraction as the technique for *ab initio* structure determination [2–5].

Despite the mentioned advances in powder diffraction methodology, single-crystal diffraction remains the technique of choice if a single crystal of adequate quality and size of the solid in question is available. At modern synchrotron sources diffraction data, sufficient for establishing the crystal structure, can be collected from a micron-size single crystal. However, when the crystal size is in the nanometer range or the structure lacks translational symmetry due to disorder, powder diffraction remains the only option on hand.

Y.G. Andreev (✉)
School of Chemistry, University of St Andrews, St Andrews, Fife KY16 9ST, Scotland, UK
e-mail: ya@st-and.ac.uk

U. Kolb et al. (eds.), *Uniting Electron Crystallography and Powder Diffraction*,
NATO Science for Peace and Security Series B: Physics and Biophysics,
DOI 10.1007/978-94-007-5580-2_18,

Full-profile analyses of powder diffraction patterns, *e.g.* Rietveld method, utilise empirical peak-shape functions which work reasonably well when long-range translational symmetry is not violated by small and anisotropic crystallite size, non-uniform deformation of the crystal lattice, loss of structural registry in 1 or 2 dimensions, *etc*. Such crystal structure imperfections are common in a number of materials of current interest, which include graphene and nanoparticles. More often than not, the shape of diffraction peaks from such disordered materials cannot be adequately described by analytical functions, rendering the application of established powder methods difficult or impossible [6]. The arrival of total scattering approach [7, 8] circumvents the use of such methods by employing basic x-ray diffraction theory which uses Fourier transforms. Based on the early methodologies of Kitaigorodsky and Guinier [9, 10] originally used to interpret diffuse scattering data, the total scattering approach takes full advantage of the modern powerful synchrotron radiation sources to collect high quality diffraction data in a wide range of values of the modulus of the wave vector, Q. The extended Q range greatly reduces the truncation errors, caused by performing a Fourier transform within a finite interval, and produces an atomic pair distribution function which takes into account both diffuse and Bragg scattering data.

In this Chapter, a different approach is used to interpret diffraction data from imperfect structures. The method utilises the fundamental equation of Debye [11] which allows one to calculate a powder pattern by considering diffraction/interference contributions from each pair of atoms in the scattering domain. Thus calculated powder profile from a trial direct-space structural model can be directly compared to the experimental diffraction pattern.

18.2 Debye Formula

In 1915 Debye derived an equation that relates directly the inter-atomic distances between each pair of atoms in the scattering volume to the observed X-ray diffraction pattern, without recourse to symmetry (crystallography) [11]. The equation is exact in the first Born, or kinematic, approximation and deals explicitly with Bragg and diffuse scattering as well as the small-angle scattering from a powder. The intensity of X-ray radiation diffracted by an array of atoms, allowing all orientations of the array to have equal probability, is

$$I(\theta) = \sum_n f_n^2(\theta) + 2\sum_i \sum_j f_i(\theta)\, f_j(\theta) \left[\sin\left(4\pi r_{ij} \sin\theta/\lambda\right) \Big/ \left(4\pi r_{ji} \sin\theta/\lambda\right)\right]$$

where $f_n(\theta)$ is the atomic form-factor of the *nth* atom in the array, λ is the wavelength and r_{ij} is the distance between atoms i and j.

To account for the effect of preferred orientation a multiplier, T_{ij}, can be added into the double sum of the above equation [12].

$$T_{ij} = \left(T^2 \cos^2 \alpha_{ij} + \frac{1}{T} \sin^2 \alpha_{ij} \right)^{-\frac{3}{2}}$$

The correction is similar to the March-Dollase formulation [13], however, in this case α_{ij} is the angle between r_{ij} and the preferred orientation vector.

18.3 Applications

18.3.1 Layered Structures with Dimensional Disorder

Layered materials with loose coupling between sheets (layers) in the structure are prone to losing the inter-layer registry (ordering) on mechanical impact (*e.g.* ball-milling) or during intercalation/deintercalation of host atoms or molecules between the layers. The classic examples of such materials are graphite and hexagonal boron nitride. Under normal circumstances both solids have a highly symmetrical hexagonal structure with only a few atoms in the asymmetric unit. Atoms in these structures are arranged in honeycomb layers, with the latter stacked in registry, forming a 3D-ordered array which gives a powder pattern with sharp symmetric peaks, Fig. 18.1a.

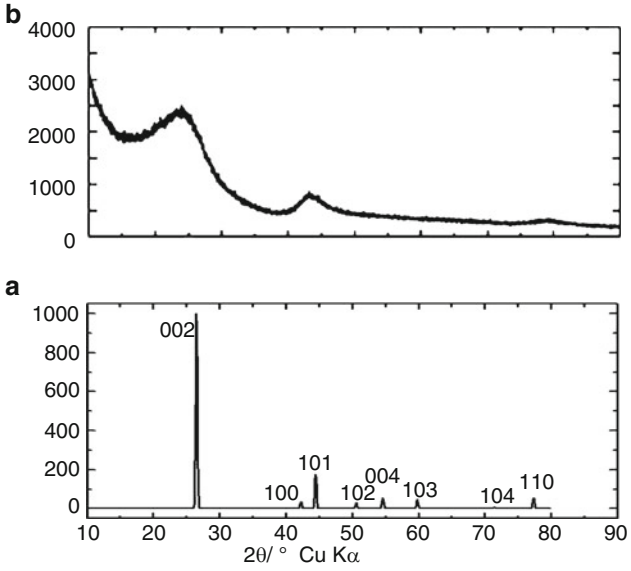

Fig. 18.1 X-ray diffraction patterns of 3D-ordered (**a**) and turbostratically disordered (**b**) graphite

When such layered materials are synthesised *via* a disorder-inducive route or subjected to mechanical or chemical treatments mentioned above, the size of the in-plane ordered regions tend to decrease along with the degree of the inter-layer registry. This type of disorder is often referred to as turbostratic distortions. Such distortions have dramatic effect on the powder diffraction pattern, Fig. 18.1b. All reflections that are not of the *00l*, *h00* or *hk0* type disappear. The *00l* peaks broaden and shift to lower 2θ (higher d-spacing) values, while the shape of the in-plane *h00* and *hk0* reflections, in addition to broadening and shifting of the position of the maximum count towards higher 2θ, becomes highly asymmetric, with significantly slower intensity decay from the peak maximum on the lower d-spacing side. The latter peak shape in some cases can be adequately described by the function derived by Warren and Bodenstein for diffraction reflections from a single circular honeycomb layer (or a collection of randomly oriented layers of this type) [14]. The profile, $Y_{hk}(2\theta)$, of such 2D reflection is defined as follows:

$$Y_{hk}\,(2\theta) = mMD\lambda^{3/2}\,F^2R^{5/2}\,\Omega\Big[2\pi A_a^2\sin\theta(\sin\theta+\sin\theta_0)^{1/2}\Big]^{-1},$$

where

$$\Omega = \int_0^1 \left\{\Big[\arccos S - S\big(1-S^2\big)^{1/2}\Big]\Big/S^{1/2}\right\}(\cos 2\pi\gamma S + \sin 2\pi\gamma S)\,dS,$$

$$A_a = a^2\sqrt{3}/2\,,\quad \gamma = (4R/\lambda)(\sin\theta - \sin\theta_0)$$

m is the multiplicity of the *hk* reflection; M is the number of randomly oriented layers in the sample; D is the distance to the receiving surface; λ is the wavelength; F, R and a are the in-plane structure factor, layer radius and lattice parameter, respectively; θ_0 is the position of the *hk0* reflection in the case of 3D ordering. Note that, unlike for 3D reflections, the position of the 2D peak maximum is a function not only of the in-plane lattice parameter but also of the layer size!

The peak-shape function of Warren and Bodenstein has been successfully applied to determine the in-plane crystallite size and lattice in a turbostratically disordered hexagonal BN, Fig. 18.2 [15].

However, modelling of 2D diffraction peak shapes from single honeycomb layers of different size, Fig. 18.3, and ensembles of parallel, but not in complete crystallographic registry, layers (to produce *00l* reflections, in addition to *h0* and *hk*) using Debye equation clearly demonstrates that the analytical formulation would fail in some cases [16].

Thus, when the radius of a layer is reduced to 10 Å deviations from perfect circular shape become more evident and the 2D profile shape suggested by Warren

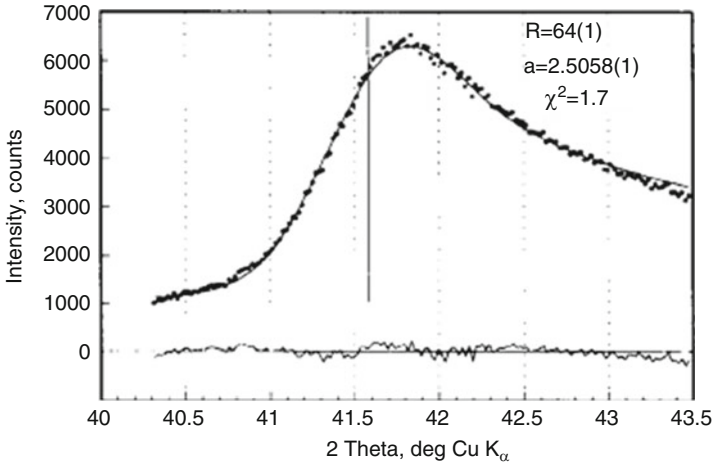

Fig. 18.2 Experimental (*dots*), calculated using the formulation of Warren and Bodenstein [14] (*solid line*) and difference (*solid line* around y = 0) X-ray diffraction profile of *10* peak of turbostratically disordered hexagonal BN. *Vertical solid line* indicates the position of *100* reflection in 3D-ordered hex-BN, *R*, and *a* (both in Å) are the in-plane radius of the ordered region and lattice parameter, respectively

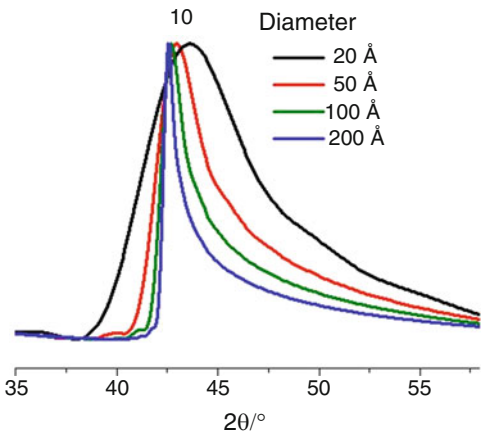

Fig. 18.3 Calculated using Debye equation X-ray diffraction profiles of *.10* reflection from single circular graphene layers of different size

and Bodenstein provides a poor match to the true profile obtained by using the equation of Debye. Similarly, even for larger layer size, when turbostratic distortions are caused by random rotations of the layers, the single-layer peak shape fails to adequately describe the 2D reflection profile, Fig. 18.4.

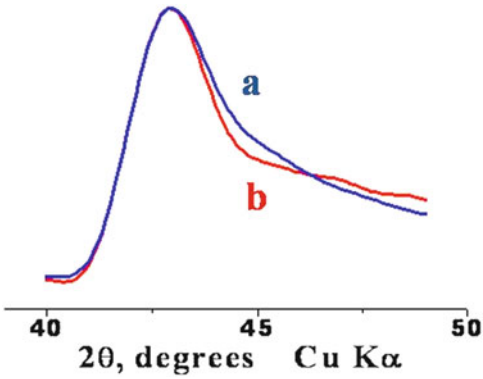

Fig. 18.4 Calculated using Debye equation X-ray diffraction profiles of *.10* reflection from (**a**) single circular graphene layer (50 Å in diameter) and (**b**) 16 such layers first stacked in the *ABAB* registry of graphite and then rotated by a randomly chosen angle around their centres

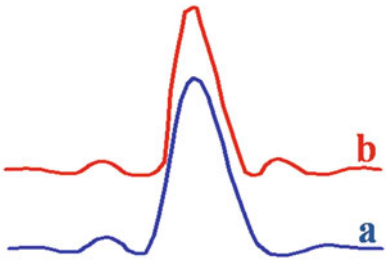

Fig. 18.5 Fragments of the experimental neutron diffraction profile of the *400* reflection from oxygen-free (*top*) 160 Å Ni particles and the same particles at an early oxidation stage (*bottom*)

18.3.2 Oxidation of Ni Nanoparticles

In the course of neutron diffraction study of oxygen insertion into spherical Ni nanoparticles, 160 Å in diameter, a pronounced peak asymmetry, Fig. 18.5, has been detected at early stages of oxidation, when the oxygen content is several atomic percents and the NiO phase is not yet formed [17].

The true diffraction profiles, $I(\theta)$, of the 400 reflection from the oxidised and oxygen-free powders, which have been extracted by solving the convolution equation

$$H(\theta) = \int I(\theta)\, G\left(\theta - \theta'\right) d\theta'$$

[$H(\theta)$ and $G(\theta)$ are experimental profiles from the nanoparticular and micron-size Ni powders, respectively], reveal that on oxidation the intensity of the left satellite of the main peak becomes greater than that of the right satellite.

In order to explain the changes in the peak shapes the profile of the *400* reflection was calculated using Debye equation. A spherical Ni particle with the ideal and non-uniformly deformed *fcc* structure was used as a model. The deformation was

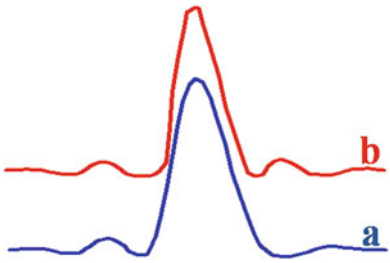

Fig. 18.6 True neutron diffraction profiles, $I(\theta)$, of the *400* reflection from 160 Å Ni particles (**a**) at an early oxidation stage and (**b**) oxygen-free

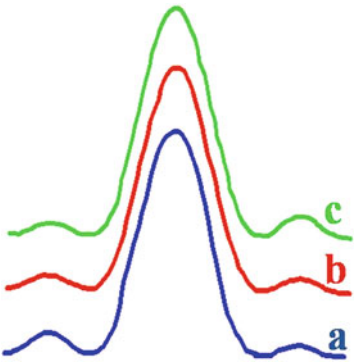

Fig. 18.7 Calculated using Debye equation neutron diffraction profiles of the *400* reflection from (**a**) non-uniformly expanded, (**b**) ideal and (**c**) non-uniformly contracted spherical Ni nanoparticles

introduced through the components of the deformation tensor implying that the greatest distortion of the ideal lattice is observed on the surface of the particle and gradually reduces towards the centre. The calculated profiles show that the satellites of the main diffraction peak are of equal height for the ideal particle (Fig. 18.6b) while non-uniform deformation causes considerable redistribution of their intensities. The left-hand side satellite is higher for the expanded particle (Fig. 18.6a) and is lower for the non-uniformly contracted particle (Fig. 18.6c). The $I(\theta)$ profile from the oxidised powder is similar to that of the expanded particle (compare Figs.18.7a and 18.6a). It is natural to assume that the observed deformation is caused by the presence of oxygen atoms in the nickel particle which form a coherent solid solution with the metal. The non-uniformity of the deformation can be explained by the concentration gradient of oxygen within the particle, with the higher oxygen content in the surface area.

18.3.3 Deformations in TiO_2-B Nanotubes

According to TEM data internal and external diameters of TiO_2-B nanotubes are 50 and 100 Å respectively, and the length can be up to tens of microns. A powder

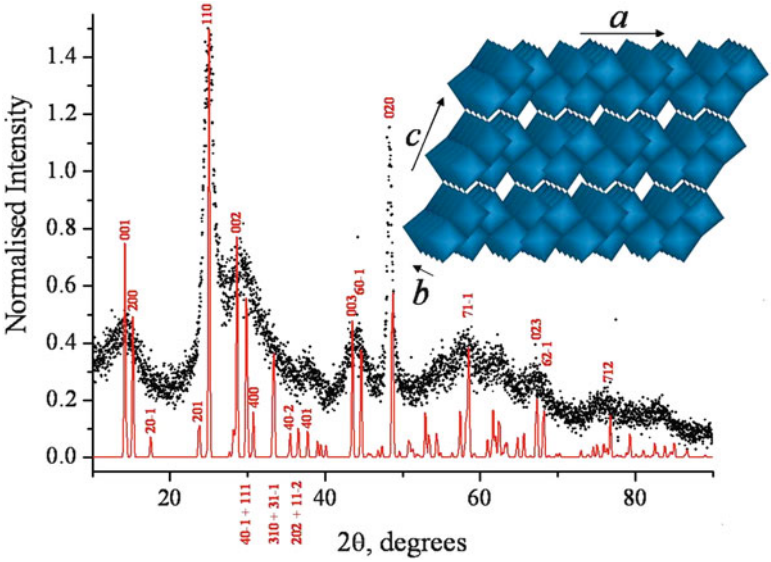

Fig. 18.8 *Dots* – observed X-ray diffraction pattern of TiO_2-B nanotubes; *red line* – simulated pattern based on the ideal TiO_2-B structure. Numbers are Miller indices. Inset shows ideal TiO_2-B crystal structure with crystallographic axes (color figure online)

X-ray diffraction pattern for the nanotubes is presented in Fig. 18.8 along with the ideal monoclinic TiO_2-B crystal structure and a simulated powder X-ray diffraction pattern based on the latter.

Comparison between the simulated and observed powder patterns highlights the severe *hkl*-dependent peak broadening/distortion of the latter, features that reflect the limited dimensions of the tube walls, the anisotropy of the nanotubes and the structural distortions (deviations from the ideal crystal structure) which are expected to occur on bending a layered crystal structure into a nanotube.

The 020 reflection in Fig. 18.8 is noticeably narrower than other peaks in the experimental pattern and by application of the Scherrer formula a coherence length in the *b* direction is estimated at 144 Å. This exceeds the diameter of the tubes and implies that the *b*-axis lies along the axial direction of the nanotubes.

Many materials have been formed as nanotubes, the vast majority are based on layered structures in which the layers fold to form the tubes. Since the layers of the TiO_2-B structure lie in the *ab* plane and since *b* lies along the axial direction, a tube may be formed by folding the *ab* plane along *a*, as shown in Fig. 18.9 (middle pattern).

Such a structure is consistent with the TEM image which indicates that the walls are composed of four layers, consistent with the wall thickness of ∼25 Å. Hence, the first structural model to be constructed was based on folding four layers of the crystal structure in the *ab* plane, as just described. The length of the tube was set

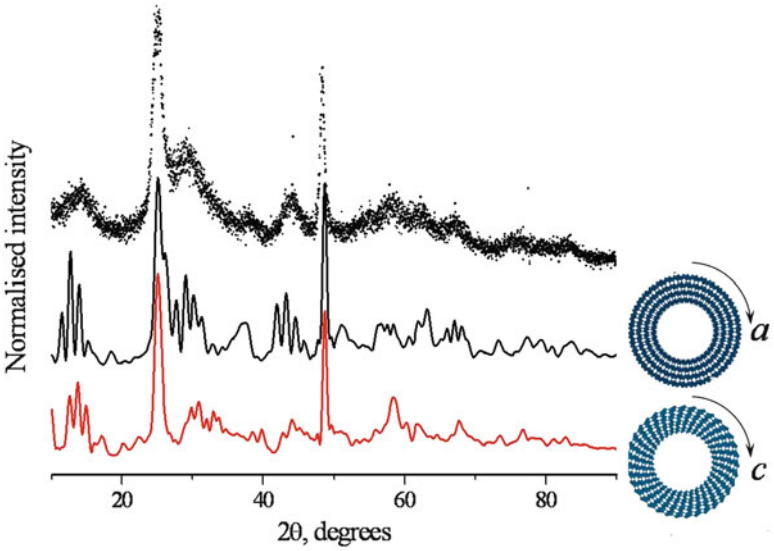

Fig. 18.9 *Dots* – observed X-ray diffraction pattern of TiO_2-B nanotubes; *black line* – simulated pattern based on folding the *ab* plane of the ideal TiO_2-B structure along *a* into a tube; *red line* – simulated pattern based on folding the *bc* plane of the ideal TiO_2-B structure along *c* into a tube. Views along the tube axis for each model are also shown (color figure online)

at 142 Å (equivalent to 38 unit cells along *b* in the ideal structure), consistent with the coherence length along *b*, and the internal diameter at 23 Å, consistent the TEM data. Bending a slab of the ideal TiO_2-B structure into a tube inevitably leads to distortions of the TiO_6 octahedra along the annulus of the tube.

A powder diffraction pattern generated from this model using Debye equation is compared with experiment in Fig. 18.9, from which it is clear that the model does not adequately describe the nanotubes. The peaks of the simulation are narrower and more abundant than in the observed powder diffraction pattern, suggesting that the model possesses more symmetry than is the case in practice. Similar problems are noted for an alternative model in which the tubes are formed by folding the *bc* plane along *c*, Fig. 18.9 (bottom pattern). Despite the inadequacies of both models, comparison between them and the observed powder diffraction pattern suggests that folding along *a* better describes the nanotubes. Also, as discussed above, folding along *a* is more physically reasonable than folding along *c*.

Recognising that a model involving order throughout the entire nanotube does not adequately describe the observed data, segments of this structure were considered, all retaining four layers in the radial direction and extending 142 Å along *b* but extending to different degrees along the circumference. A segment of dimension 32 Å best represents the observed data, Fig. 18.10.

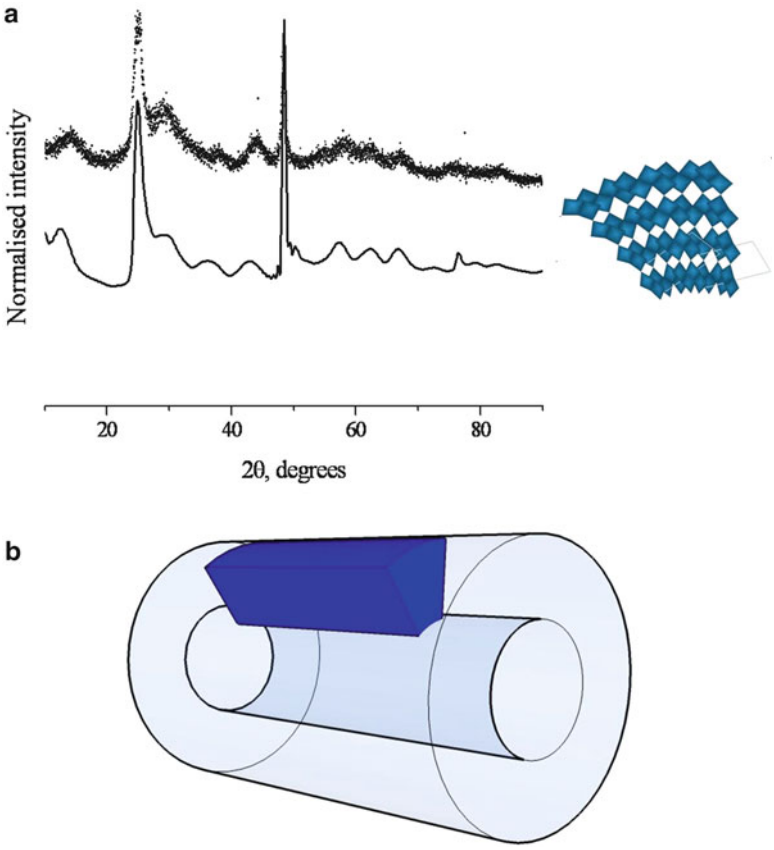

Fig. 18.10 (**a**) *Dots* – observed X-ray diffraction pattern of TiO_2-B nanotubes; *black line* – simulated pattern of a 3.2 nm tube segment with a view of the model along *y*. (**b**) Schematic representation of an ordered segment within a nanotube

A schematic representation of a segment within the tube is also shown in Fig. 18.10; the segments are not in registry with each other but are aligned along the axial direction of the tubes. Further details about this investigation can be found in [12].

References

1. Rietveld HM (1969) A profile refinement method for nuclear and magnetic structures. J Appl Crystallogr 2:65
2. Altomare A, Burla MC, Camalli M, Cascarano G, Giacovazzo C, Guagliardi A, Moliterni AGG, Polidori G, Rizzi R (1998) Toward EXPO: from the powder pattern to the crystal structure. Mater Sci Forum 278:284

3. Andreev YG, Lightfoot P, Bruce PG (1996) Structure of the polymer electrolyte poly(ethylene oxide)$_3$:LiN(SO_2CF_3)$_2$ determined by powder diffraction using a powerful Monte Carlo approach. J Chem Soc Chem Comm 2169
4. Kariuki BM, Serrano-Gonzalez H, Johnston RL, Harris KDM (1998) The application of a genetic algorithm for solving crystal structures from powder diffraction data. Chem Phys Lett 280:189
5. David WIF, Shankland K, Shankland N (1998) Routine determination of molecular crystal structures from powder diffraction data. J Chem Soc Chem Comm 8:931
6. Billinge SJL, Levin I (2007) The problem with determining atomic structure at the nanoscale. Science 316:561
7. McGreevy RL, Pusztai L (1988) Reverse Monte Carlo simulation: a new technique for the determination of disordered structures. Mol Simul 1:359
8. Petkov V, Billinge SJL, Shastri SD, Himmel B (2001) High-resolution atomic distribution functions of disordered materials by high-energy X-ray diffraction. J Non-Cryst Solid 293:726
9. Kitaigorodsky AI (1952) X-ray structural analysis of microcrystalline and amorphous, Substances Gostekhizdat, Moscow
10. Guinier A (1963) X-ray diffraction in crystals, imperfect crystals and amorphous bodies. W. H. Freeman and Co., San Francisco
11. Debye P (1915) Zerstreuung von Röntgenstrahlen. Ann Phys 351:809
12. Andreev YG, Bruce PG (2008) Demonstrating structural deformation in an inorganic nanotube. J Am Chem Soc 130:9932
13. Dollase WA (1986) Correction of intensities for preferred orientation in powder diffractometry: application of the March model. J Appl Crystallogr 19:267
14. Warren BE, Bodenstein P (1966) The shape of two-dimensional carbon black reflections. Acta Crystallogr 20:602
15. Andreev YG, Lunström T (1994) In-plane lattice-parameter and crystallite-size determination in a turbostratic graphite-like structure. J Appl Crystallogr 27:767
16. Andreev YG, Lunström T (1995) Simulation of powder diffraction diagrams from disordered and imperfect graphitic layers. J Appl Crystallogr 28:534
17. Andreev YG, Burkhanov AV, Ermolaev AG, Zelenyuk FM, Lapovok VN, Petrunin VF, Sukhovich EP, Trusov TI (1990) A neutron-diffraction investigation of the effect of oxidation on the mean-square displacement of atoms in finely dispersed nickel. Phys Chem Mech Surf 5:2560

Chapter 19
Quantitative Phase Analysis

Ian C. Madsen, Nicola V.Y. Scarlett, and Nathan A.S. Webster

Abstract The most common use of powder diffraction in analytical science is the identification of crystalline components, or phases, present in a sample of interest. The near universal applicability of the method for this purpose is derived from the fact that a diffraction pattern is produced directly from the components' crystal structure. However, for multi-phase samples, once the nature of phases present has been established, the next question usually asked of the diffractionist is "how much of each phase is there?" This chapter provides an overview of the basis and application of commonly used methods of quantitative phase abundance determination as well as references to the extensive literature on the subject.

19.1 Introduction

The mathematical basis of quantitative phase analysis (QPA) from diffraction data is well established and, in an ideal world, QPA should be a relatively straightforward science. However, there are a significant number of factors, most of them experimental, which serve to decrease the accuracy which can be obtained. Some of these, such as accuracy in measurement of peak position and intensity, resolution of overlapping peaks and counting statistics, relate to instrument geometry and data collection conditions, while other sources of error derive from sample related issues. This latter group includes effects such as preferred orientation (which distorts the observed relative intensities from those expected for a randomly oriented powder), crystallite size and strain broadening (leading to increased peak overlap) and microabsorption (where phases which strongly absorb the incident and diffracted beams are

I.C. Madsen (✉) • N.V.Y. Scarlett • N.A.S. Webster
CSIRO Process Science and Engineering, Box 312, Clayton South 3169, VIC, Australia
e-mail: ian.madsen@csiro.au; Nicola.Scarlett@csiro.au; Nathan.Webster@csiro.au

U. Kolb et al. (eds.), *Uniting Electron Crystallography and Powder Diffraction*,
NATO Science for Peace and Security Series B: Physics and Biophysics,
DOI 10.1007/978-94-007-5580-2_19,

underestimated with respect to weakly absorbing phases). Microabsorption remains the largest impediment to accurate QPA and is more pronounced in X-ray diffraction than neutron based studies.

This paper provides some of the background to methods of QPA from diffraction data. The round robin on quantitative phase analysis run under the auspices of the International Union for Crystallography (IUCr) Commission on Powder Diffraction (CPD) [1, 2] demonstrated that 87% of participants collected laboratory-based X-ray diffraction data, while the majority (75%) used whole pattern, especially Rietveld [3] based, methods for the analysis of their data.

Rietveld-based methods have the potential to produce more accurate and precise results than those obtained from conventional single peak methods. The improvement derives from the fact that (i) all of the peaks in the pattern contribute to the analysis, regardless of the degree of overlap, and (ii) the impact of some sample related effects, such as preferred orientation, are minimised by the inclusion of all reflections. The application of models for correction of other residual aberrations, serves to further improve the analysis.

While the Rietveld technique was initially developed for the refinement of crystal structure, other parameters, which must be refined to ensure best fit between the observed and calculated patterns, contain useful, non-structural information which can be of interest to the analyst. These include peak width and shape which can be related to crystallite size and strain or preferred orientation parameters which can be related to crystal morphology. However, it is the Rietveld scale factor which, in a multiphase mixture, is related to the amount of the phase present that is interesting in the current context.

There is extensive coverage of traditional 'single-peak' methods in earlier literature [4–8] plus a thorough review of the field by Zevin and Kimmel [9] to which the reader is directed for more detailed explanations. Due to the wide-spread use of the Rietveld method in QPA, this chapter will focus only on the use of whole-pattern, Rietveld based approaches. The mathematical basis will be described along with detailed discussion of various modifications which aim to produce absolute, rather than relative, phase abundances. A number of case studies and applications, which serve to illustrate selected issues in QPA, are also presented.

19.2 Mathematical Basis

19.2.1 Rietveld-Based Methods

The Rietveld method uses a model to calculate a diffraction pattern which is then compared with observed data. The difference between the two patterns is then reduced through least squares minimisation. The refinable parameters used in the models provide the analyst with information regarding the crystal structure of the

component phases, the crystallite size and strain and, importantly, their relative proportions. The Rietveld scale factor, which is a multiplier for each component's contribution to the pattern, is related to the relative abundance of that phase and can be used in the quantification of phases.

The integrated intensity I of the hkl reflection for phase α in a multi-phase mixture, measured on a flat-plate sample of infinite thickness using a diffractometer with Bragg-Brentano geometry, is given by:

$$I_{(hkl)\alpha} = \left[\frac{I_0\lambda^3}{32\pi r}\frac{e^4}{{m_e}^2c^4}\right]\cdot\left[\frac{M_{(hkl)}}{2{V_\alpha}^2}\left|F_{(hkl)\alpha}\right|^2\cdot\left(\frac{1+\cos^2 2\theta\cos^2 2\theta_m}{\sin^2\theta\cos\theta}\right)\right.$$
$$\left.\cdot Exp\left(-2B\left(\frac{\sin\theta}{\lambda}\right)^2\right)\right]\cdot\left[\frac{W_\alpha}{\rho_\alpha {\mu_m}^*}\right] \tag{19.1}$$

where I_0 is the incident beam intensity, e is the charge on an electron, m_e is the mass of an electron, r is the distance from the scattering electron to the detector and c is the speed of light. M_{hkl} and F_{hkl} are the multiplicity and structure factor of the hkl reflection respectively, V is the unit cell volume and θ and θ_m are the diffraction angles for the hkl reflection and the monochromator respectively. B is the mean atomic displacement parameter (ADP). W_α and ρ_α are the weight fraction and density of phase α respectively, while ${\mu_m}^*$ is the mass absorption coefficient of the entire sample.

Many of the terms in Eq. 19.1 can be grouped together and defined as a constant K. Equating $I_{(hkl)\alpha}$ with the overall Rietveld scale factor S_α for each phase, Eq. 19.1 reduces to:

$$S_\alpha = \left[\frac{K}{V_\alpha^2}\right]\cdot\left[\frac{W_\alpha}{\rho_\alpha}\right]\cdot\frac{1}{\mu_m^*} \tag{19.2}$$

Since this expression inherently contains the weight fraction information it can be rearranged to derive W_α:

$$W_\alpha = \frac{S_\alpha\rho_\alpha V_\alpha^2\mu_m^*}{K} \tag{19.3}$$

The value K is an 'experiment constant' that can be used to put W_α on an absolute basis. O'Connor and Raven [10] have shown that K is dependant only on the instrumental conditions and is independent of individual phase and overall sample-related parameters. A single measurement therefore is sufficient to determine K for a given instrumental configuration.

For each phase, the density ρ_α can be calculated from:

$$\rho_\alpha = 1.6604\cdot\frac{Z M_\alpha}{V_\alpha} \tag{19.4}$$

where *ZM* is the mass of the unit cell contents (*Z* is the number of formula units in the unit cell and *M* is the molecular mass of the formula unit) and *V* is the unit cell volume.[1]

Substitution and rearrangement of Eq. 19.4 in Eq. 19.3 shows that:

$$W_\alpha = \frac{S_\alpha (ZMV)_\alpha \mu_m^*}{K} \tag{19.5}$$

In this context, $(ZMV)_\alpha$ is the 'calibration constant' for phase α and can be calculated from published or refined crystal structure information alone. Determination of *K* may be carried out by:

(i) Measurement of a standard pure phase or mixture separately from the measurement of the actual unknown mixture in question, or
(ii) Using a phase which is present in the sample in known amount.

The value of *K* calculated in this way will be appropriate for the calibration of subsequent measurements as long as all instrumental conditions remain the same as those used in its determination. This methodology is important in many applications in that it produces, within the limits of experimental error, absolute phase abundances and is referred to hereafter as the external standard approach. While the use of a phase within the sample to determine *K* may be considered as an internal standard approach, in some applications, including *in situ* studies, that phase may be removed from the system through, for example, decomposition or dissolution. However, the value of *K* remains valid for subsequent determination of phase abundances as the reaction proceeds.

Equation 19.5 is directly applicable for the analysis of those phases for which detailed crystal structure information is available. For phases where only a partial structure (for example, an indexed unit cell but no atom coordinates or site occupation factors) is available, an empirical *ZMV* can be derived using mixtures of the phase of interest with known amounts of a well characterised standard [11]. QPA of phases with partial structure is also possible through the use of Eq. 19.3 but an estimate of the phase density, obtained through direct measurement, is required.

The limitations of the approach embodied in Eqs. 19.3 and 19.5 derive from the need to (i) conduct a measurement of *K* and (ii) estimate the value of the mass absorption coefficient $\mu_m{}^*$ for the sample(s) used to determine *K*, as well as each sample of interest. However, the benefits which can be derived, namely the ability to extract the absolute, rather than relative, phase abundances, make it worth pursuing in many analytical situations.

The value of $\mu_m{}^*$ can be calculated from the sum of the products of the theoretical mass absorption coefficient ($\mu_j{}^*$) of each element (or phase) and the weight fractions (W_j) of all *n* elements (or phases) in the sample. Elemental composition may be determined, for example, by X-ray fluorescence (XRF) measurement and use of this

[1]The value $1.6604 = 10^{24}/6.022 \times 10^{23}$ is needed to convert ρ in AMU/Å^3 to g/cm^3.

is more accurate than the use of phase composition as it takes into account any amorphous material not represented by peaks in the diffraction pattern but which still contributes to $\mu_m{}^*$.

$$\mu_m^* = \sum_{j=1}^{n} \mu_j^* W_j \tag{19.6}$$

The need to measure K and measure, or calculate, $\mu_m{}^*$ serves to increase the overall experimental difficulty and can be eliminated in a number of ways. For a simple two phase mixture where both phases, α and β, are fully crystalline, the sum of their weight fractions W_α and W_β equals unity and can be expressed as [12]:

$$W_\alpha = \frac{W_\alpha}{(W_\alpha + W_\beta)} \tag{19.7}$$

Substitution of Eq. 19.5 for phases α and β in Eq. 19.7 results in:

$$W_\alpha = \frac{S_\alpha (ZMV)_\alpha}{S_\alpha (ZMV)_\alpha + S_\beta (ZMV)_\beta} \tag{19.8}$$

Alternatively, in a multi-phase sample, the addition of an internal standard s in known amount W_s and taking the ratio of Eq. 19.5 for analyte and standard phases provides the relationship:

$$W_\alpha = W_s \cdot \frac{S_\alpha (ZMV)_\alpha}{S_s (ZMV)_s} \tag{19.9}$$

The method embodied in Eq. 19.9 also serves to produce absolute phase abundances $W_{\alpha(absolute)}$ and is referred to hereafter as the internal standard approach. One of the benefits accruing from the use of absolute phase abundances is the ability to estimate the presence and amount of any amorphous and/or unidentified phases $W_{(unknown)}$ present through:

$$W_{(unknown)} = 1.0 - \sum_{k=1}^{n} W_{k(absolute)} \tag{19.10}$$

The so-called matrix flushing method of Chung [13, 14] uses the additional constraint that all phases are known and included in the analysis. The consequence of this constraint is that the analysed weight fractions are summed to the assumed concentration of the crystalline components (usually unity). Hill and Howard [15] and Bish and Howard [12] have applied the matrix flushing approach to the Rietveld analysis context and shown that the weight fraction of phase α in an n phase mixture is given by the relationship:

$$W_\alpha = \frac{S_\alpha (ZMV)_\alpha}{\sum_{k=1}^{n} S_k (ZMV)_k} \tag{19.11}$$

The use of Eq. 19.11 in QPA once again eliminates the need to measure the instrument calibration constant and estimate the sample mass absorption coefficient. However, the method normalizes the sum of the analysed weight fractions to unity. This approach, while it is the most widely used in Rietveld based QPA and is almost universally coded into Rietveld analysis programs, only produces the correct relative phase abundances. If the sample contains amorphous phases, and/or minor amounts of unidentified crystalline phases, the analysed weight fractions will be overestimated. Where absolute phase abundances are required in, for example, the derivation of reaction kinetics in *in situ* studies, then one of the methods which produces absolute phase abundances must be used.

19.3 QPA Applications in Minerals Research

19.3.1 Crystallisation from Hydrothermal Solutions

The strengths and weaknesses of some of the methods described in Sect. 19.2.1 are highlighted in the recent work of Webster et al. [16]. This was a study of the mechanism and kinetics of nucleation and crystal growth in the context of the Bayer process for the extraction of aluminium from bauxite ores. Specifically, the experiments utilise synthetic Bayer liquors, consisting of Al-loaded caustic solutions to which a variety of seed material is added. Several polymorphs of $Al(OH)_3$ (gibbsite, bayerite and nordstrandite) crystallise from solution onto the seed material. The rate of crystallisation, and the ratio of the phases, depends on the sample conditions used, including the Al and caustic concentration in solution, as well as sample temperature.

The mechanism and rate of crystallisation were followed by collecting X-ray diffraction data at the powder diffraction beamline of the Australian Synchrotron over a period of about 3 h. The diffractometer incorporates a Mythen detector [17] which allows for the simultaneous collection of 80º 2θ of the diffraction pattern. A wavelength 0.826 Å was used to ensure adequate penetration of the beam in the sample. The sample environment (described in Madsen et al. [18]) consisted of a 1 mm quartz glass capillary heated to temperatures between 60 and 75 ºC using a hot air blower.

The data were analysed using the TOPAS software package [19]. A fundamental parameters approach [20] was used with an empirical instrument width and shape contribution determined using the NIST SRM660 LaB6 profile standard. For the samples in the study, refined parameters included 2θ zero offset, pattern background and, for each phase, the Rietveld scale factor, crystallite size and strain and unit cell dimensions.

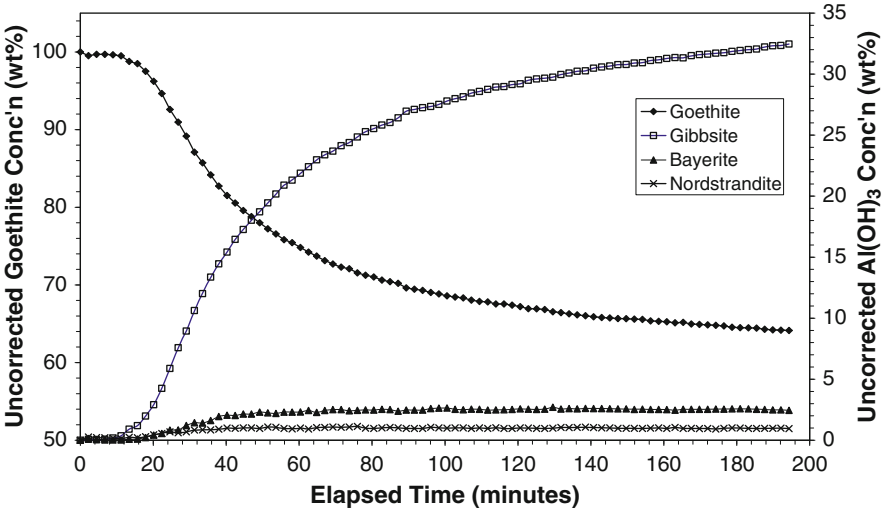

Fig. 19.1 The results of quantitative phase analysis from the seeding experiments of Webster et al. [16]. The values were derived using the Hill/Howard [15] relationship in Eq. 19.11. Note the decrease in apparent goethite concentration (*left axis*) as the polymorphs of $Al(OH)_3$ (*right axis*) crystallise from solution

A number of different approaches were used to extract the phase abundances at each stage of the reaction. Initially, QPA was derived using Eq. 19.11; the value that many Rietveld analysis programs output as their first estimate of phase abundance. Figure 19.1 shows the output from an *in situ* run in which goethite (FeOOH) was added as the seed.

At the start of the run, prior to the crystallisation of any of the $Al(OH)_3$ polymorphs, Fig. 19.1 shows that the reported concentration of the goethite seed is 100 wt.% since it is the only phase represented in the analysis at that time. On formation of gibbsite, bayerite and nordstrandite, the goethite concentration decreases progressively to about 65 wt.% and the total $Al(OH)_3$ concentration reaches about 35 wt.% at the end of the run. However, these figures are in disagreement with (i) the fact that goethite is unlikely to dissolve or otherwise be consumed in this system, (ii) the known addition of goethite to the sample and (iii) the total amount of Al available from solution.

The problem with the QPA in this case arises from the fact that only the crystalline components are considered in the analysis and that Eq. 19.11 normalises the sum of their analysed weight fractions to unity. However, aluminium, which is in solution at the start of the run, forms crystalline phases continuously throughout the reaction after an initial incubation period. In order to overcome the anomalies in the QPA results, it is necessary to consider the sample as a whole; that is, the concentration of both the solid and liquid components in the X-ray beam for the duration of the experiment.

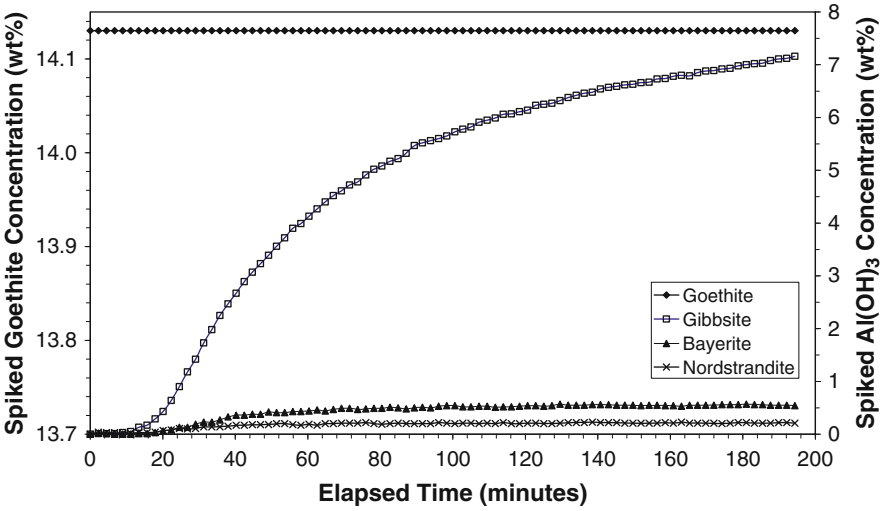

Fig. 19.2 The results of quantitative phase analysis from the seeding experiments of Webster et al. [16]. The values are absolute phase abundances derived using the relationship in Eq. 19.9. The goethite concentration (*left axis*) is now fixed at the known addition at the start of the run (14.13 wt.%)

In this sample, the goethite seed was added at a concentration of 14.13 wt.% in the slurry injected into the sample capillary. If the assumption is made that, in this environment, goethite is unreactive and hence will not change its concentration during the reaction, it can effectively be used as an internal standard to put the $Al(OH)_3$ concentrations on an absolute basis. The QPA results derived using the internal standard or 'spiked' approach in Eq. 19.9 are shown in Fig. 19.2.

The goethite concentration is now fixed at the known addition at the start of the run. The concentrations of the $Al(OH)_3$ polymorphs are put on an absolute scale, thus allowing derivation of relative rates of formation for runs conducted at different temperatures.

If, however, there is residual doubt about the reactivity of the goethite, it may be necessary to use the external standard approach embodied in Eq. 19.5. In this case the value for the instrument constant, K, can be derived using the Rietveld scale factor, ZMV and the known addition of goethite in a rearranged Eq. 19.5. For this determination, the goethite scale factor from the first few data sets was averaged to minimise any errors which may be introduced by counting statistics. The value of the sample mass absorption coefficient $\mu_m{}^*$ has been set to an arbitrary value of unity for both the determination of K and all subsequent analyses since the overall chemical content of the capillary, and hence the attenuation of the X-ray beam, does not change during the reaction.

This experimental work was conducted at the Australian Synchrotron where the ring current is boosted every 12 h. In between these times the current, and hence the incident beam intensity, decays resulting in what amounts to a change

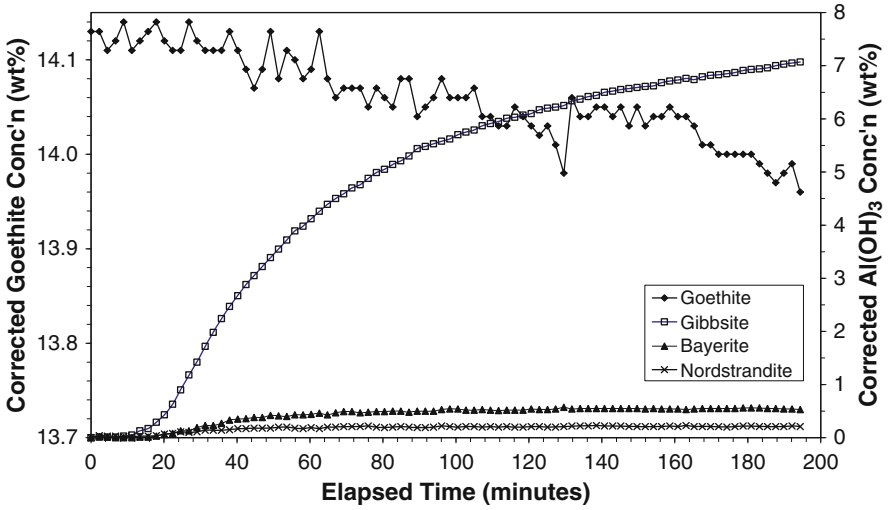

Fig. 19.3 The results of quantitative phase analysis from the seeding experiments of Webster et al. [16]. The values are absolute phase abundances derived using the relationship in Eq. 19.12. Note the slight decrease in the goethite concentration (*left axis*) during the run

in the 'instrument configuration'. This requires a modification of the K value and subsequent calculation of concentration to compensate for the changing incident intensity in a modified Eq. 19.5:

$$W_{\alpha i} = \frac{S_{\alpha i}(ZMV)_{\alpha}\mu_m^*}{K} \cdot \frac{I_0}{I_i} \tag{19.12}$$

where I_0 and I_i are the monitor count (or ring current) at the start of the run and during data set i respectively.

Figure 19.3 now shows the results of QPA derived from Eq. 19.12. In this case the concentrations of the $Al(OH)_3$ polymorphs are similar to those in Fig. 19.2. However, since the phase abundances are derived using an external standard approach, any changes in the goethite concentration can now be monitored. Figure 19.3 shows a small, but systematic, decrease in the goethite concentration as the run progresses. At the end of the run, the goethite concentration appears to be lower by about 1% relative than the concentration at the start.

This apparent decrease has been attributed to the 'shielding' of the goethite from the X-ray beam by the $Al(OH)_3$ phases as they form and coat the goethite particles. This decrease in intensity from the goethite could then be used to obtain an average thickness of the $Al(OH)_3$ phases. This layer was calculated to be about 5.5 μm (assuming a linear absorption coefficient of 9.5 cm^{-1} for gibbsite) resulting in an overall particle size of about 11 μm at the end of the run (the goethite particles are about 0.2×2 μm and hence do not contribute significantly to the overall particle size). This is in good agreement with independent SEM measurements (Fig. 19.4).

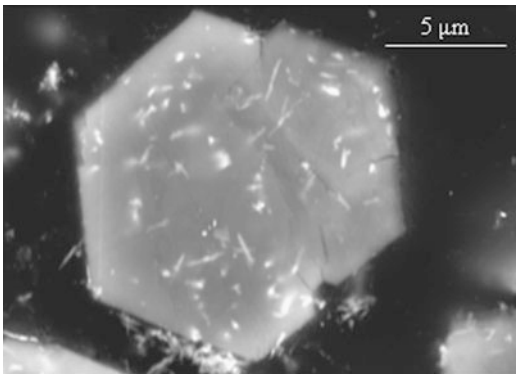

Fig. 19.4 SEM image of a gibbsite particle (*grey*) which has grown on the goethite seed (*white inclusions*). From Webster et al. [16]

Table 19.1 Comparison of errors generated during the analysis of XRD data (Cu Kα) from three sub-samples of Sample 4 from the IUCr CPD round robin on quantitative phase analysis [2]

		Phase	
n = 3	Corundum	Magnetite	Zircon
Weighed	50.46	19.46	29.90
Mean measured wt.%	56.52	17.06	26.42
Mean of Rietveld errors	0.15	0.11	0.11
S.D. of measured wt.%	0.63	0.41	0.35
Mean of bias	6.06	−2.58	−3.48
XRF	50.4(2)	19.6(1)	29.5(1)

The bias values are (measured – weighed) while the values denoted "XRF" are the phase abundances generated from elemental concentrations measured by X-ray fluorescence methods

19.4 Precision, Accuracy and Calculation of Error

The question of precision and accuracy in QPA via XRD is a difficult one. It is simple enough to calculate errors on the basis of replication or precision in the mathematical fit. However, determination of the actual accuracy of the analysis is no trivial task in a standardless method. In fact, it cannot be achieved without recourse to some other measure of the sample which does incorporate standards. Too often, analysts will report Rietveld errors calculated in the course of refinement as the errors in the final quantification. These numbers relate purely to the mathematical fit of the model and have no bearing on the accuracy or otherwise of the quantification itself.

Consider, for example, a three phase mixture of corundum, magnetite and zircon. Such a sample was presented as Sample 4 in the IUCr CPD Round Robin on quantitative phase analysis [2]. Its components were chosen with the deliberate aim of creating a sample in which severe microabsorption occurs. Table 19.1 shows the weighed amounts of each component and the results of replicate analyses of three different sub-samples of this material.

In this context, the Rietveld error represents the uncertainty in the mathematical fit between the observed and calculated patterns and is the value most often quoted as the error in the phase abundance. Contrasting with this is the standard deviation

of the mean abundances which represents the expected precision in the analysis and is 3–4 times greater than the Rietveld derived errors. The good level of fit achieved in conducting these analyses (evidenced in the low R-factors) could lead the analyst to conclude that the mean value ± the standard deviation of the mean is an adequate measure of the phase abundances and their errors.

However, the Rietveld errors and the replication errors are at least an order of magnitude smaller than the bias (measured – weighed). The bias, due to the presence of severe microabsorption, represents the true accuracy which can be achieved in this system if the analyst takes no further steps are taken to identify the cause and minimize the effect of absorption contrast or other aberrations which may affect accuracy.

In the example above, the phases are such that the chemistry is unambiguous and the phase quantification could have been derived by normative calculation from bulk elemental analysis (XRF). This is not often the case, but it is frequently possible to establish the composition of each phase within a system via electron probe microanalysis or similar and conduct the inverse of a normative calculation to derive the bulk chemistry from the XRD QPA. This can then be compared with the results of a standards based technique such as XRF to obtain a measure of the accuracy of the XRD analysis. Where this is not possible or practical, it is better to consider XRD-based QPA as a "semi-quantitative" technique at best.

References

1. Madsen IC et al (2001) Outcomes of the International Union of Crystallography Commission on Powder Diffraction Round Robin on Quantitative Phase Analysis: samples 1a to 1h. J Appl Crystallogr 34(4):409–426
2. Scarlett NVY et al (2002) Outcomes of the International Union of Crystallography Commission on Powder Diffraction Round Robin on Quantitative Phase Analysis: samples 2, 3, 4, synthetic bauxite, natural granodiorite and pharmaceuticals. J Appl Crystallogr 35(4):383–400
3. Rietveld HM (1969) A profile refinement method for nuclear and magnetic structures. J Appl Crystallogr 2:65–71
4. Cullity BD (1978) Elements of X-Ray diffraction, 2nd edn. Addison-Wesley Publishing Company, New York, 555 p. ISBN 0-201-01174-3
5. Klug HP, Alexander LE (1974) X-ray diffraction procedures: for polycrystalline and amorphous materials. Wiley, New York, 966
6. Jenkins R, Snyder RL (1996) Introduction to X-ray powder diffractometry. Wiley-Interscience, New York
7. Chung FH, Smith DK (2000) The practice of diffraction analysis. In: Chung FH, Smith DK (eds) Industrial applications of X-ray diffraction. Marcel Dekker, New York
8. Madsen IC, Scarlett NVY (2008) Quantitative phase analysis. In: Dinnebier RE, Billinge SJL (eds) Powder diffraction: theory and practice. Royal Society of Chemistry, Cambridge, pp 298–331
9. Zevin LS, Kimmel G (1995) Quantitative X-ray diffractometry. Springer, New York
10. O'Connor BH, Raven MD (1988) Application of the Rietveld refinement procedure in assaying powdered mixtures. Powder Diffr 3(1):2–6
11. Scarlett NVY, Madsen IC (2006) Quantification of phases with partial or no known crystal structures. Powder Diffr 21(4):278–284

12. Bish DL, Howard SA (1988) Quantitative phase analysis using the Rietveld method. J Appl Crystallogr 21(2):86–91
13. Chung FH (1974) Quantitative interpretation of X-ray diffraction patterns of mixtures I. Matrix-flushing method for quantitative multicomponent analysis. J Appl Crystallogr 7: 519–525
14. Chung FH (1974) Quantitative interpretation of X-ray diffraction patterns of mixtures II Adiabatic principle of X-ray diffraction analysis of mixtures. J Appl Crystallogr 7:526–531
15. Hill RJ, Howard CJ (1987) Quantitative phase analysis from neutron powder diffraction data using the Rietveld method. J Appl Crystallogr 20:467–474
16. Webster NAS, Madsen IC, Loan Melissa J, Knott Robert B, Naim Fatima Wallwork Kia S, Kimpton Justin A (2010) An investigation of goethite-seeded Al(OH)3 precipitation using in situ X-ray diffraction and Rietveld-based quantitative phase analysis. J Appl Crystallogr 43:466–472
17. Schmitt B et al (2003) Mythen detector system. Nucl Instrum Method Phys Res Sect A 501:267–272
18. Madsen IC, Scarlett NVY, Whittington BI (2005) Pressure acid leaching of nickel laterite ores: an in situ diffraction study of the mechanism and rate of reaction. J Appl Crystallogr 38(6): 927–933
19. TOPAS (2009) Version 4.2: general profile and structure analysis software for powder diffraction data, Bruker AXS, Östl. Rheinbrückenstraße 49, 76187 Karlsruhe, Germany
20. Cheary RW, Coelho AA (1992) A fundamental parameters approach to X-ray line-profile fitting. J Appl Crystallogr 25(2):109–121

Chapter 20
Quantifying Amorphous Phases

Arnt Kern, Ian C. Madsen, and Nicola V.Y. Scarlett

Abstract Traditional quantitative phase analysis using the Rietveld method fails to take into account the occurrence of amorphous material and without careful attention on behalf of the operator its presence remains undetected. In this paper the methodology of several different approaches to the determination of amorphous content and an assessment of their performance is described. All methods discussed produce reasonable results; however the study highlights some of the strengths, deficiencies and applicability of each of the approaches.

20.1 Introduction

X-ray powder diffraction (XRPD) is (i) the most direct, (ii) the only truly phase sensitive, and thus (iii) the most commonly used analytical technique for quantitative analysis of crystalline and amorphous phases in mixtures. The fundamental relationships between diffracted peak intensity in a powder diffraction pattern and the quantity of a phase in a mixture are well established. Both single peak and full pattern methods for quantitative phase analysis (QPA) are mature and extensively covered in literature, e.g. [1–5]. Recently, thorough reviews of the field have been given in [6, 7], with emphasis on current methods, sources of error, as well as accuracy and precision. This chapter builds on Chapter 19 dealing with quantification of amorphous materials as a special case.

A. Kern (✉)
Bruker AXS GmbH, Östliche Rheinbrückenstraße 49, 76187 Karlsruhe, Germany
e-mail: arnt.kern@bruker-axs.de

I.C. Madsen • N.V.Y. Scarlett
CSIRO Process Science and Engineering, Box 312, Clayton South 3169, VIC, Australia
e-mail: ian.madsen@minerals.csiro.au; Nicola.Scarlett@csiro.au

U. Kolb et al. (eds.), *Uniting Electron Crystallography and Powder Diffraction*,
NATO Science for Peace and Security Series B: Physics and Biophysics,
DOI 10.1007/978-94-007-5580-2_20,

More often than not, polycrystalline materials contain amorphous or poorly crystalline phases. In many cases, the presence of amorphous or poorly crystalline phases is undetected or simply ignored. While information about amorphous phase amounts is frequently not sought-after, this is also a result of the preferred (and sometimes indiscriminate) use of the traditional Rietveld method [8, 9], as one of the most convenient methods for QPA available. It is, however, frequently overlooked, that the traditional Rietveld method only delivers relative phase amounts by default; in the presence of amorphous and/or any amount of unidentified crystalline phases, the analyzed crystalline weight fractions may be significantly overestimated. Most phase abundances reported in literature, obtained via Rietveld analysis, are provided in a manner suggesting absolute values. However, where no allowance of amorphous and/or unidentified phases has been made/reported, it is actually reasonable to assume relative phase abundances instead. While knowledge of relative phase amounts may be sufficient for many analyses, e.g. for monitoring of trends, there is a rapidly increasing number of applications in industry and materials science, where it is essential to know absolute phase amounts including amorphous component(s). Important examples include pharmaceuticals, (geo)polymers, cements, among others, where the absolute crystalline and amorphous fractions are critical for their usefulness.

Limitations of QPA have already been discussed in Chapter 19 of "*Quantitative Phase Analysis*" and are principally the same for analysis of amorphous phases. There are some instances which require special consideration, mostly due to differences in the way X-rays are scattered by crystalline and amorphous phases. This is complicated by the fact that there is often no sharp dividing line between crystalline and amorphous materials.

Crystalline materials are frequently characterized as solids with fixed volume, fixed shape, and *long-range order* bringing about structural anisotropy, producing sharp diffraction peaks (e.g. [5]). Amorphous (or non-crystalline) materials are thus solids with fixed volume, fixed shape, characterized by *short-range order*, which, however, may also have loose long-range order (e.g. [5]). This therefore embraces disordered materials possessing only one- or two-dimensional, or lesser, degrees of order [1]. Scattering by an amorphous material produces broad diffraction bands (or halos), which may extend to some ten's of degrees 2θ. Note that terms like "short"- and "long"-range order, as well as "sharp" and "broad" diffraction maxima clearly show the ambiguity of these definitions, and why there cannot be a sharp dividing line between crystalline and amorphous materials.

A more strict definition for amorphous solids has been given by [1]: "*The term, amorphous solid, must be reserved for substances that show no crystalline nature whatsoever by any of the means available for detecting it*". In other words: The ability to detect and characterize ordering is dependent upon the principles of the analytical method and models being used. Conventional X-ray diffraction loses its power for crystalline material structures on the nano-scale, diffraction patterns become broad and features are less defined. Frequently, resulting ambiguities are paraphrased in literature by the term "X-ray amorphous" to highlight the limitations of X-ray diffraction.

Recently it has been shown by several authors, that so-called "total scattering" analysis techniques, based on pair distribution functions (PDF) obtained from Fourier transformed XRPD data, allow the extraction of structural information from amorphous materials, also providing for "finger-printing" (amorphous phase identification) and quantitative analysis (e.g. [10–13]). In this technique, all information of the powder pattern, that is Bragg-peaks as well as background (diffuse scattering) is equally used. This is in contrast to conventional XRPD methods, where the background is treated independently and frequently discarded from the analysis.

The scope of this paper is limited to conventional powder diffraction methods for quantitative analysis of amorphous phases. Total scattering is not discussed here, due to (a) the intrinsic limitation of the Q ($4\pi\sin\theta/\lambda$) range accessible in the vast majority of currently installed laboratory equipment and (b) the current lack of both dedicated and mature software tools.

20.2 Analytical Techniques

Quantification of crystalline and amorphous phase amounts relies on the determination of the intensity contribution of each component phase in a mixture to the diffraction pattern; the mathematical base is detailed in Chapter 19 of "*Quantitative Phase Analysis*". For this reason, the same methodology can be used for quantitative analysis of crystalline and amorphous phase amounts. Analysis of the latter, however, can be made difficult by the fact that the intensity contribution of amorphous phases to the diffraction pattern is not always evident, especially at low concentrations. Accordingly, available evaluation methods can be grouped into two categories:

1. Indirect methods are based on the use of internal or external standards. Only crystalline components are analyzed and subsequently put on an absolute scale. The amorphous fraction is then calculated by difference, that is indirectly. Most importantly, unidentified and amorphous phases cannot be distinguished, only the sum of these phases can be estimated. Indirect methods are suited for amorphous phases without clearly evident intensity contribution to the diffraction pattern.
2. Direct methods provide a direct measure of an amorphous compound by analyzing the amorphous intensity contribution to the diffraction pattern. Individual unidentified and amorphous phases may be distinguished, and some approaches allow the quantification of more than one amorphous phase if data quality is sufficient. Direct methods rely on the ability to observe the intensity contribution of amorphous phases to the diffraction pattern.

In the following a survey of the most commonly used conventional laboratory XRPD techniques is presented, adapted from [14]. Benefits and limitations of the methods are compared and recommendations made accordingly. Successful analysis requires careful considerations in choosing the best suited evaluation method for a given sample.

20.2.1 Single Peak Method

Single peak methods are direct methods based on the measurement of one or more peaks, for each phase of interest, and assume that the intensity of these peaks are representative of the amount of the individual phases. They rely on the availability of a suite of standard samples from which calibration constants may be determined, and on the direct estimation of the amorphous intensity contribution to the diffraction pattern. This can be done using profile fitting or simple numerical methods. The general procedure is:

1. Prepare a series of standards containing the amorphous phase at known concentrations
2. Obtain a measure of the amorphous component's intensity which may be related to its concentration
3. Generate a calibration curve, e.g.

$$W_a = A^* I_a + B \tag{20.1}$$

where W_a is the fraction of the amorphous phases and I_a is the measure of the intensity of the amorphous phase (determined in (20.1)).

The term *measure* has been chosen to highlight the fact that single peak methods do not necessarily require background determination; i.e. I_a is not required to solely represent the amorphous band intensity, it can also represent the sum of the amorphous band intensity plus background. This in an advantage in those cases where the distinction between background and amorphous band intensity is difficult and therefore unreliable. Note: If the background intensity is included, the calibration function will not go through the origin of the plot. At first glance this may be deemed to be an unconventional approach, it nevertheless can allow for very accurate analyses.

Profile fitting has the definite advantage over numerical methods in dealing better with peak overlap in the presence of crystalline phases. Numerical methods are based on some sort of numerical integration of step intensities within one or more selected 2θ ranges and are in widespread use, most notably in X-ray fluorescence analysis. The distinct advantage of numerical methods is the possibility of choosing small measurement ranges (usually optimized to regions with no or negligible peak overlap). These may include complete peaks/bands but may be limited to a single data point.

Benefits:

Single peak methods can be limited to one or a few phases, and there is no need to characterize all phases in the mixture. They generally allow for significantly longer measurement times per data point, compared to whole pattern methods. This will lead to a significant improvement in counting statistics, and thus allow for quantitative analysis at higher levels of precision and improved lower limits of detection. The method has the potential to minimize errors related to microabsorption as this

aberration is included in the calibration function. When profile fitting is used, more than one amorphous phase can be analyzed.

Limitations:

At higher degrees of overlap, the distinction between amorphous band intensities and crystalline phase peaks (tails!) can become difficult and unreliable, particularly if the latter are broad. The methods also require access to relatively pure or well-described materials for preparation of standards, and are thus only applicable to mixtures similar to the calibration suite. Neither sample properties nor the instrument setup must change between the calibration and unknown measurements, and tube ageing must be monitored, otherwise the calibration function is invalidated.

20.2.2 Whole Pattern Methods

Whole pattern methods rely on the comparison of observed wide range diffraction data with (a) calculated patterns (Rietveld methodology) or (b) measured patterns (e.g. [15, 16]). In the Rietveld methodology patterns are calculated using structure factors calculated from (i) crystal structure information, or (ii) measured from actual samples, or (iii) both. Measured pattern approaches use measured diffraction data acquired from pure phase data libraries, which need to accurately represent all phases in the mixture. Although this methodology has distinct advantages specifically if crystal structures are unknown (e.g. for disordered or amorphous materials), it is a niche approach as it does not allow for structure refinement (e.g. lattice parameters in the case of solid solutions) or preferred orientation corrections.

In the following the six most commonly used methods for the characterization of amorphous phase amounts within the Rietveld methodology are described, based on [14].

20.2.2.1 Method 1: Rietveld Method

In the traditional Rietveld Method, the weight fractions W_α of the crystalline phases present in each sample are estimated using the algorithm of Hill and Howard [9]

$$W_\alpha = \frac{S_\alpha (ZMV)_\alpha}{\sum_{j=1}^{n} S_j (ZMV)_j} \tag{20.2}$$

where S, Z, M and V are, respectively, the Rietveld scale factor, the number of formula units per unit cell, the mass of the formula unit and the unit-cell volume, and n is the number of phases in the analysis. It is assumed that all phases in the sample are crystalline and have been included in the model and thus Eq. (20.2) sums the analyzed concentrations to unity. In the presence of amorphous or non-included phases, these values will be overestimated with respect to the true concentrations.

The traditional Rietveld Method can be used as a direct method for quantitative analysis of amorphous phases, however, if a crystal structure can be found which adequately models the positions and relative intensities of the observable bands of an amorphous component in a diffraction pattern. Allowance for extreme peak broadening provides peak widths and shapes which represent those of the amorphous bands in the observed data. Since this approach treats all components as crystalline and includes them in the analysis, the amorphous phase abundance can be obtained using the traditional Rietveld methodology, applying the algorithm of Hill and Howard [9], Eq. (20.2).

Benefits:

The Rietveld Method has the potential to model more than one amorphous phase, and requires no standards or calibration.

Limitations:

Some amorphous material will not have a representative crystal structure, i.e. available crystal structures (with long-range order) may not accurately represent material which only has short-range order (e.g. glasses).

20.2.2.2 Method 2: Internal Standard Method

The Internal Standard Method is an indirect method, where the sample is "spiked" with a known mass of standard material and the QPA normalized accordingly. In this method, the weight fractions of the crystalline phases present in each sample are estimated using the Rietveld methodology (Hill and Howard [9], Eq. (20.2)). The presence of a known weight fraction of an internal standard material in the sample allows these reported concentrations to be corrected proportionately according to:

$$Corr(W_\alpha) = W_\alpha \frac{STD_{known}}{STD_{measured}} \tag{20.3}$$

where $Corr(W_\alpha)$ is the corrected weight percent, STD_{known} the weighed concentration of the standard in the sample and $STD_{measured}$ the analyzed concentration derived from Eq. (20.1).

The amount of amorphous material $W_{amorphous}$ can then be derived from:

$$W_{amorphous} = 1 - \sum_{j=1}^{n} Corr(W_j) \tag{20.4}$$

Obviously, the Internal Standard Method can also be used, if the concentration of one phase in a mixture is known (e.g. via complimentary methods such as elemental analysis or others) and thus can be defined as the internal standard.

Benefits:

The Internal Standard Method is enabled in many Rietveld analysis packages.

Limitations:

The approach is reliant upon obtaining a standard of appropriate absorption contrast to prevent the introduction of errors into the analysis via the creation of a microabsorption problem. Only the sum of all amorphous and unidentified phases can be reported. The standard addition process is laborious (weighing, mixing), and not feasible in industrial, automated sample preparation environments. Furthermore, and most significantly, the sample is contaminated.

20.2.2.3 Method 3: External Standard Method

The External Standard Method [17] is an indirect method and closely follows the approach in the Internal Standard Method in that it attempts to put the determined crystalline components on an absolute scale and derives the amorphous content by difference. An external standard – either a pure material or a mixture in which the chosen standard is present in known quantity – is used to determine a normalization constant (K) which allows the calculated weight percentages to be placed on an absolute scale,

$$W_\alpha = \frac{S_\alpha (ZMV)_\alpha \cdot \mu_m^*}{K} \tag{20.5}$$

where $\mu_m{}^*$ is the mass absorption coefficient of the entire sample.

K is dependent only on the instrumental conditions and is independent of individual phase and overall sample-related parameters. Therefore, a single measurement should be sufficient to determine K for a given instrumental configuration.

Benefits:

The External Standard Method uses an external standard, the sample is not contaminated. As good laboratory practices require regular instrument monitoring (alignment, tube aging) anyway, the choice of an appropriate standard enables to put all QPA results on an absolute basis and thus enables the calculation of the amorphous fraction, without any additional experimental effort.

Limitations:

Only the sum of all amorphous and unidentified phases can be reported. The normalization constant K is dependent on the instrumental conditions and needs redetermination to compensate for tube ageing and any instrument configuration changes.

20.2.2.4 Method 4: PONKCS Method

The PONKCS method is a direct method, its background and application is described in detail in [18, 19]. In this method, phases with partial or no known crystal structure are characterized by measured rather than calculated structure factors. Most importantly, this overcomes the requirement of the traditional Rietveld method that the crystal structures of all phases must be known. Intensity contributions

of crystalline as well as amorphous phases to the diffraction pattern may be characterized via single line or Pawley [20] or Le Bail fitting [21] methods.

The PONKCS Method follows the same general form as that used in the Rietveld Method but now includes all crystalline and amorphous phases characterized by either calculated or empirical structure factors in Eq. (20.2). However, for all phases using empirically derived structure factors (i.e. those with no defined crystal structure), ZMV "calibration constants" must be derived. This can be achieved by using a known mixture of a respective crystalline or amorphous phase α and an internal standard s,

$$(ZMV)_\alpha = \frac{W_\alpha}{W_s}\frac{S_s}{S_\alpha}(ZMV)_s \tag{20.6}$$

A one time calibration per phase with a single standard mixture is usually sufficient. It is highly recommended to create a database with "PONKCS phases"; such a database can be used in full analogy to crystal structure databases.

Benefits:

The PONKCS Method includes amorphous phase(s) in the analysis model. It has the potential to model more than one amorphous phase. It may be used simultaneously with traditional Rietveld methodology for phases in the system with known crystal structures. When ZMVs have been calibrated for all phases, microabsorption will be eliminated, as this aberration is included in the calibration. Thus, where microabsorption potentially leads to significant errors, it should be considered to use the PONKCS methodology also for all crystalline phases of which the crystal structures are known, i.e. replacing their calculated ZMVs by calibrated ZMVs.

Limitations:

This method requires availability of a standard mixture to derive an empirical ZMV.

20.2.2.5 Method 5: Linear Calibration Model (LCM) Method

The Linear Calibration Model (LCM) Method is a direct method and similar to the previous approaches, however, the information pertaining to the crystalline phases is discarded. Similar to the PONKCS Method, the intensity contribution of an amorphous phase to the powder pattern is modeled via single line or Pawley or Le Bail fitting methods, but only the refined scale factor is used in subsequent analysis. This allows the derivation of a simple linear calibration model from a suite of standard mixtures, which relates the refined scale factor, S, to the amorphous phase concentration, W_{amorph},

$$W_{amorph} = A \cdot S - B \tag{20.7}$$

where A and B are the slope and any residual offset of the calibration, respectively.

Benefits:

The LCM Method has the potential to model more than one amorphous phase. It is convenient to use when there is minimal variation of absorption contrast between the phases. For systems where there is significant variation in absorption between phases, then a sample absorption correction must be included. Errors related to microabsorption can be minimized as this aberration is included in the calibration function.

Limitations:

The approach requires preparation of a series of standards for calibration and is only applicable to mixtures similar to the calibration suite. Neither sample properties nor the instrument setup must change between the calibration and unknown measurements, and tube ageing must be monitored, otherwise the calibration function is invalidated.

20.2.2.6 Method 6: Degree of Crystallinity Method

The Degree of Crystallinity (DOC) Method is a direct method, which is relatively straightforward but different from the methods discussed earlier. For a detailed description refer to e.g. [22]. This method is based on the estimation of the total intensity or area contributed to the overall diffraction pattern by each component in the analysis. The degree of crystallinity (in literature also referred to as "crystalline index"), DOC, is then calculated from the total areas under the defined crystalline and amorphous components from

$$DOC = \frac{Crystalline\,Area}{Crystalline\,Area + Amorphous\,Area} \tag{20.8}$$

The weight fraction of the amorphous material, W_{amorph}, can be calculated from

$$W_{amorph} = 1 - DOC \tag{20.9}$$

This approach can only be used, if the crystalline phase has the same chemical composition of the whole sample. Where this requirement is not fulfilled, absolute values can be obtained via calibration based on a suite of standard materials.

Benefits:

The DOC Method is enabled in many software packages and has the potential to model more than one amorphous phase. The method does not require application of calibration constants, if the crystalline phase has the same chemical composition of the whole sample.

Limitations:

Difficulties arise in defining intensity contributions as "crystalline" or "amorphous". If the chemistry of the crystalline phase is different from the whole sample then an additional calibration step is required to obtain absolute phase amounts.

Table 20.1 Important properties of the analytical techniques discussed

Method	Calculation of amorphous content	Requires calibration suite or standard	Can correct for microabsorption errors	Can deal with more than one amorphous phase
Single peak	Direct	Calibration suite	Yes	Yes
Rietveld method	Direct	No	No	Yes
Internal standard	Indirect	Internal standard	No	No
External standard	Indirect	External standard	No	No
PONKCS	Direct	Single mixture	Yes	Yes
LCM	Direct	Calibration suite	Yes	Yes
DOC	Direct	Case dependent	No	Yes

20.3 Summary

All of the methods discussed in this paper are principally capable of determining amorphous phases in mixtures with the same accuracy (and precision) as for crystalline phases, in ideal cases even down to 1% absolute or better. Limitations are the same as for QPA of crystalline phases and are dictated by sample properties and the analytical technique used. Table 20.1 gives an overview about important properties of the latter.

Benefits and limitations of the individual analytical techniques are to be thoroughly considered when choosing the best method for a given mixture; some basic principles can be summarized as follows:

- Intensity contributions of amorphous phases to the diffraction pattern are not always evident, especially at low concentrations. In this case amorphous bands will be difficult to model and indirect methods (Internal or External Standard Method) will usually perform better.
- Where intensity contributions of amorphous phases are evident, any method based on modeling amorphous bands provides improved accuracy. These methods will usually require a sample of pure amorphous material, or a sample where the amorphous content is high, to establish an accurate model.
- For indirect methods, any errors in the structural models for the crystalline phases have the potential to decrease the overall accuracy. This is especially true when structure models for amorphous materials are selected.
- Calibration based methods usually have the potential to achieve the highest accuracy, as many aberrations, most notably microabsorption, are included in the calibration function.
- Any method based on calibration suites or standards have issues with the availability of suitable calibration samples and standards. Where single samples are to be analyzed, it is generally not practical to make a calibration suite.
- Any calibration sample and standard will contain amorphous materials which, if not accounted for, will decrease accuracy. This is also true for materials deemed to be perfectly crystalline, as any material possesses a non-diffracting

surface layer with some degree of disorder due to relaxation of the crystal structure and inclusion of surface reaction products and adsorbed species (water, hydrocarbons, . . .) Such a layer can easily account for a mass fraction of several percent in a finely divided solid.

References

1. Klug HP, Alexander LE (1974) X-ray diffraction procedures: for polycrystalline and amorphous materials. Wiley, New York
2. Jenkins R, Snyder RL (1996) Quantitative analysis. In: Bish DL, Post LE (eds) Modern powder diffraction, vol 20, Reviews in mineralogy. Mineralogical Society of America, Washington, DC
3. Zevin LS, Kimmel G (1995) Quantitative X-ray diffractometry. Springer, New York
4. Whitfield P, Mitchell L (2008) Phase identification and quantitative methods. In: Clearfield A, Reibenspiess J, Bhuvanesh N (eds) Principles and applications of powder diffraction. Blackwell, Oxford
5. Pecharsky VK, Zavalij PY (2009) Fundamentals of powder diffraction and structural characterization of materials. Springer, New York
6. Madsen IC, Scarlett NVY (2008) Quantitative phase analysis. In: Dinnebier RE, Billinge SJL (eds) Powder diffraction: theory and practice. The Royal Society of Chemistry, Cambridge
7. Madsen IC, Scarlett NVY, Riley DP, Raven MD (2011) Quantitative phase analysis using the Rietveld method. In: Mittemeijer EJ, Welzel U (eds) Modern diffraction methods. Wiley-VCH, Weinheim
8. Rietveld HM (1969) A profile refinement method for nuclear and magnetic structures. J Appl Crystallogr 2:65–71
9. Hill RJ, Howard CJ (1987) Quantitative phase analysis from neutron powder diffraction data using the Rietveld method. J Appl Crystallogr 20:467–474
10. Egami T, Billinge SJL (2003) Underneath the Bragg Peaks: structural analysis of complex materials. Pergamon, Oxford/Boston
11. Billinge SJL (2008) Local structure from total scattering and atomic Pair Distribution Function (PDF) analysis. In: Dinnebier RE, Billinge SJ (eds) Powder diffraction: theory and practice. The Royal Society of Chemistry, Cambridge
12. Proffen T, Page KL, McLain SE, Clausen B, Darling TW, TenCate JA, Lee S, Ustundag E (2005) Atomic pair distribution function analysis of materials containing crystalline and amorphous phases. Z Kristallogr 220:1002–1008
13. Billinge SJL, Dykhne T, Juhàs P, Bozin E, Taylor R, Florence AJ, Shankland K (2010) Characterization of amorphous and nanocrystalline molecular materials by total scattering. CrystEngComm 12:1366–1368
14. Madsen IC, Scarlett NVY (2011) A survey of methodologies for the determination of amorphous content via X-ray powder diffraction. Z Kristallogr 226(12):944–955
15. Chipera SJ, Bish DL (2002) FULLPAT: a full-pattern quantitative analysis program for X-ray powder diffraction using measured and calculated patterns. J Appl Crystallogr 35:744–749
16. Cressey G, Schofield PF (1996) Rapid whole-pattern profile-stripping method for the quantification of multiphase samples. Powder Diffr 11:35–39
17. O'Connor BH, Raven MD (1988) Application of the Rietveld refinement procedure in assaying powdered mixtures. Powder Diffr 3:2–6
18. Taylor JC, Rui Z (1992) Simultaneous use of observed and calculated standard profiles in quantitative XRD analysis of minerals by the multiphase Rietveld method: the determination of pseudorutile in mineral sand products. Powder Diffr 7:153–161
19. Scarlett NVY, Madsen IC (2006) Quantification of phases with partial or no known crystal structures. Powder Diffr 21:278–284

20. Pawley GS (1981) Unit-cell refinement from powder diffraction scans. J Appl Crystallogr 14:357–361
21. Le Bail A, Duroy H, Fourquet JL (1988) Ab-initio structure determination of LiSbWO6 by X-Ray powder diffraction. Mat Res Bull 23:447–452
22. Riello P (2004) Quantitative analysis of amorphous fraction in the study of the microstructure of semi-crystalline materials. In: Mittemeijer EJ, Scardi P (eds) Diffraction analysis of the microstructure of materials. Springer, Berlin/New York

Additional Reading

23. The following papers, categorized by subject and in alphabetical order, can be summarized as "Good Powder Diffraction Practice" and should be memorized by everybody working in this field:

Rietveld Structure Refinement and Quantitative Analysis

24. Hill RJ (1992) Rietveld refinement round robin. I. Analysis of standard X-ray and neutron data for PbSO4. J Appl Crystallogr 25:589–610
25. Hill RJ, Cranswick LMD (1994) Rietveld refinement round robin. II. Analysis of monoclinic ZrO2. J Appl Crystallogr 27:802–844
26. Madsen IC, Scarlett NVY, Cranswick LMD, Lwin T (2001) Outcomes of the International Union of Crystallography Commission on Powder Diffraction Round Robin on Quantitative Phase Analysis: samples 1a to 1h. J Appl Crystallogr 34:409–426
27. Scarlett NVY, Madsen IC, Cranswick LMD, Lwin T, Groleau E, Stephenson G, Aylmoree M, Agron-Olshinaa N (2002) Outcomes of the International Union of Crystallography Commission on Powder Diffraction Round Robin on Quantitative Phase Analysis: samples 2, 3, 4, synthetic bauxite, natural granodiorite and pharmaceuticals. J Appl Crystallogr 35: 383–400

Data Acquisition – General

28. Hill RJ, Flack HD (1987) The use of the Durbin-Watson d statistic in Rietveld analysis. J Appl Crystallogr 20:356–361
29. Hill RJ, Madsen IC (1984) The effect of profile step counting time on the determination of crystal structure parameters by X-ray Rietveld analysis. J Appl Crystallogr 17:297–306
30. Hill RJ, Madsen IC (1986) The effect of profile step width on the determination of crystal structure parameters and estimated standard deviations by X-ray Rietveld analysis. J Appl Crystallogr 19:10–18
31. Hill RJ, Madsen IC (1988) Effect of divergence and receiving slit dimensions on peak profile parameters in Rietveld analysis of X-ray diffractometer data. J Appl Crystallogr 21:398–405

Data Acquisition – Variable Counting Time (VCT)

32. Cockcroft JK (2002) Variable count time data collection in powder X-ray diffraction. IUCr CPD Newsletter no. 27, pp 23–24
33. David WIF (1992) Accuracy in powder diffraction: optimization of data collection strategies. Abstract P2.6, NIST special publication no. 846, p 210
34. David WIF (2004) Powder diffraction: least-squares and beyond. J Res Natl Inst Stand Technol 109:107–123
35. Madsen IC, Hill RJ (1992) Variable step-counting times for Rietveld analysis or getting the most out of your experiment time. Adv X-ray Anal 35:39–47
36. Madsen IC, Hill RJ (1994) Collection and analysis of powder diffraction data with near-constant counting statistics. J Appl Crystallogr 27:385–392

Chapter 21
Quantitative Phase Analysis: Method Developments

Luca Lutterotti

Abstract During the years several methods have been developed to identify and quantify the phases in our samples. The newly developed methods respond to precise needs like increasing accuracy, lowering detection limits, automatize and speed-up the process or overcome errors and limitations. Most of the last developments are based on the use of large set of data and full pattern analyses like the Rietveld method. The progresses have been stimulated by the need to analyze new and complex materials with the help of advanced hardware to collect quickly and reliably our data. Refinement of old and new methods will be presented for the quantification of phases as well as some examples. Particular cases will be treated for layered materials and thin films, bulk amorphous, textured samples and clay materials. The last frontier appears to be the combination of the diffraction with other techniques to improve the final analysis.

21.1 Introduction

In the quantitative analysis of our samples we may identify two principal cases that it is worth to consider. The first case is when the sample is a powder or was a bulk reduced to a powder; this is quite a common case. There is also a second important case when the sample is a bulk not reducible to a homogeneous powder or it has a special structure/distribution of phases for which it is necessary to analyze it in the original form. In the first case we can just utilize the usual methods for

L. Lutterotti (✉)
Dipartimento di Ingegneria dei Materiali e Tecnologie Industriali, Università degli Studi di Trento, via Mesiano 77, 38123 Trento, Italy
e-mail: luca.lutterotti@ing.unitn.it

U. Kolb et al. (eds.), *Uniting Electron Crystallography and Powder Diffraction*,
NATO Science for Peace and Security Series B: Physics and Biophysics,
DOI 10.1007/978-94-007-5580-2_21,

quantitative analysis, provided we take every precaution to fulfill the requisites for a good analysis: homogeneous sample, a sufficient number of small grains and randomly oriented.

When the sample is a bulk or a sample is not fulfilling all these requisites, we need to employ special methodologies and measurement techniques to perform the quantitative analysis. In this chapter we will cover this second case showing some of the methods developed to quantify the phases amount and distribution through diffraction and the help of other techniques when necessary.

21.2 Layered Materials and Thin Films

There are several cases in which the material is structured in more layers. Each layer may have different phases and a phase may be present in more than one layer. If the sample is analyzed the traditional way, by assuming an homogeneous volume, this may lead to two problems:

- The phase fraction we obtain does not really represent the composition of the sample and their quantification depends on the beam penetration.
- The absorption factor in the formula for the quantitative analysis is no more a constant value and this also will result in increasing the inaccuracy of the analysis.

In such cases it is necessary to use a model for the layered material to take into account thicknesses of the layers, absorption factors and phases distribution. The absorption factor depends on the phase content and thickness in each layer and this cause a circular dependency in the quantification method. The Rietveld method as a multi parametric fitting technique can solve the problem by including a suitable model. This has been done and demonstrated for the analysis of the oxidation of some super-alloys [1]. Following that work we can compare an analysis made assuming a homogeneous sample and subsequently adopting the correct model. In this example an Inconel 738 has been oxidized at high temperature (for details we remind to the original work) and the phases have been identified and quantified using an X-ray diffraction pattern collected in Bragg-Brentano geometry, copper radiation. Table 21.1 reports the phase quantification by the Rietveld method assuming a homogeneous sample and the layered model.

It is immediately clear how much informative is the correct model. Determining a phase fraction for the substrate using the homogeneous model does not make sense. A first indication that the sample has a layered structure is given by the B factors (a overall B factor for each phase has been used). Looking at the third row of Table 21.1 phases on top of the layers show much higher intensity at low angle respect to high angle and this is corrected in the Rietveld by a higher B factor. Instead for phases down in the sequence the reverse is observed. The correct layered model has been constructed by trial and error, observing the B factor value. This has been compared and validated using EDXS elemental maps in a cross section.

Table 21.1 Rietveld phases quantification for the oxidized Inconel 738 assuming a homogeneous sample and a layered model [1]

Rietveld homogeneous	Cr_2O_3	TiO_2	$CrNbO_4$	Al_2O_3	Alloy matrix	Ni_3Al	
Volume fraction	0.49	0.011	0.353	0.055	0.086	0.005	
B factor	0.297	−1.77	5.72	4.76	−4.75	−3	
Rietveld layered model	Volume fraction						Layer thickness (μm)
Layer #	Cr_2O_3	TiO_2	$CrNbO_4$	Al_2O_3	Alloy matrix	Ni_3Al	
1	–	–	1	–	–	–	0.089
2	0.952	0.048	–	–	–	–	2.2
3	–	–	–	0.973	0.026	0.001	0.36
4	–	0.11	–	–	0.845	0.045	5
5	–	–	–	–	0.95	0.05	∞
B factor	−0.19	0.73	−0.45	1.98	0.51	0.6	

To correctly compute the absorption factor in a layered model we point the reader at the excellent formulation in [2] (see Eq. 23) that include also the case of a general orientation of the sample surface respect to the incident and diffracted beam.

The procedure can be used successfully also for textured thin films provided a sufficient number of pattern/data is collected to characterize quantitatively the texture [3–5]. This is necessary when the texture is strong as it happens often in the thin film production. Otherwise, for the errors connected to the adoption of a simplified texture models and only one pattern, we remind at a subsequent paragraph.

21.3 Clay Materials and Turbostratic Disorder

The quantification of clay materials or in general of phases having stacking faults like turbostratic disorder (e.g. graphitic materials) has been always a big problem as the traditional Rietveld method is not able to fit the pattern with the same accuracy as for other phases. Indeed, also other methods (internal standard, RIR or PONKCS; see the work of Madsen in this book), if they can ameliorate the analysis, they do not provide a satisfactory solution, most of the time. In 2004 Ufer et al. [6, 7] have introduced an elegant way to treat the turbostratic disorder as encountered in many clay materials. This permits a good fitting of the diffraction pattern using a simple to setup model where it is only necessary to identify the faulting axis and fit the anisotropic crystallite size broadening. This has been used to successfully quantify clay materials [8] as you can see in Fig. 21.1 and carbon-carbon composites. This kind of modeling is present in both BGMN and Maud Rietveld software.

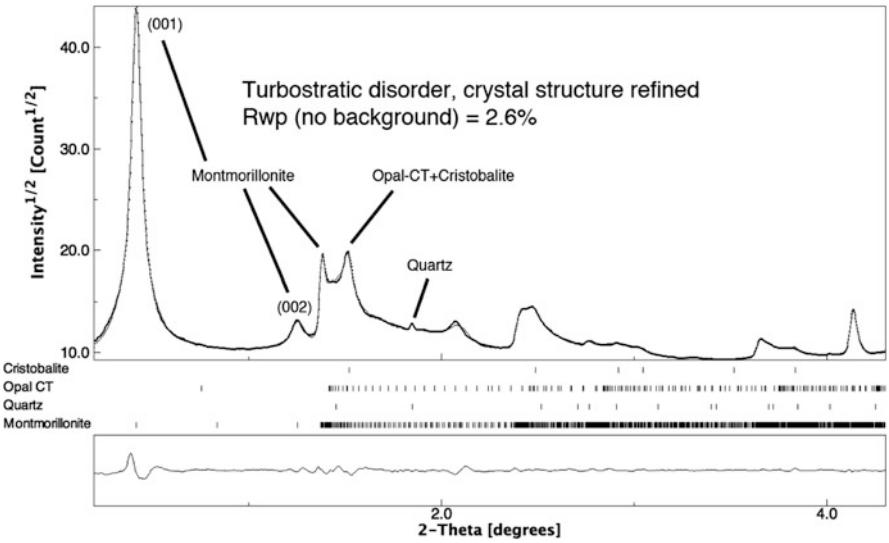

Fig. 21.1 Rietveld phases quantification of clay minerals using the model of Ufer et al. [6] for both the Ca-montmorillonite and the Opal-CT

21.4 Texture and Preferred Orientation

Preferred orientations are one of the main causes of errors in phase quantification by diffraction as enlightened in another part of this book. The best method in such case is to try to avoid them by changing the experiment or re-preparing the sample. Not always this is successful or can be done, as for example in the case of a bulk or a film. When the texture of the sample cannot be eliminated completely by the experimental procedure, we need to choose an analysis strategy to get the phase quantities as much accurate as possible. We have ideally three choices:

- Not apply any correction for preferred orientations
- Apply the texture factors computed from the Orientation Distribution Function (ODF) for this sample
- Fit and apply some corrections based on a simplified texture model.

To examine the effect of each method we have constructed a simple case with a known amount of phases and ODF. We can test the different corrections and their effect on the quantitative phase results. The test is based on a Cu-Fe bulk sample where the two phases were co-laminated for a certain extent. The original content is 1/3 in volume of Fe and 2/3 of Cu. The sample in cube form has been analyzed at the IPNS neutron TOF source in Argonne. A sufficient number of TOF pattern covering different orientation of the sample has been collected in order to obtain the true ODF for both phases. The complete analysis has been done on all patterns using the Rietveld method with the EWIMV texture model [5]. This full analysis

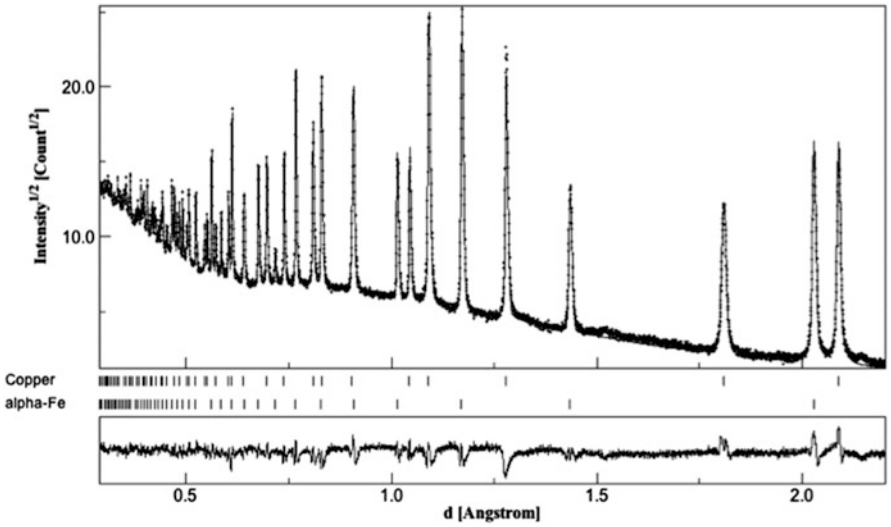

Fig. 21.2 Rietveld fit of all patterns of bank 2. Rwp = 18%

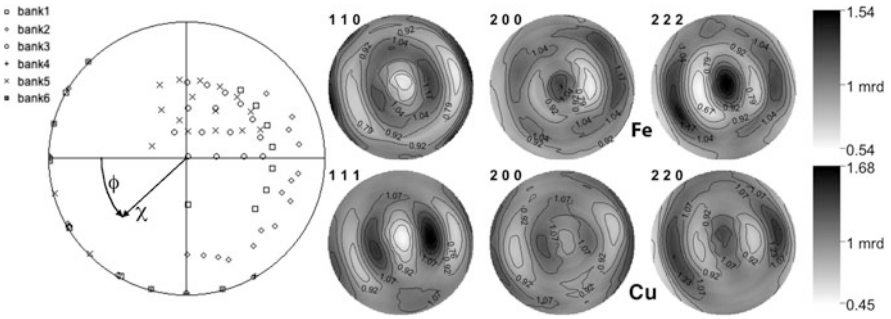

Fig. 21.3 Pole figures (recalculated from ODF, on the *right*) for the Fe-Cu sample as obtained from the full refinement of all patterns by Rietveld + EWIMV; on the *left* the measurement point of each pattern is reported as texture measurement angles (so-called pole figure coverage). *Different symbols* indicate patterns coming from different banks (detectors)

confirmed the 1/3:2/3 volume fraction for the Fe and Cu phases (0.667(2) % vol. Cu and $R_{wp} = 18\%$) and the overall fitting for only one bank is reported in Fig. 21.2. The EWIMV method provides us the ODF from which some pole figures have been calculated and are shown in Fig. 21.3 along with the measurement points in the orientation space. As we can see the texture is the typical one for such laminated phases. It is not a strong texture and nearly orthorhombic.

For our test we will use the Rietveld method for the phase analysis but with only one pattern in the center of the pole figure to be in the same usual conditions of a Bragg-Brentano experiment. In Bragg-Brentano the usual measurement only

Table 21.2 Result of quantitative analysis on Fe-Cu sample by refinement of a single pattern using different preferred orientation correction models

	0.3–2.2 Å range		0.79–2.2 Å range	
Type of P.O. correction	% vol. Cu	R_{wp} (%)	% vol. Cu	R_{wp} (%)
ODF corrected	67.8(14)	14.5	66.5(19)	15.6
No correction	65.5(25)	31.5	63.3(37)	35
March-Dollase	58.3(20)	25	57.3(38)	29
Fiber harmonic, $L_{max} = 4$	67.4(23)	27.5	62.7(41)	30.5
Fiber harmonic, $L_{max} = 6$	70.0(13)	13	66.0(25)	14.5
Fiber harmonic, $L_{max} = 8$	71.4(14)	12.7	70.2(40)	14.4

covers the center of the pole figure and consequently even if we spin the sample this does not decrease the texture and only improves the statistic. Moreover measuring only one point in the pole figures, even if for more reflections, it does not permit to discriminate the kind of texture or measure the complete ODF and in general the normalization cannot be done. All the texture models we can apply in this case are based on a fiber texture with the axe in the center of the pole figure. In Table 21.2 the results for different models are summarized. Also two different ranges in d-space were used to check the effect of the number of reflections. Not always the best fit corresponds to the best result in the quantitative analysis. Obviously correcting for the true ODF should give a good result even if only one pattern is used. But when this is not possible the test shows that using no correction at all gives the worse fit but the results are acceptable. Not always this is true for the other models. The March-Dollase produces a better fit but a wrong quantitative analysis. For the harmonic method this depends on the range and expansion used even if the texture is not strong. This is due to the fact that we suppose a certain fiber texture when it is not. The advice is that when we do not know the texture type, applying no corrections for the texture has more probability of giving a good result even if the fit is worse (Table 21.2).

If the texture is stronger the use of the wrong model (and no simplified models, harmonic included, are correct in this case) will cause a worse result.

21.5 Microabsorption

Microabsorption or absorption contrast affects the quantitative analysis when we have large grains of a highly absorbing phase with other low absorbing phases. In such cases we have few alternatives to avoid or reduce absorption contrast effects:

- Grind the powder to reduce the grain size below a certain level (usually 1 μm).
- Change the wavelength or radiation to a more penetrating one.
- Apply a model to correct the absorption contrast in the analysis (this requires the knowledge of the grain sizes of the phases).

Most of the time only the third option is feasible and the most used correction is the so-called Brindley microabsorption model [9, 10]. Applying it to the formula for quantitative analysis by the Rietveld method [10–12] we get for a mixture of N phases:

$$w_i = \frac{I_i \rho_i}{\tau_i \sum_{j=1}^{N} \frac{I_i \rho_j}{\tau_j}}$$

where I is the scale factor from the Rietveld fitting, w_i is the weight fraction for phase i, ρ_i the density and τ_i the absorption contrast effect. Brindley has reported some tables for the absorption contrast effect from which we can extrapolate a function of a form similar to the absorption characteristic [13]. For spherical particles the Brindley table can be fitted well by [13]:

$$\tau_i = -0.00229 + 2.054e - \frac{(\mu_i - \bar{\mu})\, R_i + 0.50356}{0.69525}$$

where μ_i is the linear absorption coefficient for phase i, μ the mean linear absorption coefficient of the mixture and R_i the mean particles radius. Similar formulas can be obtained also for other shapes correction.

21.6 Amorphous and Polymer Crystallinity Determination

Le Bail in 1995 [14] published how by diffraction it is impossible to distinguish between a real amorphous and a nanocrystalline structure without any long range order. So there is always the possibility to reproduce an amorphous diffraction pattern using a so-called pseudo-amorphous model in which the short range order is simulated by a particular crystal structure and the long range order is loosed by small crystallite sizes and/or high value of r.m.s. microstrain. The advantage of the description is that the short range order can be refined much better in the Rietveld framework instead of relying uniquely on Monte Carlo techniques. In 1998 Lutterotti et al. [15] demonstrated how this pseudo-amorphous model can be used in the Rietveld to accurately measure the amorphous content without any internal or external standard. The classical formula developed for Rietveld phase analysis [11, 15] works perfectly to give the amorphous content as a normal phase if the model is sufficiently accurate in describing the short range order. The benefits of this method are that no calibration, internal or external standard are needed and it can be applied also to bulk samples. Limitations are that it requires a model for the pseudo-amorphous and the background level should be estimated correctly. For the last problem it is advisable to use a monochromator in the diffracted beam to lower the background as much as possible.

The methodology can be used for crystallinity determination in polymers. An example is shown in Fig. 21.4 for polypropylene where the same crystal structure

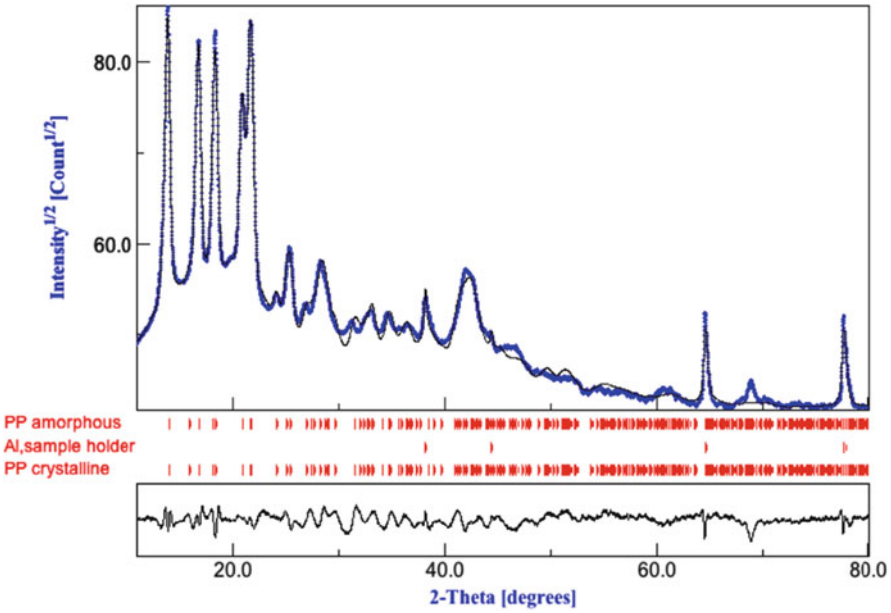

Fig. 21.4 Crystallinity determination on polypropylene by Rietveld fitting

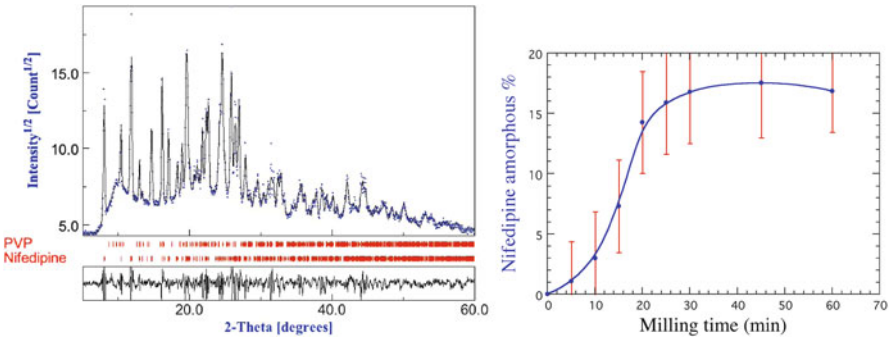

Fig. 21.5 Quantification of the nifedipine amorphization inside the PVP matrix by ball milling. On the *left* the Rietveld fit using the PVP modeled using the cell of the crystalline PVP with the PONCKS method and the pseudo-structure of the nifedipine for the amorphous part; on the *right* the nifedipine amorphous content as determine by the Rietveld fit

is assumed for both the amorphous part and the crystalline part. This assumption is quite reasonable in the polymer case and it gives results in agreement with DSC measurements. The same hypothesis do not work always in the case of ceramics or alloys, the silica glass structure by Le Bail is an example. The method requires that the pseudo-crystal structure is known. Up to now very few of them have been

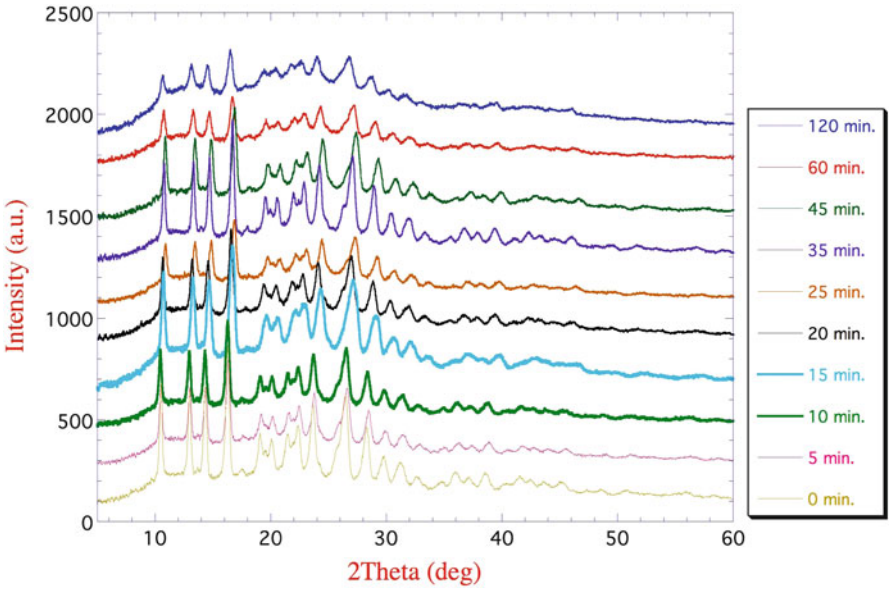

Fig. 21.6 Amorphization of the griseofulvine in the PVP matrix for different milling times. The values of griseofulvine crystallinity are reported in Table 21.3

Table 21.3 Griseofulvine crystallinity after milling at different times

Crystallinity (%)	100	70	60	51	50	40	46	50	35	32	17
Milling time (min)	0	5	10	15	20	25	35	45	60	90	120

found or tested [14, 16, 17] but in the case the pseudo-structure is unknown and a pure sample is available the same procedure as in the PONCKS can be used to calibrate the intensities. This last methodology has been used to determine the phase quantities with the presence of two different amorphous structures [18]. Two examples are reported in Figs. 21.5 and 21.6 and Table 21.3. In both examples an incipient (griseofulvine and nifedipine) in crystalline form is amorphized by ball milling with the help of a polymer (PVP) to stabilize the amorphous form. In such case the procedure has been able to quantify the incipient crystallinity with the presence of a second amorphous, the PVP polymer by the fact that the two amorphous phases have a different pattern.

Those last examples are a further proof of how flexible is the Rietveld method and how a correct quantification can be reached using the appropriate model.

References

1. Lutterotti L, Scardi P, Tomasi A (1993) Application of the Rietveld method to phase analysis of multilayered systems. Mater Sci Forum 133–136:57–62
2. Simek D, Kuzel R, Rafaja D (2006) Reciprocal-space mapping for simultaneous determination of texture and stress in thin films. J Appl Crystallogr 39:487–501
3. Ferrari M, Lutterotti L (1994) Method for the simultaneous determination of anisotropic residual stresses and texture by X-ray diffraction. J Appl Phys 76(11):7246–7255
4. Cont L, Chateigner D, Lutterotti L, Ricote J, Calzada ML, Mendiola J (2002) Combined X-ray texture-structure-microstructure analysis applied to ferroelectric ultrastructures: a case study on Pb0. 76Ca0. 24TiO3. Ferroelectrics 267:323–328
5. Lutterotti L (2010) Total pattern fitting for the combined size-strain-stress-texture determination in thin film diffraction. Nuclear Inst Methods Phys Res B 268:334–340
6. Ufer K, Roth G, Kleeberg R, Stanjek H, Dohrmann R, Bergmann J (2004) Description of X-ray powder pattern of turbostratically disordered layer structures with a Rietveld compatible approach. Zeitschrift für Kristallographie 219:519–527
7. Ufer K, Kleeberg R, Bergmann J, Curtius H, Dohrmann R (2008) Refining real structure parameters of disordered layer structures within the Rietveld method. Zeitschrift für Kristallographie 27(Suppl):151–158
8. Lutterotti L, Voltolini M, Wenk HR, Bandyopadhyay K, Vanorio T (2010) Texture analysis of a turbostratically disordered Ca-montmorillonite. Am Miner 95:98–103
9. Brindley GW (1945) A theory of X-ray absorption in mixed powders. Philos Mag 36:347–369
10. Taylor JC, Matulis CE (1991) Absorption contrast effects in the quantitative XRD analysis of powders by full multiphase profile refinement. J Appl Crystallogr 24:14–17
11. Hill RJ, Howard CJ (1987) Quantitative phase analysis from neutron powder diffraction data using the Rietveld method. J Appl Crystallogr 20:467–474
12. Bish DL, Howard SA (1988) Quantitative phase analysis using the Rietveld method. J Appl Crystallogr 21:86–91
13. Elvati G, Lutterotti L (1998) Avoiding surface and absorption effects in XRD quantitative phase analysis. Mater Sci Forum 278–281:69–74
14. Le Bail A (1995) Modelling the silica glass structure by the Rietveld method. J Non-Cryst Solids 183(1–2):39–42
15. Lutterotti L, Ceccato R, Dal Maschio R, Pagani E (1998) Quantitative analysis of silicate glass in ceramic materials by the Rietveld method. Mater Sci Forum 278–281:87–92
16. Le Bail A (2000) Reverse Monte Carlo and Rietveld modeling of the NaPbM2F9 (M = Fe, V) fluoride glass structures. J Non-Cryst Solids 271:249–259
17. Lutterotti L, Campostrini R, Di Maggio R, Gialanella S (2000) Microstructural characterization of amorphous and nanocrystalline structures through diffraction methods. Mater Sci Forum 343–346:657–664
18. Lutterotti L, Bortolotti M, Magarotto L, Deflorian C, Petricci E (2005) Rietveld structural and microstructural characterization of pharmaceutical products using the program Maud. Presented at PPXRD-4, Barcelona, Spain

Chapter 22
Texture – An Overview

Robert B. Von Dreele

Abstract Samples that are polycrystalline solids produced by some mechanical process frequently possess a non-random orientation of the crystallites due to deformation of the material during the forming operation. The resulting crystallite orientations ("texture") can be more complex that those obtained from simple packing of powders. In the course of crystal structure analysis from powder diffraction data, changes in the Bragg intensities resulting from texture / preferred orientation can strongly degrade the quality of a Rietveld refinement or prevent a structure solution. Here, we consider models for describing texture in polycrystalline samples and examine their application to real world examples.

22.1 Introduction

By definition, an ideal microcrystalline powder consists of a very large number of small crystals that are randomly oriented with respect to each other and to the macroscopic dimensions of the sample. Ignoring macroscopic effects of absorption, the diffraction intensity for any Bragg reflection from this sample is independent of its orientation in the beam because there is an equal probability of crystallites being in the diffracting condition for all sample orientations. In this circumstance, the observed intensities are proportional to the crystal structure diffraction intensities (F_{hkl}^2) after applying simple geometric corrections (e.g. Lorentz-polarization and absorption) and the appropriate reflection multiplicity.

However, the process of producing the sample by packing microcrystals in a holder (flat plate or cylinder) can force the crystal grains into a non-random orientation. For example, if the crystallites have a strong platy habit, then they will

R.B. Von Dreele (✉)
Advanced Photon Source, Argonne National Laboratory, Argonne, IL, USA
e-mail: vondreele@aps.anl.gov

U. Kolb et al. (eds.), *Uniting Electron Crystallography and Powder Diffraction*,
NATO Science for Peace and Security Series B: Physics and Biophysics,
DOI 10.1007/978-94-007-5580-2_22,

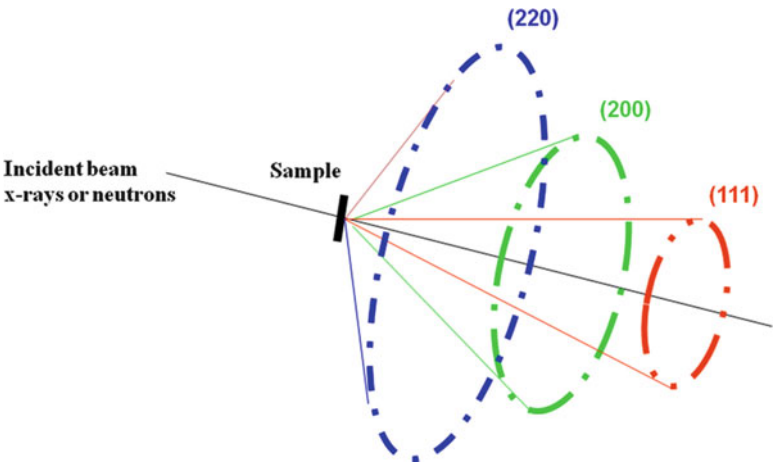

Fig. 22.1 Cartoon view of the effect of texture or preferred orientation on the diffracted intensities from a sample. Note that in general the intensity pattern around each ring will change as the sample is rotated in the beam

preferentially pack so that their plate normal aligns perpendicular to the sample surface. Conversely, crystallites with a needle-like habit will pack so that the needle axis preferentially lies in the sample surface plane. In either case the diffraction intensities are not independent of sample orientation and some intensities will be enhanced while others are suppressed for a particular sample orientation as shown in Fig. 22.1. It is important to note that this "preferred orientation" not only describes how the crystallites align with respect to each other but also with respect to the macroscopic sample dimensions.

Samples that are polycrystalline solid objects (e.g. a metal bar, wire or plate) are usually produced by some mechanical process (e.g. rolling, drawing or pressing) that frequently forces a non-random orientation of the crystallites in response to plastic deformation of the material during the forming operation. The resulting crystallite orientations ("texture") can be more complex that those obtained from packing of powders and due to anisotropy in physical properties (elasticity, conductivity, etc.) the details of the orientation can have an impact on the formed object's material properties.

In the course of crystal structure analysis from powder diffraction data, these changes in the Bragg intensities from preferred orientation can strongly degrade the quality of the result of a Rietveld refinement and can prevent a structure solution for an unknown. This nuisance factor is generally most severe for Bragg-Brentano x-ray diffraction experiments, particularly for highly absorbing materials. It is less a problem for Debye-Scherrer experiments where powders are packed in thin capillaries and frequently use is made of high energy synchrotron radiation. Neutron powder diffraction experiments with large samples and almost no absorption rarely show preferred orientation effects.

Fig. 22.2 Obverse and reverse view of a silver Roman coin; is it a fake?

On the other hand, the crystallite orientation ('texture') within a formed, polycrystalline object can be of considerable technological interest. For example, the texture can be used to infer the history of the piece – "was that piece of metal cast, rolled or drawn to give that shape?" The answer to this question might be of great interest to a museum curator of Roman artifacts looking for fakes (Fig. 22.2). Significantly, the macroscopic properties of materials (strength, stress/strain, thermal expansion, magnetization, superconductivity, thermal conductivity, etc.) are frequently dependent on direction within a crystal structure and therefore dependent on the texture in a polycrystalline object made of these materials. For example, the steel plates that make up a common electrical transformer must be produced with a very strong alignment of the steel crystal grains to have the desired magnetization properties for an efficient transformer. In another example, the formation of cuprate high-T_c superconductors into wires requires that the crystallographic c-axis be perpendicular to the wire axis because the superconductivity is largely confined to the basal plane.

Reducing the impact of preferred orientation on powder diffraction data can be done in a variety of ways. For Bragg-Brentano samples, one can use either "back mounting" or "side mounting" which attempt to prevent the alignment of the crystal grains against the surface exposed to x-rays. The samples can also be prepared by "spray drying" which agglomerates the crystallites into spherical particles which are then loaded in the sample holder; the presumption is that the crystallite grains are more randomly oriented within these particles. Additionally, a sample spinner is often used. Note that this does not eliminate preferred orientation; it simplifies it by making the distribution have cylindrical symmetry. Note that in Debye-Scherrer geometry, the sample generally is spun about the cylinder axis to remove the effect of sample grittiness and thus improve the powder average; it also makes any preferred orientation have cylindrical symmetry.

The measurement of texture requires the determination of how individual reflection intensities change as the sample is placed in a suite of orientations in the x-ray (or neutron) beam. The classical approach as done in the laboratory is to sample a few reflections in a grid of orientations (typically 5° steps on two

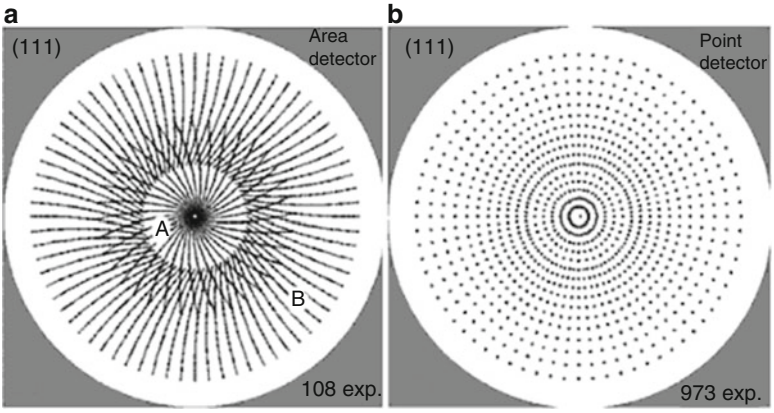

Fig. 22.3 Typical sample orientation grid for pole figure measurement at nominally 5° orientation resolution using (**a**) an area detector and (**b**) a point detector (Taken from "Two-dimensional x-ray diffraction", Bob B. He, 2009, Wiley, New York, p 230)

angles – c.f. Fig. 22.3b). After applying absorption, geometric and normalization corrections, the intensities are then displayed in a polar plot ("pole figure") of the two angles for each reflection sampled in the experiment. This measurement can be time consuming requiring 12–24 h on a laboratory diffractometer equipped with a special pole figure measuring device. Instruments equipped with area detectors can use fewer sample orientations and thus can obtain the required data in less time (c.f. Fig. 22.3a). The observed intensities must arise from cleanly separated peaks; note that the geometry used in this data collection is not optimized for peak resolution.

An alternative approach is to use "whole pattern fitting" of full diffraction patterns from a small subset of sample orientations; a model is used to represent the texture and the coefficients are obtained via Rietveld techniques. This approach can take advantage of high energy synchrotron x-rays with area detectors or spallation neutrons and time-of-flight data collection techniques and be much faster than the classical measurement of pole figures.

22.2 Texture Models

Modern Rietveld refinement programs will frequently allow inclusion of a texture model to describe the change in Bragg intensity for each reflection from that expected for an ideally random powder. The simplest is that of March [1] as simplified by Dollase [2].

$$O_h = \frac{1}{M}\sum_{j=1}^{n}\left(R_o^2\cos^2\phi + \frac{\sin^2\phi}{R_o}\right)^{-\frac{3}{2}} \tag{22.1}$$

This expression is essentially a modifier of the reflection multiplicity, M, for all equivalent h depending on the ratio, R_o, of the major and minor axes of a cylindrically symmetric ellipsoid and on the angle, ϕ, each equivalent reflection, h, makes with some user specified direction, H. The sum is over all the equivalent reflections, n. This description is suitable for either a cylindrical sample spun about its axis as in a Debye-Scherrer experiment or a flat sample spun about its normal in a Bragg-Brentano experiment.

A more complex description derives from a representation of the orientation distribution function (ODF). The ODF gives the probability of finding a particular crystallite orientation with respect to some defined sample coordinate system and is an average over all locations within the sample volume. A further elaboration not considered here is to describe the ODF(xyz) as it varies over the sample volume; this may be of interest in, for example, comparing the bulk texture of a manufactured object with its surface texture. The properties of the ODF are that it must be a real and positive function for which the integral over all orientations is unity. It may also have certain symmetries arising from both the manufacturing process used to make the sample and the crystal symmetry of material. If there is more than one crystalline phase, each will have its own ODF. An ODF has two parts; one is symmetric to inversion ("even" part) and the other is not ("odd" part). Due to Friedel's Law only the even part of the ODF will affect the diffracted intensities and the odd part is thus invisible.

Projections of the ODF are used to represent the texture. If a particular reciprocal crystal direction is chosen as hkl and a projection is made along one sample axis, the result is a "pole figure" and is plotted as a function of two sample orientation angles (ϕ, ψ) as in Fig. 22.3. Conversely, one can choose a particular sample direction (xyz) and then make a projection along some reciprocal crystal direction, and plot the projection as a function of two crystal orientation angles (μ, ν) to obtain an "inverse pole figure". These pole figures also have certain mathematical properties. They must be real and positive everywhere and their integral over all orientations must be unity. Their magnitudes are usually expressed as "multiples of random distribution" (MRD).

As noted above, a diffraction experiment is sensitive to the ODF of a crystalline phase within a solid object in that reflection intensities can differ depending on the fraction of crystallites with a particular orientation. A way of representing this effect on intensities is with the General Axis Equation [3, 4].

$$A(h,y) = 1 + \sum_{l=2}^{L} \frac{4\pi}{2l+1} \sum_{m=-l}^{l} \sum_{n=-l}^{l} C_l^{mn} K_l^m(h) K_l^n(y) \tag{22.2}$$

which is dependent on both a direction in the sample coordinates, y(ϕ, ψ), and a direction in the crystal reciprocal space, h(μ, ν), and is thus 4-dimensional in (ϕ, ψ, μ, ν). The outer summation is over the only even indices, l, to some maximum, L, thus representing the even part of the ODF that can affect the diffracted intensities.

Recall that the odd part has no impact on the diffracted intensities. The two sets of terms, $K_l^m(h)$ and $K_l^n(y)$, are spherical harmonics symmetrized according to the crystal and sample symmetries, respectively. The forms of the spherical harmonics are identical to those used for the angular part of the atomic orbitals, and form an orthogonal set of functions. The C_l^{mn} coefficients are determined by Rietveld refinement and are restricted according to both the crystal and sample symmetries; the orthogonality properties of the functions confer great stability to this refinement. If all C_l^{mn} are zero, then clearly the diffraction is the same in all directions as from an ideally random powder. By selecting either a specific h or y direction and then computing A(h, y) over the remaining orientation angles, one can produce either a pole figure for the selected h or an inverse pole figure for the selected y. The texture index, J, can be obtained from the coefficients via

$$J = 1 + \sum_{l=2}^{L} \frac{1}{2l+1} \sum_{m=-l}^{l} \sum_{n=-l}^{l} |C_l^{mn}|^2 \tag{22.3}$$

If the texture is random then $J = 1$, otherwise $J > 1$. J is very large for strongly textured materials; $J = \infty$ for a single crystal.

22.3 Applications

Here, a few applications of the spherical harmonic model are presented. One is the original test case study [4] of a calcite sample used in an earlier round robin study [5] and the other is a combined texture/microstrain study of a 3-layer hot rolled stainless/carbon steel sandwich (obtained from H. Priesmeyer (1995), private communication). Both were performed using neutron time-of-flight (TOF) diffraction data collected at LANSCE, Los Alamos National Laboratory on the High Intensity Powder Diffractometer (HIPD). In a neutron TOF experiment, the detectors are in fixed locations as is the sample, thus in the general axis equation the sample direction, y, is fixed and each powder pattern is in essence an inverse pole figure scaled by the magnitudes of the crystal structure factors. A complete texture measurement for the calcite was thus obtained from 13 sample orientations in 4 sets of detectors, comprising 52 inverse pole figure measurements. Similarly, 24 sample orientations and 3 detectors were used for the steel sample resulting in 72 inverse pole figures (Fig. 22.4).

The Rietveld refinement on the steel sandwich required two texture descriptions, one for each phase. The stainless steel texture model had 18 C_l^{mn} and the carbon steel model had 12 C_l^{mn} coefficients. These were then used in the general axis equation to generate pole figures (Fig. 22.5).

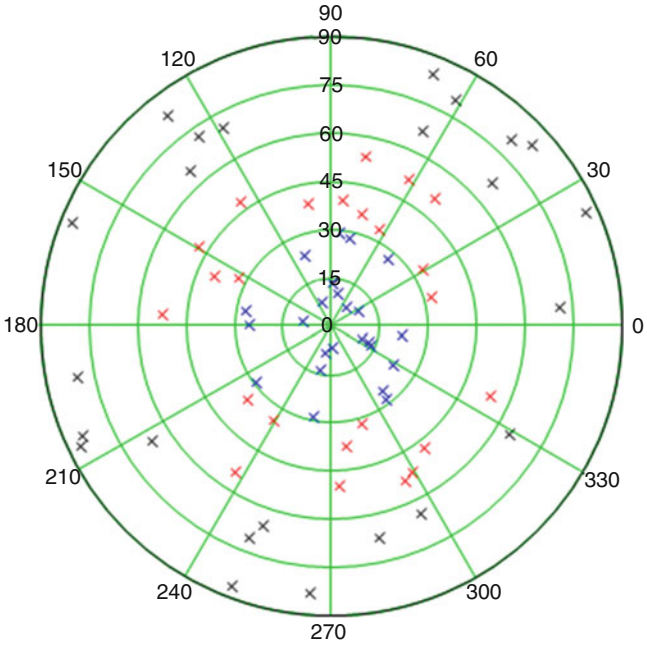

Fig. 22.4 The 72 ϕ, ψ orientations obtained in 24 settings for the steel sample on *HIPD*

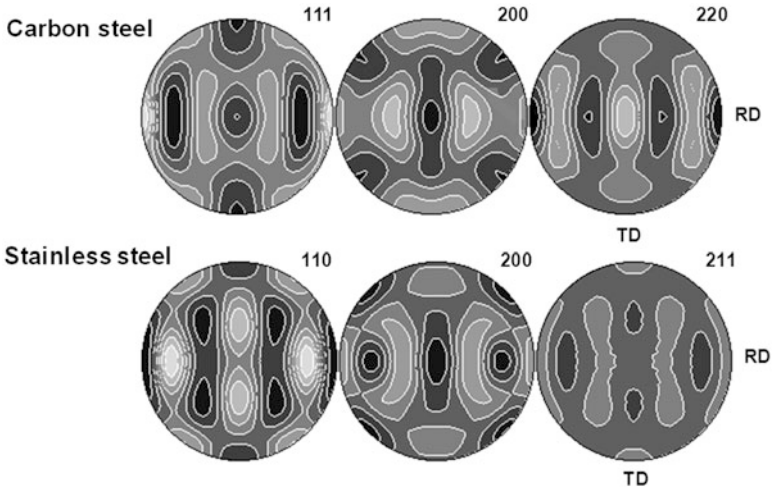

Fig. 22.5 Pole figures for carbon steel (*top*) and stainless steel (*bottom*) obtained from the hot rolled steel sandwich. They are both examples of (100) [110] rolling texture

Acknowledgments This work was supported by the US Department of Energy, Office of Basic Energy Sciences, Office of Science, under contract No. DE-AC-02-06CH11357.

References

1. March A (1932) Mathematische theorie der regelung nach korngestalt bei affiner deformation. Z Kristallogr 81:285–297
2. Dollase WA (1986) Correction of intensities for preferred orientation in powder diffractometry: application of the March model. J Appl Crystallogr 19:267–272
3. Bunge HJ (1993) Texture analysis in materials science. Cuviller Verlag, Gottingen
4. Von Dreele RB (1997) Quantitative texture analysis by Rietveld refinement. J Appl Crystallogr 30:517–525
5. Wenk HR (1991) Standard project for pole figure determination by neutron diffraction. J Appl Crystallogr 24:920–927

Chapter 23
The Future of Powder Diffraction Is 2-D

R.E. Dinnebier and B. Hinrichsen

Abstract The growing attractivenessv of two-dimensional detectors in powder diffraction does brings with it one severe drawback – the 2D to 1D data reduction. This can be a most time consuming and error prone operation, especially when the artifacts of the sample environment affect the intensities. Some developments in the field of calibrating, filtering and evaluation are presented. A selection of applications will be given throughout the oral presentation.

23.1 Introduction

The combination two-dimensional detectors, powder diffraction and synchrotron light sources has been staggeringly successful, opening doors to many new experiments [1–5]. The great advantages of such data collection lie in the short exposure times as well as in the huge redundancy. A large angular region of the Bragg cone is recorded in a single exposure; indeed most detectors are set up perpendicular and centrally to the primary beam, intercepting the Bragg cone over the entire azimuthal range. The standard practice is to integrate the image along the ellipses described by the intersection of the cone with the planar detector to a conventional powder pattern [6]. This commonly reduces the amount of information by the square root of the number of pixels. Does this represent the gamut of information contained in a powder diffraction image? A glance at an image from a calibration standard might lend itself to such a conclusion. Less perfect samples, as well as sample environments leave distinctive artifacts on images. How can they be extracted, filtered or interpreted? Methods offering answers to some of these questions are introduced.

R.E. Dinnebier (✉) • B. Hinrichsen
Max-Planck-Institute for Solid State Research, Heisenbergstrasse 1, D-70569 Stuttgart, Germany
e-mail: r.dinnebier@fkf.mpg.de

U. Kolb et al. (eds.), *Uniting Electron Crystallography and Powder Diffraction*,
NATO Science for Peace and Security Series B: Physics and Biophysics,
DOI 10.1007/978-94-007-5580-2_23,

23.2 Experimental Geometry

The experimental geometry of a plane detector used for powder diffraction has been explained in detail by others [6]. We will therefore merely give a short outline of the most important points.

Each diffraction (Bragg) cone intersecting a plane detector results in an elliptical projection (see Fig. 23.1). This projection is described most palpably using the experimental parameters of the beam centre, the sample to detector distance, the tilt of the detector out of the normal of the primary beam and finally the azimuthal rotation of the tilt with respect to an arbitrarily selected position.

In the course of the calibration of the experimental geometry a high quality image of a standard sample is used to determine and refine the required five parameters.

The standard method for refining the calibration parameters can be separated into two parts. Initially a number of radial lines are drawn from the common focus of the ellipses to the edge of the image. The profile along these lines is plotted, and the peak positions refined using a Gaussian profile. To ensure that an acceptable number of pixels are selected to contribute to the individual histograms the radial lines need to be of an acceptable width, in our case a width of five pixels for these lines returned good results. The peak positions, or rather the positions of the intersection of the radial lines with the ellipses, are now known. Each point can be uniquely associated to a given lattice spacing. The requirement that points belonging

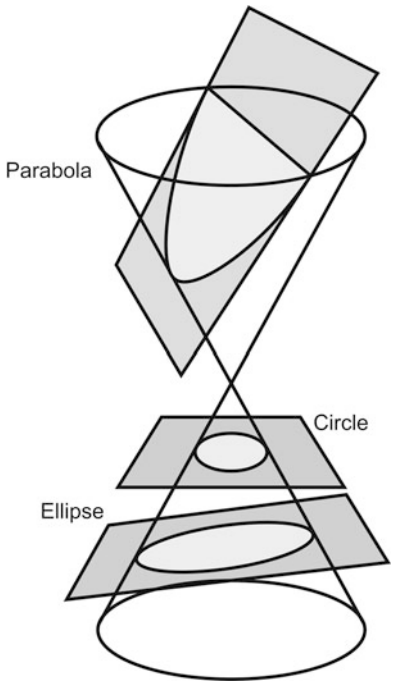

Fig. 23.1 Conic sections. The planes represent the detector plane at various angles to the primary beam. The projections of the Bragg cone trace a *circle*, an *ellipse* or a *parabola* on the detector

to the same lattice spacing should have an identical diffraction angle is sufficient for the refinement of the calibration parameters. A Levenberg-Marquard least squares minimization using the positions weighted by the statistical uncertainty of the initial peak refinement procedure leads to the final calibration values. This method leads to good results if enough radial lines are chosen and the initial six starting values, the five calibration parameters and the wavelength, are sufficiently close to the true values. To ensure this we have developed pattern recognition techniques which very successfully estimate these parameters [7, 8]. These have been described elsewhere. Recently an alternative calibration method has been proposed [9] which appears to have a high degree of automation.

23.3 Whole Image Refinement

The question poses itself, especially in view of the great computing power available to us currently, why image analysis is always synonymous with data reduction? Could not far more information be gleaned from diffraction images than a distilled I(2θ) plot? As a first step along the path of full pattern appreciation this holistic approach was applied to the calibration refinement with surprising results.

Calibration, as described earlier, is commonly a two step process. The initial step is the determination of the intersections of any number of radial lines with the Bragg ellipses. The second is the refinement of the ellipse (calibration) parameters along those points (see Fig. 23.2). The approach chosen here was to refine the sought after parameters against the difference of the observed and computed *images* (Fig. 23.3). The number of data points in such a refinement is of course rather large, a couple of million against what would normally be a couple of hundred. As ellipses furthest from the centre are most susceptible to the calibration quality, the FWHM of the highest angle peak of from the integrated pattern was chosen to give an idea of the calibration results. The material used was the common calibration standard finely ground LaB_6. Whole image refinement showed an improvement over the conventional method of 15%, reducing the FWHM from 0.122° to 0.106°.

23.4 Filtering Techniques

Experimental artefacts are a continual nuisance in the analysis of *in-situ* experiments. These generally result from the experimental environment, can however stem directly from the sample. Data becoming to powder diffraction analysis originates from an ideal sample, having all the positive attributes: random orientation, narrow size dispersion and an improved statistical distribution by sample rotation. In some cases this ideal cannot be achieved, this is especially valid for high-pressure powder diffraction experiments. Sample rotation, if any, is limited to a small angular range because of the diamond diffraction peaks and the deleterious effects of gasket

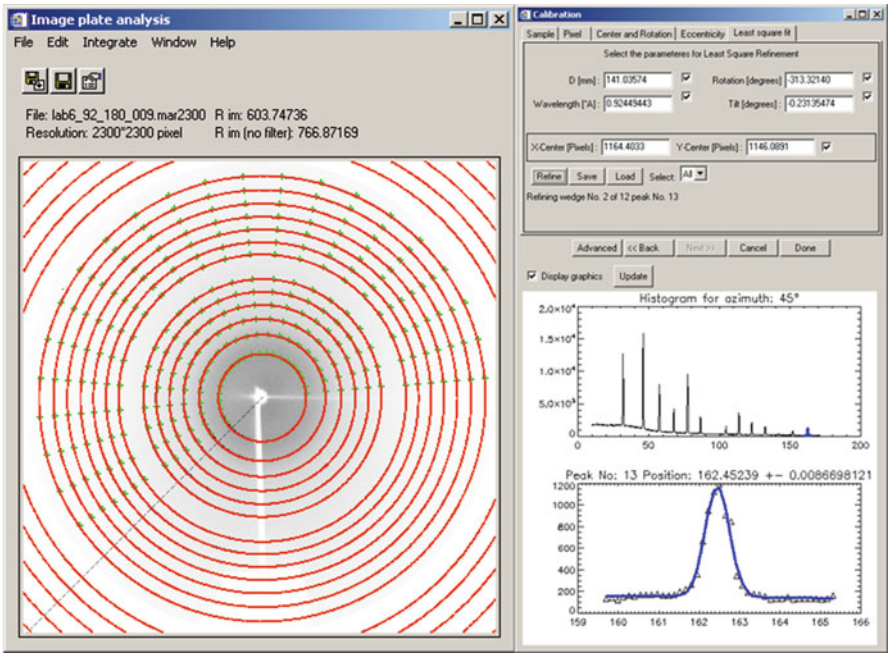

Fig. 23.2 Conventional calibration refinement method. On the *left* the *radial lines* are traced from the centre to the edge. The intensity profile is traced and the various peaks are fitted using a Gaussian profile function. The successfully refined peak positions are utilized to refine the five calibration parameters

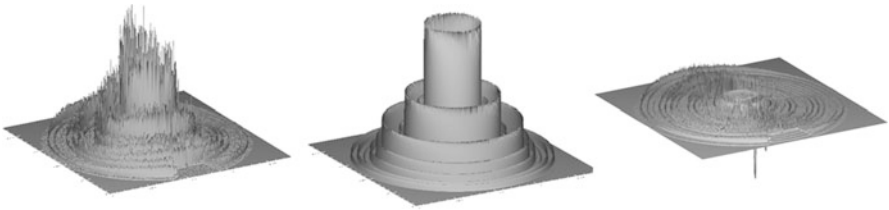

Fig. 23.3 Whole image refinement. The observed intensities (I_{obs}) are shown in the *left image*. In the *central image* the simulated images (I_{calc}) are shown. The difference is shown on the *right*. The calibration parameters are refined to minimize the difference between I_{obs} and I_{calc}

shadowing. An X-ray beam that has a diameter in the order of a few micrometers further worsens the already poor statistics of such an experiment. The general image obtained is filled with single grain spikes looming over the intensity of the Debye-Scherrer ring by at least an order of magnitude. A few peaks on a ring can cause the normal averaging process used during integration to produce data misrepresents the true powder intensities.

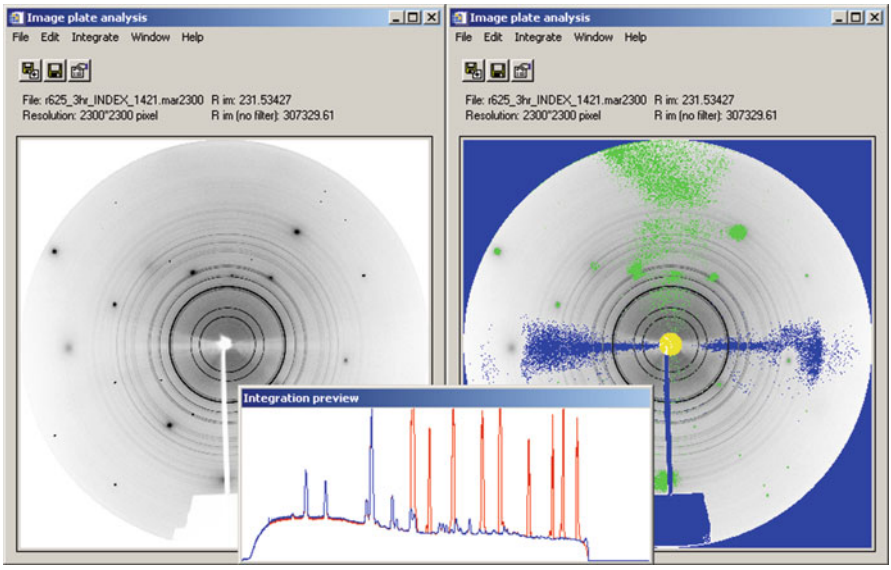

Fig. 23.4 Results of fractile filtering on an image from a high temperature experiment. *Top left*: before filtering, *top right*: after filtering. The spots of high intensity result from the sapphire capillary. *The lower image* is a preview of the finally integrated diffractogram, *red* is the unfiltered pattern, *blue* is the filtered pattern (color figure online)

When estimating the most representative value for the intensity of a single bin generally only the mean of the intensities within the bin was calculated. This of course leads to great aberrations when outlier intensities are within the bin. One way of dealing with such data would be to select the median value as a more robust estimator of the true intensity. This however still leads to variances which do not portray the true data quality. The sigmas of the intensities, which are generally used to weight the least squares refinements are completely meaningless and of no use in the refinement process.

An alternative method is to filter out the aberrant values. As a rule only very few highly deviant values cause the averaging problems. A method which can be looked upon as the inverse of the aforementioned median intensity estimation is that of fractile filtering. Here a highest or lowest intensity fraction of the data is removed. As this method has no real intensity based cut-off criteria it is very robust. An additional advantage is that it does not skew normally distributed data. The effects of this computationally cheap filter can be seen in Fig. 23.4, an example of a high temperature image.

Table 23.1 Image reliability values for some typical examples

LaB_6	R_{im} (filter applied)*100	R_{im} (no filter)*100
Good calibration	0.414	25.9
Bad calibration	10.1	45.9
Experimental data		
Sapphire tube	1.12	4,512
DAC	15.3	7,532

23.5 Reliability Values

The visual appreciation of a two-dimensional diffraction image can sometimes give an idea of the quality of the data gathered. No quantitative measure of the quality of such a data collection has yet been proposed. In lieu of appraising the effectiveness of the presented filtering algorithms an unbiased estimation of the data quality seemed opportune. A measure that has shown itself to be of good use is shown below

$$R_{im} = \frac{\frac{1}{n}\sum_{i=1}^{n}\left(\frac{1}{m-1}\sum_{j=1}^{m}(I_j - \bar{I})^2\right)}{\frac{1}{l}\sum_{k=1}^{l} I_k - I_b}$$

Where l is the total number of pixels in the image, n is the number of bins used to integrate the image and m is the number of pixels within each bin. I_k is the intensity of the kth pixel and I_b the background intensity of that pixel. This is a very simple measure of the average bin variance, normalized to the background corrected total intensity. The value is intensity and consequently detector independent. It is intentionally very sensitive to azimuthal variations in intensity. This leads to an extremely good indicator of not only the uniformity of the Bragg peaks but also of a successful calibration, as can be seen in Table 23.1.

23.6 Concluding Remarks

Some aspects in the analysis of two-dimensional powder diffraction patterns have been presented. The effectiveness of filtering methods dealing with outlier intensities has been shown, as has been a holistic approach to the calibration question. Finally an image reliability factor has been proposed to quantify the quality of a diffraction image. All the functionality has been implemented in a freely available software package, Powder3D [10].

References

1. Hanfland M, Schwarz U, Syassen K, Takemura K (1999) Crystal structure of the high-pressure phase silicon VI. Phys Rev Lett 82:1197
2. Knapp M, Baehtz C, Ehrenberg H, Fuess H (2004) The synchrotron powder diffractometer at beamline B2 at HASYLAB/DESY: status and capabilities. J Synchrotron Radiat 11:328–334
3. Norby P (1997) Synchrotron powder diffraction using imaging plates: crystal structure determination and Rietveld refinement. J Appl Crystallogr 30:21–30
4. Meneghini C, Artioli G, Balerna A, Gualtieri AF, Norby P, Mobiliob S (2001) Multipurpose imaging-plate camera for *in situ* powder XRD at the GILDA beamline. J Synchrotron Radiat 8:1162–1166
5. Wenk HR, Grigull S (2003) Synchrotron texture analysis with area detectors. J Appl Crystallogr 36:1040–1049
6. Hammersley AP, Svensson SO, Hanfland M, Fitch AN, Häusermann D (1996) Two-dimensional detector systems: from real detector to idealised image of two-theta scan. High Press Res 14:235–248
7. Hinrichsen B, Dinnebier RE, Rajiv P, Hanfland M, Grzechnik A, Jansen M (2006) Advances in data reduction of high pressure X-ray powder diffraction data from two dimensional detectors: a case study of Schafarzikite ($FeSb_2O_4$). J Phys Cond Matter 18:S1021–1037
8. Rajiv P, Hinrichsen B, Dinnebier RE, Joswig M, Jansen M (2007) Automatic calibration of powder diffraction experiments using two-dimensional detectors. Powder Diffr 22(1):3–19
9. Cervellino A, Giannini C, Guagliardi A, Ladisab M (2006) Folding a two-dimensional powder diffraction image into a one dimensional scan: a new procedure. J Appl Crystallogr 39:745–748
10. Hinrichsen B, Dinnebier RE, Jansen M (2006) Powder 3D: An easy to use program for data reduction and graphical presentation of large numbers of powder diffraction patterns. Z Kristallogr 23:231–236

Part II
Electron Crystallography

Chapter 24
Electron Crystallography – New Methods to Explore Structure and Properties of the Nano World

Ute Kolb

Abstract Electron crystallography, as the branch of science that uses electron scattering, developed in the last century into a manifold and powerful approach to study the structure of matter. Major historical milestones of this development are discussed. Especially electron diffraction experienced recently a renaissance and grew into an established method of structure analysis. The techniques of data collection and processing available nowadays are described.

24.1 Introduction

Structural elucidation of materials is a key step in the characterization of their physical properties, and therefore of particular interest to both academics and industry. The spectroscopic methods investigate the molecular structure whereas diffraction experiments are used to study the crystal structure. Quantitative crystallography dates back to 1780, when Carangeot invented the contact goniometer in order to measure the angles between the faces of a crystal [1]. Already in 1850 Bravais introduced the concept of polar axes describing a unit cell but only when Wilhelm Conrad Röntgen (University of Würzburg and Munich, first Nobel Prize in physics 1901) discovered X-rays in 1895 Bravais's concept could be featured by scaling these polar axes, called reciprocal axes [1]. First diffraction experiments on zinc-blende by Max von Laue (University of Munich, Nobel Prize in physics 1914) and co-workers Friedrich and Knipping [2] together with the interpretation of the data by William Lawrence Bragg in 1912 (University of Cambridge, Nobel Prize in physics 1915 together with W.H. Bragg) started the era of crystal structure

U. Kolb (✉)
Institute of Physical Chemistry, Johannes-Gutenberg University Mainz, Welderweg 11, 55099 Mainz, Germany
e-mail: kolb@uni-mainz.de

U. Kolb et al. (eds.), *Uniting Electron Crystallography and Powder Diffraction*,
NATO Science for Peace and Security Series B: Physics and Biophysics,
DOI 10.1007/978-94-007-5580-2_24,

analysis [3–6]. In the next decades crystallography and especially single crystal structure analysis developed rapidly. Rapid advances in technology (x-ray sources, goniometers, detectors and automation) reduced the accessible crystal size, to about 1 mm^3 for standard laboratory sources down to a few μm^3 using synchrotron radiation [7], but beyond this X-ray data collection needs to be extended to measure crystal ensembles, i.e. crystal powder.

24.2 Powder Diffraction

The first X-ray powder diffraction data (XRPD) was collected by Peter Debye and Paul Scherrer [8, 9] and in parallel by Albert Hull in 1914 [10–12] but the limitations of the one dimensional data in comparison to the three dimensional single crystal measurements hampered the development of XRPD analysis. An important step was performed by Bertram Warren with the analysis of carbon black in 1934 [13]. Using the Fourier Inversion Method to calculate the pair distribution function (PDF) he discovered that carbon black is not amorphous but consists of single or multiple graphite layers. Structure solution using XRPD developed rapidly in the following years being accelerated by the development of a method by Ernest O. Rietveld in the field of neutron diffraction in 1945 [14]. The Rietveld method allows the usage of the full diffraction profile for structure refinement. XRPD, for which well consolidated structure analysis routines exist, utilizes the diffraction of X-rays on samples consisting of many small crystallites. Exactly this circumstance provides one of the strongest advantages of XRPD namely that the data is collected from the bulk sample and not from a selected crystal which may not be representative for the material. On the other hand the simultaneous measurement of many crystallites leads to the reduction of three dimensional diffraction data to one dimensional data. The resulting reflection overlap, apart from the mere multiplicity, happens systematically in the case of high symmetry space groups (e.g. cubic case (511)/(333)) or accidentally dependent on cell dimensions and space group. This prevents the direct analysis of many peaks and enforces an estimation of the underlying intensities. Additionally, peak profile shapes may be strongly biased by broadening due to small crystallite size in the nano regime and asymmetry due to strain effects, which both may appear even in an anisotropic manner. The uncertainties in intensity determination hamper structure solution significantly. Even cell parameter determination and thus indexing of the diffraction pattern can be problematic or impossible. This problem can be exacerbated further for samples consisting of multiple phases or containing impurities. XRPD typically uses crystals of 1–10 μm but can utilize smaller crystals as well. The borderline caused by crystal-size driven peak broadening (Scherrer equation [15]) is about 100 nm for inorganic structures and approx. 300 nm for organics.

24.3 Electron Microscopy

1924 Louis de Broglie postulated that to every particle with matter and speed a wavelength can be assigned. Inspired by this, the first diffraction experiments using electrons were performed by Clinton Joseph Davisson and Lester Germer in the low-energy range [16, 17] and by George Paget Thomson and A. Reid in the high-energy range [18] both in 1927. Thomson (University of Cambridge) shared with Davisson (Bell-Laboratories, New York City) the Nobel Prize in 1937. 1931 Ernst August Friedrich Ruska (University of Berlin, Nobel Prize 1986) and Max Knoll build the first electron microscope prototype based on electron lenses and Ruska succeeded to beat the resolution of an optical microscope in 1933 [19–21]. The advantage of using electron radiation is that structural information can be collected from areas of a few tens of nanometers [22]. This is possible because the charged electron undergoes coulombic interaction and has therefore a stronger interaction with matter. In addition, electron microscopy is the only method where imaging and diffraction can be performed on the same sample volume.

A few crystal structures containing light elements were solved by single crystal electron diffraction data [23–25] but due to problems related to dynamical scattering in electron diffraction, as described by the theory of multibeam dynamical scattering developed by Cowley and Moodie 1957 [26–28] the main attention focused on high-resolution transmission electron microscopy (HRTEM) and only a few scientists continued to use quantitative electron diffraction data for structure analysis [29].

HRTEM proved to be successful in solving heavy atom positions in inorganic structures, and also some of the more radiation resistant organic molecules after the necessary point-to-point resolution of less than 4 Å has been surpassed in the late 1960s. Later imaging by scanning transmission electron microscopy (STEM) gained increasing importance [30], especially after highly sensitive high angular annular dark field detectors (HAADF) were developed. Substantial efforts were dedicated to the construction of field emission guns (FEG), delivering a highly coherent and bright electron source. Additionally, elemental analysis methods such as energy dispersive X-ray spectroscopy (EDX) or electron energy loss spectroscopy (EELS) were implemented. In parallel, various preparation methods have been invented in order to optimize the production of electron transparent samples.

With increasing interest in synthesis and characterization of nano particles high resolution transmission electron microscopy (HRTEM) gained more and more importance. Unfortunately, based on lens aberrations of axially symmetric electromagnetic lenses the resolution is limited to about 100 times the used wavelength (Scherzer theorem [31]) and is coupled to the spherical aberration of the microscope. The only chance to achieve higher resolution was to use higher acceleration voltages thus increasing beam damage. High resolution imaging in general requires a relatively strong illumination and thus a large electron dose on the sample. Under these conditions, nearly all organic and most of inorganic materials suffer a fast deterioration due to beam damage. This leads to a modification of the crystalline structure or to complete amorphization or sublimation of the sample

[32, 33]. Therefore one of the biggest improvements of TEMs, developed recently, is the design of non-axial symmetric lenses that can correct these lens aberrations [34] thus allowing the usage of low-voltage for imaging purposes. Nowadays, aberration correctors for STEM and HRTEM are available in order to achieve sub-ngstrom resolved images [35].

24.4 Electron Diffraction

Electron diffraction, which provides 3D sub-Ångstrom structural information with good signal-to-noise ratio in reciprocal space, is usually performed using a parallel illumination (Bragg diffraction) of the specimen and selecting the area of interest by insertion of a selected area aperture in the image plane of the objective lens. Illumination of the sample with a higher beam convergence leads to diffraction discs rather than focused spot patterns. Electron diffraction in high-convergence mode (convergent-beam electron diffraction – CBED also referred to as nano-beam diffraction (NBD) or micro-diffraction) traditionally uses the disc patterns to extract cell parameters and space group information including the existence of inversion symmetry [36–38]. CBED recently showed its potential for "ab-initio" structure solution of materials based on extracted intensities [39]. This technique almost has no applications to beam sensitive materials since high convergence of the beam introduces high electron dose at the sample which many materials cannot tolerate. Furthermore, long crystallographic axes cause overlap of the diffraction disks and limit the useful information in CBED patterns.

In order to utilize electron diffraction for structure solution dynamical scattering had to be reduced or taken into account. In the attempt to avoid these effects a group in Moscow used texture patterns and solved several inorganic and organic structures successfully [40–43]. Textured samples are large aggregates of regularly oriented small crystals. These are achieved by different techniques, for instance by use of orienting supports, mechanical action or application of an electrical field. Other scientists focused on organic or biological samples since for these materials dynamical effects are small and in a first approximation kinematic [44–46]. A third approach is the preparation of thin samples and the combination of information from HRTEM imaging with electron diffraction patterns [47–49]. In 1994, the precession electron diffraction (PED) technique was developed by Vincent and Midgley as another approach to reduce dynamical effects in electron diffraction patterns [50–53]. This method is based on the precession of the incident primary electron beam, which is inclined away from the optical axis of the TEM. A diffraction pattern recorded in this mode is the sum of patterns produced by the precessing beam sequentially. The intensities of the reflections are integrated throughout the reciprocal volume covered by the precessing Ewald sphere and show reduced dynamic diffraction effects. Having the ability to acquire more kinematic diffraction data *via* the PED data sets in two and three dimensional has significantly dramatically increased the number of publications in recent years [52, 54–57]

Other attempts for structure solution, were performed in combination with imaging, or focused on weak scattering objects such as organic [58, 59] or biological samples [60–62] which were expected to deliver nearly kinematical diffraction data. Early work pioneered by Klug and co-workers, focused on imaging of biological macromolecules provided the groundwork for structure solution with electron crystallography. First were the structure solution attempts by Unwin and Henderson [63] to solve membrane protein structures using both imaging and diffraction, a combination of these two pieces of work inspired Sven Hovmöller and co-workers [64] to attempt the same approach with inorganic structures, which was a significant challenge because of the increased dynamical content of the data for such structures and the assumption of kinematic data in the theoretical framework. A further approach to reduce dynamical effects was the use of very thin crystals (e.g. less than 50 Å) so that intensities can be assumed proportional to F^2 and will be sufficient for structure solution [49, 65, 66] was established.

The ability to obtain more kinematic like data from electron diffraction wither it be from PED or thinner crystals has lead to the adoption of direct methods techniques from X-ray crystallography. Making the assumption that the data is kinematic and just using the ideas of direct methods was first introduced by Fan [67] with the use of the Sayre equation to extend the resolution of the phases obtained from images from 2 to 1 Å for a structure of copper perchlorophthalocyanine; which was then followed by the use of Symbolic addition and Maximum entropy [68] in order to solve structures. Later came the use of direct methods as commonly used with X-ray data, with the increasing completeness of data sets as various methods developed [69].

There have also been developments in the opposite direction, rather than minimize the dynamical content of the data but to use the dynamical content of the data in order to resolve the structure. Jean-Paul Morniroli, John Steeds and co-workers have contributed significantly to the development of CBED as a method for determining the symmetry of a crystal system from the dynamical content of the diffraction pattern discs. This work has also been extended to the development of LACBED, to LARDIF which uses the aberration correctors on modern microscopes to obtain LACBED pattern but in image mode, there are two main advantages here, the spot patterns have a larger coverage of reciprocal space when compared to the SAED patterns and the diffracted spots are fully integrated [70]. Another interesting development has be the Large Angle Rocking curve beam diffraction (LARBED) by Christoph Koch [71]. This method combines the ideas of CBED and precession where diffraction patterns are collected by an off axis beam and the beam is precessed in order to obtain more information. There is also the ability to slightly focus the diffraction patterns to avoid disc overlap even when very large angles are used. This work is part of a technique development, which hopes to provide a solution to the phase problem for dynamical data.

In order to obtain a better understanding of dynamical diffraction patterns it has been essential that the theory of dynamical calculations and simulations is

continually evolving to help experimentalists understand what they are looking at. Primarily there are two approaches, one, the multislice method developed by Cowley and Moodie [26–28], and two the Bloch wave approach developed by Howie and Wheelan [72, 73]. Both approaches have their advantages and disadvantages. In general Multislice is preferred for HRTEM and bloc waves calculations for STEM and CBED, however much of this relies on how well characterized your system is. For a long time there has been difficulties in matching theory and experiment in electron microscopy, especially in imaging, a problem often referred to as the Stobbs factor [74] after Michael Stobbs. This is a constant effort to make the data acquired from electron microscopy more quantitative by eliminating the Stobbs factor and making theory and experiment match, which would allow for more quantitative interpretation of the data. For STEM some significant advances in the last few years most notably originated from the groups of Les Allen and Susanna Stemmer [75].

It should be noted that electron crystallography has played a significant role in the fundamental understanding of crystallography in general. The discover of Quasicrystals by Dan Shechtman et al. [76] fight to establish his finding as valid which have recently become well known after the announcement of his subsequent Nobel prize in 2011. This discovery redefined what a crystal is, from an object with a repeating unit, which is restricted in three dimensions to an object which produces Bragg diffraction, which now includes Quasi-crystals commensurate and incommensurately modulated structures [77].

Looking beyond pure crystal structure determination, electron microscopy has much to contribute to the field of crystallography, with Electron Energy Loss Spectroscopy (EELS) which can identify the coordination state of atoms in the structure to the more recent development of detecting magnetic circular dichroism [78]. It is also possible to measure the magnetic and electric fields produced by crystals *via* electron holography and Lorentz microscopy [79]. This additional knowledge is critical to the overall understanding of how these crystals interact with there surrounding and affect there overall system they are placed in, wither it be a computer disc hard drive or a biological crystal an animal. Another recent development has been the addition of Dark field holography, which allows the measurement of stress and strain within a crystal system [80]. This works by passing the beam through two different crystals and then looking at the hologram produced between the reference unstrained crystals and the system of interest. This method has been shown to produce stress strain maps with incredible detail on electronic components, which allows a deeper understanding of how the manufacturing process effects the production and operation of electronic devices [81].

Other than the direct crystal properties electron crystallography can help with the understanding crystal growth and polymorphism [82] of nano crystals in particular. The individual crystals can be studied in the microscope overcoming some of the limitations of X-ray powder diffraction which would only be able to acquire data from multiple phases simultaneously in the bulk sample.

24.5 Conclusion

Based on new technical developments electron diffraction is an upcoming method for structural investigation of matter on the nano scale. The possibility to computer control data acquisition as well as the vast improvement of computer performance for data processing supports has significantly advanced the ability to develop new methods for electron crystallography. These methods have produced improved data quantity and quality for "ab-initio" structure solution and increase the number of crystal system which it is possible to obtain data from in order to solve crystal structures. Moreover, recent developments like aberration correction, is opening up the possibilities of imaging beam sensitive materials at low beam energies. As well as the many techniques which are under development to help solve crystal structures, the significant advances in complementary techniques which help describe the crystal system more completely, from fundamental crystal properties of magnetic and electric fields, to the ability to measure stress and strain of a crystal. The topics covered in this school provide an overview of available and emerging methods in electron crystallography in order to broaden awareness of what is now possible with modern electron crystallography.

References

1. Ewald PP (1962) Fifty years of X-ray diffraction. International Union of Crystallographers, Utrecht, The Netherlands
2. von Laue M (1913) Eine quantitative Prüfung der Theorie für die Interferenzerscheinungen bei Röntgenstrahlen. Ann Phys 41:989–1002
3. Bragg WH (1912) The specular reflection of X-rays. Nature 90:410
4. Bragg WL (1913) The diffraction of short electromagnetic waves by a crystal. Proc Camb Philos Soc 17:43–57
5. Bragg WH (1913) The reflections of X-rays by crystals (II). Proc R Soc Lond A89:246–248
6. Bragg WL (1913) The structure of some crystals as indicated by their diffraction of X-rays. Proc R Soc Lond A89:248–277
7. Holton JM, Frankel KA (2010) The minimum crystal size needed for a complete diffraction data set. Acta Crystallogr D66:393–408
8. Debye P (1915) Zerstreuung von Röntgenstrahlen. Ann Phys 46:809–823
9. Debye P, Scherrer P (1916) Interferenzen an regellos orientierten Teilchen im Röntgenlicht. Physik Z 17:277–283
10. Hull AW (1917) A new method of X-ray crystal analysis. Phys Rev 10:661–696
11. Hull AW (1919) A new method for chemical analysis. J Am Chem Soc 41:1168–1175
12. Hull AW (1921) The X-ray crystal analysis of thirteen common metals. Phys Rev 17:571–588
13. Warren BE (1934) An X-ray powder diffraction study of Carbon Black. J Chem Phys 2: 551–555
14. Rietveld HM (1969) A profile refinement method for nuclear and magnetic structures. J Appl Crystallogr 2:65–71
15. Scherrer P (1918) Bestimmung der Grösse und der inneren Struktur von Kolloidteilchen mittels Röntgenstrahlen. Göttinger Nachrichten Gesell 2:98–100
16. Davisson CJ, Germer LH (1927) The scattering of electrons by a single crystal of nickel. Nature 119:558–560

17. Davisson CJ, Germer LH (1927) Diffraction of electrons by a crystal of nickel. Phys Rev 30:705–740
18. Thomson GP, Reid A (1927) Diffraction of cathode rays by a thin film. Nature 119:890–890
19. Ruska E, Knoll M (1931) Die magnetische Sammelspule für schnelle Elektronenstrahlen. Z Tech Physik 12:389–400, 448
20. Knoll M, Ruska E (1932) Das Elektronenmikroskop. Z Physik 78:318–339
21. Ruska E (1935) The electron microscope as ultra-microscope. Res Prog 1:18–19
22. Cowley JM, Goodman P, Vainshtein BK, Zvyagin BB, Dorset DL (2001) Electron diffraction and electron microscopy in structure determination. In: Shmueli U (ed) International tables for crystallography, vol B, 2nd edn, Reciprocal space. Kluwer Academic Publishers, Dordrecht
23. Cowley JM (1953) Structure analysis of single crystals by electron diffraction. II. Disordered boric acid structure. Acta Crystallogr 6:522–529
24. Cowley JM (1953) Structure analysis of single crystals by electron diffraction. III. Modification of alumina. Acta Crystallogr 6:846–853
25. Rigamonti R (1936) La struttura della catena paraffinica studiata mediante i raggi di elettroni. Gazzetta Chimica Italiana 66:174–182
26. Cowley JM, Moodie AF (1957) The scattering of electrons by atoms and crystals. I. A new theoretical approach. Acta Crystallogr 10:609–619
27. Cowley JM, Moodie AF (1959) The scattering of electrons by atoms and crystals. II. The effects of finite source size. Acta Crystallogr 12:353–359
28. Cowley JM, Moodie AF (1959) The scattering of electrons by atoms and crystals. III. Single-crystal diffraction patterns. Acta Crystallogr 12:360–367
29. Avilov AS (2003) The quantitative analysis of electrostatic potential and study of chemical bonding by electron diffraction structure analysis. Z Kristallogr 218:247–258
30. Pennycook SJ (1992) *Z*-contrast transmission electron microscopy-direct atomic imaging of materials. Annu Rev Mater Sci 22:171–195
31. Scherzer O (1936) Über einige Fehler von Elektronenlinsen. Z Phys 101:593–603
32. Spence JCH (2003) High-resolution electron microscopy, 3rd edn. Oxford University Press, New York
33. Reimer L, Kohl H (2008) Transmission electron microscopy, physics of image formation, 5th edn. Springer, New York
34. Rose H (1990) Outline of a spherically corrected semiaplanatic medium-voltage transmission electron microscope. Optik 85:19–24
35. O'Keefe MA (2004) Seeing atoms at sub-Ångstrom resolution with aberration-corrected TEM. Microsc Microanal 10:972–973
36. Tanaka M, Terauchi M, Kaneyama T, Tsuda M, Saitoh K (1985) Convergent beam electron diffraction, vol I–IV. JEOL, Tokyo
37. Sung CM, Williams DB (1991) Principles and applications of convergent beam electron diffraction: a bibliography (1938–1990). Microsc Res Tech 17:95–118
38. Buxton BF, Eades JA, Steeds JW, Rackham GM (1976) The symmetry of electron diffraction zone-axis patterns. Philos Trans R Soc Lond A 281:181–184
39. Nakashima PNH, Moodie AF, Etheridge J (2007) Structural phase and amplitude measurement from distances in convergent-beam electron diffraction patterns. Acta Crystallogr A63: 387–390
40. Pinsker ZG (1949) Diffraktsiya Elektronov. Akad. Nauk SSSR Press, Moscow/Leningrad, Engl. transl: Electron diffraction (1953). Butterworths, London
41. Zvyagin BB (1967) Electron diffraction analysis of clay mineral structures. Plenum Press, New York
42. Vainshtein BK (1956) Strukturnaya Elektronographiya. Akad Nauk SSSR Press, Moscow, Engl. transl: Structure analysis by electron diffraction (1964). Pergamon Press, Oxford
43. Vainshtein BK, Zvyagin BB, Avilov AS (1992) In: Cowley JM (ed) Electron diffraction structure analysis, vol 1. pp. 216–312. Oxford University Press, Oxford
44. Geil PH (1960) Nylon single crystals. J Polym Sci 44:449–458
45. Dorset DL (1995) Structural electron crystallography. Plenum, New York

46. Dorset DL, Gilmore C (2000) Prospects for kinematical least-squares refinement in polymer electron crystallography. Acta Crystallogr A56:62–67
47. Hovmöller S, Sjogren A, Farrants G, Sundberg M, Marinder BO (1984) Accurate atomic positions from electron microscopy. Nature 311:238–241
48. Voigt-Martin IG, Yan DH, Wortmann R, Elich K (1995) The use of simulation methods to obtain the structure and conformation of 10-cyano-9,9′-bianthryl by electron diffraction and high-resolution imaging. Ultramicroscopy 57:29–43
49. Weirich TE, Ramlau R, Simon A, Hovmöller S, Zou X (1996) A crystal structure determined with 0.02 Å accuracy by electron microscopy. Nature 382:144–146
50. Vincent R, Midgley PA (1994) Double conical beam-rocking system for measurement of integrated electron diffraction intensities. Ultramicroscopy 53:271–282
51. Avilov A, Kuligin K, Nicolopoulos S, Nickolskiy M, Boulahya K, Portillo J, Lepeshov G, Sobolev B, Collette JP, Martin N, Robins AC, Fischione P (2007) Precession technique and electron diffractometry as new tools for crystal structure analysis and chemical bonding determination. Ultramicroscopy 107:431–444
52. Gemmi M, Nicolopoulos S (2007) Structure solution with three-dimensional sets of precessed electron diffraction intensities. Ultramicroscopy 107:483–494
53. Own CS (2005) System design and verification of the precession electron diffraction technique. Ph.D. thesis, Northwestern University, Evanston
54. Gjönnes J, Hansen V, Berg BS, Runde P, Cheng YF, Gjönnes K, Dorset DL, Gilmore CJ (1998) Structure model for the phase Al*m*Fe derived from three-dimensional electron diffraction intensity data collected by a precession technique. Comparison with convergent-beam diffraction. Acta Crystallogr A54:306–319
55. Gemmi M, Zou X, Hovmöller S, Migliori A, Vennström M, Andersson Y (2003) Structure of Ti2P solved by three-dimensional electron diffraction data collected with the precession technique and high-resolution electron microscopy. Acta Crystallogr A59:117–126
56. Gjönnes J, Hansen V, Kverneland A (2004) The precession technique in electron diffraction and its application to structure determination of nano-size precipitates in alloys. Microsc Microanal 10:16–20
57. Weirich TE, Portillo J, Cox G, Hibst H, Nicolopoulos S (2006) Ab initio determination of the framework structure of the heavy-metal oxide Cs*x*Nb2.54W2.46O14 from 100 kV precession electron diffraction data. Ultramicroscopy 106:164–175
58. Dorset DL, Hauptman HA (1976) Direct phase determination for quasi-kinematical electron diffraction intensity data from organic microcrystals. Ultramicroscopy 1:195–201
59. Dorset DL (1995) Structural electron crystallography. Plenum Press, New York
60. Dorset DL (1995) Direct structure analysis in protein electron crystallography: crystallographic phases for halorhodopsin to 6-A resolution. Proc Natl Acad Sci USA 92:10074–10078
61. Kühlbrandt W, Wang DN, Fujiyoshi Y (1994) Atomic model of plant light-harvesting complex by electron crystallography. Nature 367:614–621
62. Unwin PNT, Henderson R (1976) Molecular structure determination by electron microscopy of unstained crystalline specimens. J Mol Biol 94:425–440
63. Henderson R, Unwin PNT (1975) Three-dimensional model of purple membrane obtained by electron microscopy. Nature 257:28–32
64. Hovmöller S, Sjögren A, Farrants G, Sundberg M, Marinder BO (1984) Accurate atomic positions from electron microscopy. Nature 311:238–241
65. Nicolopoulos S, Gonzalez-Calbet JM, Vallet-Regi M, Corma A, Corell C, Guil JM, Perez-Pariente J (1995) Direct phasing in electron crystallography: Ab initio determination of a new MCM-22 zeolite structure. J Am Chem Soc 117:8947–8956
66. Wagner P, Terasaki O, Ritsch S, Nery JG, Zones SI, Davis ME, Hiraga K (1999) Electron diffraction structure solution of a nanocrystalline zeolite at atomic resolution. J Phys Chem B103:8245–8250
67. Fan HF (1993) Modern crystallography proceedings of the seventh Chinese International Summer School of Physics. Chinese Academy of Science, Beijing, pp 1–10

68. Gilmore CJ (1996) Maximum entropy and Bayesian statistics in crystallography: a review of practical applications. Acta Crystallogr A52:561–589
69. Mugnaioli E, Gorelik T, Kolb U (2009) "Ab initio" structure solution from electron diffraction data obtained by a combination of automated diffraction tomography and precession technique. Ultramicroscopy 109:758–765
70. Morniroli JP, Houdellier F, Roucau C, Puiggali J, Gesti S, Redjaimia A (2008) LACDIF, a new electron diffraction technique obtained with the LACBED configuration and a Cs corrector: comparison with electron precession. Ultramicroscopy 108:100–115
71. Koch CT (2011) Aberration-compensated large-angle rocking-beam electron diffraction. Ultramicroscopy 111:828–840
72. Howie A, Whelan MJ (1961) Diffraction contrast of electron microscope images of crystal lattice defects. II. The development of a dynamical theory. Proc R Soc A 263:217–237
73. Howie A, Whelan MJ (1962) Diffraction contrast of electron microscope images of crystal lattice defects. III. Results and experimental confirmation of the dynamical theory of dislocation image contrast. Proc R Soc A 267:206–230
74. Hytch MJ, Stobbs WM (1994) Quantitative comparison of high resolution TEM images with image simulations. Ultramicroscopy 53:191–203
75. LeBeau JM, Findlay SD, Allen LJ, Stemmer S (2008) Quantitative atomic resolution scanning transmission electron microscopy. Phys Rev Lett 100:206101
76. Shechtman D, Blech I, Gratias D, Cahn JW (1984) Metallic phase with long range orientational order and no translation symmetry. Phys Rev Lett 53:1951–1953
77. International Union of Crystallography (1992) Report of the executive committee for 1991. Acta Crystallogr A48:922–946
78. Schattschneider P, Rubino S, Hübert C, Rusz J, Kunes J, Novak P, Carlino E, Fabrizioli M, Panaccione G, Rossi G (2006) Detection of magnetic circular dichroism using a transmission electron microscope. Nature 441:486–488
79. Dunin-Borkowski R, Kasama T, Wei A, Tripp SL, Hytch MJ, Snoeck E, Harrison RJ, Putnis A (2004) Off-axis electron holography of magnetic nanowires and chains, rings, and planar arrays of magnetic nanoparticles. Microsc Res Tech 64:390–402
80. Hÿtch MJ, Houdellier F, Hüe F, Snoeck E (2011) Dark-field electron holography for the measurement of geometric phase. Ultramicroscopy 111:1328–1337
81. Hÿtch MJ, Houdellier F, Hüe F, Snoeck E (2008) Nanoscale holographic interferometry for strain measurements in electronic devices. Nature 453:1086–1089
82. Kolb U, Matveeva GN (2003) Electron crystallography on polymorphic organics. Z Kristallogr 218:259–268

Chapter 25
Image Formation in the Electron Microscope

Louisa Meshi

Abstract This chapter is an introduction to electron microscopy. Instrumentation, electron optical principles, formation of an image and diffraction in the transmission electron microscope, as well as contrast and basic principles of high resolution electron microscopy are discussed.

25.1 Introduction

Nowadays electron microscopy is a well-established branch of science that uses an electron microscope for characterization of material. Unique to modern transmission electron microscopy (TEM) is the possibility of obtaining simultaneously images at atomic resolution, analytical information (using energy dispersive spectroscopy (EDS), or electron energy loss spectroscopy (EELS), for example), and structural information using various diffraction techniques available – such as selected area electron diffraction (SAED) or convergent beam electron diffraction (CBED) methods from a very small area of the specimen (approx. 1–5 nm). Due to this outstanding possibility, there is a wide range of exploitation of TEM in various fields, including the field of structure determination.

The aim of this chapter is to explain the most important electron optical principles, which must be clearly understood so that the reader can utilize the available facilities of a modern high resolution instrument to the best advantage in transmission work with crystalline materials.

An electron microscope consists of an electron gun and an assembly of electron lenses, as shown in Fig. 25.1. This depicts schematically the ray paths in a

L. Meshi (✉)
Department of Materials Engineering, Ben-Gurion University of the Negev,
Beer-Sheva 84105, Israel
e-mail: louisa@bgu.ac.il

U. Kolb et al. (eds.), *Uniting Electron Crystallography and Powder Diffraction*,
NATO Science for Peace and Security Series B: Physics and Biophysics,
DOI 10.1007/978-94-007-5580-2_25,

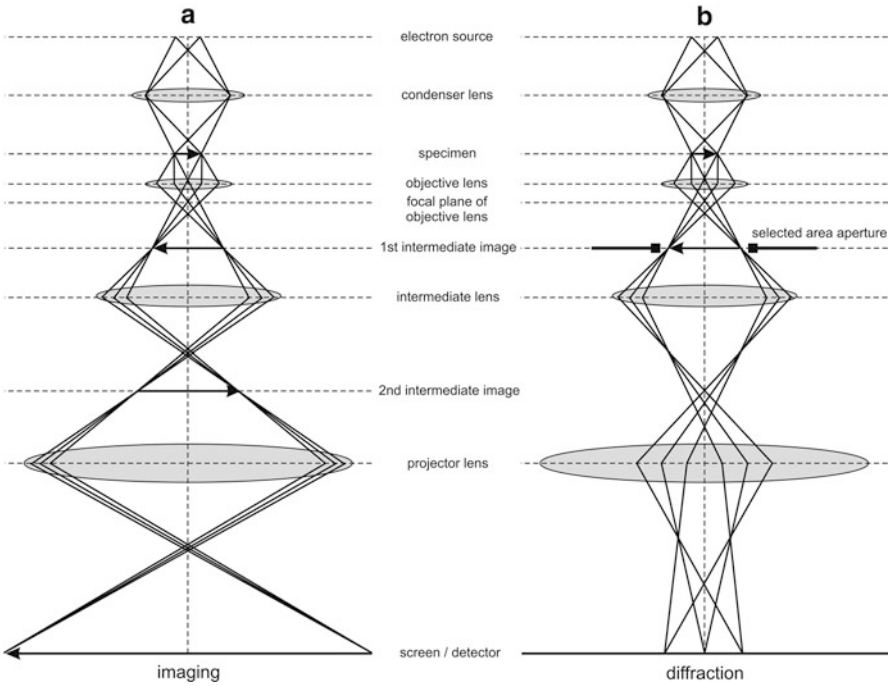

Fig. 25.1 Ray paths in the electron microscope: (**a**) imaging conditions and (**b**) diffraction conditions [1]

microscope employing three stages of magnification (objective, intermediate lens, and projector), and a single or double condenser lens system for illumination of the specimen.

There are two kinds of electron sources used in TEM: the first is called a thermionic source, which, as the name suggests, produces electrons when heated; and the second is a field-emission source, which produces electrons when a large electric potential is applied between the source and an anode.

The magnification and formation of an image in the TEM are performed by the electromagnetic lenses. The most critical component of a magnetic lens is the soft-iron pole-piece, which produces an axially symmetric magnetic field for focusing the electrons. The performance of a magnetic lens depends on its pole piece (for example: distance between the upper and bottom pole pieces of the objective lens influences the resolution of the TEM). The rest of the lens is a magnetic yoke containing the winding for energizing the lens with the d.c. current and varying the focal length of the pole-piece system.

Electromagnetic lenses, as with optical lenses, produce distortions which affect the final image produced by the microscope and limit attainable resolution. The most important lens distortions are: (1) spherical aberrations – this defect occurs when the lens field behaves differently for off-axis rays. The further off-axis the parallel

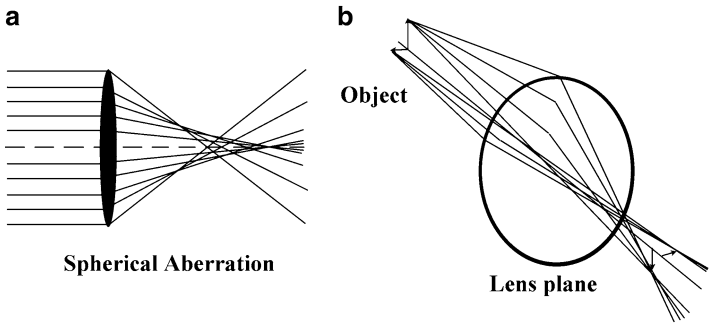

Fig. 25.2 Ray diagram when the lens suffers from (**a**) spherical aberrations; (**b**) astigmatism

beam of electrons is, the more strongly it is bent back toward the axis. Thus, as shown in Fig. 25.2a, different electron beams will be focused in different planes. As a result, a point object is imaged as a disk of finite size, which limits the resolution of the instrument; (2) chromatic aberrations – which appear due to electrons that have different energies. In TEM there are two reasons for these energy variations (energy spread) – the source and the electron-sample interactions. Electron-sample interactions produce electrons of a wide range of energies emerging from the thin foil; this effect is the major reason for energy spread. The objective lens bends the electron path of lower energy more strongly and thus electrons from a point in the object are blurred to form a disk in the Gaussian image plane (plane I_1 in Fig. 25.1); and (3) astigmatism – which occurs when the electrons sense a non-uniform magnetic field. As shown in Fig. 25.2b, beams that propagate in two perpendicular planes have different focus. If we wish to image a cross while our system suffers from astigmatism, the vertical and horizontal lines will be in sharp focus at two different distances. This defect arises because the pole pieces cannot be machined to be perfectly cylindrically symmetrical down the bore and they might also have microstructural inhomogeneities, which cause local variations in the magnetic field strength.

Astigmatism of condenser and objective lenses can be corrected in all TEMs using stigmators, which introduce a compensating magnetic field that balances the inhomogeneities causing the astigmatism. Contrary to astigmatism, aberrations are inherited properties of the lenses and they cannot be eliminated in regular microscopes. Although today C_s (spherical aberration coefficient) and even C_c correctors (chromatic aberration coefficient) can be installed, lens aberrations are still the most limiting factor of TEM resolution (aberration corrected electron microscopy will not be addressed in this chapter).

TEM assembly also includes a variety of apertures. These apertures are introduced into the bores of the lens pole pieces. With a double condenser lens system condenser 1 usually contains a fixed aperture of about 400 μm diameter, while condenser 2 may be equipped with a range of interchangeable apertures of about 10–400 μm diameter. The objective lens also has interchangeable apertures of about

5–100 μm diameter. For selected area diffraction, interchangeable apertures are inserted in the first intermediate image plane (I_1 in Fig. 25.1) during examination of the specimen (the purpose of the latest apertures will be discussed thoroughly later in this chapter).

25.2 Bright Field/Dark Field Imaging and Selected Area Diffraction

In order to understand the formation of image and diffraction patterns in the electron microscope, objective lens function should be explained. As shown in Fig. 25.1, due to electron–specimen interactions two types of beams are formed: transmitted beam and diffracted beams. On this image scattered beams, which form due to inelastic scattering, are not shown; however, we would like to emphasize that they do exist. The transmitted and diffracted beams are focused by the objective lens in the focal plane; following the ray diagram we can see that afterwards an image is formed in the image plane. In a case of crystalline materials the dominant scattering that takes place is of Bragg diffraction type; thus diffracted beams traveling at small angles with the incident beam, which are focused by the objective, form a transmission diffraction pattern in its focal plane.

Since the intermediate lens, as all electromagnetic lenses, does not have a fixed focal length, it can be focused either on the image plane and in this way a magnified image will be transferred to the fluorescence TEM screen or onto the focal plane and then a diffraction pattern will be seen (Fig. 25.1a, b). Usually diffraction from a particular place in the specimen is needed and in order to receive a pattern from only this specific area a selected area aperture is introduced in the first intermediate image plane (I_1). In this manner one specific place at the specimen can be chosen and then the diffraction formed will be related only to this particular chosen part.

Let us consider a crystalline specimen with uniformly thinned grains. The resultant image of several grains will not have any contrast! Contrast can be increased artificially by introduction of objective aperture. This aperture's position is approximately at the focal plane of the objective lens. If an aperture is inserted we can choose which beam will form an eventual image – a transmitted beam or one of the scattered/diffracted beams (see Fig. 25.3). If a transmitted beam is chosen, this means that it passes through the objective aperture hole. Such an image will be formed using only those electrons that were transmitted through the specimen without interactions; thus the place in the specimen that satisfied Bragg conditions will appear dark, since most of the electrons from such a place were scattered and only a few electrons contributed to the transmitted beam that forms the image. On the other hand – a different place in the specimen that did not satisfy Bragg conditions will appear bright, since most of the electrons were transmitted through it without interactions; thus there is a large quantity of electrons that forms an image. This type of contrast is called diffraction contrast and this particular image formation mode is called Bright Field.

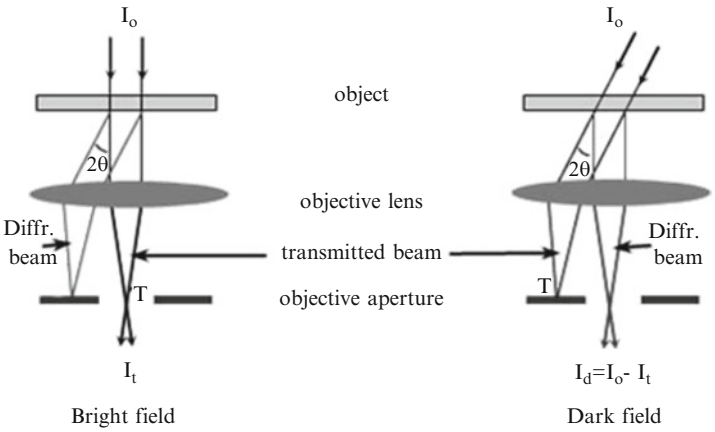

Fig. 25.3 Image formation in bright field (*left image*) and dark field conditions (*right image*)

If one of the diffracted beams is transferred through the hole in the objective aperture, the resultant image will be received in Dark Field mode. In this mode those parts of the specimen where these particular Bragg conditions were satisfied will appear bright and all the rest of the specimen will be dark.

The manner in which the contrast is introduced is not used only for crystalline samples. Since the scattering effect is proportional to z (atomic number), introduction of an objective aperture into non-crystalline material will also add a contrast. In Bright Field mode, when only the transmitted beam forms an image, heavily scattered places in the specimen will appear darker. This type of contrast is called mass or amplitude contrast.

There are two other additional types of contrast that need to be mentioned – thickness and phase contrast. Thickness contrast is seen even without the objective aperture; introduction of the aperture increases the contrast. If the place is thick – it appears darker. Phase contrast will be discussed below.

25.3 Basics of High Resolution Transmission Electron Microscopy (HRTEM) Theory and Practice

Since the transmission image is necessarily a projection of the specimen structure in the incident beam direction, an ultra-thin specimen must be used if one wishes to resolve detail at the atomic level. By definition, a HRTEM image is a micrograph that approaches atomic resolution; see Fig. 25.4 as an example.

In addition to the need for very thin specimens, in order to receive a HRTEM image, the microscope used for this purpose has to have special high or ultra-high

resolution pole pieces (with small gaps), high electronic and mechanical stability, ultra-high vacuum, and a coherent illumination source.

A high resolution transmission electron microscope is a close analogue to the optical phase contrast microscope [3]. Fresnel edge fringes, atomic lattice fringes, and images of small molecules are all examples of phase contrast, i.e., interference effects. Thus, in order to create such an image, we need the inference of several beams. The phase contrast principle is dramatically different from the conventional diffraction/mass/thickness contrast principle presented earlier. The image that is formed as the interference of transmitted and diffraction beams will be without any contrast. In both electron and optical microscopy the reasons for the lack of contrast at exact focus are the same – the thin specimens (phase objects) affect only the phase of the wave transmitted by the specimen and not the amplitude. That is, they behave like a medium of variable refractive index [4]. It is this variation in the phase from point to point across the specimen (proportional to the specimen's atomic potential in volts for electron microscopy) that must be converted into intensity variations in the image if we wish to "see", for example, atoms in the electron microscope.

Another way to explain the lack of contrast (or weakness of the contrast) in these interference images is to calculate the phase shift among the electron waves. The scattered waves, which carry the information about the crystal, suffer a 90° extra phase shift with respect to the unscattered wave. This is why the phase contrast originated by the crystal is weak when the crystal is thin and the lens is in focus. Since in the electron microscope there is a way to introduce additional phase shift by defocusing the lens and making use of the aberrations of the lens (according to formula (25.1)) – the real projected potential of the crystal (exit wave function) can be revealed.

$$\gamma(u) = \pi \Delta F \lambda u^2 + \frac{\pi C_s \lambda^3 u^4}{2} \tag{25.1}$$

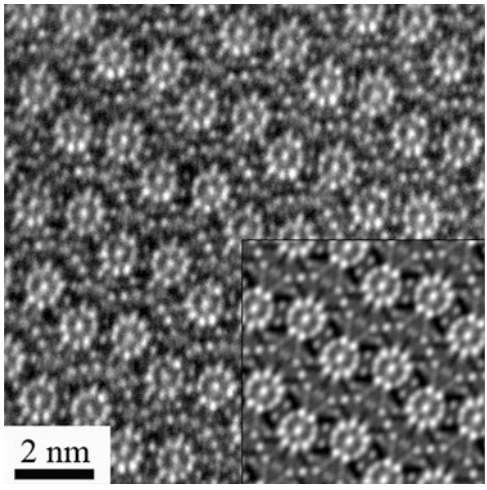

Fig. 25.4 HRTEM image taken from the Al-Rh-Ru E-phase along the [010] direction. The image corrected by crystallographic image processing method is shown in the inset. It corresponds to the optimal defocus and the exact zone axis alignment. Plane group symmetry *pmg* was imposed on the image Fourier components [2]

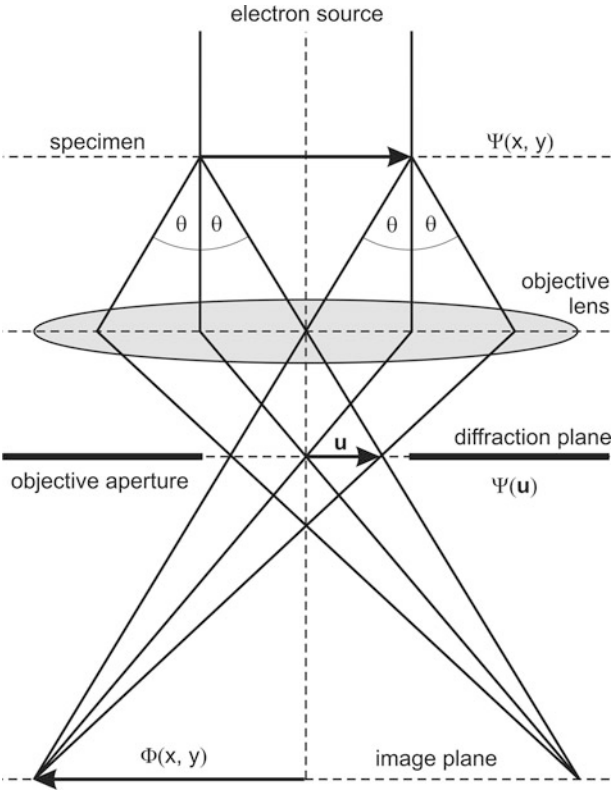

Fig. 25.5 Theory of HRTEM image formation

when: $\gamma =$ phase shift; u = reciprocal lattice vector; $\Delta F =$ defocus value of the objective lens; $\lambda =$ electron wavelength; and $C_s =$ coefficient of spherical aberrations.

Thus eventual phase contrast, enhanced by the additional shift, will enable us to resolve atomic columns in the HRTEM image.

In order to understand deeply the HRTEM image formation let us review again the ray diagram in the TEM objective lens area (see Fig. 25.5). If Ψ(x, y) is an exit wave function of electrons that leave the crystal, then in the diffraction plane, formed by the objective lens, $\psi(u)$ will be the electron intensity distribution function that will be seen (where u is the reciprocal space vector). This function describes the intensity of the diffraction beams. The exit wave and intensity distribution functions relate one to another by Fourier transform:

$$\psi(u) = \mathcal{F}\left[\Psi\left(x, y\right)\right] \tag{25.2}$$

The function of intensity distribution of the image formed by the objective lens in the image plane is Φ(x, y) and, following pure mathematics, it should be equal to inverse Fourier transform of the function $\psi(u)$. According to Eq. (25.2) this will also be equal to the exit wave function – Ψ(x, y). Mathematically:

$$\Phi(x, y) = \mathcal{F}^{-1}[\psi(u)] = \Psi(x, y) \tag{25.3}$$

Equation (25.3) means that a HRTEM image formed in this way will represent the projected potential of atomic columns; this proves the theoretical possibility to resolve atoms using HRTEM. However, as with everything else in life, the reality is not so simple, since, as stated earlier, electromagnetic lenses used in electron microscopes are not perfect and they distort the image. Thus the function of the real image formed in the image plane of an objective lens (Φ(x, y)) will not be equal to the exit wave function – Ψ(x, y) – and the final image will be distorted. Actually, the coefficient by which these two functions relate to each other is called the Contrast Transfer Function (CTF) – this function takes into account all distortions introduced by the microscope and thus is a function of the microscope used. Equation (25.4) summarizes the real relation between an atom distribution function of the specimen and the intensity distribution function of the image formed by the microscope:

$$\Phi(x, y) = \mathcal{F}^{-1} A(u) D(\alpha, \Delta) \exp(-i\gamma(u)) \psi(u) = \mathcal{F}^{-1} CTF\psi(u) \tag{25.4}$$

when: A(u) = objective aperture function that limits the number of diffraction beams that form the image; D(α, Δ) = function of chromatic aberrations, beam convergence, and defocus spread; γ(u) = phase shift of the electron wave with respect to incident electrons, see Eq. (25.1). This function depends on the coefficient of spherical aberrations (C_s), electron wavelength, and defocus (Δf).

C_s and defocus are the main factors affecting the CTF of the microscope (see Fig. 25.6). CTF function, as shown in Fig. 25.6, is a function of image intensity vs. the reciprocal vector (u). Thus at some lattice spacing we see the inverse of the contrast and some spacings have zero intensity (see points marked as u_1 and u_2 in Fig. 25.6b). For interpretable HRTEM images we prefer to choose a defocus value in which these effects will be minimized. Such a defocus value is called Scherzer focus [6]. In Fig. 25.6 this condition is satisfied when Δf = −50 nm.

Summarizing, we would like to state that minimization of the distortions of image caused by CTF will enable formation of a HRTEM image that would be straightforward interpretable. Nowadays, there are two paths in which scientists work in order to achieve this: (1) improvement of the instrumentation (such as development of C_s and C_c correctors and monochromators), and (2) HRTEM image processing (such as the crystallographic image processing method). These issues will be addressed in later chapters.

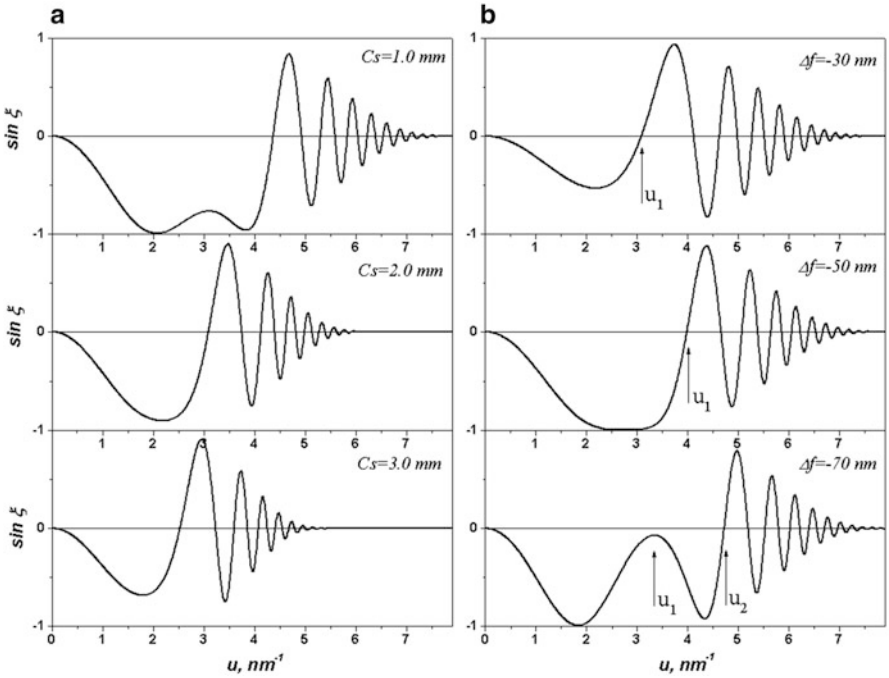

Fig. 25.6 Changes of CTF as a function of (**a**) coefficient of spherical aberrations (C_s) (for V = 200 kV and Δf = −60 nm) and (**b**) defocus (Δf) (for V = 200 kV and C_s = 1 mm) [5]

References

1. Hirsh PB, Howie A, Nicholson RB, Pashley DW, Whelan MJ (1967) Electron microscopy of thin crystals. Butterworths, London
2. Meshi L, Samuha S, Kapush D, Pavlyuchkov D, Grushko B (2011) New complex intermetallic in the Al-Rh-Ru alloy system. J Alloy Compd 509:6551–6555. doi:10.1016/j.jallcom.2011.03.108
3. Bennett AH, Jupnik H, Osterberg H, Richards OW (1951) Phase microscopy. Principles and applications. Wiley, New York
4. Spence JCH (2003) High-resolution electron microscopy, 3rd edn. Oxford University Press, New York
5. Williams DB, Carter CB (2009) Transmission electron microscopy: a textbook for materials science. Springer, New York
6. Scherzer O (1949) The theoretical resolution limit of the electron microscope. J Appl Phys 20:20–29. doi:10.1063/1.1698233

Chapter 26
Models for Precession Electron Diffraction

Laurence D. Marks

Abstract Precession Electron Diffraction has become an increasingly popular method of obtaining crystallographic data, and may well replace older methods such as selected area diffraction or microdiffraction. While a full model has to involve a dynamical calculation, some approximations give some indication how the results vary as a function of thickness and precession angle. This note reviews some of the basic models, their advantages and failures as well as some of the open issues.

26.1 Introduction

Over the last few years Precession Electron Diffraction (PED), a technique for acquiring electron diffraction intensities, invented in 1994 by Vincent and Midgley [1] has started to emerge as a viable technique for determining structures based solely upon the intensities, and/or with some assistance from crystallographic phases determined using HREM or similar techniques. An incomplete list of references is [1–50]. It was clear from the first attempts to use the method coupled with direct methods that it gave remarkably better results than conventional diffraction techniques except in relatively special cases such as surfaces where the diffraction intensities are very close to kinematical. Hence the quandary; electron diffraction can only be properly be described using dynamical diffraction, but tools based upon a kinematical formulation work. Why? While the detailed answer to this is still not fully understood, many of the details are and I will here briefly describe the main models along with their advantages and limitations.

L.D. Marks (✉)
Department of Materials Science and Engineering, Northwestern University, Evanston, IL 60201, USA
e-mail: l-marks@northwestern.edu

U. Kolb et al. (eds.), *Uniting Electron Crystallography and Powder Diffraction*, NATO Science for Peace and Security Series B: Physics and Biophysics,
DOI 10.1007/978-94-007-5580-2_26,

26.2 Kinematical Model

The kinematical model has to be mentioned as it is the simplest. The result one gets is that the intensities are proportional to the square of the crystallographic structure factor. Unfortunately except for special cases such as surfaces or graphene monolayers the method has only a very limited relevance for standard samples as an accurate model, as illustrated in Fig. 26.1, failing by 10 nm thickness.

26.3 Blackman Model

The Blackman model [51, 52] makes the assumption that the integration over angles can be considered as equivalent to a complete integration of a two-beam diffraction problem for all possible angles. In more detail, the intensity for a given reflection can be written as the integral of a Bessel function:

$$I(t) = \int_0^{A_g} J_0(2x)dx \quad A_g = \frac{\pi t}{\xi_g{}^2}$$

Where ξ_g is the standard extinction distance which scales inversely with the structure factor and t is the thickness. The result one obtains is that the intensity, for a relatively thick crystal, scales directly as the crystallographic structure factor; for a thin crystal it scales as the square of the structure factors. While this is again a useful, simple approximation which has been sometimes used and is better than kinematical, there are several fundamental problems with it:

(a) It neglects most dynamical diffraction effects, as the two-beam model really only applies for specific orientations.
(b) It neglects the fact that in a precession experiment only a limited range of angles are used.

Unfortunately it is not accurate, R1 > 40% for 200 Å, see Fig. 26.2.

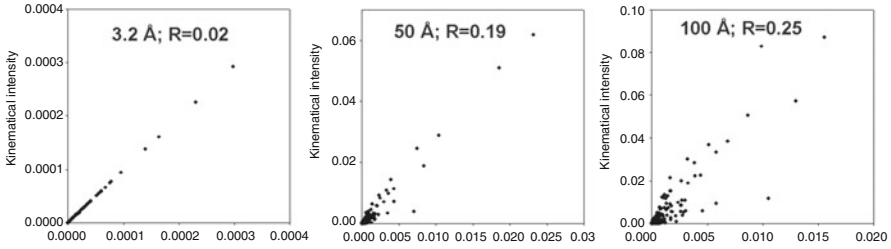

Fig. 26.1 Comparison of kinematical intensities (y axis) versus full dynamical calculations (x axis) for different thicknesses for $(Ga,In)_2SnO_4$ with the R1 shown

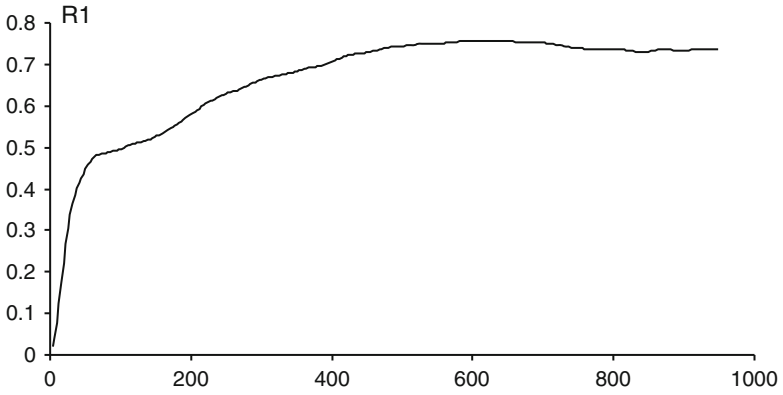

Fig. 26.2 Values of the R1 from a Blackman model versus a full dynamical calculation (y-axis) for $(Ga,In)_2SnO_4$ as a function of thickness in Angstroms along the x-axis

26.4 Methods Based Upon Lorentz-Type Corrections

From the earliest days of PED a different approach has been to try and separate the contributions associated with the integration over angle and dynamical diffraction effects, what has been called a Lorentz correction. In more formal fashion, the intensity would be written as

$$I(g) = L(g) * B(g)$$

where L(g) is an approximate form to take into account the integration range, and B(g) is purely a diffraction term, for instance Kinematical or the Blackman equation. The concept is that one might then be able to precalculate L(g) and remove it, thereby obtaining a better form. A simple form for L(g) suggested by Gjonnes [2] is

$$L(g) = g\sqrt{1 - \left(\frac{g}{2R_0}\right)}$$

Where R_0 is the precession scan angle in reciprocal Angstroms. While this is an interesting idea unfortunately to date it has not been particularly successful as illustrated in Fig. 26.3.

26.5 1s Channeling Model

The concept of a channeling approach is to expand the electron wave in terms of local orbitals rather than plane waves, e.g. [53–56]. One can then approximate by using just the 1s states, which works well for HREM and STEM imaging [57].

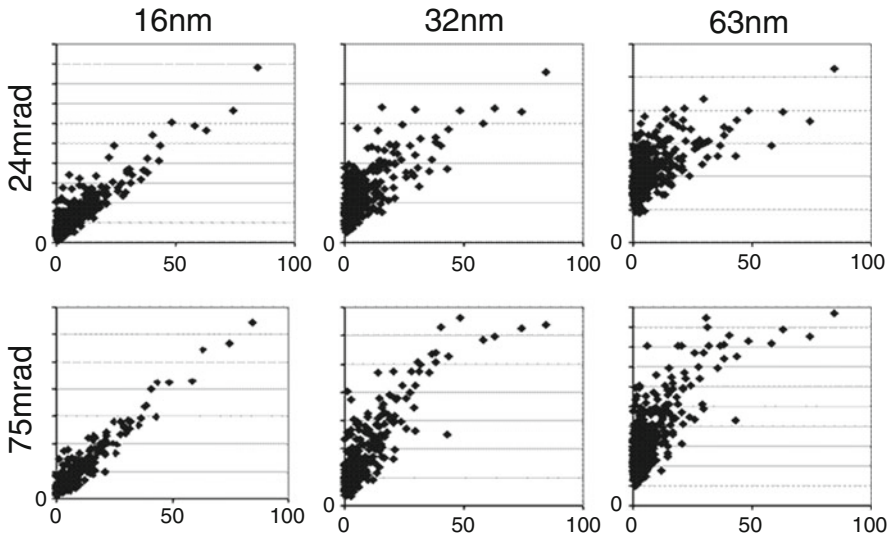

Fig. 26.3 Scatter plot of Lorentz-corrected data (y-axis) versus the true values (x-axis) for $(Ga, In)_2SnO_4$ with two different precession angles and three different thicknesses

At least in order of simplicity, this model is an attractive approach. The result of the model is "atom-like" features and it has been shown that even though the results are dynamical, the deviations from kinematical are in fact statistical in character rather than being systematic [58, 59]. Since both direct methods and refinements are (in principle) stable against statistically random deviations, it is therefore true that in some cases on a zone axis these methods will work well. Alas, while there may be some relationship to what one finds in a PED pattern, to date this approach has not proved to be useful. (A 1s-model leads to scattering which is dominated by atomic strings which is similar to what PED yields so there may be some connection, but so far there is no proof beyond qualitative intuition.)

26.6 Two-Beam Model

The first model to account for at least some of the effects present is a two-beam model with a proper tracking of the range of integration. A specific form [26] is

$$C_{2beam}(g,t,\phi) = {F_g}^2 \left(\frac{1}{{\xi_g}^2} \int_0^{2\pi} \frac{\sin^2(\pi t s_{eff})}{(s_{eff})^2} d\theta \right)^{-1}$$

Where the effective excitation error $s_{eff} = (s^2 + \xi_g^2)^{1/2}$ is used. This is better, but again not perfect and breaks down for a thickness much beyond 10 nm as illustrated in Fig. 26.4.

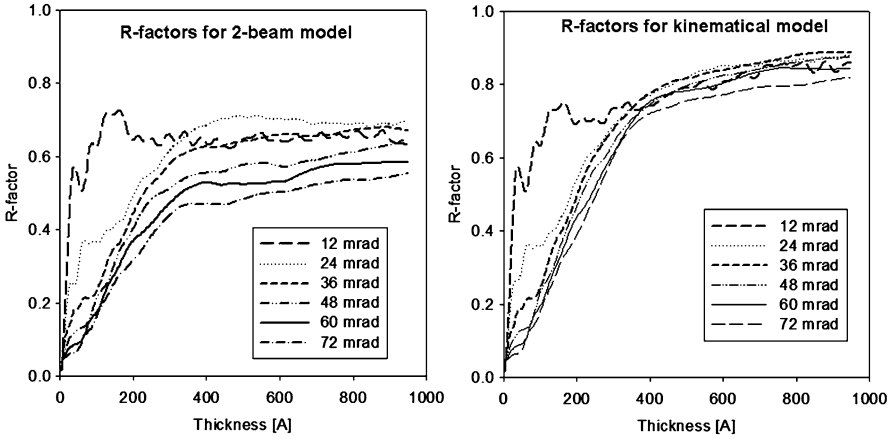

Fig. 26.4 Comparison for $(Ga,In)_2SnO_4$ of the R1 for a two-beam model versus thicknesses (*left*) compared to a kinematical model (*right*). Unfortunately while there is some improvement, it is not enough

26.7 Full Multislice or Bloch Wave Methods

Good agreement between experimental and calculated intensities has been obtained using methods where all the dynamical diffraction effects (except fine details of inelastic scattering/adsorption) are taken into account. These are based upon either the multislice method [60–63], a fast numerical integration of the intensities, or Bloch Wave methods [64–66] where a matrix problem is solved. Assuming that the potential used is the same for the two methods, it is known that they give identical results provided that they have been properly coded.

The approach [13], as illustrated in Fig. 26.5 is to consider all different incident beam directions and integrate the final intensity over these, for instance the set 1–8 below.

Without any additional refinement one can easily obtain an R1 of about 0.1, as illustrated below in Figs. 26.6 and 26.7.

26.8 Intensity Ordering

An explanation of why the methods work, which unfortunately slightly begs the question of the details of when they will fail, is intensity ordering [67]. Instead of the intensities being simply related to the structure factors as in kinematical or Blackman approaches, the hypothesis of this model is that reflections with large structure factors lead to large intensities in PED, those with small structure factors small intensities. By inspection this is largely true for the plots shown above which

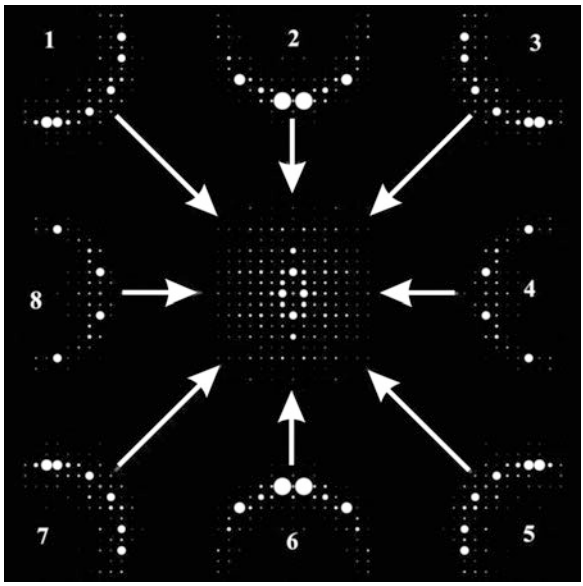

Fig. 26.5 Schematic of a dynamical simulation. For a range of different tilts a full calculation is performed and the results are summed. Specific results for eight illustrative tilts are shown; in general 512–1,024 different values are used

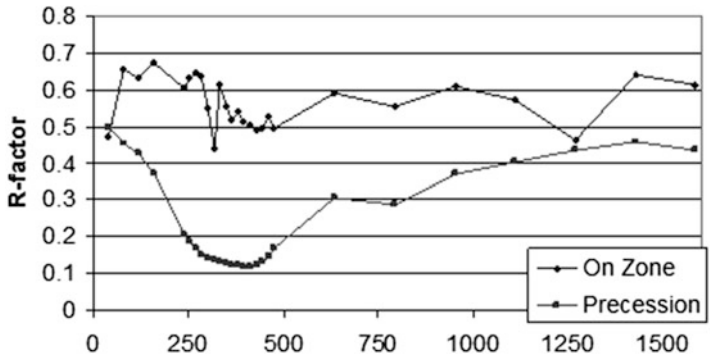

Fig. 26.6 R1 as a function of thickness in Angstroms from a multislice calculation using experimental data for $(Ga,In)_2SnO_4$ both on-zone (*upper line*) and precessed (*lower line*). The minimum with precessed data is much clearer, and the R1 much lower

plot the kinematical structure factors versus the true values. This is a sufficient condition for direct methods to work, indeed in the early days of the technique with "by eye" measurement of intensities for x-ray diffraction from film, structures were solved by dividing the intensities into those which were strong, those which were of medium intensity and the weak ones. Classical direct methods only use the strong intensities, so provided that these are representative then Σ_2 and similar relationships will be preserved.

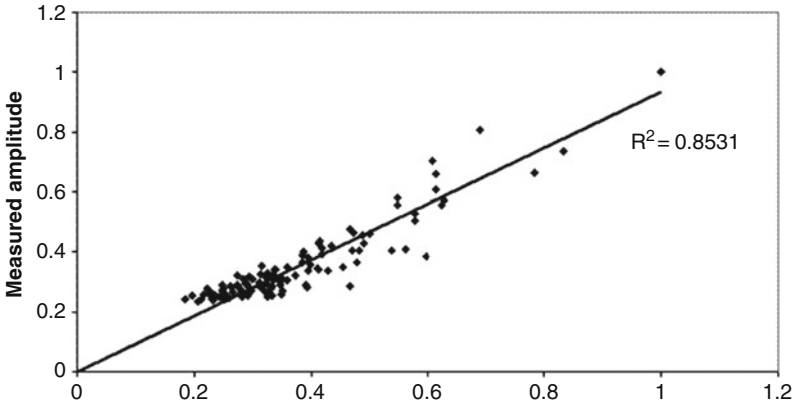

Fig. 26.7 Plot of measured amplitudes versus multislice calculations for the optimum thickness shown in Fig. 26.6

26.9 Summary

For certain PED has emerged as a powerful tool for solving structures. The intensities are much better behaved than those from zone-axis diffraction particularly if larger tilt angles are used. Unfortunately most simple models to date fail to explain fully the dynamical diffraction effects in enough detail so one has to do a full calculation.

Fortunately the PED intensities are not chaotic, but are ordered which is enough for direct methods to work and there is now extensive empirical evidence showing that this approach can be used to obtain an initial structure for later refinement either (or both) from powder x-ray data or by using a dynamical approach.

What remains as a problem is how to refine the structure, or perform structure completion – in most respects the later is a more significant issue as structure completion is in many respects why direct methods work. The large R1 values with kinematical models are problematic. In principle one might be able to use a two-beam model as an improvement upon kinematical in a refinement as implied by an initial estimate [26] and one can use it to approximately invert a set of intensity data. This might be a viable refinement approach as it would be faster than a full dynamical method, and this is currently under investigation.

There are also other alternatives. For instance, some time ago it was suggested by Peng [68] that one could use a quasi-kinematical approach, an idea that may well be worth returning to. Alternatively there are ways to exploit the implicit periodicity in reciprocal space (Brillouin Zone folding) so rather than calculating 1,024 different tilts a much smaller number of Bloch wave calculations is needed, perhaps only 1 if chosen judiciously or at most 8 [47]. This could give a 10^3 improvement in speed and might make a Bloch wave refinement viable on a reasonable computer; full

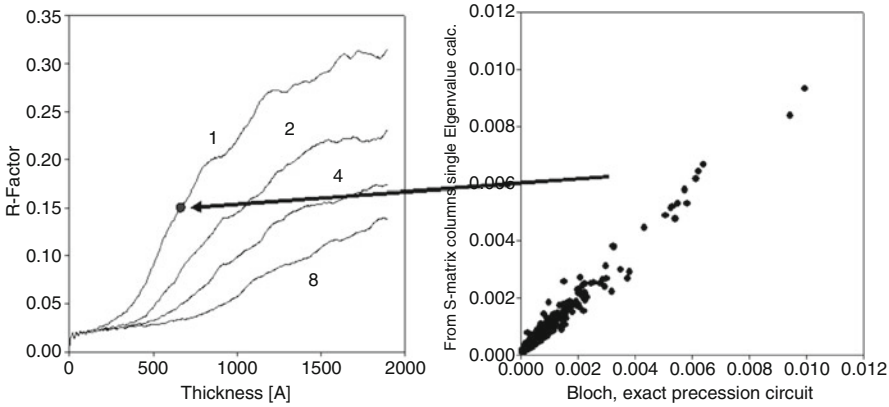

Fig. 26.8 Plot the R1 for $(Ga,In)_2SnO_4$ using a limited number of tilts exploiting Brillouin-Zone folding for different thicknesses relative to a full calculation (*left*) with a scatter plot of the intensities on the *right* for one Bloch-wave as *arrowed*

refinements will be unrealistically slow if all points are used. This is illustrated in Fig. 26.8 below which compares the results of an accurate Bloch wave calculation with 1,024 tilts to a much smaller set.

Despite these limitations, PED has moved from the early days when it was a curiosity to a mainstream tool for electron microscopists to use to determine structures where real-space imaging methods are problematic, for instance when there is beam damage or ambiguities in the interpretation of the images. Even with its current limitations the R1 values obtained are in most cases rather better than one can obtain with alternative approaches.

References

1. Vincent R, Midgley PA (1994) Double conical beam-rocking system for measurement of integrated electron diffraction intensities. Ultramicroscopy 53:271–282
2. Gjonnes K (1997) On the integration of electron diffraction intensities in the Vincent-Midgley precession technique. Ultramicroscopy 69:1–11
3. Berg BS, Hansen V, Midgley PA, Gjonnes J (1998) Measurement of three-dimensional intensity data in electron diffraction by the precession technique. Ultramicroscopy 74:147–157
4. Gjonnes J, Hansen V, Berg BS, Runde P, Cheng YF, Gjonnes K, Dorset DL, Gilmore CJ (1998) Structure model for the phase Al_mFe derived from three-dimensional electron diffraction intensity data collected by a precession technique. Comparison with convergent-beam diffraction. Acta Crystallogr Sect A 54:306–319
5. Gjonnes K, Cheng YF, Berg BS, Hansen V (1998) Corrections for multiple scattering in integrated electron diffraction intensities. Application to determination of structure factors in the [001] projection of Al_mFe. Acta Crystallogr Sect A 54:102–119
6. Midgley PA, Sleight ME, Saunders M, Vincent R (1998) Measurement of Debye-Waller factors by electron precession. Ultramicroscopy 75:61–67

7. Gemmi M, Zou X, Hovmöller S, Migliori A, Vennström M, Andersson Y (2002) Structure of Ti_2P solved by three-dimensional electron diffraction data collected with the precession technique and high-resolution electron microscopy. Acta Crystallogr Sect A 59:117–126
8. Gjonnes J, Hansen V, Kverneland A (2004) The precession technique in electron diffraction and its application to structure determination of nano-size precipitates in alloys. Microsc Microanal 10:16–20
9. Own CS (2005) System design and verification of the precession electron diffraction technique. Northwestern, Evanston
10. Own CS, Marks LD, Sinkler W (2005) Electron precession: a guide for implementation. Rev Sci Instrum 76:1866612
11. Kverneland A, Hansen V, Vincent R, Gjonnes K, Gjonnes J (2006) Structure analysis of embedded nano-sized particles by precession electron diffraction. η'-precipitate in an Al-Zn-Mg alloy as example. Ultramicroscopy 106:492–502
12. Own CS, Marks LD, Sinkler W (2006) Precession electron diffraction 1: multislice simulation. Acta Crystallogr Sect A 62:434–443
13. Own CS, Sinkler W, Marks LD (2006) Rapid structure determination of a metal oxide from pseudo-kinematical electron diffraction data. Ultramicroscopy 106:114–122
14. Weirich TE, Portillo J, Cox G, Hibst H, Nicolopoulos S (2006) Ab initio determination of the framework structure of the heavy-metal oxide CsxNb2.54W2.46O14 from 100 kV precession electron diffraction data. Ultramicroscopy 106:164–175
15. Boulahya K, Ruiz-Gonzalez L, Parras M, Gonzalez-Calbet JM, Nickolsky MS, Nicolopoulos S (2007) Ab initio determination of heavy oxide perovskite related structures from precession electron diffraction data. Ultramicroscopy 107:445–452
16. Avilov A, Kuligin K, Nicolopoulos S, Nickolskiy MS, Boulahya K, Portillo J, Lepeshov G, Sobolev B, Collette JP, Martin N, Robins AC, Fischione P (2007) Precession technique and electron diffractometry as new tools for crystal structure analysis and chemical bonding determination. Ultramicroscopy 107:431–444
17. Dudka AP, Avilov AS, Nicolopoulos S (2007) Crystal structure refinement using Bloch-wave method for precession electron diffraction. Ultramicroscopy 107:474–482
18. Gemmi M, Nicolopoulos S (2007) Structure solution with three-dimensional sets of precessed electron diffraction intensities. Ultramicroscopy 107:483–494
19. Morniroli JP, Redjaimia A (2007) Electron precession microdiffraction as a useful tool for the identification of the space group. J Microsc-Oxf 227:157–171
20. Morniroli JP, Redjaimia A, Nicolopoulos S (2007) Contribution of electron precession to the identification of the space group from microdiffraction patterns. Ultramicroscopy 107:514–522
21. Nicolopoulos S, Morniroli JP, Gemmi M (2007) From powder diffraction to structure resolution of nanocrystals by precession electron diffraction. Z Kristallogr 26:183–188
22. Oleynikov P, Hovmoller S, Zou XD (2007) Precession electron diffraction: observed and calculated intensities. Ultramicroscopy 107:523–533
23. Own CS, Dellby N, Krivanek OL, Marks LD, Murfitt M (2007) Aberration-corrected precession electron diffraction. Microsc Microanal 13:96–97
24. Own CS, Sinkler W, Marks LD (2007) Prospects for aberration corrected electron precession. Ultramicroscopy 107:534–542
25. Sinkler W, Own CS, Ciston J, Marks LD (2007) Statistical treatment of precession electron diffraction data with principal components analysis. Microsc Microanal 13:954–955
26. Sinkler W, Own CS, Marks LD (2007) Application of a 2-beam model for improving the structure factors from precession electron diffraction intensities. Ultramicroscopy 107:543–550
27. Ciston J, Deng B, Marks LD, Own CS, Sinkler W (2008) A quantitative analysis of the cone-angle dependence in precession electron diffraction. Ultramicroscopy 108:514–522
28. Ciston J, Own CS, Marks LD (2008) Cone-angle dependence of ab-initio structure solutions using precession electron diffraction. Electron Microsc Multiscale Model 999:53–65
29. Morniroli JP, Auchterlonie GJ, Drennan J, Zou J (2008) Contribution of electron precession to the study of perovskites displaying small symmetry departures from the ideal cubic ABO(3) perovskite: applications to the LaGaO3 and LSGM perovskites. J Microsc-Oxf 232:7–26

30. Morniroli JP, Houdellier F, Roucau C, Puiggali J, Gesti S, Redjaimia A (2008) LACDIF, a new electron diffraction technique obtained with the LACBED configuration and a Cs-corrector: comparison with electron precession. Ultramicroscopy 108:100–115
31. Rauch EF, Veron M, Portillo J, Bultreys D, Maniette Y, Nicolopoulos S (2008) Automatic crystal orientation and phase mapping in TEM by precession diffraction. Microsc Anal Nanotechnol Suppl 22:S5–S8
32. Xie D, Baerlocher C, McCusker LB (2008) Combining precession electron diffraction data with X-ray powder diffraction data to facilitate structure solution. J Appl Crystallogr 41:1115–1121
33. Boullay P, Dorcet V, Perez O, Grygiel C, Prellier W, Mercey B, Hervieu M (2009) Structure determination of a brownmillerite $Ca_2Co_2O_5$ thin film by precession electron diffraction. Phys Rev B 79:184108
34. Jacob D, Cordier P, Morniroli JP, Schertl HP (2009) Application of precession electron diffraction to the characterization of (021) twinning in pseudo-hexagonal coesite. Am Mineral 94:684–692
35. Ji G, Morniroli JP, Auchterlonie GJ, Drennan J, Jacob D (2009) An efficient approach to characterize pseudo-merohedral twins by precession electron diffraction: application to the LaGaO3 perovskite. Ultramicroscopy 109:1282–1294
36. Morniroli JP, Ji G (2009) Identification of the kinematical forbidden reflections from precession electron diffraction. In: Moeck P, Hovmoller S, Nicolopoulos S, Rouvimov S, Petkov V, Gateshki M, Fraundorf P (eds) Electron crystallography for materials research and quantitative characterization of nanostructured materials. Materials Research Society, Warrendale
37. Mugnaioli E, Gorelik T, Kolb U (2009) "Ab initio" structure solution from electron diffraction data obtained by a combination of automated diffraction tomography and precession technique. Ultramicroscopy 109:758–765
38. Barnard JS, Eggeman AS, Sharp J, White TA, Midgley PA (2010) Dislocation electron tomography and precession electron diffraction – minimising the effects of dynamical interactions in real and reciprocal space. Philos Mag 90:4711–4730
39. Cascarano GL, Giacovazzo C, Carrozzini B (2010) Crystal structure solution via precession electron diffraction data: the BEA algorithm. Ultramicroscopy 111:56–61
40. Eggeman AS, White TA, Midgley PA (2010) Is precession electron diffraction kinematical? Part II A practical method to determine the optimum precession angle. Ultramicroscopy 110:771–777
41. Gemmi M, Klein H, Rageau A, Strobel P, Le Cras F (2010) Structure solution of the new titanate $Li_4Ti_8Ni_3O_{21}$ using precession electron diffraction. Acta Crystallogr Sect B 66:60–68
42. Hadermann J, Abakumov AM, Tsirlin AA, Filonenko VP, Gonnissen J, Tan HY, Verbeeck J, Gemmi M, Antipov EV, Rosner H (2010) Direct space structure solution from precession electron diffraction data: resolving heavy and light scatterers in $Pb_{13}Mn_9O_{25}$. Ultramicroscopy 110:881–890
43. Jacob D, Cordier P (2010) A precession electron diffraction study of α, β phases and Dauphine twin in quartz. Ultramicroscopy 110:1166–1177
44. Ji G, Jacob D, Morniroli JP (2010) The state of order in Fe-Al studied by precession electron diffraction. Philos Mag Lett 91:54–60
45. Moeck P, Rouvimov S (2010) Precession electron diffraction and its advantages for structural fingerprinting in the transmission electron microscope. Z Kristallogr 225:110–124
46. Rauch EF, Portillo J, Nicolopoulos S, Bultreys D, Rouvimov S, Moeck P (2010) Automated nanocrystal orientation and phase mapping in the transmission electron microscope on the basis of precession electron diffraction. Z Kristallogr 225:103–109
47. Sinkler W, Marks LD (2010) Characteristics of precession electron diffraction intensities from dynamical simulations. Z Kristallogr 225:47–55
48. White TA, Eggeman AS, Midgley PA (2010) Is precession electron diffraction kinematical? Part I: "Phase-scrambling" multislice simulations. Ultramicroscopy 110:763–770
49. Zhang DL, Gruner D, Oleynikov P, Wan W, Hovmoller S, Zou XD (2010) Precession electron diffraction using a digital sampling method. Ultramicroscopy 111:47–55

50. Klein H, David J (2011) The quality of precession electron diffraction data is higher than necessary for structure solution of unknown crystalline phases. Acta Crystallogr Sect A 67:297–302
51. Blackman M (1939) On the intensities of electron diffraction rings. Proc R Soc A 173:68–82
52. Gjønnes K, Cheng YF, Berg BS, Hansen V (1998) Corrections for multiple scattering in integrated electron diffraction intensities. Application to determination of structure factors in the [001] projection of Al_mFe. Acta Crystallogr Sect A 54:102–119
53. Lindhard J (1964) Motion of swift charged particles, as influenced by strings of atoms in crystals. Phys Lett 12:126–128
54. Gemmell DS (1974) Channelling and related effects in the motion of charged particles through crystals. Rev Mod Phys 46:129–227
55. Kambe K, Lehmpfuhl G, Fujimoto F (1974) Interpretation of electron channeling by the dynamical theory of electron diffraction. Z Naturforsch 29:1034–1044
56. Tamura A, Ohtsuki YH (1974) Quantum mechanical study of rosette motion channeling. Phys Status Solidi B 62:477–480
57. Geuens P, Van Dyck D (2002) The S-state model: a work horse for HRTEM. Ultramicroscopy 93:179–198
58. Hu JJ, Chukhovskii FN, Marks LD (2000) Statistical dynamical direct methods I. The effective kinematical approximation. Acta Crystallogr Sect A 56:458–469
59. Chukhovskii FN, Hu JJ, Marks LD (2001) Statistical dynamical direct methods II. The three-phase structure invariant. Acta Crystallogr Sect A 57:231–239
60. Cowley JM, Moodie AF (1957) The scattering of electrons by atoms and crystals I. A new theoretical approach. Acta Crystallogr 10:609–619
61. O'Keefe M (1973) n-Beam lattice images IV. Computed two-dimensional images. Acta Crystallogr Sect A 29:389–401
62. Ishizuka K (1982) Multislice formula for inclined illumination. Acta Crystallogr Sect A 38:773–779
63. Ishizuka K (2004) FFT multislice method – the silver anniversary. Microsc Microanal 10:34–40
64. Humphreys CJ (1979) The scattering of fast electrons by crystals. Rep Prog Phys 42:1825–1887
65. Spence JCH, Zuo JM (1992) Electron microdiffraction. Plenum Press, New York
66. Allen LJ, Josefsson TW, Leeb H (1998) Obtaining the crystal potential by inversion from electron scattering intensities. Acta Crystallogr Sect A 54:388–398
67. Marks LD, Sinkler W (2003) Sufficient conditions for direct methods with swift electrons. Microsc Microanal 9:399–410
68. Peng L-M (2000) Quasi-dynamical electron diffraction – a kinematic type of expression for the dynamical diffracted-beam amplitudes. Acta Crystallogr Sect A 56:511–518

Chapter 27
Structure Solution Using HRTEM

Sven Hovmöller

Abstract Electron microscopy is the only method known today that allows us to directly see the atoms in a sample. Compared to X-ray crystallography, crystals billions of times smaller can be studied by electron crystallography. The fundamental difference between (electron microscopy) images and diffraction patterns is explained. Images have a one-to-one relation to each point in the object. This is not the case for diffraction patterns, where each point comes from all points in the sample. The crystallographic structure factor phases that are necessary to know in order to solve a crystal structure, can be read out numerically directly from the Fourier transform of an image, but not from diffraction patterns.

27.1 Introduction

All materials and compounds are made up of atoms. The 3D arrangement of these atoms determines the properties of everything, ranging from simple inorganic salts to biological macromolecules. Therefore it is of fundamental importance to be able to determine the atomic arrangement with high accuracy. Mankind has speculated about what the inner structure of matter was, for thousands of years. It would take until exactly 100 years ago, until the dream of revealing the inner secrets of matter was fulfilled.

It was in 1912 that father and son Bragg invented X-ray crystallography and solved the structures of NaCl and other inorganic compounds. During the following century, X-ray crystallography has evolved in a spectacular way and has been used for solving hundreds of thousands of structures, up to the complexity of viruses.

S. Hovmöller (✉)
Structural Chemistry, MMK, Stockholm University, SE-10691 Stockholm, Sweden
e-mail: sven.hovmoller@mmk.su.se

U. Kolb et al. (eds.), *Uniting Electron Crystallography and Powder Diffraction*,
NATO Science for Peace and Security Series B: Physics and Biophysics,
DOI 10.1007/978-94-007-5580-2_27,

With such a fantastic method at hand, one may wonder if it is worth while to compete, using electron crystallography. There is one good reason for this: X-rays interact so weakly with matter that it can only be used for compounds that form perfect crystals with about 10^{12}–10^{15} unit cells. Electrons interact about a million times stronger with matter than X-rays do and thus become the alternative for very small crystals. X-rays cannot in practice be focussed into images with atomic resolution, so only diffraction patterns are available. Electrons, on the other hand, can be focused into images. Electron microscope lenses have been improved over the years; they have today reached atomic resolution. Electron microscopy can be used both for crystal structure determination and for looking at non-crystalline features, including defects, grain boundaries and so on, even down to individual atoms [1].

The downside of the strong interaction of electrons with matter is that the electrons can scatter more than once on their way through the sample, even if it is only a few nanometres thick. This can make the interpretation difficult or even impossible. Another difficulty is the dramatic change of appearance of an EM image with even slight changes of focus. Unlike the multiple scattering, the focus effects are rather easy to determine and compensate for, as shown below. In summary, electron diffraction and electron microscopy are two powerful techniques for studying the atomic arrangements in crystals and in non-crystalline materials. Here we will only deal with crystals, but what is said, especially about the effects of focus, holds for any kind of specimen.

27.2 Phase Information Is Present in EM Images

There is a fundamental difference between an image and its diffraction pattern. In an image, you see directly the object. Mathematically, an image should have a one-to-one relation from a point in the object to a point in the image. An image is not the same thing as the object and it may have suffered from distortions. For one thing, the object may be in colour but the image only black and white. Most objects are 3-dimensional while almost all images are 2-dimensional. In microscopy, the images are much larger than the objects. In electron microscopy, the magnification may be as large as one million, allowing us to see individual atoms. Always when you have lenses, there will be a number of more or less serious distortions. Theses distortions can be minimized to some degree by special hardware and they may be compensated for by software (image processing).

A diffraction pattern is a different matter altogether. It does not give a one-to-one relation from the image to the diffraction pattern. In fact, every single point in a diffraction pattern carries information from all the points in the object. A diffraction pattern is a frequency spectrum of the object. Large features (low resolution) appear near the center of the diffraction pattern. Small details, such as atoms, contribute to the high resolution part, far away from the center of the diffraction pattern.

The most important difference between an image and a diffraction pattern is that the crystallographic structure factor phase is present in images but lost in diffraction patterns. Thus, there is a phase problem for diffraction data, but not for images. This phase problem is well known in crystallography and the X-ray crystallographers have developed many ways to solve the phase problem, including Patterson, direct methods, charge flipping and others that you will read about in this book. The easiest way to understand the phase problem (and many more things) in crystallography is via electron crystallography. That is because in the electron microscope you can get *both* an enlarged image of your crystal and the diffraction pattern. While an electron diffraction pattern looks very similar to the (precession) X-ray diffraction pattern of the same crystal, the EM image is a different matter! An EM image can be an enlargement of a million times, and then individual atoms are seen. This works for inorganic materials, such as metal oxides, that can resist the high electron dose. For proteins it is harder, but taking great care you can still get (almost) atomic resolution EM images also from proteins. If you now calculate the Fourier transform (FT) of an EM image, it will look just like the diffraction pattern, although the spots in the FT don't go so far out from the center.

Now to the phases: An image of a crystal is a sum of several sets of lines (black/white/black . . .) in all directions. Crystallographers would say these lines are projected Bragg planes. Each such set of lines gives rise to just a single spot (and its Friedel pair) in the diffraction pattern. From the position of that spot, you know the direction and spacing of the Bragg plane. If the spot is strong it means this set of black/white lines are strong (high amplitude). But – you don't know how all these sets of lines are positioned, relative to each other. That is the phase problem in crystallography. In an EM image, on the other hand, you see the fringes and when you calculate the Fourier transform of the EM image, you get also the phases! Numerically in degrees – just read out from the FT! This was first realized by Aaron Klug at the MRC in Cambridge around 1965 and he got the Nobel Prize for this (and more) in 1982.

In Fig. 27.1 below, you can see some of the structure factors that together make up the crystal structure, superimposed on the crystal structure. In Fig. 27.2 you see the EM image from which this structure was solved, as well as its Fourier transform and the sum of just these six structure factors shown in Fig. 27.1.

In order to solve a crystal structure from HRTEM images, we need to determine the crystallographic structure factor phases and amplitudes of sufficiently many reflections with sufficient accuracy. We must also recognize that all chemical structures are 3-dimensional, but a single EM image is always just a 2D projection. Only in some special structures with a very short ($\sim$4 Å) unit cell dimension, is it possible to determine the crystal structure from a single projection, along that short axis. This is the case for the example above. For larger unit cells, it becomes necessary to take EM-images from several different orientations; along all the three crystallographic axes and even among several diagonals for the most complex (=large) structures.

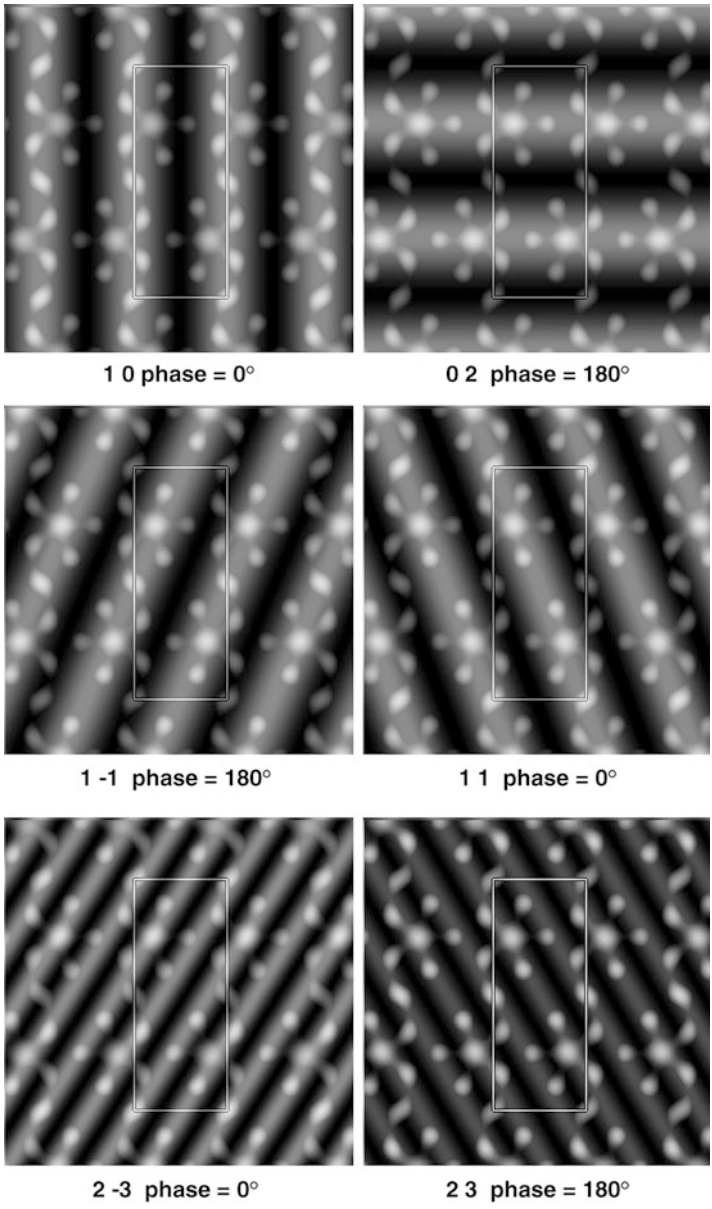

Fig. 27.1 The structure of a metal oxide $K_7Nb_{15}W_{13}O_{80}$ [2] superimposed on various structure factors. The *white dots* are the metal atoms. Each set of *white/black waves* is a structure factor. *White* stands for high electrostatic potential and so coincides with most (but not necessarily all) of the atoms. Low index structure factors (*top*) give low resolution contributions, whereas the higher indices (*bottom*) give high resolution, eventually reaching atomic resolution. This structure is centrosymmetric, so all phases have to be 0° or 180°. If the wave has its maximum (*white*) at the origin of the unit cell, its phase is 0°, since in crystallography we talk only about cosine functions and a cosine has its maximum at 0°. The sum of these six structure factors is not sufficient to create an interpretable map (see Fig. 27.2d) – another ten are needed for that [3]

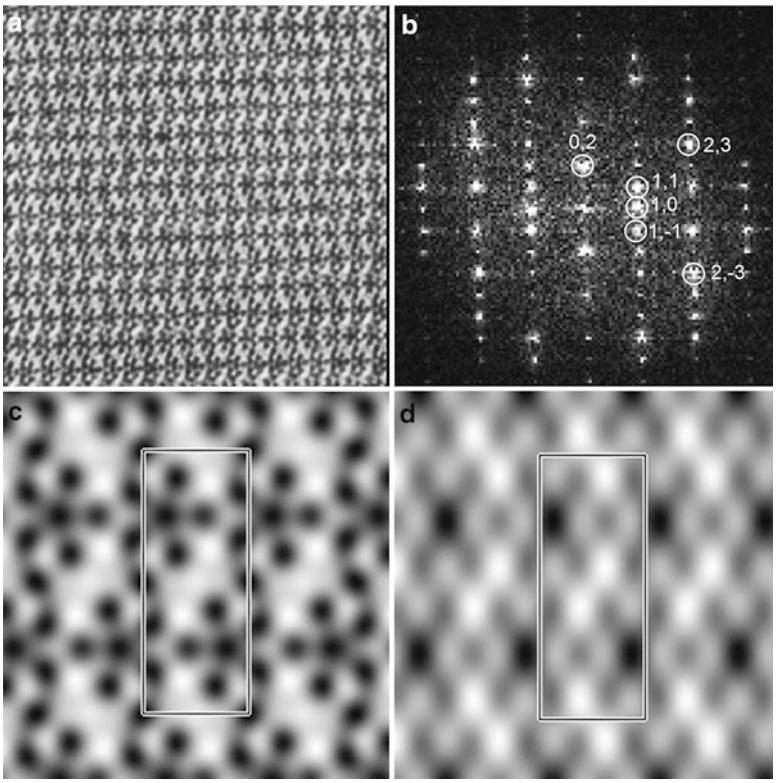

Fig. 27.2 (**a**) HRTEM image of K7Nb15W13O80 and (**b**) its Fourier transform, with the six reflections shown in Fig. 27.1 marked. In (**c**) all the 35 reflections seen in (**b**) have been used to reconstruct a very clear image of the atomic structure, while in (**d**) the reconstruction based only on those six reflections marked in (**b**) (and their Friedel mates) is not quite enough to give a clear image of the crystal structure

27.3 Importance of Amplitudes and Phases

Experimental data is always imperfect. It is important to know what the minimum quality required for atomic resolution is. We can discuss this in three parts; how many reflections do we need and how accurate must the amplitudes and phases be? The phases are more important than the amplitudes. Amplitudes extracted from HRTEM images typically are accurate only $\pm 20\%$ or so. This is much poorer than amplitudes obtained by X-ray crystallography, but that is compensated by the fact that phases are available from EM images, which is not the case for X-ray diffraction patterns. The phases are typically accurate to within about 20–30°, which is very good.

27.4 Symmetry Determination from HRTEM Images

Symmetry is fundamentally important in crystallography. In 3D there are 230 space groups, but when these are projected onto a plane (as in an EM image) there are only 17 plane groups. These are characterized by the unit cell dimensions and, more importantly, by amplitude and phase relations between symmetry-related reflections. In the image processing system CRISP [4], these relationships are tested for every image and the closeness to each of the 17 plane groups are reported in numerical form. Most plane groups are centrosymmetric, which forces all phases to be restricted to either 0° or 180°. This makes it very easy in most cases to assign the correct phase, given that the phase errors are typically less than 30°. Once the correct plane group symmetry is found, amplitudes and phases consistent with that symmetry will be imposed, resulting in clear images, as seen in Fig. 27.2c.

The number of reflections that are needed for solving a structure, and those that are available experimentally from HRTEM images, is best described with the term resolution. The resolution of a reflection is the d-value of that reflection. It can easily be calculated from its *h, k*-index and the unit cell dimensions. For example, in the structure discussed here, the unit cell dimensions are 9×21 Å. The *1 0* reflection has a d-value of 9 Å, while the *0 2* reflection has a d-value of 10.5 Å as shown in Fig. 27.3. In this case, we are not able see oxygen atoms (O), so only the metal atoms (Me = W or Nb) can be determined. The Me-O distances are ∼1.9 Å, while the Me-Me distances are ∼2.7 Å. In order to see the metal atoms, we will then

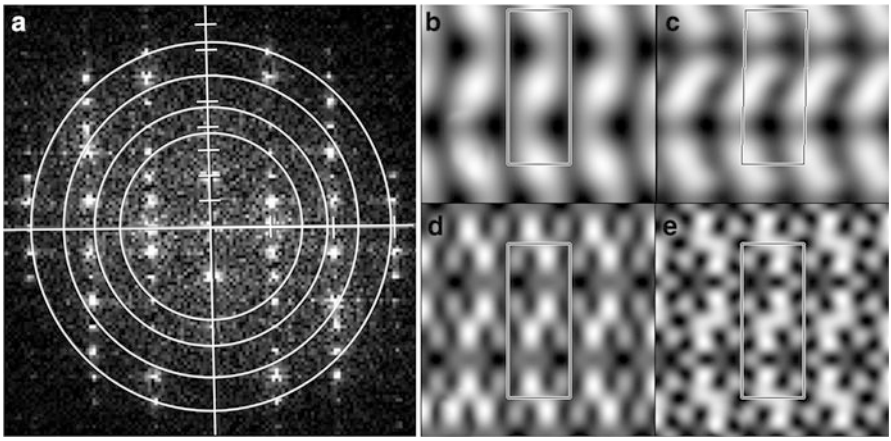

Fig. 27.3 The effect of resolution. (**a**) From the Fourier transform of the EM image seen in Fig. 27.2a, different resolution limits have been applied. These are seen as *white circles*. The innermost ring corresponds to 6 Å resolution. The next rings are at 5 Å, 3.5 Å and the largest ring is at 3.0 Å resolution, respectively. As the resolution is increased, more and more reflections are included and so the resulting image gets more and more detailed, as seen in (**b**) to (**e**), corresponding to the four resolution ranges. At 2.5 Å resolution, all reflections are used, given the result seen in Fig. 27.2c

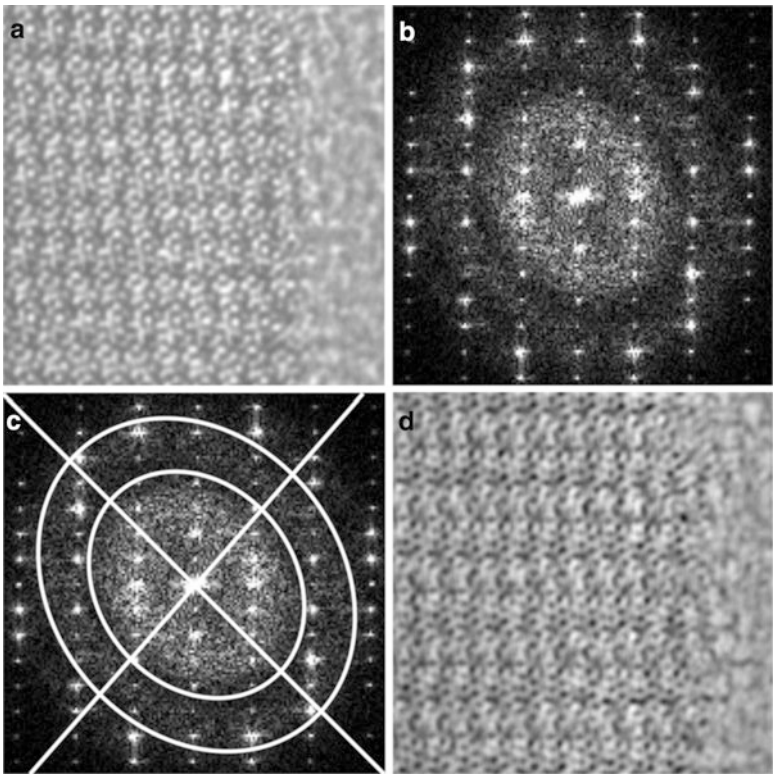

Fig. 27.4 (**a**) An HRTEM image of the same crystal as in Figs. 27.2 and 27.3, but taken away from Scherzer focus. This image cannot be interpreted directly. This is because all reflections between the first and second ring (or *ellipse* rather) seen in the FT (**b**) are reversed. Using the image processing program CRISP, these *ellipses* are marked in (**c**) and the program then switches the phases of those reflections by 180° (simply by multiplying by −1). When the inverse Fourier transform of this corrected data is calculated as in (**d**), the metal atoms become visible as *dark spots*

expect it necessary to have (good) data to ∼2.7 Å. That level of resolution became available in HRTEM instruments in the 1970s, which marked a revolution in terms of EM studies on metal oxides.

27.5 Determining the Focus and Compensating for Defocus Effects

In summary, for metal oxides, taken along a short (∼4 Å) unit cell direction, we can solve the atomic structure directly from a single HRTEM image. But this works only if the image was taken near the so-called Scherzer focus. As we shall see, it is also

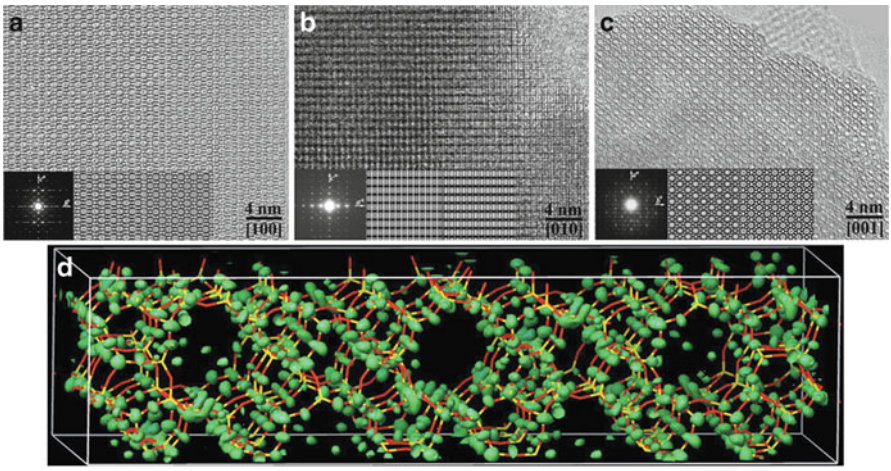

Fig. 27.5 High-resolution transmission-electron-microscopy images taken along different zone axes of IM-5. (**a**) [100], (**b**) [001] and (**c**) [010]. Shown as insets are the corresponding ED pattern (*left*), the CTF-corrected and symmetry-averaged image (*middle*), and the computer simulation from the structural model (*right*). (**d**) The final three-dimensional density map (*in green*) with a stick model of the final structure of IM-5 (Si atoms *yellow*, O atoms *red*) superimposed for comparison [3] (color figure online)

possible to solve the structure if a totally different focus is used, but then we must compensate for the effects of the focus. This is manifested in the Contrast Transfer Function, CTF, as shown in Fig. 27.4.

Notice that the amplitude and phase data are distorted as the focus is changed, but this distortion is easily determined from looking at the black rings (so-called Thon rings) in the Fourier transform. It can also easily be corrected for, as shown in Fig. 27.4. If the image was astigmatic, like in this case, the Thon rings turn into ellipses, but that can equally easily be corrected for. Unfortunately, the effects of the multiple scattering that occurs if the sample is not infinitely thin, cannot be compensated for in a similar straight-forward procedure. The best thing to do is therefore to try very hard to find the thinnest areas for HRTEM images.

27.6 From 2D to 3D Structure

For more complex structures, with all unit cell dimensions >6–8 Å or so, there is no single projection that can reveal all atoms without overlap. Then it becomes necessary to take several projections and add them all up in a crystallographic program that allows 3D data. Several such structures, including complex metal alloys [5] and zeolites [6] have been solved.

In order to combine several 2D projections into one 3D map, all the images have to be on the same origin. For the zeolite IM-5 shown in Fig. 27.5, it was enough to use the three projections along each of the crystallographic axes. For the AlCrFe alloy [2] several diagonal projections had to be included.

In summary, HRTEM is a powerful method for solving crystal structures. It becomes even more powerful when it is combined with image processing techniques, since they are capable of improving the experimental amplitude and phase data.

References

1. Zou XD, Hovmöller S (2008) Electron crystallography: imaging and single crystal diffraction from powders. Acta Crystallogr A 64:149–160
2. Hovmöller S, Sjögren A, Farrants G, Sundberg M, Marinder BO (1984) Accurate atomic positions from electron microscopy. Nature 311:238–241
3. Zou XD, Hovmöller S, Oleynikov P (2011) Electron crystallography – electron microscopy and electron diffraction. Oxford University Press, New York
4. Hovmöller S (1992) CRISP – crystallographic image processing on a personal computer. Ultramicroscopy 41:121–135
5. Zou XD, Mo ZM, Hovmöller S, Li XZ, Kuo K (2003) Three dimensional reconstruction of the v-AlCrFe phase by electron crystallography. Acta Crystallogr A 59:526–539
6. Baerlocher C, Gramm F, Massüger L, McCusker LB, He ZB, Hovmöller S, Zou XD (2007) Structure of the polycrystalline zeolite catalyst IM-5 solved by enhanced charge flipping. Science 315:1113–1116

Chapter 28
Combination of X-ray Powder Diffraction, Electron Diffraction and HRTEM Data

Christian Baerlocher and Lynne B. McCusker

Abstract A combination of X-ray and electron scattering data can facilitate structure analysis of polycrystalline materials that are problematic to study by conventional methods. Different electron diffraction data collection techniques as well as high-resolution imaging are described. A number of diverse algorithms of data combination and their applications to structural analysis of several materials systems are provided.

28.1 Introduction

X-ray powder diffraction and electron microscopy are probably the two most useful techniques for analyzing the structures of polycrystalline materials. While it is relatively easy to measure an X-ray powder diffraction pattern, a detailed interpretation of the data is not always straightforward because of the well known overlap of reflections with similar diffractions angles. This hinders structure elucidation by conventional (single-crystal) crystallographic methods, because the algorithms assume that the intensities are reliable. However, a wide variety of approaches have now been developed to deal with this overlap problem, and structures of moderate complexity can now be solved from powder diffraction data in an almost routine manner [1].

With an electron microscope, on the other hand, very tiny crystals (<100 nm) can be examined individually, because electrons interact much more strongly with matter than do X-rays. Furthermore, because electrons can be focussed easily, both diffraction patterns and high-resolution images can be obtained. These obvious advantages are offset by the fact that the operation of an electron microscope requires

C. Baerlocher (✉) • L.B. McCusker
Laboratory of Crystallography, ETH Zurich, Zurich, Switzerland
e-mail: Ch.Baerlocher@mat.ethz.ch; lynne.mccusker@mat.ethz.ch

U. Kolb et al. (eds.), *Uniting Electron Crystallography and Powder Diffraction*,
NATO Science for Peace and Security Series B: Physics and Biophysics,
DOI 10.1007/978-94-007-5580-2_28,

Table 28.1 Comparison of X-ray powder and electron diffraction data

	X-ray powder	Electron
Data collection	Easy	Difficult
Data set	Complete (up to $2\theta_{max}$)	Incomplete
Lattice parameters	Precise	Approximate
Intensities	Kinematic	Dynamical
Multiple diffraction	No	Yes
Systematic absences	Difficult	Easy
Crystallite size	μm	nm
Reflection overlap	Yes	No
Phase information	No	Yes (from HRTEM images)

considerable expertise and the measured diffraction intensities are distorted by a number of effects that are not easy to control or correct for. Nonetheless, electron crystallography has been applied successfully to various classes of materials (e.g. [2, 3], U. Kolb, this school).

These two techniques are remarkably complementary (see Table 28.1), and over the last few years, several ways of combining them have been developed to address structures that cannot be solved by either method alone. In this lecture, the relevant features of the two techniques, the algorithms used to combine the different kinds of data, and some recent examples taken from the world of zeolite structures are described.

28.2 Structure Determination from Powder Diffraction and Electron Microscopy Data

28.2.1 Powder Diffraction

As mentioned above, the main limitation of X-ray powder diffraction data is reflection overlap. In most cases, the total intensity measured for a group of overlapping reflections is simply equipartitioned over the contributing reflections. The problem can be reduced by collecting high-resolution data at a synchrotron facility, but it cannot be eliminated. It was soon recognized that single crystal methods could not be applied for diffraction patterns with severe overlap and alternative approaches would be required. Supplementing the powder diffraction data with chemical information (known bond distances and angles, coordination numbers, connectivity, etc.) was found to be a particularly effective approach [1]. This resulted in a number of automated model-building programs based on global optimization algorithms. While direct methods operate in reciprocal space (i.e. with reflection intensities and phases), the global optimization algorithms work in direct space. For more detailed information, the reader is referred to the book *Structure Determination from Powder Diffraction Data* [4], the special issue of *Z. Kristallogr.* devoted to the same topic [5] and of course to the lectures of this school.

A few algorithms, such as the shake-and-bake modification to direct methods [6], the charge-flipping algorithm that was introduced only recently [7], and the zeolite-specific program *Focus* [8], alternate between the two spaces and can therefore benefit from the individual strengths of both. On particular idea that can be used in this respect is the concept of a structure envelope [9]. A structure envelope defines regions within the unit cell that are most likely to contain atoms, and can be generated from just a few strong, low-index reflections [10].

28.2.2 Electron Microscopy

All aspects of electron crystallography are of course extensively covered in the workshop on that topic. For the benefit of the "powder people" the problems and techniques relevant for this lecture are briefly mentioned here. Whereas the main problem with powder diffraction data is the reflection overlap, the main problem of electron diffraction is the strong interaction of the electron beam with the crystal. As a consequence the diffracted beams are also strong and can, in turn act as incident beams. Thus, the interaction between the incident beam and the crystal cannot be treated as a single-scattering event for each reflection as it is for X-rays (kinematical approximation). The thicker the sample, the more severe is this effect.

28.2.2.1 Selected Area Electron Diffraction (SAED)

If the crystal in the electron beam is thin enough (∼50 nm or less), however, the dynamical effects are minimized and the diffraction intensities measured using a conventional selected area electron diffraction (SAED) technique can be treated as quasi-kinematical. In a typical SAED pattern, the incident beam is generally aligned along a zone axis, and the complete zero-order diffraction pattern for that zone (zero order Laue zone or ZOLZ) can be recorded out to a resolution of less than 1 Å in a single shot. However, because many reflections are excited simultaneously, multiple scattering effects can be severe, and the measured intensities are not very reliable.

28.2.2.2 Precession Electron Diffraction (PED)

In 1994, Vincent and Midgley [11] introduced the precession electron diffraction (PED) technique that partially solves this problem. The electron beam is deflected and then precessed around a stationary crystal, and with this tilted illumination, only a few reflections are excited at a time, so the possibilities for multiple scattering are reduced and the resulting diffraction intensities are more kinematical in nature. Although the PED intensities are still not ideal, they are significantly improved over typical SAED intensities [12], and have been used to solve several structures [13–16].

28.2.2.3 High-Resolution Transmission Electron Microscopy (HRTEM)

Because the electron beam can be focused, it is also possible to record a magnified image of the sample with an electron microscope. The advantages of having a high-resolution transmission electron microscope (HRTEM) image for structure analysis are twofold. First, the image shows approximately where the atoms are in that projection of the unit cell even if atomic resolution is not attained, so the validity of a structure envelope can be evaluated by eye. Second, the Fourier transform of the image yields a list of structure factor amplitudes *and* phases for the reflections in the corresponding diffraction pattern. Before the Fourier transform is performed, the image is usually lattice and symmetry averaged to obtain a clearer and defect-free image. Then a contrast-transfer-function (CTF) correction is applied, which allows for the modulation of the amplitudes and phases caused by various parameters of the microscope. Fourier transform of this modified image then generates the desired phase information. The crystallographic image processing software package *CRISP* [17] can be used to perform these calculations.

28.3 Dual-Space Structure Solution Algorithms

It was mentioned earlier that a few structure determination algorithms work in both reciprocal and direct space, so information from different sources can in principle be added in either realm. Such algorithms are particularly well-suited for combining data from different sources. In the last few years, two of them, *Focus* [8] and powder charge flipping *pCF* [18], which is implemented in the program *Superflip* [19], have been used successfully to combine X-ray powder diffraction and electron microscopy data.

28.3.1 Focus

Focus is a zeolite-specific structure-solution program that uses chemical information (real space) to compensate for the ambiguities in the reflection intensities (reciprocal space) extracted from a powder diffraction pattern. Structure factor amplitudes are calculated from the extracted intensities, and are then assigned starting phases (usually random). These are used to generate a (random) electron density map. The program then interprets the map and calculates a (partial) model. It is primarily in this interpretation step that the chemical information about zeolite framework structures is exploited (4-connected, 3-dimensional network of corner-sharing TO_4 tetrahedra, where T is any tetrahedrally coordinated atom such as Si or Al). If a framework model is found, it is classified and written to a file. When a sufficient number of frameworks have been found, a histogram is generated, and in general,

the framework found most frequently (from different starting phase sets) will be the correct one [20]. The algorithm has now been applied by many different laboratories with considerable success. Its only drawback is that it is specific to zeolites.

Until 2006, the germanosilicate ITQ-22 [21] had the most complex zeolite framework structure, so it was used to test the value of including some initial phases in the *Focus* input [22]. These tests showed that by prescribing the phases of just 31 of the 992 strongest reflections, the time required for structure solution could be reduced from 31 days to 44 h. Doubling the number of phases to 62 resulted in 17 solutions within 11 h. Obviously even a limited amount of phase information has a significant effect on the structure solution.

28.3.2 Powder Charge Flipping

In 2004, Oszlányi and Sütő introduced a more general algorithm for structure solution from single-crystal data, that they called charge flipping [23]. The details of this algorithm as applied to powder diffraction data is explained by L. Palatinus during this school. To start with, an electron density map is generated using random phases as in *Focus*, and therefore it is again simple to introduce already known phases in this step to help the solution process. How this and other combinations help this process is explained in the following chapters.

28.4 Combining X-ray Powder Diffraction Data with HRTEM Images

Data from high-resolution electron microscopy images can be supplied to the *Focus* and *pCF* algorithms in several different ways. For example, a structure envelope for a zeolite derived from one or more HRTEM images can be imposed in real space to limit the peak search in *Focus* or to set the electron density in the pore regions to zero in *pCF*. It is also possible to include all phases obtained from HRTEM images in the starting phase set in either program. Although it would be possible to keep these phases fixed, experience has shown that it is more prudent to allow them to change during the normal procedure, whether in *Focus* or *pCF*, to allow any incorrect phases to correct themselves. However, in *pCF*, it is critical that they be fixed for the initial 10–20% of the cycles if they are to be effective. A further option is to use an approximate or partial model that has been deduced from HRTEM images as a seed for generating sets of complete starting phase sets.

Different combinations of these options eventually led to the determination of the three most complex zeolite structures using powder diffraction data (TNU-9 [24], IM-5 [25] and SSZ-74 [26]). The relevant aspects of these structure solutions

are given in the following sections to illustrate the procedure. Although all three are zeolites, only the first was solved using the zeolite-specific program *Focus*. The more generally applicable *pCF* algorithm was used for the other two, and the concepts applied in all three cases should be readily transferable to non-zeolite materials.

28.4.1 TNU-9

The first true test of the value of including phases in the *Focus* input was performed in the structure solution of the high-silica zeolite TNU-9 [24]. It's high-resolution synchrotron powder diffraction pattern could be indexed (*C*2/*m*, $a = 28.2219$ Å, $b = 20.0123$ Å, $c = 19.4926$ Å, $\beta = 92.33°$), but there were a few unindexed peaks, so SAED data were used to confirm the unit cell. However, attempts to solve the structure with *Focus* using the powder diffraction data alone were not successful.

From three high-quality HRTEM images of TNU-9 (along the [010], [001] and [$\bar{1}$10] zone axes), the phases of 258 reflections were estimated using the *CRISP* software package. Only when these phases were included in the *Focus* input along with a structure envelope to describe the pore system, could the structure, with 24 Si and 52 O atoms in the asymmetric unit, be solved.

28.4.2 IM-5

In the case of IM-5 [25], another high-silica zeolite, a slightly different approach was used. As for TNU-9, impurities were present, so SAED experiments were performed to verify the unit cell (*Cmcm*, $a = 14.299$ Å, $b = 57.413$ Å and $c = 20.143$ Å).

Initially, the phases of 95 reflections were estimated from three HRTEM images (along the [100], [010] and [001] zone axes) and included in *pCF* runs, but the resulting electron density maps could not be interpreted on an atomic level. After careful corrections to the HRTEM images, a 3-dimensional potential map was generated in the space group *C*2*cm* and a model with 36 Si atoms in the asymmetric unit deduced. Although this structural model was geometrically strained and its calculated powder pattern did not fit the measured one very well, it was reasoned that it was probably at least partially correct (certainly more so than a random structure). Therefore it was used as a seed to generate 1,000 different starting phase sets for 1,000 *pCF* runs. To do this, the phase of each structure factor calculated from the geometrically optimized model was varied by up to 25% in a random manner. The 1,000 electron density maps resulting from these *pCF* runs were symmetry averaged assuming the space group *C*2*cm*, and then the best five were combined. Interpretation of this map was almost trivial: 35 of the 36 Si atoms and 61 of the 79 O atoms could be located directly in the strongest 106 peaks. The position of the missing Si atom was derived from the positions of the four surrounding Si atoms

and the missing bridging O atoms were added. Rietveld refinement of this model revealed that it could be described in the higher space group *Cmcm* with 24 Si atoms in the asymmetric unit.

These HRTEM images of IM-5 were later used to test the limits of electron crystallography. By careful analysis, it proved to be possible to derive the positions of the 24 Si atoms from the HRTEM data alone (Sun et al. [31]).

28.4.3 SSZ-74

The *pCF* approach was also applied to synchrotron powder diffraction data collected on the high-silica zeolite SSZ-74 [26]. In this case, no impurities were present and the pattern could be indexed with confidence with a monoclinic unit cell (*C*2/*c* or *Cc*, $a = 20.514$ Å, $b = 13.395$ Å, $c = 20.097$ Å, $\beta = 102.2°$). Unfortunately, only one HRTEM image of relatively low resolution was available, and only 29 structure factor amplitudes and phases could be derived from it. These were used to construct a structure envelope that could be imposed in real space in the *pCF* algorithm to eliminate any electron density in the pores.

The best electron density maps generated from a series of *pCF* runs were examined by eye. Those judged to have realistic pores and at least a partial framework structure were averaged, and then used as a seed within the *Superflip* program to generate 100 new starting phase sets in a manner analogous to that used for IM-5 (but with a map in this case rather than a model). The ten best maps from these runs were then averaged, and the framework structure could be recognized easily. The space group symmetry had to be reduced to *Cc*, and the final structure, with 23 Si atoms in the asymmetric unit, proved to be a most unusual one with ordered Si vacancies.

28.5 Combining X-ray Powder with Precession Electron Diffraction Data

Although it is readily apparent that HRTEM images can be extremely useful in the structure determination process, they are not always easy to obtain, especially if the sample is beam sensitive. To circumvent this problem, Xie et al. [27] investigated the possibility of using the less demanding precession electron diffraction (PED) technique in place of HRTEM. While PED and X-ray powder diffraction data have been used in combination by Dorset [28] to solve and refine the structure of the zeolite ZSM-10, in that case, the structure was solved from the PED data and then refined with the X-ray data. The question here is whether or not the two sets of data can be combined to facilitate structure solution. Two approaches have been developed: (1) PED data are used to identify weak reflections, and (2) PED data are used to estimate the phases of the reflections in the projection. Both strategies proved

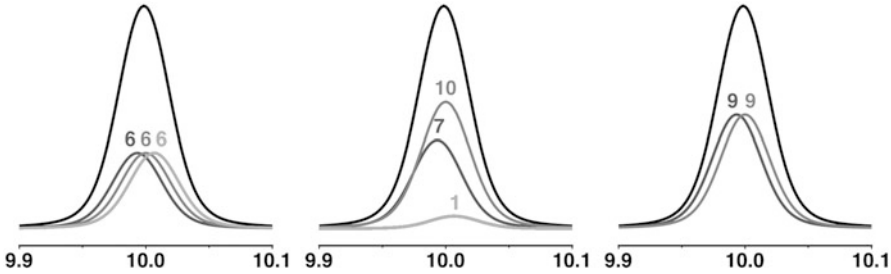

Fig. 28.1 The effect of weak reflection elimination on intensity extraction. The true intensities of three reflections (10, 7, 1) under a single peak are shown in the *center*. On the *left* is a conventional equipartitioning (6, 6, 6), and on the *right*, equipartitioning after the weak reflection has been eliminated (9, 9, 0)

to have a significant and beneficial effect on the structure solution process. To keep things simple, the structure factors derived from the PED patterns were calculated assuming kinematical scattering and no geometric corrections were applied.

28.5.1 Weak Reflection Elimination

Although the scattering factors for X-rays and electrons are not identical, they do show the same general trend, so reflections that are weak in the electron diffraction pattern should also be weak in the corresponding X-ray diffraction pattern. Thus, if those reflections are eliminated during the X-ray intensity extraction process, the intensities of the remaining reflections in an overlap group should be better estimated (see Fig. 28.1).

Tests on the zeolite ZSM-5 (*Pnma*; $a = 20.022$ Å, $b = 19.899$ Å, $c = 13.383$ Å) using just four projections ([010], [01$\bar{2}$], [02$\bar{1}$] and [10$\bar{1}$] with a total of 594 reflections) showed that the electron density map generated by *pCF* with intensities derived using this weak reflection elimination (WRE) procedure improved significantly. Of the 3,042 reflections in the powder diffraction pattern, 412 were defined to be weak and eliminated from the intensity extraction procedure. With the new set of intensities, the best maps produced by the powder charge flipping algorithm matched the correct one much better. The agreement factor R_{map}, which compares the *pCF* map with a reference map calculated from the true structure, decreased from over 55% without WRE to less than 25%.

28.5.2 Phase Retrieval from PED Data Using Charge Flipping

Precession electron diffraction data have already been used in combination with direct methods and maximum entropy methods to determine two-dimensional

structures [13–15]. This is an indication that the reflection intensities are reliable enough and have sufficient resolution for the phasing process to succeed. For three-dimensional structures, of course, a single projection is insufficient to solve the structure, but the phases for selected projections can be used in combination with X-ray powder diffraction data in the same way as those derived from 2-dimensional electron microscopy images.

Baerlocher et al. [26] used the single-crystal charge-flipping algorithm implemented in the program *Superflip* [22] to estimate the phases. Using the same PED patterns for ZSM-5 as for the weak reflection elimination study, 100 charge-flipping runs were performed on each of the 4 two-dimensional datasets (289 reflections for [010], 162 for $[01\bar{2}]$, 124 for $[02\bar{1}]$ and 246 for $[10\bar{1}]$). The resolution for each of these datasets was *ca.* 0.8 Å.

For each projection, the five maps with the best *Superflip R*-values were averaged. Then a Fourier transform was applied to calculate the phases of the corresponding reflections. Even though the symmetry of the map at this stage was *P*1, the space group symmetry was imposed for this transformation to ensure that only phases consistent with a centrosymmetric space group were obtained. The total amplitude that was correctly phased was more than 70% for each of the four zones. This number compares well with that obtained for the phases derived from HRTEM images.

28.5.3 Combining Weak Reflection Elimination and Phase Retrieval

It is to be expected that the combination of weak reflection elimination and phase retrieval will further improve the changes for a successful structure determination. This was tested with PED data recorded for the zeolite TNU-9. Five PED patterns were used to eliminate 323 reflections and to derive 176 phases. The best map showed the positions of 23 of the 24 Si atoms in the asymmetric unit and many of the O atoms. By "recycling" this map in a second series of *pCF* runs, more realistic electron densities for Si and O atoms were obtained and all 24 Si atom positions could be located.

28.6 Combining X-ray Powder with Selected Area Electron Diffraction Data

Selected area electron diffraction patterns can also be used to advantage in conjunction with X-ray powder diffraction. Not only can the unit cell dimensions be verified, but the intensities can also be used if sufficient care has been taken in recording them. In the case of the zeolite ITQ-26 (*I*4/*mmm*, $a = 26.7769(8)$ Å, $c = 13.2505(5)$ Å), Dorset et al. [29] used 41 and 17 SAED intensities taken along the [001] and

[100] directions, respectively, as input to the maximum entropy program MICE [30] to produce low resolution electrostatic potential maps. These were not sufficiently detailed to allow direct interpretation, but could be used to screen the framework structures generated by *Focus* from the X-ray powder diffraction data.

Sun et al. [31] used SAED data in a somewhat different way to solve the structure of the germanosilicate zeolite ITQ-37 ($P4_132$, $a = 26.5126(3)$ Å). Because the unit cell is cubic and rather large, many symmetry-unrelated reflections overlap exactly in the powder pattern (e.g. 511 and 333). SAED patterns were recorded along the [100], [110], [111] and [120] directions and their intensities extracted using the program *ELD* [32]. To get a better estimate of the relative intensities of the reflections in the overlap groups, the ratios of the corresponding SAED intensities were used to prepartition them. This improved set of intensities was then used as input for *Superflip*, and the resulting electron density maps could be interpreted in a straightforward manner.

28.7 Conclusions

The combination of X-ray powder diffraction and electron microscopy techniques is a powerful one for the determination of the structures of polycrystalline materials that resist solution by more conventional methods. Crystallographic phase information obtained from high-resolution electron microscopy images or from precession electron diffraction patterns has proven to be particularly useful. The powder diffraction structure determination programs *Focus* and *pCF*, both of which operate in both direct and reciprocal space, use the phase information in the critical early stages of the structure solution procedure. Electron diffraction data, whether recorded using the conventional selected area or the newer precession technique, can also be exploited to get a better estimation of the relative intensities of overlapping reflections. By combining data from these two different sources, several complex zeolite structures have been solved. The concepts used for these zeolite structure solutions are generally applicable, and can also be applied to other classes of materials, whose structures cannot be solved by more traditional methods.

References

1. David WIF, Shankland K (2008) Structure determination from powder diffraction data. Acta Crystallogr A 64:52–64
2. Dorset DL (1995) Structural electron crystallography. Plenum Press, New York
3. Zou XD, Hovmöller S (2008) Electron crystallography: imaging and single-crystal diffraction from powders. Acta Crystallogr A 64:149–160
4. David WIF, Shankland K, McCusker LB, Baerlocher C (eds) (2002) Structure determination from powder diffraction data. Oxford University Press, Oxford
5. Baerlocher C, McCusker LB (2004) Structure determination from powder diffraction data. Z Kristallogr 219(Special Issue):782–901

6. Miller R, DeTitta GT, Jones R, Langs DA, Weeks CM, Hauptman HA (1993) On the application of the minimal principle to solve unknown structures. Science 259:1430
7. Oszlányi G, Sütő A (2008) Ab initio structure solution by charge flipping. Acta Crystallogr A 64:123–134
8. Grosse-Kunstleve RW, McCusker LB, Baerlocher C (1997) Powder diffraction data and chemical information combined in an automated structure determination procedure for zeolites. J Appl Crystallogr 30:985–995
9. Brenner S, McCusker LB, Baerlocher C (1997) Using a structure envelope to facilitate structure solution from powder diffraction data. J Appl Crystallogr 30:1167–1172
10. Brenner S, McCusker LB, Baerlocher C (2002) The application of structure envelopes in structure determination from powder diffraction data. J Appl Crystallogr 235:243–252
11. Vincent R, Midgley PA (1994) Double conical beam-rocking system for measurement of integrated electron diffraction intensities. Ultramicroscopy 53:271–282
12. Oleynikov P, Hovmöller S, Zou XD (2007) Precession electron diffraction: observed and calculated intensities. Ultramicroscopy 107:523–533
13. Weirich TE, Portillo J, Cox G, Hibst H, Nicolopoulos S (2006) Ab initio determination of the framework structure of the heavy-metal oxide CsxNb2.54W2.46O14 from 100 kV precession electron diffraction data. Ultramicroscopy 106(1):64–175
14. Dorset DL, Gilmore CJ, Jorda JL, Nicolopoulos S (2007) Direct electron crystallographic determination of zeolite zonal structures. Ultramicroscopy 107:462–473
15. Gilmore CJ, Dong W, Dorset DL (2008a) Solving the crystal structures of zeolites using electron diffraction data. I. The use of potential-density histograms. Acta Crystallogr A 64:284–294; Gilmore CJ, Dong W, Dorset DL (2008b) Solving the crystal structures of zeolites using electron diffraction data. II. Density-building functions. Acta Crystallogr A 64:295–302
16. Boullay P, Dorcet V, Perez O, Grygiel C, Prellier W, Mercey B, Hervieu M (2009) Structure determination of a brownmillerite Ca2Co2O5 thin film by precession electron diffraction. Phys Rev B 79:184108
17. Hovmöller S (1992) CRISP: crystallographic image processing on a personal computer. Ultramicroscopy 41:121–135
18. Baerlocher C, McCusker LB, Palatinus L (2007) Charge flipping combined with histogram matching to solve complex crystal structures from powder diffraction data. Z Kristallogr 222:47–53
19. Palatinus L, Chapuis G (2007) SUPERFLIP – a computer program for the solution of crystal structures by charge flipping in arbitrary dimensions. J Appl Crystallogr 40:786–790
20. Zhang KYJ, Main P (1990) Histogram matching as a new density modification technique for phase refinement and extension of protein molecules. Acta Crystallogr A 46:41–46
21. Corma A, Rey F, Valencia S, Jorda JL, Rius J (2003) A zeolite with interconnected 8–10- and 12-ring pores and its unique catalytic selectivity. Nature Mater 2:493–497
22. Gramm F (2007) Kombination von Transmissions-Elektronenmikroskopie mit Pulver-Beugungsdaten zur Lösung von komplexen Zeolith-Strukturen. Ph.D. thesis, ETH Zurich, Switzerland
23. Oszlányi G, Sütő A (2004) Ab initio structure solution by charge flipping. Acta Crystallogr A 60:134–141; Oszlányi G, Sütő A (2005) Ab initio structure solution by charge flipping II. Use of weak reflections. Acta Crystallogr A 61:147–152
24. Gramm F, Baerlocher C, McCusker LB, Warrender SJ, Wright PA, Han B, Hong SB, Liu Z, Ohsuna T, Terasaki O (2006) Complex zeolite structure solved by combining powder diffraction and electron microscopy. Nature 444:79–81
25. Baerlocher C, Gramm F, Massüger L, McCusker LB, He Z, Hovmöller S, Zou X (2007) Structure of the polycrystalline zeolite catalyst IM-5 solved by enhanced charge flipping. Science 315:1113–1116
26. Baerlocher C, Xie D, McCusker LB, Hwang SJ, Chan IY, Ong K, Burton AW, Zones SI (2008) Ordered silicon vacancies in the framework structure of the zeolite catalyst SSZ-74. Nature Mater 7:631–635

27. Xie D, Baerlocher C, McCusker LB (2008) Combining precession electron diffraction data with X-ray powder diffraction data to facilitate structure solution. J Appl Crystallogr 41:1115–1121
28. Dorset DL (2006) The crystal structure of ZSM-10, a powder X-ray and electron diffraction study. Z Kristallogr 221:260–265
29. Dorset DL, Strohmaier KG, Kliewer CE, Corma A, Diaz-Cabanas MJ, Rey F, Gilmore CJ (2008) Crystal structure of ITQ-26, a 3D framework with extra-large pores. Chem Mater 20:5325–5331
30. Gilmore CJ, Dong W, Bricogne G (1999) A multisolution method of phase determination by combined maximization of entropy and likelihood. VI. The use of error-correcting codes as a source of phase permutation and their application to the phase problem in powder, electron and macromolecular crystallography. Acta Crystallogr A 55:70–83
31. Sun J, Bonneau C, Cantín Á, Corma A, Díaz-Cabañas MJ, Moliner M, Zhang D, Li M, Zou X (2009) The ITQ-37 mesoporous chiral zeolite. Nature 458:1154–1158
32. Zou XD, Sukharev Y, Hovmöller S (1993) Quantitative measurement of intensities from electron diffraction patterns for structure determination – new features in the program system ELD. Ultramicroscopy 52:436–444

Chapter 29
Automated Electron Diffraction Tomography

Ute Kolb

Abstract Ab-initio structure analysis by electron diffraction is hampered by two major problems: insufficient number of reflections sampled and an intensity alteration by dynamical scattering contribution or beam damage. Thus, in recent years the principles of automated diffraction tomography (ADT) allowing systematic reciprocal space sampling and automated data analysis were developed. Here the basic ideas of ADT and its general applicability will be discussed along with some examples of solved structures.

29.1 Principles of Automated Diffraction Tomography

In conventional electron crystallography, prominent crystallographic zones comprising approximately planar cuts through reciprocal space are recorded. To gain three dimensional diffraction data for structure solution, intensity collection from several independent single diffraction patterns or from a tilt series, derived through a crystal tilt around a crystallographically pronounced axis, is necessary. The resulting in-zone diffraction patterns can be indexed via Vainshtein plots [1]. Figure 29.1 (top), where such planar reciprocal space cuts are viewed along the tilt axis, shows that the collection of only prominent zones ignores a vast number of high indexed reflections inside the scanned reciprocal space thus reducing the total number of collected reflections. Limiting factor of the tilt range, called the *missing cone* problem, includes geometric constraints such as pole piece gap, specimen holder thickness, position of the particle on the grid.

U. Kolb (✉)
Institute of Physical Chemistry, Johannes-Gutenberg University Mainz, Welderweg 11, 55128 Mainz, Germany
e-mail: kolb@uni-mainz.de

U. Kolb et al. (eds.), *Uniting Electron Crystallography and Powder Diffraction*, NATO Science for Peace and Security Series B: Physics and Biophysics,
DOI 10.1007/978-94-007-5580-2_29,

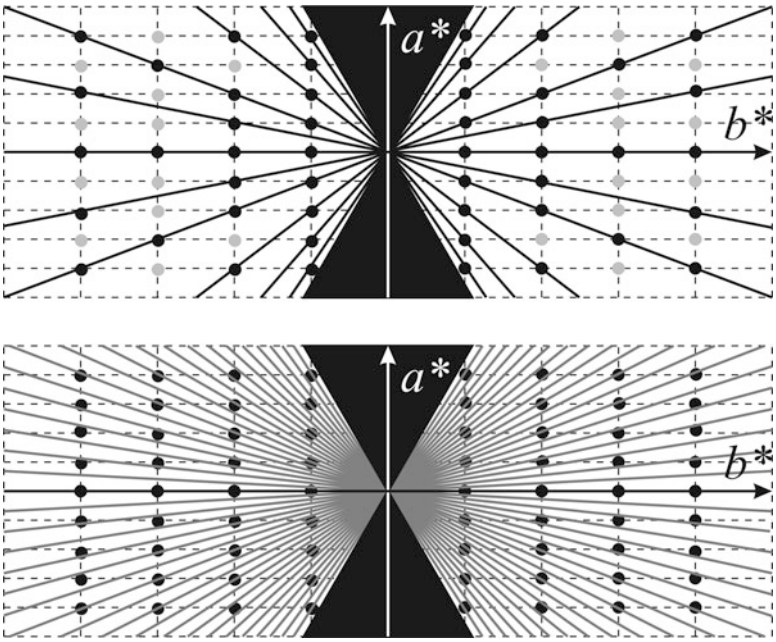

Fig. 29.1 Sketch of the reciprocal net viewed down the tilt axis c*. On the *top* a traditional tilt collecting prominent zones is sketched. Ewald sphere cuts are approximated by planes. Collected in-zone patterns are marked as *linear cuts*. Collected reflections are indicated as *dark spots* and missed reflections as *bright spots*. On the *bottom* a scan of the reciprocal space with fixed tilt steps by ADT is sketched. The off-zone cuts are marked as *dark lines*. The non-reachable area, the missing cone, is indicated in *black*

The ADT method [2] improves reciprocal space coverage by applying fixed tilt steps (Fig. 29.1 bottom). The resulting diffraction patterns are not oriented, they are off-zone, and can be indexed only by automated data analysis. Here 3D volume reconstruction from a set of sequential 2D slices, known as tomography, is utilized. Although the term tomography is associated with "real-space" tomography, each slice being a projection of the real space structure, it describes "reciprocal-space" slicing as well. For such a sampling of the nearly complete reciprocal space pre-orientation of the crystal is not necessary and should be even avoided in order to collect as many independent reflections as possible.

Oriented diffraction patterns suffer particularly from dynamic effects: as they typically have a large number of geometrically related and simultaneously excited beams, multiple scattering effects are very strong [3, 4]. Additionally, in low index zones channeling effects are strong leading to additional redistribution of diffracted intensity [5]. Being "off zone" automatically reduces dynamic effects such that the collected data set can be considered pseudo-kinematic.

Diffraction experiment inside a TEM can be performed with a large parallel beam using the selected area aperture (SAED). Focusing the beam on the sample

by the condenser lens creates a convergent beam producing diffraction discs instead of spots [6, 7]; decreasing convergence in CBED, LACBED, NBD. Nano electron diffraction (NED) can be applied, when a small condenser aperture ($\leq$10 μm) is used producing a quasi-parallel beam ($\sim$0.2 mrad convergence) with a diameter of down to 20 nm. Small discs do not hamper data processing, but may cause for large unit cells reflection overlap. Therefore diffraction patterns are focused additionally with the diffraction (intermediate) lens. This introduces an effective camera length change, which can be handled through an additional calibration, and a slight rotation of the diffraction patterns. Even crystals, perfectly adjusted in eucentric height, move slightly through crystal tilting. Therefore, the crystal position needs to be tracked manually or automatically by correlation with a reference image taken in TEM or STEM mode.

29.2 Data Collection

ADT data collection can be performed manually or automatically, following the sequence – tilt, crystal tracking, diffraction acquisition – being basically applicable to nearly every TEM on the market [8]. Preferably, the machine should be equipped with a computer-controlled goniometer. Sample holder/pole piece combination should allow at least 30° complete tilt range for cell parameter determination. Most structure solutions from ADT data were performed using FEG source at 300 kV but have been successful as well with LaB_6 at 120 kV as well [9]. Primarily, data resolution is given by the diffraction camera length necessary to ensure that the diffraction spots are uniquely resolved. In order to maintain the resolution and resolve the spots at the same time a CCD detector with larger area can be used. Automation becomes important for beam sensitive samples because an extremely low electron intensity can be chosen, where the beam is hardly visible on the screen. Exposure time can be reduced further by blanking the beam every moment it is not necessary to illuminate the sample. The acquisition module was developed in collaboration with FEI (FEI Company Eindhoven, The Netherlands), thus it is primary designed for TECNAI-class of TEMs equipped with a scanning unit (STEM). Calibration procedures, necessary prior to the measurement, were adopted from real-space tomography. During a tilt series collection the microscope is toggled between μ-STEM imaging mode for crystal tracking and NED mode for data collection. Diffraction as well as imaging data is stored in an MRC file.

29.3 Combination with Electron Beam Precession

ADT diffraction information is collected in discrete tilt steps. The intensity recorded depends on the distance of the reflection centre to the intersection with the Ewald sphere, commonly referred to as the excitation error [10, 11]. The probability to

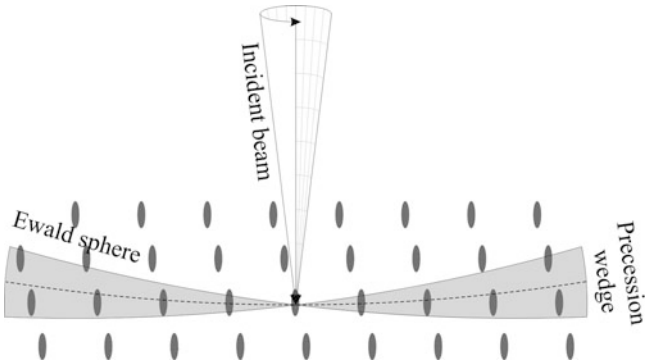

Fig. 29.2 Sketch of the reciprocal space during collection of precession electron diffraction pattern

cut a reflection close to the centre increases for smaller tilt steps. Electron beam precession (PED), developed by Vincent and Midgley [12] to reduce dynamical effects in electron diffraction patterns, can improve the situation. Using PED the electron beam is tilted away from the vertical optical axis and precessed around the optical axis. When precession speed is high the diffraction patterns produced at each azimuthal position of the beam are merged into an integrated steady pattern. As shown in Fig. 29.2, the diffraction volume within the wedge, described by the Ewald sphere precession, integrates the gap between the slices, comparable to the oscillation method used in single crystal X-ray crystallography [13, 14]. The combination of automated diffraction tomography data acquisition and electron beam precession has two substantial benefits, which lead to vastly improved data quality for structural investigations: the intensity data has less dynamical effects (which may be only a problem when approaching low index zones) and the intensities between the tilt steps are integrated by the use of precession sweeping the full reflection through Ewald sphere.

29.4 Data Processing

As mentioned above automated data processing and analysis is crucial to index off-zone diffraction patterns and to extract intensities [15]. Data processing uses the knowledge of the diffraction geometry to reconstruct the 3D reciprocal space, including diffraction pattern shift, analysis of the correct azimuthal tilt axis position and subsequent rotation of the patterns, and integration into a 3D volume by recalculation of 2D pixel-data into 3D voxel-data. Data analysis covers visual inspection of the reconstructed 3D diffraction volume, unit cell parameters determination and orientation matrix, indexing of reflections and extraction of intensities.

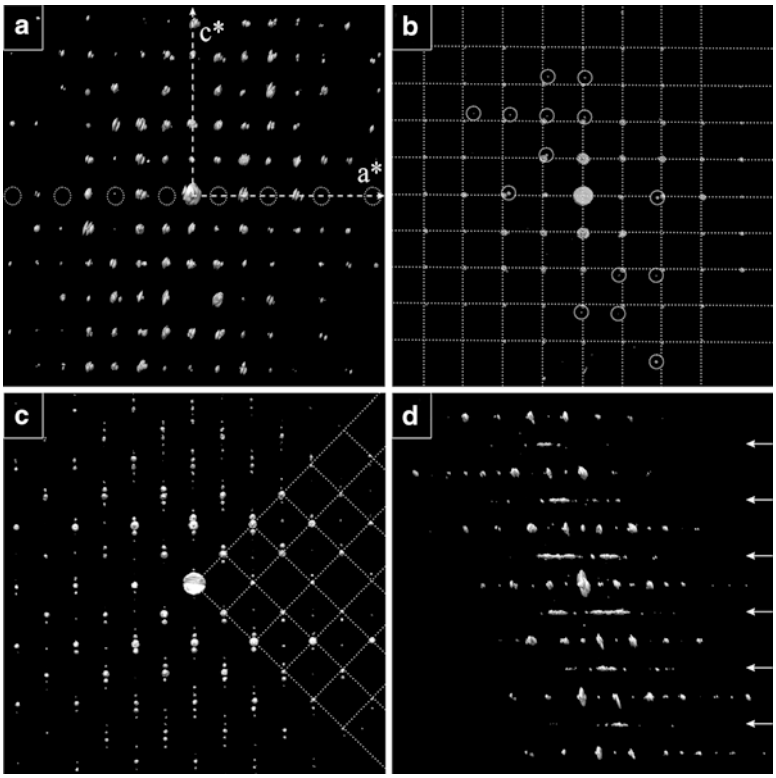

Fig. 29.3 Reconstructed reciprocal volume of crystals: (**a**) $BaSO_4$ view down b*, extinct columns caused by a-glide plane marked by *circles*; (**b**) MoO_3, view down b* plus representing lattice of the major crystal and additional reflections of an extra crystal (*circled*); (**c**) $Bi_{12}O_{17}Cl_2$ superstructure, representing lattice of the parent structure; (**d**) high-temperature modification of $Li_2O/Al_2O_3/WO_3$, partially disordered

29.4.1 Visual Analysis of the 3D Reciprocal Space

The ability to visualize the 3D reciprocal space can be used to recognize and separate superimposed crystal lattices in the diffraction volume, when crystals agglomerate so strongly that a single crystal to collect data from cannot be found. In principle, two lattices can be taken apart and treated separately (Fig. 29.3a, b) and for separated reflections there is no problem extracting intensity data sets of both lattices. Additionally, the visualization of the complete 3D volume can be very useful to analyze structural features like superstructures and partial disorder. Figure 29.3c shows a projection of the diffraction volume of a $Bi_{12}O_{17}Cl_2$ superstructure: the parent lattice (white dotted lines) is visible. Partial disorder is seen as streaking along some reflection lines (Fig. 29.3d), like in the diffraction pattern of a low temperature modification of $Li_2O/Al_2O_3/WO_3$. Indices of these lines can be easily deduced and the structure faults assigned.

29.4.2 Unit Cell Parameter Determination

Reflection positions, the basis for unit cell parameter determination, can be derived from 2D diffraction patterns and transformed into 3D coordinates or determined directly from the 3D reciprocal volume. Since all collected points can be considered as 3D vectors, a difference vector space, an autocorrelation of the reflection set, can be produced. It emphasizes the 3D periodic lattice and fills the non-sampled diffraction volume (missing cone) arising from data collection. Clouds of high difference vector density can be detected by cluster routines; three shortest non-coplanar difference vectors are taken as initial unit cell vectors and refined. The used density based clustering routine is robust but may need special parameter adjustment for strongly anisotropic cell dimensions.

29.4.3 Intensity Extraction

Once unit cell parameters and an orientation matrix have been determined it is possible to assign and integrate intensities. Within the integration boxes a "local" background function is calculated and subtracted. In order to index the reflections, a correct projection of the 3D net onto 2D diffraction patterns, thus the effective camera length and the effective radius of the Ewald sphere need to be known accurately.

Due to the effective diffraction peak size in 3D, reflections penetrate through several diffraction patterns. From the intensities collected for one reflection the maximal intensity value is associated with each (hkl) according to the assumption that this comprises the closest cut to the reflection center. As a result of intensity integration, an hkl I file, with $\sqrt{I}$ as error estimation is created analogous to single crystal X-ray data analysis. No correction is applied yet to the raw data.

29.5 Structure Analysis Using ADT Data

29.5.1 Data Evaluation

An ADT 3D data set provides information about the symmetry of the structure and the extinction conditions. Dynamical effects, which cause zonal and serial reflection extinction violations, are significantly reduced and can be detected, even for more than 100 nm thick specimens, inspecting the full 3D-reconstructed diffraction volume. In most of the cases the extinction group can be automatically determined by statistical routines implemented in structure solution programs. Visualizing the 3D reconstructed reciprocal space as a projection (integral: lattice centering, zonal: glide planes) or clipped along a main axis (serial: screw axes) shows extinctions clearly in addition.

Both quantity and quality of data are crucial for performing structure solution. The later depends on the kinematical nature of the diffraction data, i.e. how closely the intensities of reflections are proportional to the squared structure factor ($I \sim F^2$). A strict quantification is not trivial, as reflection intensities can also deviate from expected values for reasons not related with dynamical scattering. In order to judge the quality of an ADT data set before attempting structure solution, several parameters should be evaluated.

The achievable **resolution** is given by the field of view of the CCD camera and the camera length necessary to separate reflections in a reasonable way. Well-ordered inorganic structures usually deliver reflections with sufficient intensity up to resolutions above 1 Å. A reason to consider a resolution cut-off may be to compensate for poor sampling of reciprocal space at high scattering angles, where the gap between slices is too large to sample the reflections completely. Reliable small molecule structure solution needs a data resolution of at least 1.2 Å for direct methods programs [16].

For an ADT electron diffraction data set the number of reflections is, dependent on the lattice cell parameters, in the range of several thousands. The ratio of collected independent reflections to expected reflections for a given resolution is defined as **completeness**. Data sets with <50% completeness rarely give reliable structure solutions. For high symmetry structures good data completeness is relatively easy to achieve, while for a triclinic structure within a tilt range of ±60° one can get only 2/3 = 66% of data coverage.

R_{sym} or R_{int} indicates the agreement of reflections related by Friedels law. In electron diffraction the main sources of perturbations are dynamical effects, excitation error and beam damage or experimental problems such as inhomogeneity of recording media, presence of hot spots or additional intensity from another crystal. A low R_{sym}, was found to be in the range of 7–17% for ADT/PED and 12–22% for ADT data. Higher R_{sym} values are usually caused by strong beam damage of the sample or disorder effects. If R_{sym} shows high values for particular or classes of reflections, a closer inspection the data set is recommended.

$$R_{sym}\,(SIR) = \frac{\sum ||F_o| - |F_o\,(mean)||}{\sum |F_o|}; \quad R_{int}\,(SHELX) = \frac{\sum \left|F_o^2 - F_o^2\,(mean)\right|}{\sum F_o^2}$$

If the **Wilson plot** [17, 18], which relates the intensities of reflection groups to the scattering angle, is positive the data will most likely lead to a routine structure solution. Unlike conventional manual-tilt electron data [10, 19], the majority of ADT data sets delivers positive thermal factors. Therefore the Wilson plot can be used to evaluate the reliable resolution of the data set.

Reflection/parameter ratio: To achieve reliable structure solution a ratio of independent reflections to refined parameters of 10:1 or higher is normally required [18]. Atoms on general positions need at least four parameters (positions and isotropic thermal factor or occupancy). Anisotropic thermal factors are usually not refined.

29.5.2 Structure Analysis

With the exception of a few outstanding data sets electron crystallography has not been able to rely on direct methods to solve crystal structures like the single crystal X-ray community. However, ADT electron diffraction data, being of pseudo-kinematic nature, moved ab-initio structure solution closer to routine using traditional direct methods (SIR: [20], SHELX: [21]) or more exotic direct method programs such as maximum entropy methods (MICE: [22, 23]) and charge flipping (SUPERFLIP: [24]). A combined structure solution strategy implemented in Endeavour [25] has been used for electron diffraction data as well. TOPAS [26], FOX [27, 28] and DASH [29] could also be used by making the simple adjustment of changing the X-ray scattering factors to electron scattering factors.

Using ADT and ADT/PED, over 40 structures were solved ab-initio in the last 2 years; 24, 12 known and 12 unknown structures (see Table 29.1) ranging from small structures with two independent atoms to relatively complex ones including 90 independent atoms with triclinic up to cubic cells. The majority of the atoms were detected directly from SIR2008 solution even for light atoms in the vicinity of heavy atoms. The achieved R(F) values ($R1 = \sum ||Fo| - |Fc|| / \sum |Fo|$), in the range of 20–30% and for beam sensitive samples or non-precessed data about 30–40%, are at the lower limit or below those achieved for conventional electron diffraction data. The largest cell solved so far is Basolite, a metal organic framework, for which structure solution was only possible with data collected from a liquid N_2 cooled crystal. Deviations of atomic positions from structure solution in comparison to those taken from literature turned out to be in the range of 0.1–0.2 Å. Five unknown structures were refined versus X-ray powder diffraction data and showed comparable atomic position deviations. For the remaining structures, where samples turned out to contain several phases and crystals smaller than 50 nm, X-ray powder diffraction data was not suitable for structure refinement.

The advantage of ADT approach is the ability to investigate one single particle at a time. The smallest particle ever used for structure solution from ADT/PED data was 20 nm. In general all atomic positions for heavy atoms as well as the majority of light atom positions could be detected by direct methods structure solution. Using least squares refinement the 5% missing positions, which resemble mainly atoms in channels of porous materials, could be located from difference Fourier maps as well. Except for zeolite structures with remaining template residual potentials are negative or extremely low.

29.6 Conclusion

ADT is an emerging technique that combines the ability to access nano-crystalline volumes with the ability to perform a more complete sampling of the reciprocal space. Intensity data sets are significantly less dynamical than conventional zonal

Table 29.1 Crystal structures solved by ADT/PED data

	Space group	No. of indep. refl.	No. of indep. atoms	V(Å^3)	Completeness (%)
Inorganic					
Intermetallic particles (ZnSb)[30][a, b]	*Pbca*	106	2	440	70
Calcite ($CaCO_3$)[31][a]	*R-3c*	106	3	140	97
Barite ($BaSO_4$)[32][a]	*Pnma*	355	5	350	82
Mullite ($Al_6Si_2O_{13}$)[33][a]	*Pbam*	213	6	170	84
HP hydrous Al-pyroxene ($Mg_2Al(OH)_2AlSiO_6$)[34]	*C2/c*	255	8	540	86
$Na_2W_4O_{13}$[8][a, b]	*P-1*	738	10	260	68
Natrolite ($Na_2Al_2Si_3O_{10}{\cdot}2H_2O$)[35][a]	*Fdd2*	743	10	2,250	99
Sodium titanate ($Na_2Ti_6O_{13}$)[35][a]	*C2/m*	517	11	510	72
Pseudo-spinel titanate ($Li_4Ti_8Ni_3O_{21}$)[36][a]	*P-3c1*	187	11	720	91
Phosphate ($Ba_6P_{12}N_{17}O_9Br_3$)[37]	*P6$_3$/m*	1,343	11	1,540	99
Sodium titanate ($NaTi_3O_7OH{\cdot}2H_2O$)[38]	*C2/m*	628	13	670	79
Phosphate (SrP_3N_5O)[39]	*Pnam*	1,790	25	2,050	86
Intermetallic particles (Zn_8Sb_7)[30]	*P-1*	3,651	30	1,620	57
ITQ-43 ($Ge_xSi_{160-x}O_{328}$)[40]	*Cmmm*	2,735	39	14,040	91
ZSM-5 ($Na_xAl_xSi_{96-x}O_{192}$)[33][a]	*Pnma*	2,288	43	5,490	79
IM-5 ($Si_{288}O_{576}$)[33][a]	*Cmcm*	2,579	71	16,240	94
Charoite_96 ($(K,Sr)_{16}(Ca,Na)_{32}[(Si_{70}(O,OH)_{180})](OH,F)_4{\cdot}nH_2O$)[41]	*P2$_1$/m*	3,353	88	4,470	97
Charoite_90 ($(K,Sr)_{16}(Ca,Na)_{32}[(Si_{70}(O,OH)_{180})](OH,F)_4{\cdot}nH_2O$)[42]	*P2$_1$/m*	2,878	90	4,450	97
Organic and hybrid organic-inorganic					
10-CNBA ($C_{29}NH_{17}$)[43][a, b]	*P2$_1$/c*	3,519	30	1,990	87
OPBA3[44][a, b]	*P2$_1$/c*	3,078	30	1,760	81
OPBA4[44][b]	*C2/c*	3,576	39	4,550	77
Basolite ($C_6H_4CuO_5$)[33][a]	*Fm-3 m*	384	6	18,280	99
MFU_4*l* ($Cl_4Zn_5N_{18}C_{36}O_6H_{12}$)[45]	*Fm-3 m*	411	9	29,960	100
ECS-3 ($(Na,K)_3Al_3Si_4C_{12}O_{12}{\cdot}nH_2O$)[46]	*Cc*	4,417	72	5,300	72

[a]Known test structures
[b]No precession used

acquisitions, producing reliable intensities even from crystals thicker than 100 nm. The technique has been proven suitable for beam-sensitive materials because crystal pre-orientation resulting in reduction of electron dose during acquisition is not necessary. The method can be performed using standard specimen holders and TEMs. 3D reciprocal space reconstruction allows unambiguous unit cell parameters determination for any cell metric with accuracy of 2–5% and makes it possible to analyze additional structural features like partial disorder and polycrystallinity.

ADT allows for structure identification and solution within multiphase systems. The combination of ADT with PED leads to more reliable pseudo-kinematic intensities. It is highly suitable for structure solutions of nano-crystalline and beam sensitive inorganic materials with high structural complexity like charoite having more than 300 atoms in the unit cell. The ADT approach allows a significant acceleration of structure solution leading to the ability to access hot-topic structures in an acceptable time scale. In comparison with single crystal X-ray data collection and analysis, electron diffraction experiments are now achievable on similar time scales. Quality and speed of structure analysis will increase the number of solved crystal structures by electron diffraction significantly and will have a strong impact on the electron crystallography field.

References

1. Vainshtein BK (1964) Structure analysis by electron diffraction. Pergamon Press, New York
2. Kolb U, Gorelik T, Kübel C, Otten MT, Hubert D (2007) Towards automated diffraction tomography: part I – data acquisition. Ultramicroscopy 107:507–513. doi:10.1016/j.ultramic.2006.10.007
3. Peng LM, Dudarev SL, Whelan MJ (2004) High-energy electron diffraction and microscopy. Oxford University Press, New York
4. Fultz B, Howe JM (2008) Transmission electron microscopy and diffractometry of materials. Springer, Berlin
5. Van Dyck D, Coene W (1984) The real space method for dynamical electron diffraction calculations in high resolution electron microscopy: I. Principles of the method. Ultramicroscopy 15:29–40. doi:10.1016/0304-3991(84)90072-X
6. Tanaka M, Terauchi M, Kaneyama T, Tsuda M, Saitoh K (1985) Convergent beam electron diffraction, vol I–IV. JEOL, Tokyo
7. Sung CM, Williams DB (1991) A bibliography of CBED papers from 1939–1990. J Electron Micro Tech 17:95–118
8. Gorelik TE, Stewart AA, Kolb U (2011) Structure solution with automated electron diffraction tomography data: different instrumental approaches. J Microsc 244:325–331
9. Palatinus L, Klementová M, Dřínek V, Jarošová M, Petříček V (2011) An incommensurately modulated structure of η'-phase of $Cu_{3+x}Si$ determined by quantitative electron diffraction tomography. Inorg Chem 50:3743–3751
10. Dorset DL (1995) Structural electron crystallography. Plenum Press, New York
11. Williams DB, Carter CB (1996) Transmission electron microscopy, vol II. Plenum Press, New York
12. Vincent R, Midgley PA (1994) Double conical beam-rocking system for measurement of integrated electron diffraction intensities. Ultramicroscopy 53:271–282

13. Arndt UW, Champness JN, Phizackerley RP, Wonacott AJ (1973) A single-crystal oscillation camera for large unit cells. J Appl Crystallogr 6:457–463
14. Monaco HL (1994) Experimental methods in X-ray crystallography. In: Giacovazzo C (ed) Fundamentals of crystallography. Oxford University Press, New York, pp 229–318
15. Kolb U, Gorelik T, Otten MT (2008) Towards automated diffraction tomography. Part II – cell parameter determination. Ultramicroscopy 108:763–772
16. Hauptman H, Karle J (1953) The solution of the phase problem, I. The centrosymmetric crystal. Polycrystal Book Service, Pittsburgh
17. Wilson JAC (1949) The probability distribution of X-ray intensities. Acta Crystallogr 2:318–321
18. Giacovazzo C (1980) Direct methods in crystallography. Academic, London
19. Dorset DL, Gilmore CJ (2000) Prospects for kinematical least-squares refinement in polymer electron crystallography. Acta Crystallogr A 56:62–67
20. Burla MC, Caliandro R, Camalli M, Carrozzini B, Cascarano GL, De Caro L, Giacovazzo C, Polidori G, Siliqi D, Spagna R (2007) IL MILIONE: a suite of computer programs for crystal structure solution of proteins. J Appl Crystallogr 40:609–613
21. Sheldrick GM (2008) A short history of SHELX. Acta Crystallogr A 64:112–122
22. Gilmore GJ (1996) Maximum entropy and Bayesian statistics in crystallography: a review of practical applications. Acta Crystallogr A 52:561–589
23. Gilmore CJ, Bricogne G (1997) The mice computer program. Methods Enzymol 277:65–78
24. Palatinus L, Chapuis G (2007) Superflip – a computer program for the solution of crystal structures by charge flipping in arbitrary dimensions. J Appl Crystallogr 40:786–790
25. Brandenburg K, Putz H (2009) Endeavour – structure solution from powder diffraction. http://www.crystalimpact.com/endeavour/Default.htm
26. Coelho A (2007) TOPAS-academic V4.1, Brisbane. http://www.topas-academic.net
27. Favre-Nicolin V, Černý R (2002) FOX, 'free objects for crystallography': a modular approach to ab initio structure determination from powder diffraction. J Appl Crystallogr 35:734–743
28. Favre-Nicolin V (2008) Fox, free objects for crystallography. http://objcryst.sourceforge.net
29. David WIF, Shankland K, Van De Streek J, Pidcock E, Motherwell WDS, Cole JC (2002) DASH: a program for crystal structure determination from powder diffraction data. J Appl Crystallogr 39:910–915
30. Birkel CS, Mugnaioli E, Gorelik T, Kolb U, Panthöfer M, Tremel W (2010) Solution synthesis of a new thermoelectric $Zn_{1+x}Sb$ nanophase and its structure determination using automated electron diffraction tomography. J Am Chem Soc 132:9881–9889
31. Kolb U, Gorelik T, Mugnaioli E (2009) Automated diffraction tomography combined with electron precession: a new tool for *ab initio* nanostructure analysis. In: Moeck P, Hovmoeller S, Nicolopoulos S, Rouvimov S, Petrok V, Gateshki M, Fraundorf P (eds) Electron crystallography for materials research and quantitative characterization of nanostructured materials, Materials Research Society Symposia Proceedings, vol 1184, Warrendale, PA, GG01-05
32. Mugnaioli E, Gorelik T, Kolb U (2009) "Ab initio" structure solution from electron diffraction data obtained by a combination of automated diffraction tomography and precession technique. Ultramicroscopy 109:758–765
33. Mugnaioli E, Kolb U (2012) Applications of automated diffraction tomography (ADT) on nanocrystalline porous materials. Micropor Mesopor Mater (in press), doi:10.1016/j.micromeso.2012.02.024
34. Gemmi M, Fischer J, Merlini M, Poli S, Fumagalli P, Mugnaioli E, Kolb U (2011) A new hydrous Al-bearing pyroxene as a water carrier in subduction zones. Earth Planet Sci Lett 310:422–428
35. Mugnaioli E, Gorelik TE, Stewart A, Kolb U (2011) "Ab-initio" structure solution of nano-crystalline minerals and synthetic materials by automated electron tomography. In: Krivovichev SV (ed) Minerals as advanced materials II. Springer, Berlin/Heidelberg, pp 41–54
36. Kolb U, Mugnaioli E, Gorelik TE (2011) Automated electron diffraction tomography – a new tool for nano crystal structure analysis. Cryst Res Technol 6:542–554

37. Mugnaioli E, Sedlmaier SJ, Oekler O, Kolb U, Schnick W (2012) $Ba_6P_{12}N_{17}O_9Br_3$ – a column-type phosphate structure solved from single-nanocrystal data obtained by automated electron diffraction tomography. Eur J Inorg Chem 2012:121–125
38. Andrusenko I, Mugnaioli E, Gorelik TE, Koll D, Panthöfer M, Tremel W, Kolb U (2011) Structure analysis of titanate nanorods by automated electron diffraction tomography. Acta Crystallogr B 67:218–225
39. Sedlmaier SJ, Mugnaioli E, Oekler O, Kolb U, Schnick W (2011) SrP_3N_5O: a highly condensed layer phosphate structure solved from a nanocrystal by automated electron diffraction tomography. Chem Eur J 17:11258–11265
40. Jiang J, Jorda JL, Yu J, Baumes LA, Mugnaioli E, Diaz-Cabanas MJ, Kolb U, Corma A (2011) Synthesis and structure determination of the hierarchical meso-microporous zeolite ITQ-43. Science 333:1131–1134
41. Rozhdestvenskaya I, Mugnaioli E, Czank M, Depmeier W, Kolb U, Merlino S (2011) Essential features of the polytypic charoite-96 structure compared to charoite-90. Mineral Mag 75:2833–2846
42. Rozhdestvenskaya I, Mugnaioli E, Czank M, Depmeier W, Kolb U, Reinholdt A, Weirich T (2010) The structure of charoite, (K,Sr,Ba,Mn)15–16(Ca,Na)32[(Si70(O,OH)180)](OH,F)4.0*nH2O, solved by conventional and automated electron diffraction. Mineral Mag 74:159–177
43. Kolb U, Gorelik TE, Mugnaioli E, Stewart A (2010) Structural characterization of organics using manual and automated electron diffraction. Polym Rev 50:385–409
44. Gorelik TE, van de Streek J, Kilbinger AFM, Brunklaus G, Kolb U (2012) *Ab-initio* crystal structure analysis and refinement approaches of oligo *p*-benzamides based on electron diffraction data. Acta Crystallogr B 68:171–181
45. Denysenko D, Grzywa M, Tonigold M, Schmitz B, Krkljus I, Hirscher M, Mugnaioli E, Kolb U, Hanss J, Volkmer D (2011) Elucidating gating effects for hydrogen sorption in MHU-4 type triazolate-based MOFs featuring different pore sizes. Chem Eur J 17:1837–1848
46. Bellussi G, Montanari E, Di Paola E, Millini R, Carati A, Rizzo C, O'Neil Parker WJ, Gemmi M, Mugnaioli E, Kolb U, Zanardi S (2012) ECS-3: a crystalline hybrid organic–inorganic aluminosilicate with open porosity. Angew Chem 51:666–669

Chapter 30
Automated Quantitative 3D Electron Diffraction Rotation Tomography

Peter Oleynikov

Abstract Recent developments in data collection allow automated acquisition of 3D electron diffraction data from nano-sized crystals using conventional transmission electron microscopes. In the present work we show that the automated 3D electron diffraction rotation method can be successfully applied for the rapid data collection. Moreover, a dedicated data processing system can be used for the treatment of the obtained 3D data and for the quantitative extraction of integrated intensities which are required for the successful crystal structure solution.

30.1 Introduction

Investigations of atomic structure of materials improve the understanding of their unique physical and chemical properties. This knowledge is of high importance in the developments of new materials for e.g. biomedical sciences, optics, catalysis, electronics etc. Generally, synchrotrons and transmission electron microscopy (EM), which can collect data from very small crystals, are used for such investigations. However, the EM approach has a major advantage in the possibility to work with crystals a million times smaller in volume (few nanometers) than the smallest single crystals possible to use at synchrotrons (few microns). Unfortunately, the conventional EM approach for such investigations is extremely tedious, skill demanding, and time consuming. These draw backs are even more obvious when 3D data collection is required, which can easily take months.

P. Oleynikov (✉)
Berzelii Centre EXSELENT on Porous Materials, Stockholm University, 106 91 Stockholm, Sweden

Department of Materials and Environmental Chemistry, Stockholm University, 106 91 Stockholm, Sweden
e-mail: peter.oleynikov@mmk.su.se

U. Kolb et al. (eds.), *Uniting Electron Crystallography and Powder Diffraction*,
NATO Science for Peace and Security Series B: Physics and Biophysics,
DOI 10.1007/978-94-007-5580-2_30,

There is an obvious need for fast and automated methods for 3D data collection, data processing, crystal structure solution and refinement of any kind of fine structure materials. Crystallographic and numerical computation methods combined with recent advances in the hardware development such as computer controlled TEMs, Cs aberration correctors, precession/rotation, CCD cameras, and automated electron diffraction tomography have opened a new era for the EM approach. First of all, advances in both the methods and hardware have allowed us to study in detail and reveal/understand the atomic structures of different types of materials such as nanoparticles, meso-porous materials and zeolites etc., both in bulk and on their surfaces. Most importantly, these new robust tools boosted technological development and innovation by introducing and realizing automated quantitative measurements and data analysis procedures. This means significant shortening of the time required to design new materials with required properties. A good example is the solution of the full (3D) crystal structure of a very complicated quasicrystal approximant [1] which requires at least 13 electron diffraction patterns from specific zone axes. With the development of an automated rotation electron diffraction tomography, the time necessary to find and acquire these patterns is reduced from at least 3 months of tedious manual TEM work down to just 1–2 h of data collection time. This approach had never been possible before even with inorganic materials, not until the last 3–4 years. Automated 3D data collection also present as an untapped potential to collect 3D ED data from biological samples such as proteins, which could revolutionize the way protein structures are solved.

30.2 Precession and Rotation Methods

There are great scientific and applications interests in nanoparticles, meso-porous materials, metal-organic frameworks and zeolites as these materials represent a "bridge" between bulk materials and atomic/molecular structures. It has been assumed that a bulk material has constant physical properties independent of its size. However, this is often not true at the micro- and nano-scale. Size-dependency of material properties (particles become more reactive or catalytic) due to enormous increase of surface area to volume ratio has been observed in many cases [2, 3].

The structural characterization of these materials is often done using electron microscopy, both in image and diffraction modes. The drawback of conventional approaches is the low performance of an electron microscope in diffraction mode in comparison to an automatic X-ray diffraction collection method. The precession electron diffraction method, which involved conical electron beam movement [4], has gained popularity among electron crystallographers and is today often used for high quality electron diffraction data collection [5, 6]. However, this method required installation of an extra expensive hardware. We have recently developed a method to perform the same task using only software approach (no extra hardware needed) for computer controlled TEMs [7]. However, the precession method can only collect data within limited geometry (the range of accessible precession angles

is typically 1–3° both for hardware and software methods) and cannot be considered as a 3D data collection method. The real 3D data can only be recorded using other methods such as the tomography and rotation techniques [8, 9]. The latter is well known in the field of X-ray crystallography.

In the X-ray rotation method, the Bragg condition for each reflection is satisfied for monochromatic radiation by rotating the sample crystal. Each lattice plane is brought into the diffraction condition for a short period of time as the crystal rotates (see Fig. 30.1). An equivalent description is to imagine reciprocal lattice points traversing the Ewald sphere as the lattice rotates.

The wavelength for electrons is about 50 times smaller than that used in X-ray crystallography (∼0.02–0.03 Å for electrons against 1–2 Å for X-rays). This introduces a significant difference between electrons and X-rays – the radius of the Ewald sphere becomes very large in case of electron diffraction. It eliminates the influence of geometrical limits on the resolution, which then depends only on factors not related to the geometry of the experiment. We thus introduced automated electron diffraction rotation, which is robust and quite reliable in producing similar results as the X-ray rotation, into our recently developed method [9].

The main difference between the implementations of the X-ray and the electron diffraction rotation methods is the crystal tracking problem when a computer controlled TEM is used for the data collection. In order to avoid imperfections of TEM goniometers we scan reciprocal space by using the electron beam tilt within a given angular range and a small step. The beam tilt is combined with the mechanical crystal tilt to cover the full range of tilt angles available for the accessible TEM goniometer.

30.3 Data Collection

The automatic electron diffraction data collection is done through both mechanical and electronic controls. Firstly, the mechanical tilt is used in order to reach different low-index crystallographic axes. Secondly, the deflection coils of the electron microscope are used for tilting the beam electronically around some axis, thereby sampling and scanning reciprocal space with desired precision. The smallest beam tilt step depends on the TEM machine but can be as small as ∼0.0005°.

At present, our rotation method allows the 3D data collection in the range from −43° to +43°, the actual limits for our double tilt TEM sample holder, JEOL JEM-2100 LaB_6, covering ∼86° of reciprocal space, or from −75° to +75° using the single tilt holder. The complete data set contains 25 individual subsets for double tilt holder. Each subset has 80 individual frames recorded by tilting the beam with 0.05° steps between frames. Every data subset is recorded after physically tilting the sample at an interval of 3.5° to introduce some overlap (∼0.5°) between individual data subsets.

Our developed automated electron diffraction rotation tomography method can collect an impressive number of individual diffraction patterns, for example 2,880

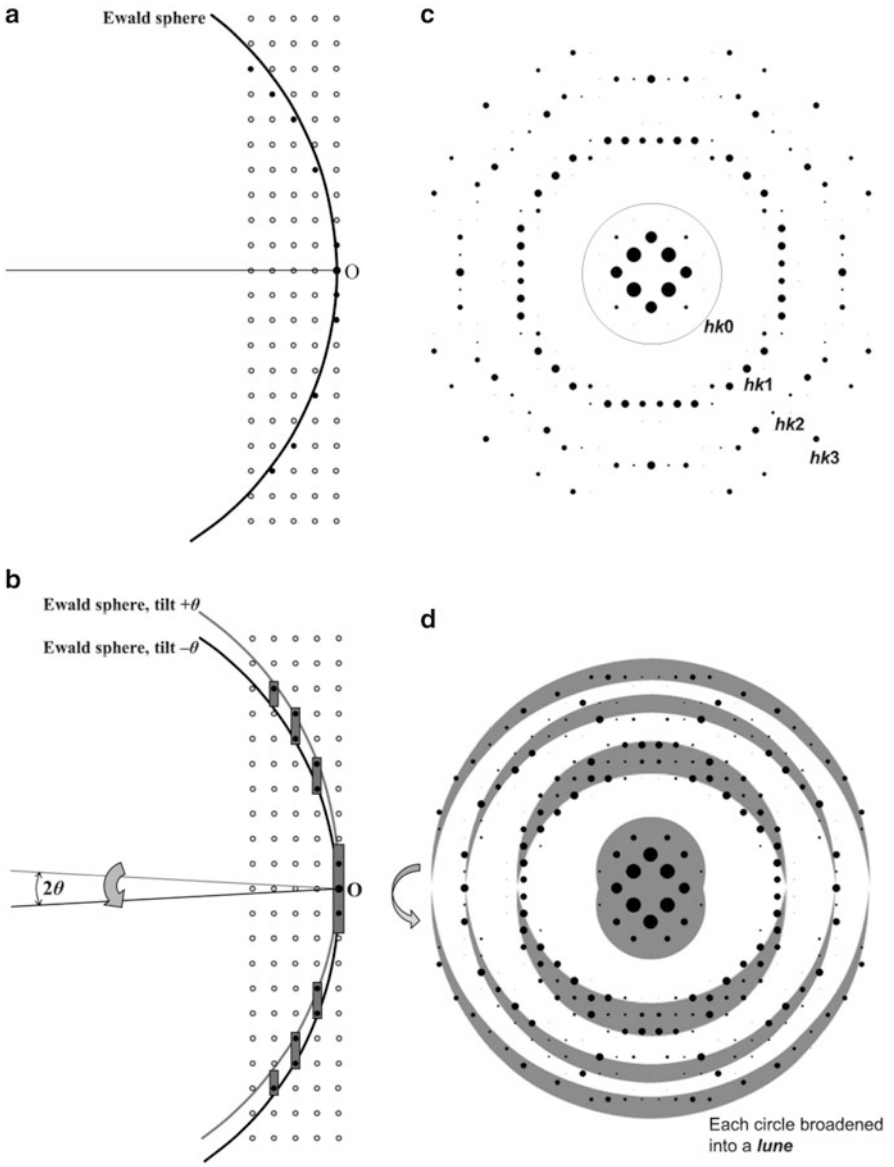

Fig. 30.1 X-ray rotation geometry. *Side views* of reciprocal space: (**a**) for the exact zone axis orientation and (**b**) during sweeping by the Ewald sphere. The schematic projection view showing the difference between (**c**) the static and (**d**) the rotating crystals (the *dark grey* regions represent the sampled areas where the reflections will be observed)

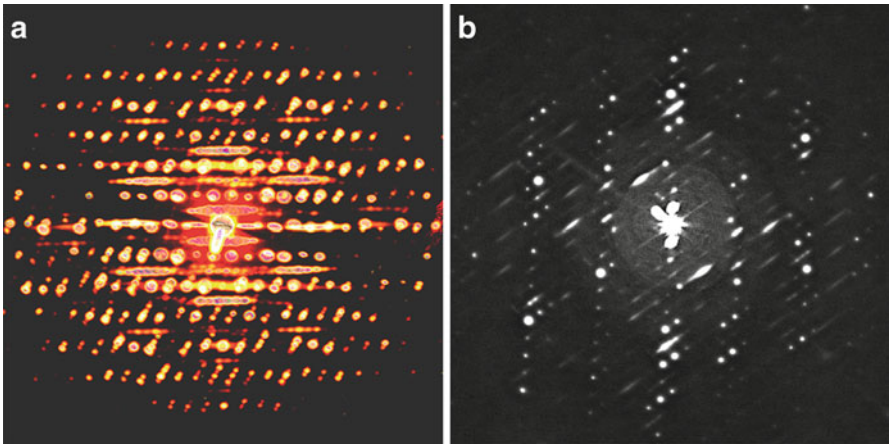

Fig. 30.2 The titanosilicate zeolite ETS-10. (**a**) A 3D reconstruction of reciprocal space after sweeping ∼150° of reciprocal space. (**b**) The accumulated electron diffraction pattern of 30 individual frames with a step of 0.15°. The diffuse scattering between main spots can be clearly observed as streaks (Data collection: P. Oleynikov, sample preparation: F. Hirotoshi, Stockholm University)

frames within 90 min. This means ∼1 frame per second, ∼60 min for 2,000 frames including *automatic crystal tracking*. The scanning of reciprocal space using rotation tomography not only allows the recording of the Bragg reflections, but also the 3D diffuse scattering intensity around and between diffraction spots (see Fig. 30.2).

There are different tilting modes that can be used in case of digital beam control: full scan, precession, or rotation [9]. The advantages of this approach are as follows. Firstly, at any beam tilt, the total number of excited reflections is low, which significantly reduces the dynamical effects [5]. Secondly, due to the integration effect during beam tilting (we "remember" all spots through the acquisition of individual diffraction patterns at each beam tilt), the final electron diffraction pattern has higher resolution than a regular selected area electron diffraction pattern.

The practical data collection and analysis shows that due to the strong dynamical interactions present in the zone-axis diffraction patterns it is normally better to avoid passing through the low-index zone axes. Thirdly, again due to the integration effect, the diffuse scattering intensity has higher amplitude on recorded diffraction patterns. This simplifies the measurements and the quantification of electron diffraction patterns from nano-sized, modulated or disordered samples.

The main problem which arises with electron diffraction tomography is the so-called "missing" cone. A part of data collected from one crystal is absent in some volume of reciprocal space. To avoid this problem a double tilt holder with capability of 360° continuous rotation of the sample can be used.

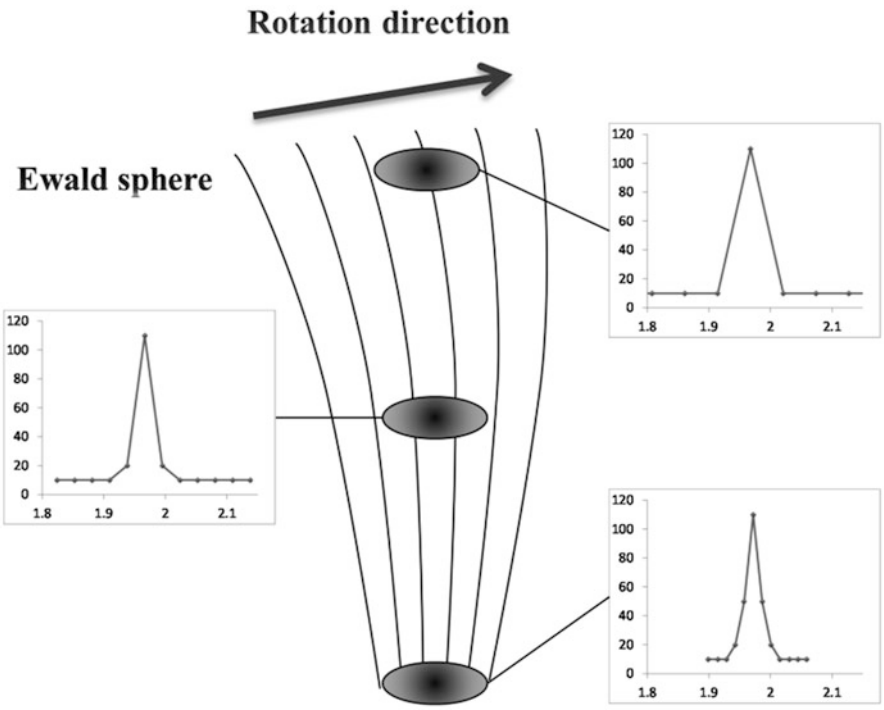

Fig. 30.3 The Ewald sphere sweeps through reciprocal space and samples reflections differently depending on their distance from the center of the reciprocal lattice. The corresponding intensity *curves* are shown for these reflections as *insets*

Another problem which shows up during the data collection and the data processing is the reflections sampling (see Fig. 30.3). If the half-width of the reflections is very small they can be sampled at only a few points (1–3) (if they appear at high resolution). Thus the beam tilt step must be chosen carefully in order to record enough sampling points for those reflections which appear at high resolution [9].

It is possible to use a specialized hardware (for example, from NanoMEGAS, Belgium) for the data collection. A single integrated frame (precession or rotation) can be recorded for each goniometer tilt instead of acquiring several individual diffraction frames at every beam tilt. The advantage of this approach is reduced data collection time per single data set since the hardware rocks the beam at high speed (60–1,000 Hz). The disadvantages are: (a) after each goniometer tilt the hardware alignment should be verified; (b) special care should be taken for the partially recorded reflections (partials of these reflections are recorded on two or more diffraction frames); (c) each reflection has uncertainty in the third dimension (e.g. for a diffraction pattern with rotation/precession angle range $-2°$ to $+2°$ and a reflection with the width $\theta°$, we can only say that it lies within the range $-2 - \theta/2 : +2° + \theta/2$).

30.4 Radiation Sensitive Materials

The use of cryo-TEM specimen holder allowed us to collect a data set and perform a partial reconstruction of a small part of reciprocal space of a sucrose sample. It was possible to maintain the data collection for ~12 min covering 16.5° in reciprocal space using the 3D rotation tomography.

30.5 Data Processing

The data from all series is combined into a 3D data set for reciprocal space reconstruction, representing a part of reciprocal space that has been sampled. This task is performed by a post data processing program "ED-tomo". After reciprocal space is reconstructed, all the reflections can be indexed. The unit cell dimensions and space group can thus be determined even for a crystal with unknown structure. When the integrated intensities of all the reflections are estimated, *hkl* files can be produced and used for solving the structure.

The collected and processed data of high quality can be used for further determination of the 3D crystal structure. Figure 30.4 shows the results of data collection and crystal structure analysis using the rotation tomography method, for a $K_2Nb_{14}O_{36}$ sample (space group *P4/mbm*, unit cell a = b = 27.5 Å, c = 3.94 Å). For a $K_2Nb_{14}O_{36}$ crystal with tetragonal symmetry, a general *hk*0 reflection appears 8 times while a general *hkl* reflection appears 16 times (8 times as *hkl* and another 8 times as *hk*–l). In other words, we only need to reconstruct 1/16 of reciprocal space to get a complete 3D reflection data set. For structures with lower symmetries, more coverage of reciprocal space during data collection is needed.

The oxygen atoms can be easily identified in the calculated 3D potential map (Fig. 30.4c, d). This is the first time, for the given structure, when the oxygen atoms have been localized and identified in the 3D potential map using electron microscopy.

30.6 Conclusions

We have developed a software-based method, for computer-controlled TEMs, to automatically collect 3D electron diffraction data from particles or crystals with a size of only a few nanometers. We have shown that up to 2000 unique diffraction patterns can be collected within 1 h using our approach, an impressive improvement over the conventional method, which can take months to collect less than a 100 frames. Both the data collection and the alignment and calibration procedures are all automatic, which opens new applications for those crystallographers and material scientist who are not experts in TEM operations. By this rotation method, reciprocal

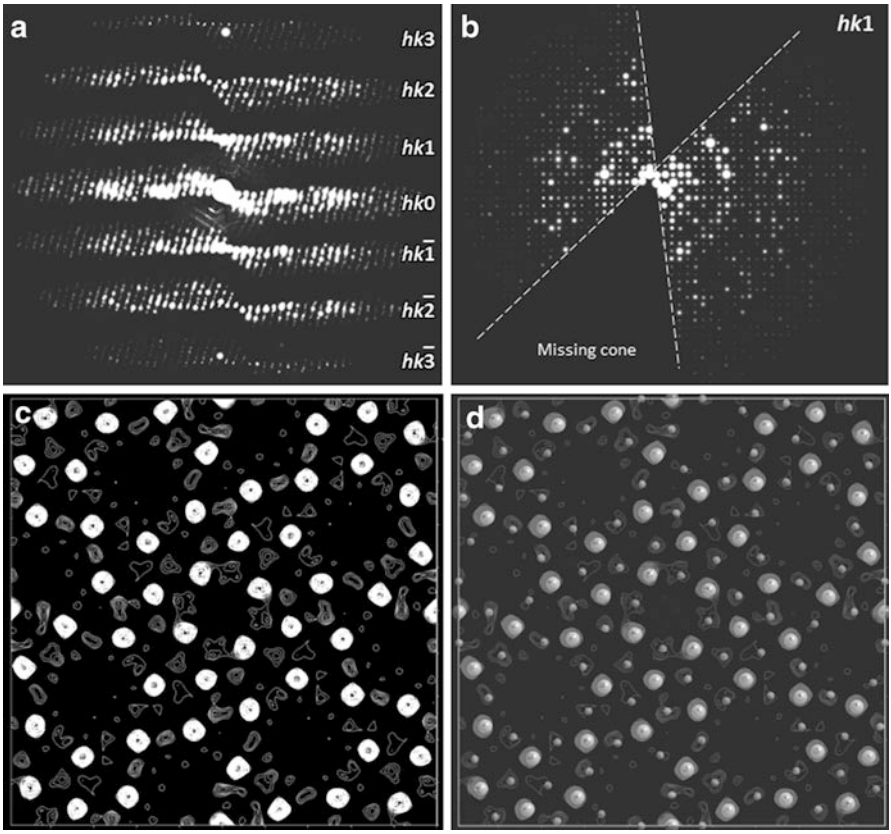

Fig. 30.4 From the 3D reconstruction of reciprocal space to 3D crystal structure solution. (**a**) The 3D reconstruction of reciprocal space after sweeping ∼120° (2,880 diffraction patterns). The pattern shows the intensity distribution within hkl reciprocal layers with different Miller index l. This is the first time such reconstruction is done for electron diffraction. (**b**) The hk1 slice of reconstructed reciprocal space (**a**) with the missing cone marked. (**c**) The calculated projected potential using the intensities extracted from reconstructed reciprocal space. (**d**) The overlay of the real atomic structure (large = niobium, small = oxygen) on the calculated potential (**c**)

space can be reconstructed with very high resolution (1–0.6 Å). With measures taken to minimize the electron beam damage, this technique may also be applied to beam-sensitive materials such as organic molecules and even bio-molecules such as proteins, allowing full 3D electron diffraction data sets from crystals of unprecedented small sizes to be collected.

Acknowledgments The Swedish Science Research Council (Vetenskapsrådet) and Göran Gustafsson Foundation are thanked for financial support. The electron microscopes used were purchased from a grant given by the Knut and Alice Wallenberg Foundation.

References

1. Zou XD, Mo ZM, Hovmöller S, Li XZ, Kuo KH (2003) Three-dimensional reconstruction of the ν-AlCrFe phase by electron crystallography. Acta Crystallogr A 59:526–239
2. Ying J (2001) Nanostructured materials. Academic, New York
3. Mnyusiwalla A, Daar AS, Singer PA (2003) Mind the gap: science and ethics in nanotechnology. Nanotechnology 14:R9–R13
4. Vincent R, Midgley PA (1994) Double conical beam-rocking system for measurement of integrated electron diffraction intensities. Ultramicroscopy 53:271–282
5. Oleynikov P, Hovmöller S, Zou XD (2007) Precession electron diffraction: observed and calculated intensities. Ultramicroscopy 107:523–533
6. Gemmi M, Klein H, Rageau A, Strobel P, Le Cras F (2010) Structure solution of the new titanate $Li_4Ti_8Ni_3O_{21}$ using precession electron diffraction. Acta Crystallogr B 66:60–68
7. Zhang DL, Grüner D, Oleynikov P, Wan W, Hovmöller S, Zou XD (2010) Precession electron diffraction using a digital sampling method. Ultramicroscopy 111:47–55
8. Kolb U, Gorelik T, Kübel C, Otten MT, Hubert D (2007) Towards automated diffraction tomography: part I – data acquisition. Ultramicroscopy 107:507–513
9. Zhang D, Oleynikov P, Hovmöller S, Zou XD (2010) Collecting 3D electron diffraction data by the rotation method. Z Kristallogr 225:94–102

Chapter 31
Introduction to ADT/ADT3D

Tatiana E. Gorelik, Sebastian Schlitt, and Ute Kolb

Abstract ADT approach was successfully used within the last years to solve crystal structure of nanocrystalline material *ab-inito* using programs initially written for X-ray diffraction data. The methodology of ADT data analysis including data extraction in a format suitable for established structure solution programs was developed. A collection of processing routines was implemented into dedicated software ADT3D. Here the main steps of ADT data processing are explained, and the complete sequence of steps from importing raw data to saving the *hklI* file is demonstrated.

31.1 Introduction

Automation of an electron diffraction experiment does not only simplify the data acquisition procedure but also drastically improves the quality of the data and its performance for structure analysis. Instrumentally two possibilities exist for 3D diffraction data collection: tilting a crystal in respect to the electron beam and tilting the beam in respect to the crystal. The beam tilt controlled by magnetic lens is much more precise, but the tilt range is limited to several degrees. Therefore in order to collect diffraction data from a reasonably large fraction of the reciprocal volume, a combination of the beam tilt and crystal (stage) tilt has to be used. This method

T.E. Gorelik • U. Kolb (✉)
Institute of Physical Chemistry, Johannes-Gutenberg University Mainz, Welderweg 11, 55128 Mainz, Germany
e-mail: gorelik@uni-mainz.de; kolb@uni-mainz.de

S. Schlitt
Institute of Mathematics, Johannes Gutenberg University Mainz, Staudingerweg 9, 55128 Mainz, Germany
e-mail: schlitt@uni-mainz.de

U. Kolb et al. (eds.), *Uniting Electron Crystallography and Powder Diffraction*, NATO Science for Peace and Security Series B: Physics and Biophysics,
DOI 10.1007/978-94-007-5580-2_31,

is called rotation electron diffraction – RED [1]. Alternatively, electron diffraction data can be collected using stage tilt solely. This approach was developed under the name Automated electron Diffraction Tomography (ADT). This chapter describes the experimental procedure to acquire ADT data as well as major processing steps necessary to prepare the data for structure analysis. The ADT method is being actively developed at the moment therefore the proposed algorithms should be seen as possible solution of the problem, thus inspiring further improvement of the method.

In contrast to traditional electron diffraction data collection approach – using zonal data, ADT data acquisition is performed through a tilt around an arbitrary crystallographic axis, intentionally avoiding low index patterns. The patterns are collected using a small tilt step sampling the reciprocal volume almost continuously. Coupling with electron beam precession geometrically integrates reflection intensities also "between" the frames.

ADT diffraction patterns do not have internal symmetry; even inversion related Friedel-pairs may not be found in one pattern. Therefore, special automated procedures are necessary to treat this kind of data. These procedures should be able to read in the data as delivered by an ADT experiment and transform it into the information which can be directly used by a structure solution program. Essentially this information is the unit cell metric, symmetry and indexed reflection intensities (*hklI* data set).

Initially a processing package was developed in MatLab (The MathWorks Inc.), later in order to improve performance and enhance visualization possibilities, all routines were implemented in ADT-3D package written in C (ADT3D, NANOMEGAS, Belgium). Below key points of the processing will be discussed in details.

31.2 ADT Experiment

An ADT experiment can principally be realized in any transmission electron microscope (TEM). Electron diffraction patterns can either be collected using nano-electron diffraction (NED) or selected area electron diffraction (SAED) beam geometry [2]. The complete acquisition sequence would include diffraction pattern acquisition, tilting and adjustment of the crystal position. An automated acquisition module, developed in collaboration with FEI for TECNAI class TEMs [3], uses NED mode for diffraction data acquisition and scanning transmission electron microscopy (STEM) mode for crystal imaging.

No matter if the diffraction data is collected using the devoted automated acquisition module or in a manual way, the output of the experiment is a stack of electron diffraction patterns representing the covered reciprocal space (see Fig. 31.1). The stack of patterns can be stored either as a set of separate 2D files, or a single 3D file (MRC file format was selected for 3D ADT data). A 2D stack can easily be transformed into a 3D file and processed further.

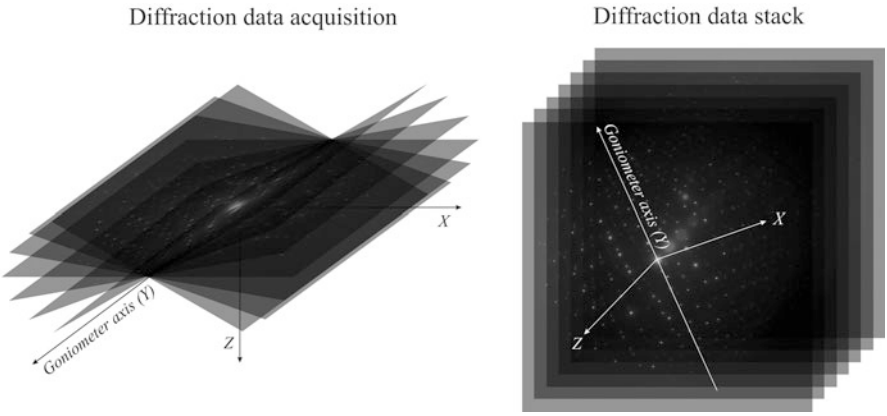

Fig. 31.1 Schematic representation of ADT acquisition geometry: the Y axis is defined along the goniometer axis, the X axis within the zero-tilt pattern and orthogonal to Y. The Z axis is orthogonal to X and Y and completes the right handed Cartesian coordinate system

ADT experimental data appears quite different in comparison to what electron crystallographers are used to, because the patterns lack symmetry (inversion-symmetry related reflections are not always present in a pattern) the azimuthal position of the tilt axis within a diffraction pattern is not known a-priori, and the centre of different diffraction patterns in a stack may be shifted for different patterns.

ADT diffraction patterns should satisfy specific quality requirements: the reflections within a pattern may not form a continuous lattice. Coexistence of several overlapping lattice parts usually is an indication of the polycrystallinity within the diffracted volume and should be avoided. The intensities of the reflections should be strong in order to use most of the available dynamic range of the recording media, but not overexposed. Exposure series may help to increase the dynamical range and record the strong reflections as well as weak. The transmitted beam should have smooth symmetrical form. The background in the patterns possibly caused by contamination/ice crystal formation when cooling is used should be low. These data then have a high success rate for ab-initio structure solution.

31.3 Preprocessing

Geometrically, diffraction patterns are collected through a tilt around a goniometer axis, so it is reasonable to consider the complete data in cylindrical coordinates. Before associating cylindrical coordinates with the data, the position of the coordinate origin and the cylindrical axis have to be determined. In other words, the patterns must be centered and the azimuthal position of the tilt axis has to be found.

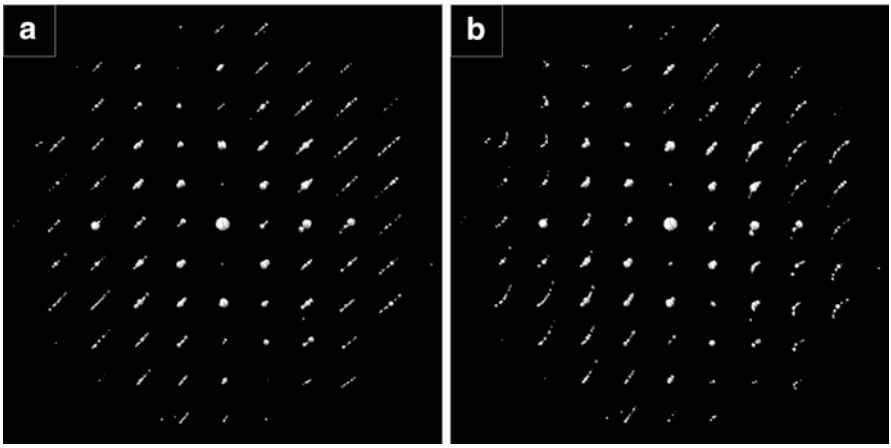

Fig. 31.2 Views of 3D reconstructed diffraction volume: (**a**) using the correct tilt axis position, (**b**) using a tilt axis position 10° off

31.3.1 Pattern Centering

The position of the transmitted beam can serve as a stable reference for pattern centering. The transmitted beam appears as a strongest "spot" in a diffraction pattern (if it does not, something is seriously wrong – maybe the crystal is too thick). Therefore, a simple approach of searching for the centre of mass in the pattern can already deliver a good centre vector. Analyzing the shape of the transmitted beam is another method to centre the patterns and sometimes delivers a more accurate result.

Both of these methods can be applied only if the shape of the transmitted beam is not disturbed significantly, which is the case when a beam stopper was used during diffraction pattern collection. In this case the patterns can be still centered when a Friedel pair can be found. In a general case the centering procedures cannot rely on 2D data solely, but on the mutual consistency of the 3D reciprocal lattice.

31.3.2 Tilt Axis Position Determination

Knowing the exact azimuthal position of the tilt axis within 2D diffraction patterns ϕ is essential for proper coordinate transformation. However this value is not trivial to estimate. A wrong assumption on the tilt axis position causes distortion of the 3D diffraction space after reconstruction, and can even compromise the lattice parameters determination. The effect is shown in Fig. 31.2.

The correct tilt axis position can be refined assuming that the correct geometry should produce a periodic equidistant net of reflections. Therefore, the geometrical consistency of the 3D lattice is used as a criterion for ϕ refinement. For different trial positions of the tilt axis a 3D net of reflections is constructed and the spatial

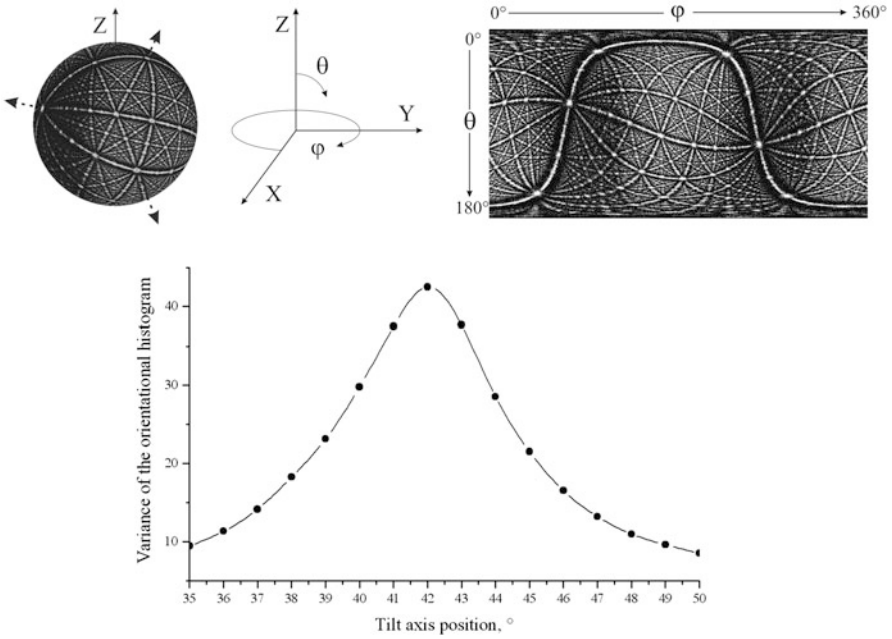

Fig. 31.3 The routine for tilt axis determination for a $BaSO_4$ data set: spherical projection of the difference vectors mimicking a stereographic projection of a crystal, an image of the cylindrical projection of the sphere surface and a variance plot of this image. A well pronounced maximum of the variance plot represents the correct position of the tilt axis

orientation of the vectors ending at reciprocal nodes is analyzed. Wrong values of ϕ cause distortion of the 3D periodical net of reflections while the correct position of the tilt axis should result in a sharp well pronounced pattern of the spatial distribution, resembling a stereographic projection. A spherical projection of all reflections (or their difference vectors) is produced and the quality of this projection is traced while ϕ is adjusted. Figure 31.3 shows a spherical projection of a $BaSO_4$ tilt series together with its cylindrical projection in (φ, θ) coordinates. The detailed description of the procedure can be found in [4]. The routine is very stable and can refine the position of ϕ down to the accuracy of 0.2°.

31.3.3 Reconstruction of a 3D Volume

A diffraction pattern is a set of reflections approaching the given position of the Ewald sphere, projected onto 2D recording media (CCD or image plate plane). Therefore, knowing the 2D coordinates of a pixel within a diffraction pattern {x, y}, tilt position α, and the radius of the Ewald sphere R, it is possible to reconstruct the 3D Cartesian coordinates {X, Y, Z}.

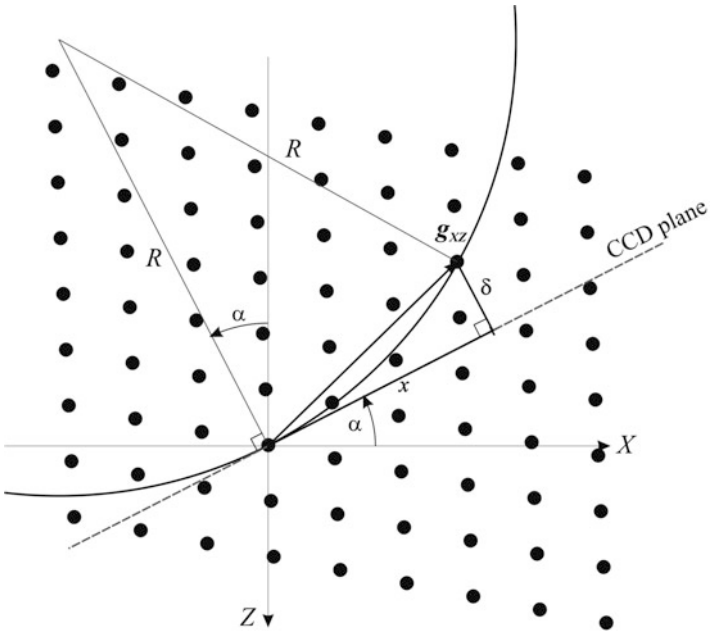

Fig. 31.4 Schematic sketch of coordinate system associated with diffraction data collection, viewed along the tilt axis direction

Figure 31.4 represents a sketch of the diffraction geometry viewed along the tilt axis. A reflection is excited when it approaches the surface of the Ewald sphere. Then it is projected onto the CCD/image plate plane. Due to the curvature of the Ewald sphere, there is an effective height of a reflection δ. For a reflection with a given vector g, having 3D coordinates {X, Y, Z}, one can write:

$$\begin{pmatrix} X \\ Y \\ Z \end{pmatrix} = \begin{pmatrix} x \cdot \cos\alpha \\ y \\ -x \cdot \sin\alpha \end{pmatrix} + \left[R - \sqrt{R^2 - x^2 - y^2} \right] \cdot \begin{pmatrix} -\sin\alpha \\ 0 \\ -\cos\alpha \end{pmatrix};$$

Here x and y are 2D coordinates of the reflection projection on the CCD plane, $\alpha$is the goniometer tilt angle, and R is the radius of the Ewald sphere.

Using these formulae a complete reciprocal volume can be reconstructed from a 2D data stack. Fixed tilt steps (1°) result in gaps in the reciprocal volume, which are filled by data interpolation. Visualization of the volume helps detecting possible extinction conditions and therefore provides hints about the symmetry of the martial. Centering of the lattice causes an extinction pattern going through the complete volume; glide planes can be detected as rows of missing reflections along specific directions (see Fig. 31.5a). Serial extinctions due to screw axes cannot be visualized directly within the volume, because of the overlap with other reflections, but can be detected in a zone clipped out of the reciprocal volume (Fig. 31.5b). Additionally

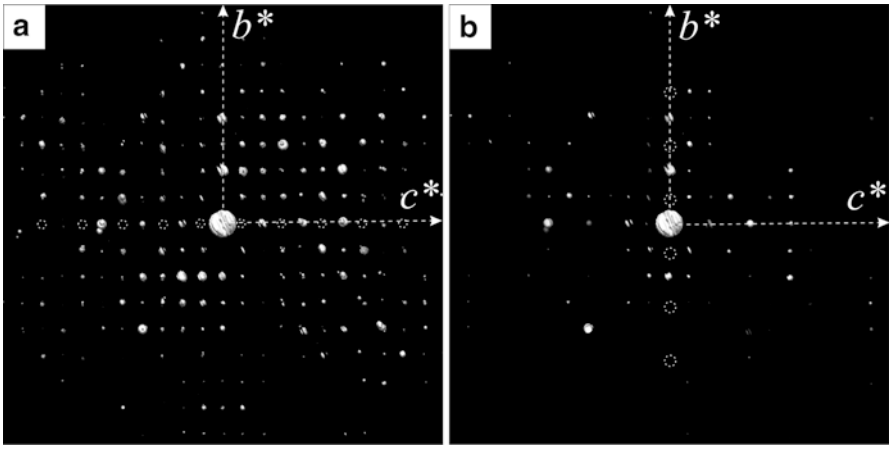

Fig. 31.5 Views of the reciprocal volume of OPBA3 $P2_1/c$: (**a**) a view of the volume along the (100) direction: zonal extinctions due to a c-glide plane are marked by dotted circles; (**b**) a planar cut close to the [100] zone clipped out of the volume: serial extinctions due to 2_1 screw axis are evident

to symmetry determination, the visualization of the reciprocal volume can deliver information about the quality of the data, possible polycrystallinity, disorder effects, superstructures, and other specific crystallographic features.

31.4 Lattice Parameter Determination

31.4.1 Determination of 3D Reflection Positions

Unit cell vectors are determined based on the 3D positions of the reflections within the reciprocal volume [5]. Therefore, first positions of reflections should be found. Principally, the reflections can either be found within the reconstructed 3D volume as 3D intensity volumes, or within 2D patterns of a data stack including a recalculation of their coordinates into 3D with the formalism described above. Either way has its benefits and drawbacks mainly based on the algorithm used for reflection identification. At the end both approaches should deliver the same unit cell parameters.

31.4.2 Difference Vectors Space Approach

A collected tilt series usually covers a large part of the reciprocal volume, but practically rarely comprises all three main crystallographic axes. Since, reflections

corresponding to the shortest reciprocal vectors and therefore to main directions are usually close to the transmitted beam a determination of their coordinates may not be accurate. It order to enhance basic lattice vectors and statistically average the unit vector over the complete reciprocal lattice, autocorrelation of the detected peak positions is used. From all collected peaks difference vectors are calculated. Three shortest linearly independent vectors should then represent the main directions of the lattice.

Figure 31.6a shows a part of an idealized reciprocal lattice. The two main directions are not included into the collected volume, so they cannot be found directly from the data. On the right side the difference vector space (DVS) of the lattice is presented. All difference vectors create an ideal lattice, which clearly exhibit the basic vectors.

Experimentally slight offset of reflections from their idealized position is always present. Figure 31.6b shows a sketch of a lattice with randomly shifted nods. For this lattice in the DVS the nodes become blurred, although the periodicity of the lattice is clearly present. When larger random shift vectors are used for the reciprocal lattice nodes (Fig. 31.6c), the lattice in the DVS appears even more unclear. More complicated situations are often met – when the displacement of the reciprocal lattice nodes is anisotropic (for instance due to thin-foil effect). In this case elongated groups of spots are seen in the DVS.

Although for distorted data the lattice nodes in the DVS are not clearly defined, the periodicity of the experimentally measured reciprocal lattice is preserved and even enhanced. Finding the centers of the groups of spots and thus determining the basis vectors in this kind of data can be done using cluster analysis approach.

31.4.3 Clustering

Cluster analysis is a technique used for data classification within sets in which the elements possess a certain dissimilarity function. This dissimilarity function can be of different nature: *e.g.* a distance between the elements. It is seen from Fig. 31.6c that the elements are not homogeneously distributed over the field, but grouped around the lattice nodes. Use of best suited clustering algorithms allows finding the centers of the nodes.

A systematic study of main clustering approaches and their application to ADT data revealed that the most robust and fast algorithms are density based, among which DBSCAN [6] was selected for implementation in ADT3D.

Once three linear independent shortest vectors are found, the primitive unit cell is determined. If the lattice is centered, the three vectors do not represent the correct cell, but can be easily recalculated.

If the lattice is centered, the reflection indices can be determined using the primitive unit cell and recalculated into a centered lattice or the intensities can be integrated using the centered unit cell directly.

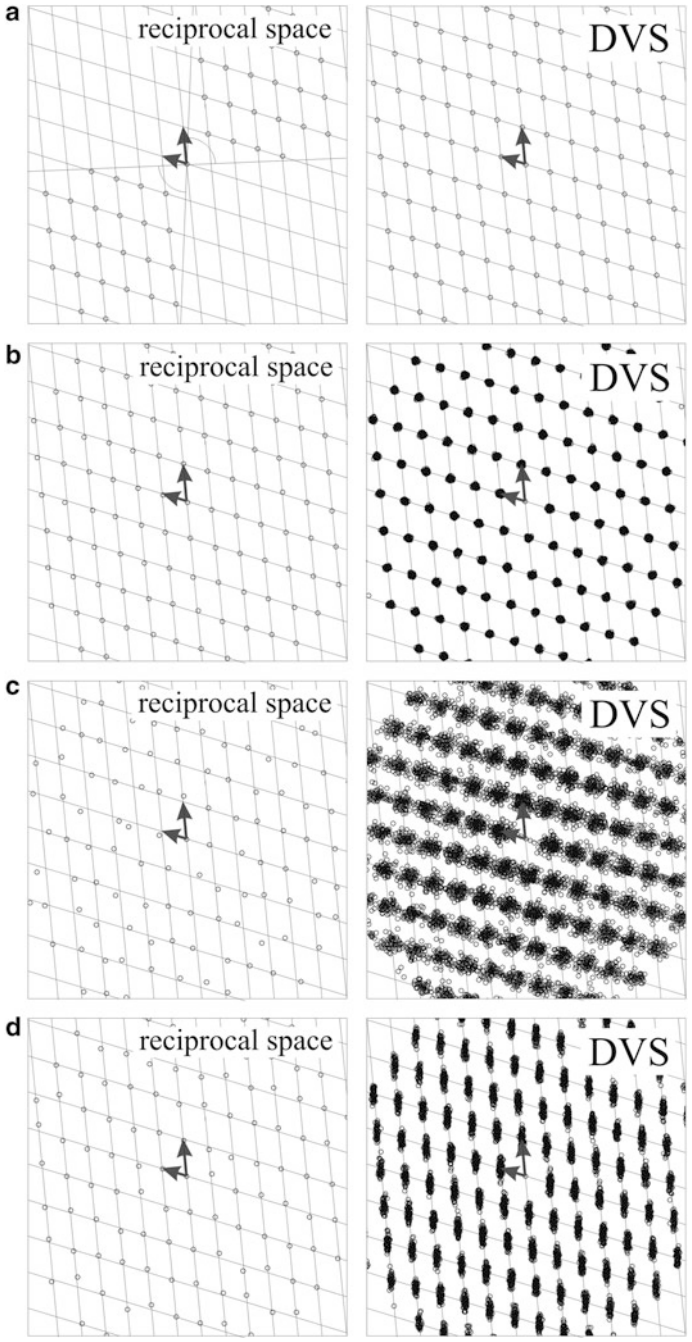

Fig. 31.6 Schematic view of reciprocal lattice (*left*) and corresponding difference vector space (*right*): (**a**) idealized lattice defined within a restricted wedge; (**b**) lattice nodes are randomly shifted from their idealized positions; (**c**) the nodes of the lattice are shifted randomly using a larger shift vector; (**d**) the shift vector components are different along the two main directions

31.5 Intensity Integration

Once unit cell parameters and the orientation matrix have been determined, the positions and indices of reflections in 2D diffraction patterns can be assigned, and therefore intensities in vicinity of these positions can be integrated and assigned to a specific (*hkl*). For the correct projection of the 3D net onto 2D diffraction patterns the effective camera length and the effective radius of the Ewald sphere need to be known accurately.

A detailed description of the integration procedure can be found in [7]. In Fig. 31.7 an original 2D pattern and the same pattern with integration boxes are shown. The size of integration boxes is related to the lattice parameters for a given crystal. Within the integration boxes a "local" background function is calculated and subtracted.

Due to the effective diffraction peak size in 3D, reflections typically penetrate through several diffraction patterns. Therefore, from the integration of the whole 2D data several intensity values can be found for the same (*hkl*) index. For all analyzed structures only the maximal intensity value associated with each (*hkl*) has been taken into consideration, no matter how many times the reflection was sampled at different tilt steps, supposing that in this slice of the reciprocal space the reflection was cut closest to its middle point. As a result of the intensity integration, an intensity *hkl* file is created analogous to single crystal X-ray data analysis.

The error in the measured intensity strongly depends on the exact position where the reflection was cut by the Ewald sphere. If the cut passes close to the center of the reflection, the maximal possible and optimum value is reached. Otherwise, if the reflection intersects the Ewald sphere further away from the center recording

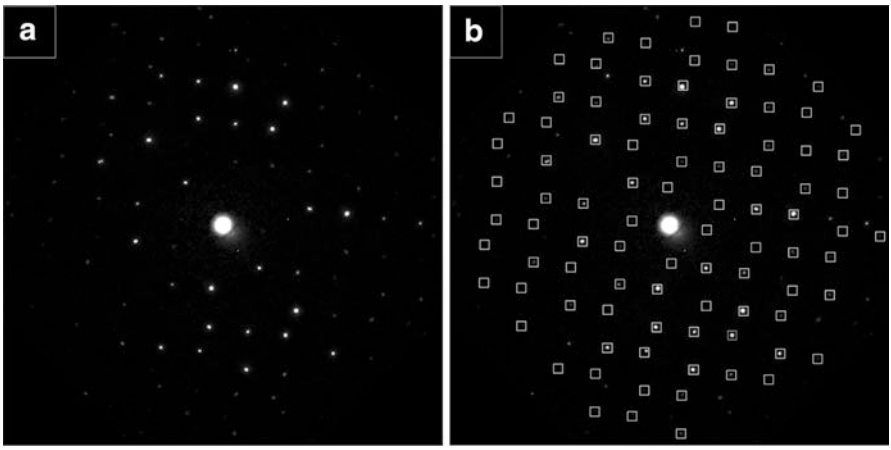

Fig. 31.7 Diffraction pattern of natrolite (**a**), the same pattern with integration *boxes* on it (**b**)

the outer part of the reflection, the experimental intensity value is likely to be underestimated. The electron beam precession, integrating a volume rather than delivering a mere cut, considerably reduces this problem.

31.6 Conclusion

ADT experiment delivers a specific kind of data. The data is not intuitive, and therefore the extraction of information needs dedicated automated routines. These routines should be able to import the data as it is produced by an ADT experiment and export the information which can be further used by a structure solution program, *i.e.*, from a stack of off-zone electron diffraction patterns, lattice cell parameters, symmetry and a *hklI* data set should be produced.

The processing routines are combined in the program ADT3D including data preprocessing and refinement of geometrical acquisition parameters. After the unit cell determination using density-based clustering algorithm the reflections are indexed and their intensity is integrated using the found set of lattice basis vectors. Finally, a *hklI* file is produced in a format taken by most structure solution programs.

References

1. Zhang D, Oleynikov P, Hovmöller S, Zou X (2010) Collecting 3D electron diffraction data by the rotation method. Z Kristallogr 225:94–102
2. Williams DB, Carter CB (1996) Transmission electron microscopy, vol 1–4. Plenum Press, New York
3. Kolb U, Gorelik T, Kübel C, Otten MT, Hubert D (2007) Towards automated diffraction tomography: part I—data acquisition. Ultramicroscopy 107:507–513
4. Kolb U, Gorelik T, Mugnaioli E (2009) Automated diffraction tomography combined with electron precession: a new tool for ab initio nanostructure analysis. Mater Res Soc Symp Proc 1184:GG01–GG05
5. Kolb U, Gorelik T, Otten MT (2008) Towards automated diffraction tomography. Part II—cell parameter determination. Ultramicroscopy 108:763–772
6. Ester M, Kriegel H-P, Sander J, Xu X (1996) A density-based algorithm for discovering clusters in large spatial databases with noise. In: Proceedings of the 2nd international conference on knowledge discovery and data mining. AAAI Press, Portland, OR
7. Mugnaioli E, Gorelik T, Kolb U (2009) "Ab initio" structure solution from electron diffraction data obtained by a combination of automated diffraction tomography and precession technique. Ultramicroscopy 109:758–765

Chapter 32
Electrostatic Potential Determined from Electron Diffraction Data

Anatoly Avilov

Abstract Modern level of the precise electron diffraction structure analysis (EDSA) provides possibility of the quantitative analysis of electrostatic potential and electron density of crystals and, therefore, brings us closer towards the ultimate goal of direct study of properties of solids. It is shown on an example of NaCl type structures with ionic bonding and Ge, which has covalent bonds. Analytical structural models of crystals built on the basis of EDSA data, enabled for the first time quantitative characterization of chemical bonding and study of topological features of electrostatic potential. It was established that the inner crystal field is well structured, and its topological analysis revealed important features of a structure which essentially enrich our understanding of the interatomic interactions in crystals.

32.1 Introduction

Fundamentals of electron diffraction structural analysis (EDSA) of crystals using high-energy electron diffraction were formulated in the book, "Structural Analysis by Electron Diffraction" by B.K. Vainshtein [1]. State of method and the main practical areas of EDSA, including theoretical foundations, experimental techniques, preparation, definition of structure amplitudes and the actual structural results are summarized in [2]. The main features of the EDSA were underlined there as:

1. Scattering on inner crystalline electrostatic potential;
2. Strong interaction of electrons with matter;

A. Avilov (✉)
Institute of Crystallography of Russian Academy of Sciences, ICRAS, Leninsky Prospekt 59, 119333 Moscow, Russia
e-mail: avilov@crys.ras.ru

U. Kolb et al. (eds.), *Uniting Electron Crystallography and Powder Diffraction*,
NATO Science for Peace and Security Series B: Physics and Biophysics,
DOI 10.1007/978-94-007-5580-2_32,

3. High intensity of the diffracted beams, comparable with the intensity of synchrotron radiation;
4. High sensitivity to the distribution of valence electrons.

Hence we see the advantages of EDSA over other diffraction methods, the main one – the opportunity to investigate the structure of nano-objects and the electrostatic potential.

Mainly polycrystalline samples are used as objects in the EDSA. In such samples, a large number of small crystals, which are either completely disordered or oriented in a certain way, fall simultaneously under the incident electron beam. This creates conditions for the formation of a special type of diffraction patterns with solid rings for polycrystals, arcs for the texture and the broadening of reflections due to the misorientation of the microcrystallites from mosaic crystals. These unique diffraction patterns contain three-dimensional set of reflections that corresponds to large scattering angles, which make it possible to perform structural analysis with high resolution [1, 2].

For the diffraction of electrons with energies over 10 keV the interaction effects between the incident electron and the electrons of the crystal can be neglected. In this case, the method gives the Fourier transforms of the electrostatic potential (ESP) of atoms, molecules and crystals (structure amplitudes). ESP determines a number of important properties of crystals, including features of atomic and molecular interactions. That is why high-energy electron diffraction is attracting attention as a method for obtaining direct information about the physical properties of crystals. It is important that for a certain arrangement of atoms in the unit cell, ESP can be calculated using the Hartree-Fock or the Kohn-Sham equations [3, 4]. Thus, the results of electron diffraction experiments allow direct comparison with the theory.

Provided high accuracy of the experiment and regarding atoms in a crystal as non-spherical, it is possible not only to improve the accuracy of atomic positions and parameters of their thermal vibrations, but also quantitatively reconstruct 3D continuous distribution of ESP. Thermal parameters are related to the quantities, derived in the theory of the dynamics of the crystal lattice. ESP is associated through Poisson equation with the full charge density, the electron part of which, as was shown by Hohenberg and Kohn [5], completely determines all the properties of ground electronic states of atoms, molecules and crystals. Electron density (ED), defining the characteristics of the crystal field and the chemical bonding in matter, is also ground variable in the quantum mechanical density functional theory, which describes the electronic properties of substances, and its characteristics are used in different physical models. Thus, if the characteristics of the ESP are obtained from electron diffraction, one can easily investigate the electron density of crystals. These relations bring EDSA on the front edge of physics and chemistry of solids.

For quantitative study of the distribution of electrostatic potential and electron density, we need to develop [6]:

– electron diffractometry with precise measurement of intensities;
– modelling techniques based on the ESP experimental data and estimate its real accuracy;

– methods for treating a continuous distribution of ESP in terms of conceptions of physics and chemistry of solids.

In general, thermal diffuse scattering leads to an underestimation of the height of the Bragg peaks and appears near the peaks and between them. Carrying the smooth lines of the background makes it possible to partially take into account the thermal diffuse scattering. We have shown that ignoring the absorption of very thin polycrystalline films of materials with low atomic numbers does not give appreciable experimental errors in determining the structure amplitudes. We may conclude that EDSA allows one to make systematic, precise electron-diffraction studies of ESP of crystals of various types.

32.2 Electron Diffractometry

For precise structural analysis of crystals, quantitative recovery of ESP and analysis of the chemical bond in crystals it is necessary to obtain the most comprehensive set of structural amplitudes with the statistical accuracy of better than 1–2%. For this purpose, we developed a system of electronic diffraction on the basis of domestic electron diffraction chamber EMR-110K, produced by Selmi Ltd. The well-known principle of measurement was used [7]: the diffraction pattern is scanned point by point before the stationary receiver. Scanning and measurement control can been made by a computer in the accumulation mode or in the time constant mode.

For precise measurements it is necessary to provide a wide dynamic range, a sufficient angular resolution and high performance of measurement systems. A new type of detector was developed in the Institute of Crystallography in Moscow, based on the principle of measuring the electron current with a Faraday cup [8]. This type of detector, as it is known, is the most linear and has a wide dynamic range. Usually it is used for checking the metrological characteristics of other detectors (e.g. CCD-cameras, imaging plates).

32.3 Topological Characteristics of the Electrostatic Potential

Electrostatic (Coulomb) potential is a scalar function depending on a charge density

$$\varphi(r) = \int_{-\infty}^{\infty} \left\{\sigma(r')/\left|r - r'\right|\right\} \cdot dv',$$

having nuclear and electronic components:

$$\sigma(r') = \sum Z_a \cdot \delta(r' - R_a) - \rho(r') \tag{32.1}$$

Here Z_a and R_a are the charge of the nucleus of an atom *a* and its coordinate, $\rho(r')$ – electron density. ESP includes the mean inner potential φ_0, which depends on the shape and surface structure of the crystal. φ_0 can be determined experimentally by electron holography or calculated theoretically. Characteristics of the atomic-molecular interactions and crystal packing can be concluded from the distribution of the ESP. In addition, knowing the ESP, gradient of the electric field at the nuclei can be defined. This quantity appears in the characteristics of nuclear quadrupole resonance and Mössbauer spectroscopy, diamagnetic susceptibility and the coefficient of the refractive index of the electrons.

ESP of the multi-electron multi-core systems has maxima, saddle points and minima corresponding to those nuclei, the internuclear lines, nuclear cycles and closed cavities in the unit cell. Consequently, as ED, the ESP may be characterized by critical point (CP), $\mathbf{r_c}$, in which $\nabla\varphi(\mathbf{r}_c) = 0$. In terms of the topological analysis [9] CP-s, corresponding to saddle points, one-and two-dimensional minima are denoted as (3, −1) and (3, +1), and maxima and minima as (3, −3) and (3, +3), respectively. Here 3 is the number of nonzero nondegenerate eigenvalues of Hessian of ESP, and the second number in parentheses is the sum of the algebraic signs of λ_i (diagonal member in Hessian).

The electrostatic potential is convenient to characterize by the vector field gradient $\nabla\varphi(\mathbf{r})$ and by the curvature $\nabla^2\ \varphi(\mathbf{r})$. Importantly, these characteristics do not depend on the constant φ_0. As it is known, the vector of intensity of the classical electrostatic field $\mathbf{E}(\mathbf{r}) = -\nabla\varphi(\mathbf{r})$, sent along the tangent to the gradient line ESP at a given point and the concentration of these lines passing through a unit area perpendicular to it, is the value of intensity of the field at this point.

Nucleus of the neighboring atoms in any crystal or molecule are separated in a field $\mathbf{E}(\mathbf{r})$ by surfaces satisfying the condition of zero flux:

$$E(n) \cdot n(r) = -\nabla\varphi(r) \cdot n(r) = 0, \quad \forall r \in S_i(r), \tag{32.2}$$

where $\mathbf{n}(\mathbf{r})$ – the unit normal to the surface. These surfaces define the specific atomic fields (atomic basins), within which the nuclear charge is completely screened by electron charge, i.e. they define electrically neutral *bonded* pseudoatoms.

ESP determining inner crystalline electrostatic field $\mathbf{E}(\mathbf{r})$, produced by all the nuclei and electrons, determines also the value of the classical electrostatic (one-electron) Coulomb force at the point $\mathbf{r}$. By condition $\nabla\varphi(\mathbf{r}_c) = 0$, the critical points of ESP are the points at which the electric field and, consequently, the electrostatic force, acting as the element of charge at the point $\mathbf{r}_c$, is equal to zero. At the nuclei positions it is consistent with the requirements of the Hellmann-Feynman theorem [10, 11] for a system in equilibrium.

Thus, the topological characteristics of ESP, in addition to those for the electron density carry physical information about inner crystalline electrostatic field.

32.4 Construction of the Electrostatic Potential

Construction of the electrostatic potential in the EDSA using electron diffraction data is usually carried out with a Fourier series. However, regardless of the progress of the reached resolution the appropriate (dynamic) ESP maps suffer from the effect of series abruption, leading to a distortion of true potential maximum and the appearance of false maximum, reaching the 5–10% of the true ones.

Our proposed method of calculating the ESP using analytical structural model parameters, through fitting of the theoretical structure amplitudes to the experimental ones, has several advantages. The method is as much as possible free from the effect of abruption and errors, associated with the experimental determination of the diffraction intensity and the transition to the structural amplitudes. As an output it gives a static ESP, which is being checked through comparison of experimental and theoretical results. It is important to point out that reconstructed from an experiment ESP should be adjusted at a "selfaction potential", without which it is impossible to obtain physically meaningful values of the electrostatic energy (the energy of electrostatic interaction between nuclei and electrons per unit cell) [12]. The calculation of the ESP using the analytical model makes it easy to take this into account by a simple subtraction of the corresponding contribution to the total charge density, see formula (32.1).

32.5 An Example of Ionic Bonding

To further treatment of the experimental data and in the analysis of chemical bonding the multipole model [13] was used, in which the electron density of each pseudoatom is represented as

$$\rho_{atom}(r) = \rho_{core}(r) + P_{val}k'^{3}\rho_{val}(k'r) + \sum_{l=1}^{4} k''^{3} R_l(k''r) \sum_{m=-l}^{l} P_{lm} y_{lm}(r/r) \tag{32.3}$$

Core ρ_{core} and valence electron density ρ_{val} the spherical density of valence shells are described by means of atomic wave functions. Structural κ-model [14] used in the analysis of ionic chemical bonding [10] was the following. Electronic structure amplitude of each atom a was expressed as the sum of a fixed component $f_{core,a}$, bound with the atomic core and variable valence component $P_{val,a}f_{val,a}$, taking into account the interatomic charge transfer and the expansion-contraction of the ion in the crystal:

$$\Phi_a(q) = (\pi\Omega|q|^2)^{-1} \sum \{Z_a - [f_{core,a}(q) + P_{val,a} f_{val,a} \cdot (q/k_a)\}$$

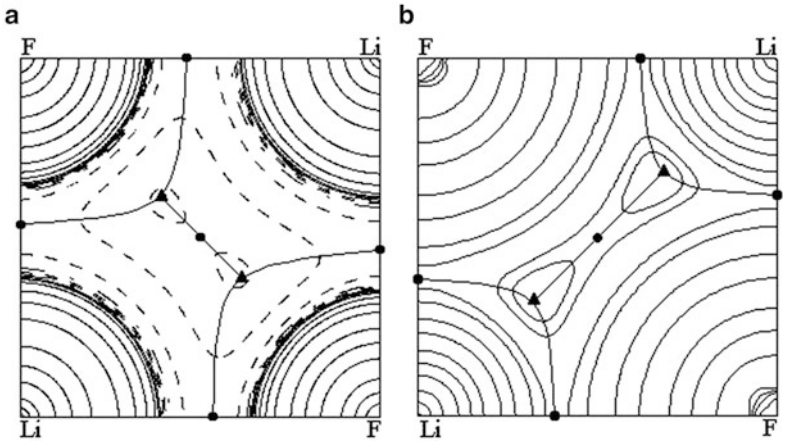

Fig. 32.1 (**a**) Electrostatic potential distribution for LiF (100 – plane). (**b**) Electron density distribution for LiF (100 – plane). Critical points are denoted: *circles* – (3,−1), *triangles* – (3,+1), *squares* – (3,+3). *Solid lines* going across CP show the atomic surfaces of zero flux defined by (32.2)

Here **q** – vector of the reciprocal lattice, Ω – unit cell volume, $f_{core,a}$ (**q**) and $f_{val,a}$, a X-ray atomic scattering amplitudes for the spherically averaged atomic (or ionic) core and the valence electron densities, normalized to one electron. κ_a- is an atomic parameter responsible for the contraction-expansion, and $P_{val,a}$ – atomic electron occupations.

Knowing the parameters of κ, values for the average inner potential φ_0 can be calculated for all crystals [15]. In [10] they were derived as: 7.07 (for LiF), 8,01 (NaF) and 11,47 V (MgO).

Figure 32.1a shows the typical distribution of the ESP for ionic LiF. In general, ESP along cation-anion bonding has a smooth character with a single axial one-dimensional minimum at distance 0.93 Å from the anion in LiF. Critical points are marked as: circles – (3, −1), triangles – (3, +1). We emphasize that the appearance of minima in the ESP is a very sensitive indicator of the interatomic charge transfer in the crystal.

Comparing the pictures of the locations of CT in the ESP and the electron density (Fig. 32.1b) crystal LiF (as typical), we can conclude that both sets of CP did not coincide. Nuclear potential also gives a picture of CP-s are different from those in the ED. These observations reflect the well-known fact: the electron density (and energy) many-electron system is not completely determined by the inner crystalline electrostatic field.

For the studied crystals, the atomic surfaces of zero flux, defined by (32.2), are shown in Fig. 32.1. These surfaces are naturally bounded by the electrostatic potential of the crystalline atom-like areas, defined by the relevant nuclear potential. Each element of the electron density, within such a “pseudoatom”, is attracted to its own nucleus. Consequently, the shape and size of these regions reflect the electrostatic energy balance between the bound atoms in a crystal.

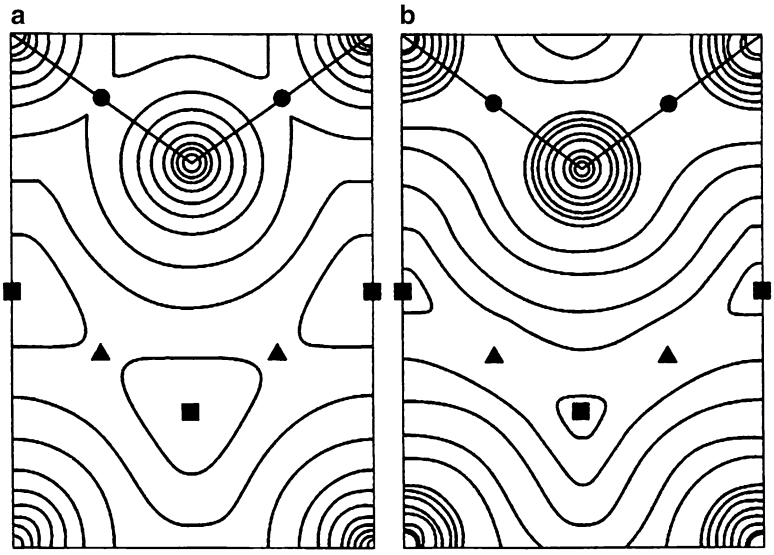

Fig. 32.2 Distributions of ESP (**a**) and ED (**b**) along (110) – plane. Critical points are denoted: *circles* – (3,−1), *triangles* – (3,+1), *squares* – (3,+3). *Solid lines* going across CP show the atomic surfaces of zero flux defined by (32.2)

The lines formed by pairs of lines the electric field gradient, ending at CP (3, −1) in the ESP, corresponds to the shortest cation-anion and cation-cation distances in the crystal with a structure of NaCl. These observations reveal the defect model of pair Coulomb interactions between all the point ions, usually used in calculations of electrostatic energy of crystals. Thus, the consideration of the gradient field leads to the conclusion that long-range Coulomb interaction between atoms having finite sizes in a crystal occur in the crystal in the form of an "atom-atom interactions", the structure which is a specific property of each compound, more precisely – each structural type.

32.6 An Example of a Crystal with a Covalent Bond (Ge)

Ge crystal has a pronounced covalent bond. So, to further treatment of the experimental data the multipole model (32.3) was used. The radial functions of the form $R_l = r^{n_l} \exp(-\kappa' \xi r)$ with $n_3 = n_4 = 4$ $(l \leq 4)$ and the values of orbital exponents $\xi_{Ge} = 2.1$ a.e. [16] were used. Ge atom is in position *43 m*, hence only the octupole P_{32}- and hexadecupole and P_{40} и $P_{44} = 0.74045 P_{40}$ terms are nonzero in (32.3). Electronic population of multipoles P_{lm} and κ' parameter can be refined by LSQ using specialized software (see, for example MOLDOS96 [17]). For germanium, value of $\kappa' = 0{,}922$ points to an 8% expansion of the spherical part

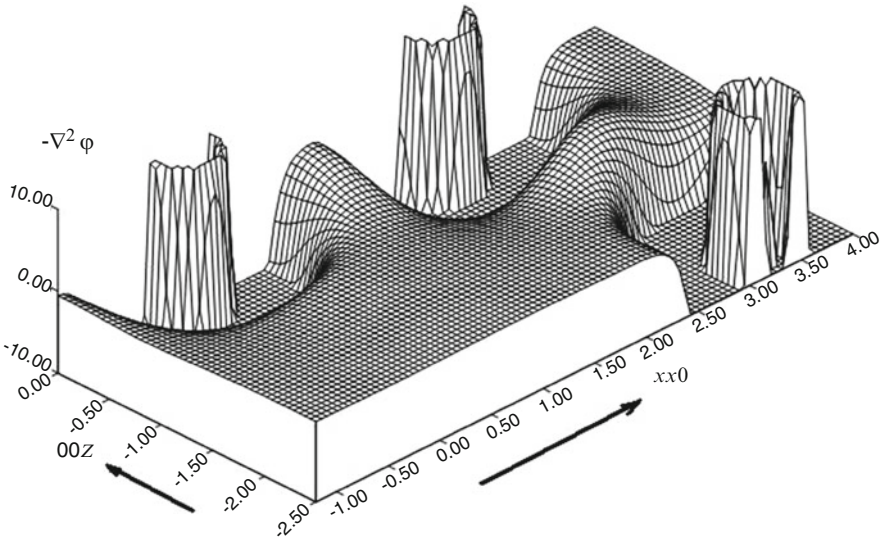

Fig. 32.3 Laplacian of ED for the fragment of Ge structure in (110) – plane

of the valence shell was obtained. The values of the multipole parameters obtained for the Ge crystals for electron diffraction data were used to calculate the static ED and ESP and the Laplacian of ED. Maps of these functions at (110) plane are shown in Figs. 32.1a, b and 32.2. Topological characteristics of CP-s in the bonds provide a quantitative description of known effect of formation of Ge crystal, which is accompanied by a strong shift of the electron density to the line of Ge-Ge. In general, the layout of the critical points of the ED and ESP does not match. However, for the Ge crystal, due to the symmetry of the electrostatic potential, electron density is homeomorphic. In this particular case, the location of critical points of the EP and ESP is equal (Fig. 32.3).

32.7 Conclusion

Distribution of ESP gives a lot more information about the nature of atomic interactions in crystals. It is important since the resulting distribution can be used in the theoretical models for the calculation of physical properties. For in-depth study of the connection of the electronic structure with the physical properties of crystals it is useful to combine electron diffraction data of the potential distribution with the distribution of an electron density data derived from precision X-ray experiment.

References

1. Vainshtein B (1964) Structural analysis by electron diffraction. Pergamon, Oxford
2. Vainshtein BK, Zvyagin B, Avilov AS (1992) Electron diffraction structure analysis. In: Cowley JM (ed) Electron diffraction techniques. Oxford University Press, New York
3. Kohn W, Sham LJ (1965) Self-consistent equations including exchange and correlation effects. Phys Rev A 140:1133–1138
4. Kohn W, Sham LJ (1966) One-particle properties of an inhomogeneous interacting electron gas. Phys Rev A 145:561–567
5. Hohenberg P, Kohn W (1964) Inhomogeneous electron gas. Phys Rev B 136:864–871
6. Avilov AS (1998) Quantitative determination of electrostatic potential of crystals by methods of electron diffraction structure analysis. Crystallogr Rep 43:925–933
7. Avilov AS, Kulygin AK, Pietsch U, Spence JCH, Tsirelson VG, Zuo JM (1999) Scanning system for high-energy electron diffractometry. J Appl Crystallogr 32:1033–1038
8. Avilov A, Kuligin K, Nicolopoulos S, Nickolskiy M, Portillo J, Lepeshov G, Sobolev B, Collette JP, Robins AS, Fischione P (2007) Precession technique and electron diffractometry as new tools for crystal structure analysis and chemical bonding determination. Ultramicroscopy 107:431–444
9. Bader RFW (1990) Atoms in molecules – a quantum theory. Oxford University Press, Oxford
10. Feynman RP (1939) Forces in molecules. Phys Rev 56:340–343
11. Hellmann H (1937) Einfuerung in die quantum-chemie. Deuticke, Leipzig
12. Tsirelson VG, Avilov AS, Lepeshov GG, Kulygin AK, Stahn J, Pietsch U, Spence JCH (2001) Quantitative analysis of the electrostatic potential in rock-salt crystals using accurate electron diffraction data. J Phys Chem B 105:5068–5074
13. Hansen NK, Coppens P (1978) Electron population analysis of accurate diffraction data 6 testing aspherical atom refinements on small-molecule data sets. Acta Crystallogr A 34:909–921
14. Coppens P, Guru Row TN, Leung P, Stevens ED, Becker P, Yang YW (1979) Electron population analysis of accurate diffraction data 7. Net atomic charges and molecular dipole-moments from spherical-atom X-ray refinements, and the relation between atomic charge and shape. Acta Crystallogr A 35:63–72
15. Spence JCH (1993) On the accurate measurement of structure-factor amplitudes and phases by electron-diffraction. Acta Crystallogr A 49:231–260
16. Lu ZW, Zunger A, Deutsch M (1995) Electronic charge-distrubution in crystalline germanium. Phys Rev B 52:11904–11911
17. Protas J (1997) MOLDOS96/MOLLY PC-DOS. Univ Nancy

Chapter 33
Domino Phase Retrieval Algorithm for Structure Solution

F.N. Chukhovskii

Abstract Novel domino-fashion-algorithm method for structure determination is being aimed to general solution of the phase retrieval problem, consequently combining the electron diffraction (ED) and the high-resolution transmission electron microscopy (HRTEM) patterns. The fusion of the direct-method technique that is described here allows realization of a full-phase restoration of complex structure factors. A numerical example, using the dynamical ED and HRTEM input data for $(Ga,In)_2SnO_5$ ceramic, shows that the method is capable of yielding unique phase retrieval solution. The clear sense is that the domino-fashion algorithm presented does work well and it is a valuable method for phasing diffraction patterns experimentally observed in electron crystallography provided that collecting the ED and HRTEM data have been consequently carried out.

33.1 Introduction. Direct Methods for Structure Determination

An application of conventional (kinematical) direct methods and refinements for purposes of electron structure determination raises some fundamental problems. There are some simple cases, for instance a surface, where such refinements are legitimate as a good first approximation, but even here correct results require the inclusion of dynamical effects. It is very well established theoretically that even one atom layer of a heavy element such as gold is a 'dynamical' scattering unit [1]. So, there are no cases with real samples where the kinematical approximation is rigorously valid. At the same time, under some optimal imaging conditions

F.N. Chukhovskii (✉)
Institute of Crystallography, The Russian Academy of Sciences,
Leninsky Prospect 59, 119333 Moscow, Russian Federation
e-mail: tschoukhowski@hotmail.com

U. Kolb et al. (eds.), *Uniting Electron Crystallography and Powder Diffraction*,
NATO Science for Peace and Security Series B: Physics and Biophysics,
DOI 10.1007/978-94-007-5580-2_33,

the high-resolution transmission electron microscopy (HRTEM) technique provides real-space information toward crystal structures though HRTEM images in general do not manifest true atom positions.

On the other hand, to obtain true real-space information concerning atom positions one may explore the direct methods relying on the electron diffraction (ED) information alone and extracting the unknown phase information among the structure factors [2].

Noteworthy is the fact that the first quantitative relationships being capable to be used for phasing diffraction patterns *via* direct methods were Sayre's equation [3] and statistical phase invariants [4, 5].

Switching to a set of structure factors, $\{U(\mathbf{g})\}$, the phase set $\{\psi(\mathbf{g})\}$ with $\psi(\mathbf{g}) = \mathrm{Im}[\ln[U(\mathbf{g})]]$ and $\mathbf{g}$ a reciprocal lattice vector, could be determined using the iterative transform algorithm based on the Sayre–Tangent formula as a convolution equation (namely, $\psi(\mathbf{g}) = \mathrm{Im}[\ln[\Sigma_{\mathbf{h}} U(\mathbf{h})U(\mathbf{g}\text{-}\mathbf{h})]]$ with the known set of moduli $\{|U(\mathbf{g})|\}$. For this, the Sayre–Tangent formula is relatively exact for pointlike atomic structures as long as the atom-scatter positions are not overlapped that coincides with the basic assumption of the ED *channeling approximation* [6, 7].

At the same time, the phase information is preserved in the HRTEM images and can be extracted sometimes using *the Fourier transform* [8, 9].

Ishizuka, Miyazaki and Uyeda [10] have developed the resolution improvement and/or phase correction method first proposed by Hoppe and Gassmann [11]. Combining the information in the electron micrograph and electron diffraction within a kinematical approach, they have applied the procedure to the model structure of the crystal of copper perchlorophthalocyanine for determining the phases (signs) of the structure factors.

The least-squares refinement and direct method technique to decode structural data from ED experiment was reviewed in many cases [12], in the most part of which dynamical ED effects have been ignored. The work [13] has to be drawn out, in which the direct methods combining with *the Fourier transform* of the HRTEM image were attempted to solving the phase problem on an example of $(Ga,In)_2SnO_5$ ceramic.

The two- and three-phase structure invariants, Σ_0 and Σ_2, within the scope of 'dynamical' direct methods has been analyzed in the works [14, 15]. It was shown that applying direct methods to dynamical ED data could be understood *via* an "effective kinematical approximation". For this, each of both the phase conditional probability Σ_0-distribution defined for a number of $(\mathbf{g}, -\mathbf{g})$-reflection pairs and the phase conditional probability Σ_2-distribution defined for a number of $(\mathbf{g}, \mathbf{h}, -\mathbf{g}-\mathbf{h})$-reflection triplets are proved to display a strong peak in many cases. This assertion is obtained, particularly using the *multislice-calculation* method.

In this lecture we push the concept of direct methods one step further, and apply the lattermost using both the two-dimensional ED and HRTEM data sets as constraints for a phase restoration [16]. To attribute this concept the iterative transform algorithm, which has at its core the Gerchberg-Saxton algorithm [17, 18] and makes the phase retrieval procedure in a domino fashion, is discussed. A prerequisite to solving the problem herein is to elaborate the appropriate numerical algorithm that creates a unique phase restoration.

For purposes of this study, some numerical simulations are given on a sample of $(Ga,In)_2SnO_5$ ceramic, which exhibits a convergence property of the domino iterative transform algorithm. In particular, the domino phase retrieval algorithm, which is described here, has been proven to be convergent in the general case of complex structure factors.

Noteworthy is the fact that its implementation can facilitate a true determination of nanometre-size crystal structures combining both the ED and HRTEM data in a sequential domino manner.

33.2 Problem Formulation. Domino Phase-Retrieval Algorithm

Before formulate the domino phase-retrieval algorithm (DPRA) issue we now use the necessary mathematical model describing the dynamical ED within the scope of 1s channeling approximation, where the electron wavefunction may be cast in the form [6]

$$\psi(\mathbf{r}, z) = 1 + 2i \sum_{j=1}^{j} a_j \psi(\mathbf{r} - \mathbf{r}_j) e^{-i\pi\left(\frac{E_j}{2E_0}\right)kz} \sin\left[\pi\left(-\frac{E_j}{2E_0}\right)kz\right], \quad (33.1)$$

where now the sum is over the *j*-atomic positions in the two-dimensional unit cell, E_0 is the incident electron energy, the wavenumber $k = \lambda^{-1}$, the eigenvalue E_j refers to the lowest lying 1s-eigenstate energy.

Equation (33.1) is the 1s channeling approximation for the wavefunction describing the electron propagation through the crystalline sample.

In the reciprocal space, which is used in structural crystallography, the structure amplitude for the **g** reflection has the form [15]

$$U(\mathbf{g}) = i F_{\mathbf{g}} = i \sum_{j=1}^{j} F_{j\mathbf{g}} e^{-2i\pi \mathbf{g}\,\mathbf{r}_j}, \quad (33.2)$$

where

$$F_{j\mathbf{g}} = 2V_j(\mathbf{g}) e^{-i\pi\left(\frac{E_j}{2E_0}\right)kz} \sin\left[-\pi\left(\frac{E_j}{2E_0}\right)kz\right] \quad (33.3)$$

is the complex atomic scattering amplitude of the *j*-atom, $\mathbf{r}_j$ is its two-dimensional position vector and J is the number of atomic columns in the two-dimensional unit cell.

It is remarkable that $V_j(\mathbf{g})$ is the Fourier transform of the two-dimensional eigenstate function $\Psi_j(\mathbf{r}–\mathbf{r}_j)$, to a first approximation the *kinematical* single-atom structure factor.

Generally, addressed to electron structure solution the direct phase-retrieval problem is related to the complex structure factor set $\{\mathrm{U}(\mathbf{g})\}$ provided that the ED magnitude set $\{|\mathrm{U}(\mathbf{g})|\}$ in your hand. They are formed as a result of an incident electron plane wave scattering by nanometre-size crystalline sample and *e.g*., can be measured using the HRTEM technique. At the same time, along with the two-dimensional ED array $\{\mathrm{U}(\mathbf{g})|\}$ the latter allows to measure the corresponding HRTEM image $\mathrm{I}(\mathbf{x})$ when the scattered electron wave propagates through an *electron optical system* consisting of selected-area apertures and focusing lens.

Intensities measured in the back focal plane are referred to the ED magnitudes $\{|\mathrm{U}(\mathbf{g})|\}$, with diverse reciprocal lattice vectors **g,** whereas the intensity distribution $\mathrm{I}(\mathbf{x})$ in the image plane is the modulus squared of the two-dimensional Fourier transform of the complex structure factor set $\{\mathrm{U}(\mathbf{g})\}$, in general taking into account all likely aberrations, particularly, defocus, spherical aberration and so on. Clearly, the two-dimensional periodical function $\mathrm{I}(\mathbf{x})$ is the HRTEM image of the crystal structure. Underline that both the two-dimensional arrays $\{|\mathrm{U}(\mathbf{g})|\}$ and $\{\mathrm{A}(\mathbf{x})\}$ with $A(X) = \sqrt{I(X)}$ can be considered as the data arrays for formulating the phase-retrieval issue underway.

From the mathematical viewpoint each of data arrays $\{|\mathrm{U}(\mathbf{g})|\}$, $\{\mathrm{A}(\mathbf{x})\}$ is non-convex. As is known, the non-convexity of both these arrays, $\{|\mathrm{U}(\mathbf{g})|\}$, $\{\mathrm{A}(\mathbf{x})\}$, is a main obstacle to applying the Gerchberg-Saxton-type algorithm [17, 18] for direct phasing solution of diffraction patterns.

Then, it is physically reasonable, as well as mathematically precise, to consider the present diffraction-pattern phase-retrieval issue for phasing structure factors using both the finite data arrays ${}_{(N)}\{|\mathrm{U}(\mathbf{g})|\}$ and ${}_{(N)}\{\mathrm{A}(\mathbf{x})\}$, which may be measured in the back focal plane and the image plane, respectively, N is the array rank (remind that the array size is equal to $N \times N$).

Thus, in order to overcome the fundamental non-convexity limitation and, as a result, to avoid numerous redundant solutions we now attempt to go beyond the conventional Gerchberg-Saxton algorithm by using the DPRA, the modified Gerchberg-Saxton-type algorithm for the structure factor phase determination in a sequential 'domino' fashion.

Presumably, let us introduce the *selected-area* constraint sets of ${}_{(\nu)}\{|\mathrm{U}(\mathbf{g})|, \mathrm{A}(\mathbf{x})\}$ for the consecutive values of $\nu = 2, 3, 4, \ldots, N$ (for sake of simplicity $\mathrm{U}(\mathbf{g})_{\mathbf{g}=0}$ is assumed to be unity for any ν).

For the *selected-area* array index rank ν fixed the DPRA flow-equation takes the form

$$
\begin{aligned}
{}_{(\nu)}\mathrm{M}_{\mathrm{k}+1}(\mathbf{x}) &= {}_{(\blacklozenge)}\mathrm{A}(\mathbf{x}) \exp\left[i_{(\nu)}\varphi_{\mathrm{k}}(\mathbf{x})\right] \\
{}_{(\nu)}|\mathrm{U}_{\mathrm{k}+1}(\mathbf{g})| &= \left|\mathit{InverseFourier}\left[{}_{(\nu)}\mathrm{M}_{\mathrm{k}+1}(\mathbf{x})\right]\right| \\
{}_{(\nu)}\psi_{\mathrm{k}+1}(\mathbf{g}) &= \mathrm{Im}\left[1\mathrm{n}\left[\mathit{InverseFourier}\left[{}_{(\nu)}\mathrm{M}_{\mathrm{k}+1}(\mathbf{x})\right]\right]\right] \\
{}_{(\nu)}\mathrm{U}_{\mathrm{k}+1}(\mathbf{g}) &= \left|{}_{(\nu)}\mathrm{U}(\mathbf{g})\right| \exp\left[i_{(\nu)}\psi_{\mathrm{k}+1}(\mathbf{g})\right] \\
{}_{(\nu)}\mathrm{A}_{\mathrm{k}+1}(\mathbf{x}) &= \left|\mathit{Fourier}\left[{}_{(\nu)}\mathrm{U}_{\mathrm{k}+1}(\mathbf{g})\right]\right| \\
{}_{(\nu)}\varphi_{\mathrm{k}+1}(\mathbf{x}) &= \mathrm{Im}\left[1\mathrm{n}\left[\mathit{Fourier}\left[{}_{(\nu)}\mathrm{U}_{\mathrm{k}+1}(\mathbf{g})\right]\right]\right],
\end{aligned}
\tag{33.4}
$$

where we calculate the $(k+1)$-th phase sets of ${}_{(\nu)}\{\psi_{k+1}(\mathbf{g}), \varphi_{k+1}(\mathbf{x})\}$ by use of the preceding k-th ones ${}_{(\nu)}\{\psi_k(\mathbf{g}), \varphi_k(\mathbf{x})\}$, and keeping in mind that the ED and HRTEM sets of ${}_{(\nu)}\{|\mathrm{U}(\mathbf{g})|, \mathrm{A}(\mathbf{x})\}$ are considered as *a priori* fixed ones (the data constrains) and do not depend on the cycle value of k over all the iteration processes of ν (particularly, they can be experimentally measured).

The two figures of merit (FOM) related to the reciprocal space, $R^{(\nu)}$, and real space, $X^{(\nu)}$, are evaluated at each cycle over k

$$
\begin{aligned}
R^{(\nu)}{}_{k+1} &= \nu\Sigma_{\mathbf{g}}||{}_{(\nu)}\mathrm{U}_{k+1}(\mathbf{g})| - |{}_{(\nu)}\mathrm{U}(\mathbf{g})||/[\Sigma_{\mathbf{g}}|{}_{(\nu)}\mathrm{U}(\mathbf{g})|^2]^{1/2}, \\
X^{(\nu)}{}_{k+1} &= \nu\Sigma_{\mathbf{x}}|{}_{(\nu)}\mathrm{A}_{k+1}(\mathbf{x}) - {}_{(\nu)}\mathrm{A}(\mathbf{x})|/[\sum\nolimits_{\mathbf{x}(\nu)} I(\mathbf{x})]^{1/2},
\end{aligned}
\tag{33.5}
$$

For reference, ${}_{(\nu)}\psi_k(\mathbf{g})$ is the given phase of the complex structure factor ${}_{(\nu)}\mathrm{U}_k(\mathbf{g})$ at the beginning of each cycle k, and ${}_{(\nu)}\psi_{k+1}(\mathbf{g})$ is the new phases calculated at the end of the same cycle k. The phase set of ${}_{(\nu)}\{\psi_{k+1}(\mathbf{g})\}$ calculated, is then fed back in the cycle iteration fashion according to the flow-equation (33.5); $k = 1, 2, 3, \ldots,$ K and the range value K is chosen to be fixed.

Our main focus is on the fact that some important restrictions are imposed onto the phase set of ${}_{(\nu+1)}\{\psi_k(\mathbf{g})\}$, specifically, the phase set of ${}_{(\nu+1)}\{\psi_k(\mathbf{g})\}$ fixedly contains the subset of ${}_{(\nu)}\{\psi(\mathbf{g})\}$, with the array size of $\nu\times\nu$, determined within the preceding iteration of ν. And clearly, the other elements of the phase set of ${}_{(\nu+1)}\{\psi_k(\mathbf{g})\}$ are chosen to be random in the range of $(-\pi, \pi)$ for the first cycle, $k = 1$, only.

Loosely speaking, the principal idea of the domino phase retrieval method is to obtain the phase fit for the complete structure factors set $\{\mathrm{U}(\mathbf{g})\}$ sequentially step by step starting from the first subsets ${}_{(2)}\{|\mathrm{U}(\mathbf{g})|\}$, and ${}_{(2)}\{\mathrm{A}(\mathbf{x})\}$, each of them has the rank size 2, and for every combined subset ${}_{(\nu)}\{|\mathrm{U}(\mathbf{g})|, \mathrm{A}(\mathbf{x})\}$, $\nu = 2, 3, 4, \ldots, N$, the conventional Gerchberg-Saxon iteration procedure is applied.

We then use the phase consistency check factor (a 'correctness' factor)

$$
C^{(\nu)}{}_{k+1} = 0.5\Sigma'_{\mathbf{g}}|{}_{(\nu)}\mathrm{U}_{k+1}(\mathbf{g}) - {}_{(\nu)}\mathrm{U}(\mathbf{g})|/\Sigma'_{\mathbf{g}.}|{}_{(\nu)}\mathrm{U}(\mathbf{g})| \tag{33.6}
$$

that is calculated in a process of numerical simulations for all the values of k, and the sum, Σ', taken over the reflections except $\mathbf{g} = 0$.

Going on from the iteration of $\nu = 2$ until the final iteration N *via* the consecutive *selected-area* iterations the true phase solution holds on up to some numerical uncertainties depending on the final iteration number N, whereas other redundant solutions can be readily detected *yielding inappropriate values of FOM*.

In principle, numerical uncertainties of the 'true' phases increase with increasing the iteration number ν (the ED reflection array rank) that might be compensated by enlarging the cycle range value of K.

Underneath the domino iterative transform algorithm above described is tested numerically simulating the input ED and HRTEM data and true solution of the $(Ga,In)_2SnO_5$ crystal structure.

33.3 DPRA Implementation for a Sample of the Ceramic $(Ga,In)_2SnO_5$

The test case we attempt to resolve the phase problem is a centrosymmetric structure of the ceramic $(Ga,In)_2SnO_5$. The structure is monoclinic with $a = 1.169$ nm, $b = 0.317$ nm, $c = 1.073$ nm, and $\beta = 99.00^{o}$. The atom positions within the unit cell obtained from direct methods and neutron diffraction are presented in the work [13], the projected two-dimensional structure of $(Ga,In)_2SnO_5$ is shown in Fig. 33.1. The incident electron beam propagates along the *b*-axis, and the accelerating voltage is 300 kV.

The true complex structure factors related to the proper dynamical ED pattern for $(Ga,In)_2SnO_5$ were calculated using 1s-state channeling approach.

The corresponding ideal HRTEM images calculated using the above values of thickness and 0.01 nm resolution are shown in Figs. 33.2a and 33.3a, respectively.

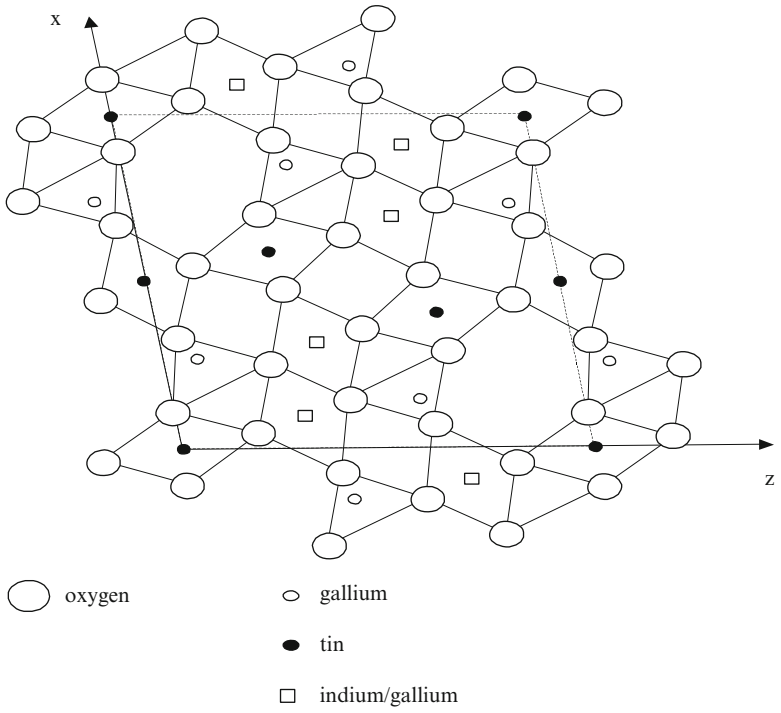

Fig. 33.1 Structure of $(Ga, In)_2SnO_5$ viewed along $[0\bar{1}0]$

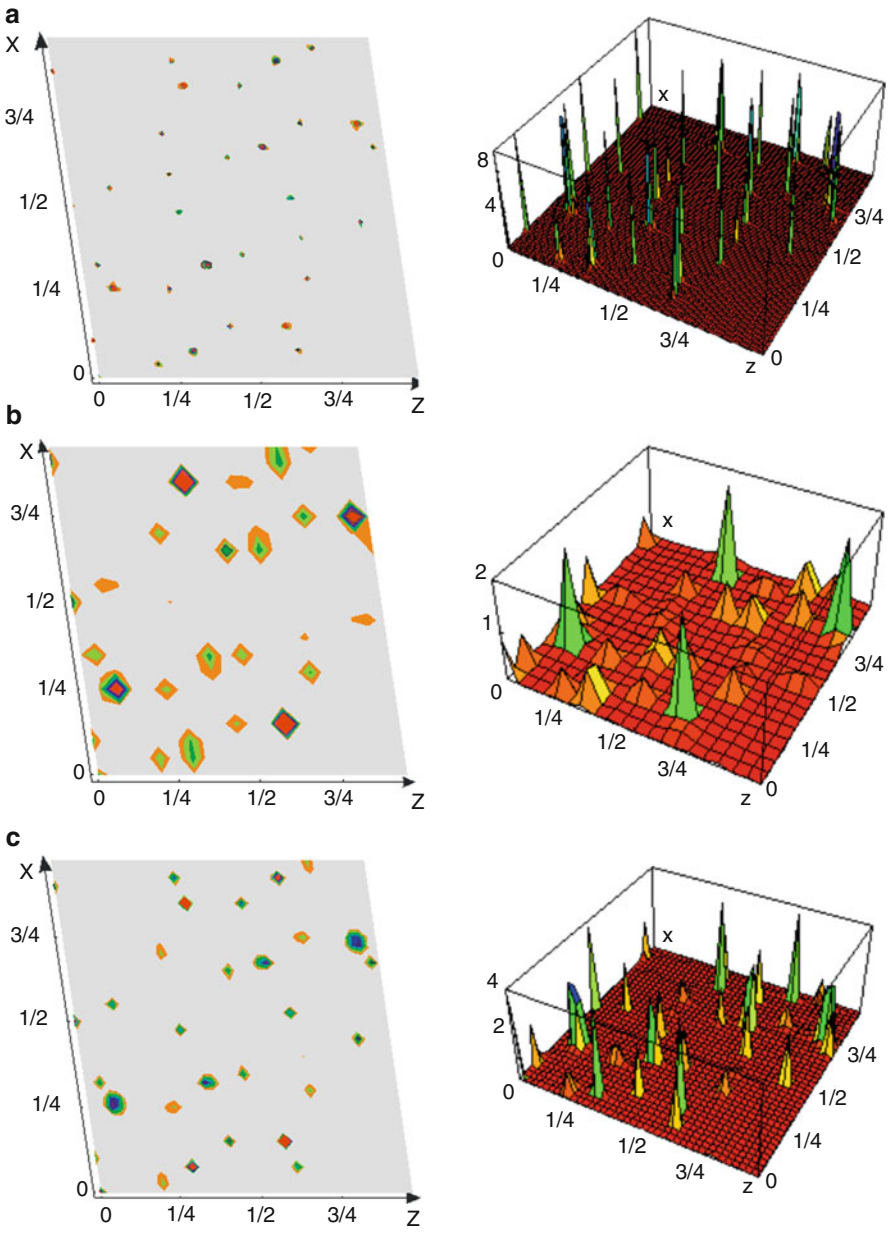

Fig. 33.2 The numerically calculated 2D- and 3D-images of the two-dimensional structure of $(Ga, In)_2SnO)_5$-ceramic with using the DPRA for the iteration range N: (**b**) = 20, (**c**) = 40 in comparison with the ideal HRTEM image in (**a**) = 100. The cycle range of K is 1,000. The sample thickness along the b-axis is 4.121 nm

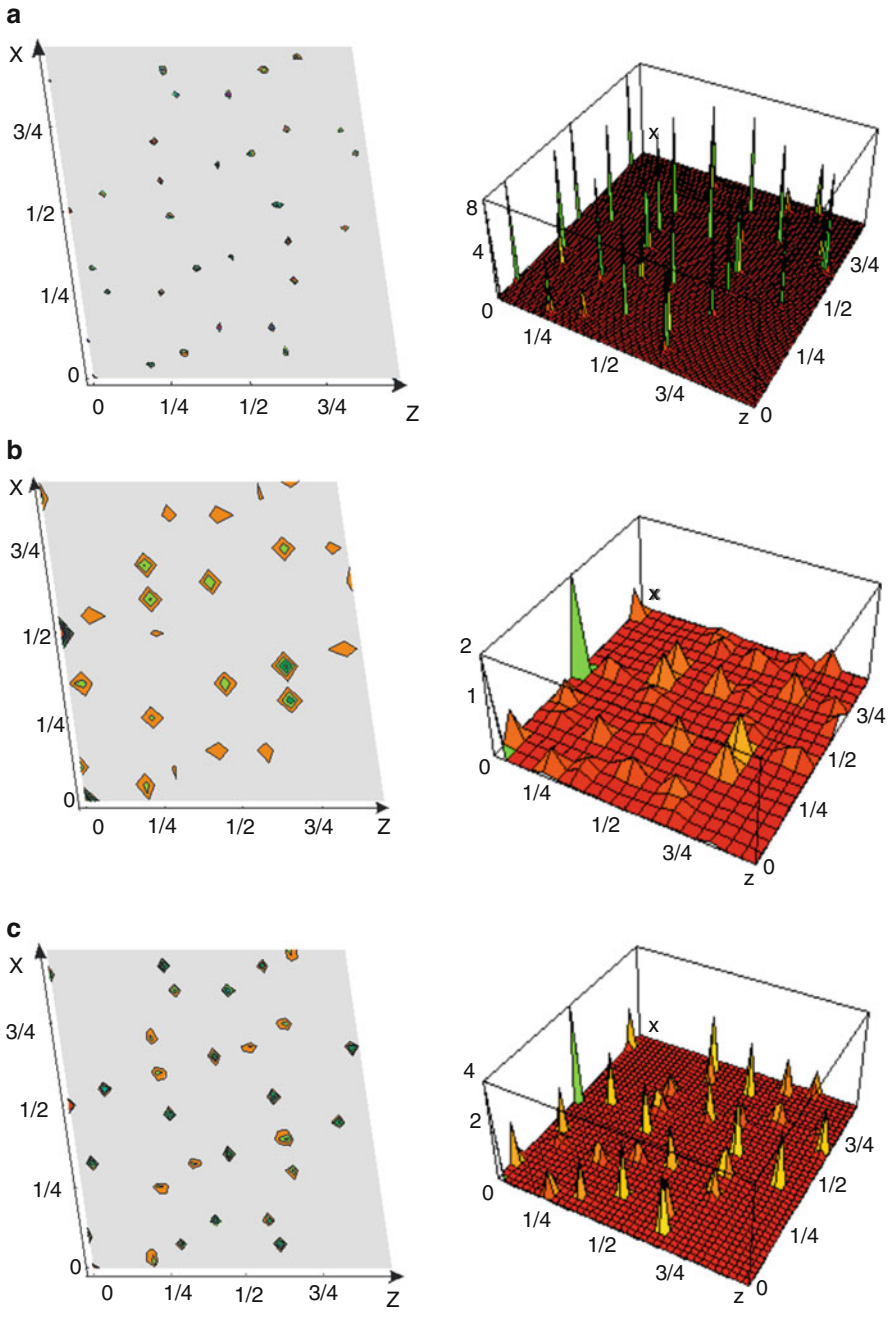

Fig. 33.3 The numerically calculated 2D- and 3D-mages of the two-dimensional structure of $(Ga,In)_2SnO_5$-ceramic with using the DPRA for the iteration range N: (**b**) = 20, (**c**) = 40 in comparison with the ideal HRTEM image in (**a**) = 100. The cycle range of K is 1,000. The sample thickness along the b-axis is 7.291 nm

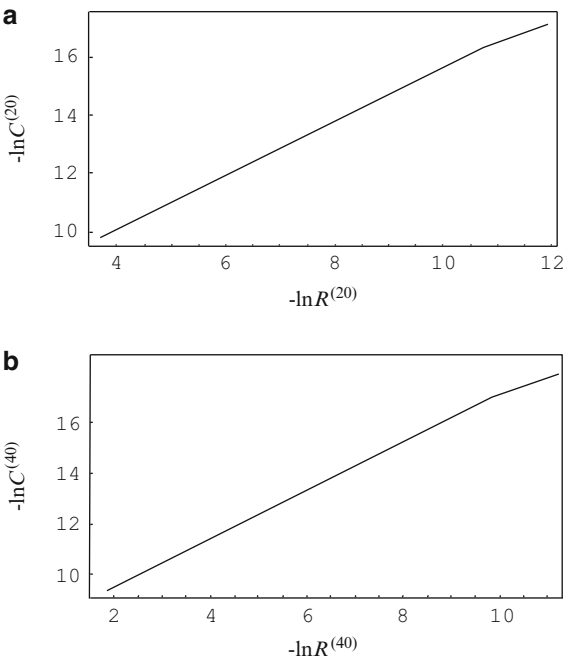

Fig. 33.4 Parametric plots of the factor $-\ln R$ versus a 'correctness' factor $-\ln C$-factor for the two iteration ranges N: (**a**) = 20, (**b**) = 40. The cycle range $K = 100$. The sample thickness along the b-axis is 7.291 nm

To illustrate the convergent features of the DPRA guiding the structure-factor-phase determination the calculated parametric plots of the *R*-FOM *versus* a 'correctness' *C*-factor (*cf*. Eqs. 33.6) is depicted in Fig. 33.4. It is found that the calculated *R*-FOM and *C*-factor achieve the values of order of 10^{-5} and 10^{-7} for the cycle range of $K = 100$ used for the calculated images given in Fig. 33.3b, c.

References

1. Spence JCH (1988) Experimental high-resolution electron microscopy. Oxford University Press, New York
2. Giocovazzo C (1998) Direct phasing in crystallography. Fundamentals and applications. Oxford University Press, New York
3. Sayre D (1952) The squaring method: a new method for phase determination. Acta Crystallogr 5:60–65
4. Cochran W, Woolfson MM (1955) The theory of sign relations between structure factors. Acta Crystallogr 8:1–12
5. Hauptman H (1982) On integrating the techniques of direct methods with anomalous dispersion 1. The theoretical basis. Acta Crystallogr A 38:632–641
6. Van Dyck D, Op de Beeck M (1996) A simple intuitive theory for electron diffraction. Ultramicroscopy 64:99–107
7. Sinkler W, Marks LD (1999) Dynamical direct methods for everyone. Ultramicroscopy 75:251–268

8. DeRosier DJ, Klug A (1968) Reconstruction of three-dimensional structures from electron micrographs. Nature 217:130–134
9. Weirich TE, Ramlau R, Simon A, Hovmöller S, Zou XD (1996) A crystal structure determined to 0.02 Å accuracy by electron crystallography. Nature 382:144–146
10. Ishizuka K, Miyazaki M, Uyeda N (1982) Improvement of electron-microscope images by the direct phasing method. Acta Crystallogr A 38:408–413
11. Hoppe W, Gassmann J (1968) Phase correction a new method to solve partially known structures. Acta Crystallogr B 24:97–107
12. Weirich TE, Zou XD, Ramlau R, Simon A, Cascarano GL, Giocovazzo C, Hovmöller S (2000) Structures of nanometre-size crystals determined from selected-area electron diffraction data. Acta Crystallogr A 56:29–35
13. Sinkler W, Marks LD, Edwards DD, Mason TO, Pöppelmeier KR, Hu Z, Jorgensen JD (1998) Determination of oxygen atomic positions in a Ga-In-Sn-O ceramic using direct methods and electron diffraction. J Solid State Chem 136:145–149
14. Hu JJ, Chukhovskii FN, Marks LD (2000) Statistical dynamical direct methods I. The effective kinematical approximation. Acta Crystallogr A 56:458–469
15. Chukhovskii FN, Hu JJ, Marks LD (2001) Statistical dynamical direct methods II. The three-phase structure invariant. Acta Crystallogr A 57:231–239
16. Chukhovskii FN, Poliakov AM (2003) Domino phase-retrieval algorithm for structure determination using electron diffraction and high-resolution transmission electron microscopy patterns. Acta Crystallogr A 59:48–53
17. Gerchberg RW, Saxton WO (1972) Practical alrogithm for determination of phase from image and diffraction plane pictures. Optik 35:237–244
18. Dainty J, Fienup J (1987) Phase retrieval and image reconstruction for astronomy. In: Stark H (ed) Image recovery: theory and application. Academic, New York

Chapter 34
LARBED: Exploring the Fourth Dimension in Electron Diffraction

Christoph T. Koch

Abstract This chapter describes a novel method for acquiring information-rich convergent beam-like patterns of thin specimen and materials with very large lattice constants. Yet, despite effective convergence angles of up to 100 mrad diffraction orders do not overlap. It is demonstrated how the 4-dimensional information carried by these patterns may be used to solve the dynamic inversion problem in electron diffraction and reconstruct 3D diffraction patterns. It is also shown how aberrations of the illumination system up to seventh order are measured in a fully automated manner and may be compensated on any TEM without installing any additional hardware.

34.1 Introduction

Because of the strong interaction of the fast electron beam with matter TEM-transparent samples must usually be not much more than 100 nm thick, in many cases even thinner.

The reciprocal space representation of a thin crystalline sample consists of a regular lattice of Bragg points (at reciprocal lattice vectors $\boldsymbol{g}$), each of which, when 'zooming in' has a rod-like shape which is why these features are also called reciprocal lattice rods or just 'relrods' (see Fig. 34.1b). In kinematical scattering theory the amplitude squared of the relrod at the point of intersection with the Ewald sphere defines the scattering intensity.

If the electron beam is tilted with respect to the zone axis of the crystal, the Ewald sphere may cut through points that lie precisely on the reciprocal lattice

C.T. Koch (✉)
Institute for Experimental Physics, Ulm University, Albert-Einstein-Allee 11, 89081 Ulm, Germany
e-mail: christoph.koch@uni-ulm.de

U. Kolb et al. (eds.), *Uniting Electron Crystallography and Powder Diffraction*, NATO Science for Peace and Security Series B: Physics and Biophysics,
DOI 10.1007/978-94-007-5580-2_34,

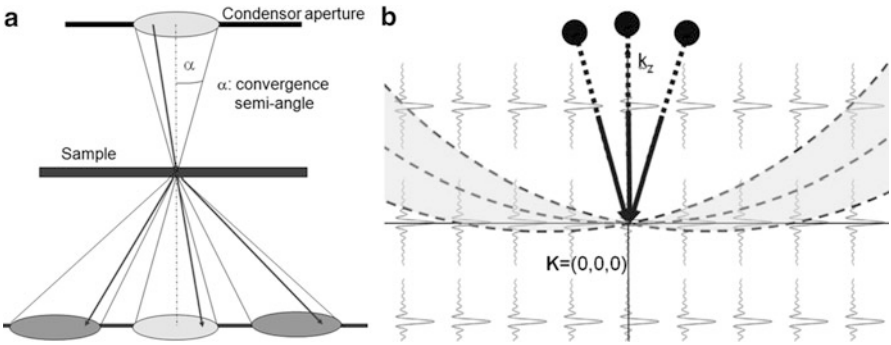

Fig. 34.1 (**a**) Illustration of CBED and (**b**) how it samples the reciprocal lattice of a crystal of finite thickness

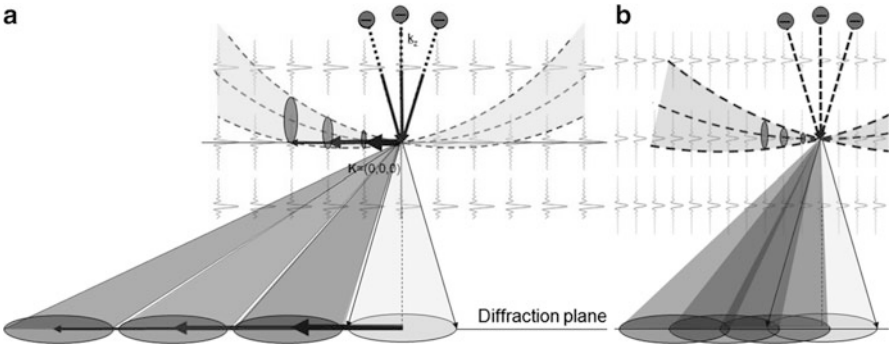

Fig. 34.2 Illustration of the relation between Bragg spacing and CBED disc size: While for crystals with small lattice constant (**a**) CBED works very well, for crystals with large lattice constant (**b**) only very small disc sizes are possible

of the crystal, bringing these reciprocal lattice vectors $\boldsymbol{g}$ (reflections) in the exact Bragg condition. Convergent beam electron diffraction (CBED – see Fig. 34.1a) is an elegant way of probing many slightly different incident beam directions in a single experiment [1].

If the beam convergence angle is matched to the crystal's lattice constant the diffraction discs may barely touch. For crystals of large unit cells, however, the reciprocal lattice is often too dense to allow the application of CBED at all, because diffraction discs corresponding to any significant illumination convergence angle would overlap (Fig. 34.2).

Proposed techniques to overcome limitation of overlapping discs (see also Fig. 34.3 for diagrams illustrating some of them):

- Recording only one disc at a time: Large-angle CBED (LACBED) [2]
- Recording integrated LACBED discs: LACDIF [3] (here, as in precession electron diffraction (PED) the rocking curve information is lost).

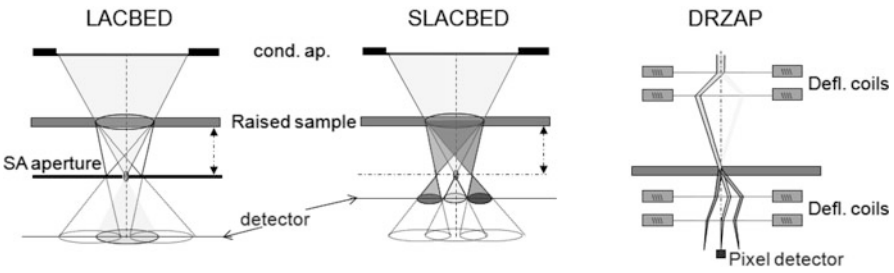

Fig. 34.3 Three examples of techniques aiming at recording diffraction information for different angles of incidence

Recording all LACBED discs simultaneously (SLACBED) [4] by working at a large defocus of the intermediate lens.

- Double-rocking zone-axis pattern (DRZAP) technique [5, 6]
- Rotation method [7]
- Large-angle rocking–beam electron diffraction (LARBED) [8]

34.2 The Dynamic Inversion Problem

While the kinematic diffraction intensity I**g** at a specific **g** is determined only by the structure factor of that particular diffraction vector, dynamic diffraction intensities depend on the complete structure factor matrix A according to the equations given in Fig. 34.4.

This means that I_g is actually the intensity of coherently adding partial waves, each having taken a different 'Umweg' (= detour) through the sample. Even for very thin samples this interference of the direct path with longer scattering paths (higher order Umweg excitations), or, as in the case of forbidden reflections, only these Umweg excitations, affects the diffraction pattern. However, for thin samples this can only be seen for large variations of the incident beam direction, much larger than that achievable by CBED (often several degrees or 10s of mrad). This is where techniques capable of exceeding the limit imposed by the Bragg spacing listed in Fig. 34.3 become very interesting.

The fast convergence of a recently developed scattering path expansion [9] allows us to expresses the diffraction pattern intensities as a set of multivariate polynomial equations. Applying a globally convergent algorithm to solve these is a direct inversion of the dynamical scattering equation and solves for the relative phases of the structure factors. Figure 34.5 shows how, by using a sufficiently high order scattering path expansion we can recover the projected crystal potential [10], without applying any iterative refinement techniques. Of course, the finite order expansion will always be an approximation, but once an approximate solution has been found, further iterative refinement will not be a problem anymore.

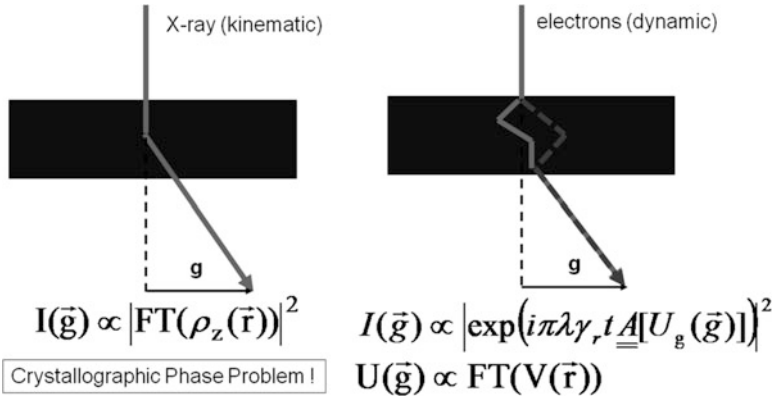

Fig. 34.4 Comparison of kinematic and dynamical diffraction. While kinematic (e.g. X-ray-) diffraction theory implies the crystallographic phase problem, dynamical diffraction intensities are interference patterns of different scattering paths, implying that the phase relation between these is encoded already in the measured intensities

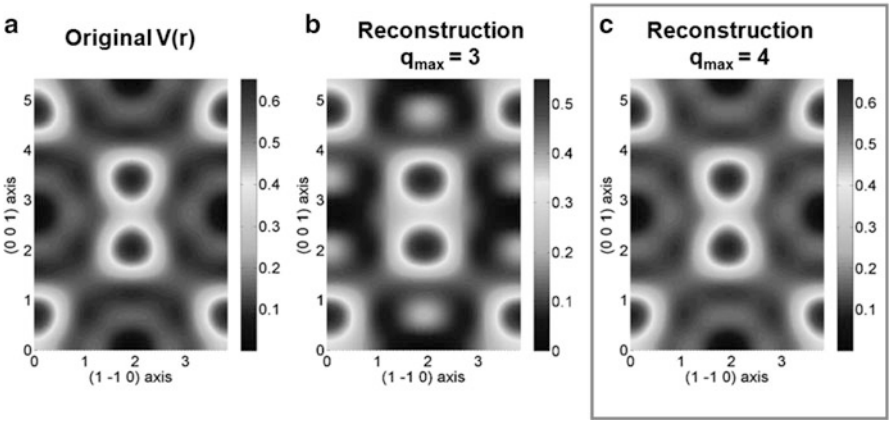

Fig. 34.5 (**a**) projected potential of Si. (**b**) potential reconstructed from a simulated LARBED pattern of 4 nm thin Si, applying a $q \leq 3$ scattering path expansion, q being the total length of the scattering path. (**c**) potential reconstructed from the same pattern using a $q \leq 4$ scattering path expansion.

Important prerequisite for being able to directly solve the dynamic inversion problem in this way is the availability of diffraction information for a rather large range of incident beam directions for all relevant reflections. Because the specimen thickness should be kept constant, this diffraction information should stem from a rather small area on the sample. Exactly this kind of data is provided by the LARBED technique described below.

34.3 The LARBED Experimental Setup

The LARBED technique works very similar to PED, except that only a partial compensation of the incident beam tilt is applied by the diffraction shift coils. In that way a constant but large and well known fraction of the tilt-induced diffraction shift is compensated, preserving the information about the original angle of incidence and the associated diffraction intensities in the pattern (Fig. 34.6).

Software control of beam tilt, beam shift and diffraction shift easily allows

- arbitrary scan patterns (ring, square, disc [see], etc.)
- compensation of objective pre-field lens aberrations, objective lens aberrations, and pivot point (shift tilt impurities, even if non-linear)
- fully automated beam alignment and calibration

34.3.1 Aberration Compensation

One very important requirement of quantitative LARBED experiments is that all diffraction information stems from exactly the same specimen area, for all angles of incidence of the electron beam. Otherwise it will be impossible to separate the effect of varying specimen thickness from the genuine rocking curve signal. This is particularly challenging if the sample is nanocrystalline and a very small probe must be used. It is thus necessary to keep the probe from wandering about the sample surface during acquisition. Within the Quantitative Electron Diffraction (QED) software (HREM Research, Japan), a commercially available plug-in for

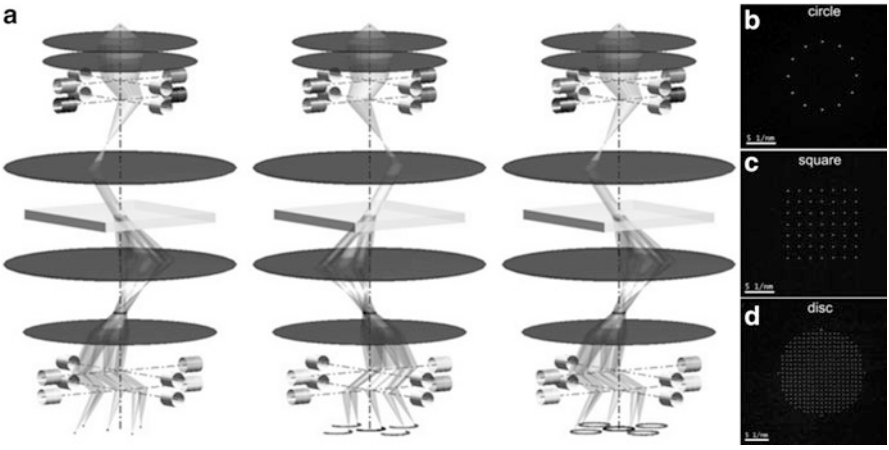

Fig. 34.6 (**a**) Sequence of ray paths in the TEM when completing a circular LARBED pattern as well as examples of a few other scan patterns: (**b**) circle, (**c**) square, (**d**) disc

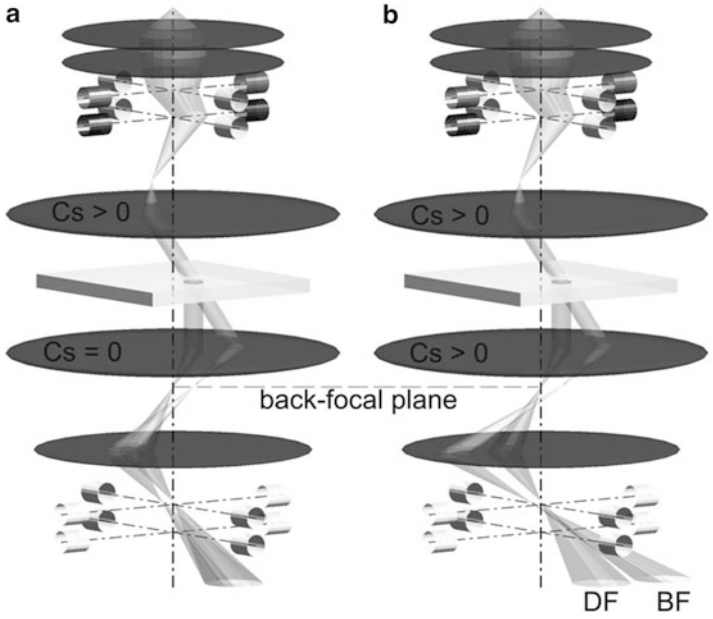

Fig. 34.7 Illustration of the effect of aberrations of the objective lens on the measurement of the spot on the sample. (**a**) Without aberrations, images of the tilted beam, as well as the diffracted beam travelling parallel to the optic axis end up at the same position on the detector. (**b**) Aberrations cause images of the diffracted and undiffracted beams to be detected at different positions

DigitalMicrograph (Gatan Inc., Pleasanton, CA) implementing LARBED as well as a few other technique, this is achieved by fitting a large set of pseudo-aberration coefficients to the movement of the spot on the sample for a large range of beam tilt angles. These parameters which include all aberration coefficients up to (and including) third, fifth, or seventh order, depending on the user's choice, are then used to predict the probe shift corresponding to any beam tilt within (and to some degree also outside) the range of tilt angles sampled during the calibration.

Such calibration may be achieved in two different ways. As illustrated in Fig. 34.7b, aberrations of the objective lens will induce a tilt-dependent image shift of the illuminating probe, exaggerating its actual movement on the sample. As discussed in detail in [8], when tracking the movement of the illuminating spot on the detector by recording its bright-field (BF) image, it is necessary to characterize in addition to the aberrations of the objective pre-field lens, also those of the objective lens. However, if one brings some amorphous sample area within the field of view, inserts a small objective aperture and aligns it with the microscope's optic axis, the movement of the probe on the sample may be tracked directly by following the movement of the dark-field (DF) image of the probe on the sample, independent of the aberrations of the objective lens. Either method has some advantages as well as disadvantages, which is why QED offers a choice of either method (BF or DF).

While the BF calibration requires both imaging as well as illumination aberrations to be calibrated, its advantage is that, once the aberrations of the objective lens have been determined, the calibration of the illumination aberrations may be performed without any sample. The DF method, on the other hand, may be simpler in that it requires only a single calibration step, but it may involve very long exposure times if the scattering of the amorphous sample is weak, which is why QED offers an auto-illumination option for the illumination aberration calibration in DF mode.

34.4 Applications of LARBED (Using the QED Plug-In for DM)

At the moment, the only tool implementing the LARBED principle is the QED Plug-In to DigitalMicrograph. This software is commercially available [11] and works on any TEM with the possibility of controlling the beam tilt and – shift through DigitalMicrograph. While the QED plug-in implements a number of diffraction techniques (e.g. PED, diffraction mapping, fluctuation electron microscopy), this section focuses on its application to LARBED-like experiments.

34.4.1 Quantitative LARBED

LARBED patterns can also be analyzed at least as quantitatively as CBED patterns. In principle, the same numerical fitting routine applied in quantitative CBED [12, 13] work may also be applied to LARBED data. Because of the large effective convergence angle one obtains diffraction discs with feature variations in intensity even for very thin specimen where conventional CBED patterns would show discs of constant contrast.

Figure 34.8 shows a LARBED pattern of a thin $SrTiO_3$ specimen. This pattern provides dynamical rocking curve information up to an illumination tilt angle of 70 mrad in all directions, i.e. the diameter of each of the diffraction disc is 140 mrad (=8°). As for conventional PED patterns, the (partial) compensation of the illumination tilt by the diffraction shift smears out any detail within the thermal diffuse scattering background, such as Kikuchi bands. Compared to conventional CBED this increases the accuracy with which quantitative information may be extracted from each of the diffraction discs of a partially compensated LARBED pattern.

Since the data presented in Fig. 34.8 was acquired by recording each of the 1,009 individual diffraction patterns, storing these in a single data potentially even higher quality (more quantitative) data can be extracted. For a diffraction pattern consisting of discrete spots, as is the case in the presented example, it is possible to subtract the background under each of the individual diffraction spots present in the diffraction

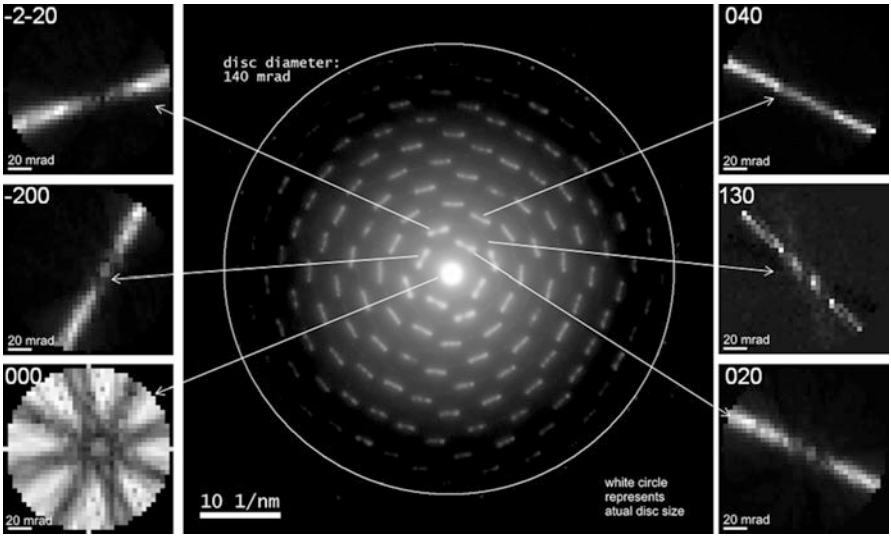

Fig. 34.8 Zero-loss filtered LARBED pattern (log scale) of very thin $SrTiO_3$ acquired using the QED software installed on a Zeiss EM912 at 120 kV. To the *left* and *right* of the pattern individual, background-subtracted diffraction discs extracted from a LARBED data stack are shown

pattern, for each discrete illumination tilt angle separately. The value of each pixel within the individual diffraction discs displayed to the left and right of the LARBED pattern in Fig. 34.8 thus represents the integrated background-subtracted diffraction intensity for the selected Bragg spot [8].

Such kind of data will extend the application of quantitative CBED to structures with arbitrarily large unit cells and also arbitrarily small specimen thicknesses.

34.4.2 Pseudo-3D Reconstruction of 4D Electron Diffraction Data

Much of what is counted as a great advantage of PED may be attributed to the washing out of 3D (dynamical) diffraction information by integrating along the relrods. Figure 34.9 shows a very extreme case of this ($K_2O{\cdot}7Nb_5O_2$, space group P4/mbm [No. 127], $a = b = 27.5$ Å, $c = 3.94$ Å). The integrated LARBED pattern for a disc scan with 70 mrad radius shows that Bragg spots from several Laue zones have been sampled by the Ewald sphere.

Looking at the background-subtracted LARBED discs (shown as insets in Fig. 34.10a, b, c) extracted from the data set shown in Fig. 34.9, we notice three features:

(a) Because of the large tilt range and the not very thin sample only sharp lines appear where the Bragg condition is satisfied exactly = > 'Bragg lines'

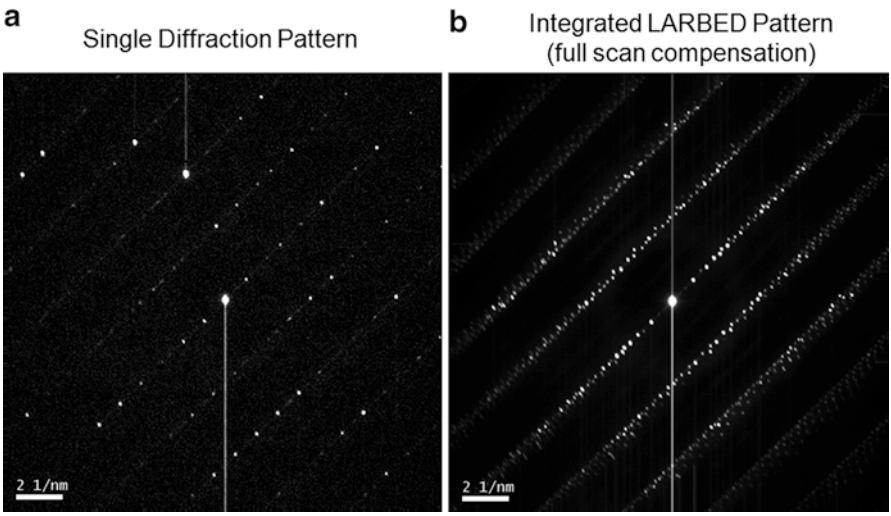

Fig. 34.9 (**a**) individual zero-loss filtered diffraction pattern of $K_2O{\cdot}7Nb_5O_2$, (**b**) LARBED pattern of the same sample with complete scan compensation (The sample was kindly provided by D. Zhang and S. Hovmöller (Stockholm university))

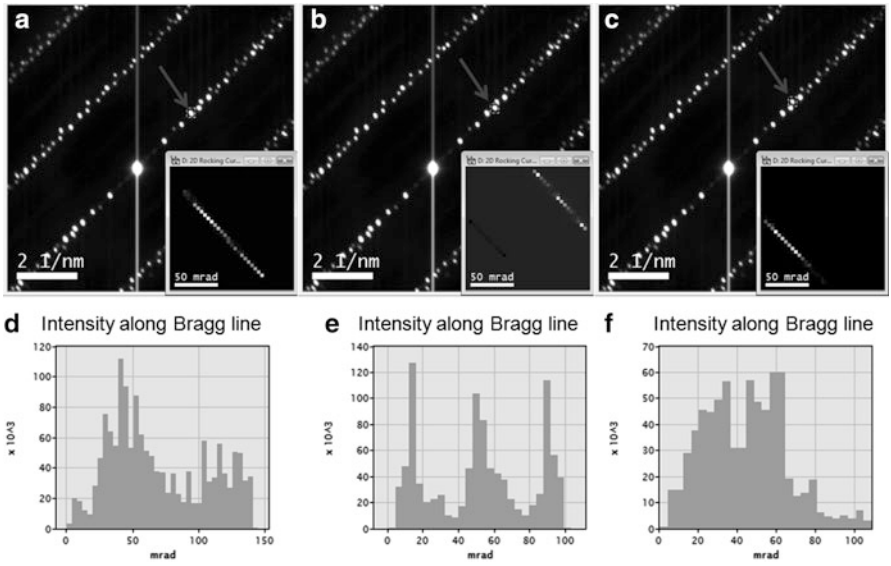

Fig. 34.10 Central part of the pattern shown in Fig. 34.9b. The *arrows* in (**a**, **b** and **c**) point to the reflections for which LARBED discs (shown in the respective *insets*) have been extracted. The related intensity variations along the Bragg are shown in (**d**), (**e**), and (**f**)

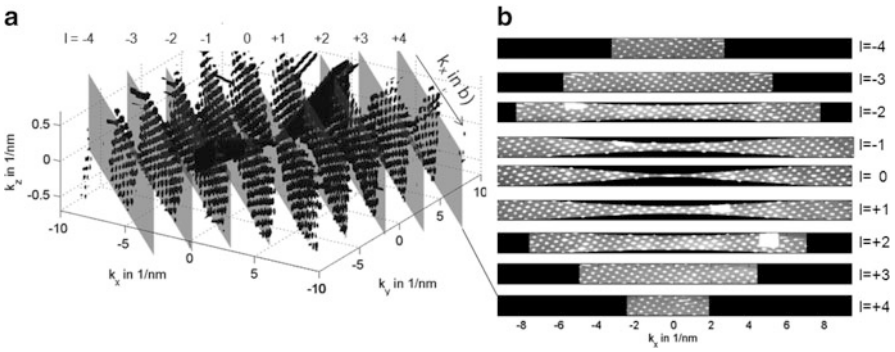

Fig. 34.11 (**a**) Isosurface plot of a small section of 3D reciprocal space of the $K_2O7Nb_5O_2$ lattice reconstructed form the LARBED data stack shown in Fig. 34.10. Note that the k_z-axis has been magnified 5 times. (**b**) Vertical cuts through the 3D volume displayed in (**a**). The intensity has been adjusted to reveal even the faint reflections. The k_x- and k_z-axes have equal scales

(b) The intensity along these Bragg lines (shown Fig. 34.10d–f) varies very much, depending on which other reflections are also excited (dynamical diffracting conditions).
(c) While the orientation of these Bragg lines is always normal to the corresponding **g**-vector, their position within the discs indicates the z-component of **g**.

Feature (b) in the above list indicates a significant advantage of LARBED over PED in this context, because PED includes at most two points along these Bragg lines. Feature (c) can be made use of for recovering the 3D information contained in this data. The combination of these two facts means that the data presented here is of 4D nature. While the position of the Bragg line indicates the z-position of a given reflection (=>3D), the intensity variation along the Bragg lines (the fourth dimension) may, in principle, be used to solve the crystallographic phase problem, as described earlier when discussing the dynamic inversion problem.

However, disregarding the fourth dimension for the moment and simply averaging the intensity along the Bragg lines one may also just reconstruct a small section of 3D reciprocal space, as shown in Fig. 34.11.

34.5 Conclusion

This chapter has presented a short introduction to the additional kind of information that can be access by collecting diffraction information for a range of different incident beam directions. Particular emphasis has been put on the importance of overcoming the limitations imposed in conventional CBED experiments and the advantages implied by the very recently developed LARBED technique. It has been shown that the availability of the kind of 4D diffraction data made

available by LARBED experiments opens the door to a whole new range of possible experiments, including the possibility of a fully automated solution to the dynamic inversion problem in electron diffraction. While this making full use of the information carried by dynamically scattered electrons is still work in progress, some other alternative applications, such as quantitative CBED for arbitrarily thin samples and arbitrarily large unit cell crystals, pseudo-3D diffraction, or the extension of the acceptance angle of imaging energy filters may already be applied routinely.

References

1. Spence JCH, Zuo JM (1992) Electron microdiffraction. Plenum, New York
2. Tanaka M, Saito R, Ueno K, Harada Y (1980) Large-angle convergent-beam electron diffraction. J Electron Microsc 29:408–412
3. Morniroli JP, Houdellier F, Roucau C, Puiggali J, Gesti S, Redjaimia A (2008) LACDIF, a new electron diffraction technique obtained with the LACBED configuration and a Cs corrector: comparison with electron precession. Ultramicroscopy 108:100–115
4. Terauchi M, Tanaka M (1985) Simultaneous observation of bright- and dark-field large-angle convergent-beam electron diffraction patterns. J Electron Microsc 34:128–135
5. Eades JA (1980) Zone-axis patterns formed by a new double-rocking technique. Ultramicroscopy 5:71–74
6. Tanaka M, Ueno K, Hirata Y (1980) Signal processing of convergent beam electron diffraction patterns obtained by the beam-rocking method. Jpn J Appl Phys 19:L201–L204
7. Zhang D, Oleynikov P, Hovmöller S, Zou X (2010) Collecting 3D electron diffraction data by the rotation method. Z Kristallogr 225:94–102
8. Koch CT (2011) Aberration-compensated large-angle rocking-beam electron diffraction. Ultramicroscopy 111:828–840
9. Koch CT, Spence JCH (2003) A useful expansion of the exponential of the sum of two non-commuting matrices, one of which is diagonal. J Phys A Math Gen 36:803–816
10. Koch CT (2008) Many-beam solution to the phase problem in crystallography. http://arxiv.org/abs/0810.3811
11. http://www.hremresearch.com
12. Zuo JM, Spence JCH (1991) Automated structure factor refinement from convergent-beam patterns. Ultramicroscopy 35:185–196
13. Deininger C, Necker G, Mayer J (1994) Determination of structure factors, lattice strains and accelerating voltage by energy-filtered convergent beam electron diffraction. Ultramicroscopy 54:15–30

Chapter 35
Shadow Imaging for Charge Distribution Analysis

Yimei Zhu and Lijun Wu

Abstract We briefly review the shadow imaging method for charge distribution analysis developed at Brookhaven. It is a unique electron-diffraction technique. Instead of focusing a small electron probe on the sample in conventional convergent beam electron diffraction, we focus the probe above (or below) the sample, resulting in parallel recording of dark-field images (shadow images), or PARODI. Because the method couples diffraction with imaging, it is thus suitable for studying crystals as well as their defects. We used this technique to accurately describe charge transfer that determines the functionality of technologically important materials. Examples are given for MgB_2 superconductor and $CaCu_3Ti_4O_{12}$ oxide that exhibits giant dielectric response. Discussions on non-spherical electron scattering factors and their parameterizations for direct observations of electron orbitals in atomic images are also included.

X-ray and electron diffraction are complementary. X-ray diffraction measures the total density of electrons in crystal; in contrast, electron diffraction measures electrostatic potential, i.e., the total electron density as well the nuclear core charge. With x rays we often collect a powder pattern containing many reflections from many crystals, while with electrons we can determine accurately a few selected structure factors, and due to the small electron probe, a tiny powdered grain or a crystal smaller than 100 nm can be easily studied as a single crystal. Electron diffraction is particularly sensitive to valence-electron distribution in crystals at short reciprocal vectors, and thus the structure factors determined from electron diffraction at small scattering angles give valuable information about electron or charge transfer over longer distances in the crystal unit cell. This becomes evident

Y. Zhu (✉) • L. Wu
Brookhaven National Laboratory, Long Island, NY 11973, USA
e-mail: zhu@bnl.gov

U. Kolb et al. (eds.), *Uniting Electron Crystallography and Powder Diffraction*,
NATO Science for Peace and Security Series B: Physics and Biophysics,
DOI 10.1007/978-94-007-5580-2_35,

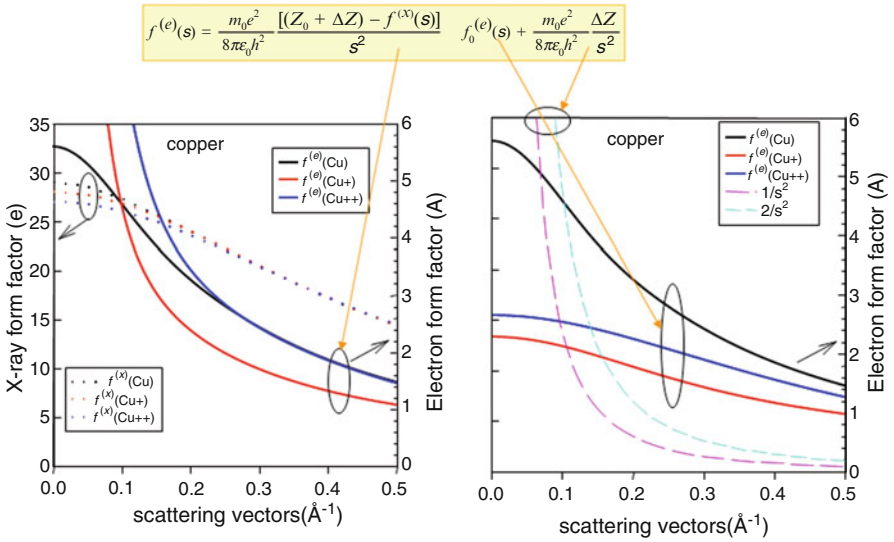

Fig. 35.1 Comparison of X-ray form factor (vertical axis on the *left*) and electron form factor (vertical axis on the *right*) as a function of scattering vector *s* for neutral Cu atom, Cu^{+} and Cu^{++} ions based on the Mott-Bethe formula. Here *f* with superindices *e* and *x* refers to the atomic scattering amplitude for electrons and x-rays, respectively, Z is the charge of the nucleus. For small s, where f (x) approaches the number of electrons at the atom that is close to Z, the electron-scattering amplitude will vary greatly with the distribution of valence electrons around the atom

when considering the Mott-Bethe formula (see Fig. 35.1), where we see clearly that the electron diffraction is more suitable for the accurate measurement of charge distribution using the innermost reflections than x-ray diffraction. Measuring accurately just a few of the low-order electron structure factors provides a useful test of electronic structure calculations of the electron density.

Conventional Convergent Beam Electron Diffraction (cCBED) have been successfully used to study charge distribution of crystals with a small unit-cell, see for example [1, 2]. However, the cCBED method is not suitable for studying crystals with a large unit-cell (where Bragg reflections are closely spaced), such as high-temperature superconductors, partly because of the wide range of incident-beam directions that is required to extract accurate information in cCBED, resulting in overlapping diffraction disks for large unit-cell crystals. Small convergent angles have to be used to avoid overlap for measuring individual structure factors. To overcome the drawback of limited angular information, we literally introduce an additional dimension, thickness, into the diffraction pattern and study the variation in diffraction intensity not only in relation to excitation error, *s*, but also as a function of the crystal thickness [3–8].

The method we developed is a new breed of CBED which is imaging and diffraction coupled. It differs from the traditional CBED in that we focus the electron probe above the sample rather than on the sample [3–9], as illustrated

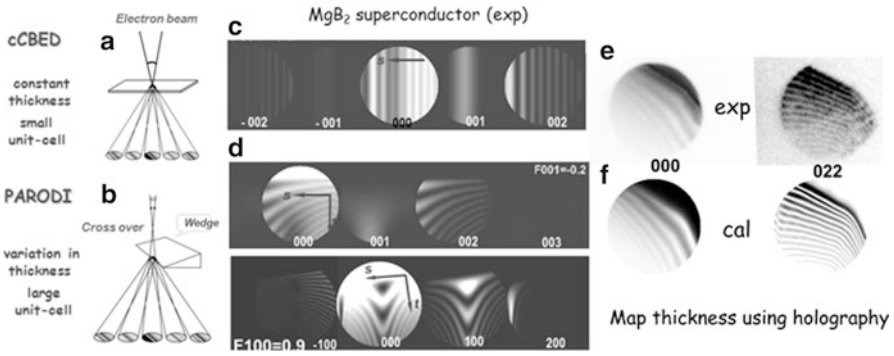

Fig. 35.2 Sketches of experimental setup for conventional convergent beam electron diffraction (cCBED) (**a**) and the shadow imaging method (Parallel Recording Of Dark-Field Images, PARODI) (**b**). Examples of experimental observations are shown in (**c**) and (**d**) for the (00 l) and (h00) systematic rows of MgB_2, respectively, to determine structure factors for charge density analysis. In cCBED, we probe an area of consistent thickness, while in PARODI an area with thickness variation. Here, *s* denotes excitation error and *t* denotes the thickness (*arrows* in (**c-d**) denote the direction of the change). Thickness measurement used in PARODI is shown in (**e-f**) with experimental observations in (**e**) and calculations, based on dynamic scattering theory, in (**f**) for the (000) and (022) reflection of Si to map the thickness of the area. (**e**) Energy filtered PARODI pattern (*left*) and experimental hologram (*right*); (**f**) calculated patterns (a 2-demensional thickness distribution) extracted from the phase map ($\phi = CV_0t$) obtained from the hologram (**e**), using a scaling factor of $I/CV_0 = 13.33$ nm/rad (where $V_0 = 11.5$ V is the mean potential). The reflections were recorded in the [1 1–1] zone with the *center* of Laue circle at (−14.2, 6.55, −7.65) position

in Fig. 35.2. In doing so, we form shadow images (mainly dark-field images) of a large illuminated area within the diffraction disks that contain not only information on orientation (as with cCBED), but also thickness profiles, or Pendellösung plots, for the many simultaneously recorded reflections. At the edge of the sample, the thickness profile usually starts from zero and goes up to a maximum that can range from 10 nm to several hundred nanometers depending on the distance from the specimen to the beam's crossover. Because this method obtains dark-field images within each diffraction disk for many reflections in a single exposure (parallel recording), we term the method Parallel Recording Of Dark-field Images, or PARODI (see also Fig. 35.3). Our PARODI method offers distinct and important advantages [7]. First, dozens of reflections (for large unit-cell crystals) are recorded simultaneously, ensuring that the incident-beam illumination and exposure are exactly the same for all reflections. Second, the dark-field images are recorded in the back focal plane of the objective lens where the aberration of the objective lens and the transfer function of the microscope can be neglected for quantitative analysis. Third, for a wedge sample, the discrete data points within each reflection (corresponding to different thicknesses of the sample) are independent for defect-free sample areas or incoherent illumination; this results in a high ratio of experimental observations versus the number of fitting parameters in model calculations, giving correspondingly higher levels of confidence. Fourth, the

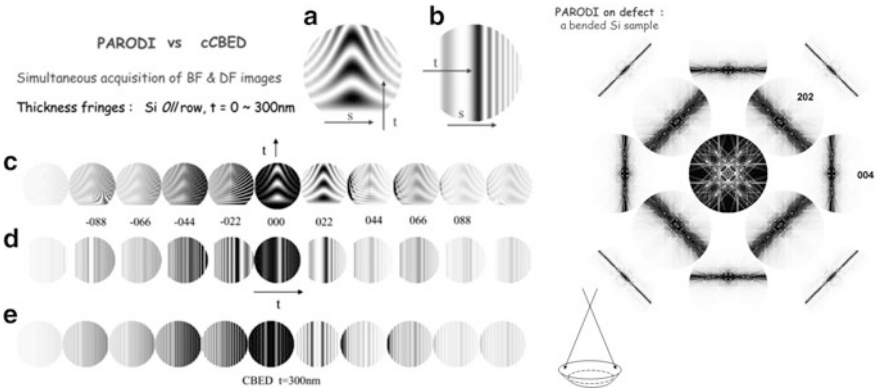

Fig. 35.3 Calculated PARODI patterns (**a-d**) for a wedge sample of Si with a linear change in thickness (t = 0–300 nm) in the vertical direction (**a** and **c**) and the horizontal directions (**b** and **d**). The vacuum area (t = 0) is at the bottom for (**a, c**) but on the *left* for (**b, d**) of the probing area. (**a-b**) the 022 reflection; (**c-d**) the *00 l* systematic row. *s* represents excitation error (or the deviation from the Bragg condition). (**e**) For comparison, a calculated cCBED pattern with a constant thickness (t = 300 nm) is included. *Right* panel: Calculated PARODI pattern of a bended Si sample showing the bend contours in 16 Bragg reflections (the corresponding dark-field images) and the *center* beam (bright-field image). Structure factor of all the reflections can be determined using a single diffraction pattern

defocused beam minimizes possible radiation damage in comparison with cCBED. Fifth, the interference fringes due to planar defects (e.g., interfaces) show strong contrast even when the defect is viewed edge on for coherent illumination [4, 9]. And last but not least, a wide range of reflections from the same illuminated area can be simultaneously analyzed in quantitative measurement of charge distribution and lattice displacement because electrons scattered at small angles are sensitive to charge arrangement, whereas those scattered at large angles are sensitive to crystal distortion. Although introducing sample thickness imposes additional complexity in measurement, for crystals with a large unit-cell this is the only way to accurately measure the low-index structure factors using CBED. We have demonstrated that the thickness distribution of the probing area can be routinely mapped using off-axis electron holography (Fig. 35.2e, f). When the area is a wedge, only one additional parameter is needed for the refinement [5].

The low-order structure factors were determined through a refinement procedure by comparing experiment with calculation based on Bloch-wave dynamic diffraction theory. The high-order structure factors are either based on experimental measurement using synchrotron X-ray, or DFT calculations, combing the low-order electron structure factors as a full dataset. The initial calculations usually start from electron structure factors (ESFs) of the procrystals (i.e., a hypothetical crystal with atoms having the electron distribution of free atoms; also so-call independent atom model (IAM)). Then iterative calculations were carried out by adjusting values of structure factors until the difference between calculated and experimental patterns

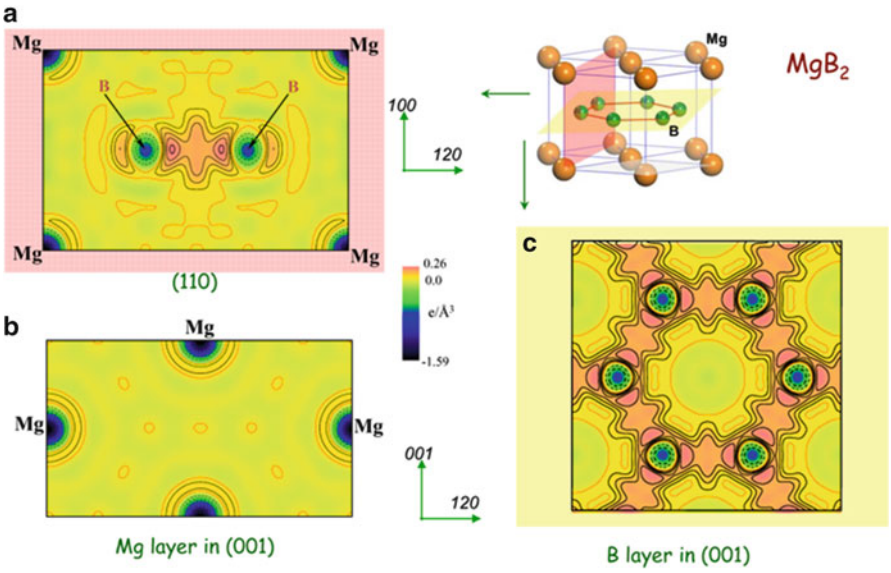

Fig. 35.4 DFT calculated difference charge-density maps $\Delta\rho(r)$ of MgB_2 superconductor incorporated with several measured low-index electron structure factors. The contours are shown as dashed *black* line for $\Delta\rho(r) < 0$ with intervals of 0.2 e/Å^3, *orange* line for $\Delta\rho(r) = 0$, and solid *black* line for $\Delta\rho(r) > 0$ with intervals of 0.05 e/Å^3. A color scheme of *black-blue-green* below zero level, *yellow-purple* at and above zero level was used. (**a-b**) Planes normal to the c-axis through the B and Mg atoms, respectively. (**c**) The 110 plane through the Mg and B atoms. The structure model of MgB_2 showing the (120) plane (*pink*) and the (001) plane (*yellow*) related to the charge-density maps in (**a**) and (**c**), respectively, is also included [6] (color figure online)

reaches minimum. To ensure that this minimum is not a saddle local minimum, we test it by selecting several different starting points and re-calculating structure factors iteratively until we reach the same lowest minimum. Multipole refinement model of Hansen and Coppens [10] are used to refine the measured structure factors for charge density analysis via computer codes of *VALRAY*:

$$\rho_{\text{atomic}}(r) = P_{\text{core}}\rho_{\text{core}}(r) + P_{\text{val}}\kappa^3\rho_{\text{val}}(\kappa r) + \sum_{l=1}^{l\,\max} \alpha^3 R_l(\alpha r) \sum_{m=1}^{l} P_{lm\pm} Y_{lm\pm}(\theta, \phi)$$

where $\rho_{\text{core}}(r)$ and $\rho_{\text{val}}(r)$ are the spherical atomic core charge density and spherical valence charge density (monopole), respectively. P_{core} and $\rho_{\text{val}}(r)$ are the electron population of core and valence parts. The last term is the multipole contribution. Several applications of charge density measurement using the PARODI method, including those illustrated in Fig. 35.4 (MgB_2 superconductor) and Fig. 35.5 ($CaCu_3Ti_4O_{12}$ dielectric oxide), will be presented. Results obtained from the PARODI method will be compared with cCBED.

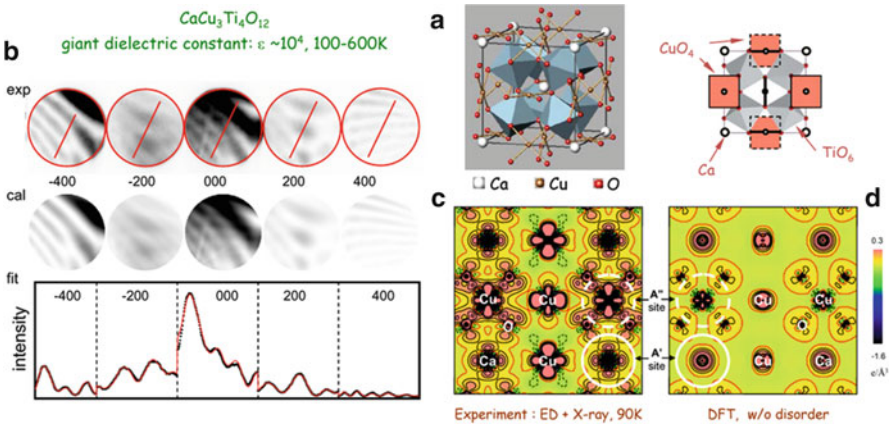

Fig. 35.5 (**a**) The structure model of $CaCu_3Ti_4O_{12}$ (CCTO), an oxide with giant dielectric response across a wide range of temperatures. (**b**) Measurement of low-order structure factors using PARODI. *Top* row: an experimental PARODI pattern of CCTO recorded on a 20 bit imaging plate showing the h00 systematical row of the 000, ±200, and ±400 reflections at room temperature. Middle row: the calculated pattern using the dynamic Bloch-wave approach. Bottom row: the line scans of the intensity oscillation from the experiment as open circles are compared with calculations as solid lines. (**c**) Experimental observation at 90 K of the charge distribution of CCTO in (001) basal plane containing Cu, Ca, and O atoms (i.e., the static deformation electron density map using neutral atoms as a reference), extracted from structure factor measurements using combined electron and x-ray diffraction data through multipole refinement and best-fit analysis. A total number of 58 independent structure factors including six from the innermost electron reflections, were used. (**d**) DFT calculation based on the ideal crystal structure. The color legend indicates the magnitude of the charge, and the contour plot has an interval of $0.1e/A^3$. The orbital-ordered Cu-*3d* states of *xy* symmetry are clearly visible, as well as its antibonding with O-*2p* states. Note the significant difference near the A' sites (circled by *white solid line*) between (**c**) and (**d**), where an anisotropic density pattern of e_g electrons is observed only experimentally, suggesting some degree of disorder with Cu replacing Ca in real material [8]

In charge density analysis the future challenges include direct observations of valence electron distribution in real-space via high-resolution imaging (HREM). Currently spherical form factors are used in most HREM image simulations, thus structure related aspherical orbitals (such as p- and d-orbitals) cannot be revealed or interpreted in HREM. To meet the challenge we have formulated and parameterized the aspherical electron scattering factors for atoms with atomic number ranging from 1 (H) to 54 (Xe) [11]. Our tabulated aspherical form factors (Fig. 35.6) might well afford a better description of the experimentally observed exit-waves in electron diffraction and imaging after they pass through the sample, thereby allowing more accurate comparisons between the experiments and the density functional theory (DFT) of functional materials. Recent HREM image simulations based on DFT calculations have demonstrated that the effect of aspherical orbitals can be visible in atomic images [12, 13]. The real-space approach is especially useful for understanding the role of valence electrons and the charge transfer associated with interfaces and defects, and is complementary to the reciprocal approach.

Aspherical electron scattering factors

$$f^{(x)}(s) = \int \rho(r)\exp(i2\pi\mathbf{q}\cdot\mathbf{r})\,d\mathbf{r} \quad \Rightarrow \quad \varphi_i(r) = R_i(r)Y_{lm}(\theta,\phi)$$

$$\exp(i\mathbf{q}\cdot\mathbf{r}) = 4\pi\sum_{l=0}^{\infty}\sum_{m=-l}^{l} i^l j_l(Sr)Y_{lm}(\beta,\gamma)Y^*_{lm}(\theta,\phi)$$

Angular dependent electron scattering factors

$$f_{ij}^{(x)}(s,\beta,\gamma) = (4\pi)^{1/2}\sum_n i^n(2n+1)^{1/2}C^n(l_i m_i, l_j m_j)\Theta_n^{m_i-m_j}(\beta)\Phi_{m_i-m_j}(\gamma)\langle j_n\rangle_{ij}$$

for p orbitals

$$f_p^{(e)}(s) = \left(\frac{3}{2}\sin^2\beta\right)f_{p,sph}^{(e)}(s) + \left(\cos^2\beta - \frac{1}{2}\sin^2\beta\right)f_{pI}^{(e)}(s)$$

for d orbitals

$$f_0(d) = \langle j_0\rangle_d - \tfrac{10}{7}\langle j_2\rangle_d + \tfrac{18}{7}\langle j_4\rangle_d,$$
$$f_1(d) = \langle j_0\rangle_d - \tfrac{5}{7}\langle j_2\rangle_d - \tfrac{12}{7}\langle j_4\rangle_d,$$
$$f_2(d) = \langle j_0\rangle_d + \tfrac{10}{7}\langle j_2\rangle_d + \tfrac{3}{7}\langle j_4\rangle_d.$$

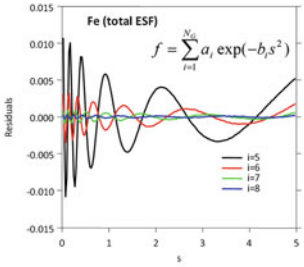

Label	a_1 / b_1	a_2 / b_2	a_3 / b_3	a_4 / b_4	a_5 / b_5	a_6 / b_6	a_7 / b_7	a_8 / b_8
29 Cu								
f(tot)	0.529112E+0	0.120921E+1	0.115166E+1	0.117554E+1	0.947268E+0	0.371478E+0	0.162101E+0	0.527718E-1
	0.108869E+3	0.432957E+2	0.148662E+2	0.510207E+1	0.192165E+1	0.664855E+0	0.185542E+0	0.295137E-1
f(core)	0.236133E-2	0.186503E+0	0.750016E-1	0.290182E+0	0.226527E+0	0.111859E+0	0.746858E-1	0.268538E-1
	0.604627E+1	0.546161E+1	0.289833E+1	0.238748E+1	0.122118E+1	0.465939E+0	0.149902E+0	0.248690E-1
f(4s)	0.387179E+0	0.897741E+0	0.585572E+0	0.222027E+0	0.798369E-1	0.285997E-1	0.891060E-2	0.237130E-2
	0.118088E+3	0.544619E+2	0.235552E+2	0.905433E+1	0.306909E+1	0.959692E+0	0.248751E+0	0.364833E-1
f(d1)	0.126412E-1	0.965902E-1	0.127679E+0	0.857683E-1	0.346609E-1	0.120229E-1	0.519026E-2	0.172532E-2
	0.731406E+2	0.241908E+2	0.957491E+1	0.390713E+1	0.155933E+1	0.541238E+0	0.165061E+0	0.272446E-1
f(d2)	0.476828E-2	0.589030E-1	0.984164E-1	0.812707E-1	0.423344E-1	0.153094E-1	0.530506E-2	0.169903E-2
	0.870598E+2	0.208898E+2	0.809949E+1	0.333448E+1	0.138063E+1	0.526814E+0	0.163076E+0	0.268266E-1
f(d3)	0.112551E-1	0.155149E-1	0.260743E-1	0.263609E-1	0.785295E-2	0.911748E-2	0.494257E-2	0.164761E-2
	0.212868E+2	0.796469E+1	0.444146E+1	0.172025E+1	0.795272E+0	0.469074E+0	0.156549E+0	0.260649E-2

Fig. 35.6 Formulation and parameterization of aspherical electron form factors: replacing charge density ρ(r) with orbital wavefunction φ(r); and expressions of angular dependent electron form factors for p-orbitals and d-orbitals. Comparison of fitting residuals with a different number of Gaussian functions using Fe as an example and parameterization of aspherical electron form factor using Cu as an example are also included [11]

Acknowledgements The author would like to thank Jin-Cheng Zheng, Johan Tafto, and Marvin Schofield for their collaborations. This work was supported by the U.S. Department of Energy (DOE), Office of Basic Energy Sciences, Materials Science and Engineering Division, under Contract No. DE-AC02-98CH10886.

References

1. Zuo JM, Kim M, O'Keeffe M, Spence JCH (1999) Direct observation of d-orbital holes and Cu-Cu bonding in Cu_2O. Nature 401:49–52
2. Tsuda K, Morikawa D, Watanabe Y, Ohtani S, Arima T (2010) Direct observation of orbital ordering in the spinel oxide $FeCr_2O_4$ through electrostatic potential using convergent-beam electron diffraction. Phys Rev B 81:1801021–1801024
3. Wu LJ, Zhu Y, Tafto J (1999) Test of first-principle calculations of charge transfer and electron–hole distribution in oxide superconductors by precise measurements of structure factors. Phys Rev B 59:6035–6038

4. Wu LJ, Zhu Y, Tafto J (2000) Picometer accuracy in measuring lattice displacements across planar faults by interferometry in coherent electron diffraction. Phys Rev Lett 85:5126–5129
5. Wu L, Schofield MA, Zhu Y, Tafto J (2004) A unique determination of boundary condition in quantitative electron diffraction: application to accurate measurements of mean inner potentials. Ultramicroscopy 98:135–143
6. Wu L, Zhu Y, Vogt T, Su H, Davenport JW, Tafto J (2004) Valence-electron distribution in MgB_2 by accurate diffraction measurements and first-principles calculations. Phys Rev B 69:064501
7. Zhu Y, Wu L, Tafto J (2003) Accurate measurements of valence electron distribution and interfacial lattice displacement using quantitative electron diffraction. J Microsc Microanal 9:442–456
8. Zhu Y, Zheng JC, Wu L, Frenkel AI, Hanson J, Northrup P, Ku W (2007) Nanoscale disorder in $CaCu_3Ti_4O_{12}$: a new route to the enhanced dielectric response. Phys Rev Lett 99:037602
9. Wu L, Zhu Y, Tafto J, Welch DO, Suenaga M (2002) Quantitative analysis of twist boundaries and stacking faults in Bi-based superconductors by parallel recording of dark-field images with a coherent electron source. Phys Rev B 66:104517
10. Hansen NK, Coppens P (1978) Testing aspherical atom refinements on small-molecule data sets. Acta Crystallogr Sect A 34:909–921
11. Zheng J-C, Wu L, Zhu Y (2009) Aspherical electron scattering factors and their parameterizations for elements from H to Xe. J Appl Crystallogr 42:1043–1053
12. Deng B, Marks LD (2006) Theoretical structure factors for selected oxides and their effects in high-resolution electron-microscope (HREM) images. Acta Crystallogr Sect A 62:208–216
13. Meyer JC, Kurasch S, Park HJ, Skakalova V, Künzel D, Groß A, Chuvilin A, Algara-Siller G, Roth S, Iwasaki T, Starke U, Smet JH, Kaiser U (2011) Experimental analysis of charge redistribution due to chemical bonding by high-resolution transmission electron microscopy. Nat Mater 10:209–215

Chapter 36
Electron Diffraction of Protein 3D Nanocrystals

Jan Pieter Abrahams, Dilyana Georgieva, Linhua Jiang, and Igor Nederlof

Abstract Protein crystallography, being one of the most established methods for structure determination of biomacromolecules, relies on the diffraction analysis using X-rays for 3D (micro-)crystals. Electron diffraction is only employed for single layer 2D nano-crystals. However, there is no established method for analysing multi-layered 3D nano-sized protein crystals. Electron diffraction may fill this important niche, but several problems have to be surmounted for this method to become mainstream. Our group aims tackling some of the bottlenecks, and although our work is still very much in progress, we can report advances in some important areas. Here we summarise improvements in (i) the induction of growth of (nano-)crystals, (ii) electron diffraction data collection using the Medipix quantum area detector, (iii) unit cell determination using single, non- oriented diffraction patterns, (iv) integration of diffraction data and (v) phasing of electron diffraction data.

36.1 Introduction

Knowledge of the atomic structures of biological molecules like DNA, proteins and their complexes, has been one of the major driving forces in life science. Crystallography is the dominant method in this field. Protein crystallography is a major justification for large-scale facilities like synchrotrons and the planned free electron lasers X-ray sources (XFELs). However, 3D protein crystals that are smaller than about 0.5 μm are too small for standard X-ray crystallography,

J.P. Abrahams (✉) • D. Georgieva • L. Jiang • I. Nederlof
LIC, Gorlaeus Laboratories, Leiden University, Einsteinweg 55, 2333, CC Leiden, The Netherlands
e-mail: abrahams@chem.leidenuniv.nl; d.georgieva@chem.leidenuniv.nl; l.jiang@chem.leidenuniv.nl; i.nederlof@chem.leidenuniv.nl

U. Kolb et al. (eds.), *Uniting Electron Crystallography and Powder Diffraction*, NATO Science for Peace and Security Series B: Physics and Biophysics,
DOI 10.1007/978-94-007-5580-2_36,

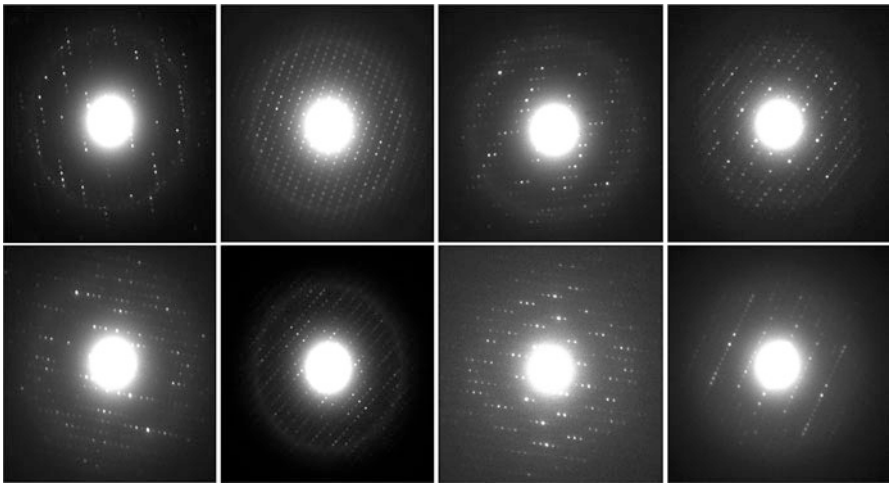

Fig. 36.1 Electron diffraction data up to 2 Å resolution of randomly oriented 3D crystals of lysozyme. Many different spacings are seen in the patterns, suggesting a broad sampling of reciprocal space. Shown is a representative sample of hundreds of diffraction patterns of lysozyme nano-crystals that we have gathered [2]

although XFEL sources may help in expanding the method towards smaller crystals [1]. This is a serious bottleneck, as about 30% of proteins that crystallize, do not grow crystals of a sufficient size, and therefore remain beyond the reach of atomic structure determination[1]. Especially membrane proteins and large (dynamic) protein-nucleic acid complexes fail to grow into crystals that are large enough. Structural information on these important drug targets is therefore severely lacking.

However, electrons are less damaging to proteins than X-rays by several orders of magnitude per diffracted quantum [2], and the groups of Profs. Abrahams and Zandbergen in Leiden and Delft recently demonstrated that useful, high-resolution electron diffraction data (up to 2.5 Å) can be obtained from nano-sized 3D protein crystals, where X-rays fail (e.g. see Fig. 36.1). For radiation sensitive material, this opens new possibilities, including full 3D data collection of 3D protein crystals to atomic resolution. However, even just qualitative knowledge of the diffraction potential of nano-sized protein crystals is important as it allows identifying positive crystallisation hits.

If electron crystallography of 3D protein crystals is so promising, why doesn't it work yet? We believe the answer to this question is the major success of X- ray crystallography as a tool for structure determination. The success of every technology is characterised by a sigmoidal curve: early on, it takes major efforts to prove the usefulness of a technique and progress is slow; then progress picks up and the popularity rapidly increases – investments in competing techniques no

[1] http://targetdb.pdb.org/statistics/TargetStatistics.html

longer seem justified. For example, the immense success of X-ray crystallography discouraged the development of 3D electron crystallography of proteins. Finally, more and more effort and investments are needed to make smaller and smaller gains in efficiency and in the end any technique will reach a plateau. We make the case that in X-ray crystallography increasingly more effort is being invested in ever-smaller gains in terms of resolution. By contrast, electron crystallography of 3D protein crystals is in the early stages, where it has to prove itself. In the case of sub-micron protein crystals, electron crystallography has the physics of diffraction on its side. It is becoming clear that tiny crystals that do not even yield to the most powerful dedicated synchrotron beamlines, can diffract well on a regular commercial electron microscope that can be obtained for a fraction of the cost.

36.2 The Disadvantages of Electron Diffraction in the Study of Protein Crystals

Being able to use smaller crystals does not solve the inherent problem of protein crystallography: obtaining crystals. Even when proteins do have the potential to crystallise, large scale screening of the many parameters that affect protein solubility has to be undertaken in order to identify suitable crystallisation conditions [3].

Detecting high-energy electrons without noise is not trivial. Off-line detectors like image plate and photographic film have advantages in sensitivity and spatial resolution respectively, but do not allow high throughput data collection. Live detectors like CCDs and direct electron detectors do not have these problems, but, like off-line detectors, these do not discriminate between high-energy electrons and other types of radiation that are generated inside the electron microscope [4]. This results in a sub-optimal signal-to-noise ratio, compromising data quality. For radiation hard materials, this may not be a major problem, as longer measuring times will increase the signal-to-noise, but for proteins, the problem is severe.

Unfortunately it is not possible to employ strategies for indexing diffraction patterns that are successful for electron diffraction of radiation hard crystals. These methods rely on careful alignment of the crystals in the microscope and this alignment requires continuous monitoring of the diffraction patterns as the crystals are oriented [5]. Protein crystals die in the beam during such alignment.

Mature software exists for the indexing and intensity measurement of diffraction data in the case of X-rays [6, 7]. In theory this software should also be able to be used on electron diffraction data, even though some types of distorion that are typical for electrons are currently not yet modeled by these programs. The extreme radiation sensitivity of protein crystals does not allow to collect complete data sets and only small wedges of data, often only single diffraction shots, can be obtained.

High-energy electrons (200–300 kV) are scattered 4–5 orders of magnitude more efficiently by organic materials, compared to X-rays, and lose only little energy when scattering inelastically. Hence, electrons are prone to scatter elastically multiple times within the crystals, a phenomenon also referred to as dynamic

scattering. In practice this implies that crystals that are more than about 200–300 nm in thickness are seriously affected by dynamic scattering, even with electron energies up to 300 keV.

36.3 Growing Nano-crystals

Crystallization of biological macromolecules is still one of the major bottlenecks in X-ray crystallography [8]. First a screening and then an optimization step characterize the process of obtaining diffraction-grade crystals. First nucleation of a microscopic crystallite must occur. Such a nucleus often composed of only a few hundred molecules and is not visible with an optical microscope. The screening step aims to identify suitable nucleation conditions, which has been shown to be the limiting step in the formation of X-ray grade crystals. Spontaneous formation of a crystal nucleus by the ordered aggregation of supersaturated proteins (homogeneous nucleation) is an unlikely event [9], but it is well known that surfaces can help in the formation of crystal nuclei.

We discovered that locally coating crystallisation plates with fragments of human hair allows automated, high-throughput crystallisation trials in a fashion that is entirely compatible with standard protein crystallisation techniques. We assessed the effect of these nucleants on the crystallisation of 11 different proteins in more than 4,000 crystallisation trials. We found additional crystallisation conditions for 10 out of 11 proteins when using the standard JCSG + screen (96 different conditions). The median increase in crystallisation hits was 14% and even membrane proteins were found to nucleate on human hair. On the basis of these numbers, we conclude that the inclusion of human hair fragments in high throughput crystallisation screens is straightforward and may be beneficial [10].

Furthermore, when crystals nucleate heterogeneously, for instance on fragments of human hair, they can be harvested straightforwardly by picking out the heterogeneous nucleant on which the protein crystals grow, even when the protein crystals themselves are sub-micron size (see Fig. 36.2). We have found that this greatly facilitates mounting nano-sized crystals on electron microscopy (EM) grids, prior to flash-freezing them using standard flash-freezing equipment.

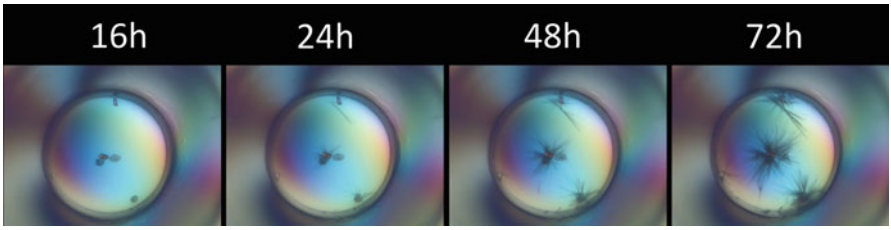

Fig. 36.2 Lysozyme needles growing on human hair fragments. These crystals can be harvested straightforwardly by picking out the hair fragments, even though the thinnest needles are sub-micron sized [10]

36.4 Measuring Electron Diffraction Data Using Quantum Area Detectors

A fundamental and often disregarded problem in electron detection in EM is that most of the energy of the electrons is converted into photons inside the microscope. These photons are produced when the electrons are being generated, focused by electromagnetic lenses, or interact with the sample, the walls of the EM or with the electron detector. Although the energy of these photons is high (hard UV and X-ray), it is not as high as that of imaging electrons. Nothing prevents these randomly scattered photons from depositing their energy along- side the imaging electrons on the electron detector. This inevitably means that conventional electron detectors have inflated signal-to-noise ratios, which often obscure essential details. This problem severely impacts studies that necessitate a limited electron dose, like time resolved studies or life science research. If there would be a way to only detect the signal (electrons), whilst disregarding the noise (photons), this would represent a quantum leap in electron microscopy, as this would allow studies with unprecedented contrast [11].

Quantum area detectors measure the energy of incoming quanta and can be programmed to only count events within a predetermined energy window [12]. Faruqi established their usefulness for TEM applications and LEEM/PEEM applications [13, 14]. In electron diffraction studies with Medipix quantum area detectors, we showed that this can result in an improved contrast in (ultra) low dose conditions: the same signal-to-noise ratio could be obtained at a dose that was 1–2 orders of magnitude lower, when compared to conventional technologies like photographic film, image plate or CCD electron detectors [11]. This finding, in addition to the high dynamic range (more than four orders of magnitude), the absence of read-out noise and comparatively fast read-out time (currently five frames/s) of the Medipix2 detector, allowed us to collect multi- degree diffraction data sets of nano-sized protein crystals (for an example: see Fig. 36.3). By employing an extremely small and parallel electron beam, we could pick out parts of the crystal with a minute mosaic spread, explaining the appearance of so-called 'lunes' due to the curvature of the Ewald sphere.

36.5 Unit Cell Determination

The first step of crystallographic data analysis is determining the unit cell parameters of the crystal. The conventional method for unit cell determination by electron diffraction is based on obtaining diffraction patterns from main crystallographic zones. Finding such zones requires carefully orienting the crystal, a process that is made easier if the diffraction pattern shows Kikuchi lines when using convergent beam. Based on the spacings between diffraction spots and the angular relationship between the patterns, unit cell parameters can be calculated. This remains a tricky

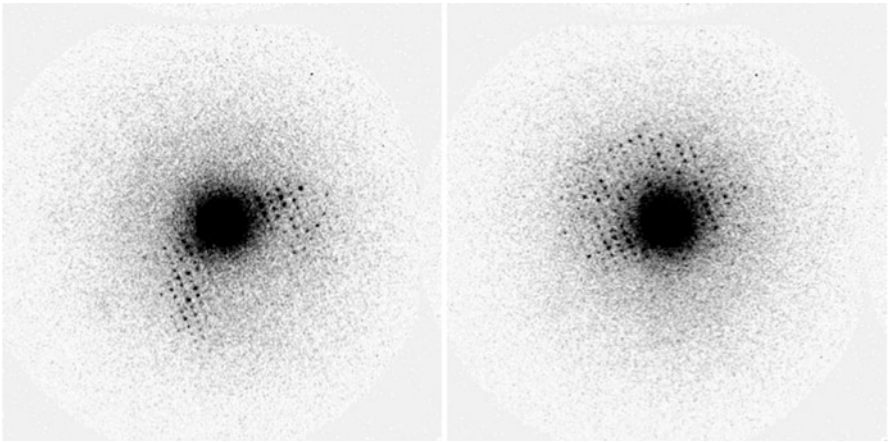

Fig. 36.3 The first and the last diffraction patterns of a series of 23 subsequent frames (0.065° per frame) collected at 200 keV with a Medipix Quad detector (512 by 512 pixels). The crystal was orthorhombic lysozyme, maximum resolution ±4.5 Å

procedure and often in the final stage, X-ray powder diffraction and electron diffraction are combined to assure accurate determination of cell parameters and their subsequent refinement.

Unit cell determination by X-ray crystallography does not rely on the avail- ability of diffraction patterns along main zone axes, and several groups have explored the possibility to likewise facilitate electron diffraction data acquisition by also allowing misoriented diffraction patterns. The Automated Diffraction Tomography technique (ADT) [15, 16] and the diffraction rotation technique [17] have recently raised major interest in this respect. In diffraction tomography, patterns are acquired in STEM mode in order to reduce beam damage and data are collected every 1° by tilting the crystal stepwise. The technique is suited for collecting data from beam sensitive materials, where the nature of the sample does not allow long exposures. The diffraction rotation technique aims at collecting a complete dataset of diffraction patterns in a fashion similar to X-ray crystallography. In this method tilting of the beam in small steps is combined with rotation of the crystal.

However, for very beam sensitive materials, like nano-crystals of proteins, it is not always possible to collect multiple diffraction patterns, or only small wedges of data can be collected (see for instance Fig. 36.3). For such cases (which we encounter frequently), we developed the program EDiff, which is a user friendly software suite for unit cell determination of 3D nano-crystals from randomly oriented electron diffraction patterns with unknown, independent orientations [18]. It can also be used for 3D cell reconstruction from diffraction tilt series. In neither case exact knowledge of the angular relationship between the patterns is required. The unit cell can be validated and the crystal system is assigned. EDiff can index the reflections in electron diffraction patterns, and can be employed as a first step in reconstructing the 3D atomic structure of organic and inorganic molecules and

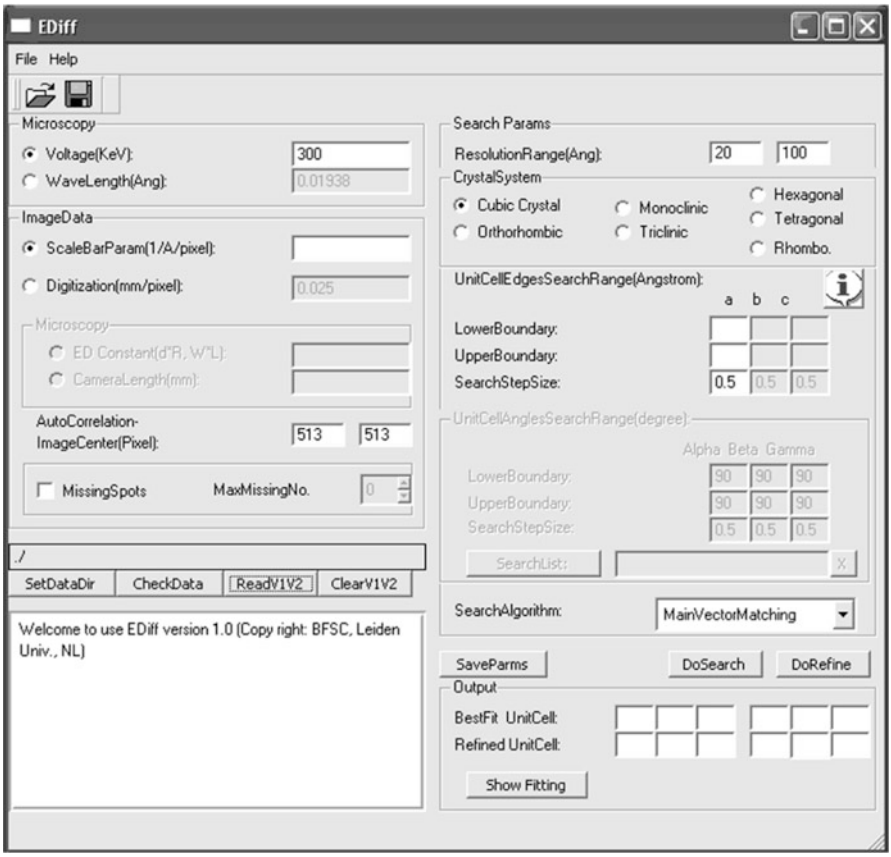

Fig. 36.4 Main graphical user interface of the program EDiff V1.0, used for finding unit cells from non-oriented electron diffraction patterns [18]

proteins. Before EDiff can suggest unit cells and indexing, the diffraction data need to be pre-processed with AMP, which forms part of the suite. AMP (Autocorrelation Mapping Program) removes the background noise from the diffraction images, picks reflection spots and determines short lattice spacings by examining the autocorrelation functions of the diffraction patterns [19].

Two reflection spots together with the direct beam position form a triangle, which we call a 'facet'. The facet defined by the two shortest vectors (corresponding to two reflection spots closest to the centre) is called a 'main facet'. In short, every reflection pair defines a facet. The main facet defines the smallest repeating unit of the 2D lattice defined by the low-resolution spacings (but not any higher-order Laue zone (HOLZ) that may be visible at high resolution). The facets found from all diffraction images contained in a dataset are used to find the cell parameters. For a more detailed explanation, please refer to [18]. EDiff also has a Graphical User Interface (GUI); see Fig. 36.4.

36.6 Integration of Diffraction Data

The current version of EDiff can also determine the intensities of indexed spots, but this feature is undergoing testing at the moment of writing. We are also testing whether the images can be integrated with X-ray diffraction data integration programs like MOSFLM [6] and XDS [7]. In some instances, notably for small molecules, XDS proved successful, but we are still facing some unexplained difficulties for the general cases.

36.7 Phasing of Electron Diffraction Data

Once data has been integrated, the phases of the structure factors must be determined in order to solve the crystal structure. In the case of protein crystals, molecular replacement – where the phases of a different but related protein structure are used as an initial guess – is likely to be a powerful phasing method for electron diffraction data too. Another possibility is to use imaging data of the crystals to infer low resolution phase information in a method that is successful for electron diffraction structure determination of 2D protein crystals. In any case, subsequent structure refinement has to include corrections for dynamical scattering, like the strong phase approximation or multi-slice simulations.

The presence of dynamical diffraction, especially if crystals are in the order of 100–200 nm in thickness, has been considered to be a serious obstacle in structure determination by electron diffraction. The regime for dynamical scattering of bacteriorhodopsin 2D crystals was indicated by Glaeser and Ceska [20]: differences between Friedel pairs caused by dynamic scattering were clearly ob- served when 20 kV electron diffraction patterns were collected; however, they were not observed in 100 kV patterns. For 3D protein crystals, which are considerably thicker than 2D protein crystals, differences between Friedel mates were anticipated even at high accelerating voltage [21]. However, these Friedel pair differences anticipated in this paper were severely overestimated, since the calculations assumed a zero scattering potential for the disordered solvent and lipid parts of the crystal (which on average occupy 50% of the unit cell in protein crystals). This results in a substantial overestimation of the phase shift of electrons that travelled through ordered protein, compared to electrons that traversed the disordered parts of the crystal. In a recent theoretical paper, we showed that dynamical diffraction may be used to retrieve phase information from diffraction patterns [22], but this theoretical result remains to be validated experimentally.

36.8 Discussion and Conclusion

The road towards structure determination of 3D nano-crystals of proteins is arduous, but important progress has been made. Although we have been able to remove some of the bottlenecks, we cannot claim success (yet). The main problems that we are facing now are all related to the experimental difficulties of collecting diffraction data of sufficient quality. We have found the vitrification of crystals on EM grids using standard cryogenic techniques that are employed routinely in single particle analysis and cryo-electron tomography, to be a major source of variability. Sometimes we have to scan up to ten grids before we find well-frozen protein crystals. So far, we have not been able to pinpoint the source of this variability, which is currently the main factor hampering progress. It may be that the cause is the larger thickness of the sample, compared to samples routinely used for single particle analysis. In this case, the inclusion of cryo-protectants should improve reproducibility (at the expense of contrast), but so far we have insufficient data to make any claims in this respect.

We anticipate that the availability of two Titan Krios microscopes, which will be installed in our lab in 2011, will be highly important for progress. With these microscopes (both equipped with an autoloader), we will be able to scan grids for well-frozen crystals in a fraction of the time we currently require (we are currently using a CM-200 microscope). Furthermore, the new microscopes allow us to combine STEM-diffraction [15, 16] with measuring the diffraction using a quantum area detector [11], which may further reduce beam damage.

References

1. Chapman HN et al (2011) Femtosecond X-ray proteinnanocrystallography. Nature 470:73–81
2. Henderson R (1995) The potential and limitations of neutrons, electrons and X-rays for atomic resolution microscopy of unstained biological molecules. Q Rev Biophys 28:171–193
3. Chayen NE, Saridakis E (2002) Protein crystallization for genomics: towards high-throughput optimization techniques. Acta Crystallogr Sect D 58:921–927
4. Plaisier JR, Koning RI, Koerten HK, van Roon AM, Thomassen EAJ, Kuil ME, Hendrix J, Broennimann C, Pannu NS, Abrahams JP (2003) Area detectors in structural biology. Nucl Instrum Methods Phys Res A 509:274–282
5. Zou XD, Hovmöller A, Hovmöller S (2004) TRICE – a program for reconstructing 3D reciprocal space and determining unit cell parameters. Ultramicroscopy 98:187–193
6. Leslie AGW (1992) Joint CCP4 + ESF-EAMCB newsletter on protein crystallography 26
7. Kabsch W (2010) XDS. Acta Crystallogr Sect D 66:125–132
8. Bolanos-Garcia VM, Chayen NE (2009) New directions in conventional methods of protein crystallization. Prog Biophys Molec Biol 101:3–12
9. Cacciuto A, Auer S, Frenkel D (2004) Onset of heterogeneous crystal nucleation in colloidal suspensions. Nature 428:404–406
10. Nederlof I, Hosseini R, Georgieva D, Luo JH, Li DF, Abrahams JP (2011) A straightforward and robust method for introducing human hair as a nucleant into high throughput crystallization trials. Cryst Growth Des 11:1170–1176

11. Georgieva D, Jansen J, Sikharulidze I, Jiang L, Zandbergen HW, Abrahams JP (2011) Evaluation of medipix2 detector for recording electron diffraction data in low dose conditions. J Instrum 6:C01033
12. Llopart X et al (2002) Medipix2, A 64 k pixel readout chip with 55 μm square elements working in single photon counting mode. IEEE Trans Nucl Sci 49:2279–2283
13. McMullan G, Faruqi AR (2008) Electron microscope imaging of single particles using the Medipix2 detector. Nucl Inst Exp Phys A 591:129–133
14. Faruqi AR (2009) Principles and prospects of direct high resolution electron image acquisition with CMOS detectors at low energies. J Phys Condens Matter 21:314004
15. Kolb U, Gorelik T, Kubel C, Otten MT, Hubert D (2007) Towards auto- mated diffraction tomography: part I – data acquisition. Ultramicroscopy 107:507–513
16. Kolb U, Gorelik T, Otten MT, Hubert D (2008) Towards automated diffraction tomography: part II – cell parameter determination. Ultramicroscopy 108:763–772
17. Zhang D, Oleynikov P, Hovmöller S, Zou Z (2010) Collecting 3D electron diffraction data by the rotation method. Z Kristallogr 225:94–102
18. Jiang L, Georgieva D, Zandbergen HW, Abrahams JP (2009) Unit cell determination from non-oriented electron diffraction patterns. Acta Crystallogr Sect D 65:625–632
19. Jiang L, Georgieva D, IJspeert K, Abrahams JP (2009) An intelligent peak search program for digital electron diffraction images of 3D nano-crystals. Image and Signal processing CISP'09: Vol 17–19
20. Glaeser RM, Ceska TA (1989) High-voltage electron diffraction from bac-teriorhodopsin (purple membrane) is measurably dynamical. Acta Crystallogr Sect A 45:620–628
21. Glaeser RM, Downing KH (1993) High resolution electron crystallography of protein molecules. Ultramicroscopy 52:478–486
22. Abrahams JP (2010) The strong phase object approximation may allow extending crystallographic phases of dynamical electron diffraction patterns of 3D protein nano-crystals. Z Kristallogr 225:67–76

Chapter 37
Parallel-Beam Diffraction and Direct Imaging in an Aberration-Corrected STEM

Ondrej L. Krivanek

Abstract Aberration-corrected scanning transmission electron microscopes (STEMs) are versatile instruments that can perform many types of investigations. The main use of such microscopes has so far been in direct imaging and analysis, but they are equally well suited to performing diffraction studies and combined diffraction + imaging experiments. The various optical modes needed for such operating modes are reviewed. They include producing electron beams with angular spreads as narrow as a few μrad, and conical precession scans with scan angles >50 mrad.

37.1 Electron Diffraction in a STEM

Crewe's original STEM [1, 2] had no lenses after the objective lens. The information projected onto its detectors was therefore always a diffraction pattern. However, this STEM also had no 2-dimensional detector – it detected its various signals on scintillator + photomultiplier type detectors, and the richness of the diffraction information available in a STEM was not fully appreciated at the time.

This situation changed fundamentally when John Cowley, the author of Diffraction Physics [3], acquired a Vacuum Generators (VG) HB5 STEM, built a camera detector for it, and started to explore the wide variety of imaging and diffraction modes available in a STEM [4]. The results of these pioneering studies were presented in many papers by Cowley and coworkers and also in Spence's and Zuo's comprehensive book [5].

Modern STEMs are able to take these studies further, because they have several features that Cowley's STEM lacked:

O.L. Krivanek (✉)
Nion Co., 1102 Eight St, Kirkland, WA 98075, USA
e-mail: krivanek@nion.com

U. Kolb et al. (eds.), *Uniting Electron Crystallography and Powder Diffraction*,
NATO Science for Peace and Security Series B: Physics and Biophysics,
DOI 10.1007/978-94-007-5580-2_37,

(a) symmetric or nearly-symmetric condenser-objective lens. This kind of lens can transform a nearly parallel beam of electrons into a convergent beam that illuminates the sample, and then transform the outgoing electron beam, widely dispersed in angle, back into a nearly parallel beam. It allows scattering angles of up to about 200 mrad to be transferred onto detectors. It also allows the STEM to operate as a parallel-beam instrument.
(b) Post-specimen lenses. These serve to magnify the parallelized exiting beam as needed on the detectors, i.e. to give an adjustable camera length, typically from a few mm to several m.
(c) Aberration correctors. In a STEM, aberration correctors primarily serve to produce smaller electron probes, by correcting aberrations to higher angles and thus making it possible to use more convergent (and therefore smaller) illuminating probes. The correctors introduce many new lenses into the column, and these lenses can also be used for setting up various diffraction experiments.

37.2 Convergent and Nearly Parallel Electron Probes

Magnetic electron lenses have one great advantage over glass lenses used for light: their focal length can be changed very easily, simply by adjusting the current flowing through their coils. This gives electron-optical columns a very large degree of flexibility. Figure 37.1 illustrates how an electron beam can be made more or less convergent simply by adjusting the strength of two electron lenses, L1 and L2.

The figure shows schematically a case of 1:1 imaging of a crossover (a), 2× reduction (b) and 2× magnification (c). In practice, a pair of lenses with adjustable focal lengths can typically cover 10:1 reduction to 1:10 magnification, and strong lenses (with short minimum focal length) can cover 50:1–1:50. To cover the range continuously, the lenses have to be individually alignable, as is done for instance for every lens in the Nion microscope column [6].

When the output crossover is made smaller, as in Fig. 37.1b, the illumination grows more convergent (as shown by the axial ray). The image of the beam-defining aperture then moves towards the first crossover and becomes larger. The total electron flux remains the same, which means that the final crossover becomes more intense (more concentrated).

When the output crossover is made larger, as in Fig. 37.1c, the illumination grows less convergent (as shown by the axial ray), and the image of the beam-defining aperture becomes smaller. The total electron flux again remains the same, which means that the crossover appears fainter (more spread out), as shown schematically in the figure.

The diagrams shown in Fig. 37.1 are very simple, but they illustrate several important points. First, in order to understand an optical system, its first-order (Gaussian) trajectories must be precisely quantified. This is because all the other properties of the system, such as its higher order aberrations, are crucially dependent on the first order trajectories. In a complicated optical system, such as one involving

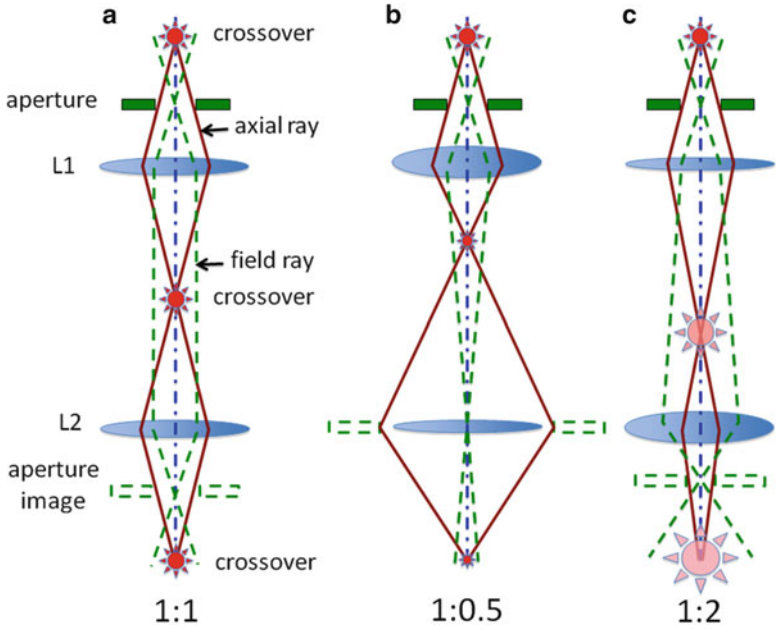

Fig. 37.1 Changing convergence and probe size by adjusting two electron lenses: (**a**) 1:1, (**b**) 1:0.5, (**c**) 1:2

aberration correctors, the widths of the electron beam in the different optical elements must typically be known with an accuracy better than 0.1%.

Second, a crossover is never a point-like object. Each new crossover is simply an image of the previous crossover, all the way through the optical column. The first crossover is typically the virtual crossover situated behind the actual electron source, from which the electrons appear to emanate.

Third, it is useful to trace two types of rays through an optical system: axial rays, which go through crossovers at recurring images of the object we are imaging, and field rays, which go through crossovers at images of the beam-defining aperture, and traverse the object plane some distance from the optic axis.

Fourth, when modeling electron-optical systems, it is often convenient to run the electrons backwards, so that their trajectories can start at a place where the optical conditions are readily defined, such as in the sample plane of a condenser-objective lens. Provided that the polarity of all the magnetic fields is reversed at the same time, the backward-traveling electrons trace out exactly the same trajectories as the forward-traveling ones. Applying this principle to Fig. 37.1, one can see that reversing the direction of the electron travel in mode (b) produces the same schematic of magnifying the crossover (and demagnifying the angular range) as depicted in mode (c).

Fifth, conservation of brightness (Liouville's theorem) means that the area of a crossover times the solid angle of the rays converging into it is constant throughout

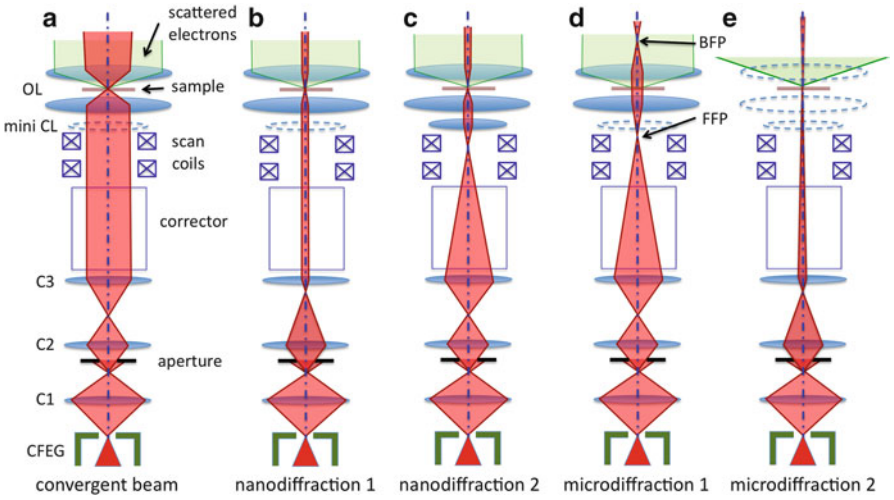

Fig. 37.2 Different ways of illuminating the sample in a STEM: (**a**) convergent beam, (**b, c**) nanodiffraction, (**d, e**) microdiffraction

any part of an optical system that contains no apertures. The magnification of each crossover is therefore simply equal to 1/angle at which the rays going through the crossover meet.

Sixth, there is no such thing as a completely parallel illuminating probe. If it were completely parallel, all the rays would have to originate from the same point in the aperture plane. The area subtended by a point being zero, this would mean that for a practical electron source of finite brightness, the electron flux through the aperture plane would also be zero. In other words, an illuminating beam with a zero spread of angles automatically means zero electron flux, and a real illuminating beam will therefore always have a finite spread of angles.

Figure 37.2 illustrates the formation of electron probes of different degrees of convergence in a complete STEM. I have placed the electron source at the bottom, with the electron beam traveling upwards, as pioneered by Vacuum Generators (VG) and currently done in Nion microscopes. The shown source is a cold field emission electron gun (CFEG), the brightest and most coherent electron source presently known. (For a "conventional" view, in which the electrons travel downwards, simply turn the page upside down.)

The angles of the rays defining the illuminating beam have been greatly exaggerated for better schematic clarity. In practice, the unscattered electrons stay close to the optic axis. The largest deviation, about 50 μm, typically occurs in the front-focal and back-focal planes (FFP and BFP) of the condenser-objective lens (OL).

Mode (a) illustrates the standard way of operating the STEM when acquiring high resolution scanning transmission images. With third-generation aberration correctors (see [7] for a description of STEM correctors), the convergence semi-angle

on the sample is typically around 30–40 mr. The smallest attainable probe size, which is given by the diffraction limit

$$d = 0.61\frac{\lambda}{\alpha_o} \tag{37.1}$$

(where λ is the electron wavelength and α_o is the illumination semi-angle) is then about 0.5 Å in a 200 keV STEM operating with a very small beam current. For larger probe currents, d grows bigger due to source-size broadening, as described quantitatively in [8]. The probe can also be broadened by aberrations and instabilities. Even so, sub-Å probes are now readily achievable in aberration-corrected STEMs operating at 100 keV and higher.

Mode (b) parallelizes the beam simply by adjusting condenser lenses C2 and C3, much like mode (c) in Fig. 37.1. The narrower beam traverses the corrector, whose precise setting then becomes much less critical, and which can even be turned off altogether. In practice, a reduction of the beam divergence by about 40x is readily possible, giving a beam with a semi-angle of 1 mr, and a diffraction-limited probe size of around 2 nm. The total beam current can be kept the same, or increased by strengthening C1, so that the beam density becomes larger on the aperture in front of C2.

Several modern microscopes have a condenser mini-lens (mini CL) just in front of the objective lens, and turning this lens on allows the beam to be switched into a nano-diffraction mode too (mode (c)). In practice, another condenser lens is then needed after the corrector, to project a beam crossover into the front-focal plane of the mini CL without requiring new trajectories through the corrector.

Mode (d) parallelizes the beam further, by projecting the aperture plane into the sample plane, and the source plane into the front-focal plane of the objective lens. For clarity of the schematic, the beam through the corrector is shown as similar to nanodiffraction mode 2. In reality, one typically starts from nanodiffraction mode 1, i.e. with a fairly narrow beam through the corrector. The probe convergence at the sample is determined by how wide the image of the source is in the front-focal plane of the OL. The half-angle of the illumination α'_o at the sample is:

$$\alpha_o{}' = \frac{d_s}{2f_o} \tag{37.2}$$

where d_s is the size of the source projected into the FFP and f_o the focal length of the objective lens. For CFEG STEM, the typical projected source size is about 20 nm. f_o of 2 mm therefore gives $\alpha'_o = 10$ μrad, i.e. the beam becomes quite parallel in this mode. At the same time, the diffraction-limited probe size at the sample is about 0.15 μm. The large probe size is why we call this mode "microdiffraction".

If the image of the source is made only about a nm in size, either by the last lenses of the corrector, or by a CL minilens preceding the OL FFP, if one is present, then α'_o can be made smaller than 1 μrad and the illumination becomes very parallel indeed. The probe on the specimen then grows to several μm in size, but it can still be largely coherent.

A problem with mode (d) is that the objective lens parallelizes the outgoing electron beam, and features of interest in the diffraction pattern obtained with the parallel illumination, which can lie at scattering angles <0.1 mrad, remain close to the optic axis. The projector lenses must then be highly excited to produce the large camera lengths, of the order of 10 m, that are needed to project a clear version of the pattern onto the final detector. This difficulty is avoided if the objective lens is turned off altogether (mode (e)). A diffraction-limited probe size of the order of between 0.01 and 1 μm is then again possible, with a correspondingly parallel illuminating beam. At the same time, the scattered electrons now spread away from the optic axis rather than become parallelized, and very large camera lengths at the detectors are much easier to attain.

37.3 Coherence, Intensity and Shape of the Illuminating Probe

A coherent electron probe is one in which the electron wave-packets extend over the full width of the probe, and electrons constituting the probe carry no information about which part of the source they came from. An incoherent probe is one in which the wave-packets are narrower than the probe, and the electrons go through the probe at locations corresponding to where they originated at the virtual source. In practice, of course, a perfectly coherent probe carries zero probe current, and hence all probes are only partially coherent.

A convenient description of partial coherence is provided by the concept of the "coherent probe current", defined as the current for which the probe size due to diffraction and the projected source size are the same [8]. The magnitude of this current is determined only by the electron source, and it does not change no matter what the optical system does to the beam: magnify or demagnify the probe, accelerate or decelerate the beam. Coherent probe currents are typically about 150 pA for a cold field emission gun (CFEG) and 30 pA for a Schottky source [8]. Both values may increase in the future; for instance, a coherent probe current of 430 pA has been measured recently for a newly developed CFEG [9].

Probes with currents less than the coherent value are largely coherent and exhibit various interference phenomena not observed with incoherent probes: e.g., interference fringes in overlap region produced by Bragg spots whose separation is less than the convergence angle of the probe. They are also at most $\sqrt{2}$ larger than the diffraction-limited probe size, whereas incoherent probes are typically much larger than the diffraction limit. One can of course pass continuously from the coherent into the incoherent regime simply by changing the amount of the beam current admitted through the final beam-defining aperture, either by changing the aperture size, or by changing the magnification of the beam projected onto the aperture.

The precise shape of the probe depends on what it images. If the probe is coherent and contains an image of the source, as in modes (a–c) and (e) in Fig. 37.2, then it typically contains the Airy disk distribution [10], somewhat smoothed by the partial incoherence. Such a probe has multiple rings around the central maximum, and can also contain pronounced and not necessarily symmetric tails arising due to remaining aberrations.

If the probe contains an image of the beam-defining aperture, as is done for instance in mode (d) in Fig. 37.2, it typically has a more square profile, but it can still contain pronounced Fresnel fringes due to the aperture being projected into the sample plane unfocused. Making sure that the aperture image is properly focused is an extra constraint, which can be satisfied if an extra lens is available. Every aberration-corrected microscope has several extra lenses, and setting up the illumination so that the aperture image is sharply in focus is therefore mostly a matter of making sure the lenses are set up correctly. Putting a beam crossover in one of the lenses, i.e. using this lens as a "field lens", which then does not change the heights of the crossovers in the column but changes the heights of the focused images of the illuminating aperture, makes the set-up especially convenient.

An illumination mode in which the illuminated spot on the sample is a focused image of an aperture rather than an image of the source is called Kohler illumination [11]. It is the main illumination mode used in optical microscopy, and it can have major advantages as an illumination mode in electron microscopy too.

37.4 Scanning Modes

A high-performance STEM typically has four layers of scan coils, and the layers can be driven independently. Two of the layers are before the sample and two layers after the sample. A variety of scan modes becomes possible with such an arrangement. Figure 37.3. illustrates two of them: regular scanning and beam rocking, as used for instance for precession diffraction [12].

For regular scanning (mode (a)), the beam is made to rock about the "coma free plane" of the objective lens, which is located between the front-focal plane of the lens and the sample. The coma-free plane can be thought of as the plane in which the objective lens effectively inserts the phase change due to its spherical aberration (C_s), i.e. the plane in which sideways beam shift must be avoided if coma is not to arise as a misalignment aberration in a C_s-producing optical element. Because the coma-free plane is located closer to the sample than the front-focal plane of the OL, coma-free scanning rocks the angle of beam at the sample slightly, and the correct ratio setting of the de-scan coils is not the same as for the scan coils. In practice, however, the rocking is quite small: less than 50 μrad for a 100 nm field of view.

De-scanning makes sure that the beam does not move on the detectors, especially the energy-loss spectrometer, in which beam movement causes a shift of spectra in energy. In practice, this correction only becomes important for scans larger than about 100 nm in size.

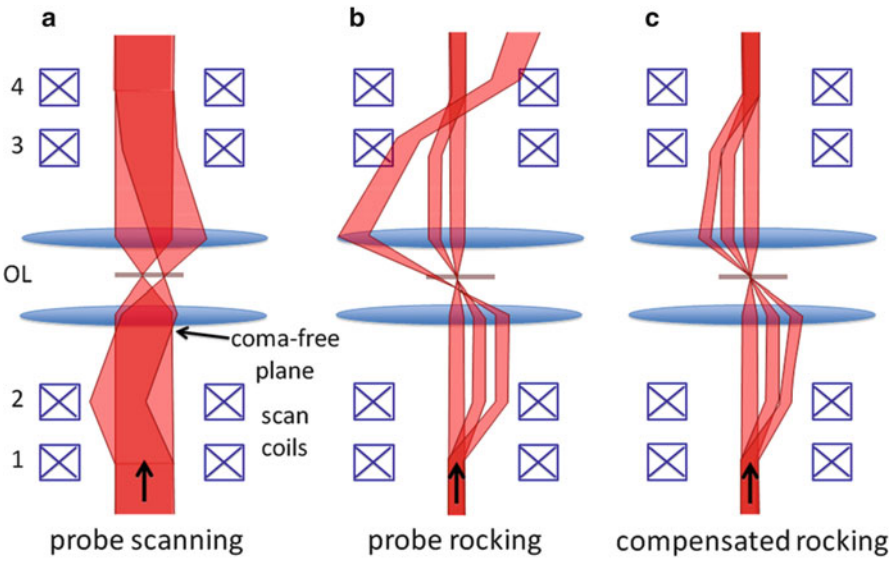

Fig. 37.3 Different ways of scanning and de-scanning the beam in a STEM: (**a**) probe scanning, (**b**) probe rocking, (**c**) compensated rocking

The beam rocking mode (b) involves setting the ratio of the first and second layers of the scan coils such that the beam is shifted while remaining nearly parallel to the optic axis as it enters the OL. The beam is typically much narrower in this mode, as needed for nanodiffraction, and rocks about a stationary point on the sample. Anti-symmetric de-rocking brings it back onto the optic axis. The scan magnitudes in this mode are typically much larger than for regular scanning used to acquire high-resolution images. With an objective lens of 2 mm focal length, the shift of the beam entering the OL amounts to 2 μm for 1 mrad of rocking, and rocking angles of 20 mrad and more are of interest.

It is also worth noting that when the objective lens is switched off, this kind of scan becomes a regular scan (parallel scan on the sample). The resultant imaging mode is very useful, because it provides a low magnification view of the sample.

Beam rocking as shown in mode (b) was first implemented by Eades in a Philips 400 EM [13], and was used soon thereafter by Higgs and Krivanek for obtaining EELS channeling maps [14]. For precession diffraction, the basic features of the scanning system are the same, but the scan is made conical rather than rectangular. There are various commercial devices able to perform such scans when added to electron microscopes [15]. Some microscopes such as the Nion UltraSTEM™ [6, 9] have the hardware needed to do the scans already built into them, but presently lack software dedicated to this type of operation.

For rocking ranges smaller than about 10 mrad, the relationship between the scans needed in the different layers of scan coils is approximately linear, and scan coil layers 2–4 of the complete scan-descan system can therefore be driven by a

linear combination of the signals sent to scan coils in layer 1. For rocking angles higher than about 10 mrad, spherical aberration and also aberrations such as three-fold astigmatism begin to affect the scan. The probe then starts wondering on the sample instead of rocking about a stationary point, and it also goes out of focus and becomes astigmatic. This is shown schematically in mode (b) for the beam that is deflected by a large amount.

A simple solution is to make the relationship between the signals sent to the different scan coil layers non-linear, as shown for mode (c). Adding a negative third-order curve to the scan signal for scan coil layers 2–3 (i.e., weakening the large-magnitude deflections from these coils) can compensate for spherical aberration, adding a parabola term can compensate for three-fold astigmatism and remnant axial coma. At the same time, the probe focus and astigmatism need to be adjusted dynamically across the scan field. (For correctly aligned conical precession scans, only the astigmatism adjustment needs to be done dynamically.) A stationary, diffraction-limited nanoprobe, with an angular range of about a mrad and a stationary size of <5 nm should then become available for rocking and precession scans of 50 mrad magnitude and beyond. To my knowledge, such a system has not yet been implemented in a STEM. The basic hardware for it exists in every Nion STEM column, and it is simply a question of spending the time needed to program the non-linear scans.

An alternate solution would be to scan the beam using scan coils located in front of the aberration corrector, which would then be able to automatically correct the effects of axial aberrations, just like it corrects the aberrations when producing a probe with a large semi-angle. However, such a system would not correct imperfections of the scan coils (such as non-linearities), and a completely corrected scan-descan system would need two correctors, one pre-sample and one post-sample. So even though a corrector could correct the scan imperfections in principle, in practice it will probably be more efficient to compensate them instead, as outlined above.

37.5 Conclusion

An aberration-corrected scanning transmission electron microscope is a very powerful instrument, which makes possible many kinds of experimental techniques. This brief summary of the optical solutions for some of the techniques is far from comprehensive, and there is no space in these printed notes for examples of applications. These will be given in the talk at the school.

A comprehensive compendium of the many aspects of STEM capabilities has appeared recently [16]. It includes chapters on STEM history, STEM imaging theory, application examples of sub-Å resolution imaging, nanodiffraction and diffraction imaging, EELS, fluctuation microscopy, low-voltage STEM, etc. I recommend it highly to all students interested in exploring electron crystallography with a STEM.

Acknowledgement I am grateful for useful discussions with Niklas Dellby, Lawrence Marks and Christopher Own.

References

1. Crewe AV, Wall J, Welter LM (1968) A high-resolution scanning transmission electron microscope. J Appl Phys 39:5861–5868
2. Crewe AV (2009) The work of Albert victor Crewe on the scanning transmission electron microscope and related topics. In: Hawkes PW (ed) Cold field emission and the scanning transmission electron microscope. Advances in imaging and electron physics. Elsevier, Amsterdam
3. Cowley JM (1995) Diffraction physics, 3rd edn. Elservier, Amsterdam/New York
4. Cowley JM, Spence JCH (1978) Innovative imaging and microdiffraction in STEM. Ultramicroscopy 3:433–438
5. Spence JCH, Zuo JM (1992) Electron microdiffraction. Plenum Press, New York
6. Krivanek OL et al (2008) An electron microscope for the aberration-corrected era. Ultramicroscopy 108:179–195
7. Krivanek OL, Dellby N, Murfitt MF (2009) Aberration correction in electron microscopy. In: Orloff J (ed) Handbook of charged particle optics, 2nd edn. CRC Press, Boca Raton
8. Krivanek OL et al (2011) Atomic resolution STEM at low primary voltages. In: Pennycook SJ, Nellist PD (eds) Scanning transmission electron microscopy. Springer, New York
9. Dellby N et al (2011) Dedicated STEM for 200 to 40 keV operation. Eur J Phys Appl Phys. doi:10.1051/epjap/2011100429
10. Born M, Wolf E (1997) Principles of optics, 7th edn. Cambridge University Press, Cambridge
11. Koehler A (1894) New method of illumination for photomicrographical purposes. J R Microsc Soc 14:261–262
12. Vincent R, Midgley PA (1994) Double conical beam-rocking system for measurement of integrated electron diffraction intensities. Ultramicroscopy 53:271–282
13. Eades JA (1980) Zone axis patterns formed by a new double-rocking technique. Ultramicroscopy 5:71–74
14. Higgs A, Krivanek OL (1981) Energy-filtered, double-rocked zone axis patterns. Proc 39th Annual EMSA Meeting, Atlanta
15. See for instance http://www.nanomegas.com/ and http://www.beamdevices.com/
16. Pennycook SJ, Nellist PD (2011) Scanning transmission electron microscopy: imaging and analysis. Springer, New York

Chapter 38
Electron Diffraction of Commensurately and Incommensurately Modulated Materials

Joke Hadermann and Artem M. Abakumov

Abstract Many materials have structures which are modulated, either displacively or compositionally, or a combination of both. A distinction can be made between commensurately modulated structures (where the period of the modulation is an integral multiple of the periodicity of the unmodulated cell) and incommensurately modulated structures (where that period is a non-integral multiple of the periodicity of the underlying unmodulated cell).

Electron diffraction (ED) is often very helpful in the analysis of modulated structures, especially if the compound is not available in the form of single crystals suitable for X-ray diffraction. Being applied to modulated structures, powder diffraction techniques face problems in the correct determination of the periodicity of the modulation waves (reflected in the modulation vector(s) in the reciprocal space) and the symmetry associated with the basic structure and the modulation waves (reflected in the superspace symmetry group). Reconstruction of the 3D reciprocal lattice using the ED data is a great help for solving these problems, especially taking into account that powder diffraction data often suffer from poor resolution (neutron powder diffraction) or low signal/noise ratio (conventional laboratory X-ray diffraction). This creates particular difficulties in recognizing weak satellite reflections, caused by some minor perturbations of the basic structure, such as displacements of the oxygen atoms or oxygen/vacancy ordering.

This chapter is an introduction to handling electron diffraction patterns of both commensurately and incommensurately modulated materials. This does not extend to the underlying theory of incommensurate crystallography due to the limited amount of space, and appropriate references are given instead.

J. Hadermann (✉) • A.M. Abakumov
EMAT, University of Antwerp, Groenenborgerlaan 171, B-2020 Antwerp, Belgium
e-mail: joke.hadermann@ua.ac.be; Artem.Abakumov@ua.ac.be

U. Kolb et al. (eds.), *Uniting Electron Crystallography and Powder Diffraction*,
NATO Science for Peace and Security Series B: Physics and Biophysics,
DOI 10.1007/978-94-007-5580-2_38,

38.1 Commensurately Modulated Structures

38.1.1 The Supercell Approach

Assume a simple primitive structure I with only one atom type A, as shown in Fig. 38.1a. For simplicity we will consider a two-dimensional lattice, but the consideration can be extended to the third axis analogously. The schematic representation of the ED pattern of this structure, is given next to the scheme of structure I and shows a rectangular pattern. All reflections have the same weight, as expressed by the structure factor $F_{II} = f_A e^{2\pi i(0h+0k+0l)} = f_A$, showing no particular cases for any *h*,*k*,*l*. If each second atom along the *b*-axis is replaced with another atom B (Fig. 38.1b) we can call this new structure II an occupationally modulated structure for which the structure I serves as the parent, or basic structure. The periodicity of the structure II along the *b*-axis is twice that of structure I, and in reciprocal space extra reflections will therefore appear at the $\mathbf{g}' = \mathbf{G} \pm 1/2\mathbf{b}^*$ positions. These reflections are the superstructure reflections, while the reflections at **G**, that were also present for structure I, are the basic reflections. In general the superstructure reflections are weaker than the basic reflections. This can be demonstrated by expressing the structure factor $F_{II} = f_A e^{2\pi i(0h+0k+0l)} + f_B e^{2\pi i(0h+\frac{1}{2}k+0l)} = f_A + f_B e^{\pi i k}$ which gives $F_{II} = f_A + f_B$ in case $k = 2n$, and $F_{II} = f_A - f_B$ for $k = 2n + 1$, the latter corresponding to the superstructure reflections.

Similar considerations can be made for structures where every *n*-th A atom is replaced by a B atom, which will give a periodicity along the *b*-axis that is *n* times that of structure I, and will give extra reflections at $h, k + m/n, l$ (with *hkl* the indices relative to the basic structure I), or in other notations at $\mathbf{g}' = \mathbf{G} \pm m/n\mathbf{b}^*$, which can then be treated using a supercell with unit cell basis vectors $\mathbf{a}'$, $\mathbf{b}'$, $\mathbf{c}'$ that are $\mathbf{a}' = \mathbf{a}$, $\mathbf{b}' = n\mathbf{b}$, $\mathbf{c}' = \mathbf{c}$ and reciprocal basis vectors $\mathbf{a}'^* = \mathbf{a}^*$, $\mathbf{b}'^* = 1/n\mathbf{b}^*$, $\mathbf{c}'^* = \mathbf{c}^*$.

The modulation does not always occur exactly along one of the axes of the basic structure. In the structure III (Fig. 38.1c) the atoms B are lying on planes (110) and $(1\bar{2}0)$, forming a rectangular pattern, and are tripling the periodicity along the directions perpendicular to (110) and to $(1\bar{2}0)$. In reciprocal space this leads to extra reflections along the directions $[110]^*$ and $[1\bar{2}0]^*$, i.e. extra reflections at $\mathbf{g}' = \mathbf{G} + m[1/3,\ 1/3,\ 0]$ and at $\mathbf{g}' = \mathbf{G} + m[1/3,\ -2/3,\ 0]$ (see right side of Fig. 38.1c). It is possible to again take basis vectors for the supercell that are lying along the same direction as those of the basic structure, $\mathbf{a}' = 3\mathbf{a}$, $\mathbf{b}' = 3\mathbf{b}$, $\mathbf{c}' = \mathbf{c}$ and reciprocal basis vectors $\mathbf{a}'^* = 1/3\mathbf{a}^*$, $\mathbf{b}'^* = 1/3\mathbf{b}^*$, $\mathbf{c}'^* = \mathbf{c}^*$ (Fig. 38.1d). However, it is possible to find a better, smaller unit cell by choosing reciprocal basis vectors for the supercell that are not lying along the same directions as those of the basic structure. In this case choosing $\mathbf{a}'^* = 1/3\,\mathbf{g}_{110}$, $\mathbf{b}'^* = 1/3\mathrm{g}_{1\bar{2}0}$, $\mathbf{c}'^* = \mathbf{c}^*$ will give a smaller primitive unit cell that allows you to index all reflections (see Fig. 38.1c for the unit cell indicated in direct space and Fig. 38.1e for the corresponding indexes in reciprocal space).

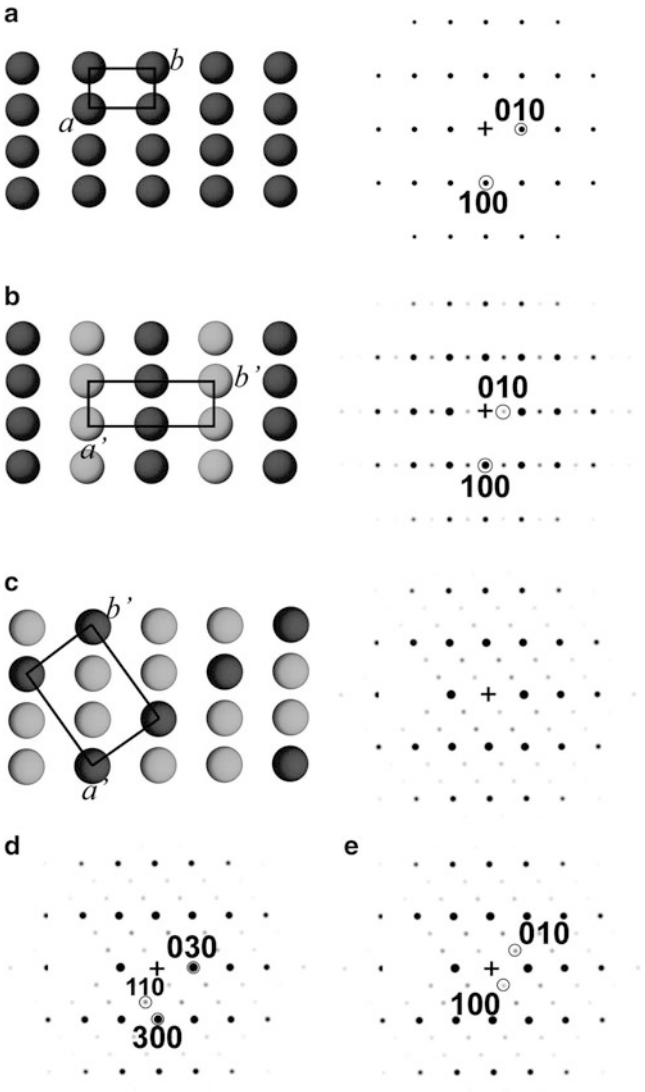

Fig. 38.1 Models for structures I (**a**), II (**b**) and III (**c**) on the *left* side, and their corresponding schematized electron diffraction patterns at the *right* side. (**d**) and (**e**) show two alternative indexation schemes for the electron diffraction pattern corresponding to the order in structure III

One can now use the transformation matrix to find the corresponding direct space basis vectors for your choice of reciprocal basis vectors. The transformation in reciprocal space between the basic unit cell and the supercell is given by

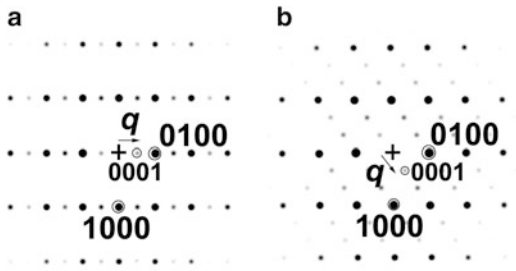

Fig. 38.2 The schematic electron diffraction patterns for (**a**) structure II and (**b**) structure III, indexed in the q-vector approach

$$\begin{pmatrix} \mathbf{a}*' \\ \mathbf{b}*' \\ \mathbf{c}*' \end{pmatrix} = Q \begin{pmatrix} \mathbf{a}* \\ \mathbf{b}* \\ \mathbf{c}* \end{pmatrix}$$

while the relation in direct space is given by $(\mathbf{a}'\ \mathbf{b}'\ \mathbf{c}') = (\mathbf{a}\ \mathbf{b}\ \mathbf{c})P$ with $P = Q^{-1}$. For the case in Fig. 38.1e:

$$P = \begin{pmatrix} 2 & -1 & 0 \\ 1 & 1 & 0 \\ 0 & 0 & 1 \end{pmatrix}$$

Thus the basis vectors of the supercell in direct space are $\mathbf{a}' = 2\mathbf{a} + \mathbf{b}$, $\mathbf{b}' = -\mathbf{a} + \mathbf{b}$, $\mathbf{c}' = \mathbf{c}$, corresponding to the unit cell in Fig. 38.1c.

As it was demonstrated with the last example, the choice of the supercell is not unique, but it should follow the requirement of keeping the highest possible symmetry and the smallest unit cell volume. If the new axes are chosen along other directions than in the basic structure, the transformation matrix should be included for clarity. More details on this aspect can be found in the International Tables for Crystallography, volume A, section 5 [1].

38.1.2 The q-Vector Approach

Instead of finding a supercell, one can describe the positions of the superstructure reflections using a modulation vector which connects the basic reflections to the superlattice reflections. This vector is expressed as $\mathbf{q} = \alpha\mathbf{a}^* + \beta\mathbf{b}^* + \gamma\mathbf{c}^*$. The basic reflections are indexed with $\mathbf{G} = h\mathbf{a}^* + k\mathbf{b}^* + l\mathbf{c}^* + 0\mathbf{q}$, while the superstructure reflections (also called satellites) are indexed with $\mathbf{g} = h\mathbf{a}^* + k\mathbf{b}^* + l\mathbf{c}^* + m\mathbf{q}$, with m an integer, $m \neq 0$. The modulation vector gives the plane on which the modulation occurs, while the reciprocal of the length of the modulation vector gives the periodicity of the modulation wave.

For the structure II, $\mathbf{q} = 1/2\mathbf{b}^*$ and the indexation using this approach is shown in Fig. 38.2a. The modulation occurs on the (010) plane, the interplanar spacings

for the satellite reflections (assuming an orthorhombic cell) can be found as $\frac{1}{d^2_{hklm}} = \frac{h^2}{a^2} + \frac{(k+m\beta)^2}{b^2} + \frac{l^2}{c^2}$ which gives a periodicity of the modulation wave as the reciprocal length of the **q**-vector:

$$\left|\frac{1}{\mathbf{q}}\right| = d_{0001} = \frac{1}{\sqrt{\left(\frac{0}{a}\right)^2 + \left(\frac{1/2}{b}\right)^2 + \left(\frac{0}{c}\right)^2}} = 2b$$

For structure III, the modulation occurs on the (110) plane with $\mathbf{q} = 1/3\mathbf{a}^* + 1/3\mathbf{b}^*$ (Fig. 38.2b) and the periodicity of the modulation is $3d_{110}$.

38.2 Incommensurately Modulated Structures

When the components α, β and γ of the modulation vector **q** are rational numbers with a reasonably small denominator (such as 1/2, 1/3, 1/4 etc.) the supercell approach seems to be the most straightforward way to describe the extra periodicity due to modulations. However, cases are frequently observed, where a very large denominator is required to represent the component of the modulation vector with sufficient precision. For example, Fig. 38.3 shows a schematic electron diffraction pattern with the same basic structure as structures I–III, and with $\mathbf{q} = 0.458\mathbf{b}^*$ (structure IV). Although the β value is not an irrational number, it requires quite a large unit cell to build a commensurate approximation. It can be approximated by $5/9 = 0.444$, in which case the supercell will be 9 times larger along the direction of the *b*-axis. It can be approximated even closer by $5/11 = 0.455$ or $6/13 = 0.462$ but this increases the size of the supercell to respectively 11–13 times along the *b*-axis, and still it will only be an approximation. The components of the modulation vector are always measured with some finite precision (i.e. they are known only up to certain digit after comma) and therefore can always be expressed as a rational number, but sometimes needing a very large denominator. In incommensurately modulated structures the modulation vector has at least one such component which cannot be approximated with a rational number with reasonably small denominator and can be regarded as an irrational component. Treating such structures with a large

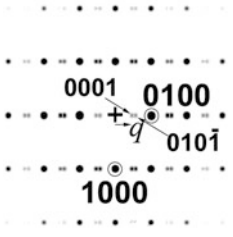

Fig. 38.3 Example of a schematical electron diffraction pattern of a structure with q = 0.458b*

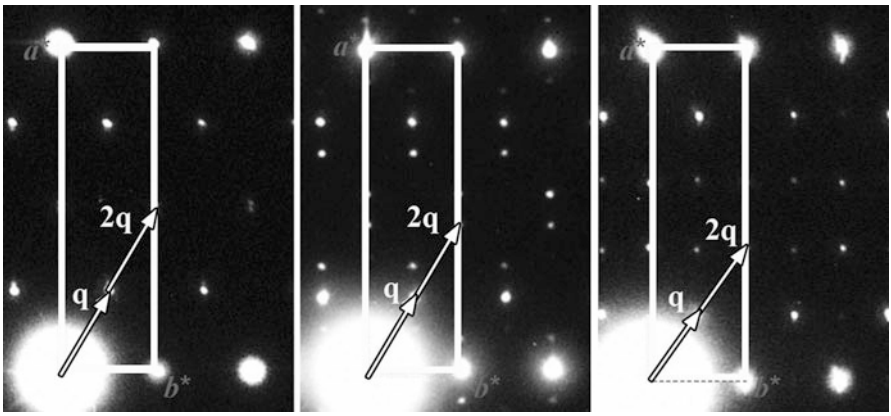

Fig. 38.4 A change of the position of the satellites upon a change in composition is shown, which can help distinguish satellites from basic reflections

supercell is impractical because it would require a very large amount of structural variables. The more rational way is to use (3 + d)-dimensional crystallography (the superspace approach). The diffraction pattern of the incommensurately modulated structure can be considered as a projection from this (3 + d)-dimensional reciprocal space onto the 3D reciprocal space. Here we restrict ourselves to the (3 + 1)D case only.

The first step in the indexation of the electron diffraction patterns of an incommensurately modulated structure consists of the separation of the reflections into a set of basic reflections ($m = 0$) and a set of satellites ($m \neq 0$). Intuitively, in many cases this can be done by choosing the brighter reflections as the basic ones, surrounded by one- or two-dimensional arrays of weaker satellites. The separation of the reflections into basic reflections and satellites can be performed, for example, by monitoring the systematic changes of the reflection positions with temperature or chemical composition (Fig. 38.4). The basic reflections should form a regular 3D reciprocal lattice. The symmetry operators of the point group of the crystal should transform any basic reflection into a reflection also belonging to the basic reciprocal lattice, i.e. the reflections with $m = 0$ and $m \neq 0$ should not be intermixed. The basis vectors of the basic direct lattice should obey the requirement of keeping the highest symmetry and lower volume. The analysis of the extinction conditions imposed on the *hkl*0 reflections will provide the possible centering of the basic structure.

The second step is the selection of the modulation vector and assigning *hklm* indexes for the satellites. This problem may not have a unique solution. The components of the modulation vector should be in correspondence with the selected crystal system and the centering type of the basic lattice. The modulation vector can be split into a rational and irrational part: $\mathbf{q} = \mathbf{q}_r + \mathbf{q}_i$. The operator R of the point group of the crystal should transform satellites into satellites and basic reflections into basic reflections: R:$\mathbf{G}(m = 0) \rightarrow \mathbf{G}'(m = 0)$ and R:$\mathbf{g}(m \neq 0) \rightarrow \mathbf{g}'$ $(m \neq 0)$. This condition is fulfilled if the operator R transforms the vector $\mathbf{q}$

Table 38.1 Allowed irrational components of the **q**-vector for different crystal systems (After [2])

Crystal system	$\mathbf{q_i}$	Crystal system	$\mathbf{q_i}$
Triclinic	(α,β,γ)	Tetragonal	
Monoclinic (γ-setting)	(α,β,0)	Trigonal	(0,0,γ)
	(0,0,γ)	Hexagonal	
Orthorhombic	(α,0,0)	Cubic	none
	(0,β,0)		
	(0,0,γ)		

Table 38.2 Compatibility between the centering types and possible rational components of the **q**-vector (After [3])

Crystal system	**q**	Crystal system	**q**
Triclinic	No rational component	Orthorhombic-P	(0, 1/2, γ)
			(1/2, 1/2, γ)
Monoclinic-P	(α, β, 1/2)	Orthorhombic-C	(1, 0, γ)
Monoclinic-B (γ-setting)	(1/2, 0, γ)	Orthorhombic-A	(1/2, 0, γ)
	(0, 1/2, γ)	Orthorhombic-F	(1, 0, γ)
		Tetragonal-P	(1/2, 1/2, γ)
		Trigonal-P	(1/3, 1/3, γ)

into itself or to $-\mathbf{q}$: $R\mathbf{q} = \varepsilon\mathbf{q} \pm \mathbf{G}$, $\varepsilon = \pm 1$. Let's assume that an orthorhombic structure has a modulation vector with only the irrational component $\mathbf{q}_i = (\alpha,\beta,\gamma)$. The mirror plane m_y transforms $\mathbf{q}_i = (\alpha,\beta,\gamma)$ into $\mathbf{q}_i{}' = (\alpha,-\beta,\gamma)$. The $R\mathbf{q}_i - \varepsilon\mathbf{q}_i = 0$ condition is fulfilled only if $\alpha = \gamma = 0$ for $\varepsilon = -1$ or $\beta = 0$ for $\varepsilon = +1$. If the β component is not zero as for the structure IV, it fixes ε to -1 for the m_y plane in this structure and automatically leads to null α and γ components. Considering the same conditions for the m_x and m_z planes will result in only a single irrational component possible for the modulation vector in the orthorhombic crystal system. The allowed irrational components of the **q**-vector for different crystal systems are summarized in Table 38.1.

For the orthorhombic basic structure let's consider the action of the m_x and m_y planes on the $\mathbf{q} = (\alpha,\beta,0)$ vector assuming that β is the irrational component: $m_x\mathbf{q} = \mathbf{q}' = (-\alpha,\beta,0)$, $m_y\mathbf{q} = -\mathbf{q}' = (\alpha,-\beta,0)$, so that $\mathbf{q}' \neq \pm\mathbf{q}$ unless we select $\alpha = 1/2$, then $\mathbf{q}' = \mathbf{q} - \mathbf{a}^*$ (i.e. it transforms into itself with adding a basis vector of the basic reciprocal lattice). Thus a rational component is allowed in the orthorhombic system $\mathbf{q} = (1/2,\beta,0) = \mathbf{q}_r + \mathbf{q}_i = (1/2,0,0) + (0,\beta,0)$. Choosing the modulation vector with both rational and irrational components one should check the compatibility of the rational part with the centering translations of the basic lattice. For example, assume that this orthorhombic basic structure is *B*-centered, i.e. the *hkl*0 reflections obey the $h + l = 2n$ reflection condition. Then the $\mathbf{q}' = \mathbf{q} - \mathbf{a}^*$ condition cannot be fulfilled because the $(2n + 1)\mathbf{a}^*$ reciprocal lattice vectors are forbidden by the *B*-centering: only the *h*00 reflections with even *h* are permitted. Thus the rational part of the modulation vector $\mathbf{q}_r = (1/2,0,0)$ is incompatible with the lattice centering. The compatibility list between the centering types and possible rational components of the **q**-vector is provided in Table 38.2.

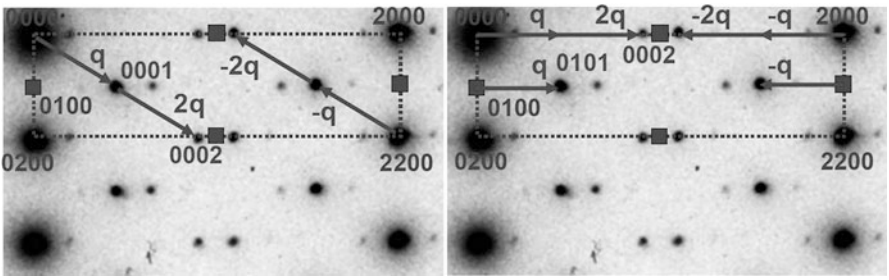

Fig. 38.5 Two alternative indexation schemes for the same electron diffraction pattern

The symmetry of the modulated structures is described in terms of the $(3 + 1)$-dimensional symmetry groups. Due to the limited volume of this chapter it is not possible to provide a comprehensive description of the concept of superspace symmetry, which can be found in Ref. [2, 3]. The superspace group symbol consists of the Hermann-Mauguin symbol of the 3D space group of the basic structure, an $(\alpha\beta\gamma)$ notation for the rational and irrational components of the modulation vector and the symbols for the symmetry generator of the 3D space group denoting whether this symmetry element introduces a phase shift of the modulation wave or not (analogous to screw axes and glide planes in 3D structures, but having a translational component along the fourth axis x_4). A typical $(3 + 1)$D superspace group symbol looks like *Pnma*$(00\gamma)000$ or *Fmmm*$(\alpha 10)0s0$. The symmetry elements of the $(3 + 1)$D superspace group can be identified from the analysis of the reflection conditions in a way similar to the conventional 3D case.

It might be possible that the standard setting of the superspace group is not the most convenient choice for subsequent structure determination. It concerns especially the cases where the **q**-vector has both rational and irrational components. The representation of the structure in $(3 + 1)$D direct space will be easier if the rational component will be eliminated, so that a new modulation vector $\mathbf{q}' = \mathbf{q}_i$ is chosen. This may cause satellites to be assigned to extinct basic reflections and also may lead to a non-standard setting for the superspace group.

In Fig. 38.5, two variants of indexation are shown for the ED pattern of an incommensurately modulated structure with a face-centered orthorhombic basic structure. For the indexation on Fig. 38.5 (left image) the modulation vector $\mathbf{q} = \alpha\mathbf{a}^* + \mathbf{b}^*$ is chosen. In this case, the reflection conditions imposed on the *hklm* reflections are $h + k = 2n$, $k + l = 2n$, $l + h = 2n$, which corresponds to the standard setting of the superspace group *Fmmm*$(\alpha 10)$. On the other hand, eliminating the rational part $\mathbf{q}_r = \mathbf{b}^*$ results in the new modulation vector $\mathbf{q}' = \alpha\mathbf{a}^*$ (right image on Fig. 38.5). Now some satellites are assigned to extinct basic reflections (such as 0101 and 0100 in right image, Fig. 38.5). This transformation changes the reflections conditions to be $H + K + m = 2n$, $K + L + m = 2n$, $L + H = 2n$ (HKL*m* are the indexes of the reflections in the new basis). These reflections conditions correspond to a non-standard set of centering vectors (1/2, 1/2, 0, 1/2), (0, 1/2, 1/2, 1/2) and

(1/2, 0, 1/2, 0) denoted as *X* in the symbol of the superspace group *Xmmm*(α00) (non-standard setting of the *Fmmm*(α10) superspace group). The relations between *hklm* and HKL*m* can be understood from the invariance of the diffraction vectors under the transformation of the basis:

$$\mathbf{g} = h\mathbf{a}^* + k\mathbf{b}^* + l\mathbf{c}^* + m(\alpha\mathbf{a}^* + \mathbf{b}^*) \equiv \mathbf{g}' = \mathrm{H}\mathbf{a}^* + \mathrm{K}\mathbf{b}^* + \mathrm{L}\mathbf{c}^* + m\alpha\mathbf{a}^*,$$

resulting in $\mathrm{H} = h$, $\mathrm{K} = k + m$, $\mathrm{L} = l$.

Both cases are crystallographically equivalent and the choice between them is a matter of convenience. Non-standard settings of superspace groups are used very frequently in incommensurate crystallography.

References

1. Arnold H (2002) Transformations in crystallography. In: Hahn T (ed) International tables for crystallography Vol A: space-group symmetry, 5th edn. Kluwer, Dordrecht
2. Van Smaalen S (2007) Incommensurate crystallography. Oxford University Press, New York
3. Janssen T, Janner A, Looijenga-Vos A, De Wolff PM (1999) Incommensurate and commensurate modulated structures. In: Wilson AJC, Prince E (eds) International tables for crystallography Vol C: mathematical, physical and chemical tables, 2nd edn. Kluwer, Dordrecht

Chapter 39
Detection of Magnetic Circular Dichroism Using TEM and EELS

Stefano Rubino, Jan Rusz, and Peter Schattschneider

Abstract Magnetic Circular Dichroism (MCD) is a phenomenon that occurs in magnetic materials whereby the intensity of transitions from core states to available states above the Fermi energy depends on the circular polarization of the exciting radiation. This is due to the fact that spin-orbit coupling breaks the degeneracy of core states with different total angular momentum (**J**) and the magnetic field gives rise to difference in spin-up/spin-down density of available states. Traditionally, those transitions are excited with X-rays (XMCD). We present here a new technique by which a virtual circularly polarized photon is absorbed in Electron Energy-Loss Spectroscopy (EELS), giving rise to EELS-MCD (EMCD). The basis of this work is the equivalence between photon polarization (ε) and electron momentum transfer ($\boldsymbol{hq}$) in the determination of the scattering cross section. The equivalent of circular polarization in EELS is achieved through special scattering conditions as interference between Bloch waves in a crystal. Angular resolved EELS is then used to measure spectra under different polarization conditions, from which information about the magnetic properties can be extracted, in particular the ratio of spin to orbital contribution to the magnetization. Measurements can be performed by

S. Rubino (✉)
Department of Engineering Sciences, Uppsala University, Uppsala, Sweden
e-mail: stefano.rubino@angstrom.uu.se

J. Rusz
Department of Physics and Astronomy, Uppsala University, Uppsala, Sweden
e-mail: jan.rusz@physics.uu.se

P. Schattschneider
Institute for Solid State Physics, Vienna University of Technology, Vienna, Austria
e-mail: schattschneider@ustem.tuwien.ac.at

U. Kolb et al. (eds.), *Uniting Electron Crystallography and Powder Diffraction*,
NATO Science for Peace and Security Series B: Physics and Biophysics,
DOI 10.1007/978-94-007-5580-2_39,

simply recording spectra at two particular symmetric points in reciprocal space or by acquiring the whole diffraction pattern trough a series of energy filtered images. Spatial dichroic maps can be obtained too either in EELS STEM or by EFTEM. The advantage with respect to XMCD lies in the higher spatial resolution (2 nm). However, since the magnetic information is intrinsically entangled with dynamical diffraction, DFT simulations of the momentum space are required to extract quantitative information from the measurement. We present an example in this work. This also means that the measured difference depends on parameters such as crystal thickness and orientation. It has been recently proposed that a way to overcome this limitation would be to use so-called electron vortex beams. EMCD would then be applied to a larger class of samples and become a true complementary alternative to XMCD.

39.1 Introduction

A material in a magnetic field is said to show Magnetic Dichroism (MD) when its absorption spectrum changes as function of the polarization of the exciting radiation. In the case of light, the absorption could be in the visible/UV region (many organic molecules are optically active in this region) or, when transition from core-shell states are involved, in the X-ray region. A technique routinely used nowadays for the characterization of magnetic material is the so-called X-ray Magnetic Circular Dichroism (XMCD), based on the observable difference between two X-ray Absorption Spectra (XAS) collected with opposite circular polarization of the exciting X-ray radiation [1–4]. The brightness and quality of modern X-ray synchrotron sources allows extracting from XMCD spectra information such as the total magnetization and its spin and orbital components by use of the sum rules, with a resolution of about 25 nm at best [5–7].

In the case of 3d transition metals (such as Fe, Co, Ni), the largest differences are observed in the intensity ratio between the L_2 and the L_3 edges, corresponding to transitions from the $2p_{1/2}$ and $2p_{3/2}$ states respectively, where the subscript indicates the total angular momentum **J**. Spin-orbit coupling is the reason behind the fact that states with different **J** have different energies (the splitting being about 10–20 eV for 3d metals). At the same time, the final states are spin polarized by the magnetic field, giving rise to a different available Density of State (DoS) for spin up or spin down electrons. It is shown schematically in Fig. 39.1 that circularly polarized photons carrying one quantum of angular momentum induce transitions whose intensity depends on the handedness of the incoming radiation [4, 8]. This remains true if the transitions are induced by electron scattering rather than photon absorption (one can imagine that a virtual photon is absorbed as result of the interaction with the fast electron). In fact, the equivalence between XAS and Electron Energy-Loss Spectroscopy (EELS [9]) has been proposed and demonstrated decades ago for the

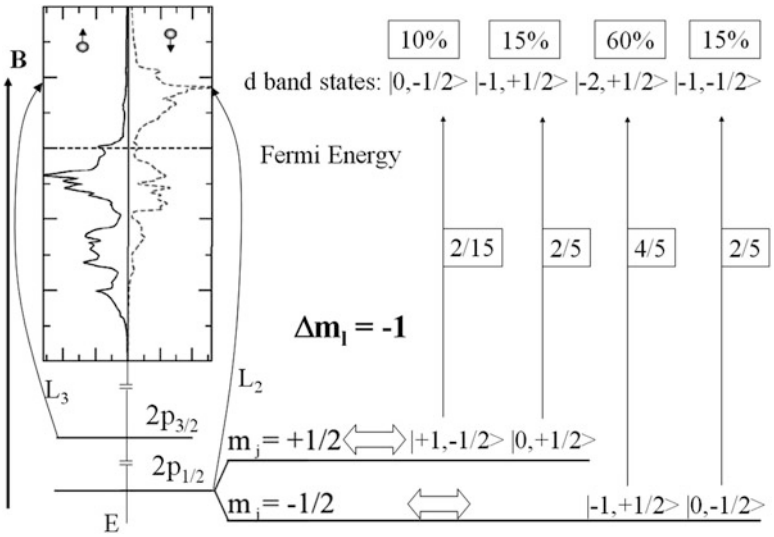

Fig. 39.1 Scheme of the electronic transitions giving rise to MCD for the absorption of a left-handed photon (carrying a quantum of angular momentum antiparallel to J). The initial states are a superposition of states with a well defined spin (S_z) and angular momentum (L_z). The absorption of the photon can only change the angular momentum, therefore the emitted photoelectron will have a certain polarization (probability to be spin up or down). The numbers next to the *arrows* are proportional to the transition probability calculated with the Fermi Golden Rule, whereas the percentage numbers on top give the photoelectron probability by taking into account the weight of the initial state in the L_z S_z decomposition. Since the available final states are spin-polarized and have therefore different occupancy (the DoS is shown on the *left side* of the figure), the resulting transitions will have different intensities for spin up or spin down photoelectrons (Figure from PhD Thesis [8])

case of linear dichroism [10, 11]. It can be easily understood by comparing the theoretical scattering intensity σ for XAS and EELS:

$$\sigma_{XAS} \propto \omega \sum_{i,f} \left| \langle f \left| \vec{\varepsilon} \cdot \vec{R} \right| i \rangle \right|^2 \delta \left(E + E_i - E_f \right)$$

$$\sigma_{EELS} \propto \frac{k_f}{k_i} \sum_{i,f} \left| \langle f \left| \vec{q} \cdot \vec{R} \right| i \rangle \right|^2 \delta \left(E + E_i - E_f \right),$$

where i and f indicate respectively initial and final states of the excited electron, ω is the photon angular frequency, $\boldsymbol{R}$ is the quantum mechanical position operator, $\boldsymbol{\varepsilon}$ is the polarization of light, $\boldsymbol{k_i}$ and $\boldsymbol{k_f}$ are the initial and final wave vectors of the incoming fast electron, $\hbar\boldsymbol{q}$ ($\boldsymbol{q} = \boldsymbol{k_i} - \boldsymbol{k_f}$) is the resulting momentum transfer to the atom, and δ is the energy Dirac function. Therefore in EELS the momentum transfer

plays the same role as the polarization of light in XAS. There are different setups that make possible to perform momentum resolved EELS experiments, the easiest is to project the diffraction pattern onto the spectrometer and use the entrance aperture to select a particular point in reciprocal space (i.e. a specific $\boldsymbol{k}_f$).

39.2 Theoretical Basis of EMCD

In the case of linear dichroism the equivalence is thus rather straightforward to implement. In $\boldsymbol{q}$-resolved EELS one simply needs to place an aperture (real or virtual) in reciprocal space in different positions, so that the $\boldsymbol{q}$ would point along different crystallographic directions. This is known in the TEM community as EELS anisotropy or EMLD (EELS Magnetic Linear Dichroism). But how to obtain a "circular" momentum transfer and therefore EELS-MCD (EMCD)? From the mathematical point of view, circular polarization can be expressed as the superposition of two perpendicular linear polarizations, out of phase by 90°. This can be formally substituted in the expression for electron scattering [12]:

$$\vec{\varepsilon}_{circ} = \vec{\varepsilon}_1 + i\vec{\varepsilon}_2 \Rightarrow \vec{q}_{circ} = \vec{q}_1 + i\vec{q}_2,$$

but what is its physical significance and how to experimentally implement it? Two perpendicular momentum transfers can be obtained if two plane waves interfere to simultaneously excite the electronic transition. If the original plane waves are also dephased by 90°, then the momentum transfers will be dephased too. In both cases (electron scattering and photon absorption) an electric field at the atomic site is the perturbation responsible for the electronic excitations [13]. The problem of obtaining two coherent electron plane waves in a TEM that only has one electron source can be solved in several ways: by means of a biprism, of holographic masks [14] or by using the sample itself as beam splitter and phase-locker [15]. The latter is the so-called "intrinsic method" and can only be used on crystalline specimens. It is the one used to first detect EMCD [8, 16] and requires only a standard TEM equipped with an EELS spectrometer or image filter. It is known from the theory of electron diffraction that when the electron beam (plane wave) enters a crystal it becomes a superposition of *Bloch waves* (solutions of the Schrödinger equation in a periodic potential), each of them uniquely identified by an index vector $\boldsymbol{k}+\boldsymbol{g}$ in their plane wave component. The amplitude and phase of each Bloch wave are a function of the boundary conditions, namely thickness and orientation of the crystal with respect to the incoming beam. It is possible to find conditions where only two or three beams are non-negligible (called the two-beam case, 2BC, or three-beam case, 3BC). For these cases, each of the beams can be considered an electron wave, source of a momentum transfer. A measured EELS spectrum will be the sum of the EELS spectra from each of the beams plus their interference terms. Another advantage due to the periodic

nature of the Bloch waves is that their relative phase shift is also periodic; therefore all equivalent atoms having the same z coordinate will see the same phase shift.

39.3 EMCD Experiments

The key factor in performing an EMCD experiment is the optimal placement of a $\boldsymbol{k_f}$-defining aperture in reciprocal space, so that spectra with opposite helicity can be obtained. The simplest method is to place the aperture as shown in Fig. 39.2. The 0 and G beams define the Thales circle; placing the aperture on this circle will give

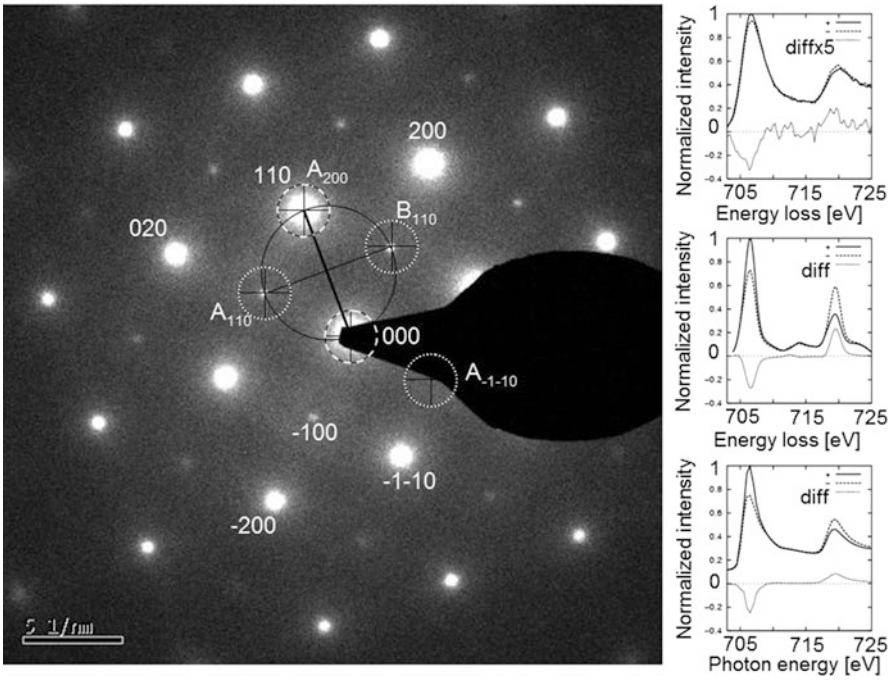

Fig. 39.2 EMCD setup. *Left*: Zone axis diffraction pattern of a 10 ± 2 nm Fe layer epitaxially grown on a [001] GaAs substrate. The 100 type reflections visible in the pattern are, in reality, 200 reflections from the GaAs substrate. The pattern is afterwards tilted to a two-beam case (2BC), strongly exciting one of the reflections (for example the 110) and projected onto the spectrometer, so that the spectrometer entrance aperture (*dotted circle*) defines the collection angle and k_f. The segment connecting the direct beam and the beam excited in the 2BC (110 in this figure) defines the diameter of the *Thales circle*, *solid black*. The two points on the Thales circle equidistant from 000 and 110 define A and B for that specific beam (hence the subscript 110). For example, in a two beam case with the 200 beam, the point A_{200} would be exactly on top of the 110 reflection. The position for A_{-1-10} is shown as another example. *Right*: EMCD measured (*top*) and simulated (*middle*) spectra, compared with XMCD measurements (*bottom*) on the same sample (Figure from paper [16])

rise to perpendicular momentum transfers: $h\boldsymbol{q}$ from 0 and $h\boldsymbol{q}'$ from G. Two positions (A and B) will also have $q = q'$. The helicity associated with the two positions is opposite, since their vectorial product $\boldsymbol{q} \hat{} \boldsymbol{q}'$ changes sign from A to B. In Fig. 39.2 spectra obtained in this way are shown. With the microscope in diffraction mode, the Spectrometer Entrance Aperture (SEA) is placed first in A_{110} then in B_{110} and spectra are recorded. This is the *detector shift* method [8, 16]. Alternatively, one could keep the aperture in one position and change the phase shift between the 0 and G beams, but this would also slightly change the illuminated area.

Ideally, there should not be other beams where the aperture is placed; if this is not the case, two signals are collected: one related to the interference between two single inelastic scattering events with non-zero momentum transfer (one for the 0 beam and one for the G beam occurring simultaneously); and one related to a double event, an elastic scattering with $\boldsymbol{q} = \boldsymbol{k}_{000} - \boldsymbol{k}_f$ (or with $\boldsymbol{q} = \boldsymbol{k}_{110} - \boldsymbol{k}_f$) and an inelastic event with $\boldsymbol{q} = \boldsymbol{0}$ (neglecting the q_z due to energy loss). The former is the origin of the EMCD signal and changes between A and B, whereas the latter is a spurious signal that disappears when calculating the difference, but affects negatively the signal-to-noise ratio S/N by increasing the Poissonian noise. In the simple approach described above (only two plane waves, point-like detector, neglecting the beam tilt away from ZA to achieve 2BC), the points A and B give the maximum EMCD signal, but when other factors are taken into account, this is no longer the case [17]. Both collection and convergence angle are non-zero (and correspondingly non-point-like in the diffraction pattern), several beams contribute to the signal and the tilt from ZA give rise to an asymmetry independent of the magnetic field [18]. In this case, dynamical diffraction simulations of the diffraction pattern are needed to estimate the optimal size and placement of the $\boldsymbol{k}_f$-defining aperture in reciprocal space [19]. A more advanced approach is to couple dynamical diffraction theory with DFT calculations to produce dichroic maps such as the one in Fig. 39.3 [20, 21]. Those maps can be obtained experimentally by acquiring a series of energy filtered images of the diffraction pattern [22–24]. Each pixel of the CCD camera collects the signal of a specific $\boldsymbol{k}_f$. Spectra can be extracted by placing a virtual aperture in the same position of every energy filtered image and plotting the resulting intensity as function of the energy loss. Sum rules [25] can then be evaluated either directly from integrating the spectra (with a somewhat arbitrary integration range) [26] or by modeling them with a combination of Gaussian, Lorentzian and double arctan functions [23, 27]. It is also very important to remove the effect of plural scattering to properly apply the sum rules [28].

Operating the TEM in diffraction mode means that the spatial resolution will be determined by the selected area aperture (usually in the 100 nm range). One way to improve the resolution is to use the objective aperture to select $\boldsymbol{k}_f$ [8, 13]. Spectra can be acquired directly with a spectrometer or extracted from an energy filtered series of real space maps (two maps have to be acquired, one for each helicity) [24]. The resolution in this case is in the nm range, with the theoretical possibility to map magnetic moments and electronic transitions with atomic resolution [29, 30]. It is also possible to obtain EMCD spectra in convergent beam modes [31] and in scanning TEM mode [32], with a resolution of 2 nm.

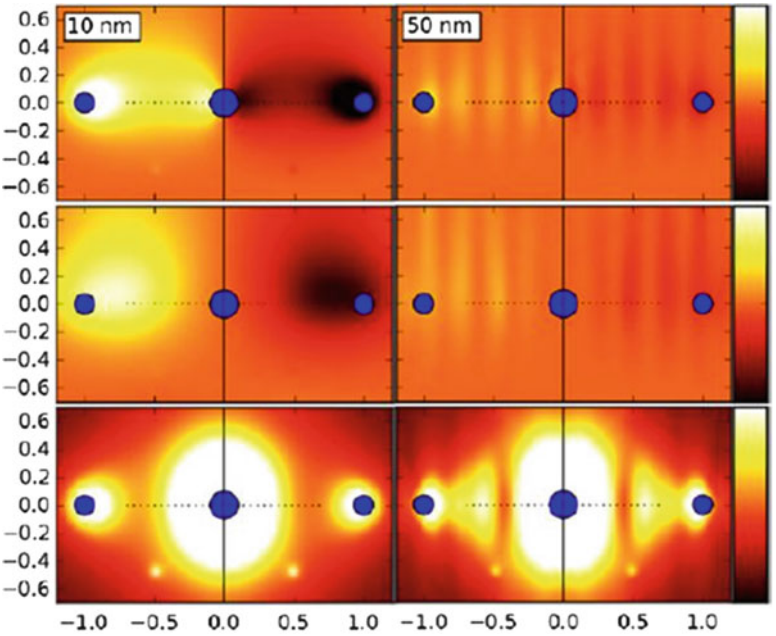

Fig. 39.3 Dichroic maps. DFT simulations for 3BC Fe showing the absolute *left/right* (l/r) difference (*upper row*), the relative l/r difference (*middle row*) and the l/r average (*lower row*) for two different thicknesses. Notice how the maximum of the dichroic signal is not on position A and B of the Thales circle and how the signal weakens for thicker samples (Figure adapted from Ref. [17])

39.4 Conclusions and Future Perspectives

EMCD has been developed as the TEM analogue of the synchrotron-based XMCD. It offers a superior spatial resolution and bulk sensitivity on instruments widely spread and more easily available than beam-time on high quality X-ray sources. On the other hand, the intrinsic EMCD method is more demanding both in terms of operator and samples. Moreover, it does not give information on the absolute magnetization but only on the ratio between its spin to orbital components, due to the fact that the effective polarization of the excitation is not known. Nonetheless, it has been already successfully used to track magnetism changes such as in magnetic phase transitions [33, 34] or magnetic diluted semiconductors [35]. High resolution real space information has been obtained [24, 32, 36], but domain contrast could not be evidenced because the strong magnetic field of the TEM lenses forces the magnetization along the optical axis. This could be possibly addressed in Lorentz mode.

Recently, electron vortex beams were successfully created in the TEM [14]. They are unique in the sense that – as vacuum solutions of the Schrödinger equation with magnetic quantum number m – they carry discrete angular momentum m. First

experiments showed surprisingly high EMCD signals using electron vortices. It could be demonstrated that Angstrom-sized vortices can be produced [37], a fact that allows EMCD experiments in scanning mode with atomic resolution. This approach would circumvent many of the disadvantages of the intrinsic method: it is straightforward to implement, it imposes no restrictions on the sample in terms of crystallinity and gives perfectly polarized beams. However, the holographic mask required to produce the vortex beams absorbs a large percentage of the fast electron which translates in low S/N. The mask is also not yet commercially available and has to be fabricated *ad hoc*. Once these difficulties are overcome, vortex beams promise to become the method of choice for EMCD experiments. But before vortices can replace the intrinsic method, more experiments and simulations are necessary in order to elucidate the details of vortex-matter interaction.

References

1. Erskine JL, Stern EA (1975) Calculation of the $M_{2,3}$ magneto-optical absorption spectrum of ferromagnetic nickel. Phys Rev B 12:5016–5024
2. Schütz G, Wagner W, Wilhelm W, Kienle P, Zeller R, Frahm R, Materlik G (1987) Absorption of circularly polarized X-rays in iron. Phys Rev Lett 58:737–740
3. Chen CT, Sette F, Ma Y, Modesti S (1990) Soft-X-ray magnetic circular dichroism at the $L_{2,3}$ edges of nickel. Phys Rev B 42:7262–7265
4. Lovesey SW, Collins SP (1996) X-Ray scattering and absorption by magnetic materials. Clarendon, Oxford
5. Thole BT, Carra P, Sette F, van der Laan G (1992) X-ray circular dichroism as a probe of orbital magnetization. Phys Rev Lett 68:1943–1946
6. Carra P, Thole BT, Altarelli M, Wang X (1993) X-ray circular dichroism and local magnetic fields. Phys Rev Lett 70:694–697
7. Chen CT, Idzerda YU, Lin HJ, Smith NV, Meigs G, Chaban E, Ho GH, Pellegrin E, Sette F (1995) Experimental confirmation of the X-ray magnetic circular dichroism sum rules for iron and cobalt. Phys Rev Lett 75:152–155
8. Rubino S (2007) Magnetic circular dichroism in the transmission electron microscope. PhD thesis, Vienna University of Technology
9. Egerton RF (1996) Electron energy-loss spectroscopy in the electron microscope, 2nd edn. Plenum Press, New York
10. Hitchcock AP (1993) Near edge electron energy loss spectroscopy: comparison to X-ray absorption. Jpn J Appl Phys 32:176–181
11. Yuan J, Menon NK (1997) Magnetic linear dichroism in electron energy loss spectroscopy. J Appl Phys 81:5087–5089
12. Hébert C, Schattschneider P (2003) A proposal for dichroic experiments in the electron microscope. Ultramicroscopy 96:463–468
13. Hébert C, Schattschneider P, Rubino S, Novák P, Rusz J, Stöger-Pollach M (2003) Magnetic circular dichroism in electron energy loss spectrometry. Ultramicroscopy 108:277–284
14. Verbeeck J, Tian H, Schattschneider P (2010) Production and application of electron vortex beams. Nature 467:301–304
15. Nelhiebel M, Schattschneider P, Jouffrey B (2000) Observation of ionization in a crystal interferometer. Phys Rev Lett 85:1847–1850

16. Schattschneider P, Rubino S, Hébert C, Rusz J, Kunes J, Novák P, Carlino E, Fabrizioli M, Panaccione G, Rossi G (2006) Detection of magnetic circular dichroism using a transmission electron microscope. Nature 441:486–488
17. Rubino S, Schattschneider P, Rusz J, Verbeeck J, Leifer K (2010) Simulation of magnetic circular dichroism in the electron microscope. J Phys D Appl Phys 43:474005
18. Rusz J, Oppeneer PM, Lidbaum H, Rubino S, Leifer K (2009) Asymmetry of the two-beam geometry in EMCD experiments. J Microsc 237:465–468
19. Verbeeck J, Hébert C, Rubino S, Novák P, Rusz J, Houdellier F, Gatel C, Schattschneider P (2008) Optimal aperture sizes and positions for EMCD experiments. Ultramicroscopy 108:865–872
20. Rusz J, Rubino S, Schattschneider P (2007) First-principles theory of chiral dichroism in electron microscopy applied to 3d ferromagnets. Phys Rev B 75:214425
21. Rusz J, Novák P, Rubino S, Hébert C, Schattschneider P (2008) Magnetic circular dichroism in electron microscopy. Acta Phys Pol A 113:599–604
22. Warot-Fonrose B, Houdellier F, Hÿtch MJ, Calmels L, Serin V, Snoeck E (2008) Mapping inelastic intensities in diffraction patterns of magnetic samples using the energy spectrum imaging technique. Ultramicroscopy 108:393–398
23. Lidbaum H, Rusz J, Liebig A, Hjörvarsson B, Oppeneer PM, Coronel E, Eriksson O, Leifer K (2009) Quantitative magnetic information from reciprocal space maps in transmission electron microscopy. Phys Rev Lett 102:037201
24. Lidbaum H, Rusz J, Rubino S, Liebig A, Hjörvarsson B, Oppeneer PM, Eriksson O, Leifer K (2010) Reciprocal and real space maps for EMCD experiments. Ultramicroscopy 110:1380
25. Rusz J, Eriksson O, Novák P, Oppeneer PM (2007) Sum rules for electron energy loss near edge spectra. Phys Rev B 76:060408(R)
26. Schattschneider P, Rubino S, Stöger-Pollach M, Hébert C, Rusz J, Calmels L, Snoeck E (2008) Energy loss magnetic chiral dichroism: a new technique for the study of magnetic properties in the electron microscope. J Appl Phys 103:07D931
27. Rusz J, Lidbaum H, Liebig A, Hjörvarsson B, Oppeneer PM, Rubino S, Eriksson O, Leifer K (2010) Quantitative magnetic measurements with transmission electron microscope. J Magn Magn Mater 322:1478–1480
28. Rusz J, Lidbaum H, Rubino S, Hjörvarsson B, Oppeneer PM, Eriksson O, Leifer K (2011) Influence of plural scattering on the quantitative determination of spin and orbital moments in electron magnetic chiral dichroism measurements. Phys Rev B 83:132402
29. Schattschneider P, Verbeeck J, Hamon AL (2009) Real space maps of atomic transitions. Ultramicroscopy 109:781–787
30. Schattschneider P, Ennen I, Stöger-Pollach M, Verbeeck J, Mauchamp V, Jaouen M (2010) Real space maps of magnetic moments on the atomic scale: theory and feasibility. Ultramicroscopy 110:1038–1041
31. Schattschneider P, Hébert C, Rubino S, Stöger-Pollach M, Rusz J, Novák P (2008) Magnetic circular dichroism in EELS: towards 10 nm resolution. Ultramicroscopy 108:433–438
32. Schattschneider P, Stöger-Pollach M, Rubino S, Sperl M, Hurm C, Zweck J, Rusz J (2008) Detection of magnetic circular dichroism on the 2 nanometer scale. Phys Rev B 78:104413
33. Rubino S, Schattschneider P, Stöger-Pollach M, Hébert C, Rusz J, Calmels L, Warot-Fonrose B, Houdellier F, Serin V, Novák P (2008) Energy-loss magnetic chiral dichroism (EMCD): magnetic chiral dichroism in the electron microscope. J Mater Res 23:2582–2590
34. Klie RF, Yuan T, Tanase M, Yang G, Ramasse Q (2010) Direct measurement of ferromagnetic ordering in biaxially strained $LaCoO_3$ thin films. Appl Phys Lett 96:082510
35. Zhang ZH, Wang X, Xu JB, Muller S, Ronning C, Li Q (2009) Evidence of intrinsic ferromagnetism in individual dilute magnetic semiconducting nanostructures. Nat Nanotechnol 4:523–527
36. Stöger-Pollach M, Treiber CD, Resch GP, Keays DA, Ennen I (2011) EMCD real space maps of magnetospirillum magnetotacticum. Micron 47:456–460
37. Verbeeck J et al (2011) Atomic scale electron vortices for nanoresearch. Appl Phys Lett 99:203109

Index

A
Aberration, 19, 177, 208, 217, 223, 226, 228, 255, 263–265, 267, 272, 273, 284, 279, 286, 328, 362, 373–375, 383, 399–407
Ab-initio structure analysis, 315
ADT. *See* Automated diffraction tomography (ADT)
Algorithm, 30, 31, 35–37, 75, 106–114, 118–122, 126, 130, 223, 224, 256, 303, 304, 306–307, 309, 310, 338, 343, 344, 347, 359–367, 371
Amplitude, 30–32, 67, 68, 74, 85, 106–111, 113, 187, 275, 276, 287, 295, 297, 298, 300, 301, 306, 309, 311, 331, 349–351, 353, 354, 361, 369, 382, 422
Angular broadening, 128
Anharmonic potentials, 152, 191
Anisotropic thermal expansion, 30, 75
Aperture, 73, 150, 264, 273–278, 283, 316, 317, 362, 374, 400–405, 422–424
18Å^3 rule, 47
Astigmatism, 273, 407
Atomic resolution, 111, 126, 271, 275, 294–297, 306, 390, 424, 426
Autocorrelation, 320, 344, 395
Automated diffraction tomography (ADT), 315–318, 320–324, 337–347, 394
Average crystallite size, 174, 175
Axial divergence, 19, 24

B
Babinet model, 126
Back focal plane (BFP), 362, 383, 402
Basis vectors, 344, 347, 410–412, 415
Beam damage, 263, 288, 321, 334, 394, 397
Beamline optics, 69–71, 76
Bessel function, 282
BF. *See* Bright field (BF)
BFP. *See* Back focal plane (BFP)
Blackman model, 282–283
Bloch wave method, 285
Bragg condition, 274, 329, 370, 376, 384
Bragg diffraction, 252, 264, 266, 274
Bragg lines, 376, 378
Bright field (BF), 274–275, 374, 375, 384
Buckminsterfullerene, 8

C
Cambridge structural database, 46, 47, 49
Camera length, 317, 320, 321, 346, 400, 404
Capillary samples, 59, 127, 214
CBED. *See* Convergent beam electron diffraction (CBED)
CCD electron detectors, 393
Centrosymmetric, 111, 296, 298, 311, 364
CFEG. *See* Cold field emission gun (CFEG)
Channeling, 283–284, 316, 360, 361, 364, 406
Charge density, 169, 350, 351, 383, 385–387
Charge flipping, 31, 76, 105–115, 295, 305–307, 310–311
Chromatic aberration, 273, 278
Clustering, 320, 344–345, 347
Coherence, 66, 71, 187, 202, 203, 404–405
Coherent scattering function, 184
Cold field emission gun (CFEG), 402–404
Commensurately modulated structures, 410–413
Completeness, 111, 114, 188, 265, 321, 323
Compton scattering, 73
Computer programs
  ADT3D, 347
  BGMN, 235

U. Kolb et al. (eds.), *Uniting Electron Crystallography and Powder Diffraction*,
NATO Science for Peace and Security Series B: Physics and Biophysics,
DOI 10.1007/978-94-007-5580-2, © Springer Science+Business Media Dordrecht 2012

Computer programs (*cont.*)
CASTEP, 169
ConQuest, 46, 47
CRISP, 299, 306, 308
DASH, 31, 322
EXPO, 31, 37
Focus, 305–308, 312
Fox, 31, 36, 37, 322
FullProf, 91
Gamess, 166
GSAS, 91, 125, 126, 141, 142
ImageD11, 130
IsoStar, 50
MAUD, 235
MICE, 31, 312, 322
Mogul, 49
MOLREP, 138
PDFfit2, 191, 192
PDFgui, 191, 192
Powder3D, 256
SHELXD, 140
SIR2008, 322
Superflip, 31, 306, 309, 311, 322
TOPAS, 24, 31, 91, 322
TotalCrystallography, 130VASP, 169
XLENS, 31
Contrast transfer function (CTF), 278, 287, 300, 306
Convergence, 36, 107, 113, 118, 121, 264, 278, 317, 361, 370, 371, 375, 401–404, 424
Convergent beam electron diffraction (CBED), 264, 265, 271, 317, 370, 371, 375, 376, 378, 379, 382–385
Convex optimization, 106
Coordination polyhedra, 36
Corrector, 264, 265, 273, 278, 328, 400–403, 407
Crossover, 120, 383, 400–403, 405
Cryoprotection, 127
Cryo-TEM, 333
Crystal analyzer, 73
CTF. *See* Contrast transfer function (CTF)

D
Dark field (DF), 266, 274–275, 374, 375, 383, 384
DASH, 31, 322
Debye and Einstein models, 153
Debye formula, 192
Debye-Scherrer geometry, 189, 190
Debye-Waller factor, 17, 184
Defocus, 276–279, 299, 300, 362, 371
Density functional theory (DFT), 38–39, 51, 166, 167, 169, 170, 350, 384–386, 420, 424, 425
Density of state (DoS), 356, 420, 421
2-D Detectors, 73, 75, 84, 89, 90
DFT. *See* Density functional theory (DFT)
Diamond-anvil cell (DAC), 96–97, 99, 100, 256
Difference vectors, 16, 320, 341
Difference vector space (DVS), 320, 343–345
Diffraction disks, 264, 382, 383
Diffuse scattering, 10, 41, 111, 183–185, 188, 196, 221, 331, 351, 375
Direct methods, 30, 31, 45, 105, 106, 120, 221, 224–227, 265, 281, 284, 286, 287, 304, 310, 322, 359–361, 364
Direct space, 35, 75, 106, 143, 166, 169, 196, 306, 410–412, 416
Disorder, 6–7, 9, 18, 24, 41, 42, 77, 78, 160, 162, 183–185, 187, 191, 192, 195, 197–200, 229, 235, 319, 321, 324, 343, 386
Displacement parameter, 151, 154, 168
DOC. *See* Dynamical occupancy correction (DOC)
Domino phase-retrieval algorithm (DPRA), 361, 362, 364–367
Double-rocking zone-axis pattern (DRZAP), 371
DPRA. *See* Domino phase-retrieval algorithm (DPRA)
DRZAP. *See* Double-rocking zone-axis pattern (DRZAP)
Dual-space methods, 106–108
DVS. *See* Difference vector space (DVS)
Dynamical occupancy correction (DOC), 36, 37

E
EDiff, 394–396
EDSA. *See* Electron diffraction structural analysis (EDSA)
EELS. *See* Electron energy loss spectroscopy (EELS)
Einstein oscillator, 152
Elastic scattering, 424
Electron density, 31, 32, 37, 106, 108, 111, 126, 131, 132, 139, 141–143, 166, 168, 306–310, 312, 350, 352–354, 356, 381, 382, 386
Electron detector, 391, 393
Electron diffraction rotation method, 329

Electron diffraction structural analysis (EDSA), 349–351, 353
Electron energy loss spectroscopy (EELS), 263, 266, 271, 406, 407, 419–426
Electron gun, 271
Electron lens, 263, 400, 401
Electron wavelength, 277, 278, 403
Electrostatic potential, 106, 139, 296, 312, 349–356, 381
EMCD, 422–426
Endeavour, 322
Energy-dispersive, 85, 87
Energy minimization, 167–169
Energy spread, 84, 273
Equipartitioning, 30, 302
Ewald sphere, 264, 316, 318, 320, 329, 330, 332, 341, 342, 346, 369, 376, 393
Excitation error, 284, 317, 321, 382–384
External standard, 210, 214, 215, 225, 228, 239
Extinction, 282, 320, 342, 343, 414
Extinction distance, 282

F
Field emission guns (FEG), 263, 317
Fluorescence, 54–55, 60, 73, 74, 89, 90, 99–101, 184, 216, 222, 274
Focal length, 272, 274, 400, 403, 406
Focal plane, 274, 403, 405
Forbidden reflection, 371
Fourier transform, 107, 109, 111, 127, 176, 185–187, 196, 277, 295, 297–300, 306, 311, 360, 361
FOX, 31, 36, 37, 322
Fractile filtering, 255
Framework, 31, 39, 108, 239, 265, 306, 307, 309, 312, 322, 328
Free electron laser, 91, 133
Friedel pair, 131, 132, 295, 338, 340, 396

G
General axis equation, 247, 248
Genetic algorithms (GAs), 106, 120, 121
Glass transition temperature, 153, 160, 161
Global minimum, 39, 118–120, 122
Global optimization, 31, 35, 48, 121, 304
Goodness of fit (GOF), 20
Guinier geometry, 150

H
Hermann-Mauguin symbol, 416
High pressure, 39, 57–59, 96–99, 101, 253
High resolution transmission electron microscopy (HRTEM), 263–266, 275–279, 293–301, 303–312, 360–366
Histogram matching, 31, 112–114
HMC. *See* Hybrid Monte-Carlo (HMC)
Holography, 266, 352, 384
HRTEM. *See* High resolution transmission electron microscopy (HRTEM)
Hybrid Monte-Carlo (HMC), 121
Hydrostatic behaviour, 100
Hypersurface, 118, 121, 122

I
IAM. *See* Independent atom model (IAM)
Incommensurately modulated structures, 266, 413–417
Independent atom model (IAM), 384
Inelastic scattering, 54, 73, 97, 285, 424
Intensity extraction, 22, 131, 310, 320
Intensity integration, 346–347
Internal coordinate description, 48, 51
Internal standard, 210, 211, 214, 224–226, 228, 235
Isomorphous replacement, 140–141
IUCr CPD round robin, 216

K
Kikuchi bands, 375
Kinematical approximation, 359, 360
Kinematical model, 282, 285, 287
Kinematical scattering, 310, 369
Kohler illumination, 405

L
LaB_6, 212, 253, 256, 317, 329
Laboratory X-ray diffractometers, 55
LACBED, 265, 317, 370, 371
LACDIF, 370
LARBED. *See* Large angle rocking curve beam diffraction (LARBED)
Large angle rocking curve beam diffraction (LARBED), 265, 369–379
Lattice, 5, 9, 11, 16–18, 22, 24, 29, 30, 40, 55, 75, 86, 89–91, 126, 130, 141–143, 151, 153, 154, 158, 160–162, 168, 177, 191, 198–201, 223, 252, 253, 276–278, 304, 306, 319–321, 329, 332, 339, 340, 342–347, 350, 354, 360, 362, 369, 370, 378, 384, 395, 410, 414, 415
Laue circle, 383
Laue zone, 305, 376

Le Bail method, 22, 29
Libration, 151, 152
Line profile analysis (LPA), 174–179
Local minimisation, 118
Local minimum, 108, 385
Local structure, 41, 186, 189–191
Lorentz-polarization factor, 17, 177
LPA. *See* Line profile analysis (LPA)

M
Magnetic dichroism, 420
Main crystallographic zone, 393
March-Dollase, 197, 238
Mass absorption coefficient, 209–210, 212 214, 225
Maximum-likelihood, 143
MICE, 31, 312, 322
Microabsorption, 207, 216, 217, 222, 225, 226, 228, 238–239
Microdiffraction, 264, 403
Microstrain, 18, 174, 175, 178, 239, 248
Microstructure, 16–19, 89, 173–178
Miller index, 334
Missing cone, 315, 316, 320, 331, 334
Modulated structures, 266, 410–417
Modulation, 306, 410, 412–416
Modulation vector, 412–416
Molecular connectivity, 46
Molecular replacement, 131, 138–140, 143, 145
Molecular volume, 46–47
Monochromator, 19, 22, 53, 54, 56, 69, 129, 209, 239, 278
Monte-Carlo method, 119
Mott-Bethe formula, 382
Multipattern fit, 131
Multiphase samples, 38, 40, 211
Multiple patterns, 138, 142
Multiple scattering, 294, 300, 316
Multiplicity, 17, 24, 177, 198, 209, 247, 262
Multislice, 266, 285–287, 360, 396
MYTHEN, 73–75, 77, 78, 80, 85, 212

N
Nanodiffraction, 403, 406, 407
Nano electron diffraction (NED), 317, 338
Nanoparticle, 89, 183, 185–187, 196, 200–201, 263, 328
Nanoprobe, 407
Nanostructured, 78, 173, 185, 188
Nanotubes, 9, 201–204
NED. *See* Nano electron diffraction (NED)
Neutron diffraction, 7, 8, 18, 86, 90, 99, 200, 201, 262, 364

O
Objective lens, 264, 272–274, 277, 373–375, 383, 399–406
Off-zone, 316, 318, 347
Optic axis, 374, 401, 402, 404–406
Orientation distribution function (ODF), 9, 236–238, 247
Overlapping reflections, 30, 31, 141, 304

P
Pair distribution function (PDF), 6, 41, 55, 75, 89, 183–192, 196, 221, 262
Parallel recording of dark-field images (PARODI), 383–386
Parametric refinement, 156, 159
Paris-Edinburgh cell (P-E cell), 99, 100
PARODI. *See* Parallel recording of dark-field images (PARODI)
Patterson map, 130, 140
Patterson method, 31, 105
Pawley method, 22, 29, 176, 226
PDF. *See* Pair distribution function (PDF)
P-E cell. *See* Paris-Edinburgh cell (P-E cell)
PED. *See* Precession electron diffraction (PED)
Pendellösung, 383
Phase, 6, 27, 36, 60, 79, 83, 101, 105, 121, 131, 138, 150, 177, 189, 200, 207, 220, 233, 247, 262, 275, 281, 294, 304, 322, 359, 371, 383, 396, 405, 416, 422
  problem, 28, 30, 105, 106, 131, 140, 265, 295, 360, 364, 372, 378
  transitions, 30, 40, 83, 88, 101, 150, 151, 154, 155, 160, 162, 189, 425
Pivot point, 373
Plane group, 276, 298
Point group, 414
Pole figure, 237, 238, 246–249
Pole piece, 272, 273, 276, 315, 317
Polychromatic radiation, 85
Polyhedra, 35–36
Polymer crystallinity, 239–241
Polymorphism, 76, 77, 143, 145, 266
PONCKS, 240, 241
Position sensitive detector, 53, 54, 72, 73, 151
Potential map, 308, 312, 333
Precession angle, 284, 328, 332
Precession electron diffraction (PED), 114, 264, 265, 281–288, 305, 309–311, 318, 320–324, 364, 370, 373–376, 378

Preferred orientation, 5, 8, 30, 129, 169, 197, 207, 208, 223, 236–238, 244–245
Probe size, 401, 403, 404
Protein, 8, 30, 76, 95, 112, 125–133, 137–145, 265, 295, 328, 334, 389–397
Protein structures, 125, 126, 132, 138, 141, 142, 265, 328, 396
PSD, 55–57, 60, 85
Pseudopotentials, 141, 167, 169

Q
Quantitative electron diffraction (QED), 263, 373–376
Quantitative phase analysis (QPA), 207–217, 219, 220, 224, 225, 228, 230–241
Quantum area detector, 393, 397
Quasi-kinematical approach, 287
Quasi-parallel beam, 317

R
Radiation damage, 30, 77, 127, 129, 131, 140, 384
Ray diagram, 273, 274, 277
Ray path, 271, 272, 373
Reciprocal space, 30, 31, 35, 36, 106, 109, 130, 143, 166, 174–177, 247, 264, 265, 277, 287, 304, 312, 315, 316, 318–321, 324, 329–334, 338, 346, 361, 363, 369, 378, 390, 410, 411, 414, 420, 422–424
RED. *See* Rotation electron diffraction (RED)
Reduced pair distribution function, 185
Refinement, 8, 10, 11, 15–25, 27–29, 32, 37, 39, 55, 59, 60, 76, 77, 85, 90, 91, 97, 100, 111, 117, 118, 125, 131–133, 138, 140–143, 145, 150, 154–159, 165–169, 176, 195, 208, 216, 223, 238, 244, 246, 248, 253–255, 262, 284, 285, 287, 288, 309, 322, 328, 340, 347, 359, 360, 371, 384–386, 394, 396
Reflection
  conditions, 416
  geometry, 54
  overlap, 28, 45, 112, 262, 304, 305, 317
Relative humidity, 60–61
Relrod, 369, 376
Resolution, 16, 18, 19, 29, 37, 56, 69–71, 73–75, 79, 84–91, 100, 111, 113, 118, 126–130, 133, 137–139, 141–143, 150, 153, 173, 184, 185, 187, 189, 207, 246, 263, 265, 271–273, 275–279, 294–300, 303–307, 309, 317, 319–321, 329, 331, 332, 334, 350, 351, 353, 360, 364, 390, 391, 394–396, 402, 406, 407, 420, 424–426
Rietveld method, 7–9, 12, 16, 18, 21, 28, 32, 138, 150, 165, 176, 177, 191, 195, 208–212, 220, 223–226, 228, 234–237, 239, 241
Rint, 321
Rocking curve, 370, 373, 375
Rotation electron diffraction (RED), 327–334, 338
R_{sym}, 321

S
SA. *See* Simulated annealing (SA)
SAED. *See* Selected area electron diffraction (SAED)
Satellites, 200, 201, 412–414, 416
Scanning transmission electron microscopy (STEM), 264, 266, 283, 317, 338, 394, 397, 399–407, 420
Scattering path, 371, 372
Scherrer equation, 17, 27
Scherrer formula, 174, 175, 178, 179, 202
Selected area electron diffraction (SAED), 265, 271, 305, 308, 311, 316, 331, 338
Self-propagating exothermic reaction, 79–81
Self-sustaining reaction, 86
Semiempirical methods, 166
SHELX, 322
Simulated annealing (SA), 31, 60, 106, 120, 121
Simultaneous refinement, 16, 154
SIR, 322
SLACBED, 371
Solid-state DFT, 167
Space group, 5, 16, 17, 23, 24, 27, 29, 39, 45, 77, 111, 117, 131, 138, 167, 168, 262, 264, 308, 309, 311, 323, 333, 376, 416
Spherical aberration, 263, 273, 278, 279, 362, 405, 407
Standardless method, 216
STEM. *See* Scanning transmission electron microscopy (STEM)
Stereochemical restraints, 125, 138, 141
Stigmator, 273
Stroboscopic, 84, 85, 90–91
Structural resolution, 126
Structure checking, 51
Structure determination, 15, 22, 27–29, 31, 35–36, 45, 46, 195, 266, 271, 294, 304–306, 309, 311, 312, 359, 390, 396, 397, 416

Structure factor, 30, 32, 106, 108, 109, 112, 113, 117, 127, 131, 132, 141, 142, 167, 177, 198, 209, 225, 248, 282, 285, 286, 295, 296, 306, 308, 310, 321, 360–364, 371, 381–386, 396, 410
Structure validation, 39
Supercell, 169, 410–414
SUPERFLIP, 31, 306, 309, 319, 320, 322
Superindices, 382
Superspace, 409, 414, 416, 417
Superstructure reflections, 410, 412
Superstructures, 40, 42, 319, 343, 410, 412
Symmetry determination, 111, 298–299, 343
Synchrotron radiation, 41, 59, 65–69, 78, 86, 112, 141, 162, 196, 244
Systematic row, 383, 384

T
Texture, 75, 130, 236–238, 243–250, 264, 350
Tilt axis, 315, 316, 318, 339–342
Time-of-flight (TOF), 85, 90, 190, 236, 246, 248
TOPAS, 9–11, 24, 31, 90, 126, 212, 322
Total scattering experiment, 184
Total scattering measurements, 184, 188
Transformation matrix, 411, 412
Transmission geometry, 54
Tungsten gasket, 97
Turbostratic disorder, 235
Two-beam model, 282, 284, 285
Two-dimensional detectors, 251

U
Undulators, 67–71, 88, 127
Unit cell parameter determination, 320

V
Vainshtein plot, 315
Variable count time (VCT), 60
Vortex beam, 420, 425, 426

W
Warren-Averbach (WA), 174–176
Wavefunction, 168, 170, 276, 353, 361, 387
Weight fraction, 209–213, 220, 223, 224, 227, 239
WH. *See* Williamson-Hall (WH)
Whole image refinement, 253, 254
Whole powder pattern fitting (WPPF), 176
Wigglers, 67–71, 87, 88
Williamson-Hall (WH), 174–176, 178, 179
Wilson plot, 321
WPPF. *See* Whole powder pattern fitting (WPPF)

X
X-ray diffraction, 3, 4, 7, 39, 53–62, 96, 106, 196, 197, 199, 200, 202–204, 208,, 220, 234, 244, 246, 286, 295, 297, 310, 328, 372, 381, 382, 386, 396, 409

Z
Zeolite, 31, 113, 300, 301, 304, 306–312, 322, 328, 331